LABORATORY AND IN-SITU CHARACTERIZATION OF DIATOMACEOUS SOIL WITH IMPLICATIONS FOR GEOTECHNICAL DESIGN

Final Report

PROJECT SPR 820

Oregon Department of Transportation

LABORATORY AND IN-SITU CHARACTERIZATION OF DIATOMACEOUS SOIL WITH IMPLICATIONS FOR GEOTECHNICAL DESIGN

Final Report

PROJECT 820

by

Jiayao Wang, Ph.D.
T. Matthew Evans, Ph.D.
Oregon State University
101 Kearney Hall
Corvallis, OR 97331

Diane Moug, Ph.D.
Portland State University
1930 SW Fourth Avenue
Portland, OR 97201

for

Oregon Department of Transportation
Research Section
555 13th Street NE, Suite 1
Salem OR 97301

and

Federal Highway Administration
1200 New Jersey Avenue SE
Washington, DC 20590

April 2024

Technical Report Documentation Page

1. Report No. FHWA-OR-RD-25-02	2. Government Accession No.	3. Recipient's Catalog No.
4. Title and Subtitle Laboratory and In-situ Characterization of Diatomaceous Soil with Implications for Geotechnical Design		5. Report Date January 2024 6. Performing Organization Code
7. Author(s), ORCID Jiayao Wang, Ph.D. T. Matthew Evans, Ph.D. (#0000-0002-8457-7602) Diane Moug, Ph.D.		8. Performing Organization Report No.
9. Performing Organization Name and Address Oregon Department of Transportation Research Section 555 13th Street NE, Suite 1 Salem, OR 97301		10. Work Unit No. (TRAIS) 11. Contract or Grant No.
12. Sponsoring Agency Name and Address Oregon Dept. of Transportation (ODOT) Research Section 555 13th Street NE, Suite 1 Salem, OR 97301 Federal Highway Admin. 1200 New Jersey Ave SE Washington, DC 20590		13. Type of Report and Period Covered Final Report 14. Sponsoring Agency Code
15. Supplementary Notes: ODOT Technical Advisory Committee: Susan Ortiz (Project Champion), Curran Mohney, Brad Hayes, Kira Glover-Cutter (Chair)		

16. Abstract

Diatomaceous soil contains large amounts of fossilized diatoms and is known to have non-textbook, often contradictory, properties: high natural water content, high liquid limit, and high compressibility, but also high shear strength. Diatomaceous deposits intersect existing and potential Oregon Department of Transportation project sites in central, eastern, and southern Oregon. This report presents results from in-situ and laboratory tests on diatomaceous soils from four such sites: Wickiup Junction, Ady Canal, Moore Park, and Pine Cone Drive. Empirical correlations across properties were developed and in-situ tests synthesized with laboratory results. Test results were used to calibrate a critical state-type constitutive model to describe mechanical behavior. The Imperial College Pile method was modified to successfully predict pile capacity as measured with a dynamic load test.

17. Key Words Diatomaceous soil, Soil characterization, Constitutive modeling, Pile design	18. Distribution Statement Copies available from NTIS, and online at www.oregon.gov/ODOT/TD/TP_RES/

19. Security Classification (of this report) Unclassified	20. Security Classification (of this page) Unclassified	21. No. of Pages 424	21. Price

SI* (MODERN METRIC) CONVERSION FACTORS

APPROXIMATE CONVERSIONS TO SI UNITS

Symbol	When You Know	Multiply By	To Find	Symbol
		LENGTH		
in	inches	25.4	millimeters	mm
ft	feet	0.305	meters	m
yd	yards	0.914	meters	m
mi	miles	1.61	kilometers	km
		AREA		
in^2	square inches	645.2	millimeters squared	mm^2
ft^2	square feet	0.093	meters squared	m^2
yd^2	square yards	0.836	meters squared	m^2
ac	acres	0.405	hectares	ha
mi^2	square miles	2.59	kilometers squared	km^2
		VOLUME		
fl oz	fluid ounces	29.57	milliliters	ml
gal	gallons	3.785	liters	L
ft^3	cubic feet	0.028	meters cubed	m^3
yd^3	cubic yards	0.765	meters cubed	m^3
~NOTE: Volumes greater than 1000 L shall be shown in m^3.				
		MASS		
oz	ounces	28.35	grams	g
lb	pounds	0.454	kilograms	kg
T	short tons (2000 lb)	0.907	megagrams	Mg
		TEMPERATURE (exact)		
°F	Fahrenheit	(F-32)/1.8	Celsius	°C

APPROXIMATE CONVERSIONS FROM SI UNITS

Symbol	When You Know	Multiply By	To Find	Symbol
		LENGTH		
mm	millimeters	0.039	inches	in
m	meters	3.28	feet	ft
m	meters	1.09	yards	yd
km	kilometers	0.621	miles	mi
		AREA		
mm^2	millimeters squared	0.0016	square inches	in^2
m^2	meters squared	10.764	square feet	ft^2
m^2	meters squared	1.196	square yards	yd^2
ha	hectares	2.47	acres	ac
km^2	kilometers squared	0.386	square miles	mi^2
		VOLUME		
ml	milliliters	0.034	fluid ounces	fl oz
L	liters	0.264	gallons	gal
m^3	meters cubed	35.315	cubic feet	ft^3
m^3	meters cubed	1.308	cubic yards	yd^3
		MASS		
g	grams	0.035	ounces	oz
kg	kilograms	2.205	pounds	lb
Mg	megagrams	1.102	short tons (2000 lb)	T
		TEMPERATURE (exact)		
°C	Celsius	1.8C+32	Fahrenheit	°F

*SI is the symbol for the International System of Measurement

ACKNOWLEDGEMENTS

This work would not have been possible without the considerable support provided by a number of ODOT employees. Dr. Kira Glover-Cutter was instrumental in countless ways throughout the entire project, including contracting, field work, sample transportation, overall project management, and being a tireless source of positivity and optimism. Curran Mohney, Susan Ortiz, and Brad Hayes were instrumental in planning the field exploration program and providing a wealth of institutional knowledge about ODOT experience with diatomaceous soils. The site investigations were successful largely because of the expertise of some fantastic ODOT geologists, Curran Mohney, Brian McNamara, and Roman Bauer. The laboratory portion of this work was extensive and benefitted from contributions by a number of individuals, including Ariadna Covarrubias Ornelas (PSU GRA), Ehsan Yazdani (OSU GRA), Talenta Pitso (OSU GRA), and Ali Dadashiserej (OSU GRA). Finally, we would like to thank the staff at the OSU Electron Microscopy Facility because, in the end, the only way to know with 100% certainty that you have diatoms is to see them.

DISCLAIMER

TABLE OF CONTENTS

LIST OF TABLES

LIST OF FIGURES

1.0 INTRODUCTION

1.1 BACKGROUND

Diatomaceous soil is a type of soil that contains large amounts of fossilized diatoms. Natural diatomaceous soils have been discovered in various areas around the world: Mexico City; Ecuador, Colombia, and Chile in South America; Osaka Bay and Oita in Japan; Taiwan; and Oregon and California in the United States, among other locations. The soil is well-known colloquially for its unique and even contradictory features: high natural water content, high consistency limits, and high compressibility, but also high shear strength. Previous research on diatomaceous soil has covered a wide range of aspects but most of the studies tend to focus on a specific subset of material behavior: physical and physiochemical properties, compressive properties, mechanical responses including monotonic behaviors, cyclic behaviors and dynamic behaviors, *in-situ* tests include standard penetration test (SPT) and cone penetration test (CPT), and a few numerical studies of time-dependent behaviors (Chapter 2). Reported properties showed large variations across the different sources, which is another feature of diatomaceous soil. In addition to work on natural diatomaceous soils, the physical and mechanical properties of mixtures of diatomite and other types of soil such as clays or sands have also been studied to show the significant influence of diatomite on soil behavior (Chapter 2). Correlations of soil properties have not been extensively and widely studied, and the lack of understanding of this soil often causes difficulties with engineering projects on diatomaceous deposits.

1.2 RESEARCH MOTIVATION

A number of diatomaceous deposits have been identified in central, eastern, and southern Oregon, and many of these deposits intersect with existing or potential Oregon Department of Transportation (ODOT) projects sites. These diatomaceous deposits vary from "pudding-like" to "chalk-like" behavior, indicating variations in soil properties. Projects built on these diatomaceous deposits have encountered assorted construction problems: excessive settlement of bridge approach embankments, early refusal during pile driving, and piles that do not reach design capacity at their design length, for example. A comprehensive understanding of the geotechnical properties of diatomaceous silt is critical for efficient and reliable design of future ODOT projects, and for effective evaluation of current ODOT structures in diatomaceous silt. A thorough characterization and examination of the physical, mechanical, and engineering behaviors of diatomaceous soil will serve as a significant contribution to the existing knowledge base and prove useful for the broader understanding of diatomaceous soils worldwide.

1.3 OBJECTIVES OF THE STUDY

Both *in-situ* and laboratory tests were conducted for four selected diatomaceous sites in Oregon: Wickiup Junction, Ady Canal, Moore Park, and Pine Cone Drive. The first goal was to extensively test soils at these sites to further facilitate our understanding of diatomaceous soil in Oregon. Previous geotechnical reports on Oregon diatomaceous soil have not covered a wide

range of tests, especially in terms of mechanical characterization. This is at least partially due to the well-recognized difficulty with retrieval of undisturbed diatomaceous soil samples. While these difficulties were also encountered in the site investigation for this project, there were a number of successful undisturbed sample retrievals. This made it possible to test the mechanical responses of diatomaceous soil in a more comprehensive manner.

The second goal was to develop correlations among various properties and provide validated interpretation of *in-situ* test results with laboratory results. As it is difficult to retrieve intact diatomaceous soil for laboratory mechanical tests, correlations for mechanical properties from easily conducted tests for physical properties will be useful and informative for engineering design guidance. Some *in-situ* tests (such as CPT) are time-efficient and reliable, so validated interpretation for diatomaceous soil from *in-situ* tests will also benefit engineering project design.

The third goal is to estimate geotechnical properties of diatomaceous deposits with a suitable constitutive model. Currently, very limited numerical analyses have been published on diatomaceous soil behavior. Numerical simulations are usually required for engineering projects and reliable constitutive models for the soil that the project is built on is essential.

1.4 OVERVIEW OF WORK

The remainder of this document is organized as outlined below:

Chapter 2 delves into a comprehensive review of existing literature concerning both mixtures of diatomite and natural diatomaceous soils. This review encompasses: index properties, compressive characteristics, monotonic shear parameters, *in-situ* responses, pile installation methodologies, and historical geotechnical documentation pertaining to diatomaceous soil deposits in Oregon. Extensive efforts were made to extract diatomaceous soil properties from each source and empirical correlations were drawn amongst various properties.

Chapter 3 is an overview of *in-situ* geotechnical testing methodologies, sample retrieval protocols, and subsurface investigation approaches. Techniques included SPT; CPT with pore pressure measurement (CPTu), shear wave velocity and dissipation tests; and in-situ vane shear tests. Split spoon and Shelby tubes were employed to collect soil samples. For each location, site characterizations were documented, inclusive of preliminary stratigraphic delineations, alongside discussions of impediments and complexities encountered during the exploration phase.

Chapter 4 details the laboratory testing program and associated protocols for characterization of physical and mechanical properties. Physical property measurements included scanning electron microscope (SEM), natural water content (w_n), *in-situ* unit weight (γ), specific gravity (G_s), grain size distribution (GSD), liquid and plastic limits (LL and PL, respectively), and specific surface area (SSA). Different methods were used to test LL and PL to compare the accuracy and limitations of each method, given the observed variances between methods and the importance of these properties in indicating soil behavior. Mechanical tests covered consolidation tests (including both incremental loading (IL) and constant rate of strain (CRS) methods), consolidated drained (CD) and consolidated undrained (CU) triaxial compression tests, direct simple shear (DSS) tests, and flexible wall permeability tests.

Chapter 5 delineates the results from both laboratory and *in-situ* tests. SEM imaging facilitates the intrinsic characterization of diatomaceous soil in virtually every split spoon sample, which is paramount for discerning soil stratigraphy in each site. Soil profiles of natural water content (w_n), *in-situ* unit weight (γ), specific gravity (G_s), fines content, consistency limits (LL and PL) are presented. Results of mechanical properties elucidate both compressive and shear responses of diatomaceous soil. Detailed consolidation parameters (i.e., compression index (C_c), recompression index (C_r), and overconsolidation ratio (OCR)) have been meticulously cataloged. Representative values of consolidation parameters for each site are provided. Shear strength parameters and shear stress-shear strain curves for both triaxial and DSS tests are presented. A critical state soil mechanics framework is adopted to interpret the results. Lastly, geotechnical profiles derived from *in-situ* investigations are showcased, encapsulating $(N_1)_{60}$ values, CPTu data (q_t, f_s, and u_2), both horizontal and vertical coefficients of consolidation (c_h and c_v), shear wave velocity (V_s), and *in-situ* vane shear strength.

Chapter 6 synthesizes the laboratory and *in-situ* results. Empirical correlations are proposed between various properties (e.g., G_s, LL, C_c, C_r, ϕ'). The soil behavioral charts are presented. Interpretations from CPTu data on unit weight (γ), OCR, friction angle (ϕ'), and undrained shear strength (s_u) are presented and discussed. Multiple interpretive correlations are evaluated, and optimal *in-situ* interpretations tailored to each diatomaceous soil category are recommended.

Chapter 7 explores the computational simulation of diatomaceous soil behavior. The Soft Soil Model, a part of the family of critical state soil mechanics models, is introduced and calibrated against laboratory test results, specifically triaxial tests and consolidation tests from this study. For comparative purposes, laboratory data extracted from literature were additionally employed for model calibration.

Chapter 8 examines the use of the Imperial College Pile (ICP) design methodology in diatomaceous soil. Detailed ICP design procedures for sandy and clayey strata are summarized. The chapter showcases two case studies: the first involving a square concrete pile embedded in Mexico City clay as detailed by Saldivar and Jardine (2005), and the second focusing on a tubular steel pile in a diatomaceous deposit in Oregon, as explored by Yazdani et al. (2021). Given the pronounced silt presence in diatomaceous soil, modifications are suggested for the canonical ICP method, traditionally limited to sandy or clayey soils.

Additional analyses, results, and supporting data are provided in the appendices for this document.

2.0 LITERATURE REVIEW

2.1 INTRODUCTION

Diatoms are unicellular microalgae found in both fresh and salt water all around the world (Antonides, 1998). The cell wall of a diatom, called a frustule, is comprised of hydrated silicon dioxide, which is effectively chemically inert in the presence of most substances in the natural environment. The life-cycle of a diatom is typically on the order of one week, after which the algae decays, leaving behind the frustule (Franklin, 2004). Because the remaining frustule was the diatom's cell wall (effectively, an "exoskeleton") it has very high intraskeletal porosity after the algal material is decomposed (Shiwakoti et al., 2002; Tanaka and Locat, 1999). Thus, the presence of diatoms in a given body of water will result in a continuous supply of environmentally persistent sediments having extremely high intraparticle porosity. This unique confluence of circumstances can result in deep deposits of materials with problematic (or, at least, uncertain) engineering properties.

The geotechnical behavior of diatomaceous soils has been studied for lacustrine deposits in Mexico City (e.g., Díaz-Rodríguez, 2003; Diaz-Rodriguez et al., 1992; Díaz-Rodríguez and Santamarina, 2001) and marine deposits in Japan (e.g., Maekawa et al., 1991; Matsumoto et al., 1995; Shiwakoti et al., 2002; Hong et al., 2006) and Korea (Lee et al., 2011). Recently, there have been more studies on diatomaceous soil from South America such as Chile (e.g. Ovalle and Arenaldi-Perisic, 2021; Wiemer et al., 2015) and Colombia (e.g., Caicedo et al., 2018; Mendoza et al., 2019). In addition to these studies on natural diatomaceous soil, a significant amount of research has focused on mixtures of diatom together with other soil (e.g., kaolin, clay, sand) to study the influence of diatom content on soil properties. These studies show non-standard geotechnical behavior for composite materials containing small fractions of diatomaceous content; for example, a soil mixture of 20% diatom particles and 80% kaolin clay had a larger liquid limit and plastic limit than 100% kaolin clay (Shiwakoti et al., 2002; Tanaka and Locat, 1999; Sonyok, 2015), whereas addition of similar sized sand particles would be accompanied by decreases in liquid limit and plasticity limit (Simpson and Evans, 2016). Small proportions of diatom particles in kaolin clay also cause increases in soil shear strength, dilation, and compressibility that are not observed with the addition of similar-sized conventional silica particles (Hong et al., 2006; Maekawa et al., 1991; Sonyok, 2015; Wiemer and Kopf, 2017). Moreover, traditional correlations between index properties and mechanical properties for fine-grained soil do not apply in diatomaceous soil, e.g., correlation between ϕ' and PI (Shiwakoti et al., 2002), or relations between index properties and liquefaction susceptibility (Wiemer and Kopf, 2017). These eccentric behaviors have been attributed to the rough surface and interlocking effects of diatom particles (Shiwakoti et al., 2002). Cyclic triaxial experiments presented in Wiemer and Kopf (Wiemer and Kopf, 2017) found that clayey-silt soils transition from cyclic softening behavior to liquefaction behavior at about 50% diatom content and that mixtures with 50% or more diatoms have higher cyclic strength but are also more susceptible to liquefaction. These studies show that standard geotechnical interpretations and correlations are not appropriate for soils with even a small proportion of diatom particles. However, little

published literature addresses geotechnical design methods, *in-situ* test interpretation, and construction methods for diatomaceous soils.

2.2 OVERVIEW OF PREVIOUS STUDIES

2.2.1 Overview

Diatomaceous soils exhibit broadly non-textbook behavior when their response is measured at the element scale ex-situ (Sonyok, 2015). Being largely comprised of silica (SiO_2), they are effectively chemically inert, but often hold more moisture than chemically active high-plasticity clays (Díaz-Rodríguez et al., 1998). While this high moisture-holding capacity implies a low shear strength, the opposite is actually true: diatomaceous soils tend to exhibit relatively high shear strengths, likely due to their irregular particle shapes (Shiwakoti et al., 2002; Wiemer et al., 2017). This complex – and non-intuitive – behavior is exacerbated by the fact that sampling and transporting undisturbed samples to the laboratory is extremely difficult due to the sensitivity of the soils (Díaz-Rodríguez and Santamarina, 1999). These aspects of laboratory-scale characterization are further explored below.

2.2.2 Two Symbolic Soil States

A unique feature of natural diatomaceous soil is that the consistency of these natural deposits varies widely between a "soft-clay" and "mudstone" material. However, there is no clear definition between the two soil states in terms of soil strength or any other parameter. Previous publications simply refer to their respective diatomaceous soil as "soft-clay" or "mudstone" without discussing differences between states. Jardine et al. (1998) briefly mentioned mudstone diatomaceous exists in Noetsu Bridge, Noto Peninsula, Japan, and soft clay diatomaceous exist in Kansai Bridge, Osaka Bay, Japan. "Mudstone" (also referred as "soft rock") diatomaceous soil widely exists in Japan, Chile, China, and Taiwan. This material has high stiffness and exceedingly high OCR, for example, OCR = 53 from Oita, Japan (Hong et al., 2006), and OCR=25 from Noto Peninsula, Japan (Jardine et al., 1998). This has been attributed to the effect of cementation and diagenesis (Iijima and Tada, 1981; Díaz-Rodríguez and Santamarina, 2001; Perisic et al., 2019; Ovalle and Arenaldi-Perisic, 2021). Figure 2.1 shows the pictures of mudstone diatomaceous soil.

Soft-clay diatomaceous soil was found in Mexico City, Osaka Bay in Japan, south Chile, and Bogota in Colombia. These soils are usually referred to as ooze, fill, and lacustrine. Compared to highly overconsolidated mudstone diatomaceous soil, they are usually normally-consolidated (e.g. OCR=1.3 from Osaka Bay, Japan (Jardine et al., 1998)). Table 2.1 summarizes the regions of soft-clay and mudstone diatomaceous soil.

(a). Mejillones Bay, northern Chile (b). Tengchong region, Yunnan, China

Figure 2.1: Pictures of mudstone diatomaceous soil (a. (Ovalle and Arenaldi-Perisic, 2021); b. (Zhang et al., 2013))

Table 2.1: Summary of regions of soft-clay and mudstone diatomaceous soil

Region	Country/Area	References
Mudstone / soft rock		
Ishikawa Prefecture	Japan	(Maekawa et al. 1992)
Noto Peninsula	Japan	(Jardine et al. 1998)(Oka et al. 2011)
Neogene section	Northern Japan	(Iijima and Tada 1981)
Oita	Japan	(Hong et al. 2006)
Hiruzenbara	Japan	(Shiwakoti et al. 2002)
Mejillones Basin	Chile	(Ovalle and Arenaldi-Perisic 2021)
Arica	Northern Chile	(Verdugo 2008)
Ulleung Basin	Korea	(Lee et al. 2011)
Yunnan	China	(Zhang et al. 2013)
Taiwan	Taiwan	(Liao et al. 2003)
Soft soil / ooze / lacustrine / alluvial / colluvial		
Osaka Bay	Japan	(Tanaka and Locat 1999)
Ariake	Japan	(Tanaka et al. 2001)
Lake Villarrica	South-central Chile	(Wiemer et al. 2015)
Bogota	Colombia	(Caicedo et al. 2018)
Guayaquil city	Ecuador	(Vera-Grunauer 2014)
Southern California	United States	(Day 1995)
Mexico City	Mexico	(Díaz-Rodríguez 2003)

2.2.3 Research Perspectives

Previous research on diatomaceous soil has a wide test type spectrum, with a focus on index properties, consolidation, and static shear, however, most of these studies tended to focus on a specific subset of those material behaviors. A majority of research is based on diatom mixtures, yet the behaviors of which do not represent natural diatomaceous soils. Several constitutive models were used to simulate triaxial, direct simple shear, and cyclic simple shear behavior. Figure 2.2 summarizes the scope of previous research on diatomaceous soil.

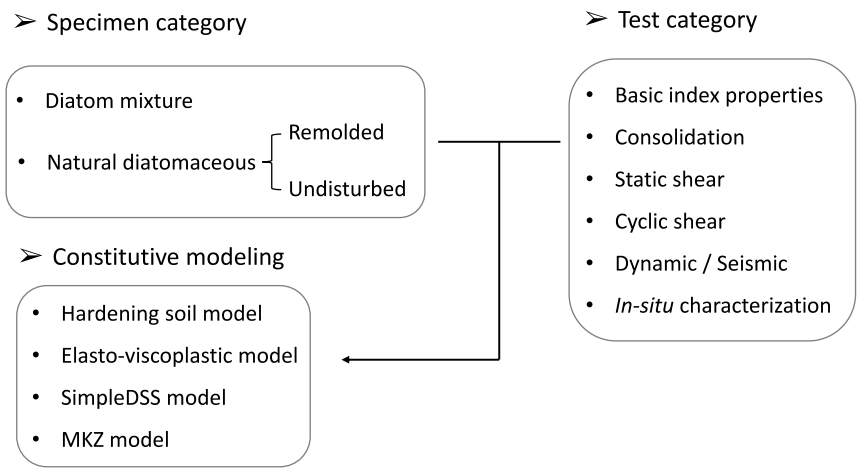

Figure 2.2: A summary of previous research on diatomaceous soil

2.3 INDEX PROPERTIES

2.3.1 Particle-scale Properties

At the most basic level, soil behavior is rooted in particle-scale properties. The most important of these are grain size distribution (Figure 2.4), particle shape (Figure 2.3), and specific surface area (Santamarina et al., 2001b). All three of these properties are clearly interrelated. The size of individual diatom particles is has been observed to generally vary from approximately 1 μm to 100 μm (Diaz-Rodríguez, 2011; Lee, 2014; Shiwakoti et al., 2002; Sonyok, 2015; Wiemer and Kopf, 2017). However, it should be noted that the measured particle size distributions could vary appreciably depending upon the measurement method. For example, Lee (2014) measured the grain size distribution using a hydrometer analysis which uses Stokes' Law predicated upon the assumption of spherical particles to infer grain size from sedimentation measurements (Bardet, 1997), thus resulting in an "equivalent sphere" diameter for the particles. Conversely, Wiemer and Kopf (Wiemer and Kopf, 2017) used laser diffraction spectroscopy to measure grain size distribution; while theoretically more precise than sedimentation analyses, this approach also suffers from the spherical particle assumption. Optical microscopy could be used to get more precise particle sizes, but these would be two-dimensional measurements. Thus, while many previous researchers report similar particle sizes for diatomaceous soils, it is not immediately clear that these measurements are directly comparable across studies, even when the same experimental procedure is employed (e.g., consider a sedimentation test on disk-like diatoms versus cylindrical or rod-like diatoms).

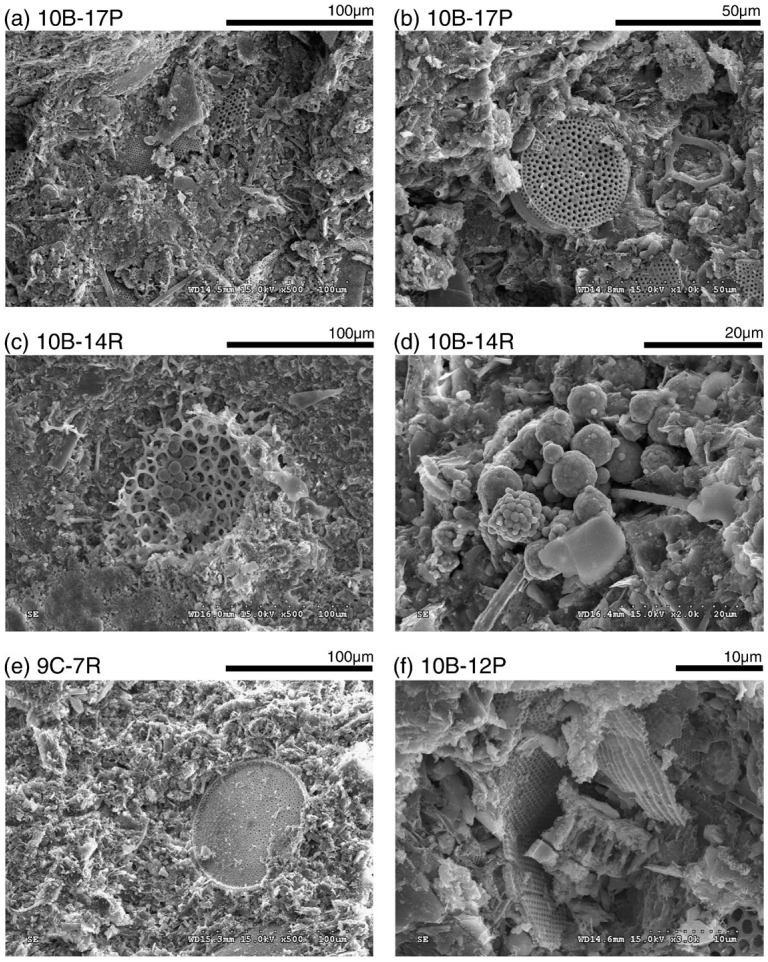

Figure 2.3: Scanning electron microscope (SEM) images of various shapes of diatomaceous soils (Lee et al., 2011)

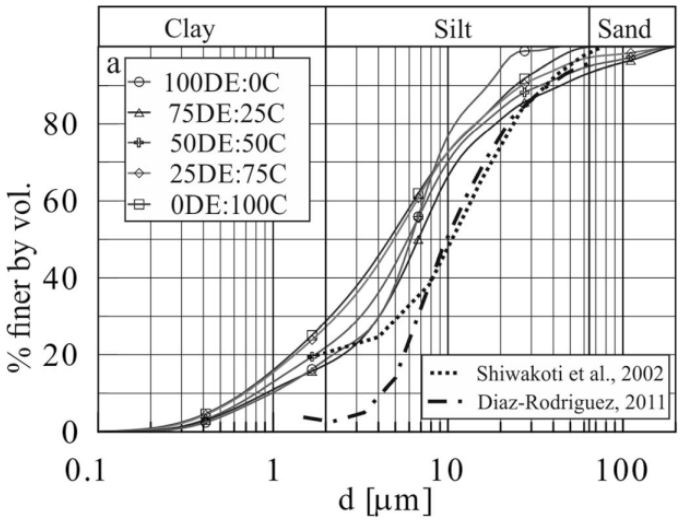

Figure 2.4: Grain size distributions of various mixtures of diatomaceous soil and clay (Wiemer and Kopf, 2017)

Specific surface area and porosity are intimately related for diatomaceous soils due to the distinct types of porosity present in these materials. Tanaka and Locat (1999) identified four different pore families present in diatomaceous soils (Figure 2.5): (i) intraskeletal; (ii) skeletal; (iii) intra-aggregate; and (iv) interaggregate, listed in order of increasing size. Thus, porosity in diatomaceous soils exists at four different scales. At the smallest scale (intraskeletal), the porosity is purely a function of the particle geometry (e.g., a perforated hollow cylinder). Particle geometry, in turn, is readily quantified by specific surface area. However, measurement of specific surface area in diatomaceous soils is, at best, nontrivial. In one example, dry measurements using nitrogen adsorption resulted in specific surface areas of 20-30 m^2/g while wet measurements on of the same material using methylene blue produce results in the range 65-110 m^2/g (Lee et al., 2011; Palomino et al., 2011). Meanwhile, Locat and Tanaka (2001) derived the specific surface area of diatoms to be 11.4 m^2/g based on their geometrical model, and claimed that it is in the range of measured specific surface area of diatoms, i.e., 10-20 m^2/g. Typically, there is a systematical difference between specific surface area (SSA) measured from dry method (e.g., N_2 absorption) and wet method (e.g, methylene blue method). Díaz-Rodríguez (2003) attributed this to the presence of swelling minerals and fine fractions. These findings indicate that while specific surface area is a fundamental parameter that provides significant insight into the engineering behavior of soils (Santamarina et al., 2001b; 2002), it is particularly difficult to measure in diatomaceous soils, largely due to their complex four-moded pore structure.

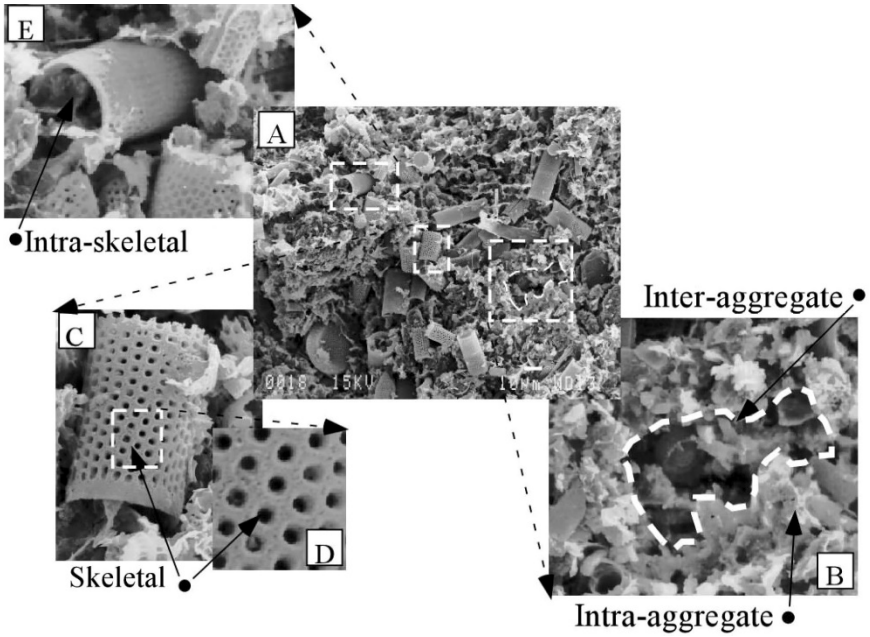

Figure 2.5: Four distinct types of porosity present in diatomaceous soils (Locat et al., 2003)

2.3.2 Specific Gravity as a Predictor of Diatom Content

A notable feature of diatomite is its low specific gravity. Despite that both diatomite and quartz are composed of silica, their specific gravities are largely different. Diatomite forms by the accumulation of amorphous silica ($G_s = 2.2 - 2.3$), while quartz forms by crystalline silica ($G_s = 2.6 - 2.7$). There is no doubt that diatom content is the key factor for engineering

properties of diatomaceous soil. However, it is difficult to quantify the amount of diatoms in natural diatomaceous soil, thus, it would be beneficial to have another parameter as an indicator of diatom content. Based on previous experimental study on diatom mixtures, specific gravity (G_s) has a strong linear correlation with diatom content (Figure 2.6 and Figure 2.7), the higher diatom content, the lower G_s. The relationship between G_s and diatom content is generally within a narrow bandwidth, indicating a reliable estimation of diatom content using G_s regardless of mixture type.

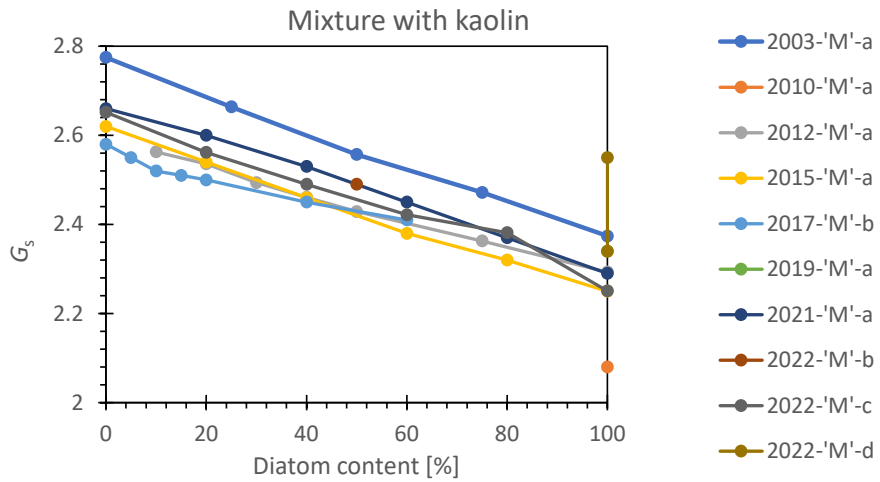

Figure 2.6: Relationship between G_s and diatom content for mixtures with kaolin (references can be referred to Section 2.9)

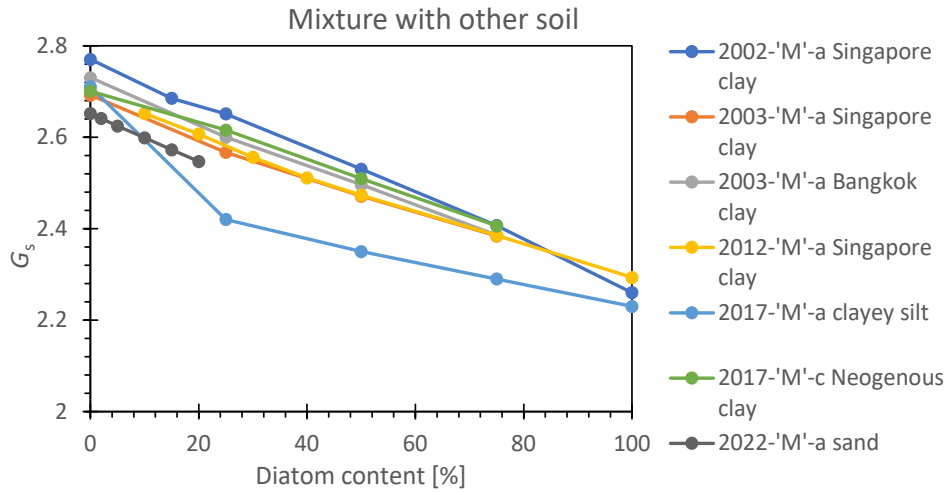

Figure 2.7: Relationship between G_s and diatom content for mixtures with other soil (references can be referred to Section 2.9)

2.3.3 Consistency Limits

Diatomaceous soils have a large intraparticle porosity, which contributes to their high water-holding capacity. The affinity of a given clay particle for water is described by the theory of

Derjaguin, Landau, Verwey, and Overbeek (DLVO; Israelachvili, 2011), which states that the amount of water that can be chemically adsorbed to the particle surface is a function of surface chemistry, specifically the balance between repulsive (double layer, Born) and attractive (van der Waals) forces. Thus, clay particles with a higher specific surface (Santamarina et al., 2001b) can absorb more water by mass (Lambe and Whitman, 1969). Diatomaceous soils do not typically have an adsorbed water layer, but they do hold significant water by mass due to capillary action in the intraskeletal pores (Palomino et al., 2011).

2.3.3.1 Diatom mixtures

A significant amount of study focuses on the properties of mixtures of diatom and other soils. It is not surprising that LL and PL increase with the increase in diatom content and decrease in G_s. Some studies show that pure diatomite shows non-plastic (i.e., LL and PL non-determinable) (Shiwakoti et al., 2002; Tanaka et al., 2003; Wiemer et al., 2017), however, the reason was not stated. Figure 2.8 and Figure 2.9 plot PI vs. LL for diatom mixtures. For mixtures with kaolin, PI does not increase with the increase of LL except for Mexican and Colombian source diatomite.

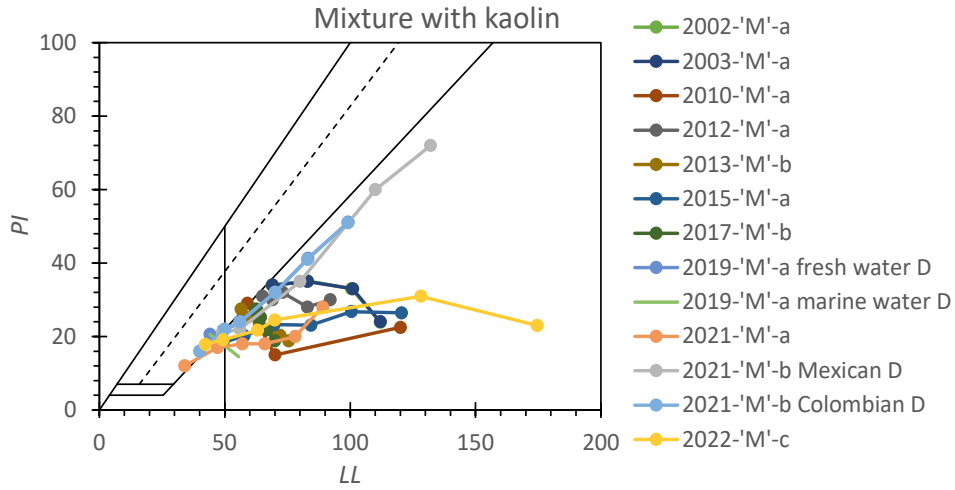

Figure 2.8: Plasticity chart of diatom and kaolin mixtures (references can be referred to Section 2.9)

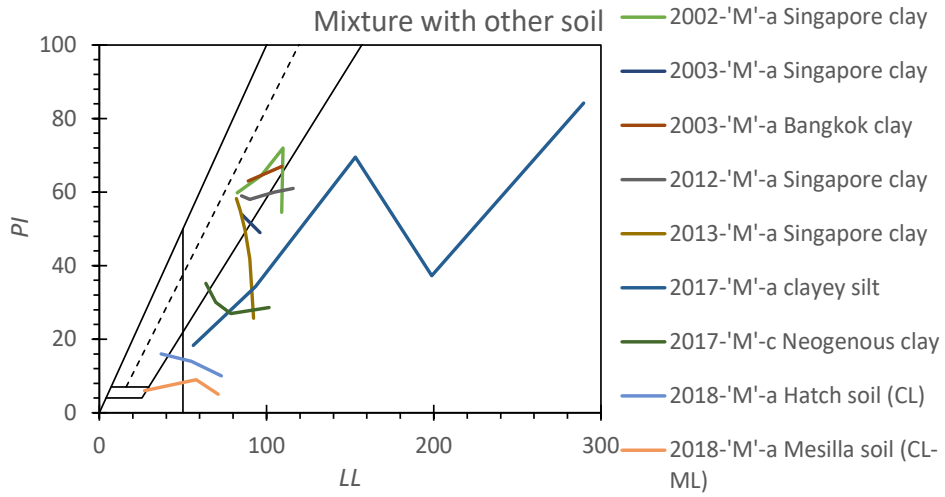

Figure 2.9: Plasticity chart of mixtures of diatom and other soil (references can be referred to Section 2.9)

2.3.3.2 Natural diatomaceous soil

Although diatomaceous soils usually have high liquid limits (LL) and plasticity indices (PI) as a result of their large water-holding capacity (Caicedo et al., 2018; Shiwakoti et al., 2002), their LL can vary between 50 to 550 across all sources of natural diatomaceous soils in the world. A striking example is the diatomaceous soils in Bogotá, Columbia, as reported by Caicedo et al. (2018). Colloquially, the soils are often termed "Bogotá clays" though, in fact, they are mostly silty. The confusion stems, in part, from the measured consistency limits presented in Figure 2.10. Over 95% of 1,024 tested soil samples had Atterberg limits that plot on or above the A-line, with many approaching the U-line. These results strongly imply a highly plastic clay soil in the classic interpretive framework (Lambe and Whitman, 1969), yet there are very few clay-sized (<2 μm) particles and very high quartz (up to 50%) and feldspar (15%-42%) contents. Indeed, on the activity chart (Figure 2.10), the diatomaceous soils plot above the region where we expect to find "classical" problem soils such as those from the smectite group (e.g., montmorillonite). Another example with exceedingly high consistency limits is Mexico City clay, which contains a significant amount of montmorillonite. Other sources of diatomaceous soil usually have LL less than 250.

As mentioned in 2.2.2 that natural diatomaceous soil has two symbolic states: mudstone like and soft clay like. To plot them separately in the plasticity chart (Figure 2.11 and Figure 2.12), they distinctively appear in different zones in the chart: the mudstone diatomaceous soil plots below A line, classified as MH in USCS classification, while soft clay diatomaceous soil generally plots above A line and classified as CH in USCS classification.

Despite the high LL of diatomaceous soil, the testing method was not emphasized in the literature. Wang et al. (2022) found that LL of diatomaceous soil from the fall cone test is

consistently higher than that tested from the Casagrande cup method, with the relative difference as high as 15%.

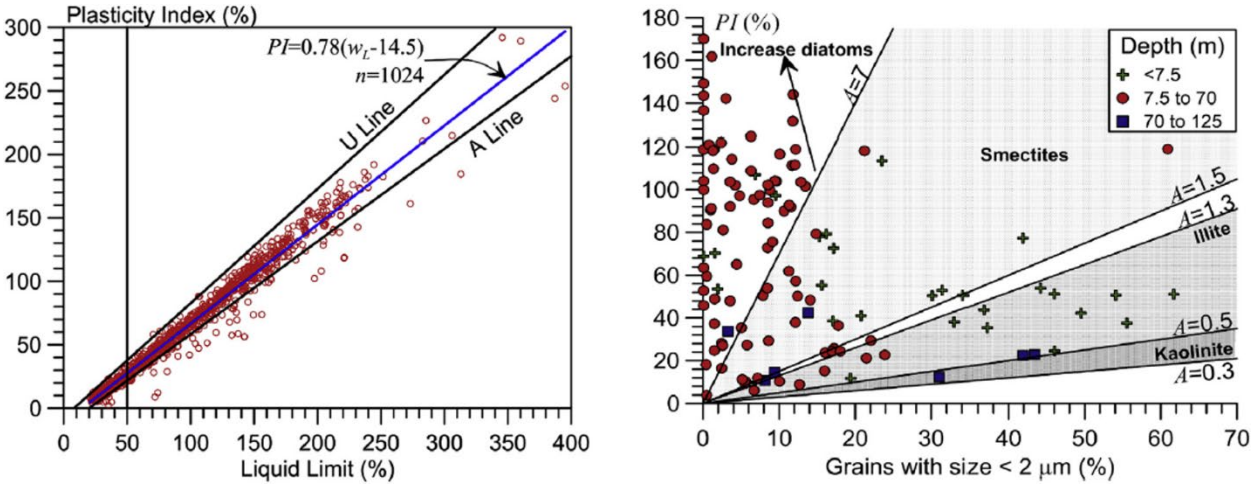

Figure 2.10: Consistency limits and activity of a diatomaceous soil from Bogotá, Columbia (Caicedo et al. 2018)

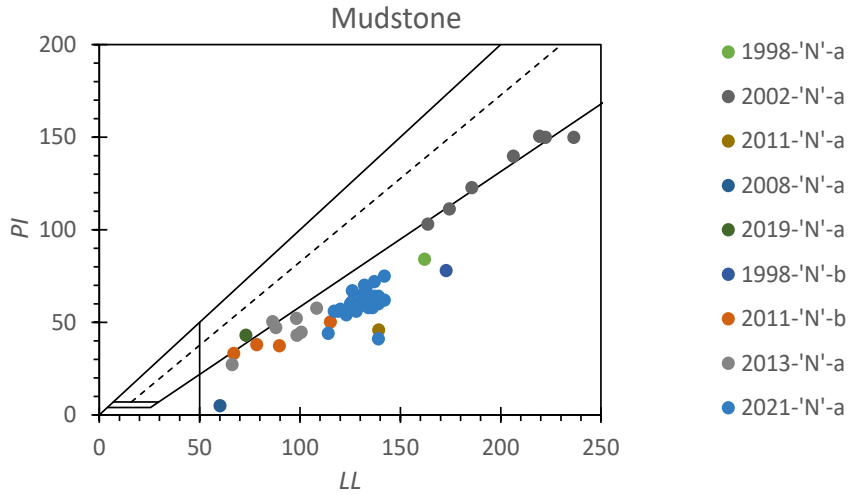

Figure 2.11: Plasticity chart for mudstone natural diatomaceous soil (references can be referred to Section 2.9)

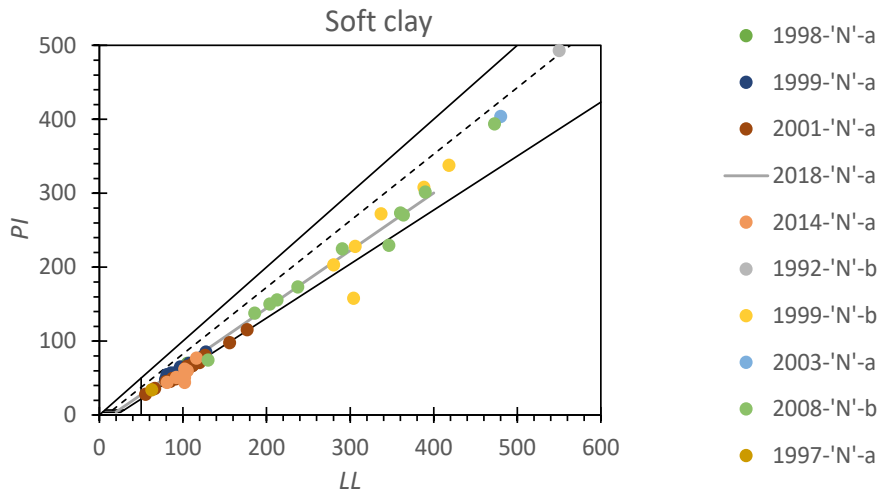

Figure 2.12: Plasticity chart for soft-clay natural diatomaceous soil (references can be referred to Section 2.9)

2.4 COMPRESSIVE BEHAVIORS

2.4.1 Consolidation Curves and Parameters

2.4.1.1 Undisturbed diatomaceous soil

Diatomaceous soil is known for its high compressibility, another consequence of its high porosity, however, there are no typical values on consolidation index (C_c) for undisturbed specimens because natural diatomaceous soil is usually a mixture of diatomite and other soils including regular clays or montmorillonite (e.g., Mexico City clay), etc. The reported C_c can vary from 0.5 (Verdugo, 2008) to 10 (Mesri et al., 1975) for undisturbed natural diatomaceous soil. The undisturbed diatomaceous soil shows a regionally different compressibility: C_c (Mexico City clay) > C_c (Japan) > C_c (Chile). Compression of interparticle pores, breakage of structural bonding, crushing of diatom skeletons, and particle rearrangement are proposed by some references (Shiwakoti et al., 2002; Hong et al., 2006) as common reasons and hypotheses attributed to high compressibility of diatomaceous soil.

Since LL is an important indicator of engineering behaviors, correlating C_c with LL would be beneficial for engineering purposes. Figure 2.13 summarizes C_c plotted against LL. Caicedo et al. (2018) proposed an empirical correlation between C_c and LL on 78 sets of data for Bogotá clays (the linear line in Figure 2.13). The example of Mexico City clay also shows increasing trend of C_c with increasing LL, varying over a large span. Other sources of data tend to cluster on LL around 100. Figure 2.14 plots C_c vs. G_s. Due to the limited data and various sources of diatomaceous soil, it is hard to find an empirical correlation between C_c and G_s.

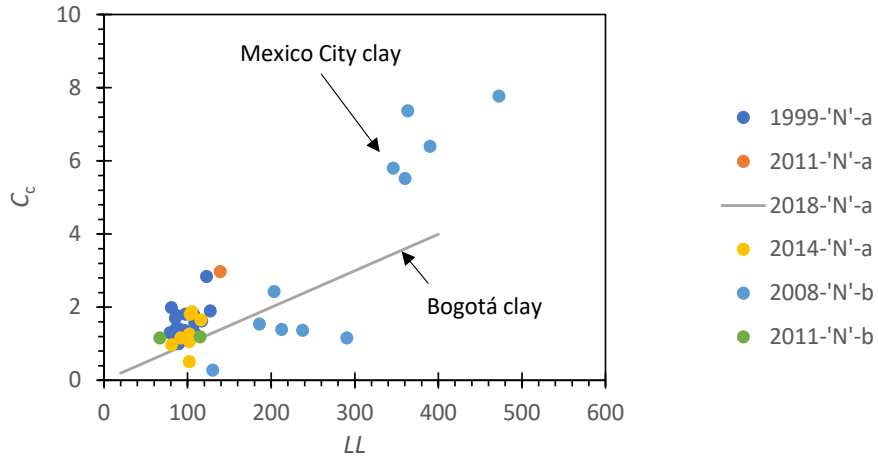

Figure 2.13: Relationship between consolidation index and LL on natural diatomaceous soil (references can be referred to Section 2.9)

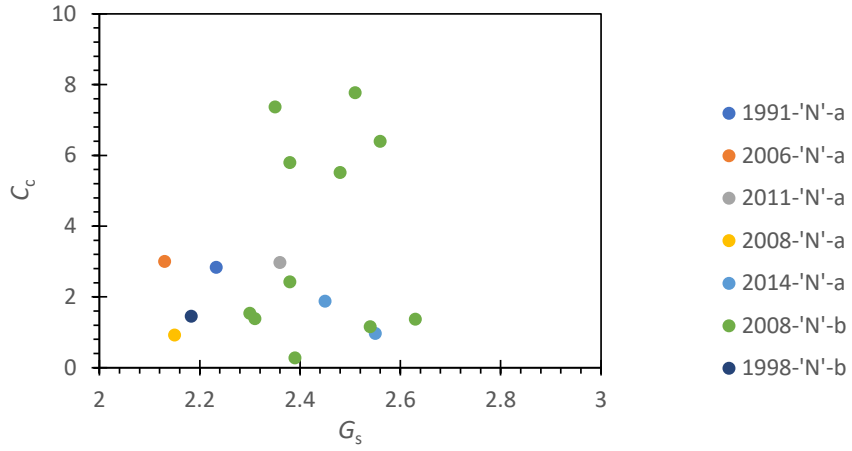

Figure 2.14: Relationship between consolidation index and specific gravity on natural diatomaceous soil (references can be referred to Section 2.9)

2.4.1.1 Remolded diatomaceous soil

Remolded diatomaceous soil usually has lower compressibility (C_c) due to the loss of fabric bonding and the reduction of inter-particle pores (Shiwakoti et al., 2002). This is shown by expected convergence of remolded and undisturbed consolidation curves at larger pressure (Figure 2.15 (a)). Some natural diatomaceous soil can even be remolded into paste consistency just like quick clay (Shiwakoti et al., 2002). Consolidation tests on remolded diatomaceous soil can be divided into two categories depending on the soil state: consolidate from slurry state (type 1) and consolidate from reconstituted specimen that has been preconsolidated to certain stress (type 2). In the latter case, the consolidation curve would show a turning point just like undisturbed specimen (e.g., Figure 2.15 (a)). Consolidation tests that start from slurry usually do not have a turning

point because the soil has no stress history (e.g., Figure 2.15 (b) and (f)). However, there are some counter examples where consolidation tests from a slurry state can show an apparent preconsolidation stress (e.g., Figure 2.15 (c) and (d)). Mesri et al., (1975) attributed it to thixotropic hardening where the Mexico city clay was remolded at natural water content and rested for a period of time when thixotropic hardening was gained up. Wiemer et al. (2017) attributed it to diatom crushing because apparent preconsolidation stress shows up around 100 kPa vertical stress when diatom content is 75% or higher and no preconsolidation stress shows up when diatom content is 50% or less (Figure 2.15 (d)). Verdugo (2008) also intended to prove diatom crushing by consolidating remolded diatomaceous soil to as high as 6500 kPa vertical stress but found no turning point which disproved the theory (Figure 2.15 (e) and (f)). Shiwakoti et al., (2002) proved diatom crushing at vertical stress of 10 MPa by running SEM images before and after applying the vertical stress. It is still an open question whether diatoms would crush under pressure or not and what pressure level would cause diatoms to crush if crushing can occur.

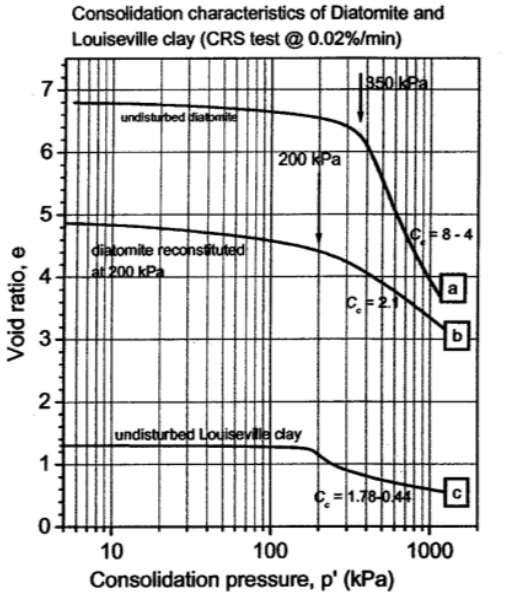

(a) (Shiwakoti et al., 2002)

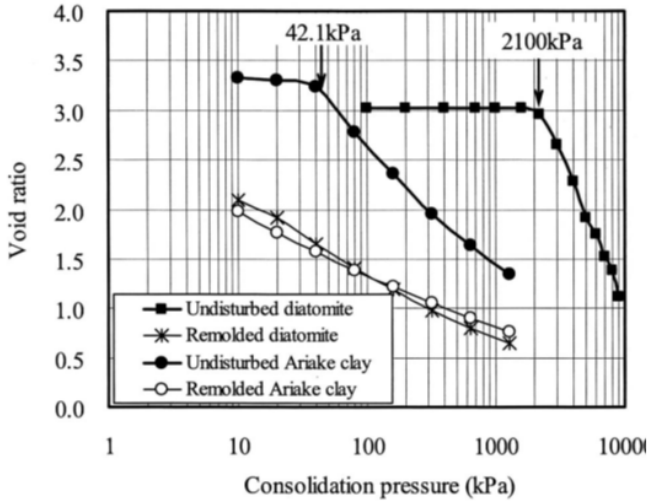

(b) (Hong et al., 2006)

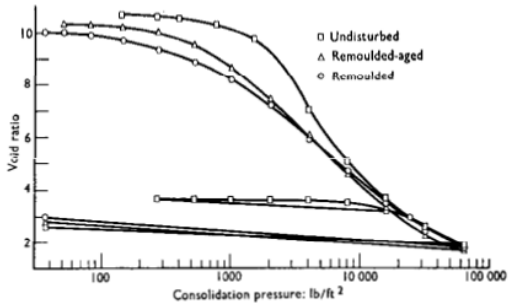

(c) (Mesri et al., 1975)

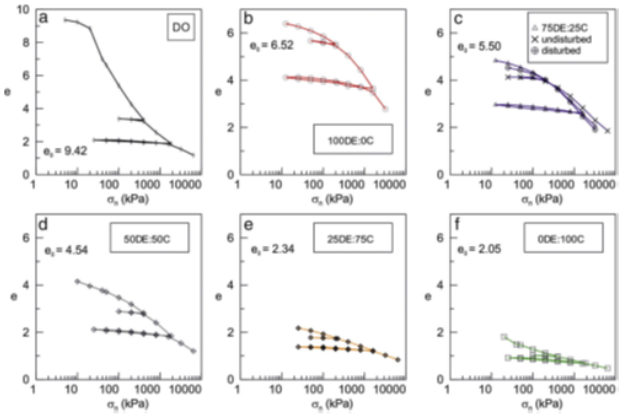

(d) (Wiemer et al., 2017)

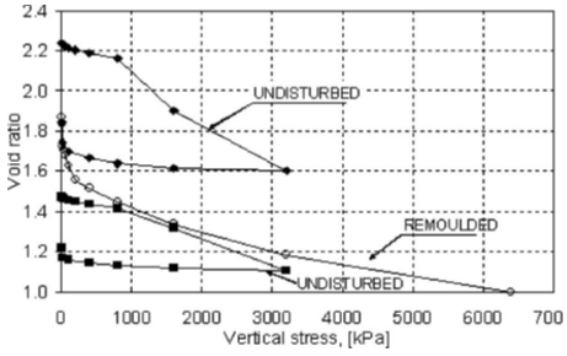

(e) (Verdugo, 2008)

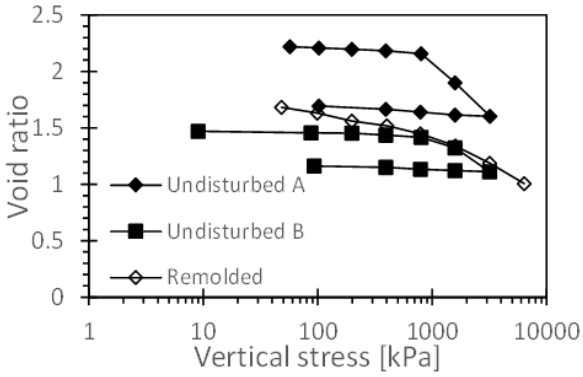

(f) replot (e) in semilogarithmic scale

Figure 2.15: Various consolidation curves of remolded and undisturbed diatomaceous soil

In addition to the high primary compression indices observed in diatomaceous materials, Wiemer et al. (2017) argue that the compression index post-yield is a function of the applied effective stress. However, close observation of the data implies that, while this may be true near the yield stress, where the compression curve is highly nonlinear, the argument is less convincing at higher stress levels (Figure 2.16 (a)). Another alternate interpretation is that the compression index varies smoothly with applied effective stress (Figure 2.16 (b)). This approach has the advantage that a closed-form solution for stiffness as a function of vertical effective stress (i.e., $C_c = C_c(\log\sigma_v')$) may be developed, which would be beneficial for computational modeling of material behavior. The results from such an analysis provide stiffness values very similar to those reported by the authors (Figure 2.16 (b), inset). However, this approach has several potentially concerning drawbacks which may preclude its use: (i) it is not appropriate for materials with a well-defined yield stress; (ii) the data supporting this analysis are from remolded specimens; and (iii) it is possible to have nonsensical (e.g., negative) stiffness values at the function extrema. Clearly, this is an area where more data and analysis are required. There are some other cases where C_c varies with effective vertical stress after yielding during consolidation. Figure 2.15 ((a) and (c)) shows that C_c decreases with vertical stress under virgin compression for diatomaceous soil.

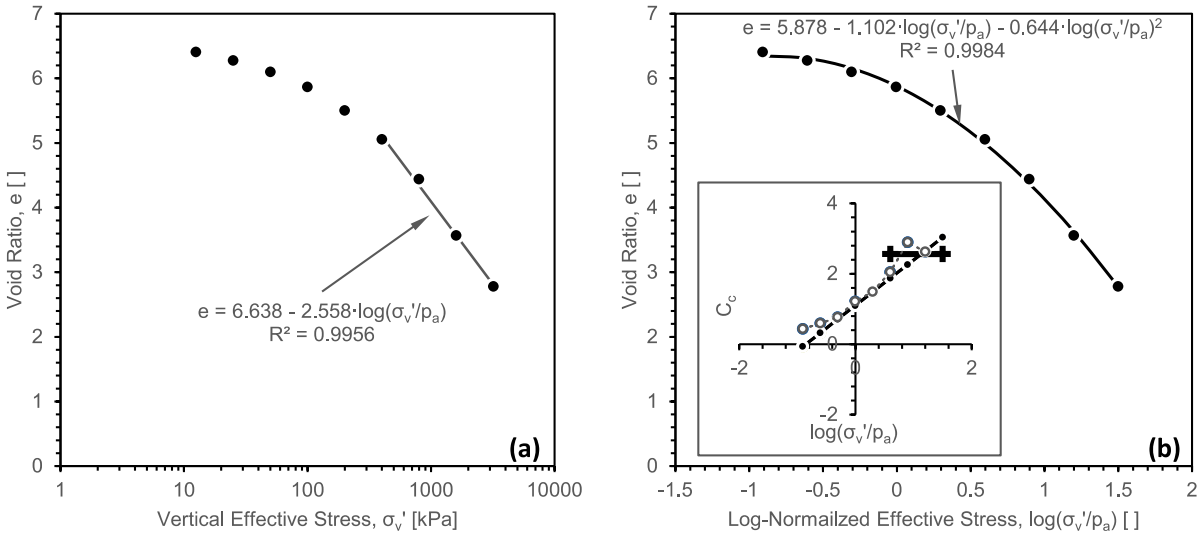

Figure 2.16: Replotted virgin oedometric compression data (i.e., Figure 2.15 (d)) after Wiemer et al. (2017). (a) A nearly constant compression index (C_c = 2.56) is observed after yielding, in contrast to the original authors' interpretation. (b) A smooth function fit to the data, resulting in a continuously varying compression index. The inset shows compression index versus vertical effective stress; the straight line with solid symbols is the derivative of the fitted function, the open circles are the values reported by the authors, and the bold horizontal line is the coefficient of compression from the line in (a).

Consolidation tests on diatom and other soil mixtures were conducted in order to study the effect of diatom content shown in Figure 2.17, predictably, the more diatom, the higher compression index. But unlike G_s which is closely related to diatom content regardless of the source of

diatomite, C_c varies at different levels of diatom content, especially at high diatom content.

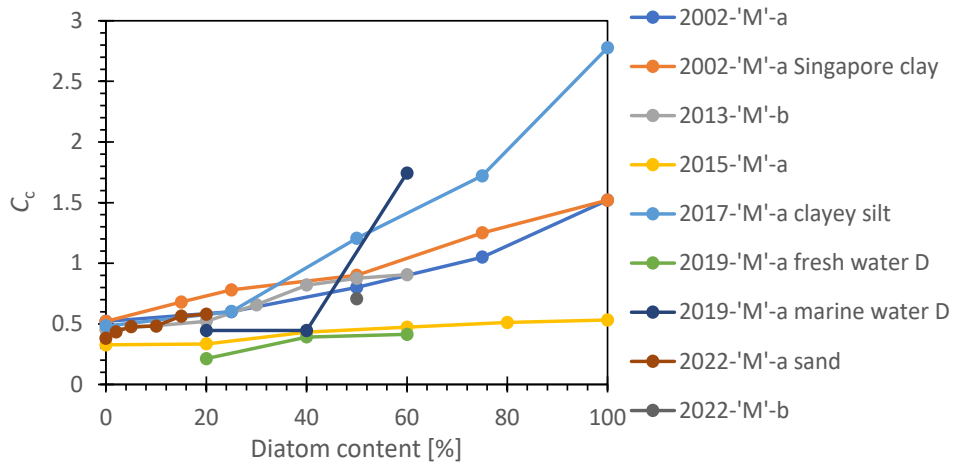

Figure 2.17: Summarized C_c vs. diatom content (soil mixtures are diatom and kaolin unless specified) (references can be referred to section 2.9)

2.4.2 Settlement-time Curves

Logarithmic-linear time dependent one-dimensional consolidation behavior has been observed for some diatomaceous soils (e.g., Shatnawi and Bandini, 2019; Sonyok, 2015; Sonyok and Bandini, 2019), see Figure 2.18. For these types of curves, their end of primary consolidation is difficult to determine, unlike with a typical "S-shaped" log time-settlement curve predicted by Terzaghi theory (Terzaghi, 1943; Bardet, 1997). Similar time-settlement curves can also be observed in other soils; Robinson (2003) observed logarithmic-linear time dependent compression curves in kaolinite but at a low load increment ratio (LIR = 0.2). He observed that the beginning of secondary compression is strongly dependent on the LIR with a small LIR corresponding to an early start of secondary compression (i.e., at an average degree of consolidation of $U_{ave} \cong 55\%$). However, diatomaceous soil can also exhibit logarithmic-linear compression behavior, even at a high LIR (Figure 2.18). The deformation mechanism of this type is not fully understood (Shatnawi and Bandini, 2019).

The time rate of consolidation of a diatomaceous mudstone from Japan was investigated by Maekawa et al. (1991) and found to be well-described by an elasto-viscoplastic model. They performed single-increment isotropic consolidation tests beginning from an isotropic effective stress of $p_i' = 0.5\, kgf/cm^2$. Five tests were performed, each with a different final isotropic effective stress: $p_f' \in \{20, 30, 40, 55, 70\}\, kgf/cm^2$ (Figure 2.19 (a)). Similar to the behavior reported by Sonyok (2015) for diatom-kaolin mixtures, Maekawa et al. (1991) observe that excess pore water pressure in the diatomaceous mudstone dissipates in less than 24 hours (Figure 2.19 (b)) but that secondary compression continues to occur for some time afterwards (Figure 2.19 (a)). Similar observations also found in Mexico City clay (Díaz-Rodríguez and Martínez-Vásquez, 2008; Díaz-Rodríguez and López-Flores, 1999).

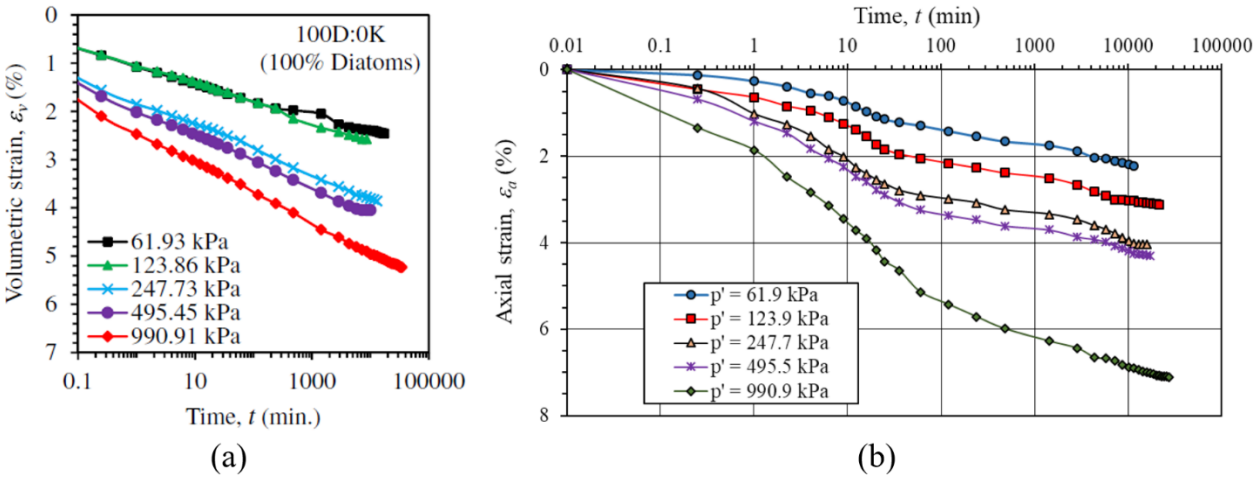

Figure 2.18: Time – settlement curves for 100% diatomite ((a). (Sonyok and Bandini, 2019); (b). (Shatnawi and Bandini, 2019))

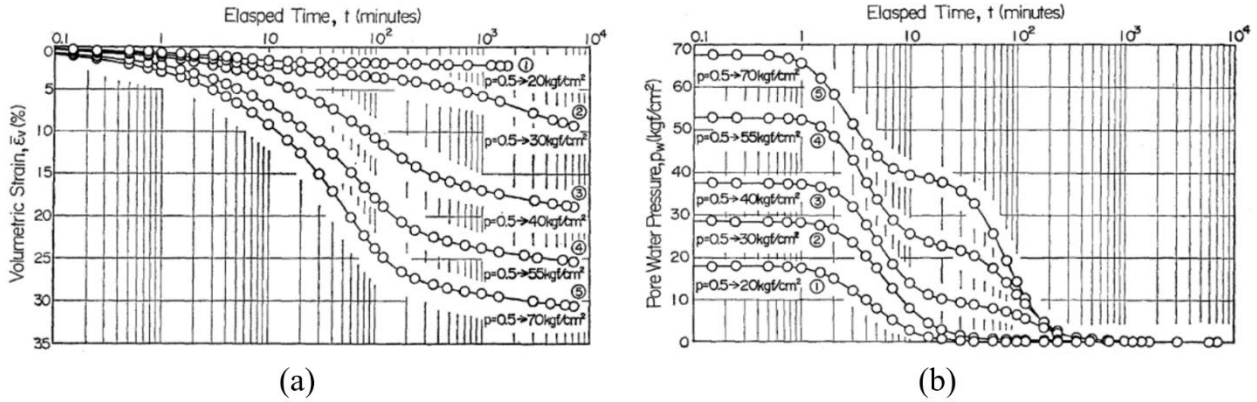

Figure 2.19: Isotropic compression behavior for a diatomaceous mudstone (Maekawa et al., 1991): (a) volumetric strain with time; (b) excess pore water pressure with time. Note that 1kgf/cm^2 = 98.1 kPa = 1.02 tsf

2.4.3 Particle Crushing

The high degree of compressibility of diatomaceous soil has been attributed to the crushing of diatomite frustules during loading by some researchers (Shiwakoti et al., 2002; Sonyok, 2015; Wiemer and Kopf, 2017). This is consistent with the observation of oedometric (i.e., K_0) compression of silica soils, where the yield point (i.e., the preconsolidation stress in clays) is generally understood to correspond to the onset of substantial particle crushing (Hagerty et al., 1993). The assertion that particle crushing is significant is further supported by the findings of Caicedo et al. (2018) who observe a strong linear correlation between liquid limit and compression index (i.e., $C_c = 0.01(LL - 0.58), R^2 = 0.92, n = 78$). However, there are remarkably few results of direct quantification of particle size distribution before and after loading reported in the literature.

Wiemer et al. (2017) used laser diffraction spectroscopy to measure the grain size distribution of a diatomaceous earth specimen both before and after oedometric compression and found that the clay-sized fraction increased (11.2%↦19.6%) while the silt-and sand-size fractions decreased (81.0%↦74.9% and 7.8%↦5.5%, respectively) during loading to 1600 kPa. They state that this breakage may begin to occur at stresses below what they term the "systematic apparent" preconsolidation stress[1]. The observed yield point (Figure 2.15 (d)) is not as well-defined as in silica sands and the authors claim that this is due to progressive particle crushing in the specimens and note that similarly-shaped consolidation curves have been reported for diatomaceous soils (Díaz-Rodríguez and González-Rodríguez, 2013; Shiwakoti et al., 2002) and high water content clays at very low effective stresses (Hong et al., 2010).

Day (1995) came to a slightly different conclusion based on oedometric compression tests on an undisturbed sample of a silty clay containing 65% diatoms and on a remolded specimen that had all of the non-diatomite material removed. He found that the two compression curves were significantly similar (Figure 2.20) and concluded that the diatom fraction of the material was responsible for the overall high degree of compressibility of the diatomaceous fill. Interestingly, while no effort was made to observe or quantify particle breakage, Day (1995) noted that there was a "distinct popping sound" at an applied vertical effective stress of 1600 kPa, which is much higher than the breakage stresses presumed by Wiemer et al. (2017).

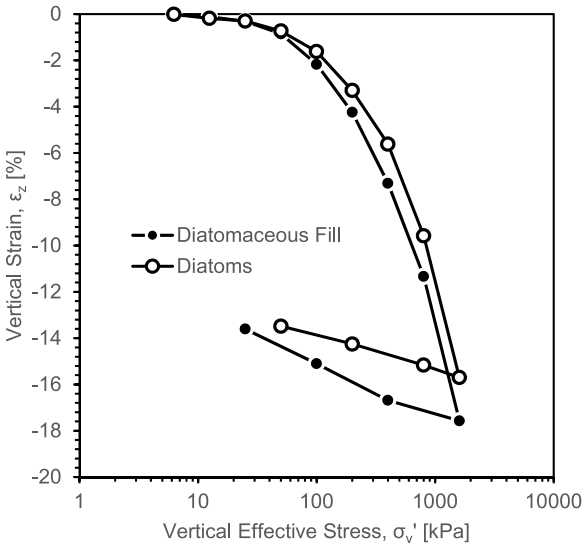

Figure 2.20: Compression curves for an undisturbed sample of diatomaceous fill and a corresponding remolded specimen with all non-diatomite fraction removed (Day, 1995)

Particle breakage occurring only at very high effective stresses was also observed by Hong et al. (2006) in a study of the micro- and macroscale behaviors of Oita diatomite from Japan. They

[1] Wiemer et al. (2017) observe a marked yield stress even in specimens that are reconstituted at their liquid limit (e.g., Figure 2.15 (d)). They attribute this to the high permeability of diatomaceous soils at low overburden stresses, consistent with the findings of Pittenger et al. (1989)

report an oedometric yield stress of 2100 kPa and a hydrostatic yield stress of 1500 kPa (Figure 2.15 (b)) despite an estimated *in-situ* effective overburden stress of approximately 39 kPa and geologic evidence that the deposit is normally consolidated. The resulting oedometric yield stress ratio is 53, which the authors take to imply that the soil is highly structured with intact silica cement bonds prior to yield. This assertion is further substantiated by the fact that the soil is essentially rigid prior to the yield stress for both one-dimensional and hydrostatic loading[2]. While particle size determinations were not made pre- and post-loading, particle breakage was substantiated visually (scanning electron microscopy, SEM) and using mercury intrusion porosimetry (MIP) to measure the evolution in pore size distribution. SEM images of the Oita diatomite after loading to 1.2, 2.0, 4.0, and 8.0 MPa are presented in Figure 2.21. Very little breakage is observed below the hydrostatic yield stress (i.e., 1500 kPa), but progresses noticeably as the stress is further increased. Contrary to some other studies (Pittenger et al., 1989; Wiemer et al., 2017), Hong et al. (2006) do not observe an apparent preconsolidation stress in the remolded specimen and, in contrast to Day (1995), found that there is substantial difference in the compressibility of undisturbed and remolded specimens. Specifically, after the undisturbed sample's yield surface has been engaged, it becomes highly compressible – much more so than the remolded specimen (contrast to Figure 2.20).

[2] Interestingly, the oedometric and hydrostatic compression curves are quite similar. If crushing is assumed to be a mean stress rather than a maximum stress phenomenon, then the two yield stresses are equivalent for an at-rest earth pressure coefficient of $K_0 = 0.571$, which while slightly high for a structured material, is not unreasonable. This point may deserve further investigation.

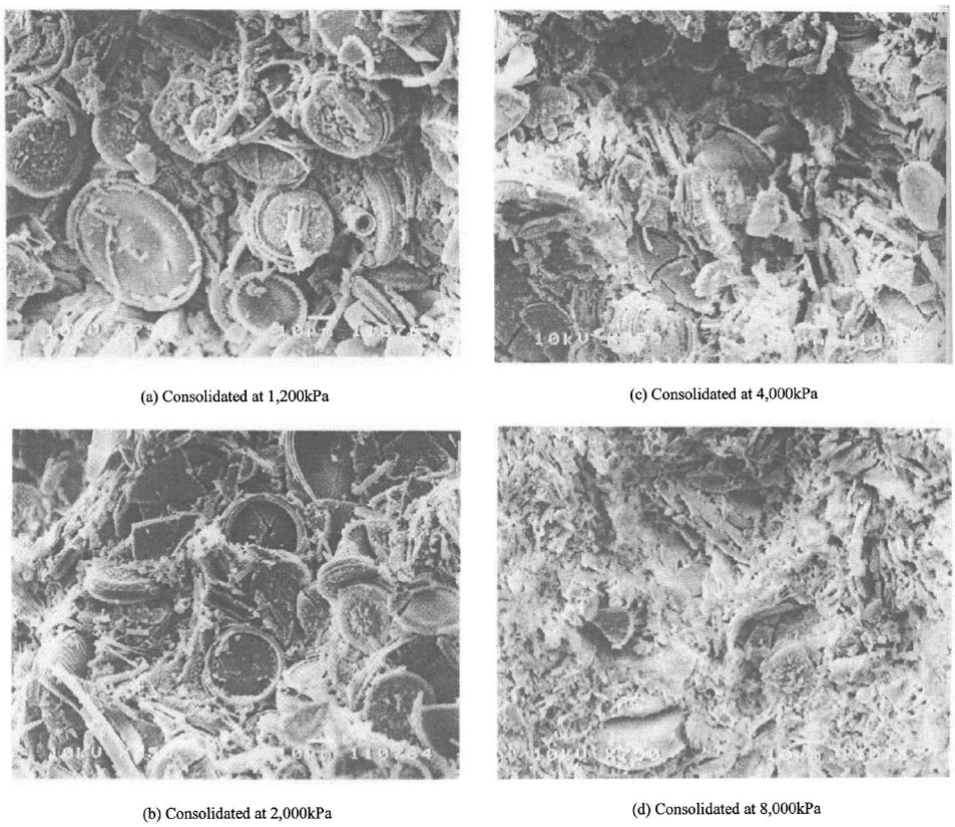

Figure 2.21: SEM images of Oita diatomite after being loaded to various hydrostatic stresses (Hong et al., 2006). Note the progression of particle crushing with increasing effective stress.

Other studies have found relatively less particle breakage in oedometric loading of diatomaceous soils. Tanaka and Locat (1999) measured compression curves for Osaka Bay clay (Figure 2.22) that exhibited near-rigid response at low stresses followed by a well-defined yield stress, which is common to other diatomaceous soils (Díaz-Rodríguez and González-Rodríguez, 2013; Shiwakoti et al., 2002; Wiemer et al., 2017). They further observed that the skeletal and intraskeletal pore space of the diatoms in Osaka Bay clay remained largely unaffected by large vertical strains while the volume of intra-aggregate and inter-aggregate pores decreased significantly. Hong et al. (2006) infer – but never state outright – that this is due to the shielding effect of the surrounding clay and the ease with which the rigid diatoms can rearrange when floating in a clay matrix. Alternately, Verdugo (2008) argues that since no obvious "breakdown point" is observed in the compression curve for remolded specimens (Figure 2.15 (e)), there is no substantial particle crushing.

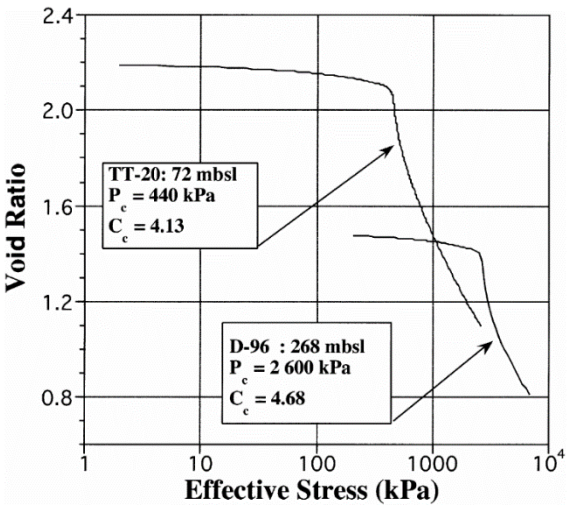

Figure 2.22: Constant rate of strain oedometer test results for diatomaceous Osaka Bay clay (Tanaka and Locat, 1999)

2.4.4 Consolidation History

As discussed in 2.2.2, natural diatomaceous soil can be divided into soft-clay and mudstone states. Although there is no distinct definition to differentiate the two, their apparent overconsolidation ratio (OCR) usually differ significantly. The soft-clay like diatomaceous soil tends to be normally consolidated (Tanaka and Locat, 1999; Tanaka et al., 2001), whereas, the mudstone diatomaceous soil tends to be highly overconsolidated (e.g., OCR = 53 at Oita Japan, OCR = 25 at Noto Peninsula Japan, Maekawa et al. 1991; Hong et al. 2006). Such phenomenon of overly higher OCR than its geological history has been named "quasi-preconsolidation" by Bjerrum (1967). Quasi-preconsolidation is the result of delayed compression (i.e., compression under constant effective stress) and usually occurs in clays. Consider, for example, the conditions illustrated in Figure 2.23. A soil deposit exists at a constant vertical effective stress of σ_0' for some (geologic) time. Due to delayed compression, the void ratio of the soil decreases from $e_0 \mapsto e_1$ at a constant stress state. If the soil is then subjected to an incremental load consolidation test, "Curve b" will be measured, exhibiting an apparent preconsolidation stress of σ_1' even though the vertical effective stress remains unchanged at σ_0'. Bjerrum (1967) attributed delayed compression to the inability of soil voids (i.e., the pore water) to retard the compression (i.e., a lack of primary consolidation). In the case of diatomaceous soil, several research studies attributed this to the mechanisms of diagenesis, cementation, and aging (Iijima and Tada, 1981; Díaz-Rodríguez and Santamarina, 2001; Ovalle et al., 2019; Ovalle and Arenaldi-Perisic, 2021).

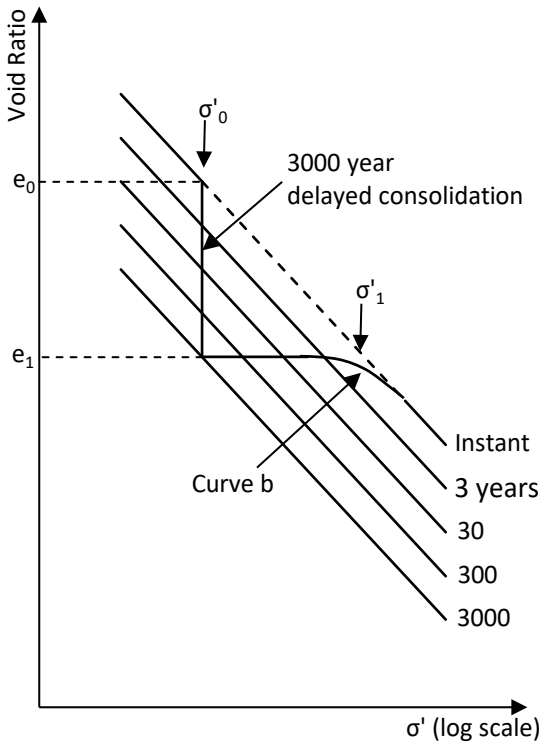

Figure 2.23: A schematic illustration of the quasi-preconsolidation effect (Bjerrum, 1967)

2.5 STATIC SHEAR BEHAVIORS

It is generally accepted that shear strength decreases with increasing plasticity index (PI) for fine-grained soils (Díaz-Rodríguez and Santamarina 2001; Kenney 1959; Wiemer and Kopf 2017). Based on trends published by Kenney (1959) and Bjerrum and Simons (1960), a diatomaceous soil with PI=300 (e.g., Mexico City clay) is expected to have a friction angle in the range $5° \leq \phi' \leq 15°$ (*American Society for Testing and Materials. 2018a. "Test Method for Field Vane Shear Test in Saturated Fine-Grained Soils."* n.d.). Many diatomaceous soils, however, are noticeable exceptions to this trend (Caicedo et al. 2018; Díaz-Rodríguez and Santamarina 2001). In spite of their high compressibility and natural water content, diatomaceous soils are typically reported to exhibit effective stress friction angles that are comparable to those of angular sands (Caicedo et al. 2018; Diaz-Rodriguez et al. 1992). This high strength is typically attributed to the rough surface and irregular shapes of diatom frustules. Locat and Tanaka (2001) note that after the yield stress of the diatoms, shear strength will decrease due to particle crushing.

2.5.1 Diatom Mixtures

Mixtures of diatom and other soil (typically kaolinite) were tested for direct shear, simple shear, triaxial shear, and unconfined compression tests (Diaz-Rodríguez 2011; Shiwakoti et al. 2002; Sonyok 2015; Wiemer and Kopf 2017; Wiemer et al. 2015; Tanaka et al. 2003). It has been reported an increase in the shear strength of diatomite-clay (typically kaolinite) mixtures with

increasing diatom content except in unconfined compression tests. Both Tanaka et al. (2003) and Sonyok (2015) reported a decrease in shear strength with increase in diatom content.

Recent work (Wiemer and Kopf 2017), however, has shown that some prior studies (Shiwakoti et al. 2002) may possibly be reporting unrealistically high values of friction angles for diatomaceous soils. Wiemer and Kopf (2017) posit that the high friction angles reported by Diaz-Rodríguez (2011) and Shiwakoti et al. (2002) overestimate the true strength of the material, particularly at low effective stresses, because they are based on a single experiment. Specifically, if a straight-line failure envelope (in $\tau - \sigma'$ space) is drawn from the origin to the failure point for a single test, then a friction angle of 40°-45° is obtained. For tests performed at low confining (or overburden) stresses, this approach neglects the dilation that is expected in drained shear (Bolton 1986). There are two immediately evident alternate interpretations: (i) a curved failure envelope (Schellart 2000); or (ii) a linear failure envelope that does not pass through the origin. Wiemer and Kopf (2017) adopted the second approach to interpret results from direct shear tests and report friction angles of $\phi' \cong 30^{\circ}$ along with apparent cohesions in the range of 35~70 kPa. Such an interpretation may more appropriately represent shear strength at high effective stresses, but it also tends to overpredict shear strength at low effective stresses. While this methodology reconciles the strengths measured by Wiemer and Kopf (2017) and Shiwakoti et al. (2002), it is important to note that all of these analyses are founded upon a limited number of tests. Additionally, the reported strengths were measured in direct shear tests, which have a number of significant drawbacks (e.g., Budhu 2010). Figure 2.24 summarizes the friction angle as a function of diatom content from direct shear tests or direct simple shear tests.

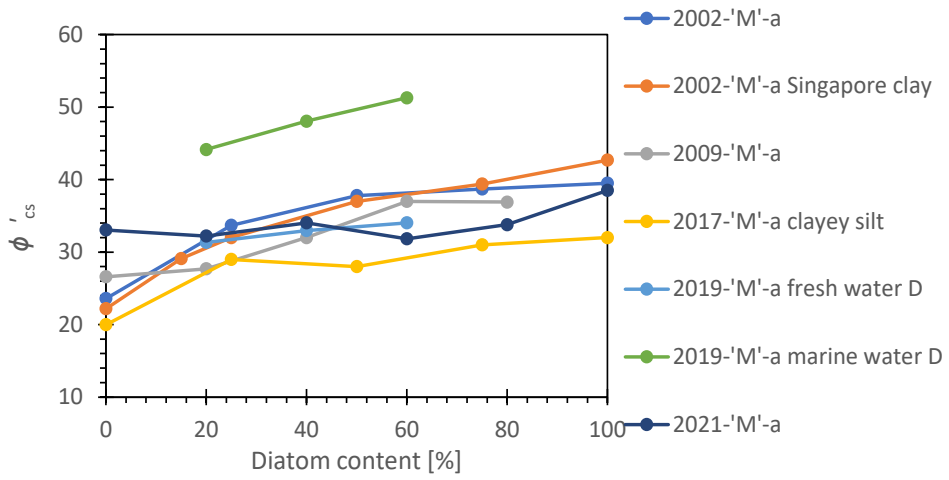

Figure 2.24: Friction angle vs. diatom content (mixture with kaolin unless specified) (references can be referred to section 2.9)

2.5.1 Natural Diatomaceous Soil

Caicedo et al. (2018) investigated the relationship between shear strength and consistency limits for the lacustrine diatomaceous deposits in Bogotá, Columbia. They attempted to describe the data using the equation proposed by Wood (1990) and subsequently modified by Vardanega and Haigh (2014), but found that it did not provide good agreement with measured data, even when

the values of $s_{u_{LL}}$ and R_{MW} were adjusted outside of their typical ranges. They found better agreement between measurements and predictions when using plasticity index (PI) to describe fundamental soil properties and water content to describe state. These relationships are summarized in Table 2.2. Of particular note is that the expressions developed for the Bogotá soils indicate that undrained shear strength increases monotonically with plasticity index and effective stress friction angle increases monotonically with liquid limit.

Table 2.2: A few semi-analytical and empirical relationships for index properties and shear strength

Empirical Correlations	References	Symbol Definitions
$s_u = s_{u_{LL}} R_{MW}^{1-LI}$	Wood (1990) Vardanega and Haigh (2014)	LI = liquidity index LL = liquid limit p_a = atmospheric pressure PI = plasticity index R_{MW} = a function of clay mineralogy, typically in the range 30-160 (see Note 1) s_u = undrained shear strength $s_{u_{LL}}$ = undrained shear strength at the liquid limit (see Note 2) w = water content γ = shear strain $\gamma_{M=2}$ = shear strain when half of the shear strength is mobilized ϕ'_{cs} = effective stress friction angle at critical state τ_{mob} = mobilized shear strength
$\frac{s_u}{p_a} = \frac{14PI}{w^{1.8}}$ $\phi'_{cs} = \left(0.323 + \frac{LL}{512}\right)\frac{180°}{\pi}$ $\ln\frac{\tau_{mob}}{s_u} = 0.455 \ln\frac{\gamma}{\gamma_{M=2}} - 0.71$	Caicedo et al. (2018)	
NOTES: 1. Based on an extensive database, Vardanega and Haigh (2014) recommend a value of 35. 2. Typically in the range 1.7-2.4 kPa, but often 1.7 kPa is assumed.		

Díaz-Rodríguez et al. (2009) studied the effects of shear rate on undisturbed Mexico city clay. They found that the higher shear rate, the higher normalized undrained strength, reversely, for specimens with higher normalized undrained strength, they are more sensitive to the shear rate. In their study, the specimen exhibits strain softening behavior when sheared at a rate of 100%/hr and 800%/hr regardless of OCR, and there is no strain softening behavior when sheared at a rate of 1%/hr regardless of OCR.

The SHANSEP model describes the relationship between the normalized shear strength to OCR (Ladd and Foott 1974). It can be used to predict the soil strength. Figure 2.25 summarizes the normalized undrained shear strength from triaxial tests for natural diatomaceous soils.

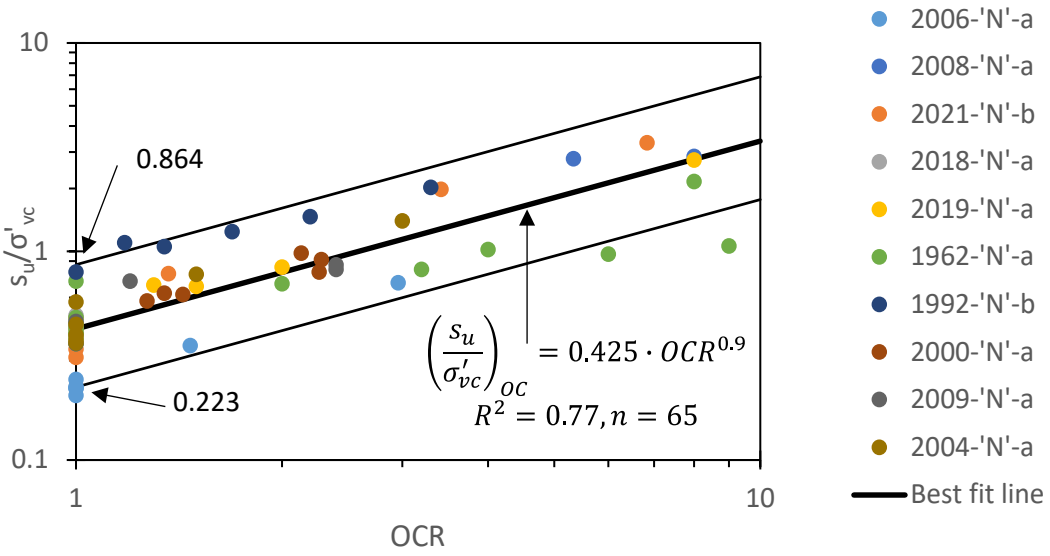

Figure 2.25: Normalized undrained shear strength vs. OCR on natural diatomaceous soil (references can be referred to section 2.9)

2.6 *IN-SITU* BEHAVIORS

2.6.1 Overview

In-situ testing can be used to infer the engineering properties of in-place soils, either with or without extraction of samples for laboratory testing. In general, reports of *in-situ* testing on diatomaceous soils in the literature is limited. Occasionally, *in-situ* tests have been performed in support of pile installation or remedial investigations in diatomaceous soils (Benson and Rippe 2008; Matsumoto et al. 1995; Matsumoto et al. 1995). Others have been executed to investigate slope failure mechanisms within diatomaceous deposits (Díaz-Rodríguez 2003; Díaz-Rodríguez et al. 1998; Wiemer et al. 2015). The most common in-situ tests reported in the literature in diatomaceous soils are the standard penetration test (SPT) and the cone penetration test (CPT).

2.6.2 Standard Penetration Testing

Relatively few SPT results are presented in the literature, but in sum, it is consistently observed that unconsolidated diatomaceous soils are characterized by very low blow counts (N≲10 in most cases) while diatomaceous mudstones afford somewhat more SPT resistance. An example of particular interest is the Wickiup Dam, which is located less than 20 km nearly due west of Wickiup Junction. In 2001, a substantial jet grouting program was initiated under the direction of the United States Bureau of Reclamation (USBR) to stabilize two deposits (upper and lower) of liquefiable diatomaceous soils beneath the foundation of the left abutment dike (Bliss 2005; Gillette 2008). As part of the geotechnical investigation for that work, blow counts of $N_{60} \cong 1{\sim}2$ in the upper deposit and $N_{60} \cong 0{\sim}3$ in the lower deposit were reported. These values are consistent with the blow counts ($N \cong 0$) recorded for potentially liquefiable diatomaceous deposits underlying Rotorua, New Zealand (Pearse-Danker 2013).

The Notojima bridge was constructed over a thick (50-65 m) deposit of diatomaceous mudstone at Nanao Bay on the Noto Peninsula, Japan in 1982. As part of the site exploration, drivability assessment, and load testing program, several SPTs were performed and the results reported by Nishida (1985). These results are presented in Figure 2.26 and indicate blow counts in the range $N \cong 13{\sim}32$. These values are approximately constant to slightly increasing with depth. Matsumoto et al. (1995) subsequently performed standard penetration testing in support of a pile load testing program and report $N \cong 10{\sim}20$ in the diatomaceous mudstone by the Notojima bridge (Figure 2.27). This load testing program was undertaken because a large number of the bridge's open-ended pipe piles encountered refusal prior to reaching their design embedment depth. These piles were designed using the SPT-based specifications from the Japan Road Association, indicating that SPT may not be a reliable design input for piles driven into mudstone.

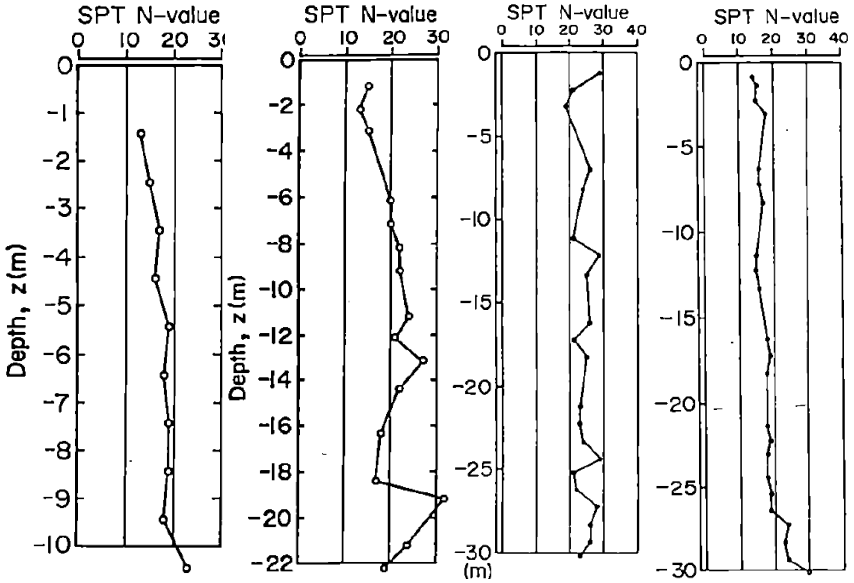

Figure 2.26: SPT blow counts recorded during site exploration and load testing for Notojima bridge (Nishida 1985)

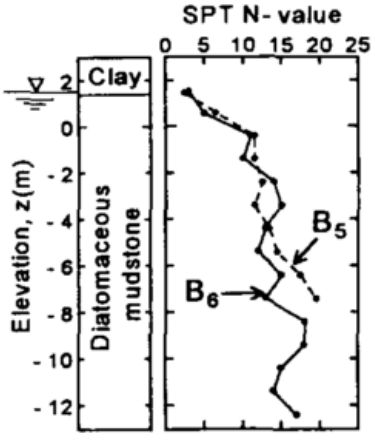

Figure 2.27: Results of SPTs at Boreholes B5 and B6 (Matsumoto et al. 1995)

The alluvial deposits that are predominant in Guayaquil, Ecuador are also characterized by significant diatom content and have been well-characterized by Vera-Grunauer (2014). Of interest, diatoms are often present to one degree or another in the upper 40 m of soil in Guayaquil rather than being concentrated in a specific stratum. There are fine materials (CH, CL, MH, ML, and OH) that can be quite soft ($1 \leq LI \leq 12$) and coarser materials (SC, SM) that have a lower fraction of diatoms, but "non-textbook" behaviors nonetheless. That study reports blow counts generally in the range $N_{60} \leq 10$ in the fine-grained deposits and in the range $20 \leq N_{60} \leq 60$ with high variability in the sandy layers (Figure 2.28).

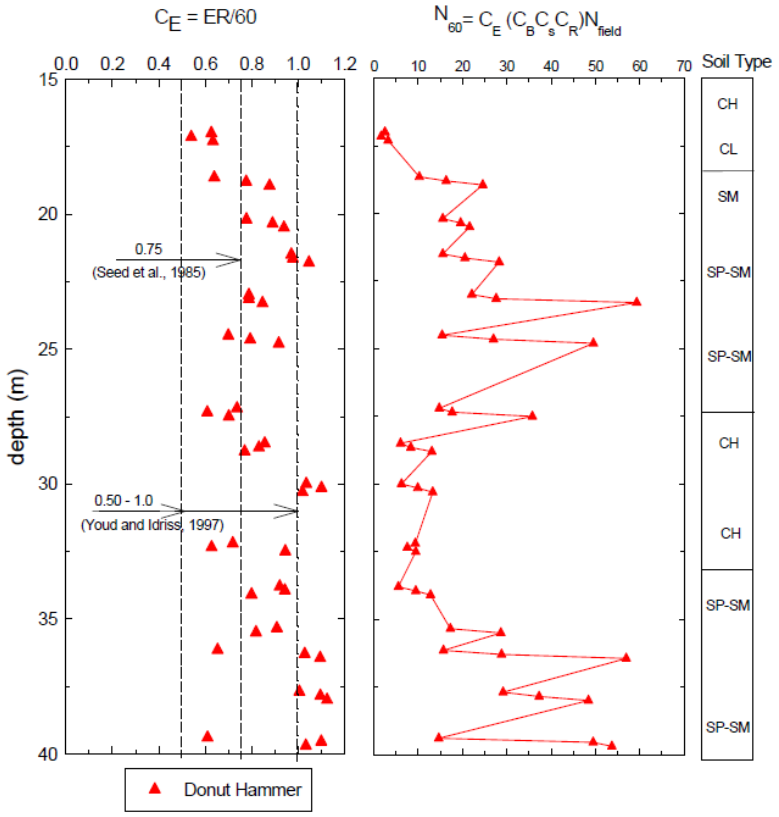

Figure 2.28: Variation in energy correction, N_{60}, and soil type with depth in Guayaquil, Ecuador (Vera-Grunauer 2014)

2.6.3 Cone Penetration Testing

There are several reports of cone penetration testing in diatomaceous soils in the literature, but the coverage is far from comprehensive. Díaz-Rodríguez (2003) and Díaz-Rodríguez et al. (1998) performed CPTs on Mexico City Clay (a known diatomaceous soil) at the Ramón López-Velarde Park (RLVP); typical results are presented in Figure 2.29(a). Cone tip resistance of approximately 0.05-0.20 MPa was observed throughout the profile (i.e., to a depth of 35 m), indicating extremely soft soil. Similarly, Saldivar and Jardine (2005) performed CPTs in Mexico City clay in the Texcoco Lake zone and measured tip resistances of 1-2 MPa in the upper diatomaceous layer (Figure 2.29(b)). Similar results (i.e., low tip resistance and sleeve friction)

are also reported by Vera-Grunauer (2014) for the diatomaceous deposits in Guayaquil, Ecuador (Figure 2.30).

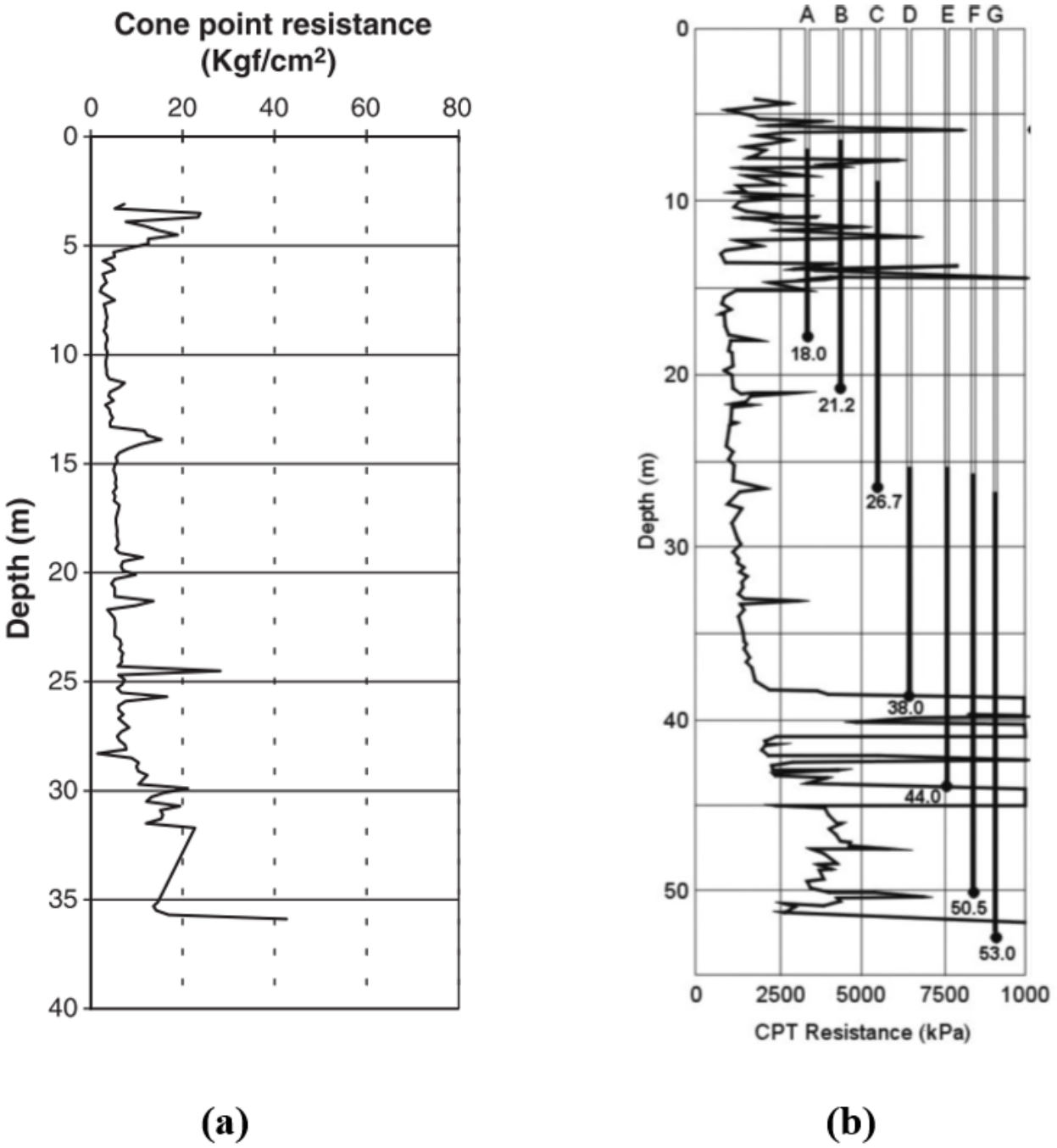

Figure 2.29: Typical profile of cone tip resistance in Mexico City clay at (a) Ramón López-Velarde Park (Díaz-Rodríguez 2003); and (b) the Texcoco Lake zone (Saldivar and Jardine 2005)

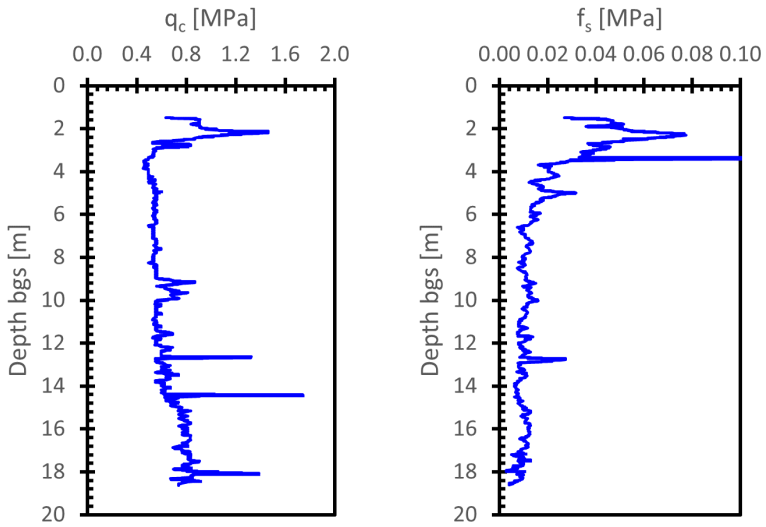

Figure 2.30: Example CPT sounding from Guayaquil, Ecuador: corrected tip resistance (L) and sleeve friction (R) (Vera-Grunauer 2014)

Matsumoto et al. (1995) performed CPTs both before pile installation and after static load tests in the diatomaceous mudstone on Noto Peninsula, Japan. Typical results of CPT soundings before pile driving are presented in Figure 2.31. The results are characterized by a tip resistance of approximately 3 MPa, rapidly oscillating sleeve friction, and high (>1 MPa) induced pore water pressure. These values are generally consistent with, though slightly higher than, values reported by Pearse-Danker (2013) for diatomaceous deposits in Rotorua, NZ: $q_c \cong 0.4 - 1.5\ MPa$ and $f_s \cong 0.01\ MPa$.

Wiemer et al. (2015) combined in-situ and laboratory work to investigate subaqueous slope failure mechanisms in Lake Villarrica, South-Central Chile. They did not report raw CPT results, but rather interpreted soil properties (e.g., undrained shear strength, s_u) and factors of safety; these results are presented in Figure 2.32. The results show that safety factors are relatively high, implying that gravitational slope failures under drained conditions are unlikely due to high friction angles. Their interpretation is that diatomaceous sediments have fundamentally different physical properties and conventional geotechnical analyses are not sufficient.

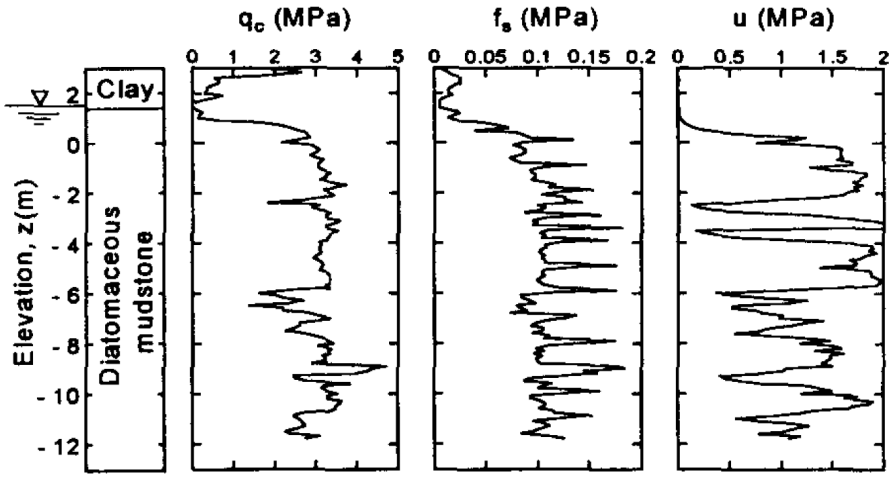

Figure 2.31: Typical results from CPTs in diatomaceous mudstone at Noto Peninsula, Japan before pile driving (Matsumoto et al. 1995)

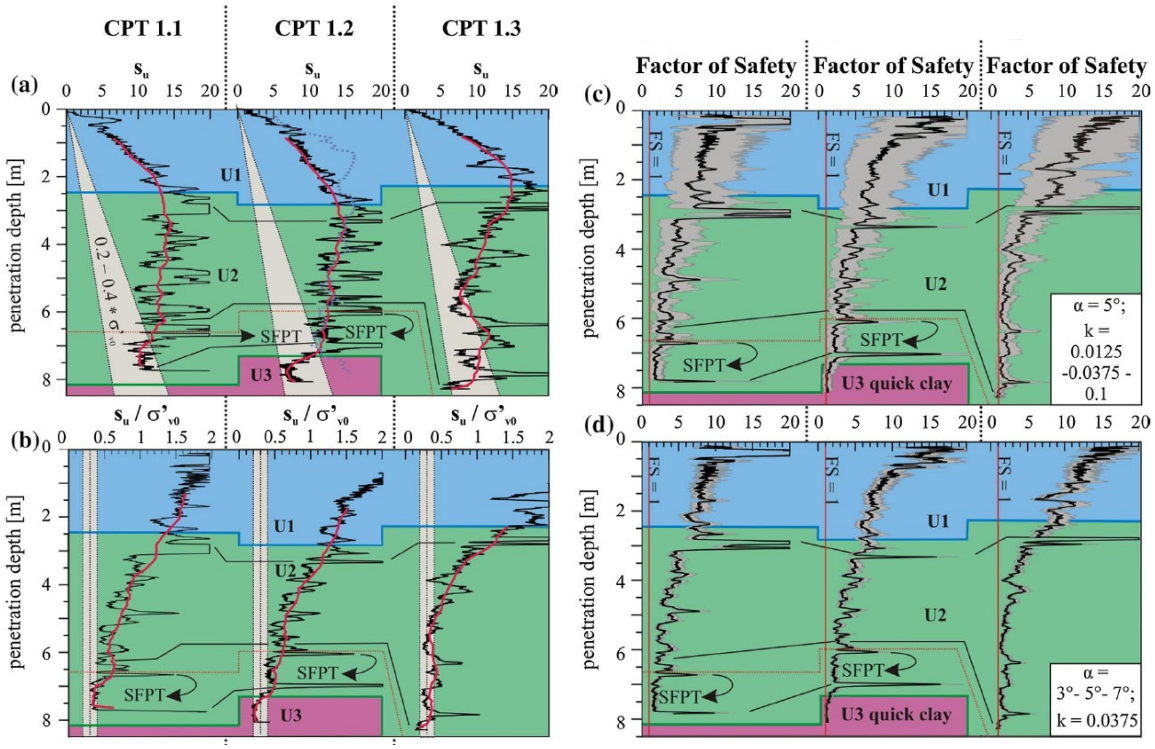

Figure 2.32: Undrained shear strength and factor of safety from CPT results in Lake Villarrica, Chile (Wiemer et al. 2015)

2.6.4 *In-situ* Shear Wave Velocity Measurement

There is also some data in the literature for other *in-situ* tests, specifically measurements of wave propagation velocity (e.g., crosshole tests) and vane shear tests. Díaz-Rodríguez and Santamarina (2001) report that the shear wave velocity from crosshole tests is relatively constant in Mexico

City clays at approximately 80 m/s. They note that the effective stress dependence of the constant-fabric shear modulus is typically modeled with a power law:

$$G_{max} = \alpha {\sigma_0'}^{\beta} \tag{2-1}$$

where α and β are fitting parameters and the modulus is computed from shear wave velocity by:

$$G_{max} = \rho V_s^2 \tag{2-2}$$

where ρ is the bulk density of the soil. Specifically, they note that the exponent back-calculated from crosshole tests is a relatively low $\beta = 0.22$, which indicates that the material exhibits apparent overconsolidation *in-situ*, which is consistent with the discussion in 2.4.4.

2.6.5 Vane Shear Testing

The limited VST data in diatomaceous soils that we have identified is from the remedial investigation following the 2006 break of the Geary Dike on Upper Klamath Lake in south central Oregon (Benson and Rippe 2008). They report generally consistent results between laboratory and in-situ VST results with very low observed undrained shear strengths: $s_{u,peak} \cong 25\ kPa$ and $3\ kPa \lesssim s_{u,residual} \lesssim 25\ kPa$. Profiles of undrained vane shear strength with depth are presented in Figure 2.33.

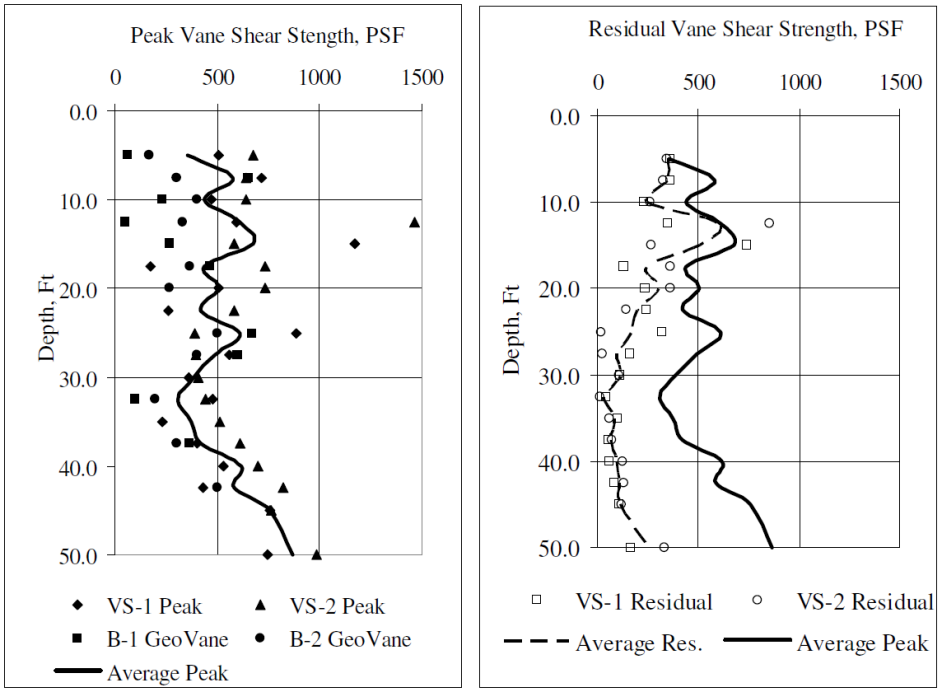

Figure 2.33: Peak and residual undrained vane shear strengths for diatomaceous soils near Upper Klamath Lake in south-central Oregon (Benson and Rippe 2008)

2.7 PILE INSTALLATION IN DIATOMACEOUS SOIL

There are exceedingly few case studies presented in the literature for piles driven into diatomaceous soils, but two prominent studies are discussed here. Saldivar and Jardine (2005) applied the Imperial College effective stress design framework to piles driven in the well-characterized diatomaceous Mexico City clay deposit and made several observations of note:

- The measured soil-steel and soil-concrete effective stress interface friction angles were quite high ($\phi' = 36°$), particularly given the high plasticity ($PI = 160$) of the soil deposit being considered;
- Driven piles in Mexico City are commonly pre-bored for some distance to "reduce driving disturbance to nearby structures," but the effects on drivability were not specifically considered;
- Of the 26 piles in the database, 25 were pre-drilled, including 21 that were pre-drilled to over 63% of their total embedded length;
- The Imperial College design approach tended to overpredict capacity by 6%, on average, whereas the more commonly employed total stress approach (i.e., the α-method) tended to overpredict capacity by approximately 26%, on average; and
- There was significant scatter in all data, but slightly less in the Imperial College approach.

Construction of the Notokima Bridge on the Noto Peninsula in Japan required driving a significant number of piles into a soft diatomaceous mudstone (Nishida 1985). Notably, during construction of the bridge many of the open-ended pipe piles could not be driven to their design embedment depth. A total of 68 open-ended pipe piles were driven to support piers P10-P13 and 44 of them (65%) could not be driven to design embedment. This behavior was considered surprising, given the relatively modest SPT N-values observed during site exploration ($13 \lesssim N \lesssim 30$). However, near the end of a 30-m pile drivability test performed prior to design, refusal was met at 22.5 m with permanent sets on the order of 1.4 mm and rebound on the order of 12 mm near then end of driving. The unit skin friction was calculated as approximately 200 kPa based on the results of static load tests and the authors attribute the drivability issues to this high frictional resistance (Nishida 1985).

Because of the extensive difficulties encountered during previous construction activities (i.e., Nishida 1985), an extensive field testing program (11 CPT soundings and three test piles) was undertaken prior to construction of a new highway on the Noto Peninsula in Japan (Matsumoto et al. 1995). During driving of the test piles, the authors observed generation of large positive pore pressures when the pile tip reached the level of a piezometer, but at farther distances away from the pile, pore pressures could be negative. They also performed redriving tests and static load tests and noted that, in both cases, the generated pore water pressures were small and that resistance was much larger than during initial driving – three times as large during redriving and twice as large during static load testing. These observations point to a significant setup effect, which is potentially in contrast to the behaviors observed by (Nishida 1985).

2.8 PREVIOUS OREGON GEOTECHNICAL REPORTS

2.8.1 Introduction

Since the 1990s, Oregon Departmenet of Transportation (ODOT) has constructed numerous bridges in Klamath County where diatomaceous soils are prevailingly identified. Investigations at these sites were conducted to provide *in-situ* characterization and laboratory test performance of the diatomaceous soils. The locations of investigated sites are shown in Figure 2.34. Here we focus on three components of the site investigations: standard penetration testing (SPT), cone penetration testing (CPT), and laboratory testing.

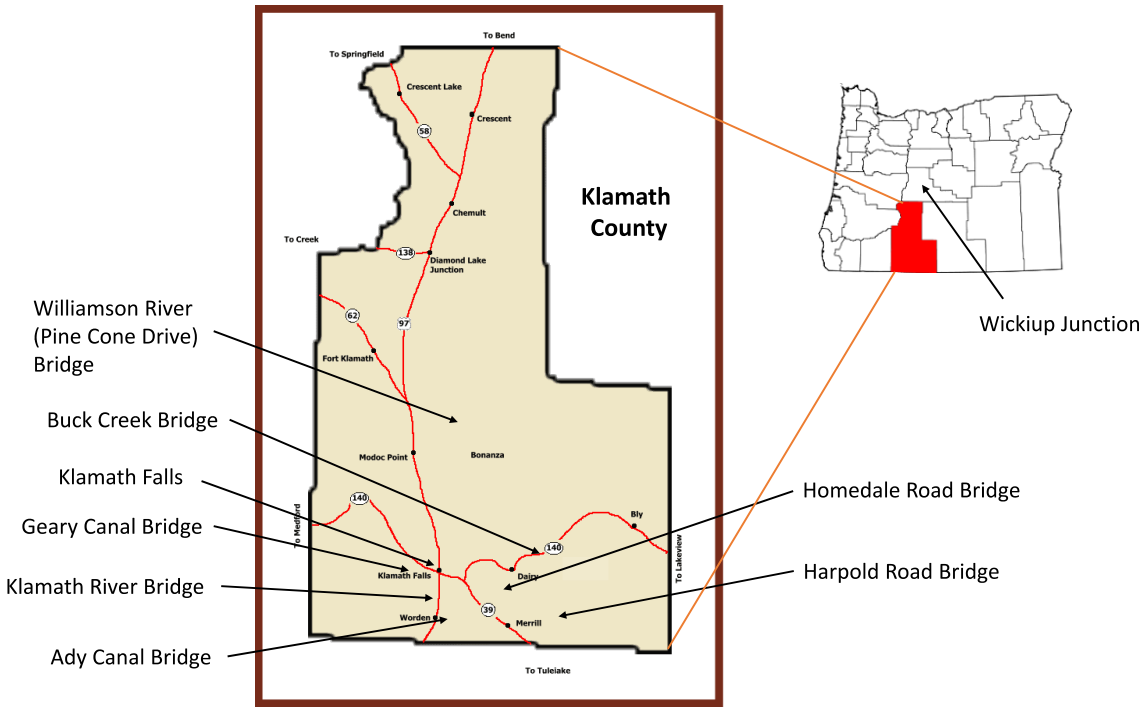

Figure 2.34: Locations of investigated diatomaceous sites in Oregon

2.8.2 Standard Penetration Testing

Standard penetration testing (SPT) is the major test type ODOT has conducted on diatomaceous deposits. As shown in Figure 2.34, except for Wickiup Junction, all other investigated diatomaceous sites are located in Klamath County, OR. In the drill logs of the geotechnical reports, the majority of diatomaceous deposits in Klamath County are described as stiff and hard, likely mudstone state diatomaceous soil. In Wickiup and Ady Canal, there are both soft and stiff diatomaceous soils. Figure 2.35 plots uncorrected N value for various diatomaceous sites (non-diatomaceous SPT are excluded). For those described as stiff diatomaceous sites (Figure 2.35 (a)), N values are clustered around 20 blows, the highest N value being 90 in Pine Cone Drive. Whereas in Ady Canal and Wickiup, 0 blow counts occasionally occurred. The natural water content logs are plotted in Figure 2.36, there is no distinction between stiff and soft diatomaceous, natural water content between 50 and 250. Table 2.3 summarizes the diatomaceous soil characteristics from the different sites. Generally speaking, all diatomaceous

soils are classified as MH from USCS classification method. The colors vary from gray to brown. As stated before, all diatomaceou sites, except Ady Canal and Wickiup which soils vary from soft to stiff, are identified as stiff.

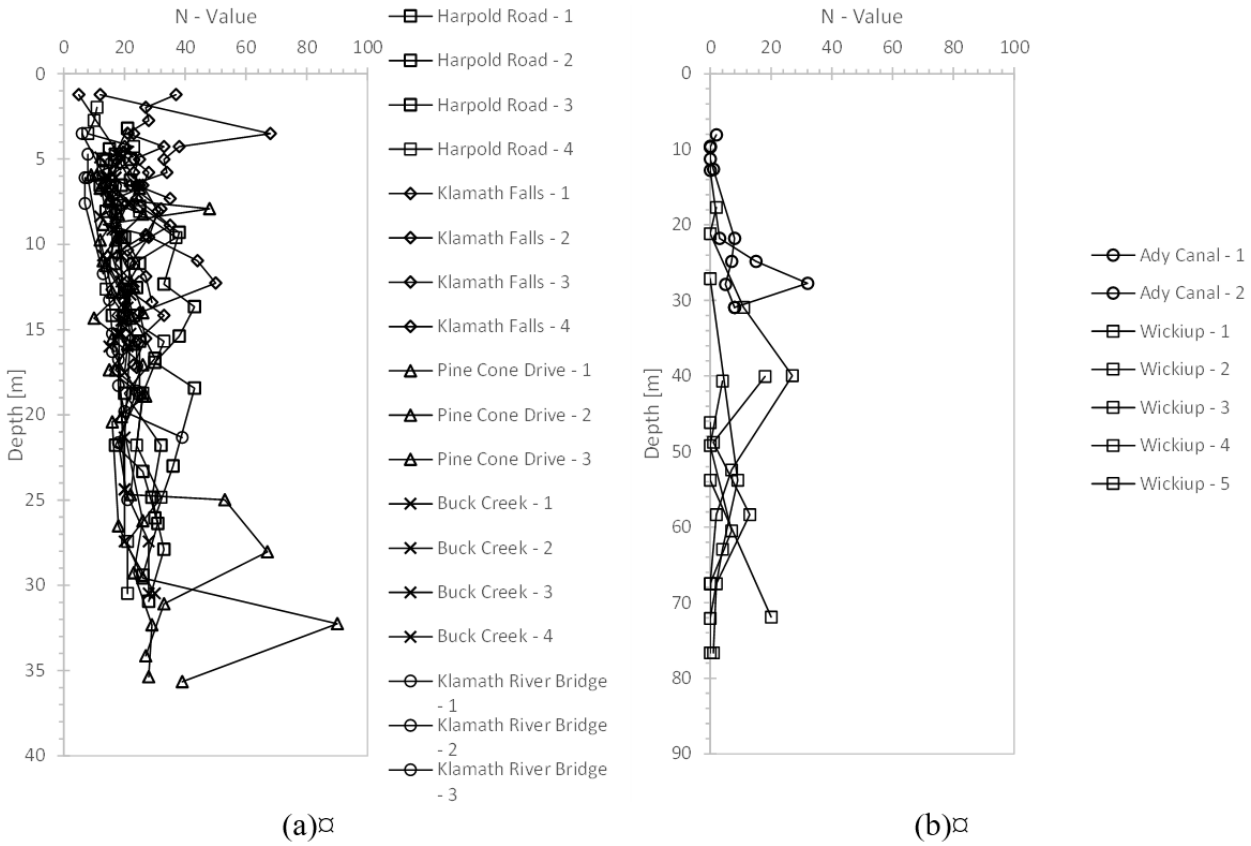

Figure 2.35: Uncorrected N values from various sites from previous ODOT reports: (a). diatomaceous soil described as hard and stiff; (b). diatomaceous sites with both soft and stiff soils

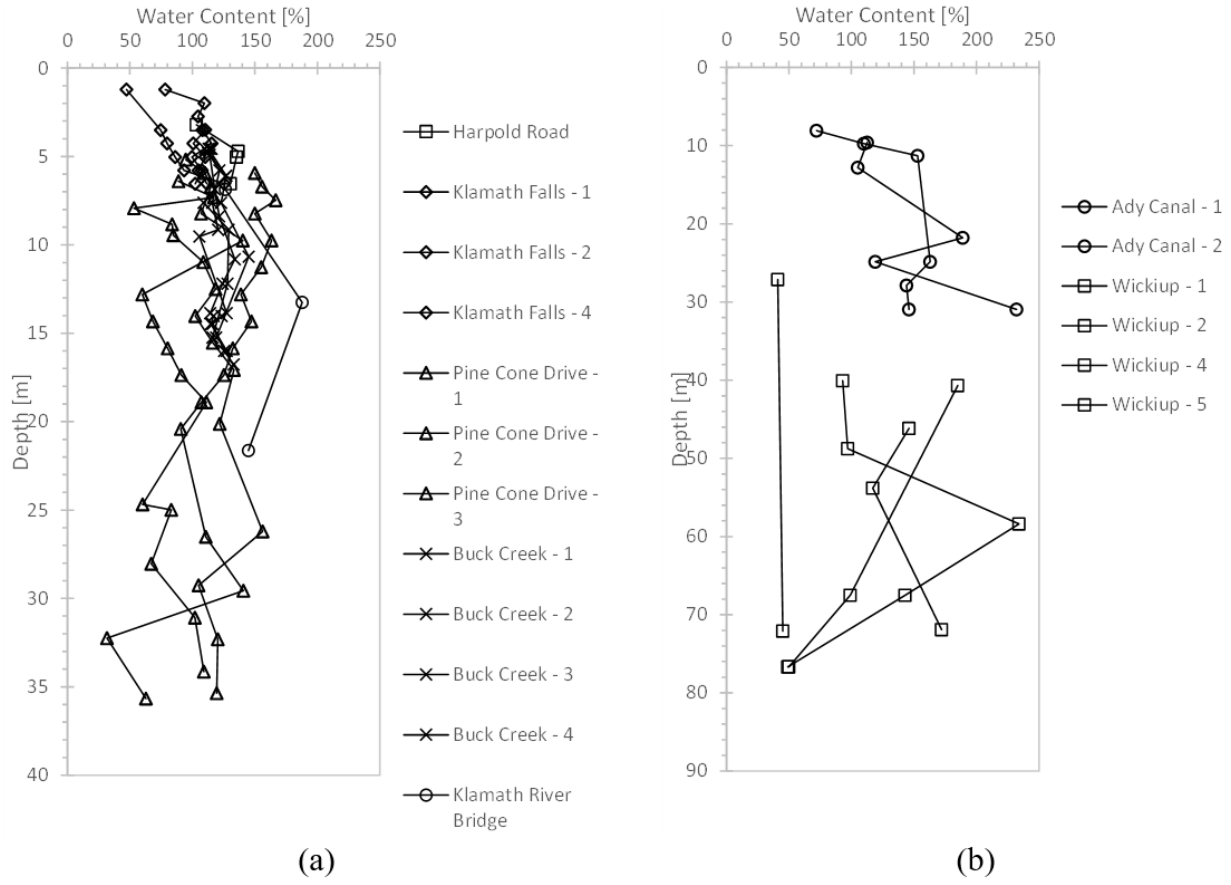

Figure 2.36: Natural water content vs. depth for various sites from previous ODOT reports: (a). diatomaceous soil described as hard and stiff; (b). diatomaceous sites with both soft and stiff soils

Table 2.3: Summary of diatomaceous soil characteristics from different sites

Site	USCS classification	Color	Plasticity	Moisture	Stiffness
Harpold Road	MH	Gray	no to low plasticity	wet	stiff
Klamath Falls	MH	Brown	low plasticity	wet	very stiff
Pine Cone	MH	Gray/Brown	medium to high plastic	wet	very stiff
Buck Creek	MH/ML	Gray/Green-Gray	medium to high plasticity /non-low plasticity	wet	very stiff
Klamath River Bridge	MH	Olive	Not provided	moist	stiff, weakly cemented
Ady Canal	MH	Gray	nonplastic	wet	soft to stiff
Wickiup	MH/ML	Gray/Black	No to medium plastic	wet	Very soft to medium stiff

2.8.3 Cone Penetration Testing

Cone penetration testing (CPT) were conducted in Klamath River Bridge, Geary Canal, Buck Creek and Wickiup (Figure 2.37). The resistance (q_t and f_s) and pore pressure (u_2) are relatively low in Geary Canal and Wickiup. The Geary Canal report (ODOT 1996) mentioned that the undisturbed samples (Shelby tubes) were very difficult to retrieve, which is a further indication of the extremely soft consistency of the soil. In contrast, the diatomaceous soil in Klamath River Bridge and Buck Creek have surprisingly high resistance and pore pressure.

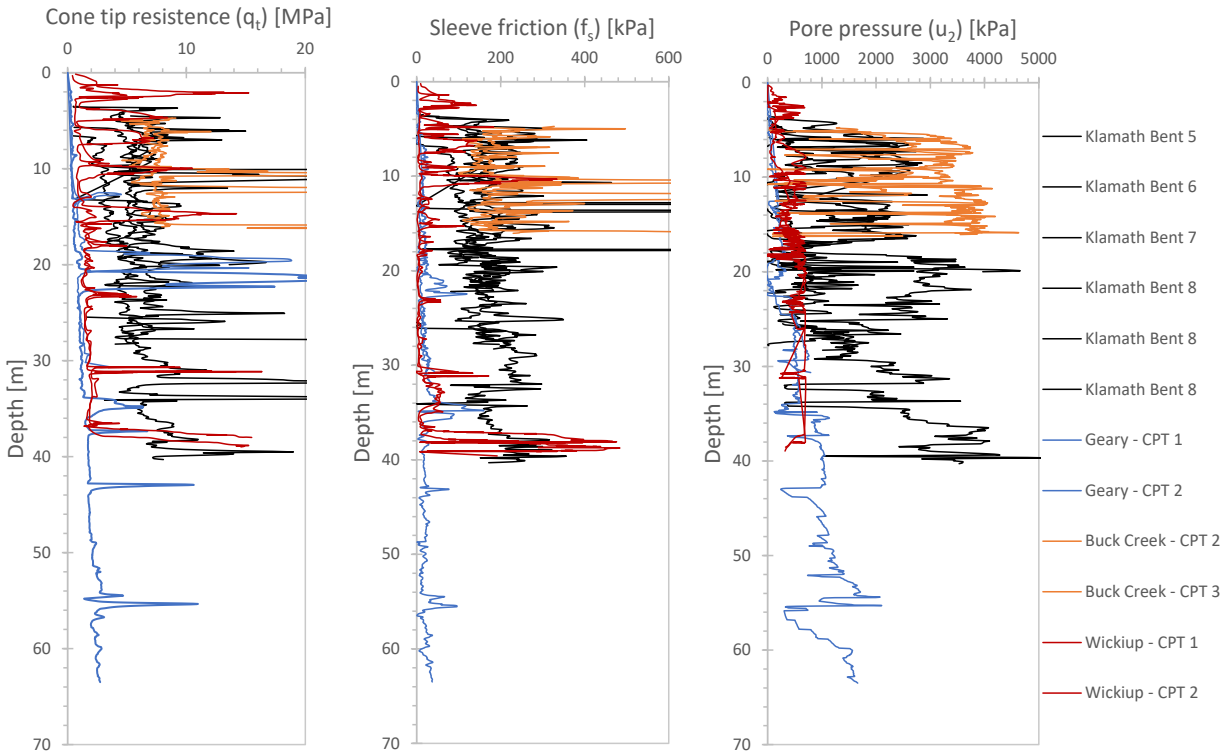

Figure 2.37: CPT sounding results of diatomaceous soil from previous ODOT reports

2.8.4 Laboratory Testing

Consistency limits and specific gravity were widely tested for these diatomaceous soils. Figure 2.38 shows the plasticity chart of diatomaceous soil from different sites. The majority diatomaceous soils can be classified as MH in USCS classification. There is relatively larger scattering for diatomaceous soil from Homedale Road and Wickiup. Figure 2.39 summarizes the relationship between LL and G_s, as expected, specimens with lower G_s show higher LL.

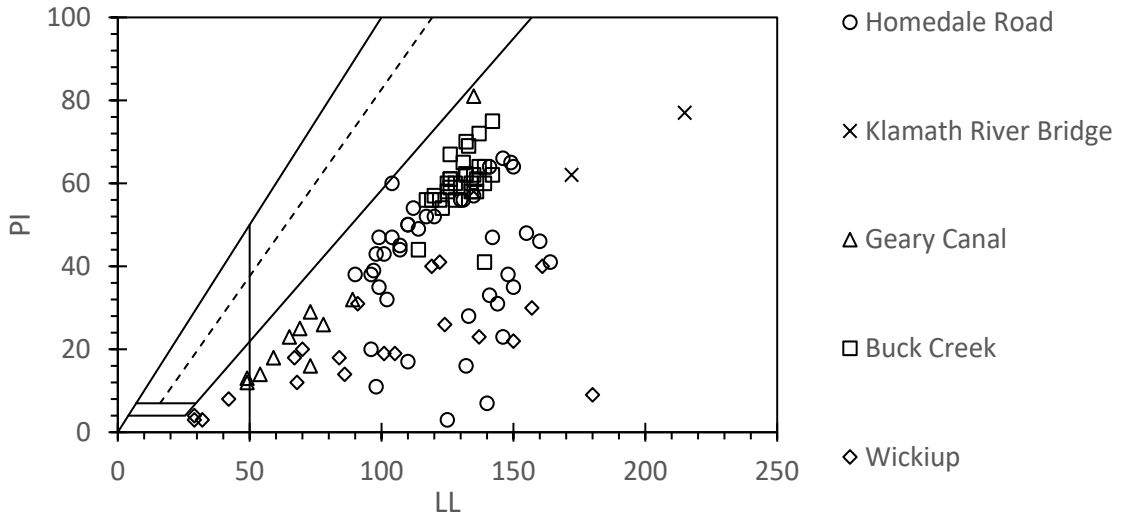

Figure 2.38: Plasticity chart of diatomaceous soil from previous ODOT reports

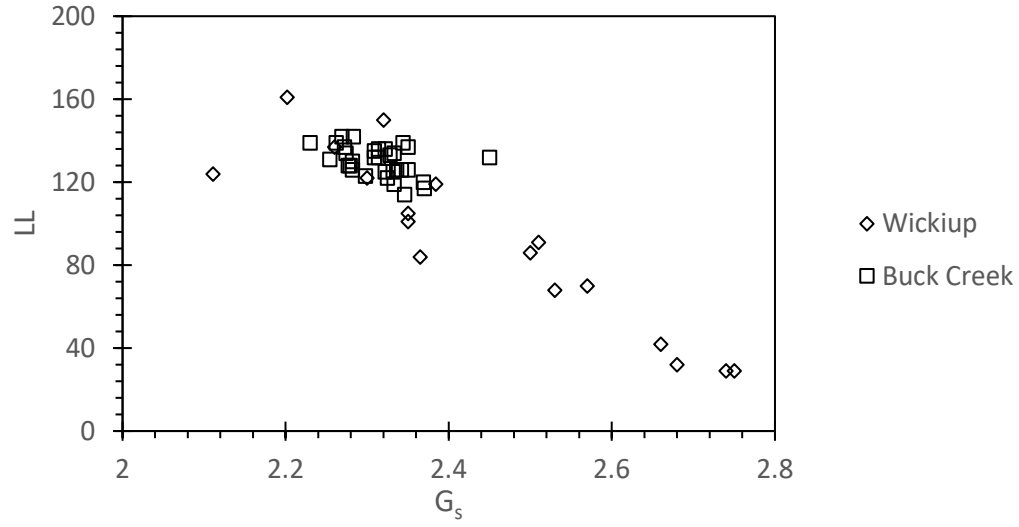

Figure 2.39: Relationship between LL and specific gravity of diatomaceous soil from previous ODOT reports

The compressive and triaxial strength parameters are not widely reported in the previous Oregon reports on diatomaceous soil. Figure 2.40 summarizes C_r vs. C_c and Figure 2.41 summarizes ϕ' vs. LL. It is difficult to see clear trends in these figures due to the limited amount of data.

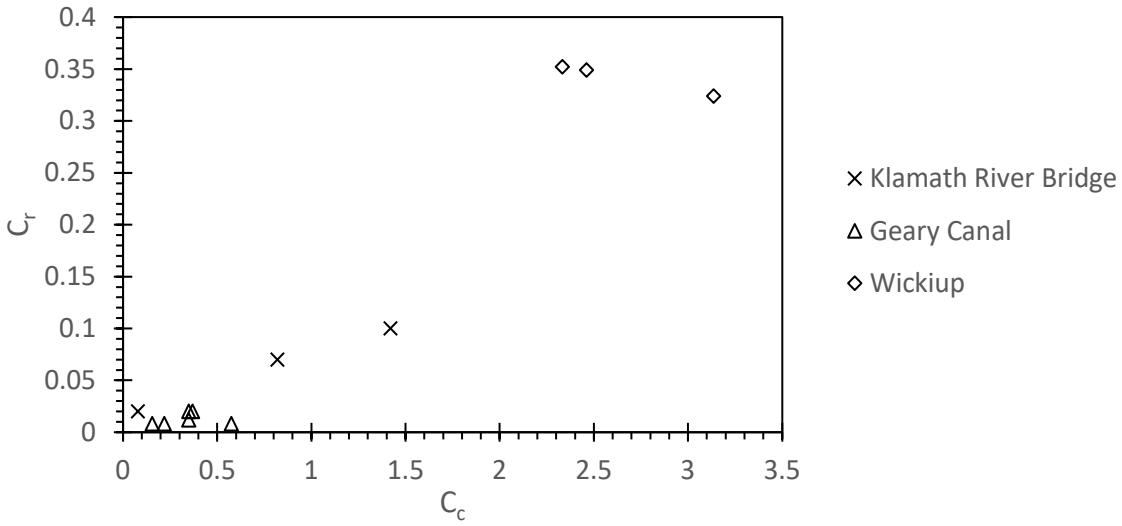

Figure 2.40: Relationship between recompression index and consolidation index of diatomaceous soil from previous ODOT reports

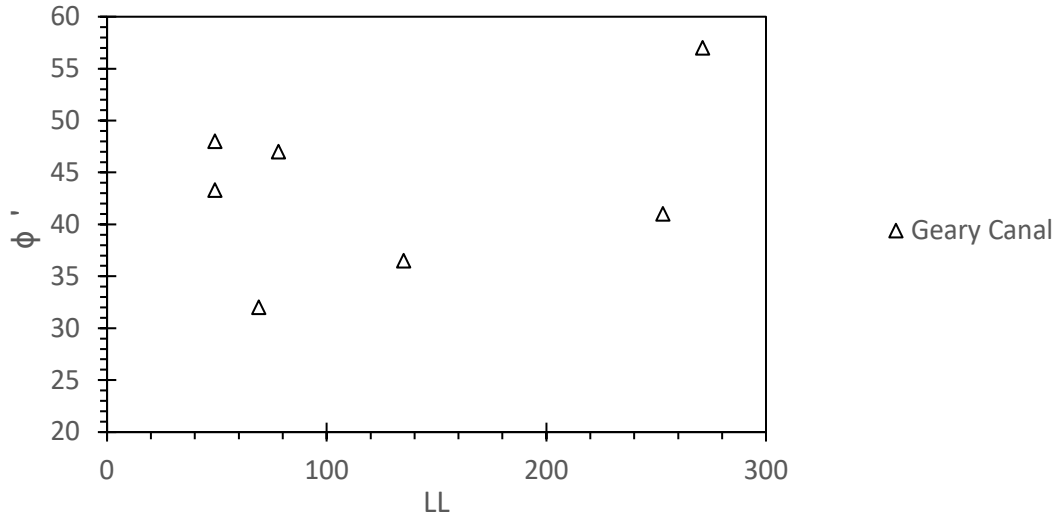

Figure 2.41: Relationship between effective friction angle and liquid limits of diatomaceous soil from previous ODOT reports

2.9 NOTATIONS FOR LITERATURE

2.9.1 Literature on Diatom Mixtures

2002-‘M’-a: (Shiwakoti et al. 2002); 2003-‘M’-a: (Tanaka et al. 2003); 2009-‘M’-a: (Díaz-Rodríguez and Lopez-Molina 2009); 2010-‘M’-a: (Palomino et al. 2010, 2011); 2012-‘M’-a: (Tanaka et al. 2012); 2013-‘M’-a: (Tanaka et al. 2013); 2013-‘M’-b: (Díaz-Rodríguez and

González-Rodríguez 2013); 2015-‘M’-a: (Sonyok 2015); 2017-‘M’-a: (Wiemer et al. 2017; Wiemer and Kopf 2017); 2017-‘M’-b: (Díaz-Rodríguez and Moreno-Arriaga 2017); 2017-‘M’-c: (Frýbová et al. 2017); 2018-‘M’-a: (Shatnawi and Bandini 2018); 2019-‘M’-a: (Caicedo et al. 2019b); 2021-‘M’-a: (Zuluaga et al. 2021); 2021-‘M’-b: (Slebi-Acevedo et al. 2021); 2022-‘M’-a: (Hoang et al. 2022); 2022-‘M’-b: (Perez Leon et al. 2022); 2022-‘M’-c: (Xu et al. 2022); 2022-‘M’-d: (Zuluaga-Astudillo et al. 2022)

2.9.2 Literature on Natural Diatomaceous Soil

Japan:
1991-‘N’-a: (Maekawa et al. 1991); 1992-‘N’-a: (Maekawa et al. 1992); 1998-‘N’-a: (Jardine et al. 1998); 1999-‘N’-a: (Tanaka and Locat 1999); 2001-‘N’-a: (Tanaka et al. 2001); 2002-‘N’-a: (Shiwakoti et al. 2002); 2006-‘N’-a: (Hong et al. 2006); 2011-‘N’-a: (Oka et al. 2011)

South America:
2008-‘N’-a: (Oka et al. 2011); 2019-‘N’-a: (Ovalle et al. 2019; Perisic et al. 2019); 2018-‘N’-a: (Caicedo et al. 2018); 2019-‘N’-b: (Caicedo et al. 2019a); 2019-‘N’-c: (Mendoza et al. 2019); 2014-‘N’-a: (Vera-Grunauer 2014)

Mexico city:
1992-‘N’-b: (Diaz-Rodriguez et al. 1992); 1999-‘N’-b: (Díaz-Rodríguez and López-Flores 1999); 2003-‘N’-a: (Díaz-Rodríguez 2003); 2008-‘N’-b: (Díaz-Rodríguez and Martínez-Vásquez 2008)

Asia:
1998-‘N’-b: (Liao et al. 1998); 2011-‘N’-b: (Lee et al. 2011); 2013-‘N’-a: (Zhang et al. 2013)

United States:
1997-‘N’-a: (Day 1997); 2021-‘N’-a: (Wang et al. 2021; Yazdani et al. 2021)

3.0 SITE CHARACTERIZATION

3.1 SITE SELECTION

Diatomaceous soil is widely spread across southern, central, and eastern Oregon, with many of these deposits being coincidental to ODOT right-of-way. ODOT has conducted numerous construction projects over these deposits, often encountering engineering problems such as excessive settlement and early pile refusal. Four sites along the Highway 97 corridor were selected for field investigation and in-situ testing: three in Klamath County, OR and one in Deschutes County, OR. The map of site locations is shown in Figure 3.1.

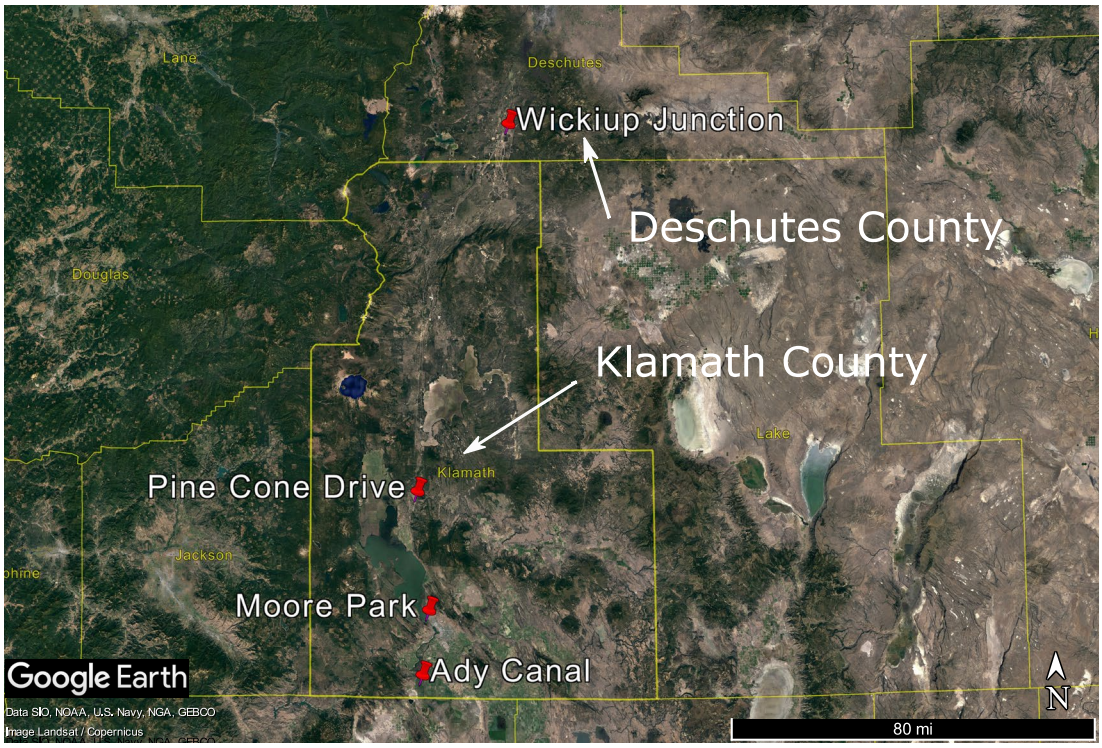

Figure 3.1: A vicinity map showing all four project sites.

At Wickiup Junction, ODOT began construction of an overpass bridge to eliminate the at-grade crossing of US 97 by the BNSF Railway. While construction was paused during the rainy season, excessive settlement of the bridge approach embankment was observed, calling the long-term performance of the structure into question. Site investigation prior to construction showed the existence of diatomaceous soil at the site. *In-situ* and laboratory tests were performed to quantify the engineering properties of soils at the site. The embankment was subsequently designed and constructed in a manner consistent with the current state of practice and standard of care for such a project.

The Ady Canal Bridge is located about 2.4 km east of the intersection of Township Road and Highway 97. A site investigation was conducted at Ady Canal in 1999 in support of the construction of a precast, prestressed concrete bridge to replace the old timber bridge built by the

Klamath Drainage District. Substantial diatomaceous silt was encountered during this investigation with the boring logs identifying five distinct soil units: fill, an upper sand unit, an upper diatomaceous silt unit, a lower sand unit, and a lower diatomaceous silt unit. Standard penetration tests (SPT) were performed during the site investigation.

Pine Cone Drive crosses the Williamson River about 460 m west of the intersection of Pine Cone Drive and Pine Ridge Road. In 1999 a site investigation was conducted at Pine Cone Drive as part of a project to replace a concrete pier. Three boreholes were drilled, revealing a thick diatomaceous silt deposit interspersed with occasional sand lenses. Similar to Ady Canal, only SPTs were conducted and disturbed samples were collected for basic material characterization.

The fourth site investigated was Moore Park, near upper Klamath Lake. Although there was no record of prior site investigations at the site, the geologic setting, including outcrops of stiff diatomaceous materials, and results from proximal site investigations implied that diatomaceous soils would likely be encountered at the site. A brief summary of site descriptions is shown in Table 3.1.

Table 3.1: Summary of site descriptions

	Wickiup Junction	**Ady Canal**	**Pine Cone Drive**	**Moore Park**
Vicinity	La Pine	Klamath Falls	Chiloquin	Klamath Falls
County	Deschutes	Klamath	Klamath	Klamath
Coordinates	43.697542N 121.476967W	42.038927N 121.844196W	42.594132N 121.860604W	42.235226N 121.816065W
Boreholes (depth, m)	B-W1 (77.4) B-W2 (23.6)	B-AC1 (31.7)	B-PC1 (32.8)	B-MP1 (30.9)
CPT (depth, m)	C-W1 (0.7) C-W2 (1.3) C-W3 (61.8)	C-AC1 (18.6) C-AC2 (12.6)	C-PC1 (3.5)	C-MP1 (17.3)
Selection Rationale	Experience indicated the diatomaceous soils at the site are particularly problematic	Previous site investigation encountered very soft diatomaceous soils	Previous site investigation encountered very stiff diatomaceous soils	Geologic indicators of diatomaceous materials, including surficial outcroppings in site vicinity

3.2 IN-SITU TESTING AND SAMPLE RETRIEVAL PROCEDURES

3.2.1 Standard Penetration Test

The standard penetration test (SPT) is one of the oldest *in-situ* site investigation tests. The test drives a split-spoon sampler with a 63.5-kg (140-lb) hammer and uses the number of hammer blows as a measure of soil resistance while collecting a disturbed soil sample for identification purposes (ASTM D 1586; American Society for Testing and Materials (ASTM). 2018b.). This test method requires a borehole into which the split spoon is driven. Two common approaches for advancing boreholes are mud rotary drilling (ASTM D 5783-18; American Society for Testing and Materials (ASTM). 2018.) and hollow-stem auger (HSA) drilling (ASTM D 6151-97; American Society for Testing and Materials (ASTM). 2017.). This test can be performed at any depth interval greater than the 0.45 m (1.5 ft) length of the split spoon sampler. The number of blows for each 0.15 m (0.5 ft) of penetration are counted, and the blows for the last two 0.15 m (0.5 ft) segments are summed to produce a blow count, also commonly referred to as the N-value. The N-value recorded in the field is not directly used to assess soil properties, as it needs to be corrected to a reference condition. The correction for efficiency (coefficients C_E, C_B, C_S, C_R) and correction for overburden effects (coefficient C_N) are needed (Robertson and Fear 1997). The equation for corrected standard penetration resistance, $(N_1)_{60}$, and related coefficients are listed in Equation (3.1):

$$(N_1)_{60} = C_E C_B C_S C_R C_N N_{field} \tag{3-1}$$

where:
$(N_1)_{60}$ = corrected standard penetration resistance, blows/ft;
C_E = energy correction factor; depends mainly on the way that hammer is lifted and released, Table 3.2;
C_B = borehole diameter correction factor, Table 3.2;
C_S = liner correction factor; depends on the sampler used to perform the test, Table 3.2;
C_R = rod length correction factor; depends on the total length of the drill rod, Table 3.2;
C_N = overburden correction factor; calculation shown in Equation (3.2); and
N_{field} = N-value recorded in the field, blows/ft.

$$C_N = \sqrt{\frac{p_{atm}}{\sigma'_{v0}}} \leq 1.5 \tag{3-2}$$

where:
p_{atm} = atmospheric pressure (i.e., 101.3 kPa); and
σ'_{v0} = effective *in-situ* overburden stress.

Table 3.2: Correction factors for measured SPT blow count (Aggour and Radding 2001)

Term	Factor	Equipment variable	Correction
C_E	Energy ratio	Donut hammer	0.5–1.0
		Safety hammer	0.7–1.2
		Automatic hammer	0.8–1.5
C_B	Borehole diameter	65–115 mm	1.0
		150 mm	1.05
		200 mm	1.15
C_S	Sampling method	Standard sampler	1.0
		Non-standard sampler	1.1–1.3
C_R	Rod length	3–4 m	0.75
		4–6 m	0.85
		6–10 m	0.95
		10–> 30 m	1.0

3.2.2 Cone Penetration Test with Pore Pressure Measurement

The cone penetration test (CPT) is a powerful *in-situ* test method for soil investigation. During the test a cone-tipped penetrometer is advanced vertically into the soil at a steady rate (ASTM D 5778-20; American Society for Testing and Materials (ASTM). 2020.). Typically two parameters are measured during the test: q_c (cone tip resistance), f_s (friction sleeve resistance). Most modern penetrometers also measure pore water pressure (PWP), and the test is denoted as CPTu. The pore water pressure can be measured at three different locations on the probe: cone tip (u_1), cone shoulder (u_2; the most common), and friction sleeve (u_3). In this project, the pore water pressures at the cone shoulder (u_2) are measured.

The cone tip resistance (q_c) should be corrected to account for the pore water pressure effects at tip shoulder (Campanella 1988), using Equation (3-3):

$$\boldsymbol{q_t = q_c + (1 - a_n)u_2} \quad \textbf{(3-3)}$$

where:

q_t = corrected tip resistance;
q_c = measured cone tip resistance; and
a_n = net area ratio, constant for a given cone and commonly determined in a calibration chamber.

The CPTu results are often used for soil behavioral classification. There exist several different methods for behavioral classification. One of the most common is presented below:

The Robertson (1990) soil classification chart uses three normalized parameters which are normalized sleeve friction (F_N), pore pressure ratio (B_q), normalized corrected cone tip resistance (Q_t). Their equations are listed from Equation (3-4) – (3-6). A demonstration of the behavioral chart is shown in Figure 3.2.

$$F_N = \frac{f_s}{q_t - \sigma_{v0}} \times 100\% \tag{3-4}$$

$$Q_t = \frac{q_t - \sigma_{v0}}{\sigma'_{v0}} \tag{3-5}$$

$$B_q = \frac{u_2 - u_0}{q_t - \sigma_{v0}} \tag{3-6}$$

where:
F_N = normalized sleeve friction;
u_0 = hydrostatic pore pressure;
σ_{v0} = total vertical stress;
Q_t = normalized corrected cone tip resistance; and
B_q = pore pressure ratio.

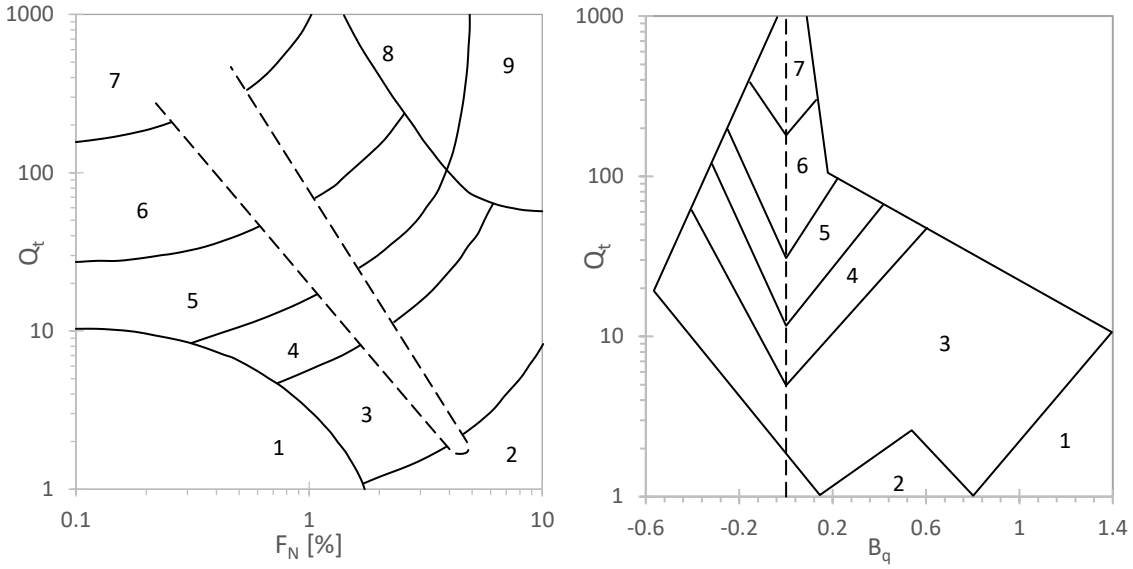

Figure 3.2: Soil behavioral chart (after Robertson 2009, 2016) (Numbers represent soil behavior type delineated in Table 3.3)

The soil behavior type numbers in Figure 3.2 are delineated in Table 3.3. The soil behavior type 2 through 7 are determined by the soil behavior type index (I_c) which is calculated following the iterative steps from Equation (3-7) – (3-9).

Step 1: compute I_c using Equation (3-7):

$$I_c = \sqrt{[3.47 - log(Q_t)]^2 + [log(F_N) + 1.22]^2} \quad \textbf{(3-7)}$$

Step 2: compute stress normalization exponent (n) using Equation (3-8):

$$n = 0.381 I_c + 0.05\left(\frac{\sigma'_{v0}}{p_{atm}}\right) - 0.15 \leq 1.0 \quad \textbf{(3-8)}$$

Step 3: recalculate I_c using Q_{tn} (Equation (3.9)) in place of Q_t:

$$Q_{tn} = \left(\frac{q_t - \sigma_{v0}}{p_{atm}}\right)\left(\frac{p_{atm}}{\sigma'_{v0}}\right)^n \quad \textbf{(3-9)}$$

Table 3.3: Soil behavior type (after Robertson 1990, 2009, 2016)

Soil behavior type index, I_c	Zone (SBTn)	Soil behavior type
-	9	Very stiff fine-grained
-	8	Very stiff sand to clayey sand
$I_c < 1.31$	7	Gravelly sand to dense sand
$1.31 < I_c < 2.05$	6	Sands – clean sand to silty sand
$2.05 < I_c < 2.60$	5	Sand mixture – silty sand to sandy silt
$2.60 < I_c < 2.95$	4	Silt mixture – clayey silt to silty clay
$2.95 < I_c < 3.60$	3	Clays – silty clay to clay
$I_c > 3.60$	2	Organic soils – peat
-	1	Sensitive, fine-grained

Dissipation tests were also performed along with cone advancement at multiple depths to assess the hydrodynamic behavior of the soil. During dissipation tests, radial drainage is much more significant than vertical drainage, and the horizontal coefficient of consolidation (c_h) can be calculated from the dissipation tests at various degrees of consolidation (Baligh and Levadoux 1986; Wroth 1984). In this study, predictions of c_h from Teh and Houlsby (1991) and Burns and Mayne (1998) methods are adopted. Basically, the horizontal coefficient of consolidation is computed by Equation (3-10) for both methods. The difference, though, is in the computation for T^*. The Teh and Houlsby (1991) solution combines the strain path method and large strain finite elements to derive a dissipation model to obtain the distribution of pore water pressures at various stages of dissipation. Table 3.4 provides T^* at different degrees of consolidation at cone shoulder introduced by Teh and Houlsby (1991). Meanwhile, Burns and Mayne (1998) proposed a dissipation model through a combination of cavity expansion theory and critical state soil mechanics. The time factor (T^*) is a function of the friction angle (ϕ') and overconsolidation ratio (OCR). The normalized dissipation curves at various ϕ' and OCRs proposed by Burns and Mayne (1998) are shown in Figure 3.3 - Figure 3.5.

$$c_h = \frac{T^* r^2 \sqrt{I_r}}{t} \tag{3-10}$$

$$I_r = \frac{G}{s_u} \tag{3-11}$$

where:

T^* = modified time factor;
r = radius of the cone, $r = 1.784\ cm$ (area $= 10\ cm^2$) in this project;
I_r = rigidity index, calculated as Equation (3-11);
t = various stages of dissipation;
G = undrained shear modulus, can be estimated as $E_{50}/3$;
E_{50} = secant modulus at half of the undrained shear strength; and
s_u = undrained shear strength.

Table 3.4: Time factor at different stages of dissipation (after Teh and Houlsby 1991)

Degree of consolidation	20%	30%	40%	50%	60%	70%	80%
T^* at cone shoulder	0.038	0.078	0.142	0.245	0.439	0.804	1.6

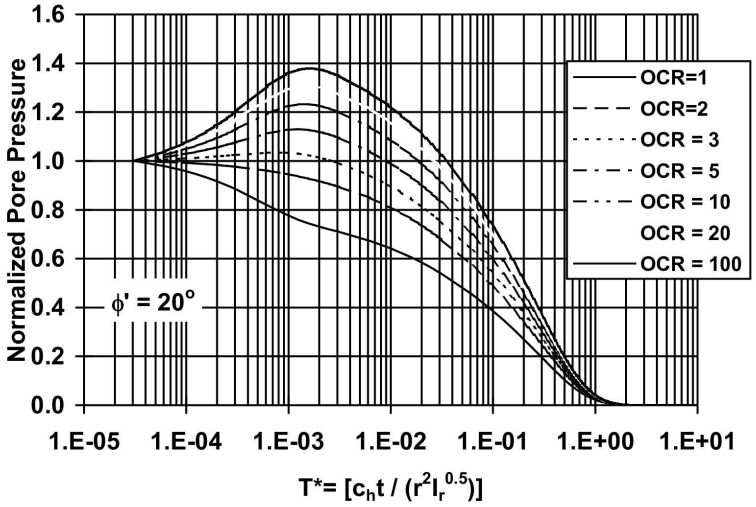

Figure 3.3: Normalized dissipation curves for $\phi' = 20^\circ$ (after Burns and Mayne 1998)

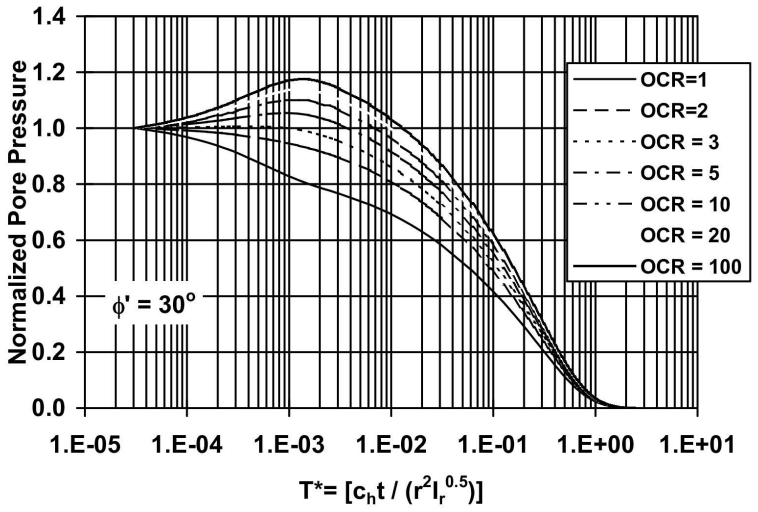

Figure 3.4: Normalized dissipation curves for $\phi' = 30^{\circ}$ (after Burns and Mayne 1998)

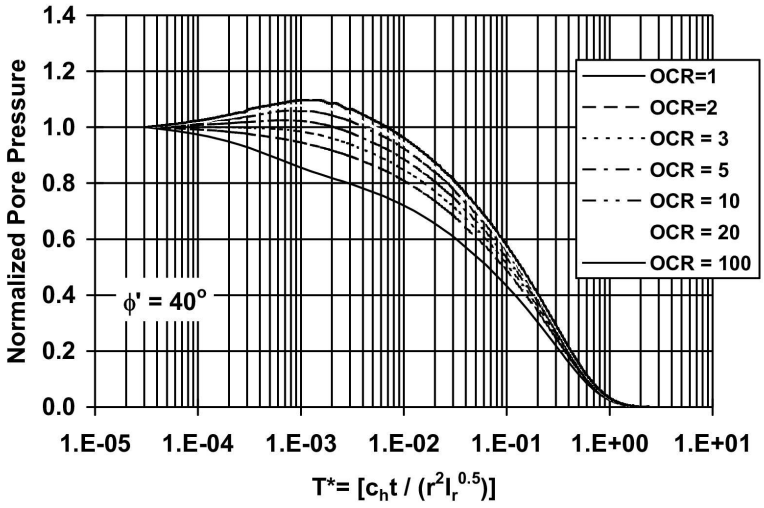

Figure 3.5: Normalized dissipation curves for $\phi' = 40^{\circ}$ (after Burns and Mayne 1998)

3.2.3 *In-situ* Vane Shear Test

The *in-situ* vane shear test (VST) is used to provide a measure of the undrained shear strength of saturated fine-grained soils in the field (ASTM D 2573-18; American Society for Testing and Materials (ASTM). 2018a.). VST is usually used as a supplemental test method in addition to SPT, CPTu, or other undrained shear strength measurement. A four-bladed vane (Figure 3.7) is inserted into the intact soil at the bottom of a borehole and rotated at a defined rate by an operator on the surface to measure the torque required to shear a cylindrical surface with the vane. This torque is then converted to a unit shearing resistance of the failure surface through a limit equilibrium analysis. The system friction is measured with the same procedure except that the bladed vane is taken off while shearing. For a rectangular vane where the height of the blade is twice the width, the conversion from torque to undrained shear strength is calculated as

Equation (3-12), and for a tapered vane (the case of this project), the undrained shear strength is calculated as Equation (3-13):

$$\boldsymbol{s_u = \frac{6T}{7\pi D^3}} \tag{3-12}$$

where:

s_u = peak undrained shear strength from the vane, kPa;
T = measured torque corrected for apparatus and rod friction, $N \cdot m$; and
D = vane diameter, mm, Figure 3.6.

$$\boldsymbol{s_u = \frac{12 \times T}{\pi D^2 \cdot \left(\frac{D}{\cos(i_T)} + \frac{D}{\cos(i_B)} + 6H\right)} \times K} \tag{3-13}$$

where:

H = height of vane, mm;
i_T = angle of taper at vane top, Figure 3.6;
i_B = angle of taper at vane bottom, Figure 3.6; and
K = 1×10^6 for SI units.

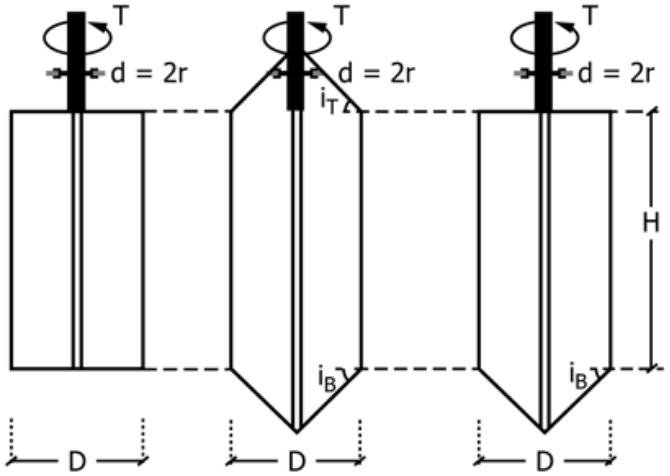

Figure 3.6: Geometry of field vanes, (after ASTM D 2573; American Society for Testing and Materials (ASTM). 2018a.)

The field vane shear test usually reaches a peak torque followed by a residual torque at large strain. The ratio of the peak undrained shear strength to the residual undrained shear strength is the sensitivity, calculated as Equation (3-14):

$$\boldsymbol{S_T = s_u / s_{ur}} \tag{3-14}$$

where:
S_T = sensitivity;
s_u = peak undrained shear strength from the vane; and
s_{ur} = residual undrained shear strength from the vane.

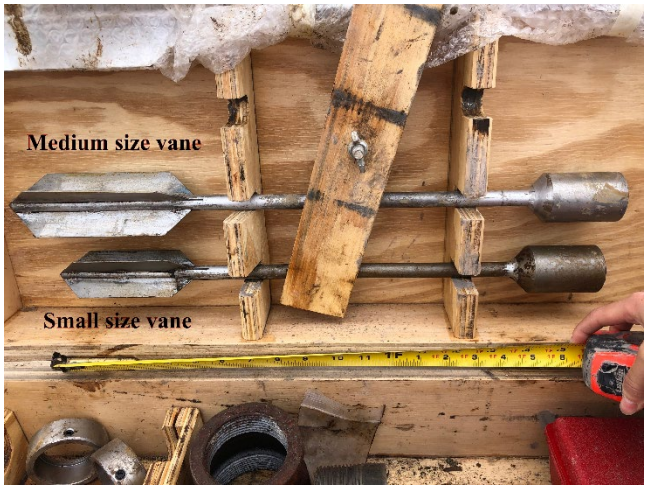

Figure 3.7: *In-situ* vanes used during testing at the project sites (both medium size and small size were used)

3.2.4 Difficulties on Retrieving Shelby Tubes

Shelby tube sampling methods are used to collect undisturbed samples of soft, fine-grained (cohesive) soils in an effort to recover intact samples which are representative of the *in-situ* soil conditions. The stainless steel, thin wall, 36-inch Shelby tubes were pushed into the soil at the bottom of the borehole at select intervals. It has been very difficult to retrieve Shelby tubes from diatomaceous deposits not only from previous geotechnical reports (Geary Canal, OR; ODOT 1996) but also from this project. Diatomaceous soils vary between "pudding-like" and "chalk-like" states, both contribute great challenges to Shelby tube retrievals. "Pudding-like" diatomaceous soil exists more in Wickiup Junction and Moore Park out of four investigated sites. In Wickiup Junction, around 40% (9 out of 23) Shelby tube retrievals were zero recovery, which indicates very soft material, likely "pudding-like" diatomaceous soil. In Moore Park, soil extruded from Shelby tubes shows a mixture of "pudding-like" and "chalk-like" material. The complex feature made the drilling hard to push at the site and the soil difficult to test at the lab: most of Shelby tubes in Moore Park only drilled around 1.5 ft out of 3 ft of Shelby tube total length, the stiffness and hardness of soil made the tube bottom damaged deeply which questions the "un disturbance" of the soil; meanwhile, part of the extruded soil from Moore Park Shelby tubes was so soft that it was very difficult to run any shear tests or consolidation tests. Pine Cone Drive has more "chalk-like" diatomaceous soil. Shelby tubes were pushed down around 2.5 ft in Ady Canal and 1.5 ft in Pine Cone Drive. The recoveries were around 1.5-2 ft for Ady Canal and 1-1.5 ft for Pine Cone Drive. The similar problem that the Shelby tube bottom damage happened in Pine Cone Drive as well. Like Moore Park, it was difficult to obtain intact specimens for lab tests from Pine Cone Drive.

3.2.5 Sample Storage

Proper sample handling and storage are critical post-extraction to maximize the likelihood of having absolute best-quality samples for testing. Split spoon samples were immediately transferred to plastic bags and sealed in the field. All bags were stored in a lidded bucket away from the direct sunlight. At the end of each day, each bag was placed into an individual long-term storage bag and vacuum sealed to isolate each sample from the environment. Under these conditions the moisture content should remain constant for extended periods, even at room temperature, which is critical for measurement of natural water content (w_n) and estimation of *in-situ* unit weight (γ).

A similar level of care was exercised in handling Shelby tubes after retrieval of intact specimens. Immediately upon retrieval, melted wax was used to seal both ends of the tube prior to affixing the plastic end caps with multiple layers of electrical tape. The ends of the tubes were then wrapped in duct tape to protect the electrical tape. On site, Shelby tubes were stored upright in buckets. At the end of each day, the buckets were moved to a vehicle and firmly secured to prevent overturning during transport. The samples were temporarily stored indoors, off-site. Every two days the tubes were transported to the ODOT moist room for storage. As needed the tubes were subsequently taken to the OSU geotechnical laboratory for testing. Specimens were extracted for testing using a vertical piston-type extruder. At no point from extraction to testing were the tubes permitted to be in any orientation other than vertical.

3.3 SUBSURFACE EXPLORATION

3.3.1 Wickiup Junction

Mud rotary drilling was used to advance two boreholes at Wickiup Junction, B-W1 and B-W2. Photographs showing the mud rotary drilling approach are presented in Figure 3.8. The majority of testing and sample collection were conducted in the first borehole, B-W1. The second borehole, B-W2, was advanced to explore lateral variability in the diatomaceous deposits. Less testing and sampling was performed in this borehole.

From prior site explorations, the diatomaceous deposit at Wickiup Junction was known to be deep. Thus, work above a depth of 16.76 m (55 ft) consisted only of SPT and split spoon sampling at 3.05 m (10 ft) intervals. Below that depth, a pattern of Shelby tube sampling, vane shear testing (VST), and SPT with split spoon samples was followed every 1.52 m (5 ft) until 30.48 m (100 ft) depth. From 30.48 m (100 ft) to the end of the borehole, VST was no longer performed, but Shelby tube sampling and SPT with split spoon samples were continued at 1.52 m (5 ft) to 3.05 m (10 ft) intervals. Shelby tube samples proved difficult to retrieve. Nearly 40% (11/28) of attempts resulted in zero recovery. The piston sampler was employed for Shelby tubes above 43.6 m depth, and the non-piston sampler was used at greater depths in an attempt to improve recovery. During SPT, it was common to encounter resistance of ‘weight of rods’ (WOR) or ‘weight of hammer’ (WOH), indicative of soft soil. The *in-situ* VST were conducted, but susceptible to torque wrench breakdown, slippage, and inconsistent readings. For borehole B-W2, three Shelby tube samples, three VST, and one SPT with split spoon sample were obtained.

(a) (b)

Figure 3.8: Drilling at Wickiup Junction: (a) drill rig; and (b) closeup of mud rotary operation.

Through inspection of split spoon samples, it is possible to preliminarily identify subsurface soil strata based on the soil texture, color, moisture content, and consistency. Accordingly, six soil layers were initially delineated based on soil texture and apparent moisture content, as shown in Table 3.5. There are two sand layers in the profile: from the ground surface to a depth of 12.65 m and again from 46.33–51.82 m depth. Between the two sand layers two distinct clay/silt layers were identified based on their texture and apparent water content. From 12.65–28.80 m depth, the soil appears wetter and more clayey, and the color is darker (Figure 3.9 (a)). From 28.80–46.33 m depth, the soil is siltier, and the color is grey to brown (Figure 3.9 (b)). The soil beneath the lower sand lenses is appreciably stiffer and appears much drier (Figure 3.9 (c)).

Table 3.5: Preliminary layer identification for Wickiup Junction

Layer Depth	Layer Description	Example Photo
0–12.65 m (0–41.5 ft)	Sands, wet, nonplastic	n/a
12.65–28.80 m (41.5–94.5 ft)	Dark clay, wet, soft, plastic	Figure 3.9 (a)
28.80–46.33 m (94.5–152 ft)	Grey to brown silt, mid-stiff, damp	Figure 3.9 (b)
46.33–51.82 m (152–170 ft)	Sands, wet, nonplastic	n/a
51.82–68.43 m (170–224.5 ft)	Brown to dark grey silt, stiff, damp to dry	Figure 3.9 (c)
68.43–77.37 m (224.5–253.83 ft)	Dense sand and gravel, possibly weathered rock	n/a

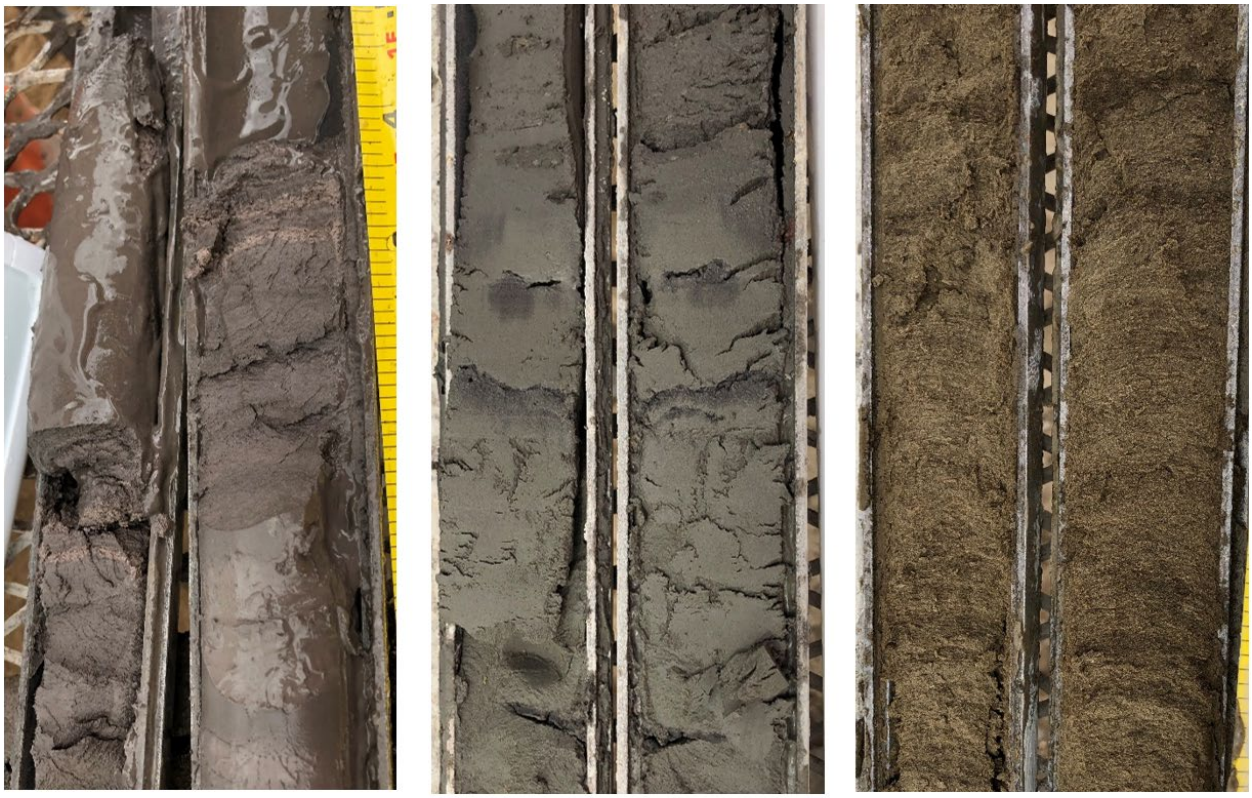

(a). W1N8 (depth: 20.88 m) (b). W1N15 (depth: 37.34 m) (c). W1N26 (depth: 65.91 m)

Figure 3.9: Selected split spoon samples from three silt layers in Wickiup Junction

The CPTu soundings at Wickiup Junction were conducted concurrently with drilling. The CPTu was located approximately 27.43 m (90 ft) from the drill rig so that the drill operations would not interfere with the shear wave velocity (V_s) measurements, which were taken every 1 m during the push. Two initial CPTu were attempted but experienced refusal at shallow depths (C-W1: 0.7 m; C-W2: 1.25 m). A 3.66 m (12 ft) pilot hole was predrilled prior to attempting the third sounding, which was successful. The cone was pushed to a depth of 61.75 m (203 ft) before system capacity was reached. Eleven dissipation tests were conducted during the push for a total

dissipation time of 215 minutes with most dissipation tests finishing in 20 minutes. Photographs of the CPTu push are shown in Figure 3.10.

(a) (b)

Figure 3.10: (a) pre-boring the hole for the third attempted CPT push; and (b) view inside of the cone truck during cone advancement.

3.3.2 Ady Canal

The borehole at Ady Canal was advanced to 31.70 m (104 ft) below ground surface (bgs) using a hollow stem auger (HSA), owing to the relatively stiff soil. The drilling approach is shown in Figure 3.11. The pattern for *in-situ* operations, in order, was: Shelby tube sampling, VST, and SPT with split spoon samples followed by advancing the borehole for 1.52 m (5 ft). The 3-ft Shelby tubs were pushed 2.5 ft, and the recoveries were between 1.5–2.3 ft. No Shelby tubes had zero recovery. Above a depth of 17.22 m (56.5 ft) SPT resistance was mostly WOR or WOH. SPT blow counts trended higher in the remainder of the borehole. A total of 5 VST were performed at intervals of 3.05–9.14 m (10–30 ft). The last three VST had no residual shear strength measurements after peak.

Four soil layers were identified based on observation of the split spoon samples, as summarized in Table 3.6. The color of split spoon samples was mostly green in the silt layers, example photos are shown in Figure 3.12.

(a) (b)

Figure 3.11: Hollow stem auger (HSA) drilling rig at Ady Canal

Table 3.6: Preliminary layer identification for Ady Canal

Layer Depth	Layer Description	Example Photo
0–9.14 m (0–30 ft)	Organic soil and sands, fill	n/a
9.14–12.19 m (30–40 ft)	Green silt, damp to dry	Figure 3.12(a)
12.19–16.76 m (40–55 ft)	Sands	n/a
16.76–31.70 m (55–104 ft)	Green to grey silt, stiff, damp to dry	Figure 3.12(b)

Two CPTu soundings were advanced at Ady Canal. The first CPTu reached refusal at a depth of 18 m (59 ft). Shear wave velocities (V_s) were measured at 1 m (3.3 ft) intervals. Two dissipation tests were performed at depths of 7.6 m (24.9 ft) and 11.75 m (38.5 ft). Both reached approximately 90% dissipation in 20 minutes. The second CPTu stopped at 12 m (39.4 ft) depth. Two dissipation tests were run at depths of 8.7 m (28.5 ft) and 10.65 m (34.9 ft). Pore pressure dissipated slowly during the test at 8.7 m (28.5 ft) and was stopped after 40 minutes. The second one, at 10.65 m (34.9 ft) depth, reached approximately 80% dissipation in 30 minutes.

(a). AC1N4 (depth: 9.45 m) (b). AC1N9 (depth: 20.27 m)

Figure 3.12: Selected split spoon samples from the two silt layers at Ady Canal

3.3.3 Pine Cone Drive

The soil at Pine Cone Drive was quite stiff, so HSA was adopted to advance the borehole. Images of the site and HSA drilling are shown in Figure 3.13. At the start of drilling, substantial mud was being produced at the ground surface (Figure 3.13(b)), which was not observed at other sites where HSA drilling was employed. Shelby tube samples were retrieved every 3.05 m (10 ft) followed by SPT with split spoon samples. Upon retrieval, a number of Shelby tubes were observed to have severely damaged leading edges due to the high soil stiffness, as seen in Figure 3.14. Unlike pushing full length of Shelby tubes at Wickiup and Ady Canal, only 1.2 ft of the length was pushed on average when retrieving samples. The subsurface at Pine Cone Drive was largely uniform, based on split spoon samples retrieved during drilling (Table 3.7). The material was very stiff, brittle, and only lightly moist Figure 3.15. Due to the high stiffness of the soil, VST was not conducted at this site.

Pushing a CPT at Pine Cone Drive proved infeasible. Both the on-site Geoprobe and a powerful track-rig Geoprobe attempted to advance a starter hole but did not succeed. Refusal occurred at a depth of 3.5 m.

(a) Beginning of HSA advancement (b) Generation of mud from HSA operations

Figure 3.13: Site view and HSA at Pine Cone Drive

(a). PC1U3 (b). PC1U5 (c). PC1U6

Figure 3.14: Examples of damaged bottom of Shelby tubes from Pine Cone Drive

Table 3.7: Preliminary layer identification for Pine Cone Drive

Layer Depth	Layer Description	Example Photo
0–32.77 m (0–107.5 ft)	Light grey silt, very stiff, damp to dry	Figure 3.15

(a). PC1N1 (depth: 3.51 m) (b). PC1N5 (depth: 14.48 m) (c). PC1N8 (depth: 23.71 m)

Figure 3.15: Selected split spoon samples in Pine Cone Drive

3.3.4 Moore Park

Unlike the other three sites where there had been previous construction and a former site investigation, there was no prior subsurface data for Moore. Moore Park is located in the upper Klamath lake area and local geology implies the presence of diatomaceous soil in the subsurface profile. One borehole was advanced to 30.94 m (101.5 ft) using an HSA. The start of HSA drilling is shown in Figure 3.16. Shelby tube samples were collected every 3.05 m (10 ft) above 13.72 m (45 ft) depth bgs followed by SPT with split spoon samples. Below 13.72 m (45 ft), the frequency for Shelby tubes retrieval and SPT with split spoon samples was every 1.52 m (5 ft). It was extremely difficult to obtain Shelby tube samples due to the high stiffness of the soil. It was often not possible to push the full length of the tube into the soil deposit, resulting in many tubes that were severely damaged, likely causing significant disturbance to the sample that was recovered (similar to Figure 3.14). Relatively high SPT blow counts were observed during sampling, gradually increasing with depth. Only one VST was attempted, at a depth of 5.94 m (19.5 ft), where the soil was relatively soft.

Inspection of split spoon samples indicated that the subsurface is largely uniform below 6.10 m (20 ft) depth. The soil color is from green to grey, stiffness is high, and soil is damp to dry (Figure 3.17). The preliminary layer identification is shown in Table 3.8.

Figure 3.16: Start of HSA drilling at Moore Park

Table 3.8: Preliminary layer identification for Moore Park

Layer Depth	Layer Description	Example Photo
0–6.10 m (0–20 ft)	Coarse sands, wet	n/a
6.10–30.94 m (20–101.5 ft)	Green to grey silt, stiff, damp to dry	Figure 3.17

One CPTu sounding was advanced at Moore Park, reaching refusal at a depth of 17.3 m. Excess pore water pressures were very high, consistently in the range of 2000-2500 kPa and spiking to over 5000 kPa. Four dissipation tests were performed and all reached dissipation in 5–10 minutes.

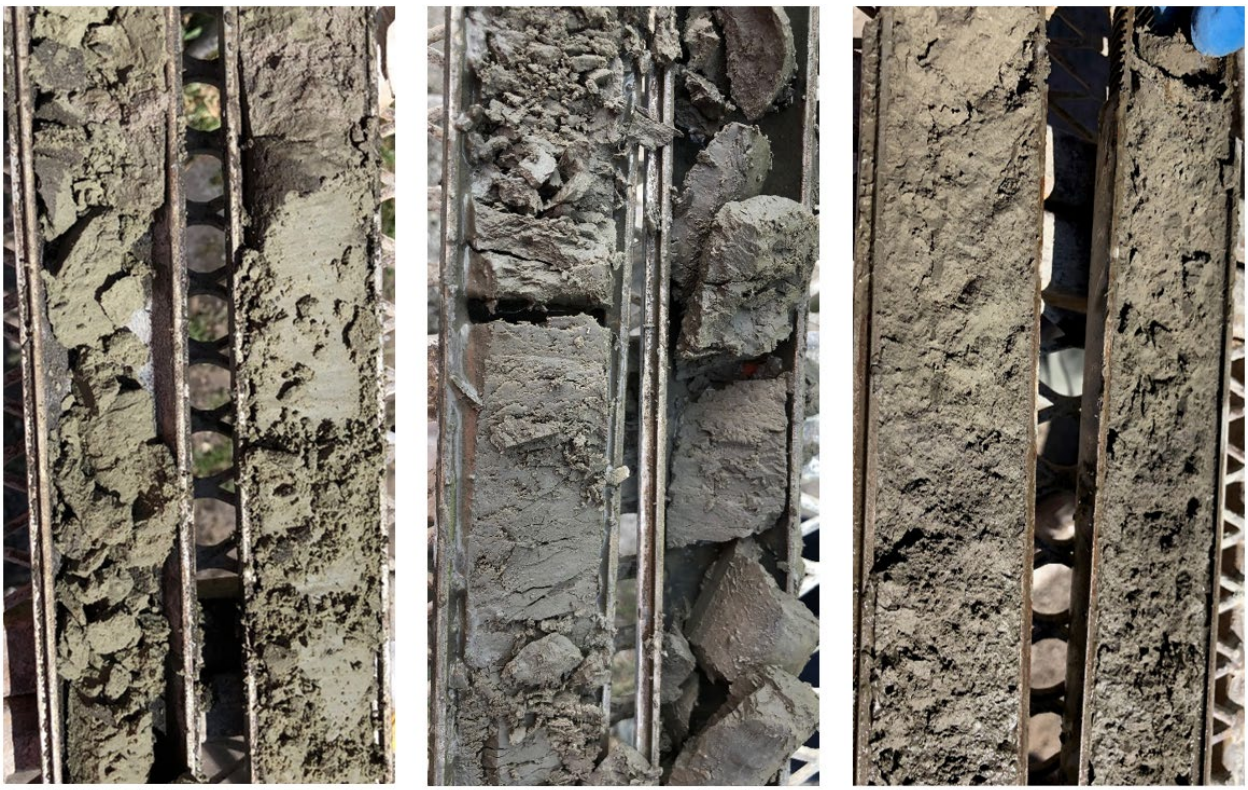

(a) MP1N3 (depth: 8.84 m) (b) MP1N8 (depth: 20.27 m) (c) MP1N13(depth: 30.94 m)

Figure 3.17: Selected split spoon samples from the silt layer at Moore Park

3.4 TEST AND SAMPLE NAMING CONVENTION

Each of the *in-situ* tests and samples were named following a specific pattern: *site acronym* + *drill log#* + *test/sample acronym* + *test/sample#*. The acronyms of sites and tests/samples are shown in Table 3.9. The tests or samples are numbered sequentially along depth. For example, the first SPT and split spoon sample at the first Wickiup Junction borehole is named as W1N1 and the third undisturbed sample recovered in the first Ady Canal borehole is AC1U3. The field work is summarized visually in Figure 3.18.

Table 3.9: Acronyms of sites and tests/samples

	Name	Acronym
Borehole	Wickiup Junction	B-W1 B-W2
	Moore Park	B-MP1
	Ady Canal	B-AC1
	Pine Cone Drive	B-PC1
CPTu Sounding	Wickiup Junction	C-W1 C-W2 C-W3
	Moore Park	C-MP1
	Ady Canal	C-AC1 C-AC2
	Pine Cone Drive	C-PC1
Test/sample	Split spoon sample/SPT	N
	In-situ vane shear test	V
	Undisturbed sample (Shelby)	U
	Dissipation test	D

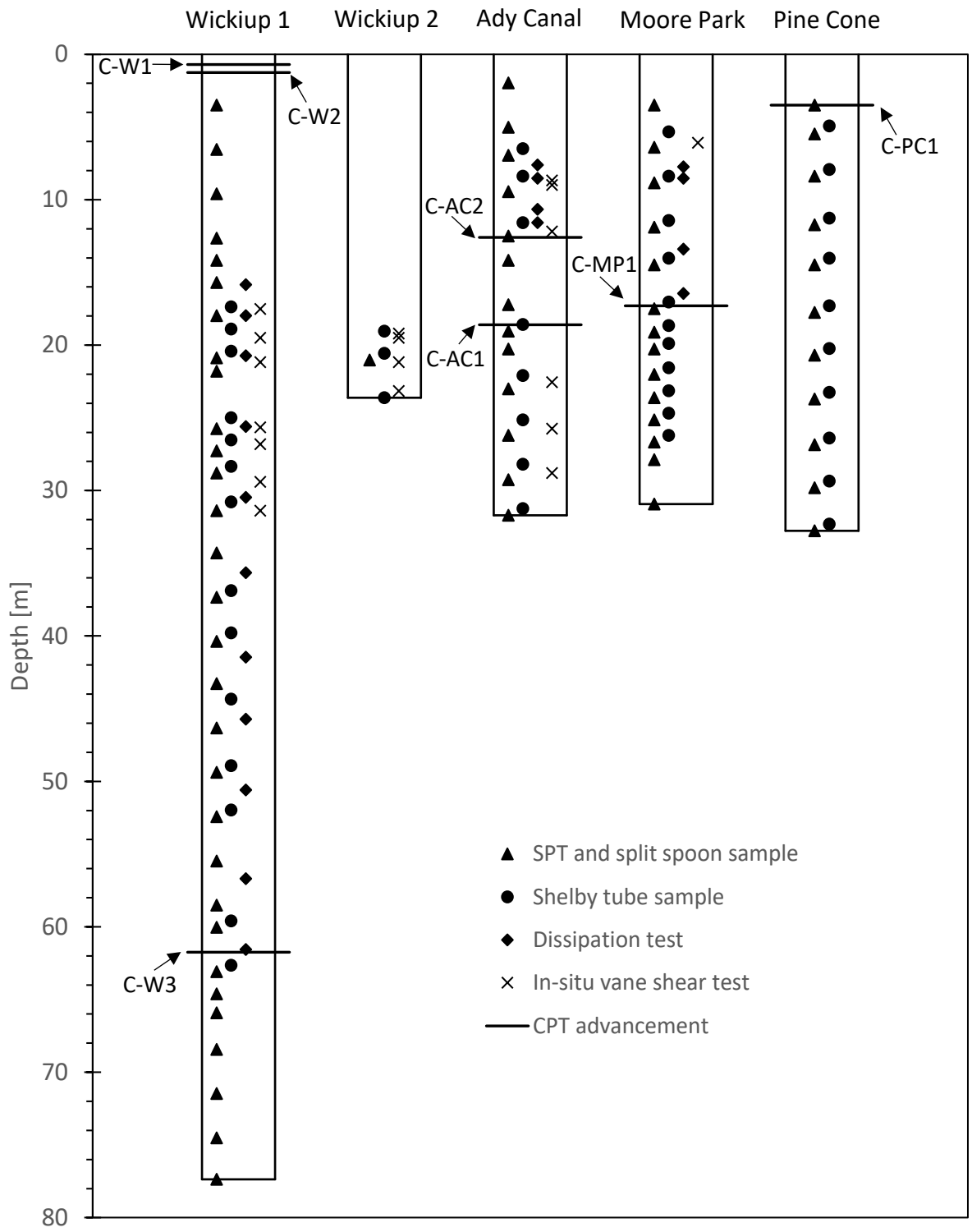

Figure 3.18: Field work scheme

4.0 LABORATORY TEST PROGRAM AND PROTOCOLS

4.1 INTRODUCTION

The laboratory test program is mainly divided into two categories: physical properties and mechanical properties. Physical-property tests were predominantly conducted on split spoon samples. Physical property tests are relatively easy to perform and because diatomaceous soil has very unique features, it is often possible to identify diatomaceous soil layers using these tests alone. The mechanical properties are directly related to engineering behavior. Intact (i.e., Shelby tube) samples from diatomaceous layers (as identified through physical property tests) were used for mechanical property testing. Some tests were performed on both split spoon samples and intact samples to provide a direct link between split spoon and Shelby tube samples, which were taken vertically adjacent to each other in the soil column. Table 4.1 summarizes the test program scheme.

Table 4.1: Test program scheme

Soil type	Test type	Tested sample selection
Fine-grained samples	Specific gravity (G_s), unit weight (γ), grain size distribution (GSD), scanning electron microscope (SEM) images	Samples selected for tests every 2-3 m in depth
Fine-grained samples	Consistency limits (LL, PL)	Nearly every diatomaceous sample
Fine-grained samples	Specific surface area (SSA)	Less frequent due to the time-consuming process
Sands or fine-grained samples	Natural water content (w_n),	All samples

Results from physical property tests on split spoon samples were used to screen for diatomaceous soils. Shelby tubes deemed to have a high likelihood of containing diatomaceous soil were opened and undisturbed specimens were extruded for lab tests. Testing was focused on compression characteristics and shear strength. Hydrodynamic consolidation behavior was measured in constant rate of strain (CRS) or increment loading (IL) tests for nearly every Shelby tube. Triaxial tests or direct simple shear (DSS) tests were performed to measure soil monotonic shearing behavior. Consistency limits were measured on specimens extracted from every Shelby tube to assess similarity between the Shelby tube materials and those from adjacent split spoons.

This chapter describes the laboratory testing program, including specimen preparation, test procedures, standards and references, and data reduction.

4.2 PHYSICAL PROPERTY TESTING

4.2.1 Scanning Electron Microscope Imaging

Scanning electron microscopy is used to directly study the surfaces of solid objects using a focused beam of electrons. Diatoms have a unique hollow structure that comes from the death of inner algae organics. The size of diatom particles typically varies from 1-75 μm (Diaz-Rodríguez 2011; Wiemer and Kopf 2017). It is easy to identify them under an electron microscope. While other physical properties such as high liquid and plastic limits, high natural water content, high compressibility can imply the presence of diatoms, the most robust mechanism for identifying diatomaceous soils is by performing SEM imaging to seek visual confirmation of diatoms in the soil matrix. SEM imaging was performed on all fine-grained materials obtained from split spoon sampling. Specimens were oven dried and ground into fine particles with a mortar and pestle. To obtain uniform specimens, the ground soils were mechanically mixed. Then, fine soil particles were sprinkled onto a circular stub with a copper tape. The SEM imaging was performed with FEI QUANTA 600FEG environmental SEM. The goal was to look for diatom particles and qualitatively identify the relative amount of diatom particles. Images of different locations of the stub were captured with different magnifications.

4.2.2 Natural Water Content

The natural water content (w_n) was measured on all collected soil samples in general accordance with ASTM D2216 (American Society for Testing and Materials (ASTM). 2019.). Three different subsamples of soil (each ≳20 g) from one specimen were oven dried to measure w_n, and the average was calculated. A drying oven with a temperature of 110 ± 5℃ was used to hold the specimens at temperature for 12-16 h. Longer drying hours was also conducted to confirm the mass remains constant after 12-16 h. The equation to calculate the water content is as Equation (2-1):

$$\boldsymbol{w_n = \frac{M_w}{M_s} \times 100} \tag{4-1}$$

where:
w_n = natural water content, %;
M_{cms} = mass of container and moist specimen, g;
M_{cds} = mass of container and oven dried specimen, g;
M_c = mass of container, g;
M_w = mass of water ($= M_{cms} - M_{cds}$), g; and
M_s = mass of soil solids ($= M_{cds} - M_c$), g.

Natural water content provides a convenient means to compute the in-situ void ratio of the material via the following simple relationship:

$$\boldsymbol{S_r \cdot e = w_n G_s} \tag{4-2}$$

where:
S_r = degree of saturation (in decimal form; i.e., $0 \leq S_r \leq 1$);
e = void ratio of the specimen;
w_n = natural water content (in decimal form); and
G_s = specific gravity of soil solids (see Section 4.2.4 below).

However, Equation (4-2) suffers from the fact that it relies upon knowledge of the degree of saturation (see Section 4.2.3 below) of the specimen to allow for direct computation of void ratio. To this end, it is often assumed that $S_r = 1$ below the groundwater table, but this is not always valid and inevitably introduces some error into the determination of weight and volume relationships.

4.2.3 *In-situ* Unit Weight

Due to their hollow structure, diatomaceous soils typically have a unit weight lower than many other soils (often 12-13 kN/m^3). Thus, unit weight can provide a qualitative indication of diatomaceous soil. The wax immersion method was adopted to measure the unit weight in general accordance with ASTM D7263 (American Society for Testing and Materials (ASTM). 2021b.). For a given test, a cohesive "chunk" approximately $3 \times 3 \times 1.5\ cm^3$ was extracted from a split spoon sample and the initial weight was measured. The sample was then coated by dipping it into a container of melted wax, making sure not to trap air bubbles under the wax. The wax-coated weight of the specimen is then measured in air and in water, the latter by immersing the specimen while suspended by a wire. The total unit weight of the soil is then calculated using Equation (4-3) to (4-5).

$$\boldsymbol{V = \left(\frac{(M_c - M_{sub})}{\rho_w}\right) - \left(\frac{(M_c - M_t)}{\rho_x}\right)} \tag{4-3}$$

$$\boldsymbol{\rho_t = \frac{M_t}{V}} \tag{4-4}$$

$$\boldsymbol{\gamma = \rho_t g} \tag{4-5}$$

where:
V = volume of test specimen, cm^3;
M_c = mass of wax-coated specimen, g;
M_{sub} = mass of wax-coated specimen submerged in water, g;
ρ_w = density of water at test temperature, g/cm^3;
M_t = mass of moist specimen, g;
ρ_x = density of wax, g/cm^3;
ρ_t = total density, g/cm^3;
g = acceleration of gravity, taken as 9.8 m/s^2; and
γ = unit weight of specimen, kN/m^3.

Two different soil chunks were selected from a given fine-grained stratum in a split spoon sample and the final unit weight is determined as the average of the two measurements. Due to the need for immersion in melted wax followed by suspension of the wax-coated soil specimen in water, this method is only suitable for soil samples that can be cut into cohesive chunks without appreciable volume change. Thus, sticky, clayey, or granular soil samples are not amenable to the wax immersion method for determination of unit weight (e.g., Figure 4.1).

In conjunction with specific gravity (G_s) and natural water content (w_n), the unit weight can be used to calculate degree of saturation using Equation (4-6).

$$S_r = \frac{\gamma G_s w_n}{G_s \gamma_w (1 + w_n) - \gamma} \tag{4-6}$$

where:
S_r = saturation, [ ];
w_n = natural water content, [ ];
G_s = specific gravity;
γ_w = unit weight of water, kN/m^3; and
γ = unit weight of soil specimen, kN/m^3.

(a) PC1N2 (b) W1N11

Figure 4.1: Typical split spoon samples showing (a) specimens suitable for unit weight measurement using the wax immersion method; and (b) other specimens that are not amenable to this procedure.

While nearly all samples were collected from below the groundwater table, some of the split spoon samples appear to be quite dry (e.g., Figure 3.15), calling into question any assumptions about full saturation. An accurate determination of saturation is helpful for interpretation of observed soil behaviors.

4.2.4 Specific Gravity

Specific gravity (G_s) is the ratio of the density of soil solids to water density at $20^{\circ}C$. It is an important parameter in mass-volume relationships for soils. For most geologic materials, the specific gravity lies in a narrow range of approximately 2.60-2.75, but for diatomaceous soils, it can be appreciably lower (≈1.9-2.2). Thus, the specific gravity is often a reliable indicator of the presence of diatomaceous soils.

The water pycnometer method (ASTM D854-14; American Society for Testing and Materials (ASTM). 2014.) was used to measure the specific gravity of specimens obtained from the split spoon samples. The test procedures in this study are:

a) Calibrate the pycnometer to obtain its actual mass and volume;
b) Prepare oven-dried specimen with mass of 35 ± 5 g, and grind the soil as fine as possible with a mortar and pestle;
c) Carefully direct the soil solids into the pycnometer with a funnel, add water until the water level is between 1/3 and 1/2 of the depth of the main body, and agitate the water until slurry is formed;
d) The boiling method was used to deair the soil slurry: place the pycnometer on the burner for at least 2 h after the soil slurry comes to a full boil, agitate the slurry during boiling to prevent it from sticking to the glass;
e) Cool the pycnometer with soil slurry and filling it with distilled water, and place it in an insulated container overnight to achieve thermal equilibrium;
f) Measure the total mass of pycnometer, soil, and water as well as the temperature of the soil-water mixture.

Calculate the specific gravity using Equations (4-7) and (4-8)

$$\boldsymbol{G_t = \frac{\rho_s}{\rho_{w,t}} = \frac{M_s}{M_p + V_p \cdot \rho_{w,t} - \left(M_{\rho ws,t} - M_s\right)}} \quad \textbf{(4-7)}$$

$$\boldsymbol{G_{20^{\circ}C} = K \cdot G_t = G_s} \quad \textbf{(4-8)}$$

where:
G_t = specific gravity of soil solids at test temperature;
ρ_s = density of soil solids, g/cm^3;
$\rho_{w,t}$ = density of water at test temperature, g/cm^3;
M_s = mass of the oven dried soil solids, g;
M_p = calibrated mass of dry pycnometer, g;
V_p = calibrated volume of the pycnometer, mL;
$M_{\rho ws,t}$ = mass of pycnometer, water, and soil solids at the test temperature, g; and
K = temperature correction coefficient, given in ASTM D854.

4.2.5 Grain Size Distribution

Knowledge of the grain size distribution (GSD) of a soil is necessary for classification purposes as it plays an important role in determining its engineering properties. Diatomaceous soils are typically silt-size (d < 0.1 mm; e.g., (Diaz-Rodríguez, 2011) (Wiemer and Kopf, 2017)), precluding the need for sieve analysis (ASTM D 6913; American Society for Testing and Materials (ASTM). 2017e.). In this study, the washing method was used to determine the fines content (i.e., material passing the No. 200 sieve, d < 0.075 mm), and the hydrometer test was then used to measure the GSD of the fines.

4.2.5.1 Fines content by washing

Fines contents of specimens were measured in accordance with ASTM D 1140 (American Society for Testing and Materials (ASTM). 2017c.). This method specifies washing soil material on a 75-μm (No. 200) sieve to separate fine- from coarse-grained materials. Approximately 50 g of oven dried soil (originally from a split spoon sample) is ground with a mortar and pestle before soaking in distilled water for 24 h. The entire specimen is transferred onto a 75-μm (No. 200) sieve, washed by hand using a stream of water until no fine material remains on the sieve. The retained material is rinsed into a container and oven dried. The fines content is calculated using Equation (4-9):

$$FC = \frac{M_i - M_c}{M_i} \tag{4-9}$$

where:
FC = mass fraction of the specimen finer than 75-μm (typically expressed as a percentage);
M_i = initial oven-dry mass of the specimen, g; and
M_c = oven-dry mass of the specimen retained on the 75-μm (No. 200) sieve, g.

4.2.5.2 Hydrometer test

The hydrometer test (ASTM D7928-21; American Society for Testing and Materials (ASTM). 2021a.) is used to determine the GSD of soil materials that are finer than 75-μm (No. 200) sieve and larger than about 0.2 μm (the diameter at which Brownian motion overwhelms gravitational settling; (Ludwig, 1997)). Sedimentation analysis is based on Stokes' Law, which says that larger particles will fall through a fluid faster than smaller particles, and thus, particles are sorted by size in both time and position. A hydrometer is used to measure the density of a soil-fluid suspension which is then used to infer the quantity of particles in suspension at a specific time and position. A 151H-type hydrometer was used for the work described herein. A summary of the procedures used are as follows:

a) Obtain a specimen of approximately 30-50 g of oven dried soil that is finer than the 75-μm (No. 200) sieve. Add distilled water to make a slurry. Dissolve 5 g of sodium hexametaphosphate in 100 mL distilled water and mix the solution with the slurry in a dispersion cup. Rest for 24 h.

b) On the day of testing, use a stirring apparatus to agitate the soil-fluid mixture for 1 minute to break soil agglomerates. Transfer the soil slurry into a 1000-mL sedimentation cylinder, rinse all remaining slurry from the dispersion cup, into the cylinder, and then add distilled water to the sedimentation cylinder to the 1000 mL mark. Similarly, prepare a control cylinder filled with the reference solution (5 g of sodium hexametaphosphate dissolved in distilled water) for calibration.
c) The tipping method was used to mix the slurry inside the cylinder: place a rubber stopper in the open end and use palms to cover both ends and turn the cylinder upside down and back for 1 minute. Quickly remove any possible foam and add water to the 1000 mL mark, start the timer.
d) Hydrometer readings shall be taken at elapsed times of approximately, 1, 2, 4, 8, 15, 30, 60, 240, and 1440 minutes. For each time of reading, gently lower the hydrometer into the solution about 15 to 20 s prior to the reading time. At the prescribed time, record the hydrometer reading (r_m) and the total elapsed time (t_m). Gently remove the hydrometer from the suspension and use a thermometer to measure the temperature. The same procedure is followed to take hydrometer and temperature readings for the control cylinder at five approximately evenly spaced intervals throughout the testing period.

A temperature-based calibration relationship is needed, and the readings from the control cylinder are used. The offset reading for temperature-density correction is calculated with Equation (4-13).

The GSD is then calculated from the collected data using Equations (4-10) – (4-16) below.

$$\boldsymbol{D_m = \left(\sqrt{\frac{18\mu}{\rho_w g(G_s - 1)} \cdot \frac{H_m}{t_m}}\right) \times 10} \tag{4-10}$$

$$\boldsymbol{N_m = \left(\frac{G_s}{G_s - 1}\right)\left(\frac{V_{sp}}{M_d}\right)\rho_c\left(r_m - r_{d,m}\right) \times 100} \tag{4-11}$$

$$\boldsymbol{H_m = H_{r2} + \left(\frac{H_{r1} - H_{r2}}{r_2 - r_1} \times (r_2 - r_m + C_m)\right) - \frac{V_{hb}}{2A_c}} \tag{4-12}$$

$$\boldsymbol{r_{d,m} = A - 7.784 \times 10^{-6} \times T_m - 4.959 \times 10^{-6} \times T_m^2} \tag{4-13}$$

$$\boldsymbol{A_n = R_{151,n} + 7.784 \times 10^{-6} \times T_n + 4.959 \times 10^{-6} \times T_n^2} \tag{4-14}$$

where:

D_m = particle diameter, mm;

μ = 0.0100 $g/(cm \cdot s)$, dynamic viscosity of water at 20℃;

ρ_w = 1.00 g/cm^3, mass density of water at 20℃;

g = 980.7 cm/s^2, acceleration due to gravity;

t_m = elapsed time, s;

H_m = particle fall distance, Equation (4-12), cm;

N_m = mass percent finer at reading m, %;

V_{sp} = 1000 mL, total volume of suspension;

ρ_c = 0.99821 g/cm^3, mass density of water at the temperature of manufacturer calibration;

M_d = dry soil mass, g;

G_s = specific gravity of soil;

r_m = hydrometer reading in suspension;

$r_{d,m}$ = specific gravity hydrometer offset reading, Equation (4-13);

V_{hb} = volume of the hydrometer bulb up to the base of the stem (i.e., the volume of the bulb up to r_2 in Figure 4.2), cm^3;

A_c = cross-sectional area of the sedimentation cylinder, cm^3;

H_r = distance between the center of buoyancy (Figure 4.2) and the minimum (H_{r1}) and maximum (H_{r2}) hydrometer readings, cm;

r = minimum ($r_1 = 0.995$) and maximum ($r_2 = 1.038$) reading for a 151H hydrometer;

C_m = meniscus correction, given as 0.0005 for a 151H hydrometer;

A = average of the specific gravity shifts ($A_n \in A_1 \ldots A_5$, see Equation (4-14) for a 151H hydrometer over the control cylinder measurements; $\sigma_A < 0.0005$ where σ_A is the standard deviation of A_n;

$T_{m(n)}$ = temperature at reading $m(n)$, ℃;

A_n = specific gravity shift for 151H hydrometer at reading number n; and

$R_{151,n}$ = the 151H hydrometer reading at reading number n.

In practice, the calculated percent finer from the first hydrometer reading (N_1) may be > 100 due to random errors. In this case, the N_m are corrected proportionally by requiring $N_1 = 100$ and using Equation (4-15):

$$\boldsymbol{N_{m,corrected} = N_m \text{ if } N_1 \leq 100}$$

$$\boldsymbol{N_{m,corrected} = \frac{N_m}{N_1} \times 100 \text{ if } N_1 > 100} \qquad \textbf{(4-15)}$$

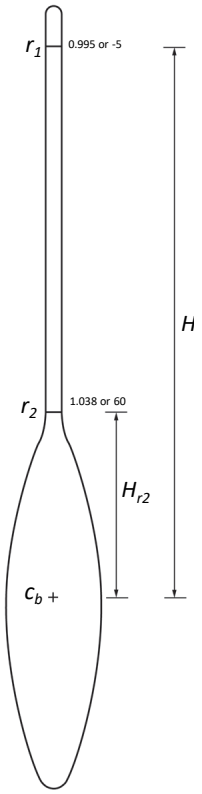

Figure 4.2: Effective depth dimensional measurements (ASTM D7928)

4.2.5.3 Final grain size distribution

Since the hydrometer test is only performed on the portion of the soil specimen finer than the 75-μm (No. 200) sieve, the results from fines washing and hydrometer testing are combined to obtain the final grain size distribution (GSD). The calculation is shown in Equation (4-16):

$$\boldsymbol{N_{m,final} = FC \text{ for } D_m = 75\ \mu m}$$

$$\boldsymbol{N_{m,final} = N_{m,corrected} \times FC/100 \text{ for } D_m < 75\ \mu m} \quad \textbf{(4-16)}$$

where all terms are previously defined.

4.2.6 Consistency Limits

Consistency limits are relatively simple measurements often used as a proxy for inferring quite complex information about fine-grained soils, including clay electrochemistry, shear strength, and compressibility. The liquid limit (LL) and plastic limit (PL) form the basis of the plasticity chart, which is critical for the USCS soil classification of any soil with a fines content greater than 5% (i.e., $P_{200} > 0.05$ where P_{200} is the fraction of material passing the #200 sieve). Wang et al. (2022) found that there is inconsistency between the Casagrande method and the fall cone method in determining LL. The determination methods of consistency measurements of

diatomaceous soil have never been emphasized in the literature, therefore, different methods are compared in this project on measuring LL and PL.

Unlike other physical properties that were mostly tested on split spoon samples, consistency limits (LL and PL) were measured for nearly all split spoon and undisturbed samples that were deemed to potentially be diatomaceous. Three distinct procedures were used to measure LL: the Casagrande cup test (ASTM D4318–17; American Society for Testing and Materials (ASTM). 2017d.), the fall cone test (BSI 2022), and the lab vane test (ASTM D4648/D4648M–16; American Society for Testing and Materials (ASTM). 2016c.). Three approaches were also used to determine PL: direct measurement via thread rolling (ASTM D4318–17; American Society for Testing and Materials (ASTM). 2017d.), semi-direct measurement with a fall cone (Wood and Wroth, 1978), and indirect measurement with a fall cone (Feng, 2001).

4.2.6.1 Liquid limit measurements

1. Casagrande cup test

Two types of Casagrande cup were used to measure LL: motorized cup and hand-operated cup (Figure 4.3). The hand-operated cup was used on split spoon samples which were tested in the early stage of the study, whereas the motorized cup was used on undisturbed samples tested later in the work. While results (Wang et al. 2022) show good consistency between the two types of cups, the motorized cup was obtained to facilitate consistency across operators.

Overall, the procedures outlined in ASTM D4318-17 (American Society for Testing and Materials (ASTM). 2017d.) were followed, but there was one adaption made based on experience with diatomaceous soils: the use of grooving tool. The standard specifies a flat grooving tool (Figure 4.4 (a)) to make a groove in the soil. In this study, the curved grooving tool specified in AASHTO T 89 (AASHTO T 89; Standard Method of Test for Determining the Liquid Limit of Soils) was used (Figure 4.4 (b)). The flat grooving tool has the advantage that it controls the depth of soil when grooving. In the case of diatomaceous soil, its viscous properties make the soil easily slide in the cup (Figure 4.5). Therefore, it is difficult to use the flat grooving tool as it tends to slide the diatomaceous soil along the surface of the cup.

Figure 4.3: Casagrande cups (left: motorized; right: hand-operated)

(a) (b)

Figure 4.4: Casagrande cup grooving tool: (a) flat grooving tool; (b) curved grooving tool.

Figure 4.5: Example of diatomaceous soil sliding along the surface of the cup to close the groove.

The test procedures are as follows:

a) Grind a specimen of oven-dried soil and pass it through the 425-μm (No. 40) sieve. Obtain 100-200 g of the soil passing the No. 40 sieve and mix it with distilled water to make a paste (the water content is usually around 1.5 LL). Rest the soil paste for 24h.
b) Gradually dry the specimen to a water content that requires 7-10 blows to close the groove. Repeat the test three times at the same water content and confirm that the relative difference in number of blows across the replicate measurements is less than 10%. Record the number of blows and measure the water content of a specimen extracted from near the closed groove.
c) Continue drying the specimen to get similar measurements at higher numbers of blows. Experience indicates that it is difficult to obtain numbers of blows >25, but best effort was made to obtain as wide a range of blow counts as possible. Data should be acquired at a minimum of four different points.
d) Plot the relationship between the water content (w) and the corresponding blow counts (N) on a semilogarithmic scale ($w - \log(N)$), best fit the data points with a

line of the form $w = a + b \log N$ (a, b = fitting parameters). The water content corresponding to $N = 25$ is the LL.

2. Fall cone test

The fall cone test is an alternative to the Casagrande cup to determine LL. The fall cone test is a fundamentally strength test (Hansbo 1957; Houlsby 1982; Wroth and Wood 1978) with a criterion that depends on the size and the weight of the cone. In BSI (2022), a 30° cone of total mass 80 g is used, and the water content corresponding to penetration of 20 mm corresponds to the LL. This is predicated upon the fact that the shear strength at the liquid limit for all remolded fine-grained soils is in the range 1.7 – 2.4 kPa.

The British standard (BSI 2022) specifies that "the water content of the specimen should not be alternately increased and reduced but either increased or reduced in stages" during fall cone tests, which means that the test should proceed consistently from the drier to the wetter condition or the wetter to the dryer condition. Wang et al. (2022) observed that the testing directions (wet-to-dry or dry-to-wet) have an influence on the results for diatomaceous soil but not for Kaolinite (Figure 4.6) even though the British standard (BSI 2022) accepts both testing directions (wet-to-dry or dry-to-wet). The schematic demonstration of how testing directions influence the determination of LL and PL using Feng (2001) is shown in Figure 4.7, more details of determining PL using Feng (2001) is seen in 4.2.6.2.

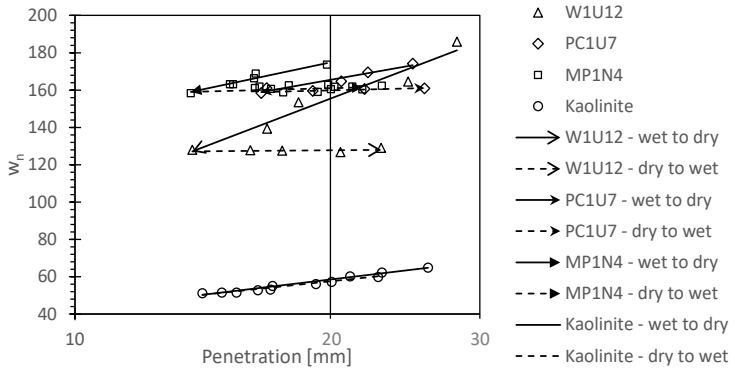

Figure 4.6: Wetting drying cycles in the fall cone test (W1U12, PC1U7, and MP1N4 are different diatomaceous soil specimens) (after Wang et al. 2022)

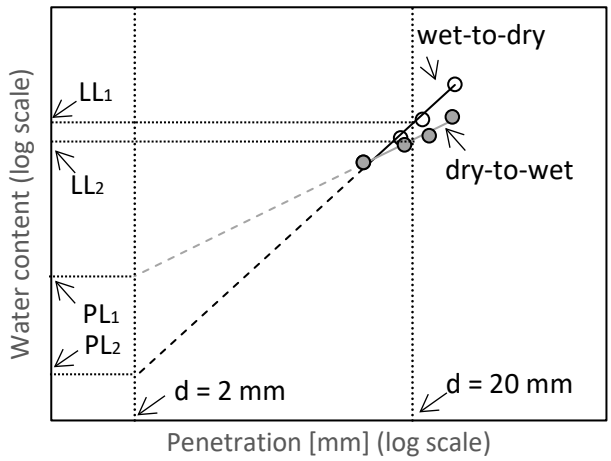

Figure 4.7: Influence of testing cycles on LL and PL determination using Feng (2001) (note: the sub notation '1' means results from wet-to-dry cycle, and the sub notation '2' means results from dry-to-wet cycle)

In this study, some specimens were prescribed to study the influence of testing directions and compare the LL and PL results from the opposite testing directions. The fall cone device used in this study is shown in Figure 4.8. The test procedures are as follows:

a) Prepare a soil paste using approximately 300 g of oven-dried soil in the same manner used for the Casagrande cup test.
b) Thoroughly mix the paste for at least 10 min and then carefully fill the testing cup without trapping air bubbles. Use a palette knife to obtain a smooth level surface. Release the cone for a period of 5 ± 1 s then record the penetration reading. Repeat penetrations two more times. If the overall penetration difference is less than 1 mm, then record the average penetration and take a water content sample of about 10 g around the cone area.
c) Gradually dry the soil specimen and obtain at least four data points with two less than 20 mm and two higher than 20 mm penetration.
d) For prescribed specimens, penetrations on reversed directions were also conducted after reaching the lowest penetration (the driest end): gradually wet the soil specimen and obtain at least four data points with two less than 20 mm and two higher than 20 mm penetration.
e) Plot the relationship between the water content (w) and the corresponding penetrations (d) on a semilogarithmic scale ($w - \log(d)$), best fit the data points with an equation of the form $w = f + g \log d$ (f, g = fitting parameters). The water content corresponding to a penetration of 20-mm is the LL.

Figure 4.8: The fall cone device (30°, $80g$ cone)

3. Lab miniature vane test

It is generally acknowledged that the LL is the water content at which the undrained shear strength of fully remolded fine-grained soils is around 2 kPa (typically 1.7-2.4 kPa). Therefore, the lab vane test can be adopted to directly measure the soil strength and determine the LL using the critical soil mechanics (Schofield and Wroth, 1968). It can be used to verify the LL when the Casagrande cup test and the fall cone test provide different results of LL. In this study, an electric lab vane device (Figure 4.9) is used to measure the remolded soil strength and the test procedures are as follows:

a) Prepare a test specimen the same way as prepared for the Casagrande cup test or the fall cone test, though the amount of specimen will be appreciably more than (5 ~ 10 times more) in the other two tests to satisfy the testing requirements (step b)).
b) Place the soil in a cylindrical container such that: the distance between the shearing surface to the outer edge of the sample is at least two blade diameters; the distance between the blade bottom to the sample top surface is at least two blade heights.
c) Slowly rotate the vane at a constant rate that ranges from 20 ~ 30°/min, the shear strength can be directly read from the device, and it should reach equilibrium in 2 ~ 3 min.
d) Record the shear strength reading, then perform 2-3 replicate trials. If the relative difference across trials is less than 10%, record the average shear strength and obtain 10 g of soil around the shearing zone for water content measurement.
e) Take at least four readings surrounding 2 kPa shear strength measurements, plot the relationship between the water content (w) and the corresponding shear strength (s_u) on a semilogarithmic scale ($w - \log(s_u)$), best fit the data points with a straight line and the water content corresponding to the 2 kPa is the calculated LL.

Figure 4.9: The lab vane device

4.2.6.2 Plastic limit measurements

1. Thread rolling

The PL is the water content at which the soil transitions from a state in which it can deform plastically to a semi-solid (i.e., more brittle) state. This point is defined to be the water content at which the soil crumbles when being rolled out into a thread (Atterberg, 1911). The following procedure was used for measuring the PL, consistent with ASTM D4318-17:

a) Obtain a 1.5-2.0 g specimen of soil and roll the mass by hand on a glass plate. If the thread can be rolled to a diameter $< 3.2\ mm$, remold it and repeat the rolling. When the thread crumbles at a diameter of 3.2 mm, collect the soil and place it in a sealed container.
b) Repeat the same procedures until at least 6 g of crumbled soil is collected. Measure the water content of the crumbles. This water content is the PL.
c) Repeat 2-3 trials. If the difference in measured water contents 1%, the average water content is the final PL.

2. Semi-direct measurement with a fall cone (Wood and Wroth 1978)

Two fall cone-based PL determination methods have been reported in the literature (e.g., Evans and Simpson, 2015) as being widely used: the dual cone weight method developed by Wood and Wroth (1978), and the linear $\log(w) - \log(d)$ model developed by Feng (2001).

Wood and Wroth (1978) combined concepts from critical state soil mechanics and the generally held belief that soil strength at the PL is 100 times that at the LL ($s_{u,PL}/s_{u,LL} = 100$) to develop a dual cone weight method. Two fall cone tests are conducted: one uses the regular cone mass (80 g) while the other uses a heavier cone mass (usually 240 g, but in this study, 180g is adopted). Each set of data is fit with a straight line in $w - \log(d)$ space. Theory specifies that the two lines should be parallel to each other, so their slopes are typically forced to be identical during fitting. Based on the critical state soil mechanics, the plasticity index (PI) is a function of the vertical separation of the two fitted lines (i.e., the absolute difference between their ordinal intercepts). The demonstration of Wood and Wroth (1978) theory is shown in Figure 4.10. The equation

to calculate PI is shown in (4-17), and PL can then be determined directly from the definition of PI, as shown in Equation (4-18).

$$\boldsymbol{PI = \frac{2\Delta}{log\left(\frac{W_1}{W_2}\right)}} \tag{4-17}$$

$$\boldsymbol{PL = LL - PI} \tag{4-18}$$

where:
Δ = separation of the two fitted lines in terms of water content;
W_1 = heavier cone weight; and
W_2 = regular cone weight (usually 80 g).

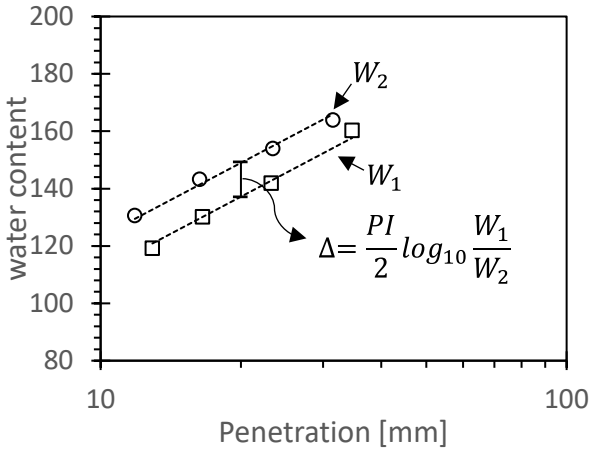

Figure 4.10: Demonstration of dual cone weight method ($W_1 > W_2$) (Wood and Wroth, 1978)

3. Indirect measurement with a fall cone (Feng 2001)

Feng (2001) developed a linear $\log(w) - \log(d)$ model for determination of PL that is founded in the same concept as that used by Wood and Wroth (1978). The procedures as previously discussed are used except that the water content and the penetration readings are plotted on a log-log scale. Given that undrained shear strength is proportional to the square of cone penetration ($s_u \propto d^2$; Hansbo 1957), a 100-fold strength increase ($s_{u,PL} = 100 s_{u,LL}$) corresponds to a 10-fold decrease in penetration ($d_{PL} = d_{LL}/10 = 20\ mm/10 = 2\ mm$). Due to the extreme difficulty of measuring penetrations that small with the fall cone, Feng (2001) suggests determining the PL as the water content extrapolated from the best-fit line of the measured data to a penetration of 2 mm in $\log(w) - \log(d)$ space. The demonstration of the linear $\log(w) - \log(d)$ model is shown in Figure 4.11 and the calculation is shown in Equation (4-19):

$$\log(w) = \log(c) + m\log(d) \tag{4-19}$$

where:
c = water content at $d = 1$ mm; and
m = slope of the log-log flow curve.
Thus, the PL can be simply calculated using Equation (4-20).

$$PL = c(2)^m \tag{4-20}$$

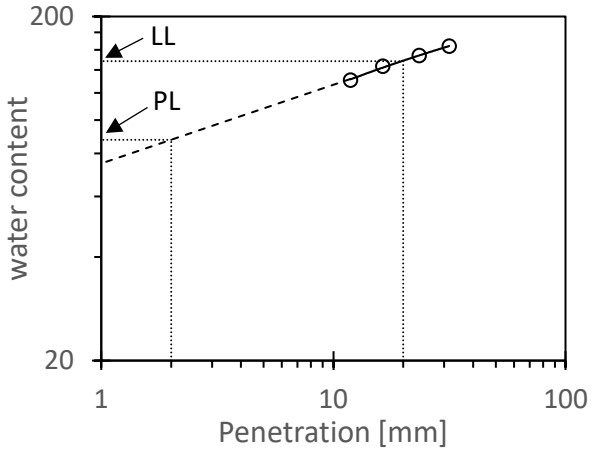

Figure 4.11: Demonstration of the linear $\log(w) - \log(d)$ model developed by Feng (2001)

4.2.7 Specific Surface Area

The specific surface area (SSA) is defined as the surface area of an object (e.g., a soil grain) divided by its mass (typically reported in units of m^2/g). The core idea of SSA measurement is to measure the amount of adsorbate molecules that are absorbed on the soil particle surface and calculate the surface area based on the contact area of the adsorbate molecules. Usually, it can be divided into dry method if the adsorbate molecules are gas (such as N_2 or water vapor) and wet method if the adsorbate molecules are dye (such as methylene blue). In this study, both wet method and dry method were attempted to measure SSA of soil specimens from the four sites. A total of 18 soil samples (six from Wickiup Junction, five from Ady Canal, four from Pine Cone Drive, and three from Moore Park) were tested with the methylene blue (MB) method and two were tested with the Guggenheim, Anderson and de Boer (GAB) method. A detailed procedure for MB method is presented below. The GAB method test was conducted in an independent lab that provided only the results; therefore, the procedures and analysis of the GAB method are omitted here.

4.2.7.1 The methylene blue method

Santamarina et al. (2002) described the determination of SSA using methylene blue as the dye. To obtain better precision, the titration method is adopted in this study, the test procedures are as follows:

a) Prepare the methylene blue solution by mixing 1.0 g of dry powder with 200 mL of deionized water.
b) Mix 2.0 g of oven-dry NO. 200 sieved soil specimen with 200 mL of deionized water.
c) Add 0.2 mL of methylene blue solution to the soil suspension while continually mixing the suspension for about 2 h, then let it sit overnight to reach absorption equilibrium and allow particle settlement.
d) Carefully remove 1 mL of the fluid, place it in a test tube, and centrifuge it.
e) Use a spectrophotometer (set the wavelength equal to 665 nm) to test the methylene blue remnant concentration.
f) Repeat steps (c) - (e) until a sudden increase in the methylene blue remnant concentration is observed. Record the total mass of methylene blue added. Use Equation (4-21) to calculate the SSA.

$$\boldsymbol{SSA_{MB} = \frac{m_{MB}}{M_{MB}} A_V A_{MB} \frac{1}{m_s}} \quad \textbf{(4-21)}$$

where:
SSA_{MB} = specific surface area measured by methylene blue method, m^2/g;
m_{MB} = total added methylene blue in mass, g;
M_{MB} = molecular weight of methylene blue, taken as 319.87 g/mol;
A_V = Avogadro's number ($6.02 \times 10^{23}/mol$);
A_{MB} = area covered by one methylene blue molecule (typically assumed to be 1.3 nm^2); and
m_{MB} = mass of soil specimen, g.

4.3 MECHANICAL PROPERTY TESTING

4.3.1 Consolidation Test

Consolidation tests were performed to measure oedometric (i.e., K_0) compression properties and stress history: compression index (C_c), recompression index (C_r), and preconsolidation stress (σ'_P). Both incremental loading tests (IL test, ASTM D2435-11; American Society for Testing and Materials (ASTM). 2020d.) using a lever arm consolidometer and constant rate of strain (CRS test, ASTM D 4186-20; American Society for Testing and Materials (ASTM). 2021.) tests were performed, as each has its own advantages. For example, the CRS test is quick and easy to perform, whereas the IL tests can provide a method to determine the hydrodynamic consolidation coefficient (c_v) for each loading stage. In this project, some specimens were subjected to both tests to verify the consistency between IL and CRS tests, other specimens were subjected to only CRS or IL tests due to the limited amount of intact soil samples.

4.3.1.1 Test procedures

The specimen preparation for either IL test or CRS test is relatively straightforward compared to the triaxial test. One critical step is to create well-trimmed specimen surfaces. However, this may not be easy for chalk-like diatomaceous soils (Figure 4.12 (a)). Chalk-like diatomaceous soils are relatively stiff and prone to peeling off or crumbling when trimming with a wire saw. For cases like Figure 4.12 (a)), trimmings were used to fill surface holes and obtain a smooth and flat surface (Figure 4.12 (b)). The disturbance induced by this process will need to be considered when interpreting results.

(a) PC1U4 (before trimming and filling) (b) PC1U4 (after trimming and filling)

Figure 4.12: An example of CRS specimen (chalk-like)

Several measurements are made while fitting the specimen into the consolidation ring: initial soil water content, initial specimen mass, and specimen height and diameter. Once the specimen is ready after careful trimming, the IL and CRS test will follow different loading procedures under different loading devices. Their corresponding test procedures are listed below separately.

For IL tests, the test procedures are as follows:

a) Assemble the consolidation cell, placing a porous stone and layer of filter paper on the top and bottom of the specimen, which is contained within the consolidation ring. Inundate the reservoir with distilled water. The images of consolidation cell are shown in Figure 4.13.
b) Place the consolidometer in the loading device and apply a series of loading steps using a load increment ratio of $LIR = 1$. Once the applied vertical stress exceeds the approximate preconsolidation stress (as determined by monitoring load-deformation response during the test), unloading-reloading steps are performed to measure recompression index.
c) The load can be incremented following one of two schedules, as specified in ASTM D2435-11. In Method A, the standard load duration is 24 hours for each loading step. In Method B the load is incremented when the end of primary consolidation is

observed by drawing deformation-log(time) ($\delta - \log t$) curves. Method B was adopted for most of the IL tests, but some specimens from the same Shelby tube were subjected to both methods to assess the impacts of changing load duration.

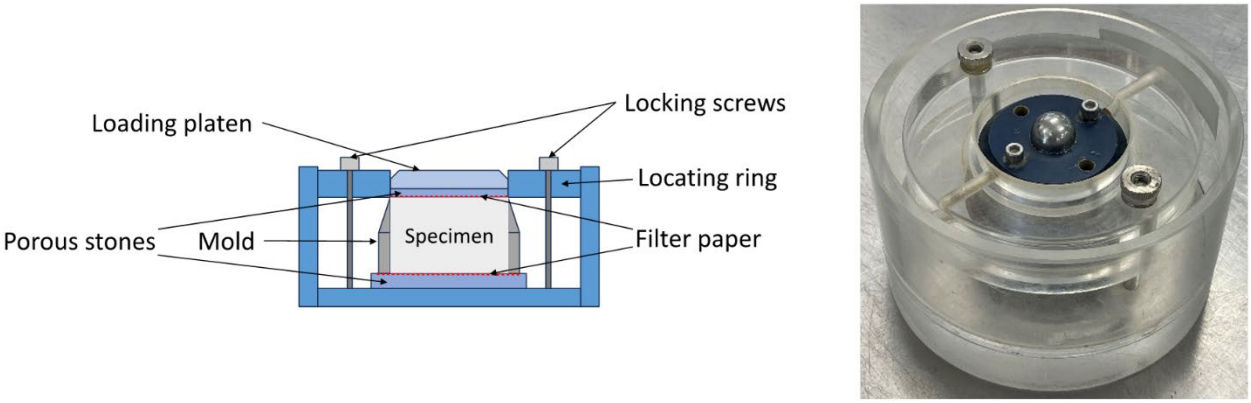

Figure 4.13: Consolidation cell: (a). schematic set-up; (b). assembled consolidation cell used in this project

The CRS test does not require manual incrementing of the load. Once the specimen is assembled in the consolidometer with porous stones and filter paper, it is placed in the loading frame, the same as in the triaxial tests, the test apparatus set-up is shown in Figure 4.14. The load is then applied at a rate of 0.0003 mm/min (corresponding to a strain rate of $1.97 \times 10^{-7}/s$ for a specimen height of 25.4 mm). Similar to the IL tests, the recompression index is measured by conducting unloading-reloading steps after the applied vertical stress exceeds the approximate preconsolidation stress.

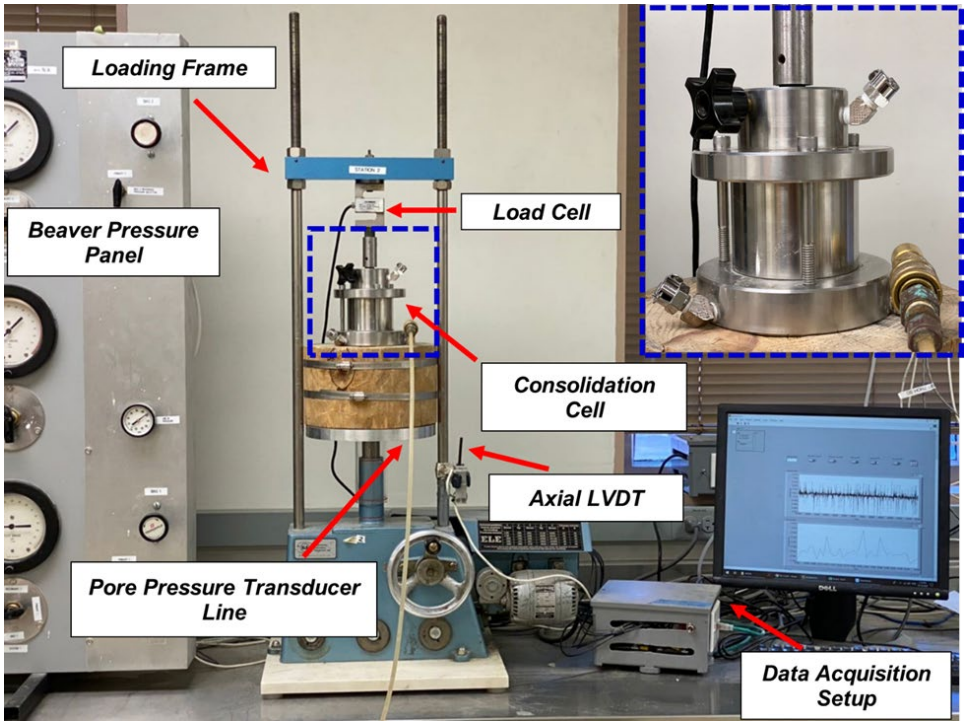

Figure 4.14: CRS test apparatus used in this project (after Dadashi, 2022)

At the end of both consolidation tests, the specimen mass and final water content were measured to calculate the consolidation curve.

4.3.1.2 Calculation of stiffness and stress history

The calculation of the compression index (C_c), recompression index (C_r), and preconsolidation stress (σ_p') are all based on the consolidation curve ($e - \log \sigma_v'$). The initial void ratio (e_0) can be calculated from specimen mass and water content measured at initial using Equation (4-22), or alternatively, e_0 can be calculated from the final void ratio (e_f) using Equation (4-24) and e_f can be calculated from specimen mass and water content measured at the end of the test using Equation (4-22). Once e_0 is determined, the void ratio at any time (e_t) can be calculated using Equation (4-25).

$$\boldsymbol{e = \frac{G_s(1+w)\rho_w}{\rho_t} - 1} \tag{4-22}$$

$$\boldsymbol{e = \frac{G_s(1+w)\rho_w}{\rho_t} - 1} \tag{4-23}$$

$$e_0 = \frac{e_f + \frac{\Delta z_f}{H_0}}{1 - \frac{\Delta z_f}{H_0}} \tag{4-24}$$

$$e_t = e_0\left(1 - \frac{\Delta z}{H_0}\right) - \frac{\Delta z}{H_0} \tag{4-25}$$

where:
G_s = specific gravity;
w = water content;
ρ_t = specimen density, g/cm^3, see Equation (4-23);
ρ_w = water density, = $1 g/cm^3$;
m_s = specimen mass, g;
d = specimen diameter, cm;
h = specimen height, cm;
Δz_f = total consolidation settlement, cm;
H_0 = initial specimen height, cm; and
Δz = settlement at load P, cm.

The compression index (C_c) is the slope of the linear portion of the virgin compression line on $e - \log \sigma_v'$ plot, and the recompression index (C_r) is the slope of unloading and reloading line. Figure 4.15 shows the actual and idealized behaviors of consolidation curve where the recompression and virgin compression line are simplified to two linear lines in $e - \log \sigma_v'$ plot. The accuracy of C_c may be influenced by the disturbance of the specimen, shown in Figure 4.16. Although "undisturbed" is used to refer to those consolidation tests that show a relatively distinct turning point near preconsolidation stress, all specimens are more or less disturbed.

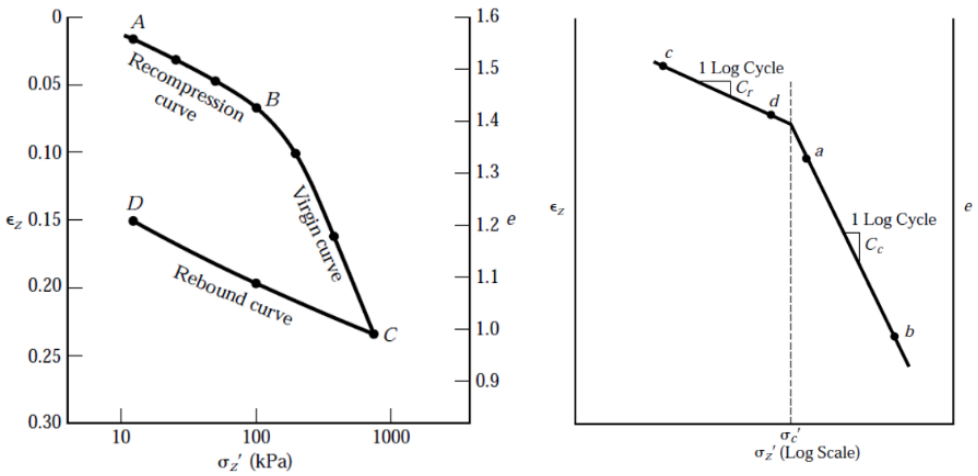

Figure 4.15: Consolidation curves between actual behavior (a) and idealized behavior (b) (after Coduto, 2003)

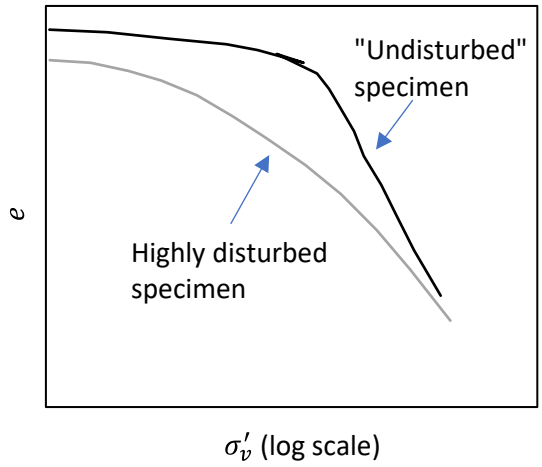

Figure 4.16: Demonstration of disturbance on consolidation curve

The preconsolidation stress (σ_p') is determined using three different methods: the Casagrande method (Casagrande, 1936), the Silva method (Pacheco Silva, 1970), and the strain energy method proposed by Becker et al. (1987). The Casagrande and Silva methods are empirical methods involving manual geometric constructions on the $e - \log \sigma_v'$ curve, whereas the Becker et al. method transforms the stress-strain curve to an energy-stress curve to identify the stress at which energy dissipation shows a marked increase, which they define as the yield stress (σ_{vy}', analogous and mechanically equivalent to σ_p'). A brief summary of the procedures for determining σ_p' with each of the three methods is provided below.

The Casagrande method (Figure 4.17):

a) Choose the point of maximum curvature on the $e - \log \sigma_v'$ curve.

b) Draw a horizontal line and a line tangent to the curve from this point.
c) Bisect the angle made by the horizontal line and the tangent line.
d) Back-project the linear portion of the virgin compression curve up to the bisector line.
e) The intersection of the bisector line and the back-projection of the virgin compression line is the preconsolidation pressure.

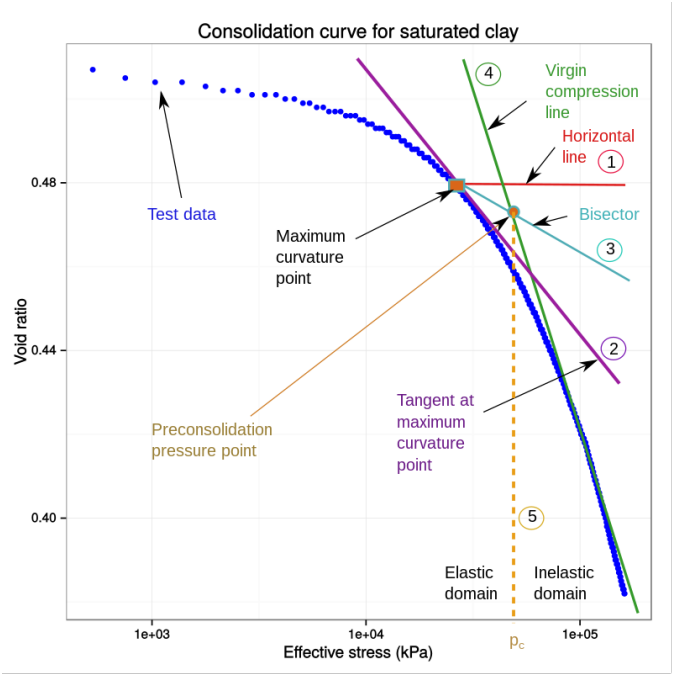

Figure 4.17: Preconsolidation stress determination using Casagrande method (after Wikipedia)

The Silva method (Figure 4.18):

a) Draw a horizontal line (Line A) passing through the initial void ratio (e_0) of the specimen (i.e., the specimen void ratio before any load has been applied).
b) Extend the straight line portion of the virgin compression curve (Line B) to intercept with Line A.
c) Draw a vertical line (Line C) passing through the intersection of Line A and B, and intercept with the $e - \log \sigma_v'$ curve.
d) Draw a horizontal line (Line D) passing through the intersection of Line C and the consolidation curve until it intercepts with Line D, the corresponding vertical stress of the intersection is σ_p'.

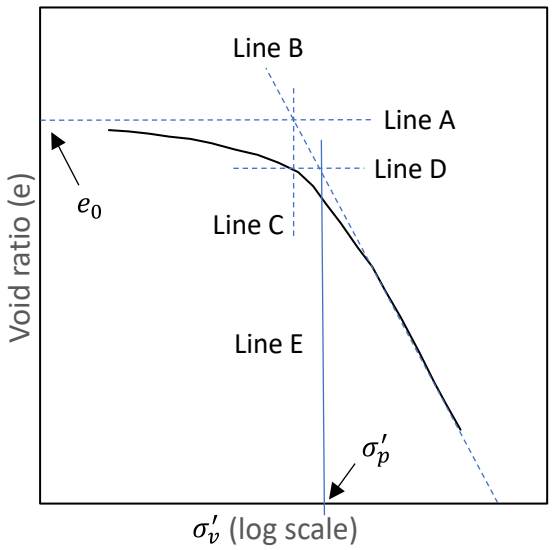

Figure 4.18: Preconsolidation stress determination using Silva method

The Becker method (Figure 4.19):

a) Calculate energy per unit volume using Equation (4-26).

$$\Delta \boldsymbol{W_{i+1}} = \left(\frac{\boldsymbol{\sigma'_i + \sigma'_{i+1}}}{\mathbf{2}}\right)(\boldsymbol{\varepsilon_{i+1} - \varepsilon_i}) \quad \forall\, \boldsymbol{i} \in \{\mathbf{1}, \mathbf{2}, \ldots \boldsymbol{N}\} \tag{4-26}$$

b) Sum the energy per unit volume using Equation (4-27), and plot accumulated energy against vertical stress.

$$\boldsymbol{W} = \sum_{\boldsymbol{i=1}}^{\boldsymbol{N}} \Delta \boldsymbol{W_i} \tag{4-28}$$

c) The intercept of the two straight line segments of the energy-stress curve is σ'_p.

where:
σ'_i = vertical stress at the i^{th} load increment;
ε_i = axial strain at the i^{th} load increment;
N = total number of loading increments;
ΔW_{i+1} = energy per unit volume between ε_i and ε_{i+1}; and
W_i = summed energy at σ'_i.

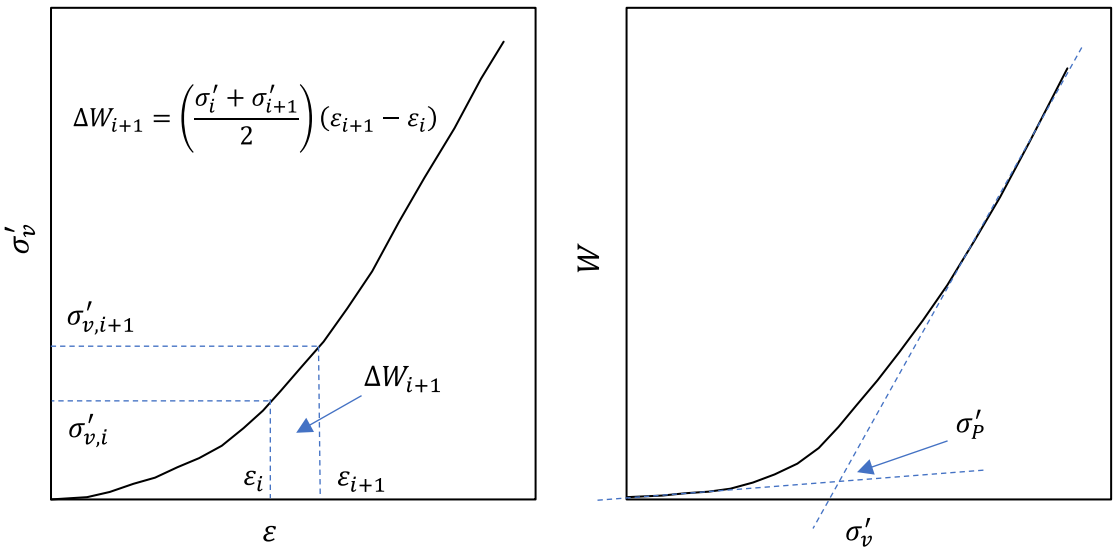

Figure 4.19: Preconsolidation stress determination using Becker method

4.3.1.3 Computing the coefficient of hydrodynamic consolidation

The vertical coefficient of consolidation (c_v) can be determined from each vertical stress increment in the IL test. It describes the rate at which excess pore pressures dissipate after a change in total stress. The most widely adopted methods for evaluation of c_v are the so-called "log time" (Casagrande and Fadum, 1940) and "root time" methods (Taylor, 1948). These methods are carefully described in ASTM D2435-11. Barros and Pinto (2008) introduced a more theoretically attractive approach that uses a nonlinear regression approach to fit the entire time–deformation data series to Terzaghi's solution of the consolidation equation. In this approach, c_v emerges as a parameter of the minimization (i.e., a "fitting parameter"). The shortcoming of this approach is that it might be computationally expensive. We adopt the Barros and Pinto (2008) approach to obtain c_v through a computationally efficient implementation in MATLAB.

4.3.2 Consolidated Drained and Undrained Triaxial Compression Tests

A triaxial shear test is performed on a cylindrical soil specimen to measure shear strength. The test attempts to replicate the *in-situ* stress during shearing and failure is influenced by a combination of stresses applied, stress history of the soil, and the internal properties of the soil. The triaxial test is often favored over other means to assess shear strength because of its advantages: the soil is free to fail on the weakest plane rather than a predefined failure plane, such as in the direct shear test; pore pressure changes (undrained test) and volume changes (drained test) can be measured directly; and the precise stress state is known throughout the test, so the Mohr circle can be drawn at any stage of shear. In this work, the intent was to perform as many triaxial tests as possible. However, the total number of tests was limited by the specimen dimension requirements for the test. Due to the brittleness of the soil, it was not possible to obtain 5.5 in tall intact specimens from and of the Pine Cone Drive Shelby tubes and extremely difficult for the Moore Park samples. A total of seven specimens from Wickiup Junction, four

specimens from Ady Canal, and one from Moore Park were obtained and subjected to consolidated undrained/drained triaxial testing. All of the triaxial specimens were extruded from Shelby tubes.

4.3.2.1 Test procedures

Triaxial tests were performed in general accordance with ASTM D4767 for undrained (American Society for Testing and Materials (ASTM). 2020b.) and ASTM D7181 for drained (American Society for Testing and Materials (ASTM). 2020a.) tests. The triaxial test procedures can be divided into five major steps: specimen preparation, specimen mounting, saturation, consolidation, and shear. The test procedures are listed below:

a) Extrude specimen of height between 140-152 mm (5.5-6 in) from the Shelby tube, the inner diameter of the Shelby tube is approximately 71 mm. Trim both ends of the specimen to level surfaces and use the trimmings fill up any possible cracks or imperfectness from extrusion (Figure 4.20 (a)).
b) Boil the porous stones for at least 10 min and saturate the end filter paper (no filter strips on the outer surface, drainage only allowed from the top and bottom of the specimen). Assemble the specimen in order from bottom to top: specimen base, porous stone, filter paper, specimen, filter paper, porous stone, specimen cap, see Figure 4.20 (b).
c) Use a membrane expander to place a rubber membrane on the mounted specimen and seal it with two rubber O-rings at top and bottom. Attach the top drainage lines and seal with silicone grease. Assemble the triaxial cell, enclosing the specimen, and fill the cell with deaired water, Figure 4.20 (c).
d) Apply back and cell pressure following ASTM D4767-20/D7181-20 to obtain the B-value (an indication of specimen saturation). The calculation of B-value is shown in Equation (4-28). Repeat applying back and cell pressure in steps until the B-value is greater than 0.95.

$$\boldsymbol{B = \frac{\Delta u}{\Delta \sigma_3}} \qquad \textbf{(4-28)}$$

where:
Δu = excess pore water pressure induced by the change in cell pressure; and
$\Delta \sigma_3$ = change in cell pressure.

e) Once a satisfactory B-value is achieved, isotropically consolidate the specimen to the desired effective stress (*in-situ* effective horizontal or vertical stress in this study) until the end of primary consolidation is reached.
f) Place the specimen chamber under the loading system and set the desired strain rate. The guideline (ASTM D 4767 and ASTM D 7181) is to calculate the strain rate using Equation (4-29) for both undrained and drained (without side drain) scenarios. If no consolidation data is available, ASTM D 4767 suggests a strain rate of 1%/hr. The primary drainage valves remain closed for undrained shearing or open for drained

shearing. A data acquisition system was used to record axial load, axial deformation, and pore pressure (undrained) or volume change (drained).

$$\dot{\varepsilon} = \frac{4\%}{10t_{50}} \tag{4-29}$$

where:

$\dot{\varepsilon}$ = strain rate; and

t_{50} = time needed for 50% primary consolidation (see discussion about consolidation coefficient in 4.3.1.3).

g) Continue loading to critical state or until a global axial strain of $\varepsilon_1 \geq 15\%$ (Figure 4.20 (d)). Dismount the specimen and collect a small portion for water content determination.

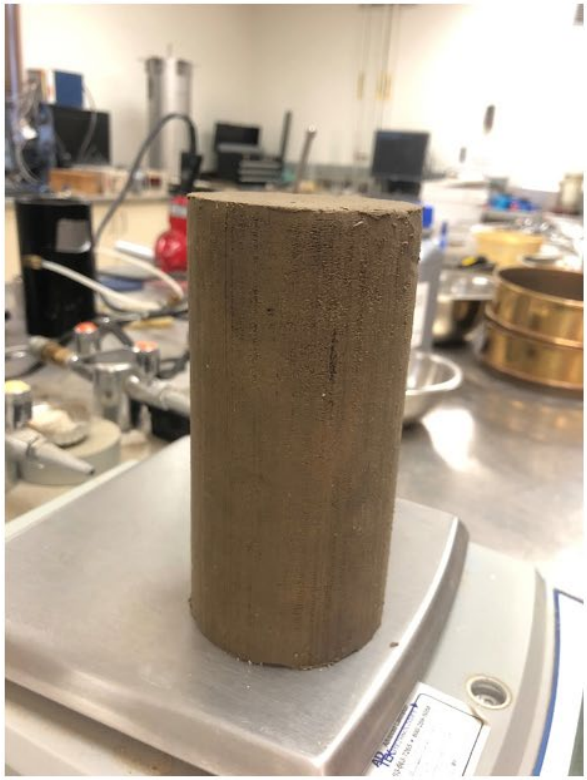

(a) Trimmed intact specimen

(b) Specimen enclosed in a membrane with top and bottom platens in place

(c) Specimen mounted in the confining cell

(d) End of triaxial test

Figure 4.20: Overview of the triaxial testing sequence

4.3.2.2 Calculations

During the triaxial test, several parameters are recorded by the data acquisition system: axial load (P), vertical deformation (Δz), and either volume change (ΔV) or excess pore pressure (Δu), depending on whether the test was drained or undrained, respectively. These measurements are synthesized to develop the constitutive quantities used to describe engineering behavior: volumetric strain (ε_p; drained test), deviatoric strain (ε_q), deviatoric stress (q), and mean effective stress (p'). The necessary steps are outlined below in Equations (4-30) through (4-37).

Major principal (i.e., axial) strain:

$$\boldsymbol{\varepsilon_1 = \frac{\Delta z}{H_0}} \tag{4-30}$$

Volumetric strain (drained):

$$\boldsymbol{\varepsilon_p = \frac{\Delta V}{V_0} = \varepsilon_1 + 2\varepsilon_3} \tag{4-31}$$

Minor principal (i.e., radial) strain:

$$\boldsymbol{\varepsilon_3 = \frac{1}{2}(\varepsilon_p - \varepsilon_1)} \tag{4-32}$$

Deviatoric (shear) strain:

$$\boldsymbol{\varepsilon_q = \frac{2}{3}(\varepsilon_1 - \varepsilon_3)} \tag{4-33}$$

Cross-sectional area correction:[3]

$$\boldsymbol{A = A_0 \frac{1 - \varepsilon_p}{1 - \varepsilon_1}} \tag{4-34}$$

Deviatoric (shear) stress:

$$\boldsymbol{q = \frac{P}{A} = \sigma_1' - \sigma_3' = \sigma_1 - \sigma_3} \tag{4-35}$$

[3] Assumes deformation as a right circular cylinder:
$A = V/H = (V_0 - \Delta V)/(H_0 - \Delta z) = (V_0/H_0) \cdot [(1 - \Delta V/V_0)/(1 - \Delta z/H_0)] = A_0 \cdot \left[\left(1 - \varepsilon_p\right)/(1 - \varepsilon_1)\right]$.

Mean total stress:[4]

$$\boldsymbol{p = \frac{\sigma_1 + 2\sigma_3}{3} = \frac{1}{3}q + \sigma_3}$$

(4-36)

Mean effective stress:

$$\boldsymbol{p' = p - \Delta u}$$

(4-37)

where:

H_0 = initial height of specimen;
V_0 = initial specimen volume;
A_0 = initial cross section area;
σ_1' = major principal (axial) effective stress;
σ_3' = minor principal (radial) effective stress;
σ_1 = major principal (axial) total stress; and
σ_3 = minor principal (radial) total stress.

The stress and strain calculations in the (p', q) domain for CD and CU triaxial tests are summarized in Table 4.2.

Table 4.2: Stress and strain calculation in (p', q) domain

	CU test	**CD test**
$\boldsymbol{\varepsilon_p}$	$\varepsilon_p = 0$	$\varepsilon_p = \frac{\Delta V}{V_0}$
$\boldsymbol{\varepsilon_q}$	$\varepsilon_q = \varepsilon_1$	$\varepsilon_q = \varepsilon_1 - \frac{1}{3}\varepsilon_p$
$\boldsymbol{q}$	$q = \frac{P}{A}$	
$\boldsymbol{p, p'}$	$p = \frac{q}{3} + p_0', p' = p - u$	$p = p' = \frac{q}{3} + p_0'$

In addition to calculation of stress and strain in the (p', q) domain, the friction angle (ϕ') is calculated in CD tests, and the undrained shear strength (s_u) is calculated for CU tests. Strength parameters are calculated using Equation (4-38) and (4-39) respectively.

$$\boldsymbol{s_u = \frac{q_{peak}}{2}}$$

(4-38)

[4] Assumes $\varepsilon_3 = \varepsilon_r = \varepsilon_\theta$.

$$\boldsymbol{\phi'_{cs} = \sin^{-1}\left(\frac{\sigma'_{1,cs} - \sigma'_{3,cs}}{\sigma'_{1,cs} + \sigma'_{3,cs}}\right)} \quad \textbf{(4-39)}$$

where:
q_{peak} = peak deviatoric stress, kPa;
$\sigma'_{1,cs}$ = major principal (axial) effective stress at critical state, kPa; and
$\sigma'_{3,cs}$ = minor principal (radial) effective stress at critical state, kPa.

Note that in Equation (4-39) the point of maximum obliquity definition of drained shear strength is adopted by convention.

4.3.3 Direct Simple Shear Test

Unlike triaxial tests where specimens will be back-pressure saturated, the direct simple shear (DSS) test does not check for saturation or back pressure. It is relatively fast and easy to perform. The soil specimen is subjected to a state of pure shear, resulting in uniform deformation without forming a single shearing surface. The soil usually exhibits different strengths under DSS and triaxial tests (Mayne, 1985), running both tests will provide different perspectives of soil behavior.

The DSS tests were conducted in this project due to its various advantages. First, the height of DSS specimen is only about 21 mm compared to 140 mm height needed in triaxial test. This is a great advantage considering that it is sometimes very difficult to obtain tall intact diatomaceous specimens. Both "pudding-like" and "chalk-like" diatomaceous soil yields great difficulty in retrieving and extruding undisturbed specimens. Second, the SHANSEP (Stress History and Normalized Soil Engineering Properties) (Ladd and Foott, 1974) procedure can be adopted where specimens from the same source will be consolidated and unconsolidated to different OCRs, the normalized undrained shear strength and OCR follow a power law relationship, therefore, the normally consolidated undrained shear strength (S) which is independent of soil stress history can be determined.

4.3.3.1 Test procedure

The DSS procedure is much simpler than the triaxial test, the actual procedure may also subject to change depending on the shear device adopted. The schematic set-up of DSS tests is shown in Figure 4.21. ASTM D 6528-17 (American Society for Testing and Materials (ASTM). 2017.) is generally followed. In this project, the DSS device was used to consolidate the specimen and perform constant volume shearing. The data acquisition is automated by the device, the specimen preparation is briefly listed as follows:

a) Stack confining rings surround the specimen (Figure 4.22 (a)) and trim the specimen with a spatula or a wire saw (Figure 4.22 (b)). The height of the specimen should be around 21 mm, the diameter is 72.6 mm.
b) Carefully take out the stacked rings (Figure 4.22 (c)), measure the height of the specimen, place the specimen on the platen, and flip up the rubber around the

specimen. Carefully stack back the rings and mount it in the loading frame (Figure 4.23, zoomed-in DSS cell).

c) Consolidate the specimen to a vertical stress that is higher than its preconsolidation stress, then unload it to create an overconsolidated specimen with known OCR.

d) According to ASTM D 6528-17 (American Society for Testing and Materials (ASTM). 2017.), the strain rate should not result in specimen failure in a time that exceeds twice the time for 90 % consolidation. Much of the practical experience uses a shear strain rate of 5%/hour, which is adopted in this study. The shear test lasts 5 hours in order for the critical state to develop.

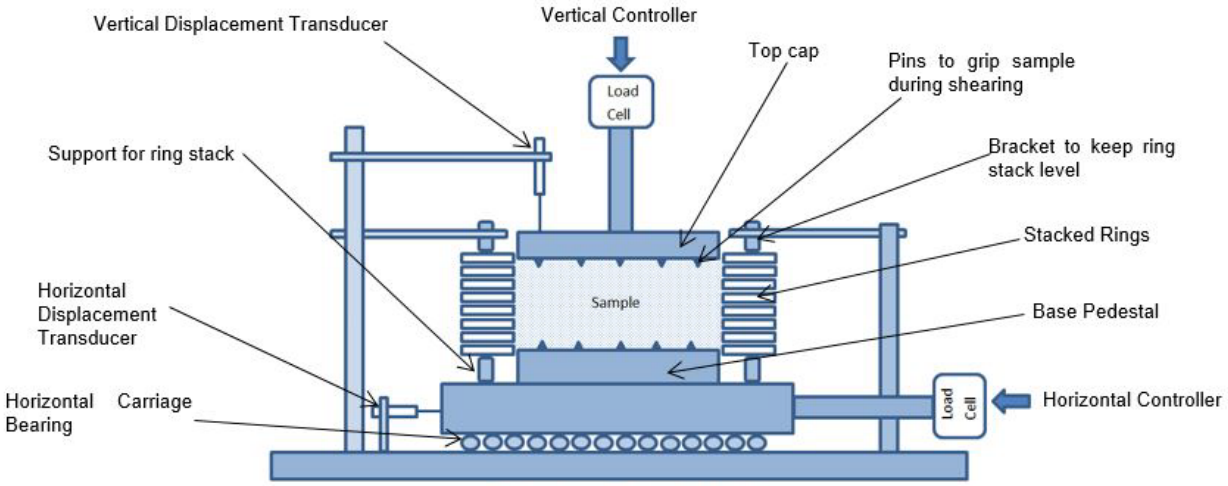

Figure 4.21: The schematic set-up of DSS tests (after VJ Tech)

(a) Before trimming (b) After trimming (c) Ready specimen

Figure 4.22: Examples of specimen trimming for DSS test

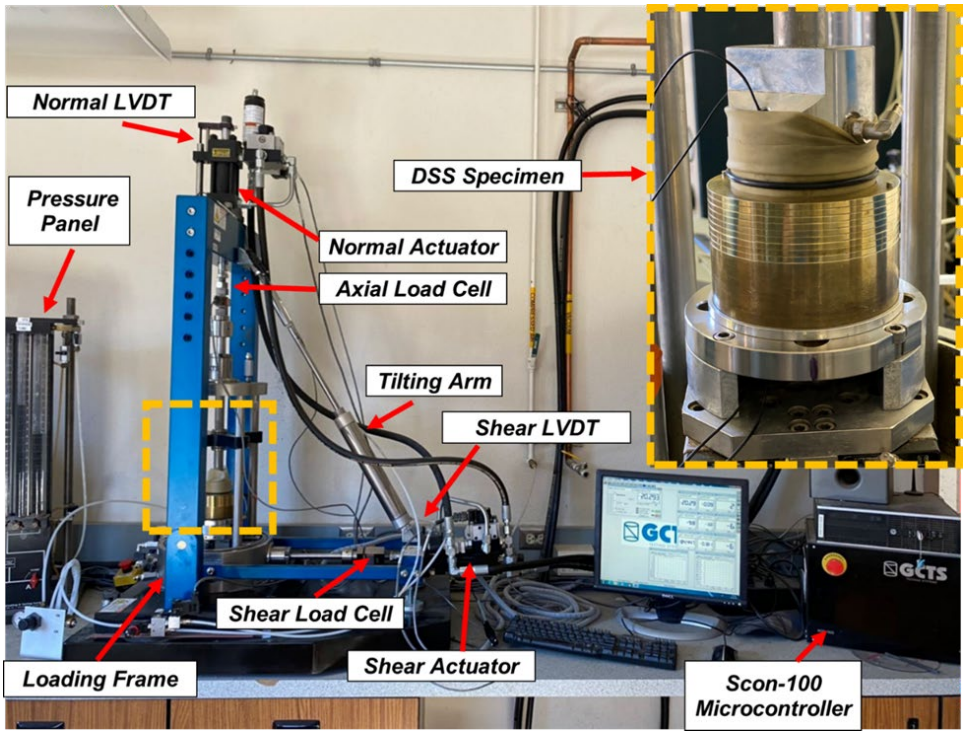

Figure 4.23: DSS test apparatus used in this project (after Dadashi 2022)

4.3.4 Flexible Wall Permeability Test

Permeability tests were conducted to measure the hydraulic conductivity (k) of saturated specimens under *in-situ* stress conditions. Following ASTM D5084-16 (American Society for Testing and Materials (ASTM). 2016d.), there are six different ways to measure permeability depending on the hydraulic system being used. We conducted permeability tests as part of the preparation of triaxial tests. The falling head method with constant tailwater elevation was used.

The test follows the procedure outlined in Section 4.3.2.1 above from specimen setup through isotropic consolidation (i.e., steps (a)-(e)). Prior to shearing the specimen, the permeability test was performed as follows:

a) Place the specimen below the bottom of the falling head (i.e., below the bottom of the burettes)
b) Open the valve to let water fall along the burettes under no pressure and measure the falling time and falling length, calculate the permeability (k) using Equation (4-40).

$$k = \frac{a \cdot L}{A \cdot \Delta t} ln\left(\frac{h_1}{h_2}\right) \quad \textbf{(4-40)}$$

where:
a = cross-sectional area of the reservoir containing the influent liquid (i.e., the burette), m^2;
A = cross-sectional area of specimen, m^2;

L = length of specimen, m;
Δt = interval of time, s;
h_1 = upstream heads at the beginning of the test, m;
h_2 = upstream heads at the end of the test, m; and
k = permeability, m/s.

5.0 RESULTS OF LABORATORY AND FIELD WORK

5.1 OVERVIEW

Results from laboratory and *in-situ* tests are presented in this chapter. Brief discussions of results from each test are provided in each individual section. A more sophisticated and robust synthesis of findings across different test types and modalities is provided in Chapter 6.

5.2 LABORATORY RESULTS ON PHYSICAL PROPERTIES

5.2.1 Scanning Electron Microscope Images

While certain physical test results, such as high natural water content, high consistency limits, low unit weight, and low specific gravity imply the presence of diatomaceous soils, SEM imaging is the most direct and reliable way to identify the existence of diatoms. Figure 5.1 presents a representative image of diatomaceous soils from split spoon samples at each of the four sites. Based on qualitative observation, the most common diatom shape across sites is cylindrical, particularly at Pine Cone Drive. Other diatom shapes include disks and cracked frustules. A total of 33 specimens were sent for SEM imaging; observational identification is shown in Table 5.1, the SEM images of individual specimens along with photos of the split spoon samples and physical properties are summarized in Appendix A. The selected soil specimens covered a wide range of features in terms of soil color, consistency, and texture. The SEM images were used to definitively identify the presence and extents of diatomaceous deposits at each site which facilitates positive correlations between the existence of diatoms and other soil properties (e.g., water content, Atterberg limits). Specifically, the following diatomaceous layers were positively identified (all depths are below ground surface, bgs):

- Wickiup Junction: 29.8 – 47.6 m, 50.7 – 67.2 m;
- Ady Canal: 9.1 – 31.7 m (end of borehole), with two thin non-diatomaceous layers at 12.2 – 15.7 m and 17.9 – 19.7 m;
- Moore Park: 8 – 30.9 m (end of borehole); and
- Pine Cone Drive: 0 – 32.8 m, throughout the depth of the borehole.

Table 5.1: Identification of diatomaceous soil layers from SEM images.

Soil ID	Depth [m]	Color	Consistency	Texture	Apparent moisture	Diatoms?
W1N6	15.7	Black	Soft	Fine grained, clayey	Wet	N
W1N8	20.88	Dark grey	Soft	Fine grained, clayey	Wet	N
W1N11a	27.05	Black	Soft	Fine grained, clayey	Wet	N
W1N11b	27.28	Black	Soft	Fine grained, clayey	Wet	N
W1U7	30.78	Dark grey	Soft to stiff	Fine grained	Moist	Y
W1N13c	31.18	Dark grey	Soft to stiff	Fine grained	Moist	Y
W1N13a	31.39	Dark grey	Soft to stiff	Fine grained	Moist	Y
W1N14	34.29	Brown	Soft to stiff	Fine grained	Moist	Y
W1N15	37.34	Grey	Soft to stiff	Fine grained	Visually dry	Y
W1N17	43.28	Grey	Medium stiff	Fine grained	Visually dry	Y
W1U10	44.35	Dark grey	Medium stiff	Fine grained	Moist	Y
W1N21	55.47	Brown	Stiff	Fine grained	Visually dry	Y
W1N26	65.91	Brown	Stiff	Fine grained, silty	Visually dry	Y
W1N28	71.48	Dark grey	Soft	Fine grained, clayey	Wet	N
W2N1	3.51	Dark grey	Soft	Fine grained, clayey	Wet	N
AC1N4	9.45	Dark grey	Soft	Fine grained, clayey	Wet	Y
AC1N5a	12.19	Dark grey	Soft to stiff	Fine grained	Moist	Y
AC1N7	17.22	Green	Soft to stiff	Fine grained	Moist	Y
AC1N8	19.05	Green	Stiff, friable	Silty, sandy	Visually dry	N
AC1N9	20.27	Green	Stiff, friable	Fine grained, small coarse fraction	Visually dry	Y
AC1N11	26.21	Dark grey	Soft	Fine grained	Wet	Y
PC1N1	3.51	Light grey	Stiff, friable	Fine grained	Visually dry	Y
PC1N2	5.49	Light grey	Stiff, friable	Fine grained	Visually dry	Y
PC1N4a	11.43	Brown	Soft to stiff	Fine grained	Moist	Y

Soil ID	Depth [m]	Color	Consistency	Texture	Apparent moisture	Diatoms?
PC1N4b	11.58	Dark brown	Soft to stiff	Fine grained	Moist	Y
PC1N4c	11.73	Dark brown	Soft to stiff	Fine grained	Moist	Y
PC1N6b	17.75	Light brown	Stiff, friable	Fine grained	Visually dry	Y
PC1N8	23.71	Light grey	Stiff, friable	Fine grained	Visually dry	Y
MP1N3a	8.53	Black	Loose	Sandy	Wet	N
MP1N3b	8.84	Green	Soft to stiff	Fine grained	Moist	Y
MP1N7a	19.02	Dark grey	Soft to stiff	Fine grained	Moist	Y
MP1N9	22.02	Dark grey	Soft to	Fine grained	Moist	Y
MP1N12	26.67	Dark grey	Soft to stiff	Fine grained	Moist	Y

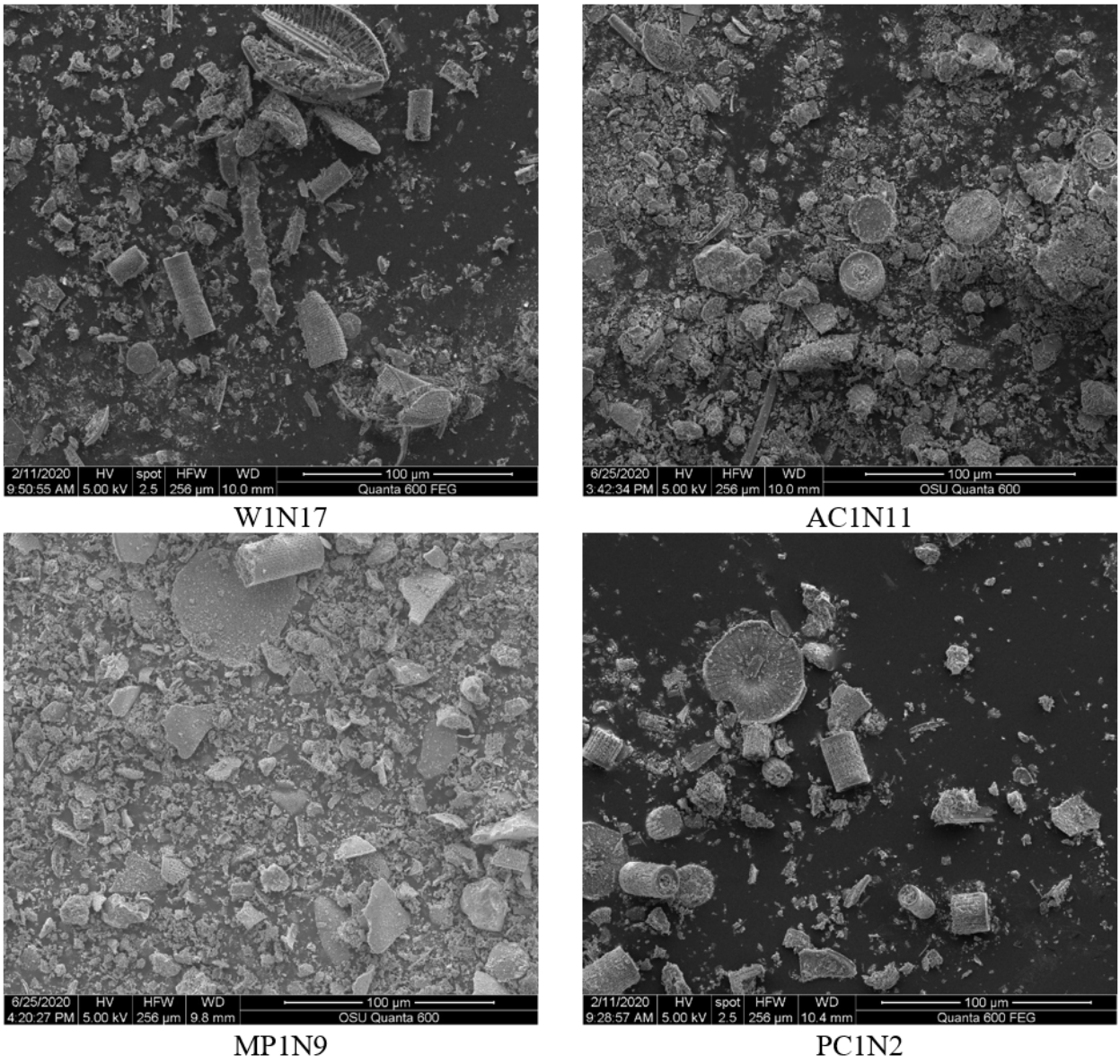

Figure 5.1: Example SEM images of diatomaceous soil from each of the four sites.

5.2.2 Water Content, Unit Weight, and Specific Gravity

The natural water content (w_n) profiles are shown below, divided into diatomaceous soil (Figure 5.2(a)) and non-diatomaceous soil (Figure 5.2(b)). The range of w_n for diatomaceous soils is $39\% \leq w_n \leq 211\%$ across the four sites. There are no consistent trends in w_n with depth: in some cases, it weakly increases and in others it weakly decreases. In non-diatomaceous soils, we generally observe that $w_n \lesssim 50\%$ with a maximum of $w_n \cong 81\%$ occurring at Moore Park. While diatomaceous soils have generally higher w_n than other soils at the sites, this is not exclusively the case – there is overlap between the two groups. This is a clear indicator that high water content alone is not a reliable indicator or identifier of diatomaceous soils.

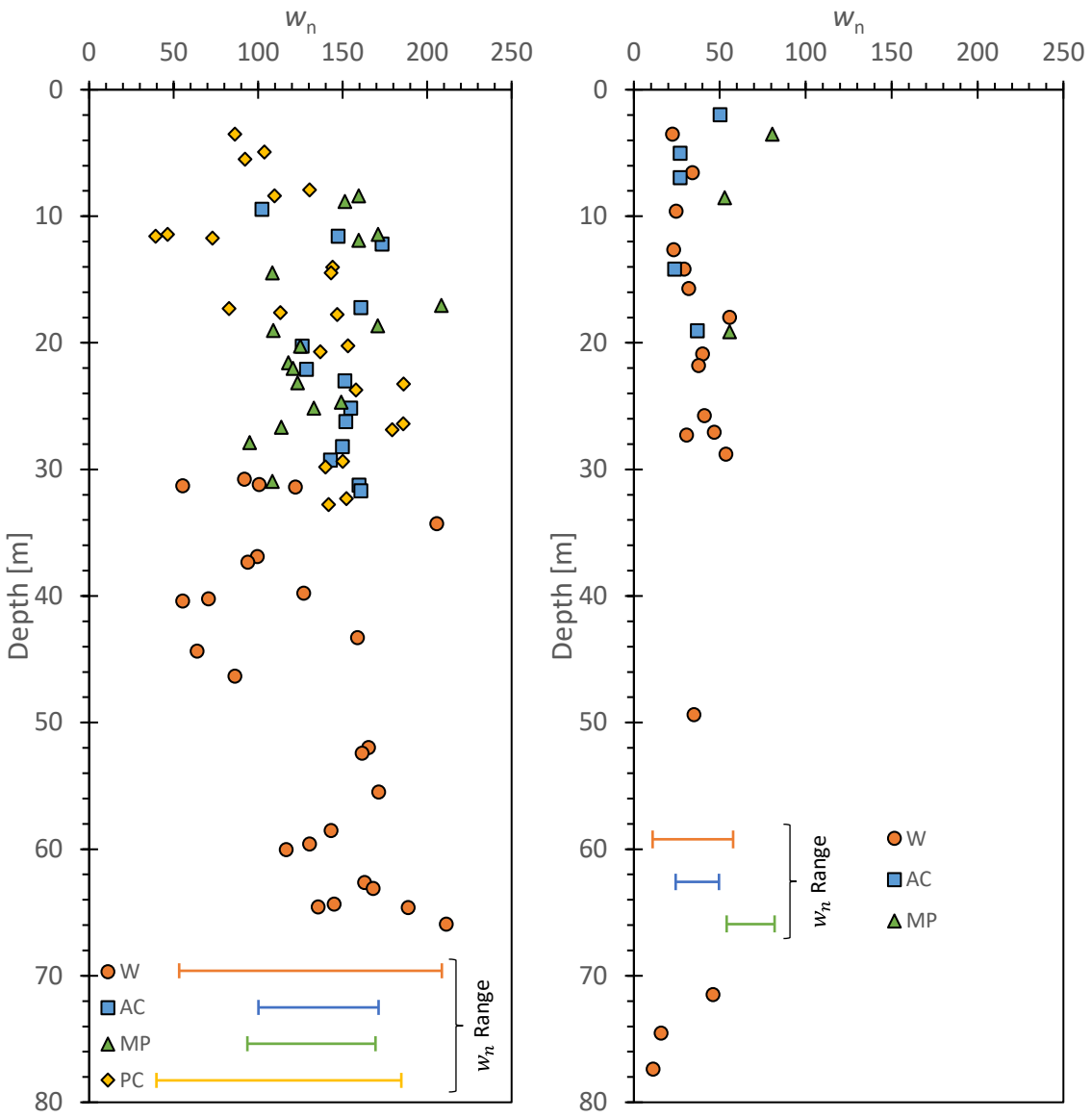

(a) Diatomaceous soil (b) Non-diatomaceous soil

Figure 5.2: Summary of natural water content

Natural water content is measured on all samples. By assuming full saturation beneath the groundwater table (GWT) and selecting an appropriate value for specific gravity (G_s) and w_n makes it possible to compute an estimate of the *in-situ* unit weight of the material. However, soils may not be fully saturated beneath the GWT because of occluded air bubbles and the specific gravity of diatomaceous soils shows much more variability ($2.00 \lesssim G_s \lesssim 2.40$) than for most geologic materials ($2.62 \lesssim G_s \lesssim 2.72$). Given these complexities and the counterintuitive properties of diatomaceous soils (e.g., some split spoon samples appear very dry and crumbly, even though they were recovered from below the GWT; see Appendix B), we elected to also measure unit weight (γ) and specific gravity (G_s) on a high proportion of bulk samples. When combined with w_n, γ and G_s complete the phase information for a soil *in-situ*. That is, these three

pieces of information are sufficient to unambiguously determine the relative proportion of soil solids, water, and air present in the bulk material. Therefore, γ and G_s were measured on a number of split spoon samples in addition to w_n. Measured values of γ are shown in Figure 5.3 (a) and those inferred through assuming full saturation ($\gamma_{calc} = G_s\gamma_w(1 + w_n)/(1 + w_n G_s)$) are presented in Figure 5.3 (b).

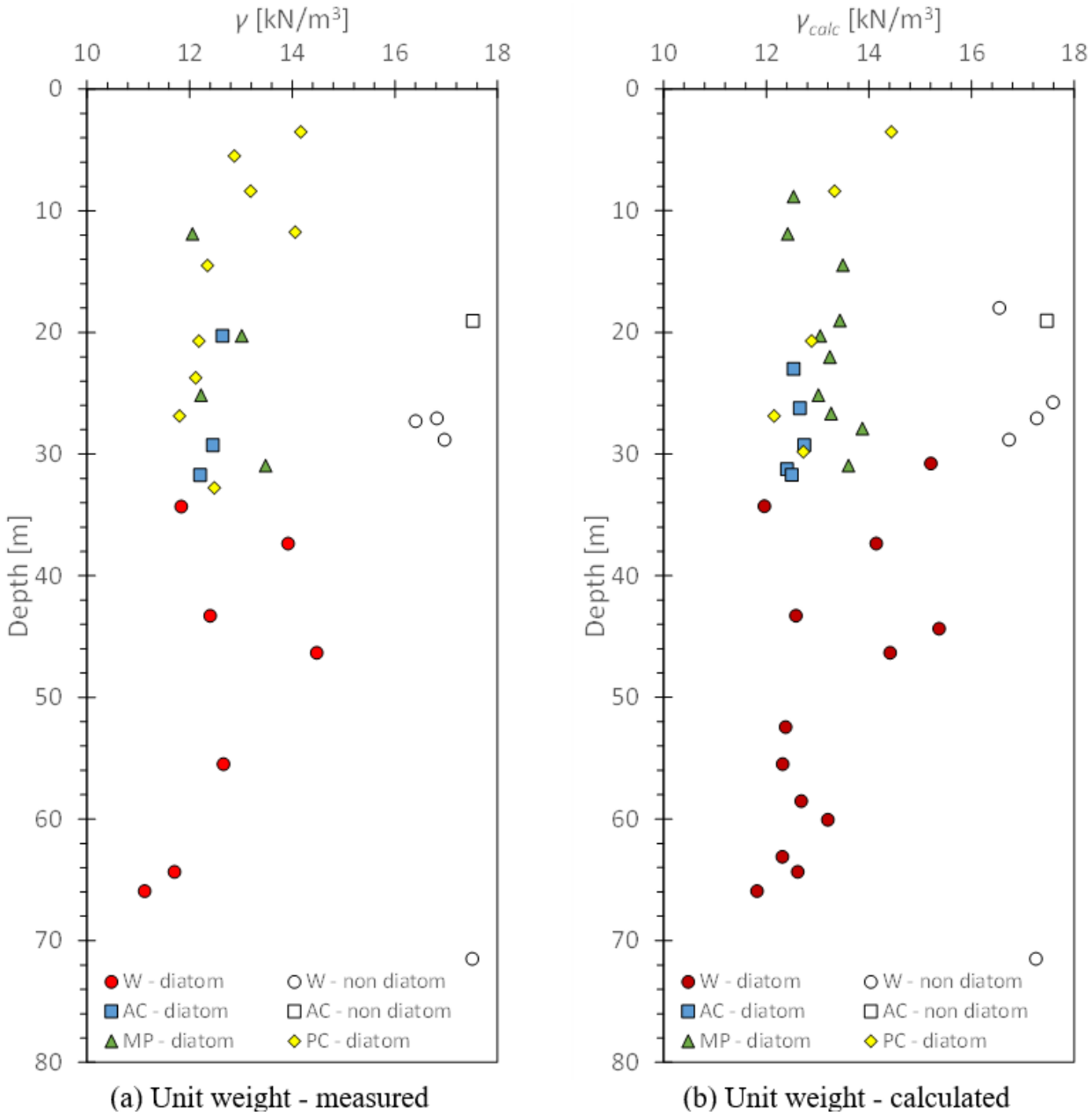

Figure 5.3: Summary of unit weight

In engineering practice, specific gravity (G_s) and unit weight (γ) are not always measured due to the complexity of the lab procedures. The value of G_s is usually estimated in order to obtain γ. The influence of specific gravity and water content on unit weight is shown in Figure 5.4. It can

be seen that the water content has a greater impact on γ, measuring w_n would be necessary for engineering practice in order to obtain accurate γ. Despite less influence of G_s on γ (Figure 5.4 (b)), it is still necessary to have a confident estimate of G_s if the soil is suspected to be diatomaceous. Figure 5.5 shows the comparison of calculated γ based on the actual G_s or G_s assumed to be 2.7. Clearly, assuming G_s equal to 2.7 would yield higher γ, which is incorrect. Good consistency is observed between the actual γ and γ calculated from the actual G_s. Therefore, it is important to have an accurate estimate of G_s if the soil is suspected to be diatomaceous.

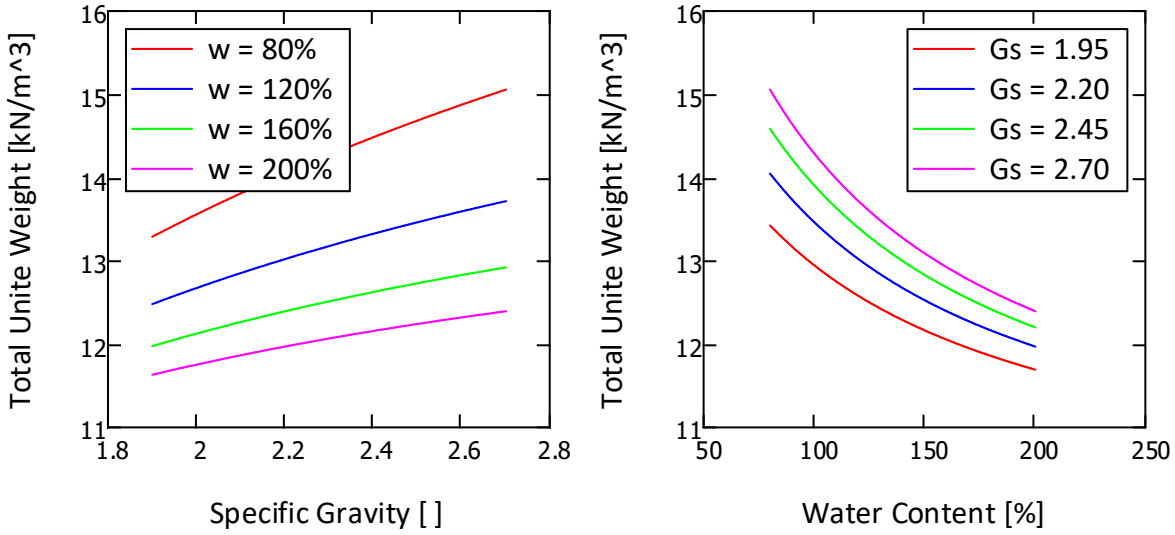

Figure 5.4: Influence of specific gravity and water content on unit weight assuming full saturation

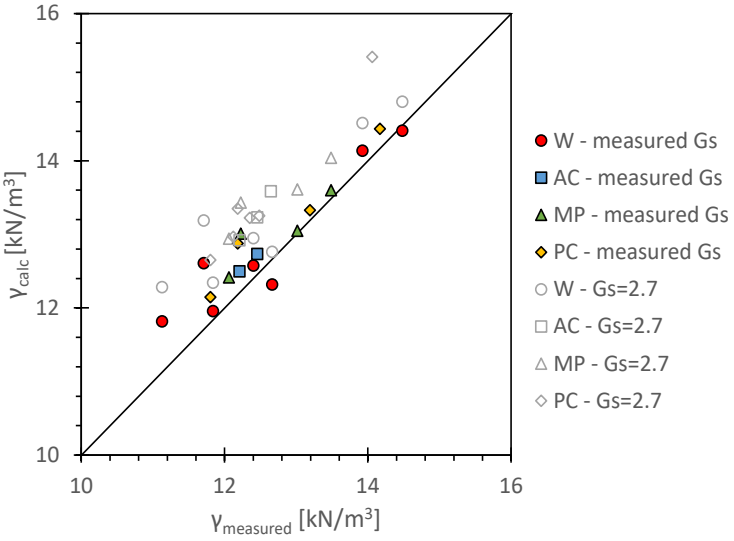

Figure 5.5: Comparison of unit weight between measured and calculated (closed symbols represent γ calculated from measured G_s, whereas, open symbols represent γ calculated from assuming $G_s = 2.7$)

Specific gravity (G_s) and saturation (S_r) profiles for the sites are shown in Figure 5.6. The separation between diatomaceous soil and non-diatomaceous soil is more distinct in terms of γ and G_s. The range of γ for diatomaceous soil is approximately 11.0–14.5 kN/m^3, and the range of G_s for diatomaceous soil is approximately 2.0–2.5. Generally, the diatomaceous soils tested had a calculated saturation higher than 90%.

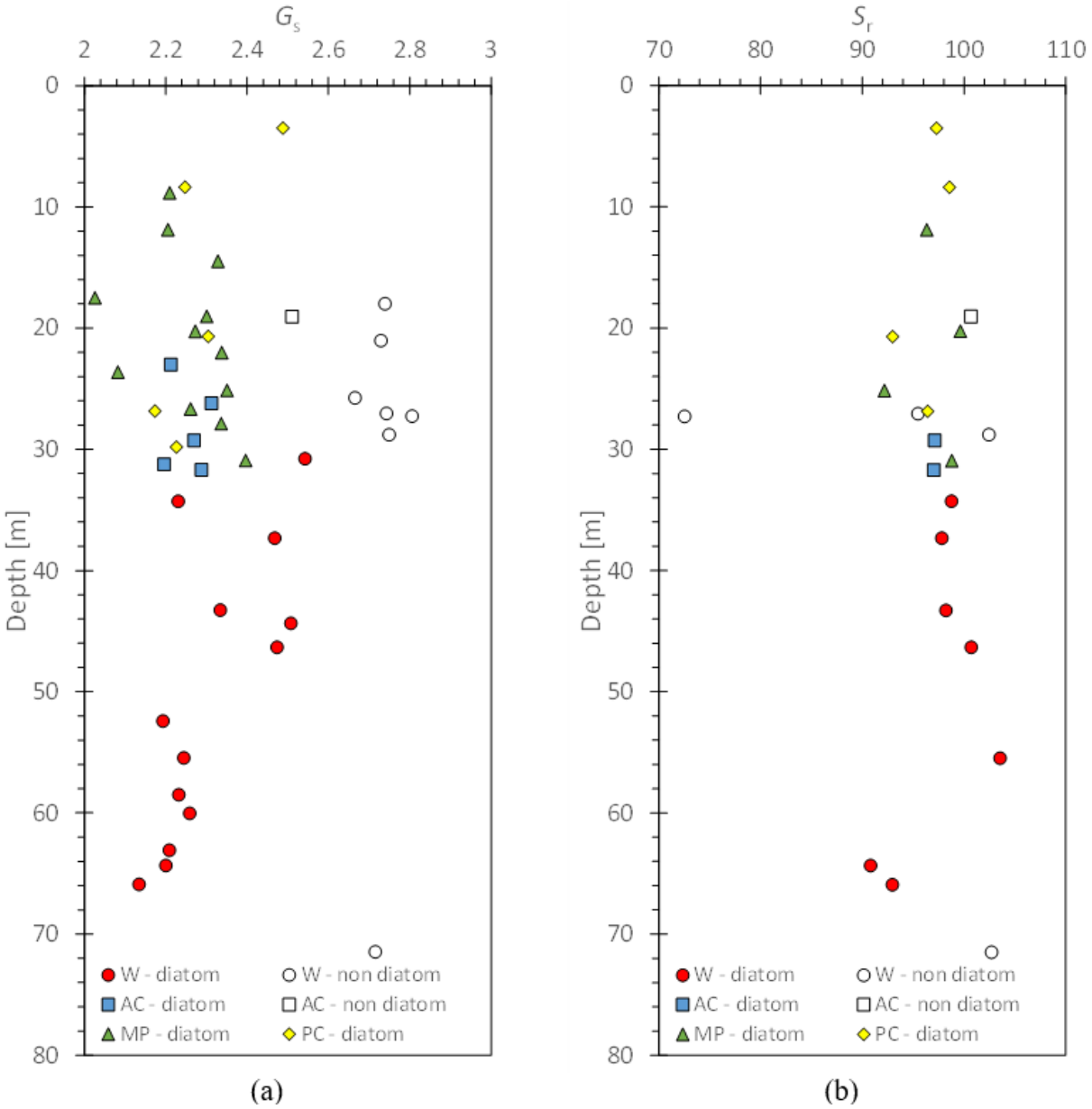

Figure 5.6: Summary of specific gravity and saturation

5.2.3 Fines Content and Grain Size Distribution

The fines content profile is shown in Figure 5.7. Generally, the tested diatomaceous soil specimens had fines contents of $FC > 90\%$. The complete grain size distribution (GSD) curve is

obtained by using nonlinear least squares regression to fit a smooth curve to the measured data (Fredlund et al. 2000), one representative specimen was selected from each site plotted in Figure 5.8 (note: not every sample measured fines content conducted hydrometer test), Appendix D summarizes all tested specimens and their GSD curves. The particle size of diatomaceous soil is generally in the range of 1 - 75 μm, which is typical value for diatomaceous soil and agrees well with reported in literature (Wiemer and Kopf, 2017).

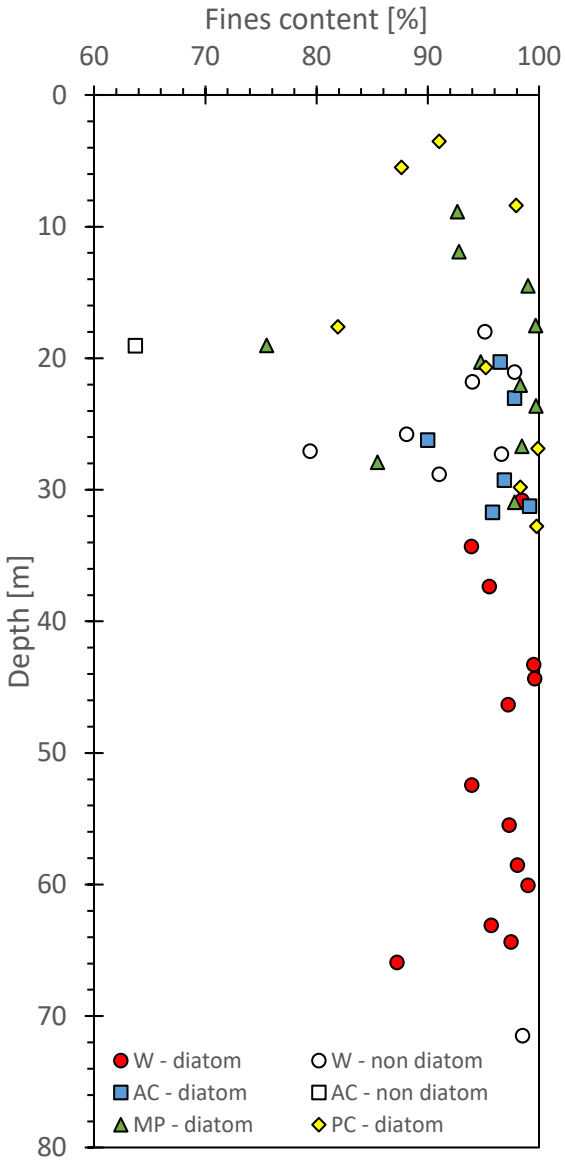

Figure 5.7: Summary of fines content

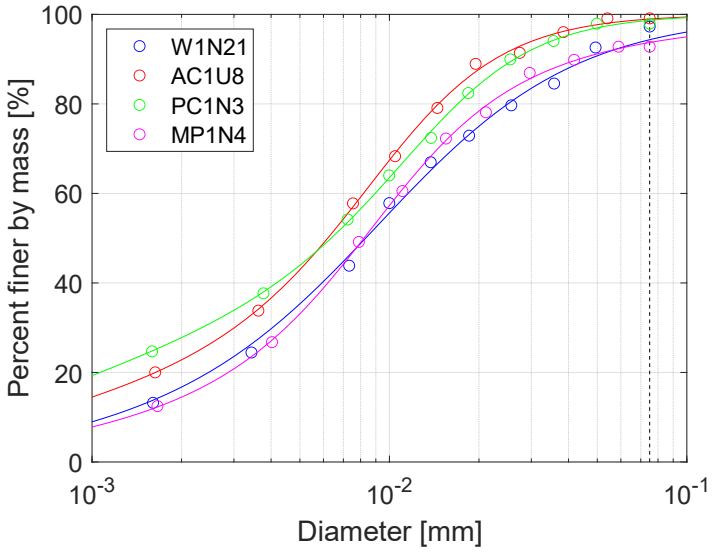

Figure 5.8: Representatives of grain size distribution of diatomaceous soil from each site fitted with Fredlund et al. (2000) equation (curves show the approximate extent of the GSDs measured in this study, remaining GSDs are presented in Appendix D)

5.2.4 Consistency Limits

5.2.4.1 Liquid limit

The liquid limit has been tested with three different methods (Casagrande cup, fall cone, and lab vane) for selected specimens. Because the lab vane test directly adopts the well-accepted definition that the undrained shear strength of soil at LL is around 2 kPa (Youssef, 1965; Sherwood and Ryley, 1970; Wroth and Wood, 1978; Wood, 1985), it is used as a metric to compare with results from fall cone tests and Casagrande cup tests. Figure 5.9 summarizes the LL determined from the fall cone and Casagrande cup tests compared with the lab vane. Similar to findings from Wang et al. (2022), the fall cone results are consistent with the lab vane test results while the Casagrande cup tests resulted in lower (around 18% lower) measured values of LL for these diatomaceous soils. In most engineering practices, the Casagrande cup method (ASTM D 4318; American Society for Testing and Materials (ASTM). 2017d.) was adopted in measuring LL for diatomaceous soil, an empirical correlation converting LL from Casagrande cup to LL from fall cone method is proposed in Figure 5.10 and Equation (4-40). In other words, the correct LL (from fall cone method) is 20% higher than that determined from Casagrande cup method. Though the Casagrande cup is the test method required by ASTM D 4318 (American Society for Testing and Materials (ASTM). 2017d.), the fall cone method (BSI 2022) should be adopted for diatomaceous soil.

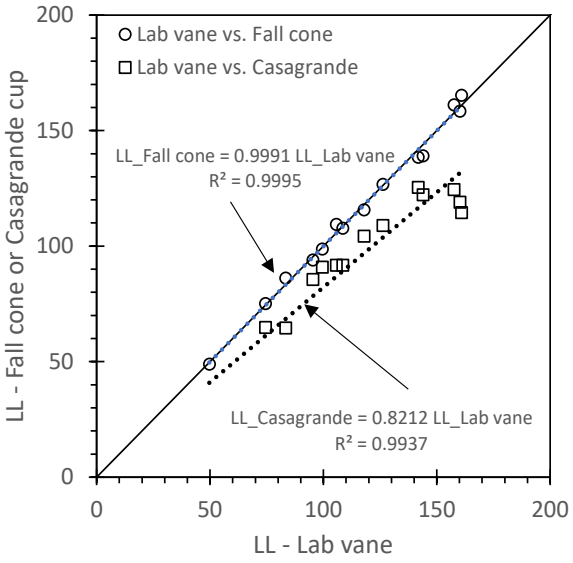

Figure 5.9: LL tested from fall cone and Casagrande cup tests compared with lab vane tests

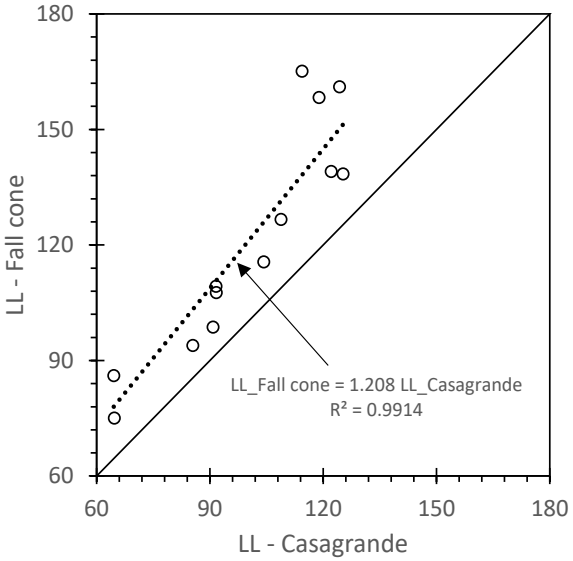

Figure 5.10: LL from fall cone method vs. LL from Casagrande cup method

$$LL_{FC} = 1.2\ LL_{CC} \tag{5-1}$$

Wang et al. (2022) found different flow curves of the fall cone tests on diatomaceous soil in terms of testing directions, therefore, prescribed specimens were tested from both wet-to-dry and dry-to-wet directions during the fall cone tests. The comparison of LL values is shown in Figure 5.11. It can be seen that LL determined from dry-to-wet direction is consistently lower than that from wet-to-dry direction. Although the relative difference (about 4%) is negligible in LL values, the influence of testing directions on PL determination using (Feng, 2001) method is considerably higher (full discussion is seen in 5.2.4.2).

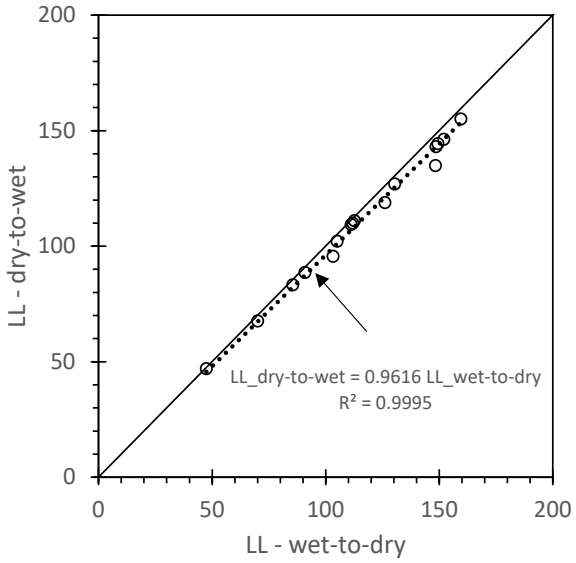

Figure 5.11: LL tested from dry-to-wet direction vs. LL tested from wet-to-dry direction on fall cone tests

5.2.4.2 Plastic limit

The comparison of PL measured from three different methods is shown in Figure 5.12. It can be seen that none of the methods are highly consistent. PL from the thread rolling method is roughly 13% higher than PL determined from Feng (2001) method when tested from wet-to-dry direction and is roughly 10% lower than PL determined from Feng (2001) method when tested from dry-to-wet direction. PL from the Wood method tends to be susceptible and does not show any consistency with the other methods. Empirical correlations are drawn from the current data between the Feng method and the thread rolling method, shown in Equation (5-2) and (5-3). The comparison between PL tested from dry-to-wet direction and PL tested from wet-to-dry direction using the Feng method is presented in Figure 5.13. There is approximately 24% relative difference between the PL as a result of the testing directions.

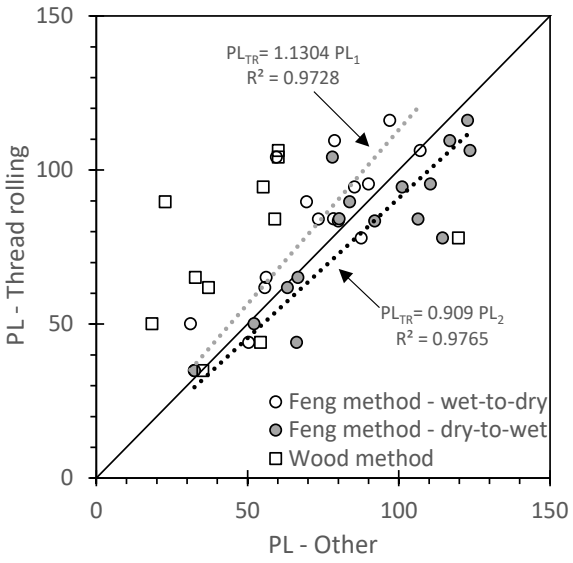

Figure 5.12: PL measured from Feng method and Wood method compared with thread rolling method (PL_1 is PL determined from Feng (2001) method when tested from wet-to-dry direction; PL_2 is PL determined from Feng (2001) method when tested from dry-to-wet direction, PL_{TR} is PL determined from the thread rolling method)

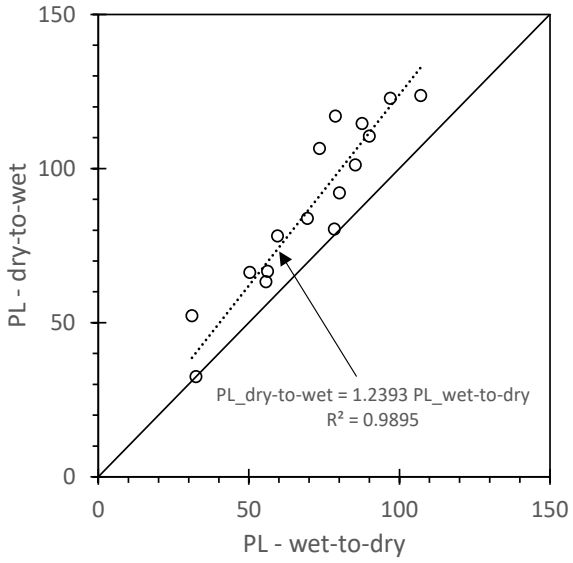

Figure 5.13: PL tested from dry-to-wet direction vs. PL tested from wet-to-dry direction using Feng method

$$PL_{Thread\ rolling} = 1.13\ PL_1 \quad \textbf{(5-2)}$$

$$PL_{Thread\ rolling} = 0.91\ PL_2 \quad \textbf{(5-3)}$$

Where,
PL_1 is PL determined from Feng (2001) method when tested from wet-to-dry direction;
PL_2 is PL determined from Feng (2001) method when tested from dry-to-wet direction.

5.2.4.3 Recommendation for liquid limit and plastic limit determination for diatomaceous soil

It is observed that different methods produce inconsistent measurements of LL and PL for diatomaceous soil. As the consistency limits are used as a proxy for inferring quite complex information about fine-grained soils, including clay electrochemistry, shear strength, and compressibility, it is critical to have accurate measurements on LL and PL. Based on the discussion in 5.2.4.1 and 5.2.4.2, it is recommended to use the fall cone method (BSI 2022) to determine LL and the thread rolling method to determine PL (ASTM D 4318; American Society for Testing and Materials (ASTM). 2017d.). The fall cone test is fundamentally a strength test and corresponds to the well-accepted definition for LL that the undrained shear strength at LL is 2 kPa. Therefore, the fall cone method should be adopted in determining LL rather than the Casagrande cup tests for diatomaceous soil. If LL is tested from the Casagrande cup tests, Equation (4-40) can be used to convert to LL from fall cone tests.

The PL determined from various methods for diatomaceous soil are not consistent with one another. The thread rolling method is fundamentally a cohesion-based method for PL determination dated back to Atterberg (1911) where the author defined PL as the state of soil at which the soil crumbles when being rolled out into threads. The Wood method (Wood and Wroth, 1978) uses the strength-based theory that the soil strength at the PL is approximately 100 times of that at the LL (Skempton and Northey, 1952). Lastly, the Feng method (Feng, 2001) uses an indirect measurement that extrapolates the flow curve ($\log(w) - \log(d)$) from the fall cone test and suggests PL is the water content at penetration of 2 mm in $\log(w) - \log(d)$ space. The Wood method is not recommended due to its low practicality. Meanwhile, the thread rolling method and Feng method are relatively easy to conduct and capable of correlating to one another. Since ASTM D 4318 adopts the thread rolling method, we recommend using it to determine PL for diatomaceous soil. If fall cone tests are conducted to determine LL, it would be straightforward to calculate PL using Feng method, in this case, Equations (5-2) and (5-3) can be used to correlate to PL from thread rolling method.

In this study, the LL presented are either measured from fall cone tests or correlated to fall cone tests, and the PL are from thread rolling method or correlated to thread rolling method.

5.2.4.4 Plasticity chart

The plasticity chart is presented in Figure 5.14. The majority of the data points are located below “A” line with LL greater than 50, which is classified as “MH” (i.e., elastic silt) in the Unified Soil Classification System (USCS). Specimens from Ady Canal, Pine

Cone, and Moore Park all have LL greater than 100. The Wickiup specimens have largest span in LL, ranging from 50 to 200.

In contrast, the data from the diatomaceous literature (covered in Chapter 2) are plotted above and below the "A" line, showing higher PI than diatomaceous soil from this project. The literature data extend to $LL \cong 500, PI \cong 500$ owing to the existence of Mexico City clay. While it is diatomaceous soil, it also contains a significant amount of montmorillonite clay, thus, having LL that are far out of trend with other diatomaceous soils.

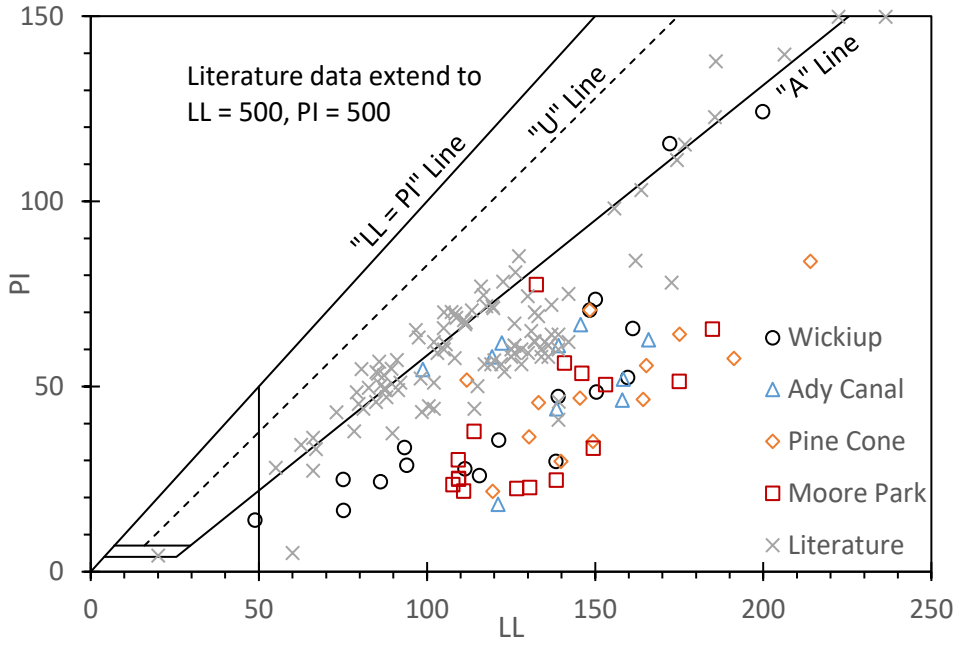

Figure 5.14: Plasticity chart on diatomaceous soil from this project and diatomaceous literature (from Chapter 2)

5.2.4.1 Soil profile of consistency limits

The soil profiles of consistency limits are presented in Figure 5.15. It can be seen that the natural water content (w_n) is generally on the upper end of the LL-PL straight line or even greater than LL, indicating a liquidity index greater than 1. However, the visual appearance of those split spoon samples actually look "dry", especially for samples from Pine Cone (see Appendix B). The variation of $w_n - LL - PL$ is most significant in Wickiup, while it remains relatively uniform in other sites. Moore Park shows a decreasing trend of $w_n - LL - PL$ along depth, whereas the trend is less obvious for other sites.

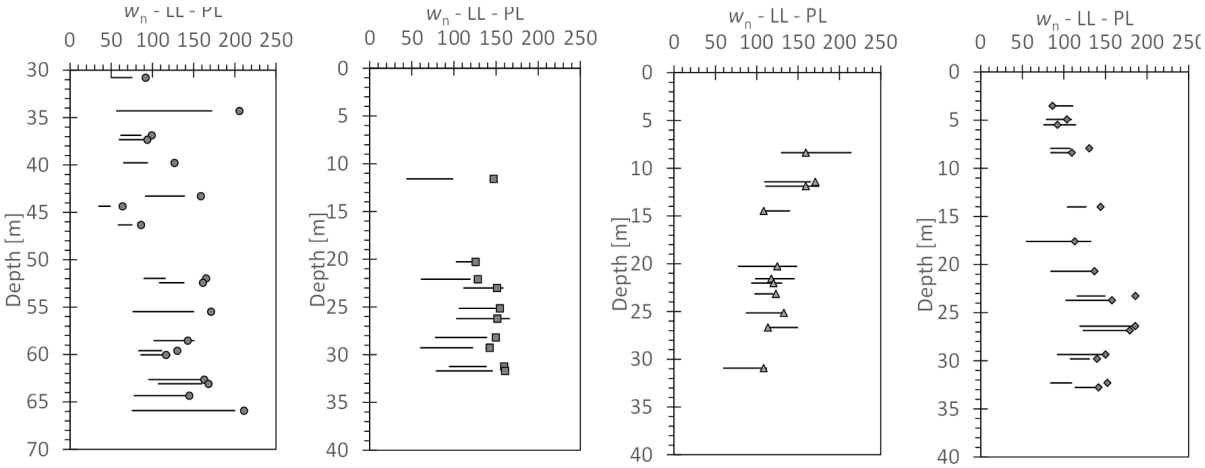

Figure 5.15: $w_n - LL - PL$ profiles of four sites (w_n is represented by the individual data points, the upper end of the straight line is LL and the lower end is PL)

5.2.5 Specific Surface Area

The specific surface area (SSA) is the ratio of a particle's surface area to its mass (e.g., Santamarina et al., 2001). It is a powerful tool for understanding the engineering properties of clays, due to the complexity and importance of particle surface chemistry on bulk material behavior. While diatom frustules are not chemically active, SSA potentially provides a mechanism to partition relatively less accessible intraparticle pores (Tanaka and Locat, 1999) from the remainder of the porous matrix, perhaps providing a clue to understanding the apparent dichotomy between very high liquid limit co-existing with high shear strength. The SSA can be measured using a variety of methods, with each having its applicability and limitations, though not all will provide the same result. For example, Hang and Brindley (1970) reported Florida kaolinite has a SSA of 35.2 ± 2 m^2/g, Santamarina et al. (2002) reported a SSA of 10~20 m^2/g for kaolinite, and in this project, the SSA of kaolinite was measured as 45.3 m^2/g. Nonetheless, SSA is widely accepted (e.g., Petersen et al., 1996; Díaz-Rodríguez and Santamarina, 2001) as a strong indicator of material behavior through a fundamental particle-scale lens.

The SSA was measured using the methylene blue method for a total of 18 soil specimens. Six of those were tested twice to confirm the repeatability, shown as Figure 5.16. It can be seen that the titration method by itself is quite repeatable regardless of whether the soil is diatomaceous. The profile of SSA against depth is shown in Figure 5.17. The measured diatomaceous soil samples have $20\,m^2/g \lessapprox SSA \lessapprox 220\,m^2/g$, and the non-diatomaceous soils exhibit $28\,m^2/g \lessapprox SSA \lessapprox 120\,m^2/g$. Because the other soils tested were generally clays (which also typically have high SSA), there is not a real distinction between the tested diatomaceous and non-diatomaceous soils in terms of SSA. Two diatomaceous split spoon samples (W1N21, AC1N12) were measured with both the methylene blue and N_2 methods, but it is difficult to draw conclusions for them results presented in Table 5.2. AC1N12 exhibits relatively consistent results between the two methods, whereas W1N21 does not.

Table 5.2: Specific surface area (unit: m^2/g) obtained from N_2 method compared with MB method

	MB method	N_2 method
W1N21	19.57	95.96
AC1N12	66.67	77.23

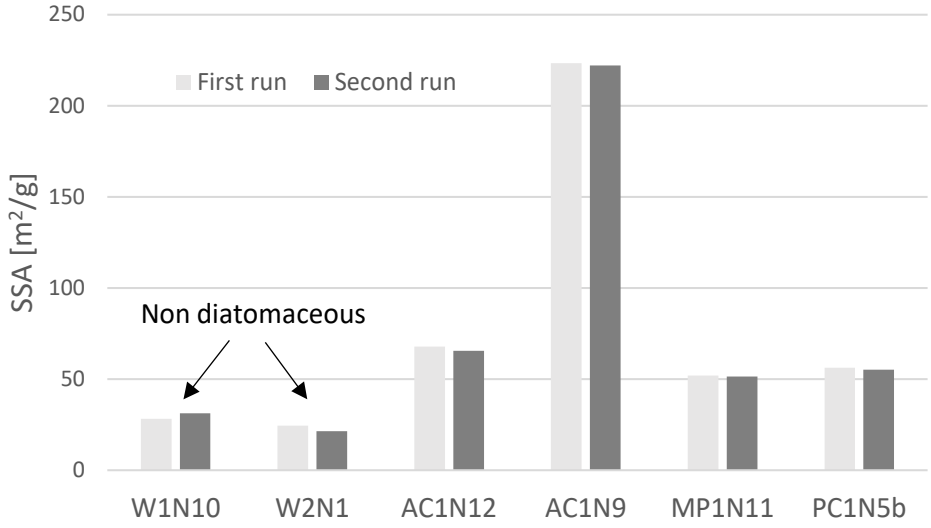

Figure 5.16: Repeatability of specific surface area by methylene blue method (non-diatomaceous soil samples are marked)

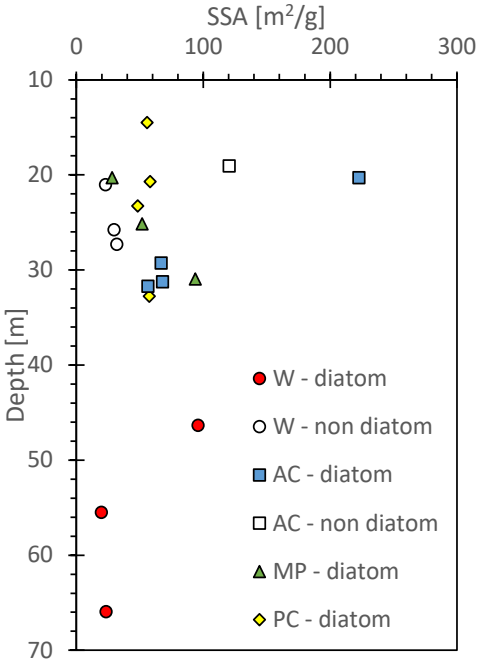

Figure 5.17: Specific surface area profile by methylene blue method

5.3 LABORATORY RESULTS ON MECHANICAL PROPERTIES

5.3.1 The Usage of Shelby Tubes

Shelby tubes were collected during the site investigation for the purpose of retrieving undisturbed samples of diatomaceous soil. Figure 5.18 shows the detailed usage of Shelby tubes in all four sites. Basically, all possible intact soil was extruded to run mechanical tests named as 'Triaxial', 'IL', 'CRS', 'DSS', respectively. The legend 'Hyprop' represents the specimens used to conduct the Hyprop tests intended to obtain soil-water retention curves. Amongst the six Hyprop specimens suggested in the figure, four of them were trial samples (i.e., soil was either sandy or slurry like or crumbled which was not useable for other tests), two of them (AC1U3, AC1U7) were intended to obtain reasonable results, however, all results were not ideal to elucidate the relation of soil-water retention. The cyclic simple shear tests (CSS) were attempted to understand the cyclic behaviors of diatomaceous soils; however, the test results did not provide adequate information for interpretation. Therefore, we omit the results of DSS tests here. Also note that the tests shown in Figure 5.18 indicate tests attempted, if tests failed or results are abnormal (e.g., IL test in PC1U7 was entirely disturbed), the results were not included for analysis.

Figure legends represent the soil status or the tube status. A 'Slurry' example is shown in Figure 5.19, where the soil is completely jelly-like making these samples inconducive for mechanical tests. If designated as Slurry, it is also unclear whether the sample was diatomaceous soil or not. Slurry soil substantially appeared in Wickiup Junction. 'Tossed' usually means the soil is at the cutting open side of the tube or right next to the extruding stone, therefore, the soil is tossed due to possible disturbance induced by cutting the tube or extruding specimen. The tossed soil is usually short length likely 1 – 2 inch, one particular example is PC1U4, where the wax deeply infiltrated into the soil along hollow portions of the soil (Figure 5.20). 'Damaged' means the tube was wrecked or damaged while being pushed in the borehole (Figure 5.21). It most frequently happened in Moore Park and Pine Cone Drive where the diatomaceous soil is chalk-like or mudstone-like. Moreover, Shelby tubes from these two sites have the lowest recoveries in all four sites. 'Soil crumbled' means that the soil did not stick together like regular clay or silt, but broke apart like 'rocks' or 'sands', however, the crumbled soil can easily turn into fine grained soil if pinched between fingertips and there are not actual 'rocks' or 'sands' (Figure 5.22). Soil like this is undoubtedly impossible to conduct any mechanical tests.

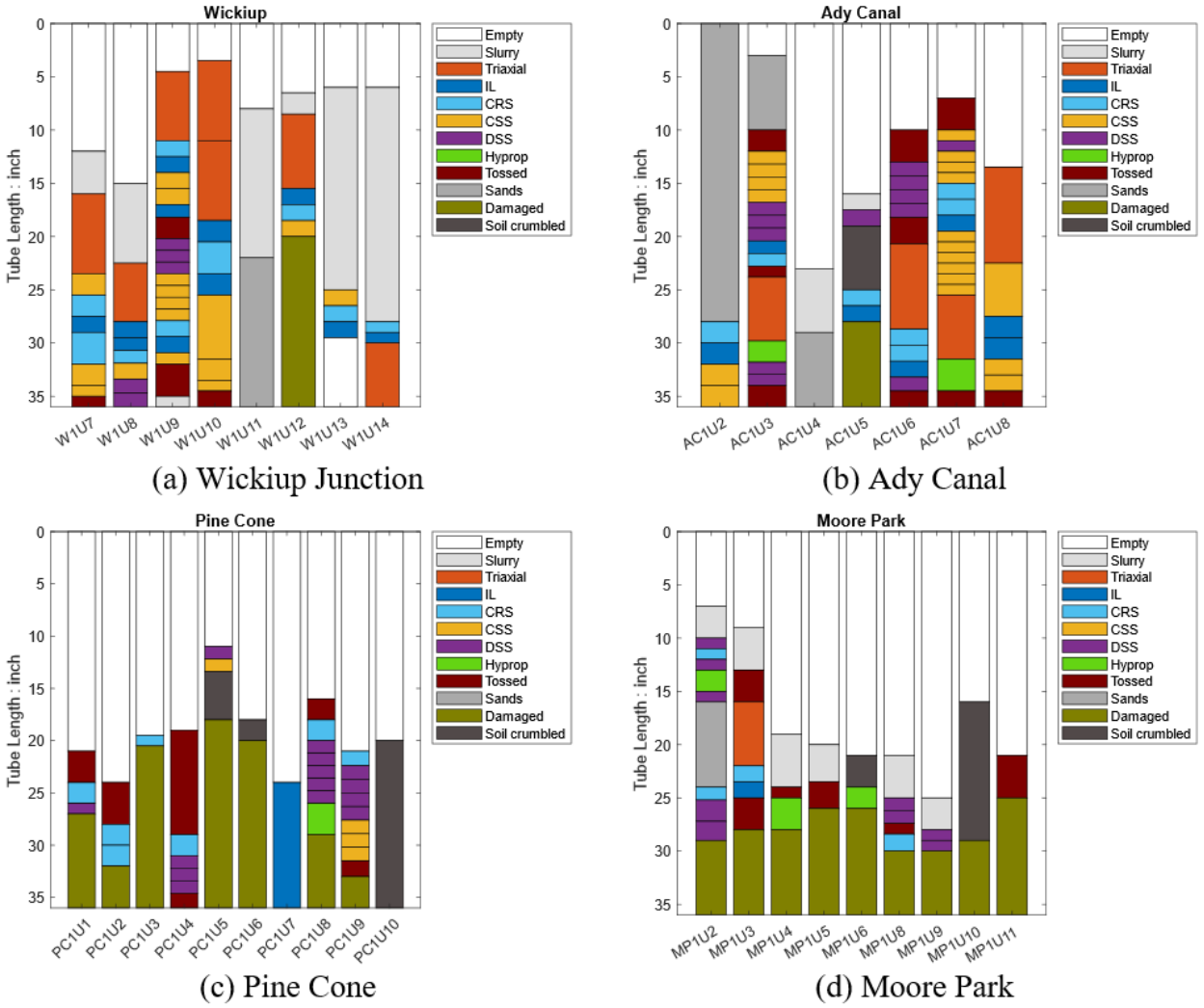

Figure 5.18: The usage of Shelby tubes

(a) W1U11 (b) W1U14

Figure 5.19: Slurry examples

Figure 5.20: Wax infiltrated into the soil (PC1U4)

(a) PC1U3 (b) PC1U6

Figure 5.21: Examples of tube damaged at the bottom

(a) MP1U6 (b) MP1U10 (c) PC1U10

Figure 5.22: Examples of soil crumbled

5.3.2 Consolidation Test

5.3.2.1 Introduction

Compressibility and hydrodynamic consolidation were measured with constant-rate-of-strain (CRS) and incremental load (IL) oedometric testing. A total of 20 Shelby tubes were used to extrude specimens for consolidation tests: seven from Wickiup, five from Ady Canal, five from Pine Cone, and three from Moore Park. In order to verify the

consistency of the two tests, a total of 12 specimens were used, most of which were from Wickiup and Ady Canal. The rest of the specimens were subject to either CRS or IL tests. Detailed summaries of the tests, including specimen photos, consolidation curves, and consolidation parameters, are included in Appendix E. Specimens from a small, selected number of tubes were subjected to multiple CRS or IL tests to assess repeatability and investigate the effects of load duration. For simplicity, only one CRS and one IL test for each specimen are used for analysis in Sections 5.3.2.2–5.3.2.5; the tests not included in the analyses are explicitly indicated in Appendix E. In Section 5.3.2.6, the replicate CRS and IL tests are presented for comparison. It is apparent from specimen photos in Appendix E that specimens are of different qualities, exhibiting more or less disturbance. Overall, specimens from Wickiup and Ady Canal are of higher quality. In contrast, Moore Park and Pine Cone soils are mudstone-like and often times they easily break into stiff clumps which can be crushed into fine particles when pinched between fingertips (e.g., photos of MP1U3 in Appendix E). In this case, it is much more difficult to trim the specimen (e.g., MP1U3, PC1U1, PC1U2), but the best effort was made to fill gaps in the specimen with trimmings to create a smooth surface for testing.

5.3.2.2 Consolidation curves

Three important material parameters can be obtained from the load-deformation (i.e., consolidation) curve: the compression index (C_c), the recompression index (C_r; also commonly referred to as the swell index, C_s), and the preconsolidation stress (σ_p'). There may be some small differences in consolidation curves depending on whether the initial or final water content measurement is used for calculation (see Section 4.3.1.2 for calculation procedure). These differences are detailed in Appendix E. Some of this difference likely arises because specimens are not at full saturation when initially placed in the consolidometer. The $\varepsilon - \log \sigma_v'$ and $e - \log \sigma_v'$ curves presented in Figure 5.23 were calculated based on specimen mass and water content measured at the end of the test because the specimen is more likely to be fully saturated at this point. The stress-strain curves of CRS tests generally show less variability across specimens than the IL tests. The $e - \log \sigma_v'$ curves indicate that almost all tests have well-defined virgin compression lines (VCLs) and yield points (i.e., σ_p'), indicating good specimen quality.

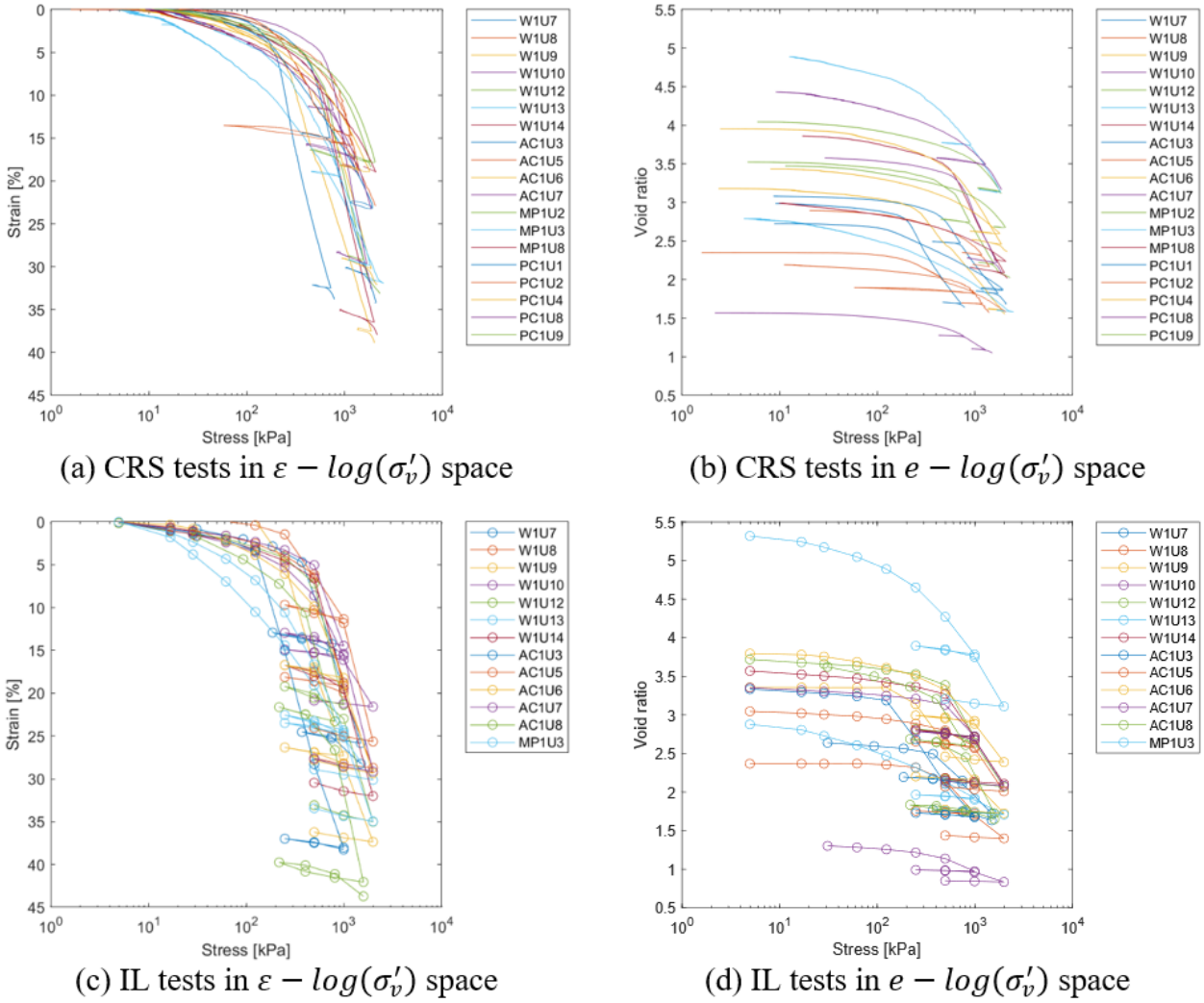

(a) CRS tests in $\varepsilon - log(\sigma_v')$ space

(b) CRS tests in $e - log(\sigma_v')$ space

(c) IL tests in $\varepsilon - log(\sigma_v')$ space

(d) IL tests in $e - log(\sigma_v')$ space

Figure 5.23: Consolidation curves in $\boldsymbol{\varepsilon - log(\sigma_v')}$ and $\boldsymbol{e - log(\sigma_v')}$ space

5.3.2.3 Compression index and recompression index

The definition of C_c is the slope of the VCL and C_r is defined as the slope of the unloading-reloading line (URL) in $e - \log \sigma_v'$ space. Both C_c and C_r were determined by regressing a best-fit line through the data points on VCL or URL. The determination of C_c is susceptible to error depending on the extent of disturbance of the specimen. The profiles of C_c, C_r, and C_r/C_c against depth are shown in Figure 5.24 - Figure 5.26. The compression and recompression indices for the diatomaceous specimens tested are mostly in the range $0.5 \lesssim C_c \lesssim 2.9$ and $0.04 \lesssim C_r \lesssim 0.22$, respectively. We have observed that the measured C_c values and soil texture are qualitatively related. For diatomaceous soils which are mudstone-like (the case of Moore Park and Pine Cone), the compression index (C_c) is lower than for the clay-like diatomaceous soils (the case of Wickiup and Ady Canal). The ratios of C_r to C_c generally fall in the range of $0.04 \lesssim C_r/C_c \lesssim 0.2$, about the same range for most fine-grained soils (Bardet, 1997). Figure 5.27 plots C_r vs. C_c

with a best-fit line showing the ratio of C_r to C_c is 0.081. In Chapter 6, the correlation between C_r and C_c is further discussed and compared to literature review data.

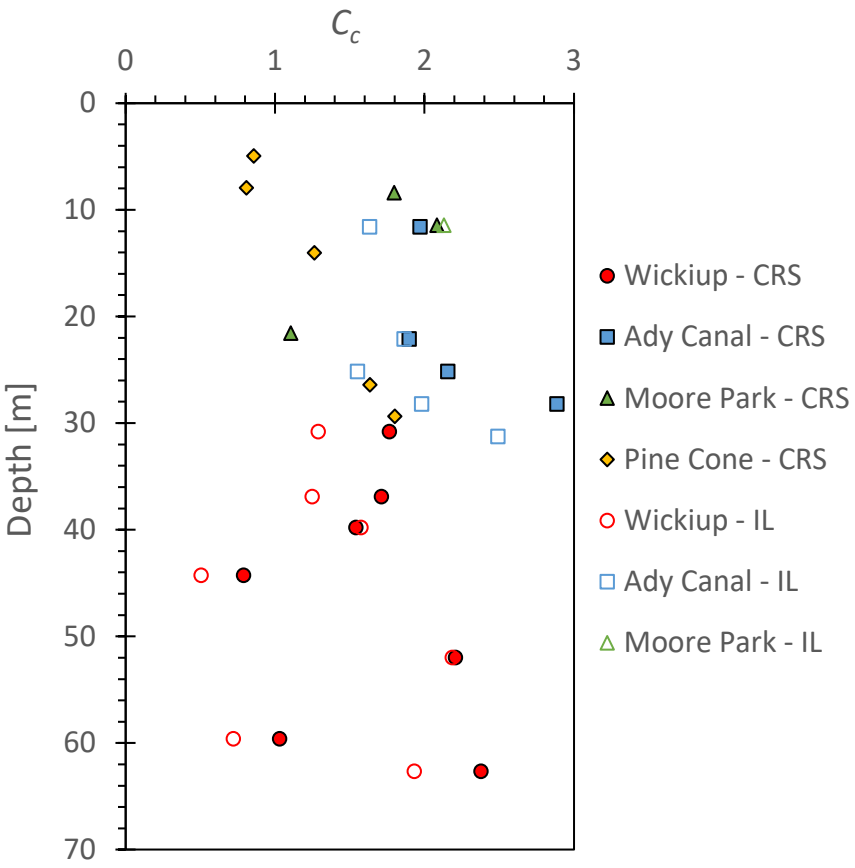

Figure 5.24: C_c profiles along depth

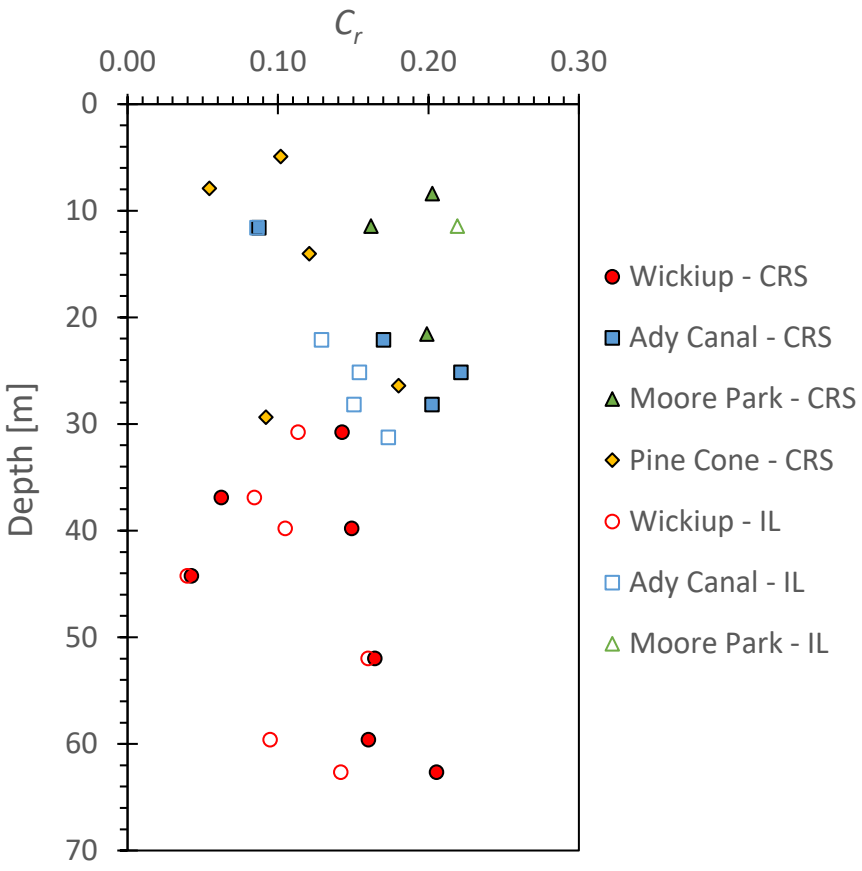

Figure 5.25: C_r profiles along depth

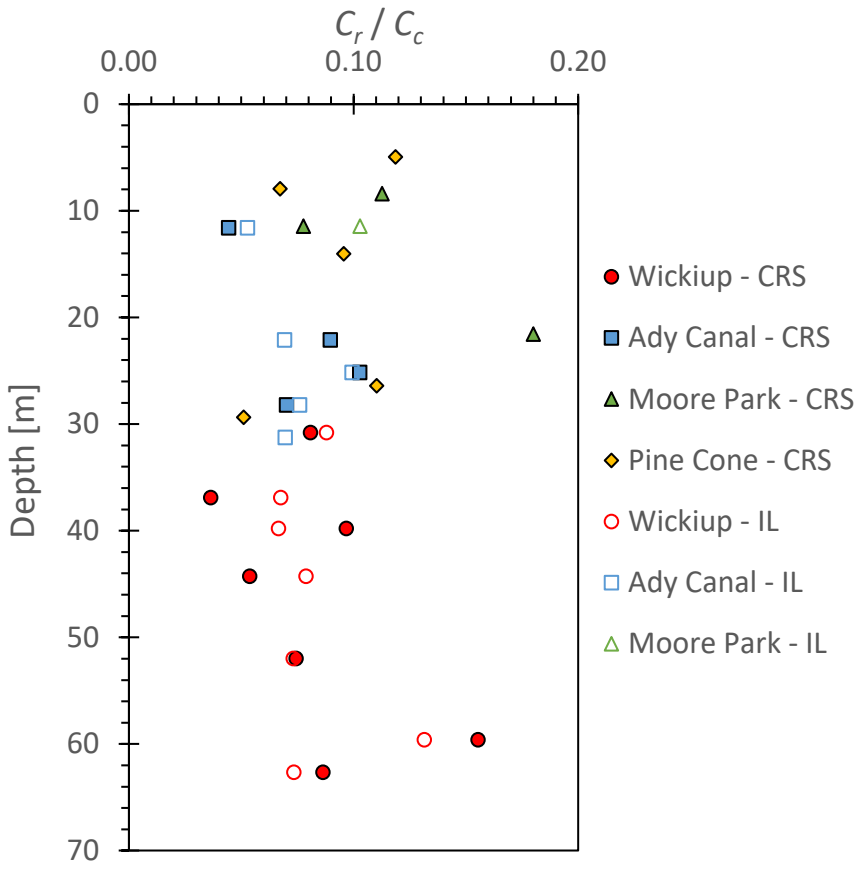

Figure 5.26: C_r/C_c profiles along depth

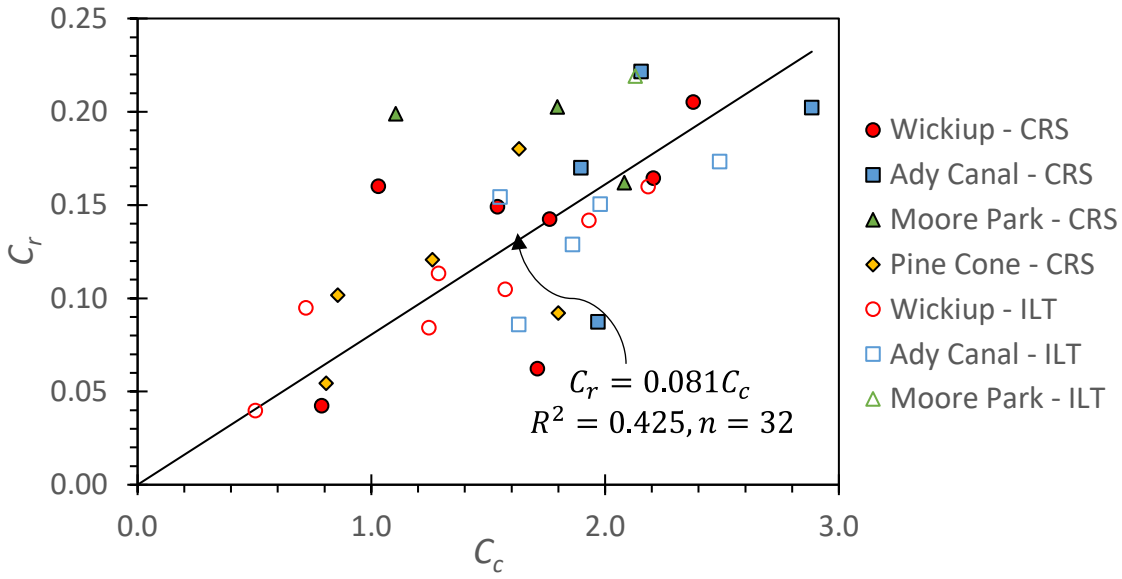

Figure 5.27: C_r $vs.$ C_c

For some specimens, there is discrepancy in the compression index (C_c) from CRS and IL tests, and the CRS tests usually yields a higher C_c than the IL test. One of the examples (W1U14) is shown in Figure 5.28. The comparisons between CRS and IL tests on C_c and C_r are shown in Figure 5.29. We can see that C_c from CRS tests is consistently higher than (or equivalent to) C_c from IL tests. An empirical correlation between evaluated C_c through the origin is presented in the figure, indicating that C_c from IL test is about 17% lower than C_c from CRS test. Similar findings have been reported in Chai et al. (2006), where the authors conducted both CRS and IL tests on soils from Saga, Japan, and found that CRS test resulted in a higher C_c than IL test although there was not much difference in σ_p'. However, the opposite findings were also observed: Gorman (1976) conducted CRS and IL tests on soil common to Kentucky, and the results show that C_c from IL test are generally (up to 35%) higher than C_c from CRS. Smith and Wahls (1969) studied CRS tests on different strain rates (0.06 and 0.024 %/min) and found that CRS test results are generally in good agreement with IL tests, especially at a lower strain rate (i.e., 0.024 %/min).

There has not been widely reported the discrepancy between CRS and IL tests. Such phenomenon may be soil specific. Similarly, the comparison on C_r between the two tests is shown in Figure 5.29 (b). Unlike Figure 5.29 (a) showing that C_c from CRS tests are consistently higher, there are two specimens showing the C_r from IL tests are higher. Still, the majority of CRS results yield a higher C_r than IL results. An empirical correlation between evaluated C_r through the origin is presented in the figure, indicating that C_r from IL test is averagely 20% lower than C_r from CRS test. Note that although the empirical correlations of C_c and C_r between the two tests are drawn, it is not to derive C_c and C_r from one test to the other, rather, it is to qualitatively understand the discrepancy between the two tests.

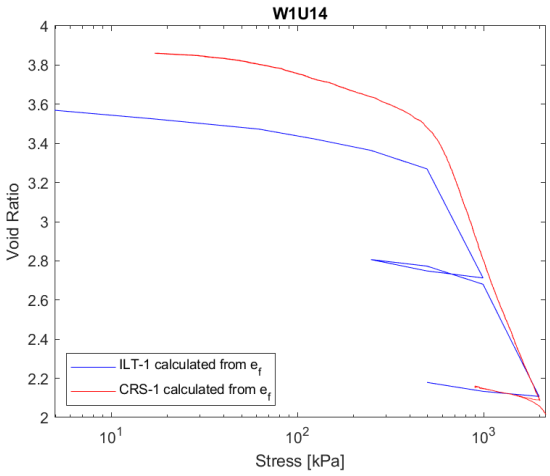

Figure 5.28: An example of higher C_{c-CRS} than C_{c-IL} ($C_{c-CRS} = 2.37, C_{c-IL} = 1.93$)

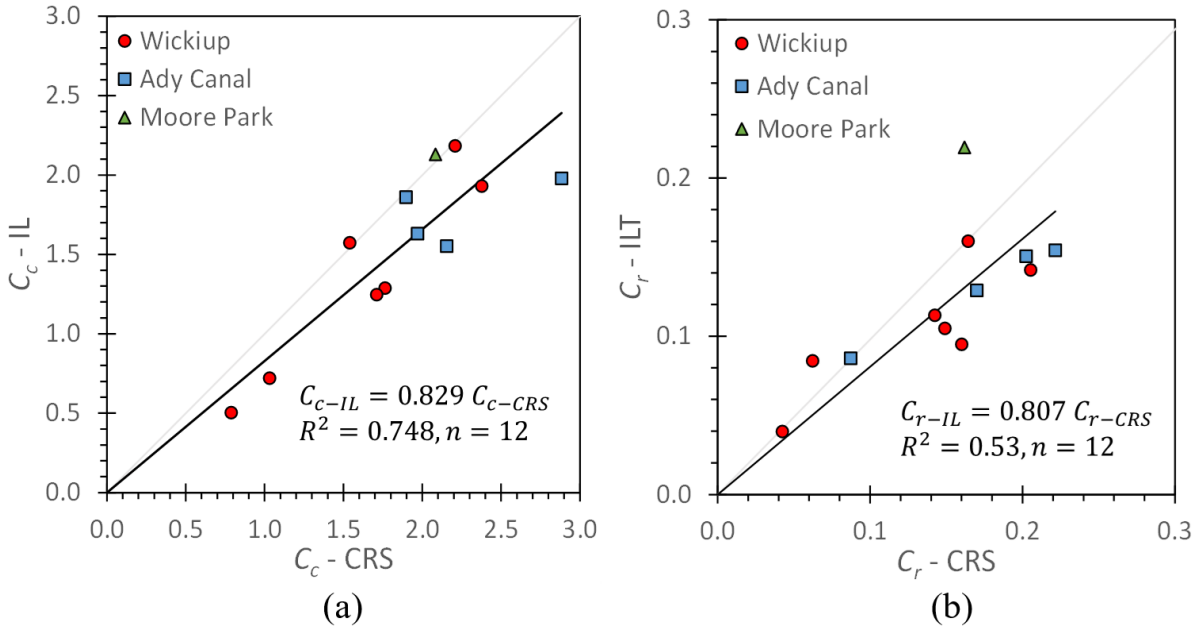

Figure 5.29: C_c and C_r comparisons between CRS and IL tests

5.3.2.4 Overconsolidation ratio

The overconsolidation ratios (OCR) evaluated by three different approaches introduced in Chapter 4 are shown in Figure 5.30. There are inevitably some differences among various methods of evaluation and testing, but for most specimens, the three different approaches yield similar evaluations for the preconsolidation stress (σ_p') on the same test results. Three specimens that caught attention are W1U13, PC1U1, and PC1U2, which show varied OCRs across different evaluations. Their specimen photos and consolidation curves are summarized in Appendix E together with all other specimens. Some disturbance can be observed in the specimen preparation and consolidation curves, which may be attributed to the discrepancies of different OCR evaluations. When comparing CRS and IL test results, W1U8 and W1U13 show different OCR evaluations. We have discussed the possibility of disturbance attributable to the observation for W1U13, but W1U8 specimens were of high quality (see Appendix E) and this observation is unexpected. However, a second IL test was conducted for W1U8 and provided results similar to those from the first IL test (details discussed in Section 5.3.2.6 below), implying that the IL test value is more appropriate than those from the CRS test for W1U8. Another noticeable specimen is W1U9 which shows slightly underconsolidated based on the OCR evaluations. Although we do not expect soils to be underconsolidated from geological inference, the evaluated OCR from CRS tests is around 0.9, only slightly less than 1. In Chapter 6, we interpret OCR from CPTu tests, and the profile of OCR does show some underconsolidation near where W1U9 was retrieved. Moreover, we conducted repetitive tests on the soil retrieved from this Shelby tube (2 CRS and 2 IL tests, details see Appendix E), the specimens were all of good quality, and the results show good repeatability and consistency across all test results.

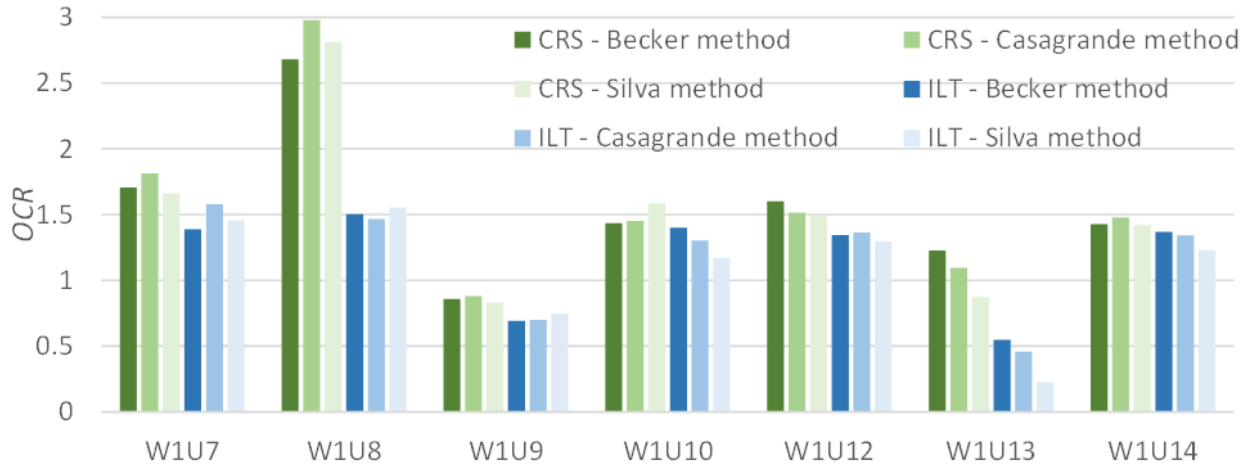

(a) Wickiup

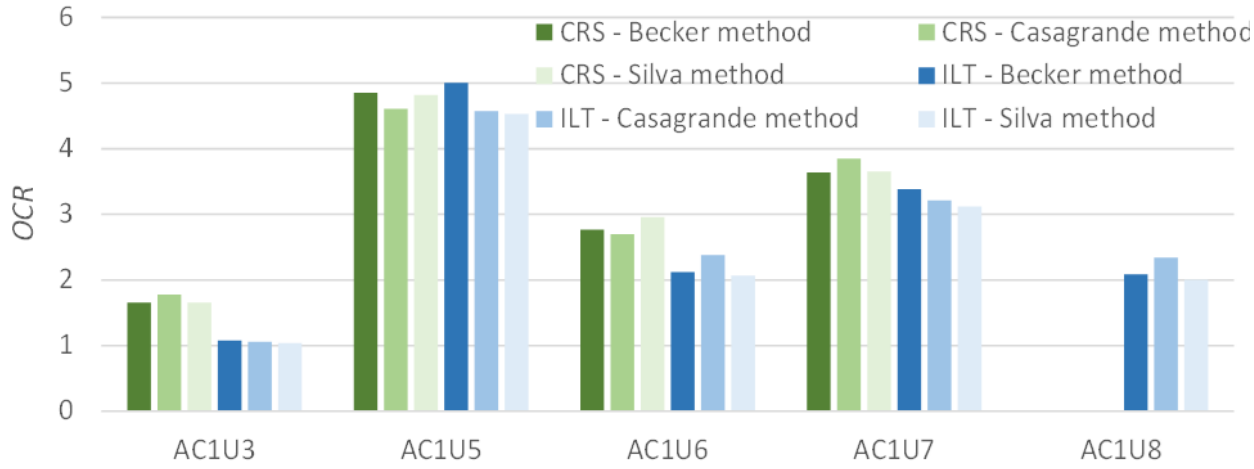

(b) Ady Canal

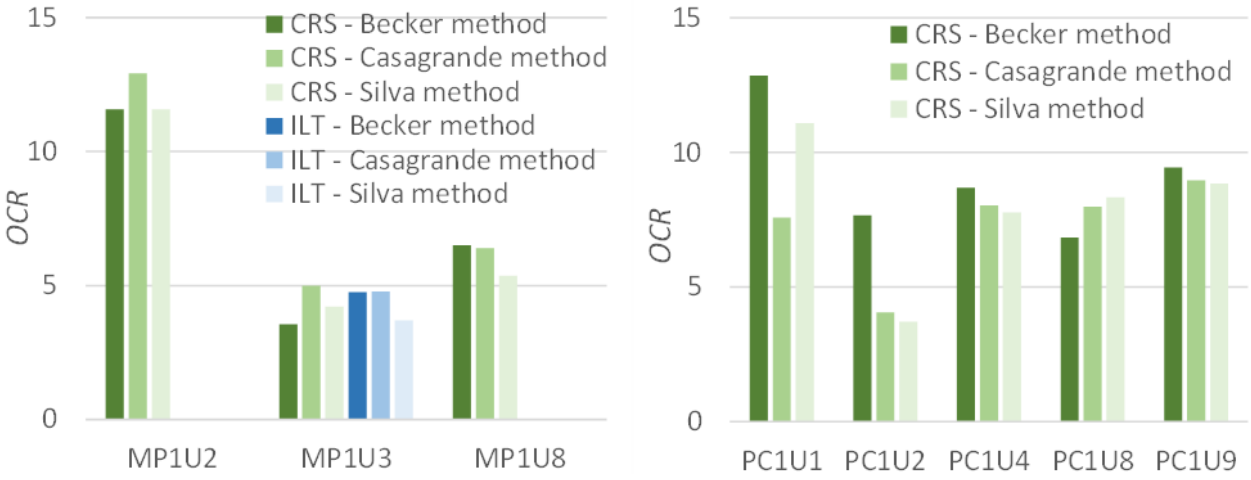

Figure 5.30: *OCR* evaluation from different methods for all for sites (note change of ordinal scales across figures)

The OCR evaluated from CRS tests with Becker method (except for W1U8, which uses Becker method from IL test) are plotted against depth in Figure 5.31. The diatomaceous soil layers at Wickiup Junction are much deeper than the other sites and consistently exhibit $OCR \approx 1.5$. The diatomaceous soils at Ady Canal are lightly to moderately overconsolidated without a strong trend with depth. Specimens from Moore Park and Pine Cone Drive have higher OCRs, which is consistent with their mudstone-like texture. The overconsolidation ratio often exhibits a relationship with depth: $OCR \propto \frac{1}{z}$. The brief derivation is shown in Equation (5-4), where γ' and $\Delta\sigma_v'$ can be seen as constants. Therefore, we can approximate OCR with depth by fitting into an equation $OCR = \frac{A}{z^B}$ (A and B are constants). In Figure 5.31, we demonstrate two correlations, while they are close to each other, they also well fit OCRs at deeper depth in Wickiup and Ady Canal.

$$\boldsymbol{OCR = \frac{\sigma_p'}{\sigma_{v0}'} = \frac{\sigma_{v0}' + \Delta\sigma_v'}{\sigma_{v0}'} = 1 + \frac{\Delta\sigma_v'}{\sigma_{v0}'} = 1 + \frac{\Delta\sigma_v'}{\gamma' \cdot z}} \quad \textbf{(5-4)}$$

where:
γ' = effective unit weight; and
$\Delta\sigma_v'$ = the decrease of overburden stress.

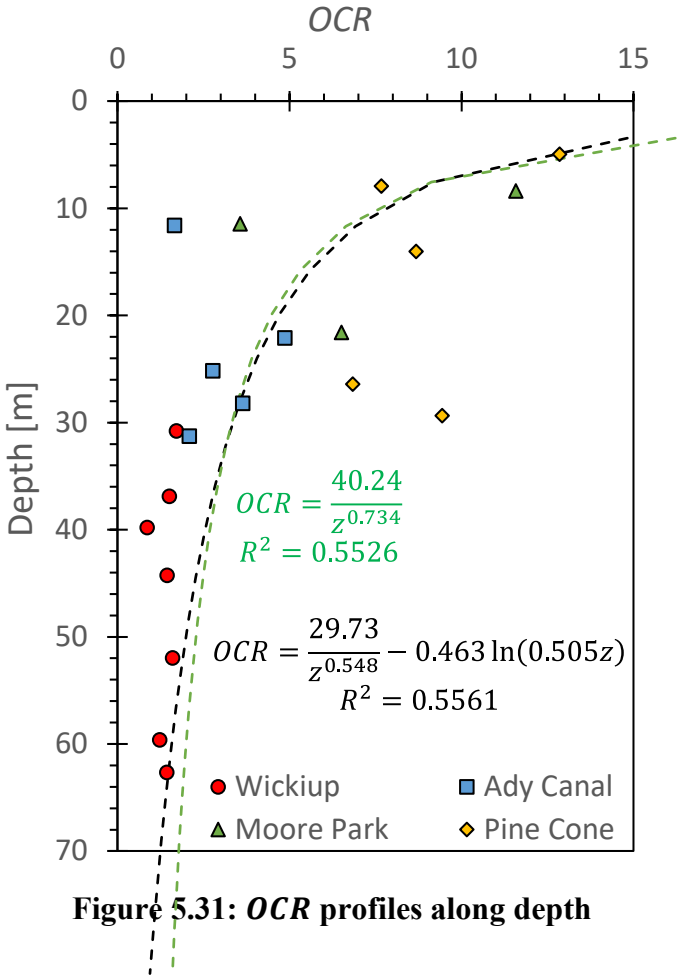

Figure 5.31: *OCR* profiles along depth

5.3.2.5 Coefficient of consolidation and permeability

The coefficient of consolidation is the parameter used to describe the rate of consolidation of saturated soil when subjected to an increase of pressure. Depending on the drainage direction, it can be referred to as the vertical coefficient of consolidation (c_v) or horizontal coefficient of consolidation (c_h). The vertical coefficient of consolidation (c_v) can be obtained from the traditional consolidation test (i.e., IL test) where only the vertical drainage is accessible. Meanwhile, the horizontal coefficient of consolidation (c_h) is often obtained from dissipation tests during CPTu investigation. The evaluation of c_h is discussed in 5.4.3.

Four representative specimens are selected to present c_v as a function of σ_v', shown in Figure 5.32. During the IL tests, the specimen underwent overburden stresses from 10 – 2000 kPa. The vertical coefficient of consolidation (c_v) is evaluated from the settlement-time curve at each loading stage, which varies between 0.005 – 5 cm^2/s. Generally, c_v shows a decreasing trend with σ_v'. Considering the incremental load increases with the overburden stress ($\because LIR = 1$), it takes longer time to dissipate the excess pore water pressure under higher incremental load. Therefore, c_v is expected to decrease with σ_v'.

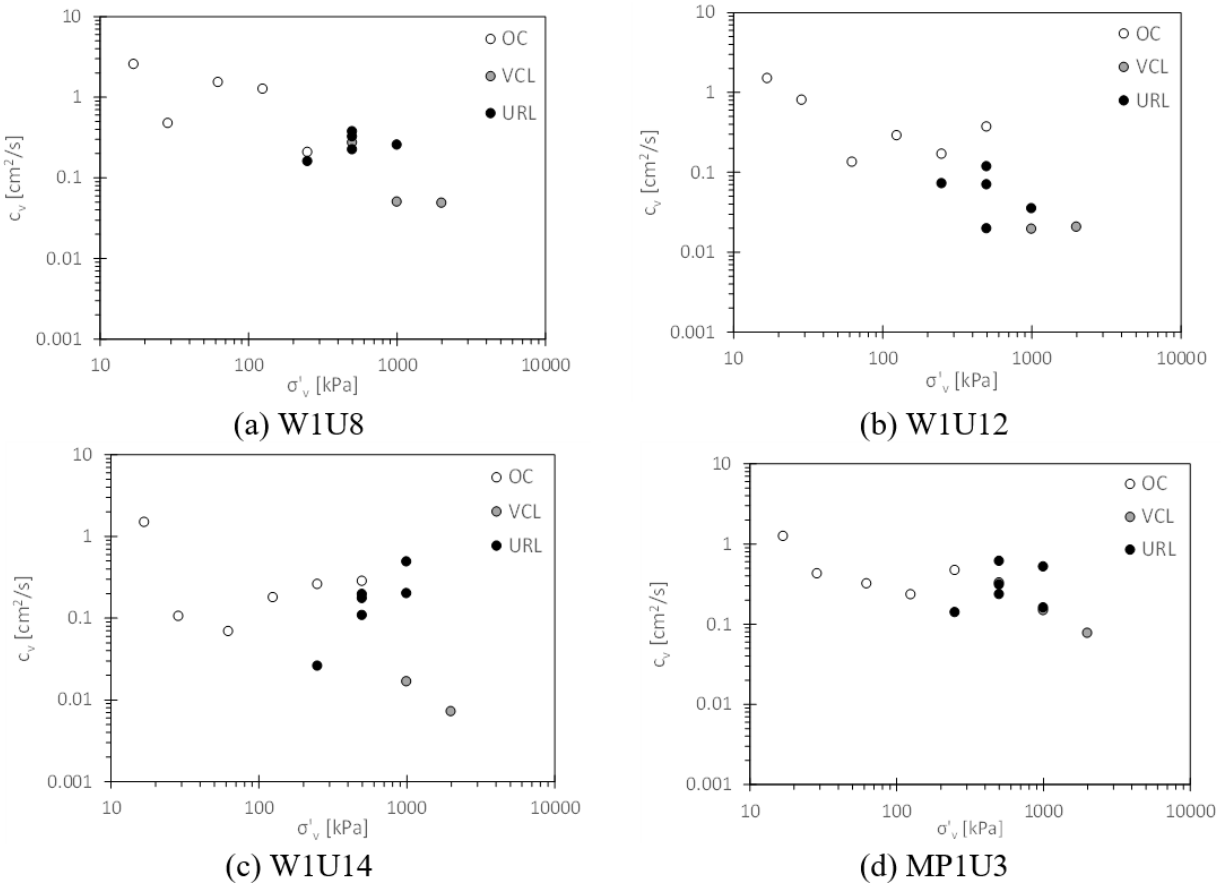

Figure 5.32: c_v vs. σ_v' on representative tests (OC: overconsolidated; VCL: virgin compression line; URL: unloading-reloading line)

Based on Terzaghi's 1-D consolidation theory (Terzaghi, 1943), the relationship between permeability (k) and the vertical coefficient of consolidation (c_v) is derived as Equation (5-5). With this relationship, the permeability (k) can be computed from c_v at corresponding loading stages. The comparison of measured and c_v-evaluated k is shown in Figure 5.33. The measured k values are close to the evaluated k values at near overburden stress stages, typically it is near OC stages as the permeability was measured under *in-situ* stress conditions which is overconsolidated. It shows that k and c_v evaluations are consistent. Our measured permeability is generally between 1e-5 and 1e-6 cm/s.

$$c_v = \frac{k}{\gamma_w}\frac{1+e_0}{a_v} \tag{5-5}$$

where:

a_v = coefficient of compressibility, defined as $\frac{\Delta e}{\Delta \sigma_v'}$;

γ_w = water unit weight; and

e_0 = initial void ratio.

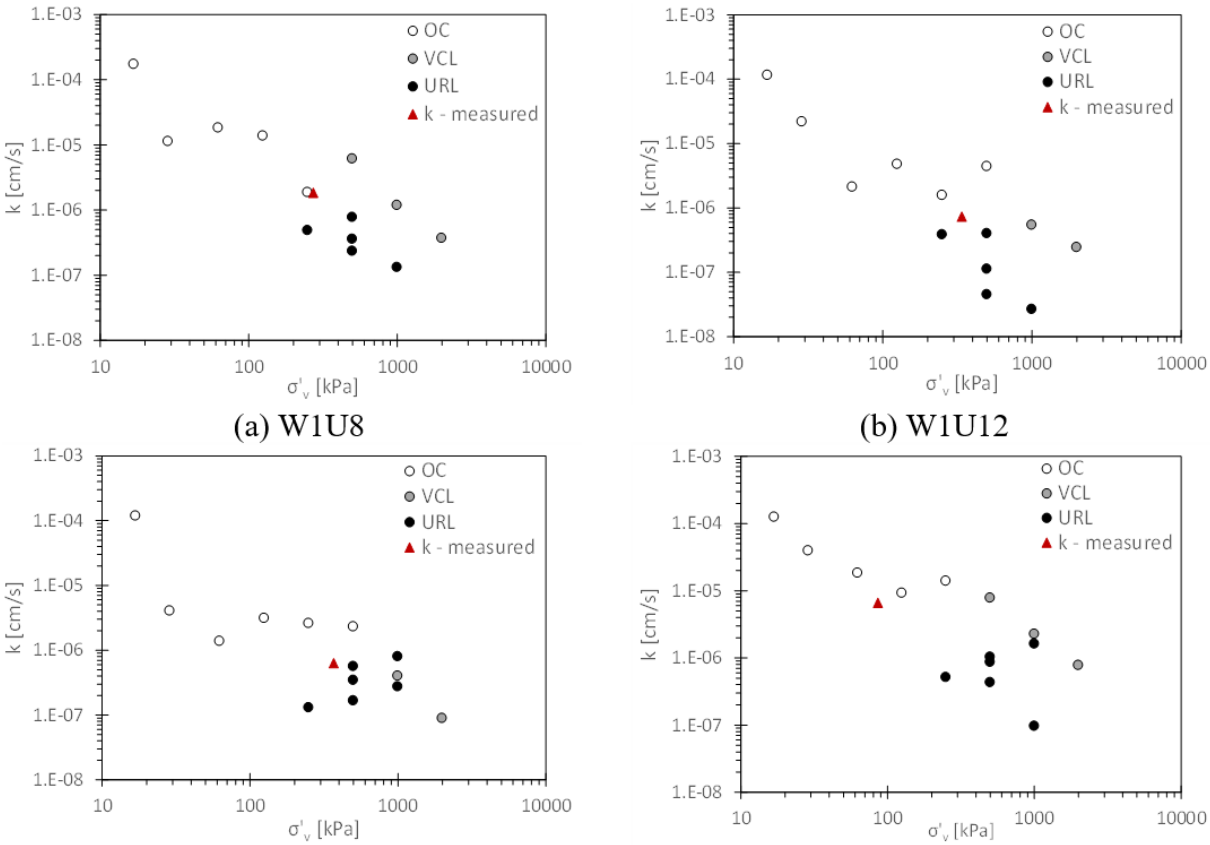

Figure 5.33: Comparison between measured k and c_v-evaluated k by Equation (5-5).

The permeability of diatomaceous soil is only scarcely reported. Tamaki et al. (1989) and Maekawa et al. (1991) reported k as a function of void ratio on diatomaceous soil found in Japan. The comparison of their k values with this study is shown in Figure 5.34. The straight lines represent best-fit lines from Tamaki et al. (1989) and Maekawa et al. (1991). Both our k values and void ratios are at the upper end of Tamaki et al. (1989)'s proposed lines.

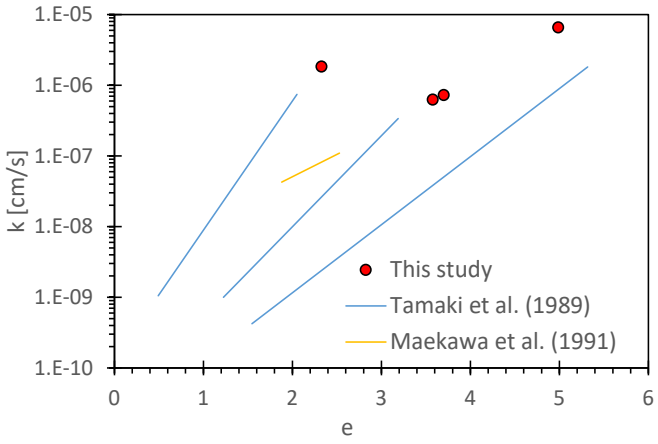

Figure 5.34: k vs. e (after Tamaki et al. 1989; Maekawa et al. 1991)

5.3.2.6 Repeatability of tests

Repeated tests were conducted on both IL and CRS for selected Shelby tubes, i.e., two specimens from the same Shelby tubes were extruded and subjected to the same consolidation tests. Specifically, W1U8, W1U9, and W1U10 were subjected to two IL tests such that in one test the load was incremented at the approximate end of primary consolidation (EOP) and for the other, the load duration was always 24 hours (note that both procedures are in conformance with ASTM D 2435 American Society for Testing and Materials (ASTM). 2020d.). The results were used to assess the repeatability of the consolidation tests and the effects of load duration. For CRS tests, W1U9 and PC1U2 were selected to assess the repeatability of the CRS test.

The consolidation curves of repeated IL tests are shown in Figure 5.35. There is reasonable agreement between the two load durations. The details of the repetitive tests on each Shelby tube specimen are summarized in Appendix E. Figure 5.36 and Figure 5.37 summarized consolidation parameters (C_c, C_r) and stress history parameters (σ_p', and OCR). The results for specimen PC1U2 have relatively more variation due to the aforementioned difficulties associated with the mudstone-like diatomaceous soils. The results from Wickiup Junction show variability in the computed σ_p', yet the OCRs between replicate tests are quite consistent. The Wickiup Junction diatomaceous deposits are quite deep, and thus, they exhibit high overburden stress and low OCR. As an example, for an overburden stress of 300 kPa, σ_p' measurements of 350 kPa and 450 kPa result in OCR values of 1.2 and 1.5, respectively.

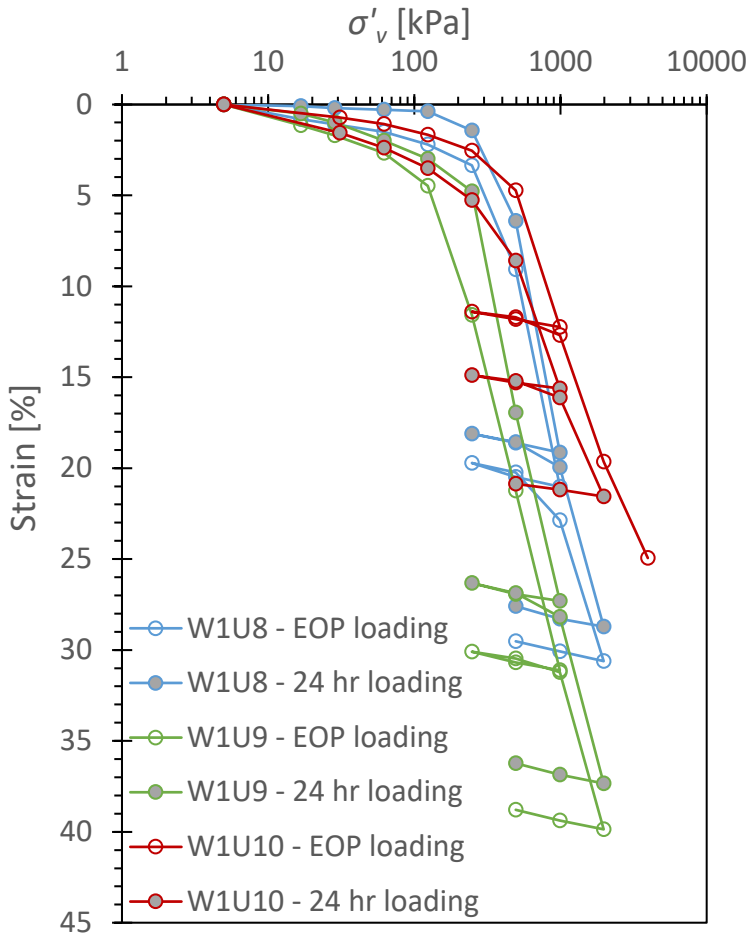

Figure 5.35: $\varepsilon - log(\sigma'_v)$ curves on two loading mechanisms (EOP: end of primary)

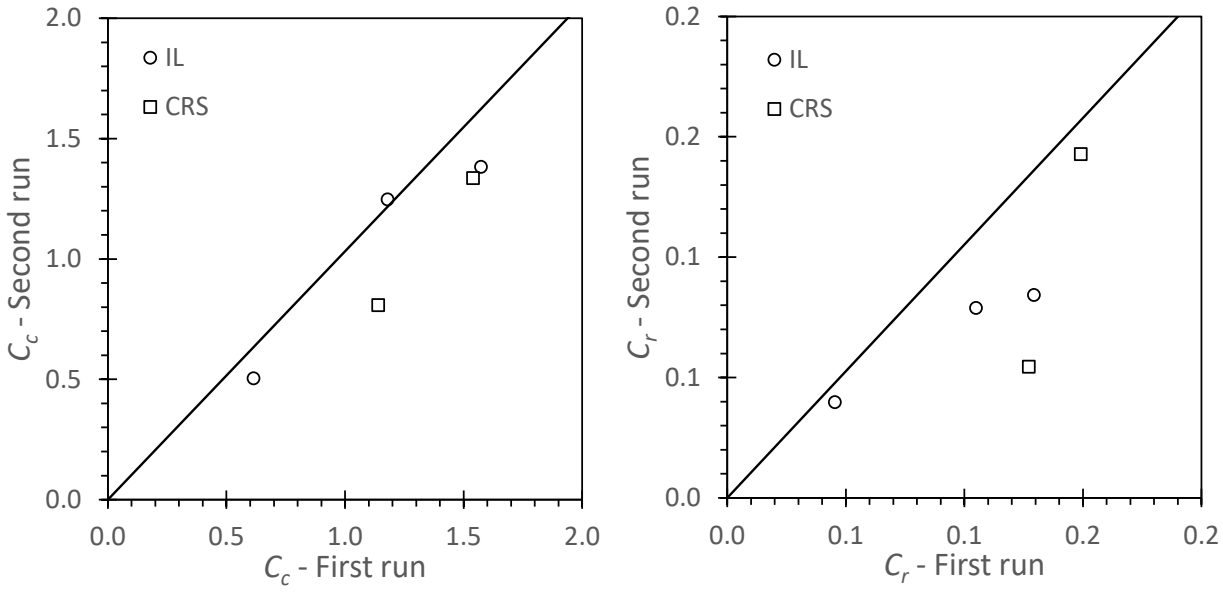

(a) C_c (b) C_r

Figure 5.36: Comparisons on C_c and C_r on repeated tests

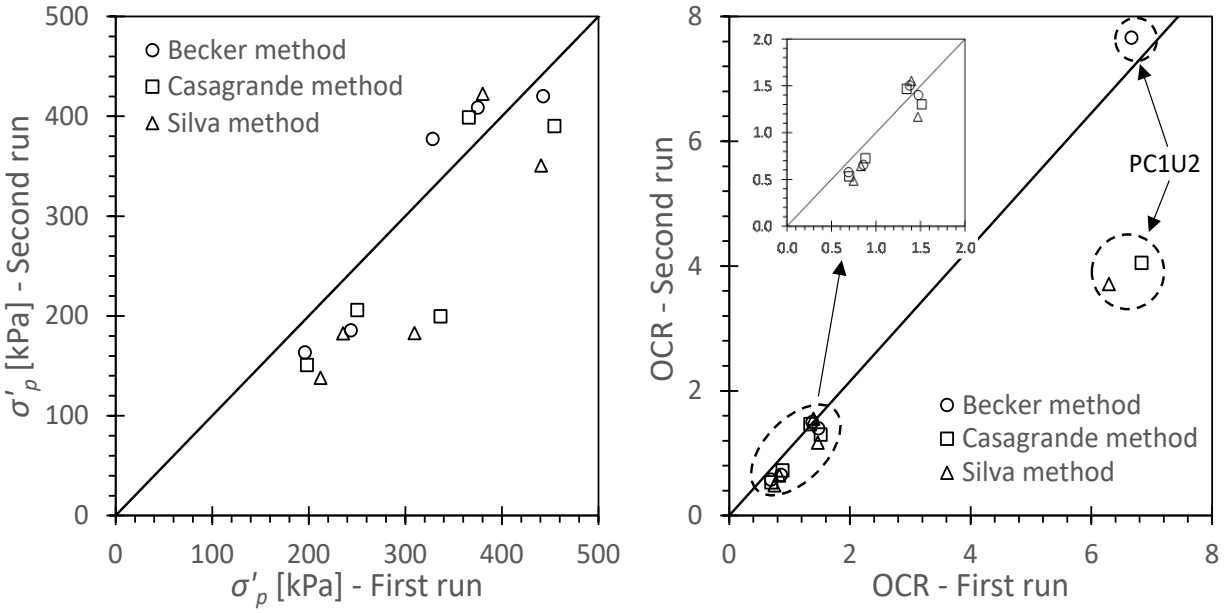

(a) σ'_p [kPa] (b) OCR

Figure 5.37: Comparisons on σ'_p and OCR on repeated tests

5.3.2.7 Summary

The summary of consolidation parameters of individual specimens is presented in Table 5.3. For each site, representative values of C_c and C_r are selected to be the average values

of the specimens from the site, presented in Table 5.4 together with upper and lower bound values of C_c and C_r.

Table 5.3: Consolidation parameters of individual specimens

	CRS					IL				
	C_c	C_r	σ'_p [kPa]	OCR	e_0	C_c	C_r	σ'_p [kPa]	OCR	e_0
W1U7	1.763	0.143	431	1.71	3.08	1.288	0.113	351	1.58	2.64
W1U8	1.711	0.062	729	2.68	2.19	1.247	0.084	409	1.47	2.37
W1U9	1.540	0.149	244	0.86	3.18	1.573	0.105	196	0.70	3.36
W1U10	0.788	0.042	430	1.43	1.57	0.504	0.040	420	1.30	1.30
W1U12	2.207	0.164	541	1.60	3.52	2.185	0.160	454	1.36	3.72
W1U13	1.031	0.160	442	1.23	2.79	0.721	0.095	197	0.46	2.88
W1U14	2.377	0.205	525	1.43	3.86	1.931	0.142	504	1.34	3.57
AC1U3	1.970	0.087	193	1.65	2.99	1.632	0.086	126	1.06	3.33
AC1U5	1.897	0.170	812	4.86	2.89	1.861	0.129	837	4.57	3.05
AC1U6	2.155	0.222	486	2.77	3.95	1.552	0.154	372	2.38	3.80
AC1U7	2.884	0.202	669	3.64	3.58	1.980	0.150	622	3.21	3.35
AC1U8	/					2.490	0.173	400	2.34	3.62
MP1U2	1.796	0.203	910	11.58	4.04	/				
MP1U3	2.083	0.162	304	3.56	4.89	2.130	0.219	406	4.77	3.62
MP1U8	1.105	0.199	792	6.51	2.99	/				
PC1U1	0.857	0.102	505	12.85	2.72	/				
PC1U2	0.808	0.054	377	7.66	2.35	/				
PC1U4	1.262	0.121	616	8.68	3.43	/				
PC1U8	1.633	0.180	679	6.84	4.43	/				
PC1U9	1.800	0.092	1014	9.44	3.47	/				

Table 5.4: Representative values of C_c and C_r of each site

	C_c			C_r		
	Average	**Upper bound**	**Lower bound**	**Average**	**Upper bound**	**Lower bound**
Wickiup	1.631	2.377	0.788	0.132	0.205	0.042
Ady Canal	2.227	2.884	1.897	0.170	0.222	0.087
Moore Park	1.661	2.083	1.105	0.188	0.203	0.162
Pine Cone	1.272	1.800	0.808	0.110	0.180	0.054

5.3.3 Triaxial Test

5.3.3.1 Test specimens

A total of 12 diatomaceous specimens were tested in triaxial compression. Nearly every diatomaceous soil Shelby tube from Wickiup Junction and Ady Canal had extruded a

specimen for triaxial test, whereas, only one specimen from Moore Park and no specimen from Pine Cone Drive was tested for triaxial shear due to their brittle nature of mudstone-like diatomaceous soil. The Moore Park specimen was subjected to drained shearing and all other specimens were undrained. Figure 5.38 depicts the photos of an example of triaxial specimen (W1U7), all other triaxial specimen photos can be found in Appendix F.

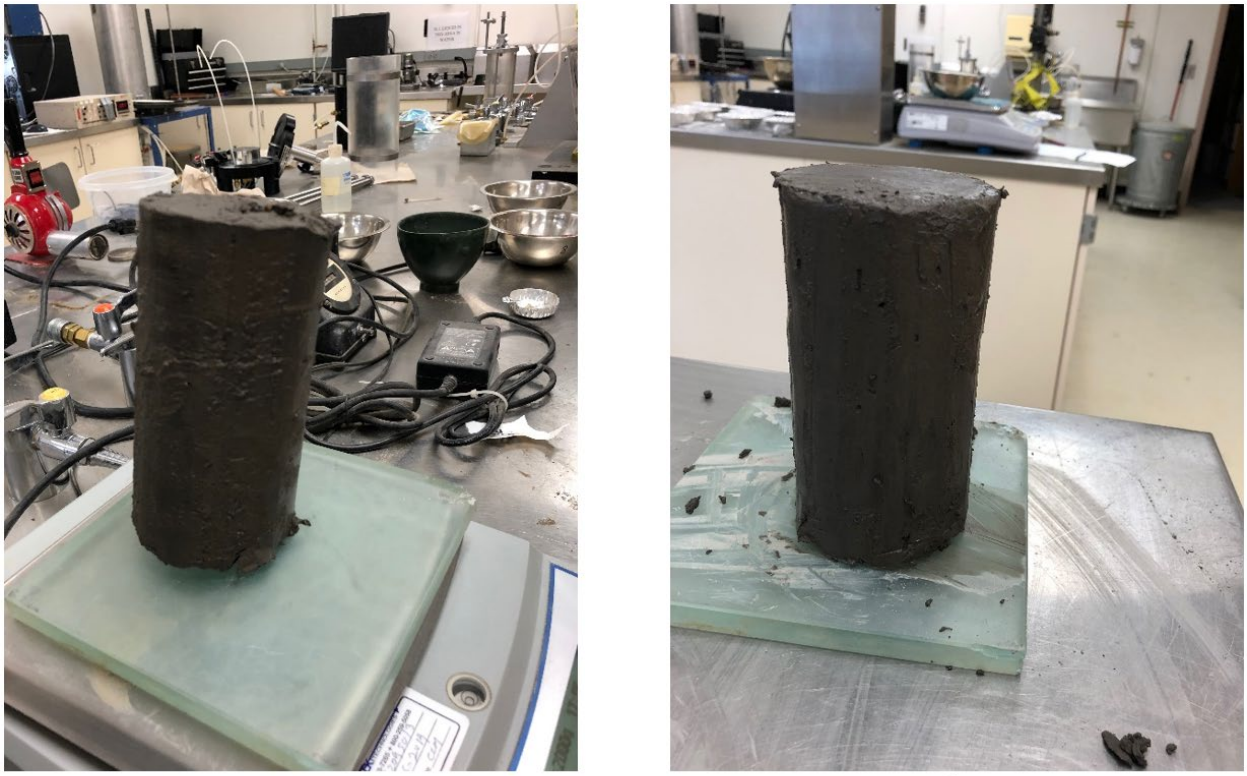

(a) (b)

Figure 5.38: W1U7 (before trimming: (a); after trimming: (b))

5.3.3.2 Triaxial test parameters and post-failure images

The triaxial test parameters for all tested specimens are summarized in Table 5.5, corresponding post-failure specimen images are presented in Figure 5.39. The strain rate was set at 1%/hr for most specimens and 2-4%/hr for limited specimens. The initial confinement (p'_0) was set to be the *in-situ* horizontal effective stress (σ'_{h0}) for nearly all specimens (except AC1U3 and AC1U7) in order for comparison of s_u between triaxial tests and CPTu interpretations, which are discussed in Chapter 6. The *in-situ* vertical effective stress (σ'_{v0}) is computed based on measured/assumed soil unit weight and soil depth, adjusted for the pore water pressure for a specific soil stratum. The *in-situ* horizontal effective stress (σ'_{h0}) is computed by Equation (5-6), where OCR and ϕ' are estimated from CPTu interpretation.

$$\boldsymbol{\sigma'_{h0} = K_0^{OC} \cdot \sigma'_{v0}} \quad \textbf{(5-6)}$$

$$K_0^{OC} = (1 - \sin\phi')OCR^{\sin\phi'} \quad \textbf{(5-7)}$$

where:
K_0^{OC} = coefficient of earth pressure for overconsolidated soil.

Except for W1U9, all other specimens showed brittle failure pattern with one or two shear planes, some are more distinct (e.g., W1U12) some are less obvious (e.g., AC1U3). Two triaxial specimens were extruded from Shelby tube W1U10 and they were subjected to the same initial confinement (p_0') and shear rate for comparison. It shows that they nearly have the same failure pattern. The shear strain at which the shear stress (q) peaked is between 1-3% for Wickiup specimens, whereas, it is 2-12% for Ady Canal specimens. The liquid limit (LL) and initial void ratio (e_0) of specimens from Wickiup have larger variation than Ady Canal specimens. $LL = 47 - 149, e_0 = 1.627 - 3.595$ for Wickiup specimens, and $LL = 103 - 160, e_0 = 3.357 - 4.077$ for Ady Canal specimens. The higher variation of LL and e_0 of Wickiup specimens may introduce additional variables when analyzing soil strength. All these triaxial specimens were confirmed as diatomaceous soil based on SEM imaging on nearby split spoon samples, meanwhile W1U7 and W1U10 specimens were directly confirmed with SEM imaging.

Table 5.5: Triaxial test parameters and related physical properties

Specimen	Test type	Strain rate [%/hr]	σ'_{v0} [kPa]	σ'_{h0} [kPa]	p'_0 [kPa]	$\varepsilon_{q=peak}$ [%]	LL	e_0	w_n/LL
W1U7	CU	2.11	253	150	150	1.55	70	1.797	1.009
W1U8	CU	1.07	272	169	169	1.49	86	2.484	1.210
W1U9	CU	1.05	284	178	178	2.48	91	3.449	1.582
W1U10-1	CU	1	300	180	180	1.3	47	1.627	1.391
W1U10-2	CU	0.8	300	180	180	1.23	47	1.627	1.391
W1U12	CU	0.98	338	200	200	2.23	112	3.595	1.464
W1U14	CU	1.05	368	218	218	2.71	149	3.524	1.073
AC1U3	CU	2.64	118	70	118	6.29	103	4.077	1.580
AC1U6	CU	1.00	176	90	90	11.9	160	3.840	1.041
AC1U7	CU	2.74	184	110	163	2.87	148	3.357	0.997
AC1U8	CU	4.45	192	160	160	5.62	130	3.499	1.222
MP1U3	CD	0.94	86	161	161	13.71	152	4.392	1.310

W1U7
$w_n/LL = 1.009, e_0 = 1.797$
$LL = 70, PL = 31$
$\varepsilon_{\tau=peak} = 1.55\%$

W1U8
$w_n/LL = 1.210, e_0 = 2.484$
$LL = 86, PL = 56$
$\varepsilon_{\tau=peak} = 1.49\%$

W1U9
$w_n/LL = 1.582, e_0 = 3.449$
$LL = 91, PL = 56$
$\varepsilon_{\tau=peak} = 2.48\%$

W1U10-1
$w_n/LL = 1.391, e_0 = 1.627$
$LL = 47, PL = 32$
$\varepsilon_{\tau=peak} = 1.30\%$

W1U10-2
$w_n/LL = 1.391, e_0 = 1.627$
$LL = 47, PL = 32$
$\varepsilon_{\tau=peak} = 1.23\%$

W1U12
$w_n/LL = 1.464, e_0 = 3.595$
$LL = 112, PL = 69$
$\varepsilon_{\tau=peak} = 2.23\%$

W1U14
$w_n/LL = 1.073, e_0 = 3.524$
$LL = 149, PL = 90$
$\varepsilon_{\tau=peak} = 2.71\%$

AC1U3
$w_n/LL = 1.580, e_0 = 4.077$
$LL = 103, PL = 50$
$\varepsilon_{\tau=peak} = 6.29\%$

AC1U6
$w_n/LL = 1.041, e_0 = 3.840$
$LL = 160, PL = 107$
$\varepsilon_{\tau=peak} = 11.9\%$

AC1U7
$w_n/LL = 0.997, e_0 = 3.357$
$LL = 148, PL = 88$
$\varepsilon_{\tau=peak} = 2.87\%$

AC1U8
$w_n/LL = 1.222, e_0 = 3.499$
$LL = 130, PL = 85$
$\varepsilon_{\tau=peak} = 5.62\%$

MP1U3
$w_n/LL = 1.310, e_0 = 4.392$
$LL = 152, PL = 79$
$\varepsilon_{\tau=peak} = 13.71\%$

Figure 5.39: Failure patterns of all triaxial specimens and related physical properties

5.3.3.3 Stress-strain curves and effective stress paths

The CU triaxial test curves are presented in Figure 5.40 and Figure 5.41 for Wickiup and Ady Canal specimens respectively. The shear stress-shear strain curves ($q - \varepsilon_q$) are presented in subplot (a), the effective stress paths ($q - p'$) are presented in subplot (b), the excess pore water pressure-shear strain curves ($\Delta u - \varepsilon_q$) are presented in subplot (c), the normalized shear stress-shear strain curves ($q/p' - \varepsilon_q$) are presented in subplot (d), and the normalized excess pore water pressure-shear strain curves ($\Delta u/p' - \varepsilon_q$) are presented in subplot (e). Specimens that show post-peak softening behavior also exhibit clear strain localization (shear banding), as expected (when second order work becomes negative Drucker's stability postulate is violated and material response bifurcates, requiring the development on a strain discontinuity (Peric et al., 1992; Vardoulakis, 1979, 1983, 1985)). The shear strain at which they reach peak stress are between 1.23%-2.71% for Wickiup specimens, and 2.87%-11.9% for Ady Canal specimens. More pronounced strain softening behavior was observed in the Wickiup specimens. The two tests on W1U10 provide nearly identical $q - \varepsilon_q$ curves, demonstrating repeatability in the triaxial tests. In the framework of critical state soil mechanics (CSSM, Budhu, 2010), the stress paths for Wickiup specimens and two Ady Canal specimens (i.e., AC1U3 and AC1U8) showed normally consolidation or lightly overconsolidation (i.e., $1 < R_0 < 2$). In contrast, the stress paths of specimens AC1U6 and AC1U7 showed heavily overconsolidation (i.e., $R_0 > 2$). The overconsolidation ratio R_0 is obtained from the isotropic compression in CSSM by Equation (5-8), whereas, the overconsolidation ratio OCR is obtained from the oedometric compression which is discussed in section 5.3.2.4. The relationship between R_0 and OCR can be described by Equation (5-11), and the derivation can be referred to as Equation (5-9) and (5-10). Therefore, the overconsolidation ratio R_0 from CSSM framework can be computed for the tested specimens, shown in Table 5.6. It can be seen that specimens AC1U6 and AC1U7 have R_0 greater than 2, while all other specimens remain R_0 between 1 and 2. This is consistent with the effective stress paths pattern shown in the tests. The ultimate normalized shear stress (q/p') range is from 1.3-2.2 ($s_u/p'_0 \approx 0.65 - 1.1$). Typically, the normally shear strength ratio for clays is between 0.2 to 0.4 (Ladd and Foott, 1974), this indicates that the specimens were overconsolidated at shearing.

$$\boldsymbol{R_0 = \frac{p'_c}{p'_0}} \tag{5-8}$$

$$\boldsymbol{p'_c = \frac{1 + 2K_0^{NC}}{3}\sigma'_p} \tag{5-9}$$

$$\boldsymbol{p'_0 = \frac{1 + 2K_0^{OC}}{3}\sigma'_{v0}} \tag{5-10}$$

$$R_0 = \frac{1 + 2K_0^{NC}}{1 + 2K_0^{OC}} OCR \tag{5-11}$$

where:
R_0 = overconsolidation ratio from the isotropic compression;
p_c' = preconsolidation mean effective stress;
p_0' = initial mean effective stress (during triaxial tests);
σ_p' = preconsolidation *in-situ* vertical effective stress;
σ_{v0}' = *in-situ* vertical effective stress;
K_0^{NC} = coefficient of earth pressure for normally consolidated soil, $= 1 - \sin\phi'$; and
K_0^{OC} = coefficient of earth pressure for overconsolidated soil, Equation (5-7).

Table 5.6: Overconsolidation ratio (R_0) for triaxial specimens

Specimens	ϕ_{cs}' [°]	K_0^{NC}	σ_p' [kPa]	p_c' [kPa]	p_0' [kPa]	R_0
W1U7	34.9	0.427	431	267	150	1.78
W1U8	34.6	0.432	409	254	169	1.50
W1U9	34.9	0.428	244	151	178	1.00
W1U10-1	38.6	0.376	430	251	180	1.40
W1U10-2	40.6	0.349	430	244	180	1.35
W1U12	48.2	0.254	541	272	200	1.36
W1U14	40.5	0.351	525	298	218	1.37
AC1U3	34.2	0.437	193	121	118	1.02
AC1U6	41.6	0.336	486	271	90	3.03
AC1U7	36.9	0.4	669	402	163	2.46
AC1U8	37.2	0.395	400	239	160	1.49
MP1U3	38.1	0.383	406	239	161	1.48

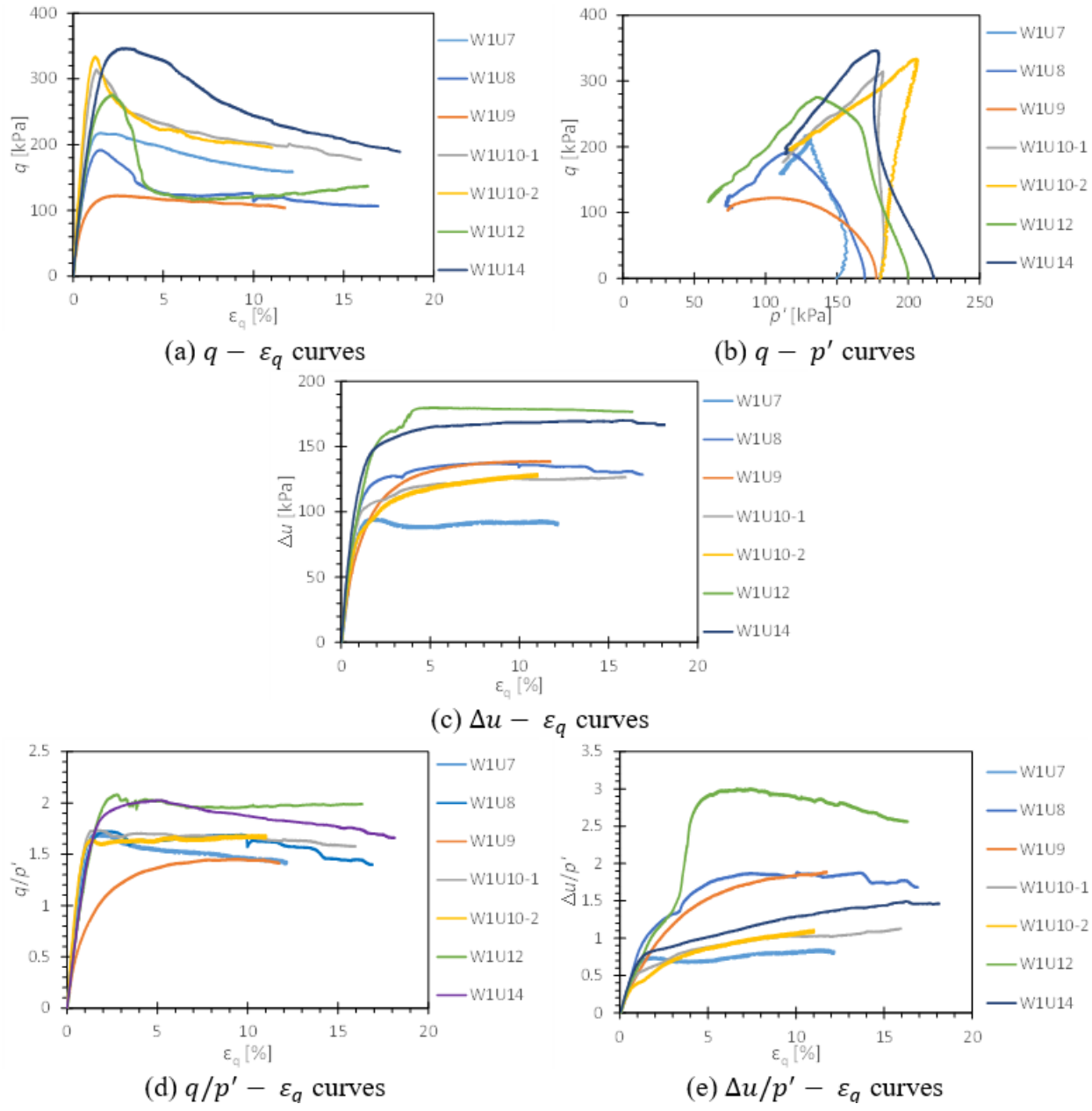

(a) $q - \varepsilon_q$ curves

(b) $q - p'$ curves

(c) $\Delta u - \varepsilon_q$ curves

(d) $q/p' - \varepsilon_q$ curves

(e) $\Delta u/p' - \varepsilon_q$ curves

Figure 5.40: Triaxial test curves for Wickiup specimens

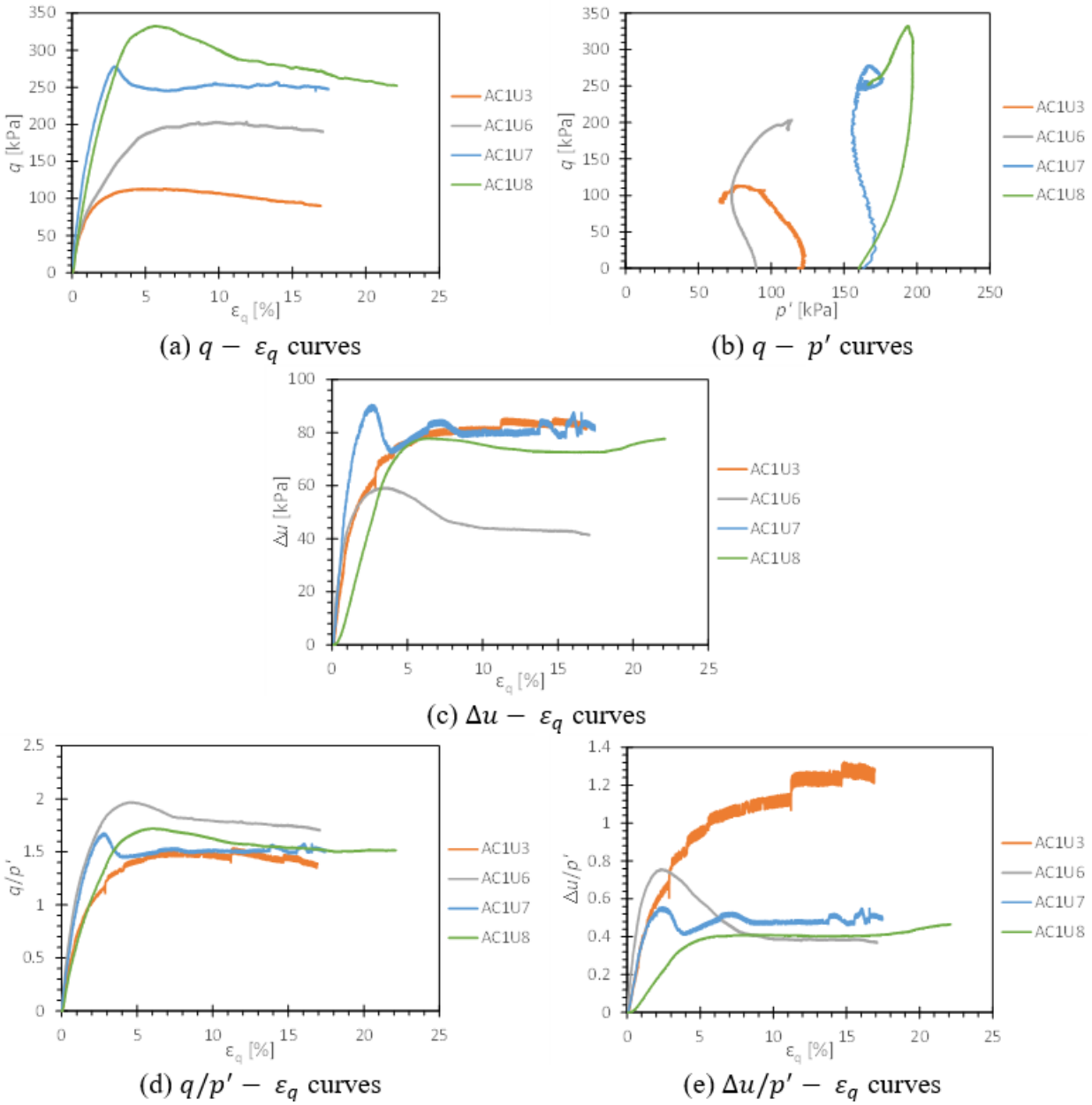

Figure 5.41: Triaxial test curves for Ady Canal specimens

The CD triaxial test curves on MP1U3 are presented in Figure 5.42. It took extensively long shear strain (13.7%) to reach peak shear stress. The ultimate normalized shear stress (q/p') range from 1.3~2.2 ($s_u/p'_0 \approx 0.65$~1.1), which indicates the specimens were overconsolidated at shearing. Contractive behavior was observed based on volume change during shear.

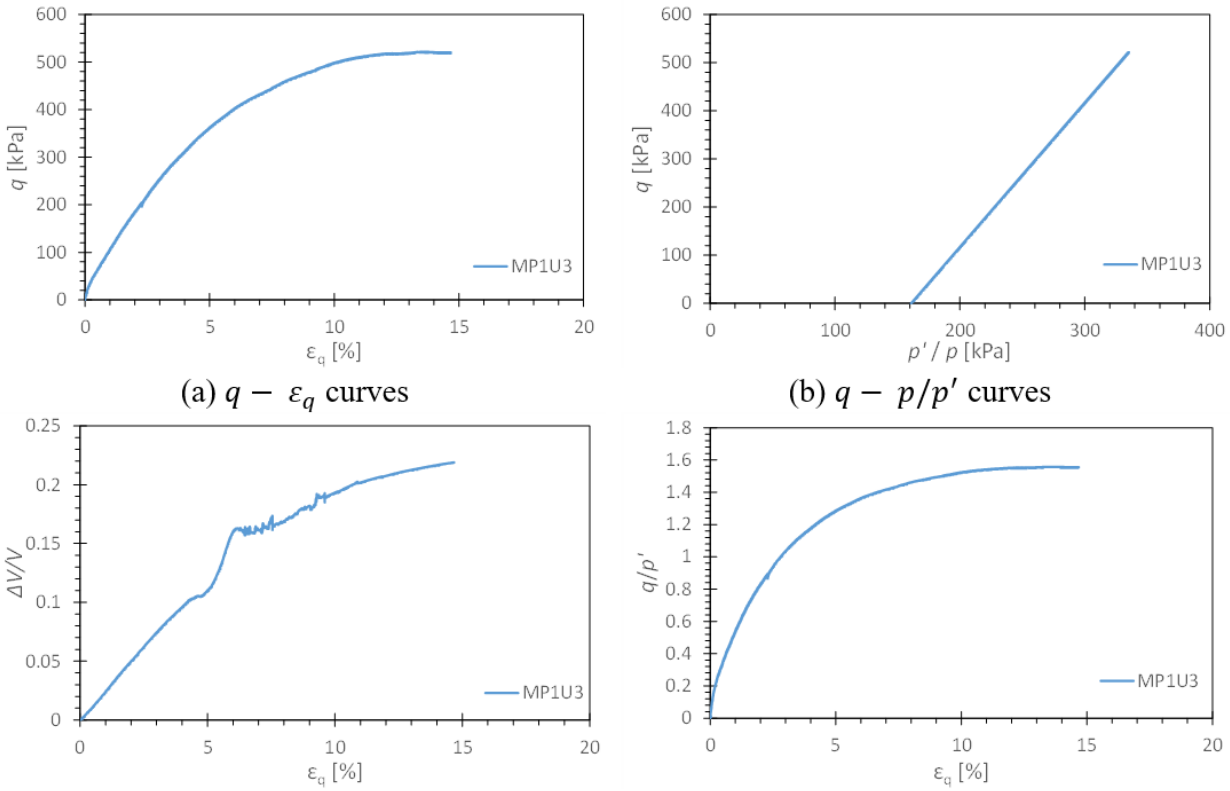

(a) $q - \varepsilon_q$ curves

(b) $q - p/p'$ curves

(c) $\Delta V/V - \varepsilon_q$ curves (compression is positive)

(d) $q/p' - \varepsilon_q$ curves

Figure 5.42: Triaxial test curves for Moore Park specimen

5.3.3.4 Undrained shear strength and friction angle

Normalized undrained shear strength profiles from triaxial testing are plotted in Figure 5.43 (a). Undrained shear strength shows some variability within and across sites but does not necessarily demonstrate well-defined trends with depth. At Wickiup, normalized undrained shear strength falls in the range $0.35 \lesssim s_u/p_0' \lesssim 0.90$, while at Ady Canal this range is $0.50 \lesssim s_u/p_0' \lesssim 1.15$. The variation is not inconsistent with that typically observed in testing of intact specimens of natural soil deposits, particularly when the difficulty associated with the sampling and subsequent specimen preparation of diatomaceous soils. These results imply that the normalized undrained shear strength at Wickiup might be appropriately characterized by an average value (e.g., 0.7-0.8) over the diatomaceous profile. This may not be true for Ady Canal where there is a cluster of data from 25–31 m showing $s_u/p_0' \cong 1.0$ and another point at 12 m with $s_u/p_0' \cong 0.5$.

The effective stress friction angles presented in Figure 5.43 (b) show variability similar to that observed in undrained shear strength. Most values for critical state friction angle at Wickiup and Ady Canal vary from 34° to 42° with the exception of one Wickiup specimen measuring 48°. The one specimen from Moore Park has a measured critical state friction angle of 38°, which is in-line with values from the other two sites.

A complete analysis of shear strength requires information on stress history (OCR), also as a function of depth. The stress normalization framework being used for interpretation of triaxial results is based upon concepts from critical state soil mechanics (e.g. Schofield and Wroth, 1968; Wood, 1990; Budhu, 2010; Puzrin, 2012) and incorporates the effects of stress history on shear strength to provide a more robust interpretation of shear strength profiles (i.e., because stress history also varies with depth). Based on the critical state soil mechanics framework, the relationship among the normalized undrained shear strength, friction angle, and overconsolidation ratio can be derived as Equation (5-12). The friction angles at critical state are plotted against the normalized undrained shear strength in Figure 5.44. The overconsolidation ratio (R_0) is within the range between 1 and 3, with the best fit value 2.12. Overall, the friction angle increases with the normalized undrained shear strength.

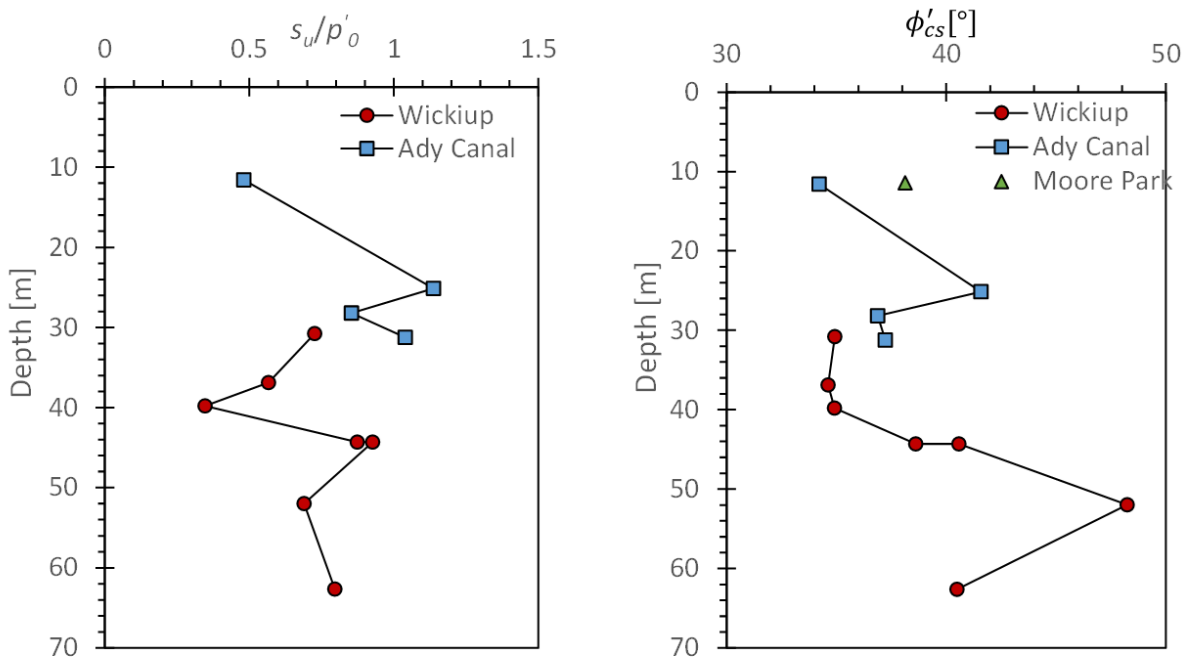

(a) Normalized undrained shear strength (s_u/p'_0)

(b) Critical state friction angle (ϕ'_{cs})

Figure 5.43: Strength parameters along depth

$$\frac{s_u}{p'_0} = \frac{1}{2} M \cdot \left(\frac{R_0}{2}\right)^{\Lambda} \tag{5-12}$$

$$M = \frac{6 \sin \phi'_{cs}}{3 - \sin \phi'_{cs}} \tag{5-13}$$

where:

M = strength parameter in critical state soil mechanics;

Λ = plastic volumetric strain potential, $=1-\frac{\kappa}{\lambda}=1-\frac{C_r}{C_c}$;

λ = slope of the normal consolidation line in a plot of void ratio versus the natural logarithm of mean effective stress; and

κ = the average slope of the unloading/reloading curves in a plot of void ratio versus the natural logarithm of mean effective stress.

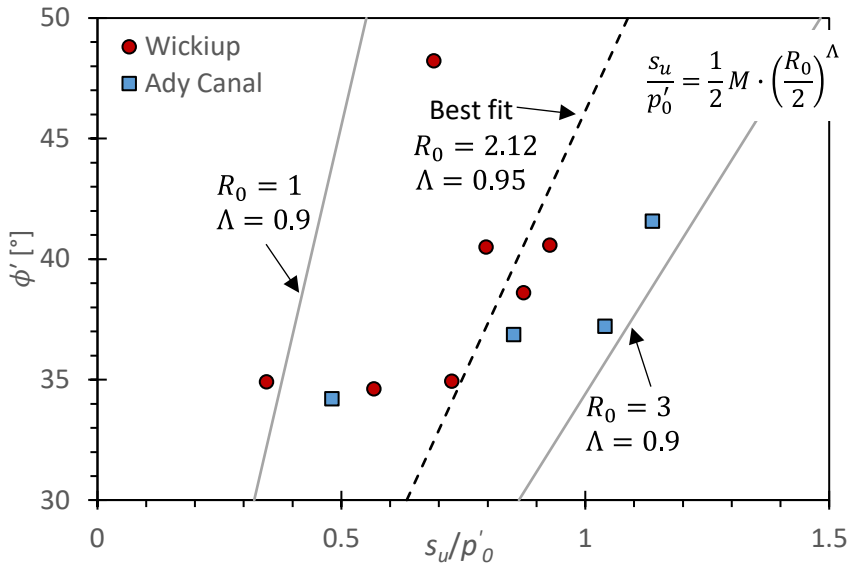

Figure 5.44: Relation between friction angle and normalized undrained shear strength

5.3.4 Direct Simple Shear Test

5.3.4.1 Soil behaviors under different OCRs (AC1U6 as an example)

Direct simple shear (DSS) tests were performed at a variety of OCR values to facilitate stress and strength normalization in the interpretation of stress history effects on material behavior. As an example, results from DSS testing of AC1U6 are presented in Figure 5.45 – Figure 5.47. Complete test results are summarized in Appendix G. Good consistency is observed for tests conducted under the same OCR. All DSS tests were conducted under a constant-volume condition and a notional excess pore water pressure was inferred from the variation in normal effective stress throughout the test (note that references (Finn and Vaid, 1977; Dyvik et al., 1987; Zhang, 2017) have shown that this is equivalent to testing with backpressure saturation and excess pore water pressure measurement). That is, the notional excess pore water pressure can be computed by Equation (5-14).

$$\boldsymbol{u = \sigma'_{vc} - \sigma'_{v}} \tag{5-14}$$

where:

u = notional excess pore water pressure;

σ'_{vc} = initial effective vertical stress;
σ'_{v} = effective vertical stress measured during DSS tests.

The stress-strain curves of AC1U6 under different OCRs are shown in Figure 5.45, unlike triaxial tests where the shear strain at peak stress is around 2%, the shear strains at peak stress in DSS are around 10% – 15%. There is a tendency that at higher OCR, the shear stress peaked at higher shear strain (refer to stress-strain curves of other specimens under various OCRs). The notional excess pore water pressures (EPWP) versus shear strain are shown in Figure 5.46. It can be seen that the soil exhibits contractive behavior for $OCR = 1$ and dilative behavior when $OCR > 1$, illustrating the importance of stress history when interpreting the shear strength of soils. The effective stress paths are shown in Figure 5.47. The critical state line (failure line) is fitted by passing through the shear stress at failure state. For AC1U6, the friction angle is 36 degrees. Similar to Figure 5.46, the stress path with OCR = 1 shows a contractive behavior, i.e., the stress path turned inward when reaching failure, whereas, the stress paths with OCR > 1 show a dilative behavior, i.e., the stress paths turned outward when reaching failure. In summary, the generic behaviors from DSS tests are consistent across all tested specimens.

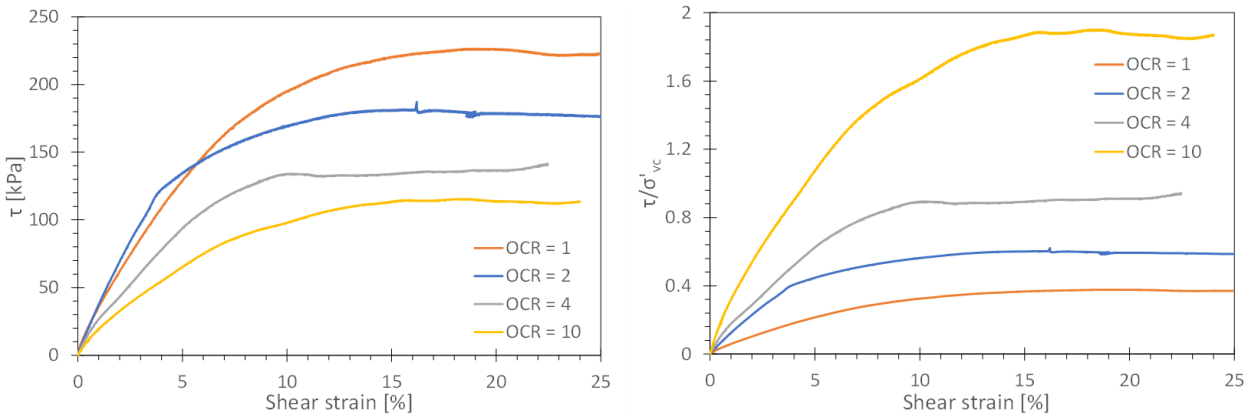

(a) Shear stress vs. shear strain (b) Normalized shear stress vs. shear strain

Figure 5.45: Stress-strain curves from DSS tests on AC1U6 prepared at different OCRs

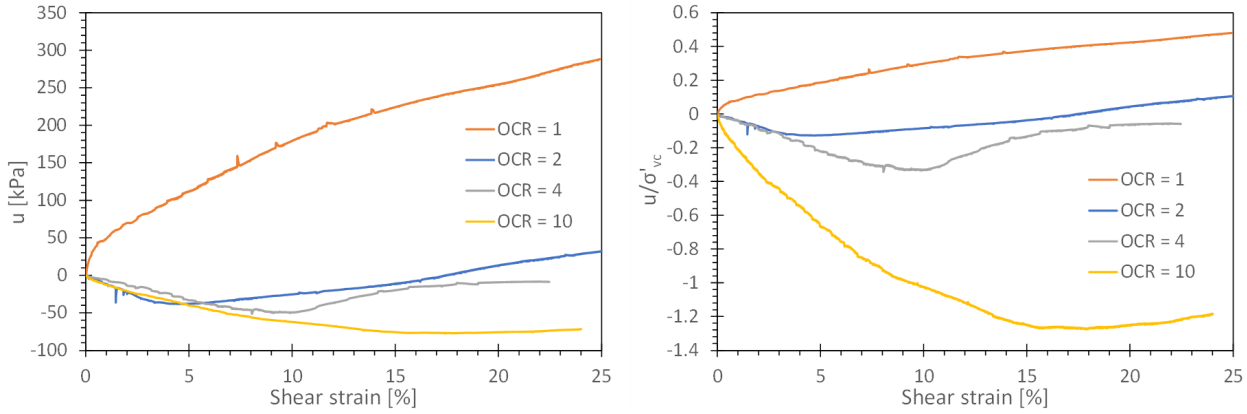

(a) Notional EPWP vs. shear strain (b) Normalized notional EPWP vs. shear strain

Figure 5.46: Notional excess pore water pressure-strain curves on AC1U6 prepared at different OCRs

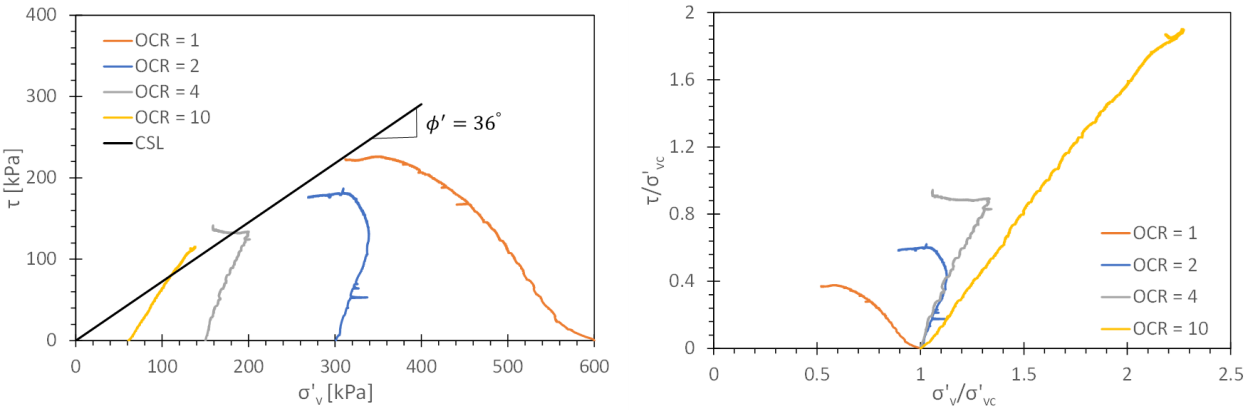

(a) Stress paths and CSL (b) Normalized stress path

Figure 5.47: Stress paths on AC1U6 prepared at different OCRs

5.3.4.2 Normalized undrained shear strength versus OCR

During DSS tests, specimens were prepared to different OCRs by consolidating the specimens to a vertical effective stress greater than the *in-situ* preconsolidation stress and then unloading to achieve a desired OCR. The effects of stress history (OCR) can be observed by plotting normalized undrained shear strength versus OCR in log-log space (Figure 5.48). The results are then fitted to Equation (5-15) to determine the values of the normally consolidated strength ratio ($S = (s_u/\sigma'_{vc})_{NC}$) and the stress exponent, m. Results are summarized in Table 5.7. The normally consolidated strength ratio (S) for Wickiup exhibits a marginally diminished value in comparison to the other sites. This observation can be attributed to the limited scope of the specimen spectrum, with only specimens W1U8 and W1U9 undergoing DSS testing. Typically, the normative consolidated strength ratio (S) for diatomaceous soil typically surpasses that of conventional soft clays ($S = 0.22$) (Ladd et al. 1977). Pertinently, the m parameters derived for all four locations demonstrate homogeneity, suggesting that the progressive

augmentation of the strength ratio with OCR remains invariant for diatomaceous soils investigated in this research.

$$\left(\frac{s_u}{\sigma'_{vc}}\right)_{OC} = \left(\frac{s_u}{\sigma'_{vc}}\right)_{NC} \cdot OCR^m \quad \textbf{(5-15)}$$

where:

$\left(\frac{s_u}{\sigma'_{vc}}\right)_{OC}$ = normalized undrained shear strength at OCR > 1;

$\left(\frac{s_u}{\sigma'_{vc}}\right)_{NC}$ = normalized undrained shear strength at OCR = 1;

m = fitting parameter.

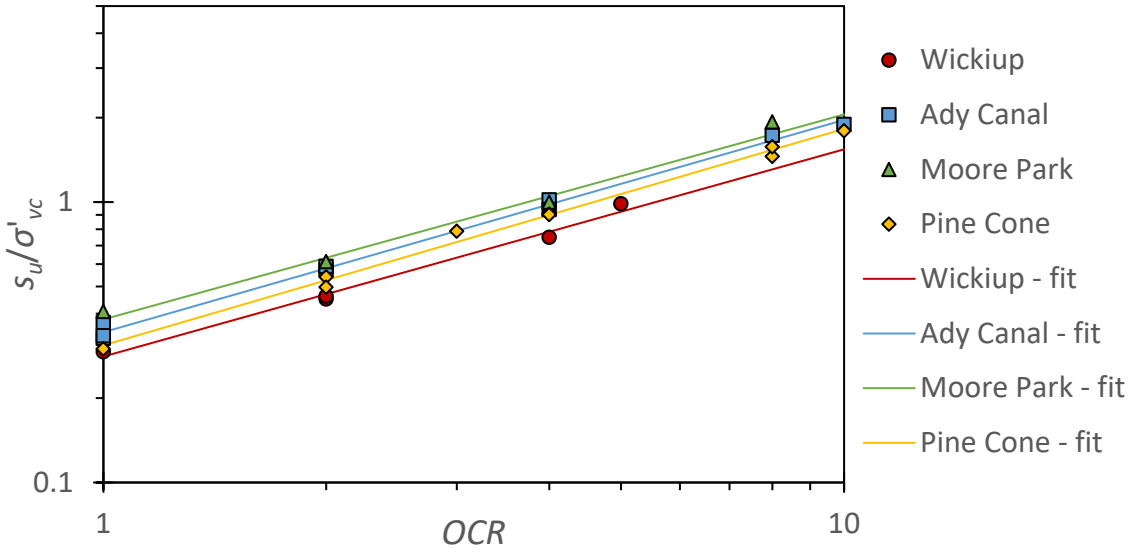

Figure 5.48: Normalized undrained shear strength vs. OCR for DSS tests

Table 5.7: Summarized *S* and *m* parameters

	S	***m***	**R^2**
Wickiup Junction	0.281	0.739	0.989
Ady Canal	0.344	0.756	0.996
Moore Park	0.381	0.731	0.980
Pine Cone	0.308	0.772	0.994

5.4 FIELD TEST RESULTS

5.4.1 Standard Penetration Test

The $(N_1)_{60}$ values from SPT tests are plotted together with CPTu profiles in Figure 5.49 to Figure 5.52 from both current project and previous investigated boreholes. In Wickiup Junction, repeated zero blow counts were encountered and the whole profile has very low $(N_1)_{60}$ values

from the current project investigation. Wickiup has relatively versatile soil layers in depth, varying between sand and fine-grained soil layers. The higher $(N_1)_{60}$ values (>21) are actually from the sand layers. The extreme values of $(N_1)_{60}$ are cut off in order to see variation of small $(N_1)_{60}$ values. There are some differences between $(N_1)_{60}$ profiles from this project and previous investigations, especially in the depth of 30 to 50 m.

In Ady Canal, the current and previous projects showed surprisingly good agreement in $(N_1)_{60}$ profiles. The soil layer has nearly zero $(N_1)_{60}$ values between 9 to 13 m depth. An extreme $(N_1)_{60}$ value of 60 shows up at the depth of 20 m. Below 20 m depth, $(N_1)_{60}$ gradually decreases.

In Moore Park and Pine Cone Drive, the $(N_1)_{60}$ values are much higher than the other two sites. $(N_1)_{60}$ values gradually increase with depth in Moore Park and slightly decrease with depth in Pine Cone. No previous site investigation was conducted in Moore Park. There is a distinction of $(N_1)_{60}$ values at higher depth in Pine Cone Drive between the current project and previous projects.

5.4.2 Cone Penetration Test with Pore Water Pressure Measurement

The cone penetration test results together with soil behavior type profiles are shown in Figure 5.49 - Figure 5.52 for each individual site. In the case of the Wickiup Junction, the preceding q_t and f_s profiles exhibit a considerable degree of conformity with the current investigation. Within the upper 15 m of the soil profile, discernible elevations in both q_t and f_s are evident, in conjunction with virtually negligible excess pore water pressure. The soil behavior type index (I_c) ranges between 6 to 8, indicating the presence of a sand-based layer. Subsurface regions lying below the 15-m mark witness a rapid decrease in q_t values to the range of 2 to 4 MPa, accompanied by f_s values predominantly falling below 150 kPa, except for sporadic scattering spikes. Simultaneously, the pore pressure (u_2) progressively increases with depth, reaching up to 1800 kPa by the end of the penetration. In the meantime, the soil behavior type index (I_c) is centered around 3, which characterizes the material as predominantly clayey. The SPT and CPTu results are consistent overall. Despite the prior knowledge of non-diatomaceous clay being present at the Wickiup site, no sudden alterations manifest within the SPT and CPTu profiles at depths lower than 15 m. This suggests a challenge in differentiating between diatomaceous and non-diatomaceous soil solely relying on these SPT and CPT representations.

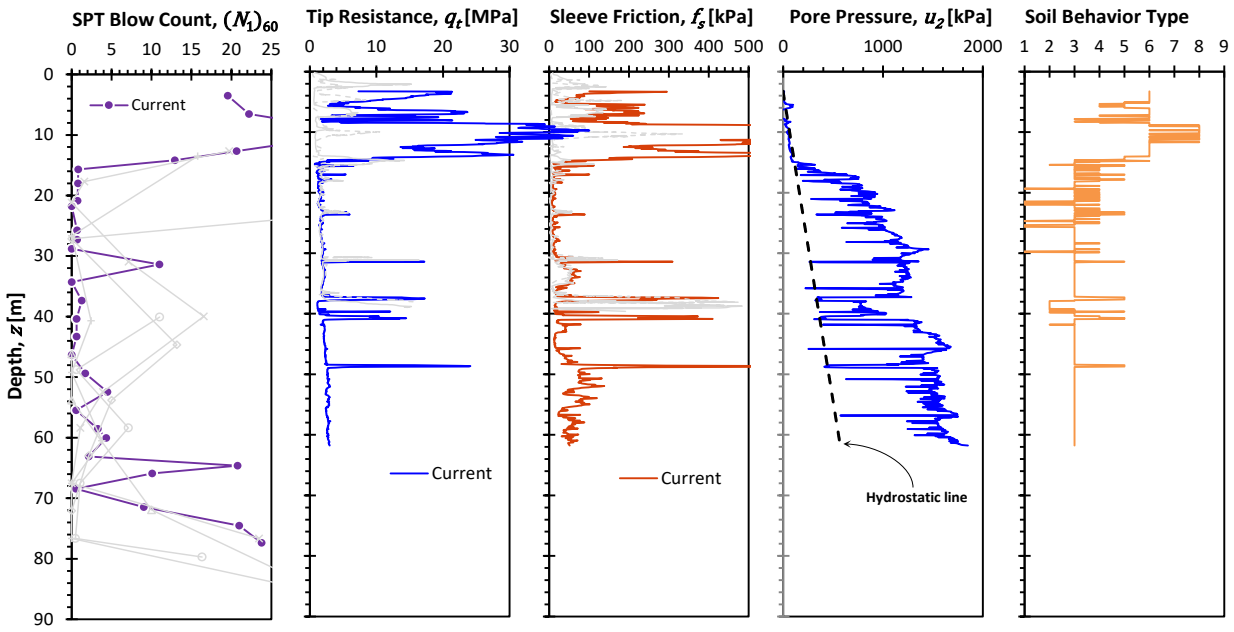

Figure 5.49: SPT, CPTu and I_c profiles in Wickiup (note that previous investigations are in grey color) (Soil behavior types are listed in Table 3.3)

Table 5.8: Soil behavior type (after Robertson 1990, 2009, 2016)

NO.	Soil behavior type
1	Sensitive fine-grained
2	Organic soils – peat
3	Clays – silty clay to clay
4	Silt mixture – clayey silt to silty clay
5	Sand mixture – silty sand to sandy silt
6	Sands – clean sand to silty sand
7	Gravelly sand to dense sand
8	Very stiff sand to clayey sand
9	Very stiff fine-grained

At the Ady Canal site (Figure 5.50), two CPTu were conducted, with one probe reaching a depth of 13 m and the other extending to 19 m. The data from both probes demonstrated high consistency. For clarity and analytical rigor, subsequent evaluations will focus on the dataset from the CPTu probe that advanced to the 19-m depth. Between 7 and 13 m depth, the CPTu data show low q_t and f_s, contrasted by elevated u_2, and I_c is characterized near 3, indicative of a clayey layer. The CPTu encountered refusal around 19 m depth where the $(N_1)_{60}$ value is also exceedingly high. From 13 to 19 meters, CPTu measurements and I_c values exhibit marked variability, suggesting a complex, heterogeneous soil stratum.

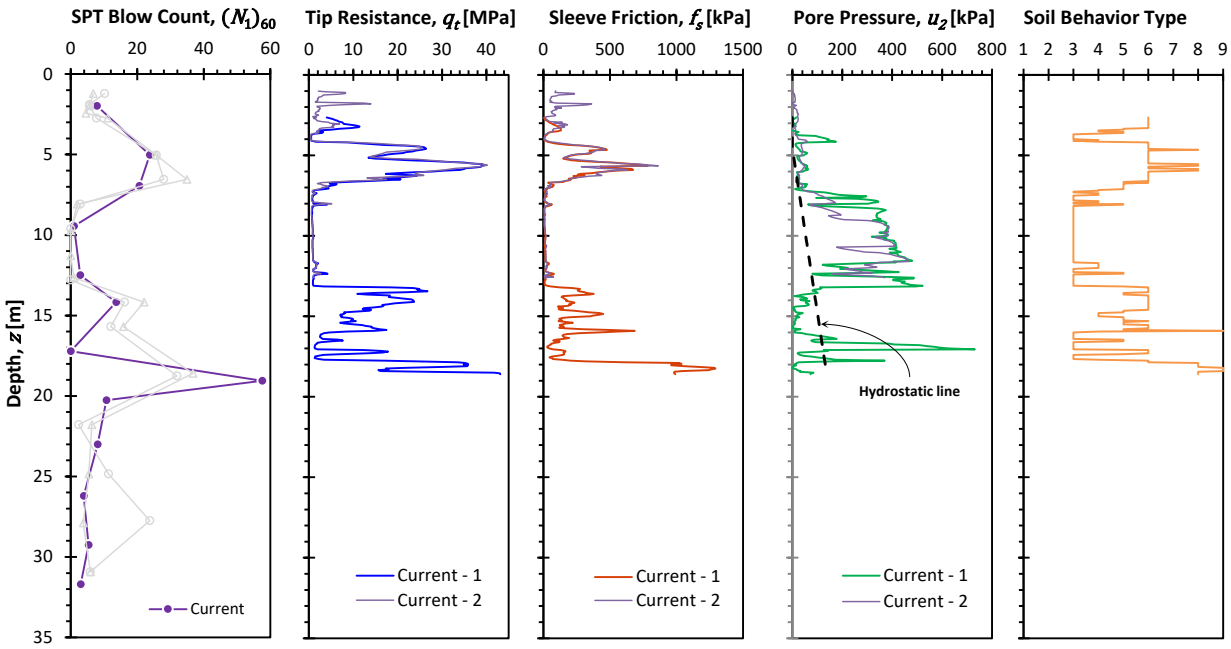

Figure 5.50: SPT, CPTu and I_c profiles in Ady Canal (note that previous investigations are in grey color) (Soil behavior types are listed in Table 3.3)

At Moore Park (Figure 5.51), no prior investigation was conducted. The presence of diatomaceous soil is informed from geological inference. Moore Park has the highest $(N_1)_{60}$ values overall. From 38 m depth, the excess pore water pressure is nearly zero, which may indicate presence of sand, however, the soil behavior type index is mostly characterized to be 3, indicative of clay. Below 8 m depth, all CPTu measurements increased, extraordinary excess pore water pressure was generated, however, the soil behavior type index varies amongst 4, 5, and 9, indicative of silt, sand, and stiff fine-grained soil. These seemingly contradictive phenomena may result from the mudstone diatomaceous soil which largely exists in Moore Park and Pine Cone.

In Pine Cone Drive site, there is barely any CPTu advancement due to exceedingly high refusal at early depth. The CPTu profiles are presented in Figure 5.51. Due to such circumstances, the soil behavior type profile is omitted (though the $Q_{tn} - F_N$ and $Q_t - B_q$ scattering plots are shown in Chapter 6).

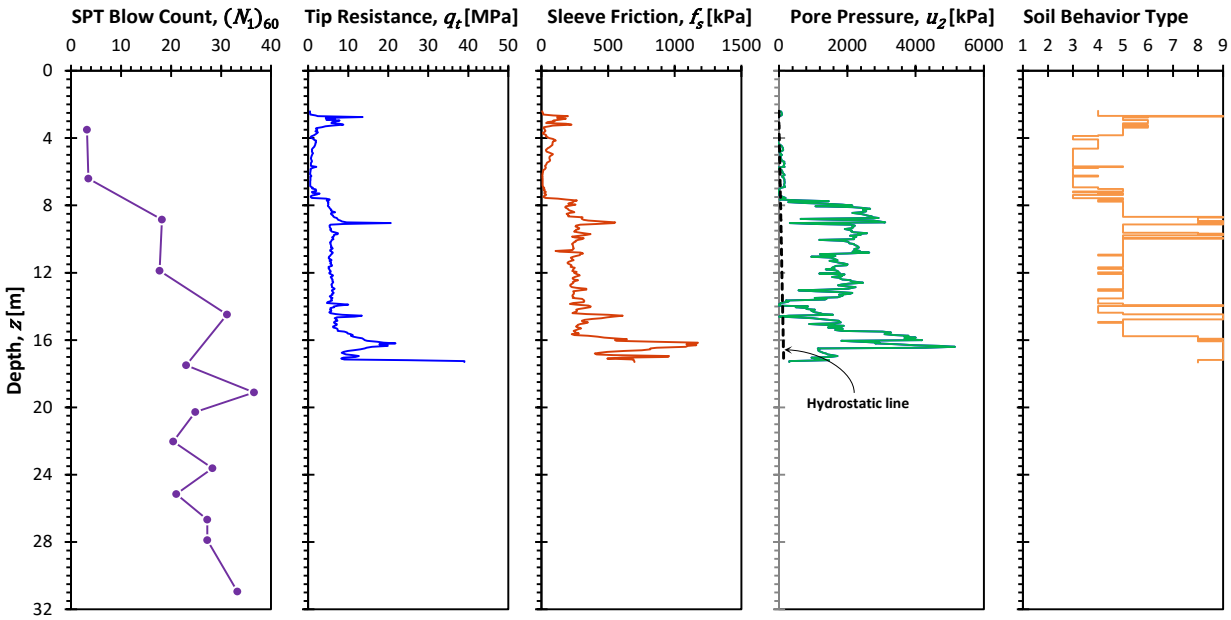

Figure 5.51: SPT, CPTu and I_c profiles in Moore Park (Soil behavior types are listed in Table 3.3)

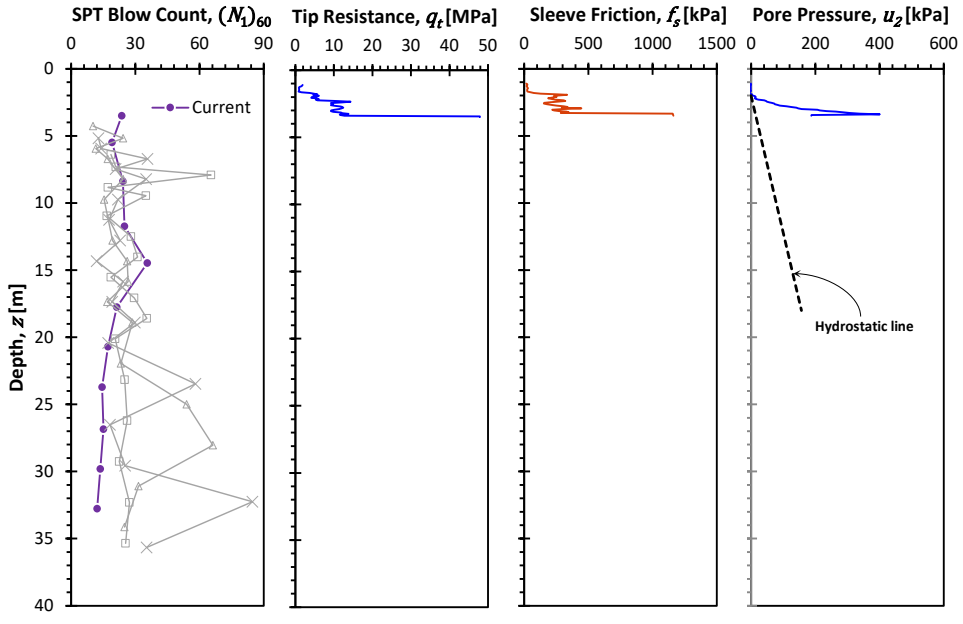

Figure 5.52: SPT, CPTu and I_c profiles in Pine Cone (note that previous investigations are in grey color) (Soil behavior types are listed in Table 3.3)

5.4.3 Dissipation Test: Horizontal Coefficient of Consolidation

The dissipation tests were conducted along with CPTu advancement, the dissipation curves are presented in the form of normalized pore water pressure vs. time in Figure 5.53. There is no

dissipation test performed in Pine Cone. The normalized pore water pressure is calculated by Equation (3-10).

$$u_{nor} = \frac{u - u_0}{u_i - u_0} \tag{5-16}$$

Where:
u_{nor} = normalized pore water pressure;
u = measured pore water pressure at time t;
u_0 = hydrostatic pore water pressure;
u_i = measured pore water pressure at time zero.

In Wickiup, a total of 11 dissipation tests were conducted in depth between 15 – 62 m. Most dissipation tests finished in 20 minutes. In Ady Canal, two dissipation tests were conducted at each CPTu. In the first CPTu (7.62 m and 11.582 m), both tests reached 90% dissipation in about 20 minutes, whereas, in the second CPTu (8.53 m and 10.67 m), one test was dissipating very slowly and was forced to stop at 40 minutes, the other test reached about 80% by 30 minutes. In Moore Park, the dissipation was fairly fast in the upper 13 m depth, the test conducted in 16.46 m depth reached 80% dissipation in about 20 minutes.

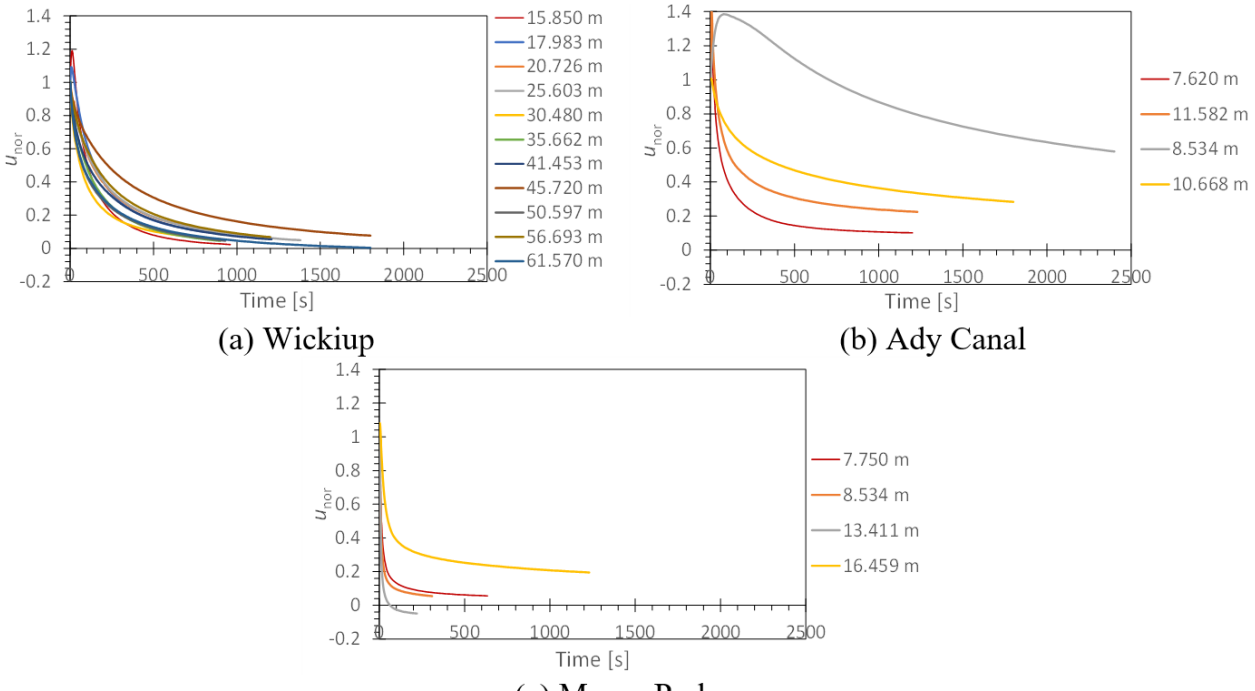

(a) Wickiup

(b) Ady Canal

(c) Moore Park

Figure 5.53: u_{nor} over elapsed time at different depths during dissipation tests

From the dissipation tests, the horizontal coefficient of consolidation (c_h) can be computed at various stages of dissipation. In Chapter 3, we introduced two evaluations of c_h proposed by Teh and Houlsby (1991) and Burns and Mayne (1998) respectively. Figure 5.54 - Figure 5.56 present c_h at different stages of dissipation ($u_{nor} = 0.8, 0.6, 0.4, 0.2$) together with vertical coefficient of

consolidation (c_v) evaluated from IL tests at different loading stages. Both coefficients of consolidation (c_h, c_v) vary to a magnitude of 2 to 3 (0.001 – 1 cm^2/s). The horizontal coefficient of consolidation (c_h) increases with the degree of consolidation (i.e., degree of dissipation) as the time factor (T^*) increases with the degree of consolidation. The c_v higher than c_h at certain depth are typically from the lower loading stages of IL tests (see 5.3.2.5). Generally speaking, both c_v and c_h are consistent with one another.

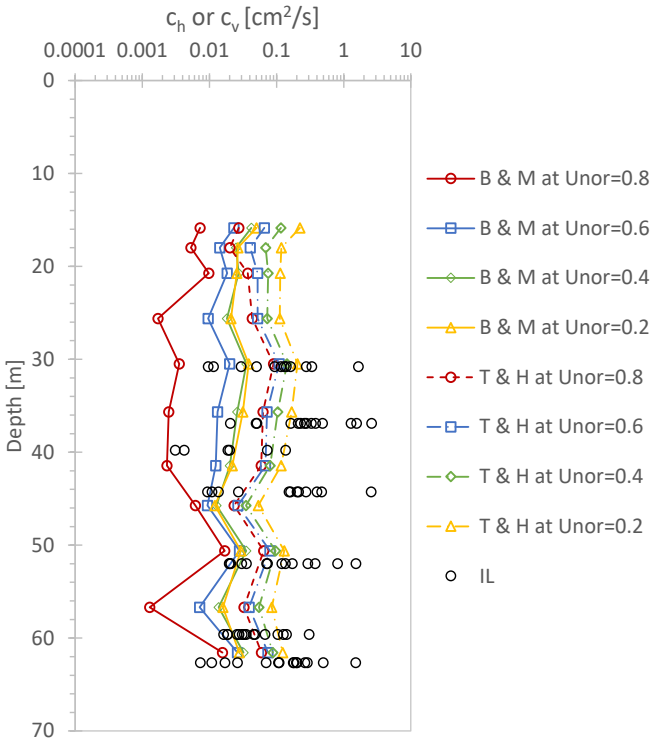

Figure 5.54: Horizontal (c_h) and vertical (c_v) coefficient of consolidation in Wickiup (note that B & M represents (Burns and Mayne, 1998b) evaluation on c_h, T & H represents (Teh and Houlsby, 1991) evaluation on c_h, IL represents c_v from IL tests)

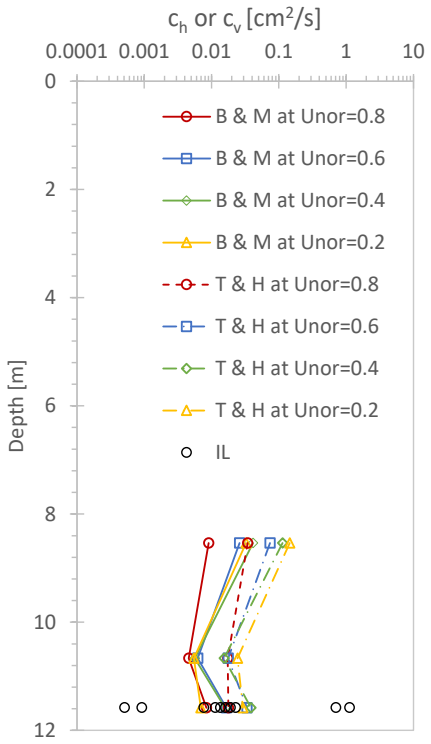

Figure 5.55: Horizontal (c_h) and vertical (c_v) coefficient of consolidation in Ady Canal (note that B & M represents (Burns and Mayne 1998b) **evaluation on c_h, T & H represents (Teh and Houlsby 1991) evaluation on c_h, IL represents c_v from IL tests)**

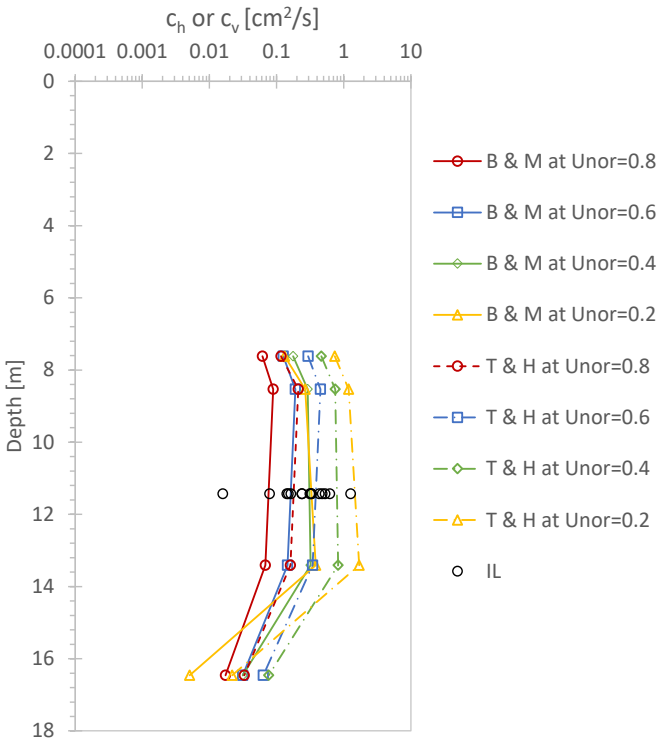

Figure 5.56: Horizontal (c_h) and vertical (c_v) coefficient of consolidation in Moore Park (note that B & M represents (Burns and Mayne, 1998b) evaluation on c_h, T & H represents (Teh and Houlsby, 1991) evaluation on c_h, IL represents c_v from IL tests)

5.4.4 Shear Wave Velocity

The profiles of shear wave velocity (V_s) and computed shear modulus (G_{max}) of three investigated sites are presented in Figure 5.57. The shear modulus (G_{max}) can be computed by Equation (5-17). The interval of V_s measurements is every 1 m. In Wickiup, V_s predominantly ranges between 150 to 250 m/s below 20 m depth, indicating consistent soil properties. In contrast, the Ady Canal site reveals a pronounced soft layer around the 10 m depth, characterized by a significantly reduced V_s of approximately 100 m/s, suggesting a potential zone of weak material. In Moore Park, there's a noticeable gradation in V_s with depth. Commencing from a lower bound of 80 m/s at shallow depths, V_s increases to 600 m/s deeper in the profile, indicative of a transition from softer soils to more consolidated or possibly mudstone layers. Based on the relation between shear modulus (G_{max}) and V_s shown in Equation (5-17). The shear modulus (G_{max}) in Wickiup is around 100 MPa consistently below 20 m depth. The soft layer in Ady Canal around 10 m depth shows a much lower shear modulus where G_{max} is about 20 MPa, which is similar to the case of typical soft clays. In contrast, Moore Park exhibits exceedingly high levels of shear modulus, representing a mudstone type soil material.

$$G_{max} = \rho \cdot V_s^2 \tag{5-17}$$

where:

G_{max} = shear modulus, Pa;
ρ = soil density, kg/m^3; and
V_s = shear wave velocity, m/s.

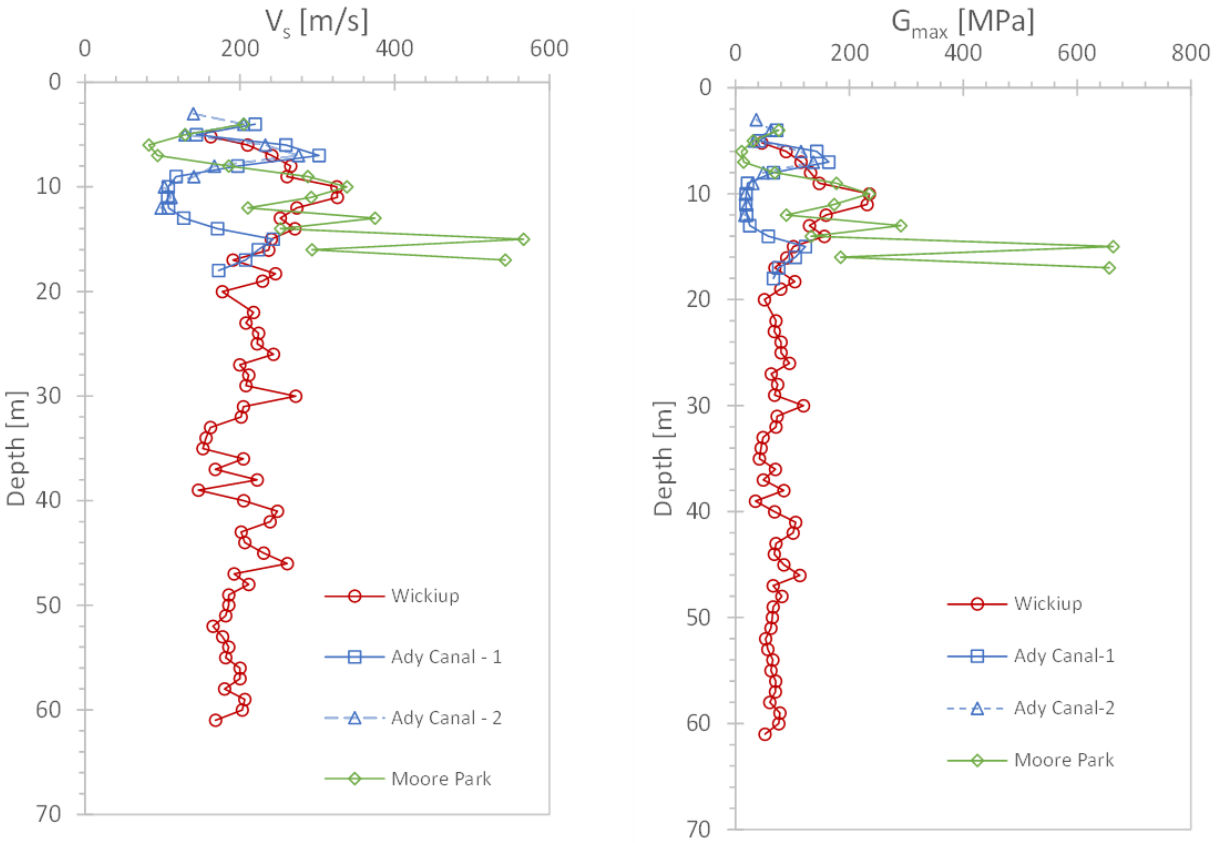

(a) Shear wave velocity (b) G_{max}

Figure 5.57: Shear wave velocity and G_{max} profiles

5.4.5 Vane Shear Test

Figure 5.58 presents the results of in-situ vane shear tests, which were performed at 10 different depths in Wickiup Junction, 5 different depths in Ady Canal, 1 in Moore Park, and 0 in Pine Cone Drive due to the extra stiffness of the soil. In practice, the whole test procedure was quite susceptible in these fields, unexpected sudden stop, sudden breaking, slippage, and inconsistent system friction measurements occurred. Whether it was the soil or the conduction that attributed to these eccentric behaviors is unknown. Moreover, based on a preliminary soil profile determination, in Wickiup Junction and Moore Park, the *in-situ* vane shear tests were not performed in the diatomaceous soil layer. At Ady Canal, a handful of *in-situ* vane shear tests were performed in the diatomaceous soil layer. In summary, the *in-situ* vane shear test results from this project should be used with caution.

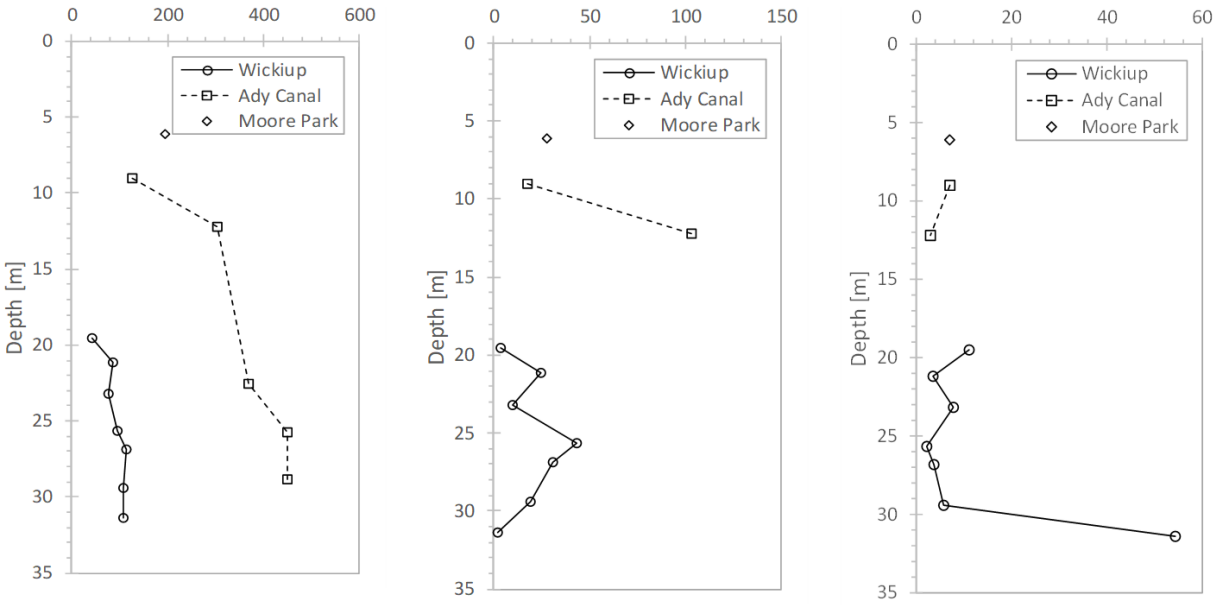

(a) Peak undrained shear strength

(b) Residual undrained shear strength

(c) Sensitivity

Figure 5.58: Field vane shear tests

6.0 SYNTHESIS OF LABORATORY AND IN-SITU TEST RESULTS

6.1 SPECIFIC GRAVITY AS A PROXY FOR DIATOM CONTENT

Natural diatomaceous soil usually is a mixture of diatom frustules and other soil such as clay or even sand. The diatom fraction in diatomaceous soil will no doubt impact the properties of the soil. The only direct way to identify the proportion of diatoms in a mixture is through robust stereological analysis of a statistically representative number of SEM images. However, this method involves a large number of SEM images and morphological operations that are difficult to automate for a highly variable material. It is well-known (e.g., Shiwakoti et al. 2002), however, that the specific gravity of diatom frustules ($G_s \approx 1.9 - 2.3$) is significantly lower than that of most common soil minerals ($G_s \approx 2.6 - 2.8$). Considering diatomaceous soil as a four-phase material (i.e., diatoms, other soil minerals, water, and air), it is possible to derive Equation (6-1) which describes diatom content as a function of the specific gravities of the diatoms, other minerals, and the total soil (G_s^d, G_s^m, G_s^T, respectively). Because pure diatom has very distinct specific gravity, and generally the other soil has G_s around 2.7, the diatom content can be inferred from the overall G_s if G_s of diatom and other soil are assumed.

$$\frac{M^d}{M^T} = \frac{G_s^d G_s^T - G_s^d G_s^m}{G_s^d G_s^T - G_s^T G_s^m} \tag{6-1}$$

where:
M^d = mass of diatoms; and
M^T = total mass of soil.

Figure 6.1 shows the relationship between G_s^T and diatom content for some representative specific gravity values. A consistent trend between diatom content and G_s^T can be seen with little variation for the range of G_s^d and G_s^m considered, indicating that knowledge of the exact values of the constituent specific gravities is not necessary in order to make an approximate prediction of diatom content. This is significant because we are aware of only one limited study in the literature reporting the diatom content of natural diatomaceous soils (Covarrubias Ornelas et al. 2022), likely due to the measurement complexities discussed previously. There are, however, a number of published studies on synthetic diatom mixtures, including measurement of G_s^T and diatom content. Results of these studies were presented in Figure 2.6 and 2.7 in Chapter 2, same data from literature are replotted in Figure 6.1. Despite some variation of G_s^T at certain diatom contents across the literature, the G_s^T generally decreases approximately linearly with the increase of diatom content for specified soil mixtures. Based on these observations, we use G_s^T as a proxy for the amount of diatoms in a natural diatomaceous soil.

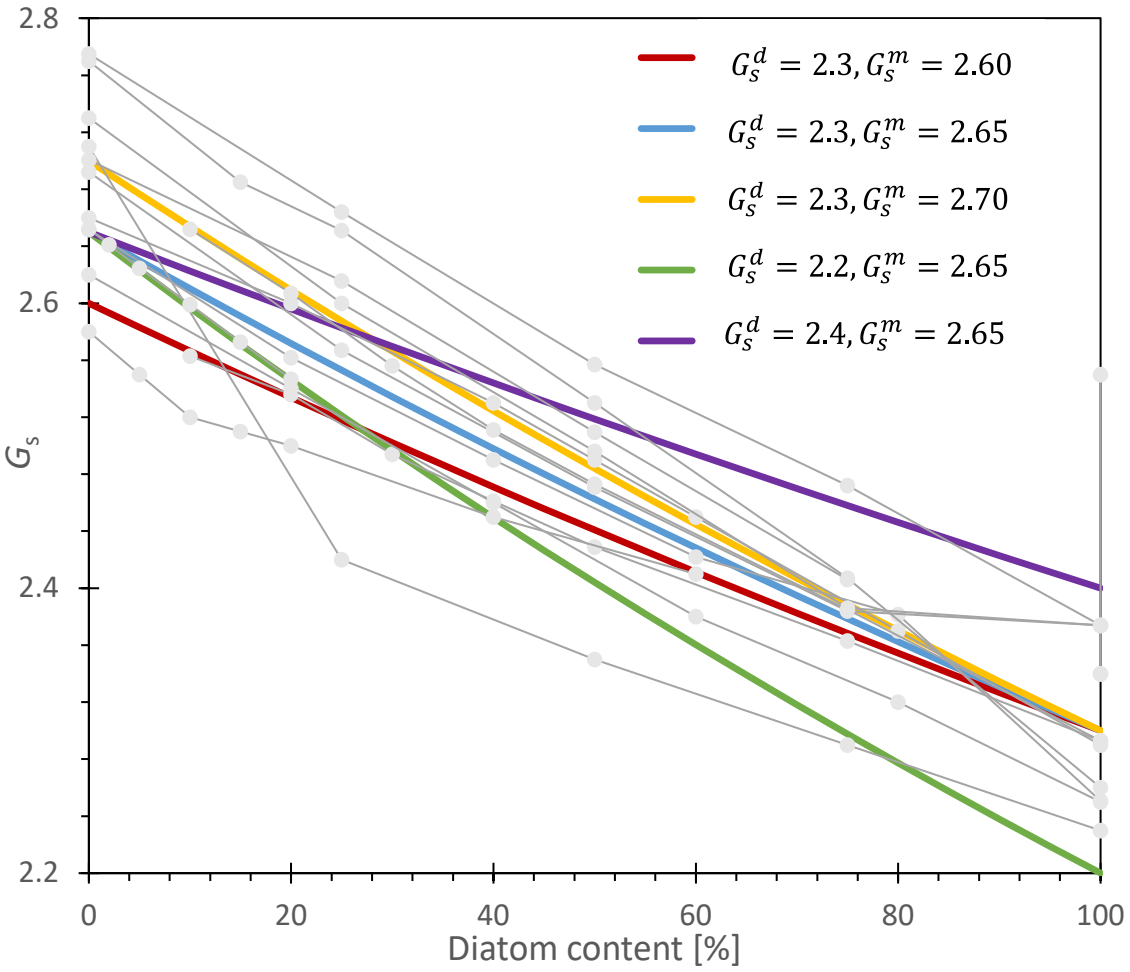

Figure 6.1: Relationship between G_s and diatom content. Colored lines are theory (Equation 6-1), and others are data from the literature (refer to Figure 2.6 and 2.7)

6.2 SPECIFIC GRAVITY AS A PREDICTOR OF OTHER PHYSICAL PROPERTIES

6.2.1 Consistency Limits

Consistency limits (LL, PL, and PI) are important physical properties for fine-grained soils in that they are necessary for soil classification, are strong indicators of soil behavior, and strongly correlate with soil mechanical properties. Given the unique structure of diatoms, we expect that diatomaceous soils will exhibit distinctive consistency limits that vary with the fraction of diatoms in the matrix. The relationship between LL and G_s is shown in Figure 6.2 together with literature data. It can be seen that LL of diatomaceous soil decreases with the increase of G_s, which means that LL is strongly influenced by diatom content for diatomaceous soil. The empirical correlation between LL and G_s from this study is presented in Equation (6-2). Figure 6.2 also shows the plots of LL vs. G_s of diatom mixtures from various references. The trend drawn from this work is generally consistent with diatom mixtures from the literature. LL of natural diatomaceous soil exceeds 550 mainly as a result of Mexico City clay. The Mexico City

clay, while diatomaceous, it also contains a significant amount of montmorillonite, and thus has LL that are far out of trend with other diatomaceous soil. For natural diatomaceous soils, the correlation between consistency limits and G_s has not previously been directly presented. The extracted data of LL and corresponding G_s from literature on natural diatomaceous soil are also presented in Figure 6.2 and compare with the trendline from this project. It is worth noting that the natural diatomaceous soils are located in different region in the plot in terms of their origin. The trendline from this project is well in line with the data from Wang et al. (2021) (i.e., the Buck Creek data) which also reported diatomaceous soil properties from Oregon. It is hard to see a universal trend for natural diatomaceous soil from different sources.

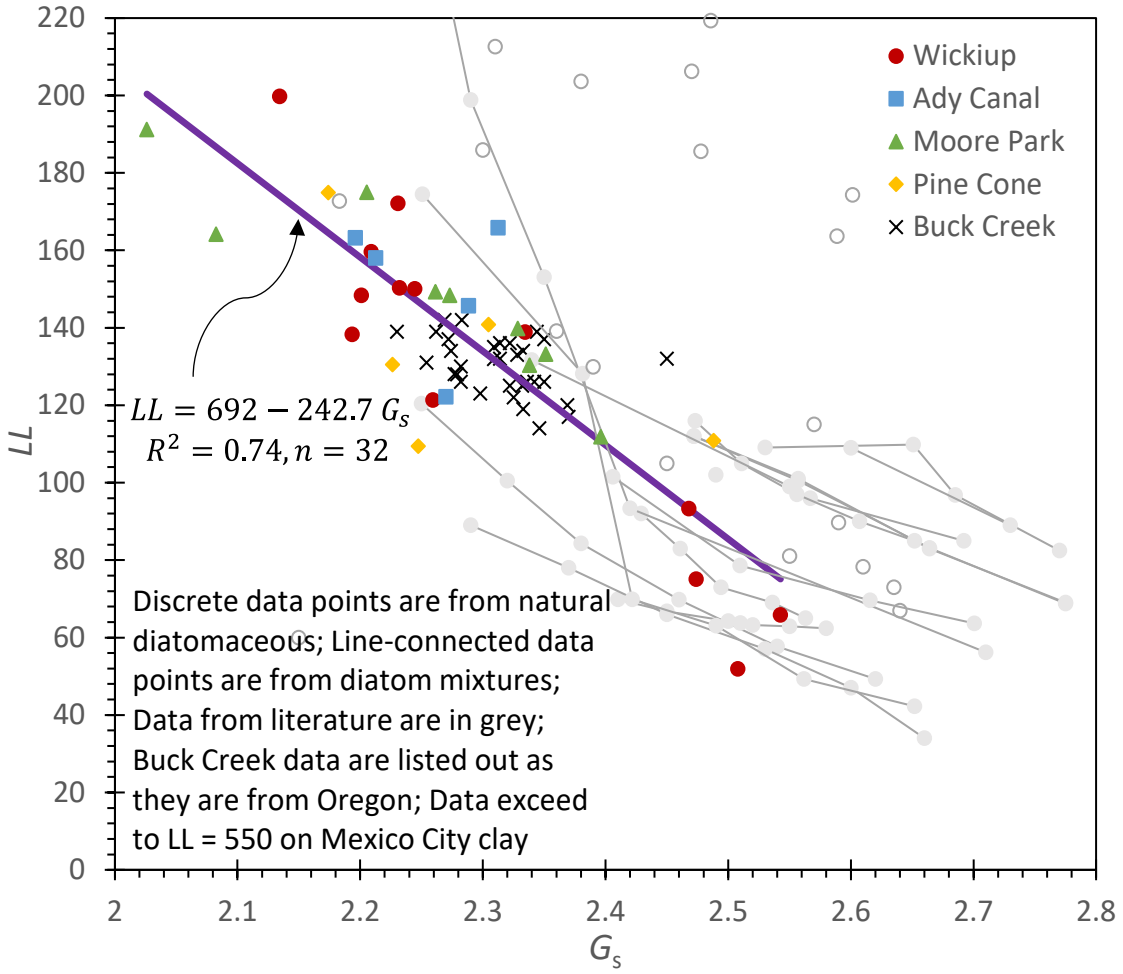

Figure 6.2: Relationship between LL and G_s collectively from this study and literature

Similar relationships are also observed for PL and PI as a function of G_s. Figure 6.3 shows the relationship between PL and G_s. A similar empirical correlation (Equation (6-3)) can be drawn from the data with a lower R^2. Note that the presented PL are either tested from or correlated to the thread rolling method. In Chapter 5, it has been discussed the differences among different methods on testing PL. Wood and Wroth (1978) method is not recommended due to its low practibility, and there is no strong theoretical support behind Feng (2001) method, thus, the thread rolling results are used. For $G_s > 2.35$ the $PL - G_s$ data for diatom mixtures from the

literature is quite consistent with the observed trend developed for Oregon diatomaceous soils. The PL values for diatom mixtures with $G_s < 2.35$ are somewhat larger than those predicted by Equation (6-3). We note, however, that the data falling above the trend shown is all for marine diatoms. Thus, it is possible that hydromechanical behavior near the plastic transition may be different for marine and lacustrine diatoms or perhaps that PL values for marine diatoms may be influenced by test protocols (e.g., if the materials are harvested from saltwater and tested using freshwater). Data from the literature on the PL and G_s for natural diatomaceous soils is somewhat more scattered, reflecting the regional, geological, and biological diversity of the diatoms.

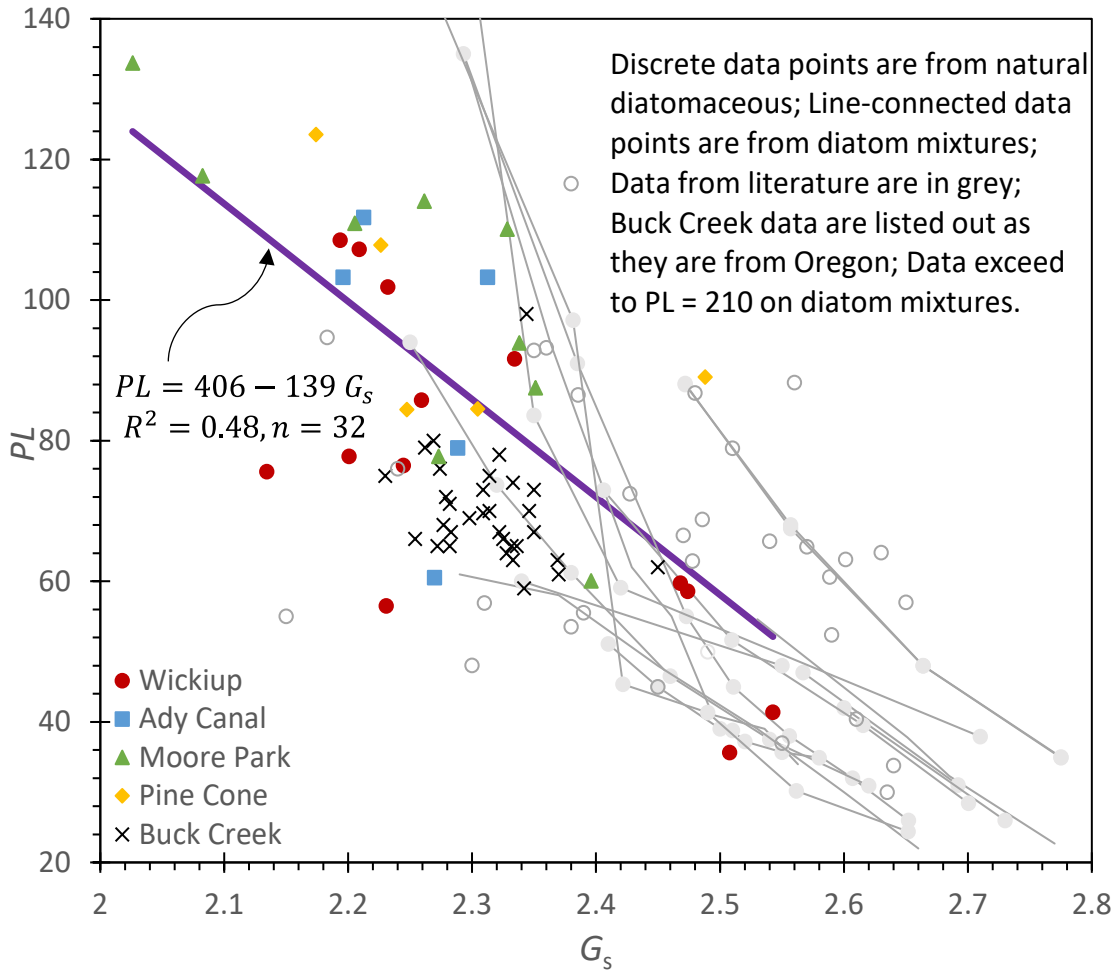

Figure 6.3: Relationship between PL and G_s collectively from this study and literature

Figure 6.4 shows that PI is not as well-correlated with G_s as LL and PL are. The best-fit line for the $PI - G_s$ data is presented as Equation (6-4). That PI is not a strong function of G_s (i.e., diatom content) is intuitively appealing. We suspect that the intraparticle water in diatomaceous soils is both trapped inside the frustules through surface tension (capillarity) and relatively constant as the global moisture content in the soil changes. Thus, this intraparticle water serves to "prop up" the LL and PL by approximately the same amount and also does not actively

participate in much of the hydromechanical response that the soil displays to external stimuli. This is presented schematically in Figure 6.5.

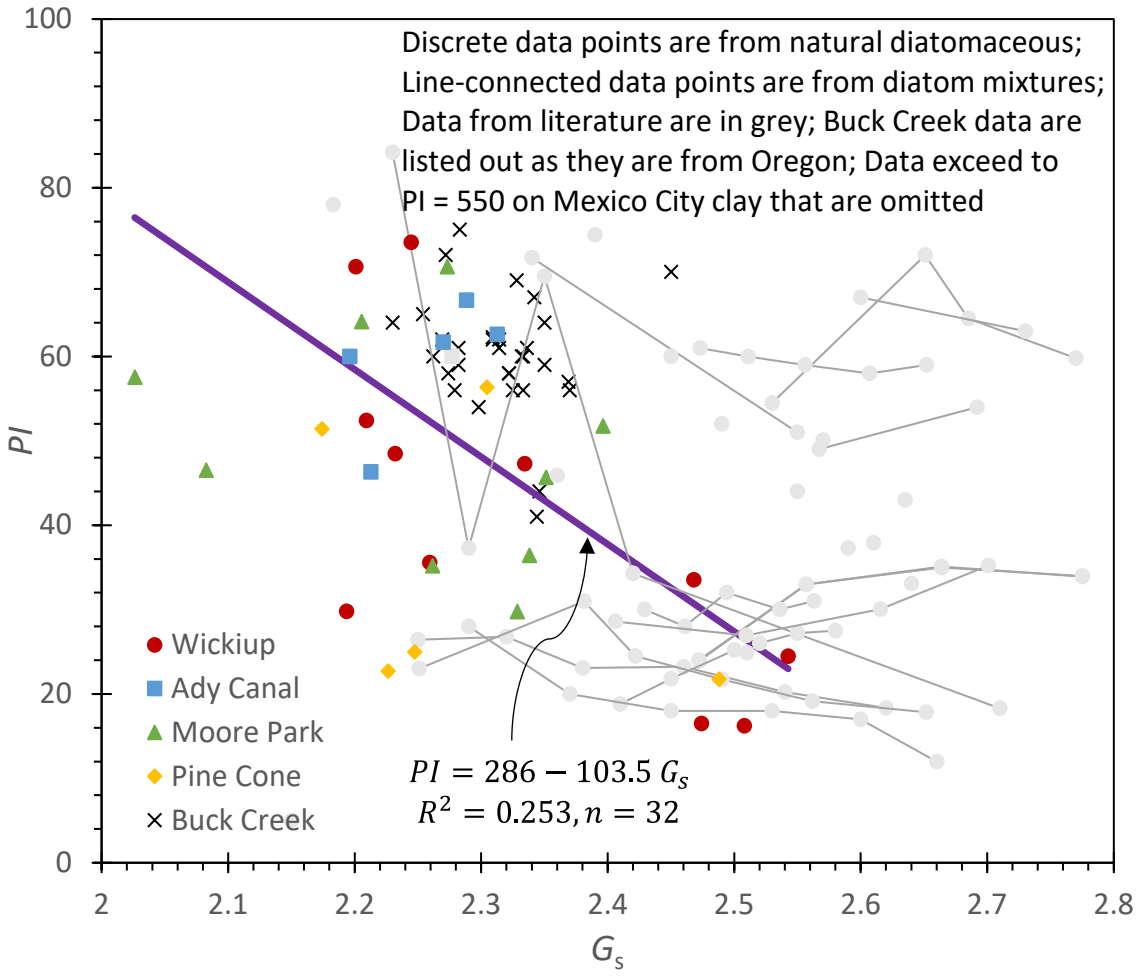

Figure 6.4: Relationship between PI and G_s collectively from this study and literature

$$\boldsymbol{LL = 692 - 242.7\ G_s} \tag{6-2}$$

$$\boldsymbol{PL = 406 - 139\ G_s} \tag{6-3}$$

$$\boldsymbol{PI = 286 - 103.5\ G_s} \tag{6-4}$$

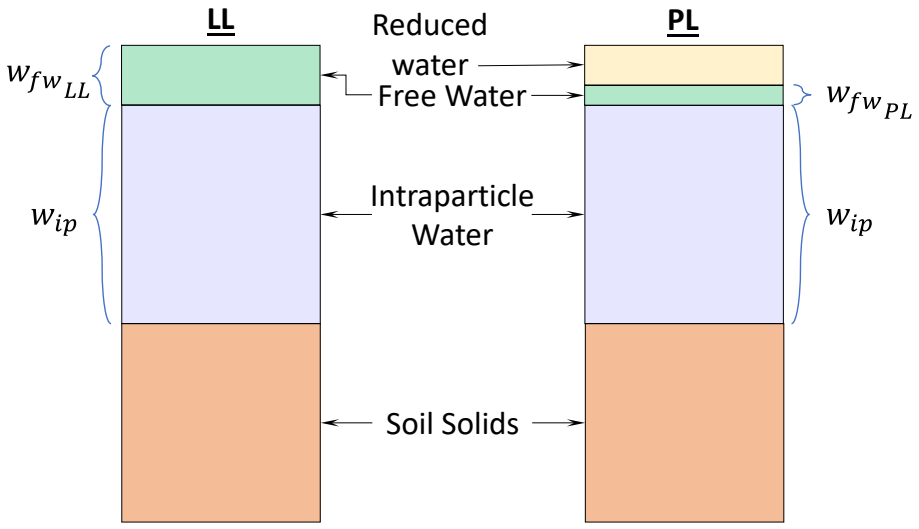

$$PI = LL - PL = \left(w_{fw_{LL}} + w_{ip}\right) - \left(w_{fw_{PL}} + w_{ip}\right)$$

$$PI = LL - PL = w_{fw_{LL}} - w_{fw_{PL}}$$

Figure 6.5: Schematic representation of why *PI* is relatively unaffected by diatom content. The intraparticle water content (w_{ip}) changes little between the *LL* and the *PL*. The *PI* is largely independent of the amount of intraparticle water and, thus, the diatom content.

6.2.2 Specific Surface Area

The values of SSA for diatomaceous soils published in the literature can vary widely, from 20 to 400 m^2/g. In this work, SSA was measured with methylene blue and gas absorption method, including multiple replicates for selected specimens. The SSA results are plotted against G_s in Figure 6.6. The data on natural diatomaceous soils found in the literature (also in Figure 6.6) show similar scatter to those reported here. We hypothesize that the methylene blue molecules may be too large to fit into some of the intraparticle void space and complex surface topography exhibited by the diatoms, thus causing an underestimate of SSA. Only two samples were sent for the gas absorption (N_2) method, one result is close to the MB method, one is four times higher than the MB result (see Chapter 5). A new method is necessary to accurately measure the SSA of diatomaceous and other complex soils. Recent work on a procedure similar to that of methylene blue, but instead using crystal violet as the staining agent, shows promise, but is not yet widely adopted.

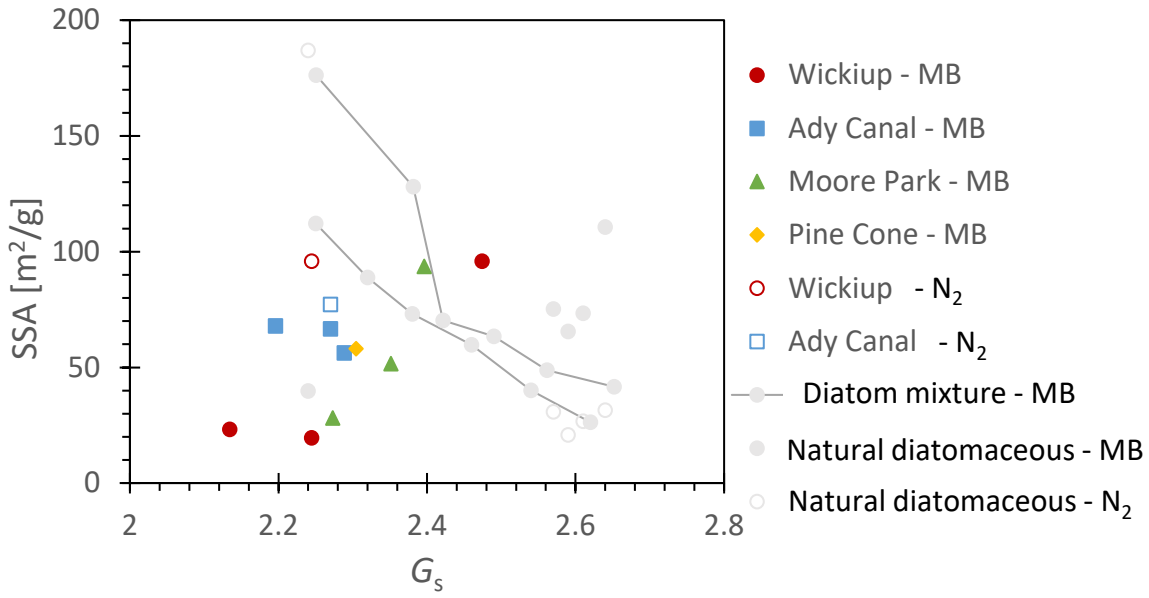

Figure 6.6: Relationship between SSA and G_s collectively from this study and literature (discrete data points are from natural diatomaceous; line-connected data points are from diatom mixtures; data from literature are in grey)

6.2.3 Activity

Activity (A) is defined as the ratio of PI to the clay content and has been widely used to infer the mineralogy of the colloidal fraction of clays (e.g., Skempton, 1948, 1953; Skempton and Bishop, 1950). Activity is often a strong indicator of clay behavior because it is an indirect measure of the size of the adsorbed water layers surrounding the individual clay particles. Thus, activity is widely considered to be approximately constant for a given soil: e.g., $A \approx 0.5$ for kaolinite (small adsorbed water layer) and $A \approx 7$ for Na-montmorillonite (large adsorbed water layer). Put another way, activity is largely understood (or assumed) to be a function of the chemistry of the colloidal (i.e., $d < 2\mu m$) fraction within the soil matrix.

The activity chart for diatomaceous soils is shown in Figure 6.7. The clay fraction for diatomaceous soils tested in this work varies from 8% to 30%, and the activity varies approximately $0.7 < A < 15$ with a concentration of specimens falling in or near the range $3 \lesssim A \lesssim 5$. Soils with $A > 1.25$ are typically considered "active". Skempton (1984) notes that the region $A > 2$, "…includes only bentonitic clays, no others are known with such high activity values." Diatomaceouls soils are comprised largely of silica, and quartz is reported to have an activity of A < 0.5 (Grim, 1949). Thus, while a number of previous researchers have reported the activity of diatomaceous soils, it would seem that it is not an appropriate measure of behavior, at least not in the classical sense, because their propensity to hold water is a mechanical rather than an electrochemical phenomenon. Literature data are also presented in Figure 6.7. The Buck Creek data largely overlap with the current study as both soils are from Oregon. Other natural diatomaceous soils in Figure 6.7 have activity between 1 to 5 with clay content up to 57%.

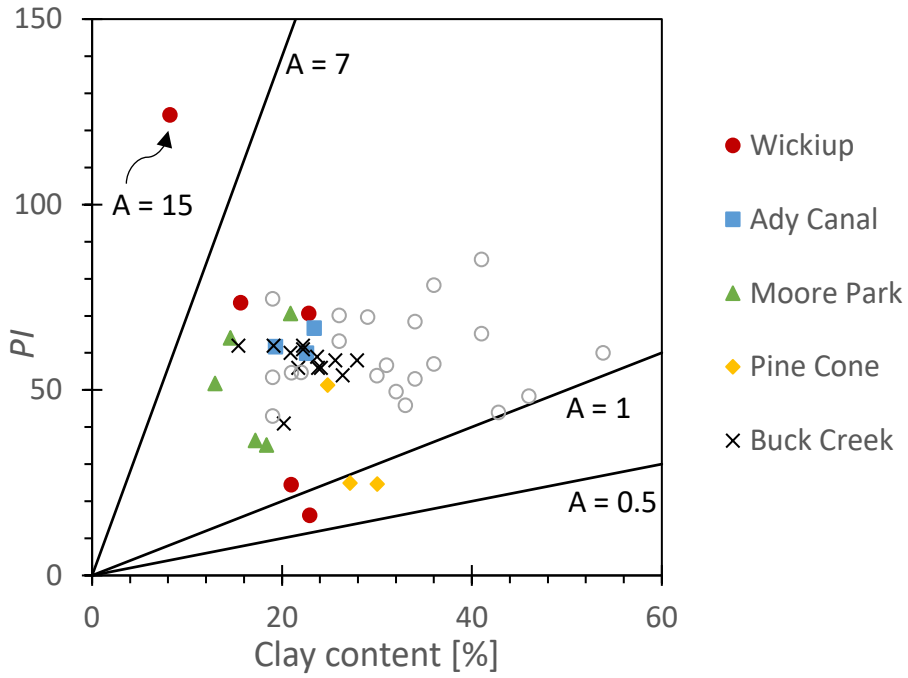

Figure 6.7: Activity chart (open symbols are natural diatomaceous from literature)

Figure 6.8 presents the variation of activity with specific gravity. There is, in general, a slight downward trend in activity with increasing specific gravity, but it is not pronounced especially for natural diatomaceous soil. The activities of natural diatomaceous soils reported in the literature are generally higher than for diatom mixtures, but the diatom mixtures often have a non-diatomaceous fraction that does not contribute appreciably to activity, such as kaolinite. While activity may yet prove to be a useful means for predicting the engineering behavior of diatomaceous soils (or other soils with mechanical water-holding capacity), we do not currently have robust diatomite correlations.

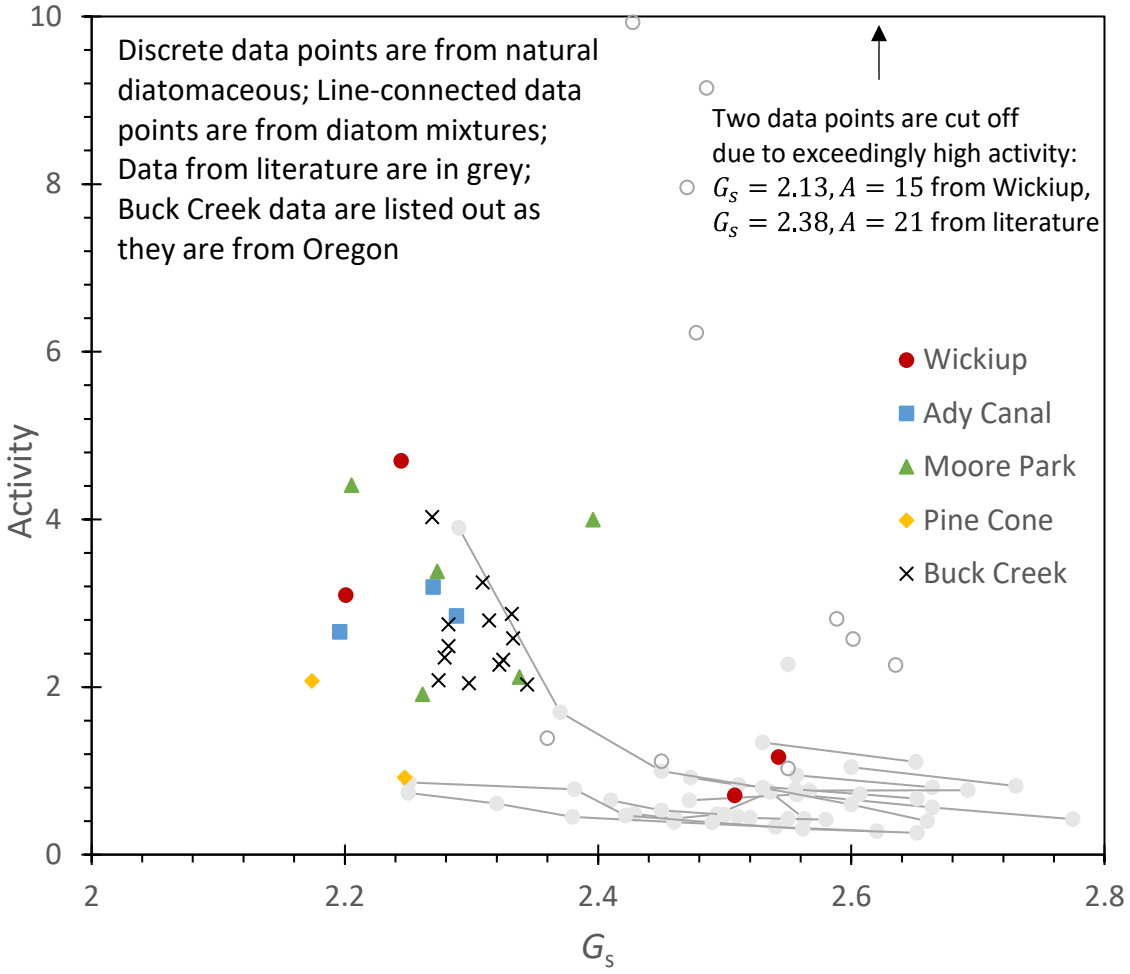

Figure 6.8: Relationship between activity and G_s collectively from this study and literature

6.3 CORRELATING MECHANICAL PROPERTIES WITH PHYSICAL PROPERTIES

In section 6.2, different physical properties (LL, PL, PI, SSA, and activity) were correlated to specific gravity because it is a direct proxy for diatom content. As seen above, amongst those physical properties, LL is most closely related to specific gravity and the fall cone method has been proved to be the correct measurement of LL. Therefore, LL will be mainly used to correlate to mechanical properties of diatomaceous soil.

6.3.1 Liquid Limit and Compressibility

As is known (e.g., Shiwakoti et al., 2002), the high compressibility of diatomaceous soil is a result of high porosity from the diatom particles. There should be a connection between the compressibility and diatom content (or G_s and LL). There is some literature data on the relation between LL and compressibility, however, these studies used diatom mixtures where compressibility was measured on reconstituted specimens. So far, only Caicedo et al. (2018) explicitly reported an empirical correlation between LL and C_c on natural Bogotá clays, a type of

diatomaceous soil in Colombia. In this study, the relationship between LL and C_c is plotted in Figure 6.9, although C_c overall increases with LL as expected, a strong linear relationship is not seen for the whole dataset. However, a separation can be seen between the group of Wickiup and Ady Canal, and the group of Moore Park and Pine Cone.

In the upcoming section 6.4.1, we classify diatomaceous soils of different layers into soft, stiff and mudstone in terms of their SPT and CPT resistance. The soft and stiff diatomaceous soils are only assigned to Wickiup and Ady Canal sites, while the mudstone diatomaceous soil is only assigned to Moore Park and Pine Cone sites. The separation between the two groups indicates that diatomaceous soils of different stiffnesses have different compressive behaviors. Linear empirical correlations were drawn for the two diatomaceous soil categories separately (Equation (6-5) and (6-6)). While the R^2 values are not very high suggesting potential limitations in the predictive capacity of the equations, they effectively elucidate underlying data trends, making them valuable for evaluating behavioral trajectories in the dataset.

$$\boldsymbol{C_c = 0.014\,LL + 0.491 \text{ at W and AC}} \tag{6-5}$$

$$\boldsymbol{C_c = 0.009\,LL + 0.133 \text{ at MP and PC}} \tag{6-6}$$

Although Caicedo et al. (2018) described the Bogotá clays as lacustrine clay, and in Chapter 2, we classified them as soft-state diatomaceous soil, their C_c vs. LL correlation is close in line with the mudstone (from Moore Park and Pine Cone) diatomaceous soil from this project. Scattered data from other natural diatomaceous soils are also plotted in Figure 6.9 based on their origins. It is hard to see any trend on the natural diatomaceous soils from literature. The diatomaceous soil from Asia (circle symbols in Figure 6.9) have a relatively narrow range of LL (around 100) but higher range of C_c (1.2 to 3). The results of Mexico City clay are spreading far beyond C_c equal to 8, and there is no simple correlation between C_c and LL for Mexico City clay. In reality, $C_c/(e_0+1)$ practically controls the ground settlement rather than C_c alone. So, the relationship between $C_c/(e_0+1)$ and LL are also plotted in Figure 6.10. For diatomaceous soil from this project, the trends on C_c vs. LL and $C_c/(e_0+1)$ vs. LL resemble each other, which means that soil with higher C_c also tends to have higher e_0. However, for Mexico City clay, their $C_c/(e_0+1)$ are well below 0.8, which means that the settlement of Mexico City clay is not necessarily higher than other diatomaceous soil despite their exceedingly high C_c. Comparing diatomaceous soil from Asia and Wickiup and Ady Canal from this study, Asian diatomaceous soils tend to have higher $C_c/(e_0+1)$ but lower C_c meaning that the settlement would be more significant for Asian diatomaceous soils.

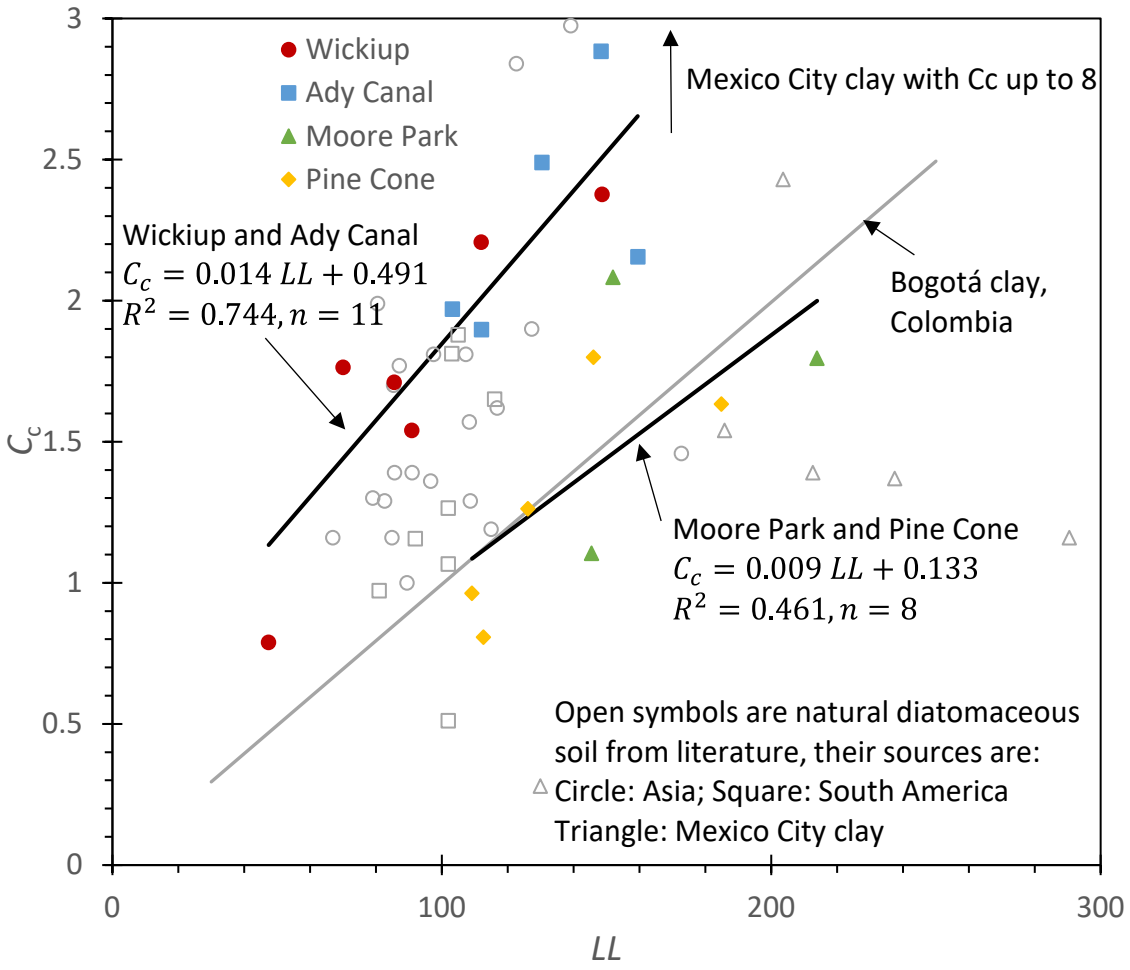

Figure 6.9: Relationship between C_c and LL collectively from this study and literature (note that data from Wickiup and Ady Canal are fitted together, while Pine Cone and Moore Park are fitted together)

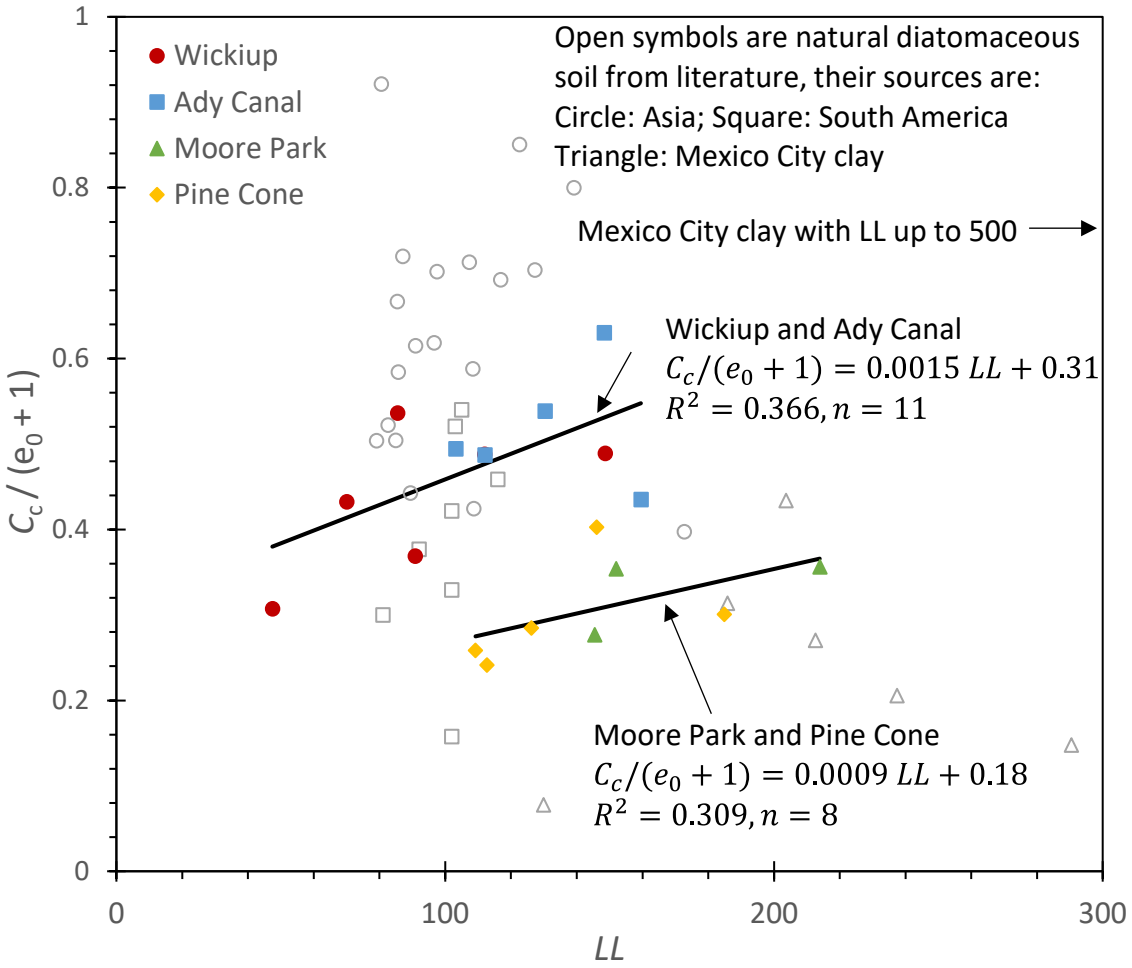

Figure 6.10: Relationship between $C_c/(e_0+1)$ and LL collectively from this study and literature (note that data from Wickiup and Ady Canal are fitted together, while Pine Cone and Moore Park are fitted together)

The results of C_r vs. LL are plotted in Figure 6.11, unlike C_c vs. LL, results of C_r vs. LL from different sites tend to mingle together, therefore, a single empirical correlation between C_r and LL for all specimens is shown in Equation (6-7). Much less data from literature are reported and they tend to scatter except for Bogotá clays where an empirical correlation is drawn by Caicedo et al. (2018).

$$C_r = 0.001\ LL + 0.027 \quad \textbf{(6-7)}$$

In summary, despite the intuition that compressibility of diatomaceous soil is expected to have a correlation with LL (or G_s and diatom content), such relationship has rarely been reported in the literature for natural diatomaceous soils except for Caicedo et al. (2018) (Bogotá, Colombia). For further assessment, C_c and LL were extracted from the literature to look for any correlations, however, results of Mexico City clay tend to scatter widely in the region of $100 < LL < 500, 0.5 < C_c < 8$, and results of Asian diatomaceous soils tend to have a narrow range of LL

(centered around 100) but larger span of C_c (0.5 to 3). Results from this study show a promising correlation between C_c and LL dependent on the type of diatomaceous soil (soft or mudstone).

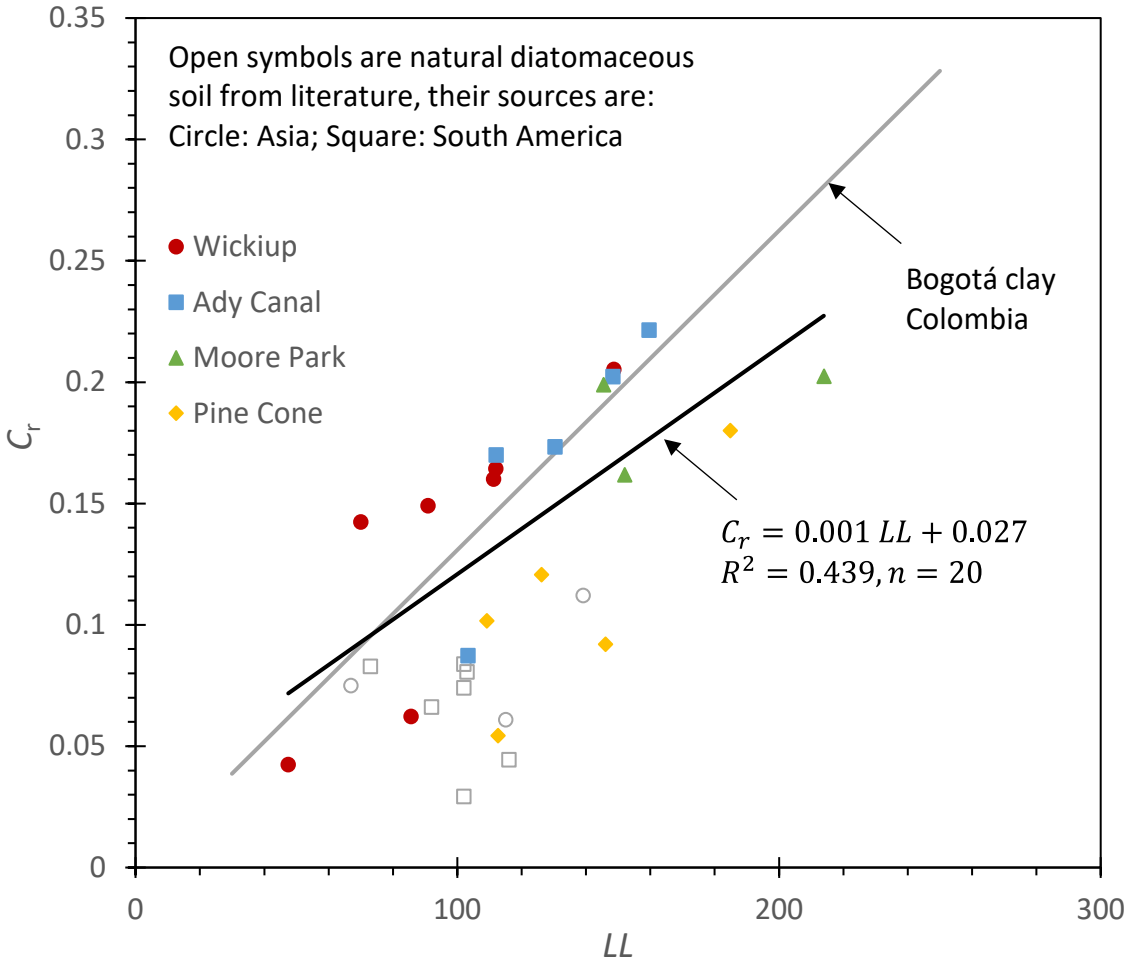

Figure 6.11: Relationship between C_r and LL collectively from this study and literature (note that data from this study are all fitted together)

The ratio of C_r to C_c is important in critical state soil mechanics (Schofield and Wroth, 1968; Wroth and Wood, 1978) as it implies a material constant $\Lambda = 1 - C_r/C_c$ which is used to relate soil compressive behaviors to shear strength. C_r/C_c is usually reported between 0.1 to 0.2 for clays. Figure 6.12 plots the relationship between C_r and C_c. There is some variation of C_r/C_c (from 0.036 to 0.18). A linear correlation between C_r and C_c for this study is presented in Equation (6-8) and Figure 6.12. Literature data from other diatomaceous soils are plotted in the same figure. Caicedo et al. (2018) observed a ratio of 0.132 between C_r and C_c for Bogotá clays, whereas diatomaceous soil from other sources have a ratio of 0.03 – 0.08 between C_r and C_c.

$$\boldsymbol{C_r = 0.081\ C_c} \tag{6-8}$$

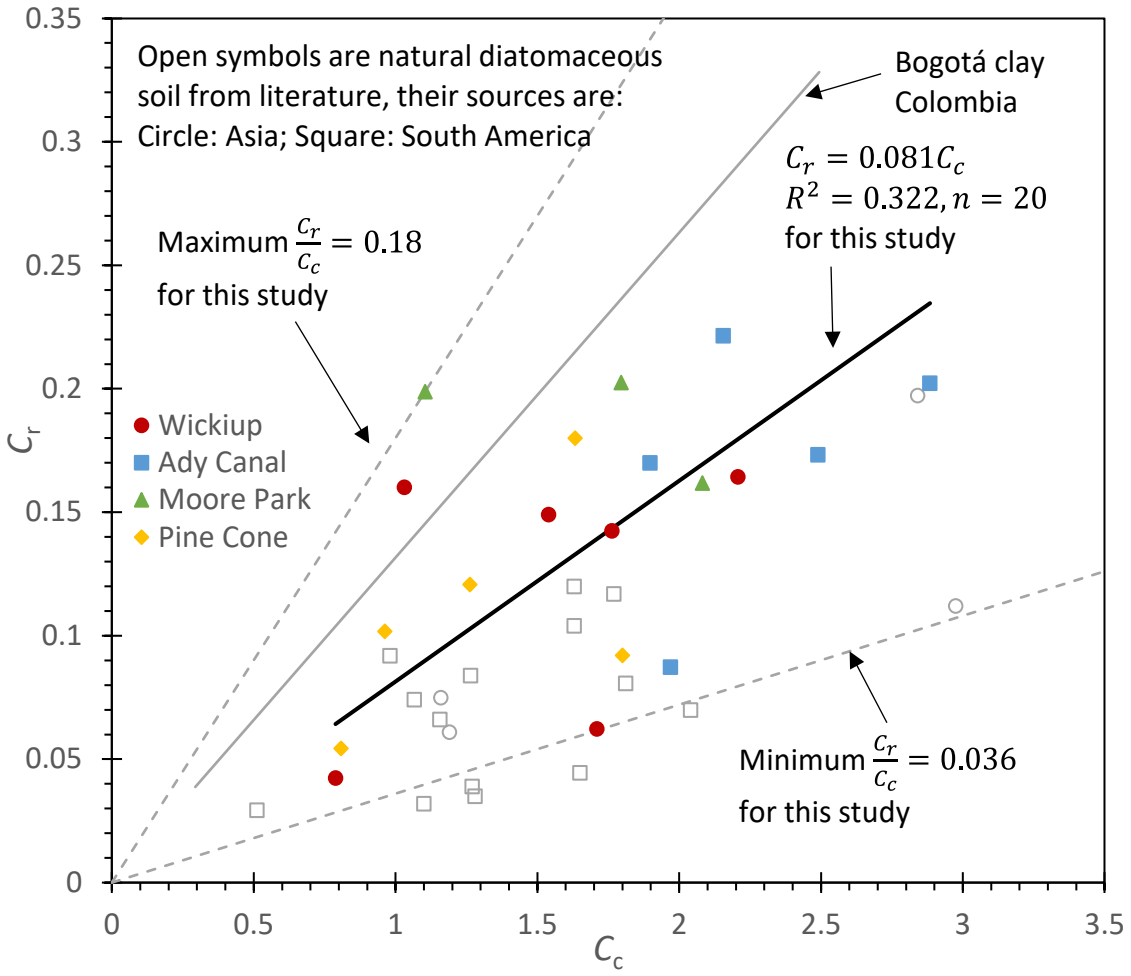

Figure 6.12: Relationship between C_r and C_c collectively from this study and literature

6.3.2 Liquid Limit and Friction Angle

Friction angle (ϕ') is widely correlated to PI on fine-grained soils (e.g., Bjerrum and Simons 1960; Ladd et al. 1977) and ϕ' generally decreases with PI for regular clays. Correlations between consistency limits and friction angle (ϕ') for diatomaceous soils are rarely reported. Caicedo et al. (2018) introduced an empirical correlation between ϕ' and LL for Bogotá clays with equation $\phi'_{cs} = 18.5 + 0.112\ LL$. Both LL and ϕ' extend a wide range: LL = 50 – 250, $\phi' = 24^\circ - 46.5^\circ$. Shiwakoti et al. (2002) reported ϕ' vs. PI for diatomaceous soil located in Japan where PI = 25 – 120, $\phi' = 22^\circ - 40^\circ$. Both references show that ϕ' of natural diatomaceous soil increases with consistency limits, contradictory to regular fine-grained soils. However, it is sensible for diatomaceous soils because higher consistency limits indicate higher diatom content. Diatom particles are actually major contributions to shear resistance owing to the surface roughness (Shiwakoti et al., 2002; Day, 1995; Wiemer et al., 2015). Figure 6.13 plots ϕ' vs. LL from this study and literature data. Data points from this study follow a consistent trend with only a few outliers. Although a best-fit line can be drawn for these data points (Equation (6-9)), it is not recommended to rely on the correlation to obtain ϕ' from LL. It is more appropriate to introduce an upper and a lower bound for ϕ' vs. LL, seen as Equation (6-10) and (6-11).

$$\textbf{Overall: } \phi' = 0.051\,LL + 29.65 \tag{6-9}$$

$$\textbf{Upper bound: } \phi' = 0.074\,LL + 29.73 \tag{6-10}$$

$$\textbf{Lower bound: } \phi' = 0.074\,LL + 22.29 \tag{6-11}$$

The friction angles calculated from DSS tests are relatively less varied, in the range of 32˚- 40˚. For triaxial tests, ϕ'_{cs} varies between 34˚- 48˚. Except for W1U10 and W1U12, results of other specimens are in the similar trend with the results from DSS tests. In most literature, friction angles are not directly reported but the stress-strain curves, therefore, we extracted p' and q from the stress-strain curves and calculated corresponding friction angles. It can be seen that the same diatomaceous soil (same LL) tends to have different ϕ' because of the different stress paths, OCR, confinements, etc.

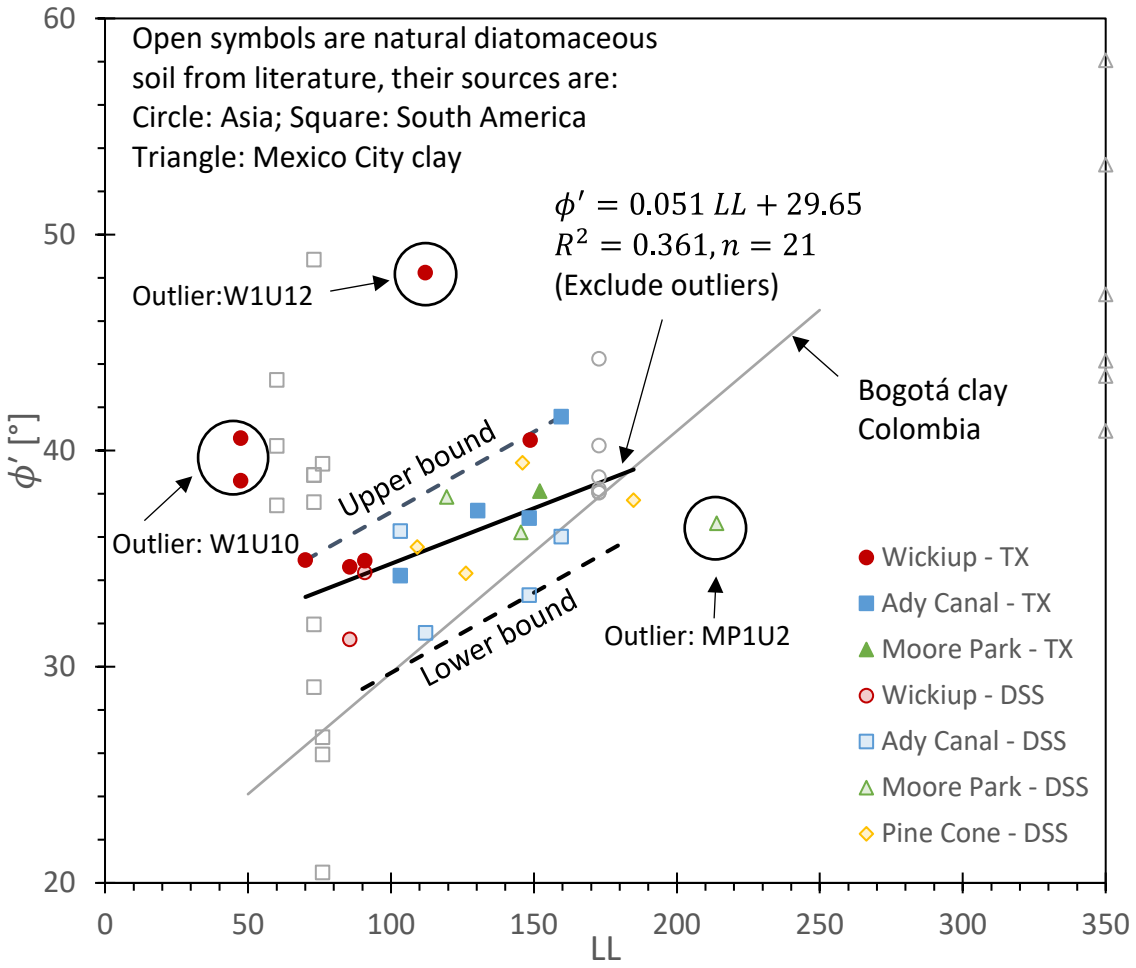

Figure 6.13: Relationship between ϕ'_{cs} and LL collectively from this study and literature

6.3.3 Stress History and Normalized Undrained Shear Strength

It is widely recognized that soil stress history will influence the normalized undrained shear strength (s_u/σ'_{vc}) of fine-grained soils (Ladd and Foott, 1974; Ladd et al., 1977). The log-log linear relationship between s_u/σ'_{vc} and OCR is widely adopted for fine-grained soils (i.e., $(s_u/\sigma'_{vc})_{oc} = S \cdot OCR^{\Lambda}$). Results from the triaxial tests and DSS tests are plotted together with literature data in Figure 6.14. Note that the literature data are all from triaxial tests of various diatomaceous sources. The best-fit line for all literature data returns $S = 0.425, \Lambda = 0.9$. Results of DSS tests from this study give $S = 0.325, \Lambda = 0.76$. This is not surprising because undrained shear strength from triaxial tests is higher than that from DSS tests (Ladd and Foott, 1974; Mayne, 1985). There is a large variation in normalized undrained shear strength for diatomaceous soils at certain OCRs. In Chapter 2, we reported that the upper and lower bounds of S for natural diatomaceous soils as 0.864 and 0.223, respectively. The triaxial results from this study, though at the lower boundary of the data pool, are consistent with results from other diatomaceous soils.

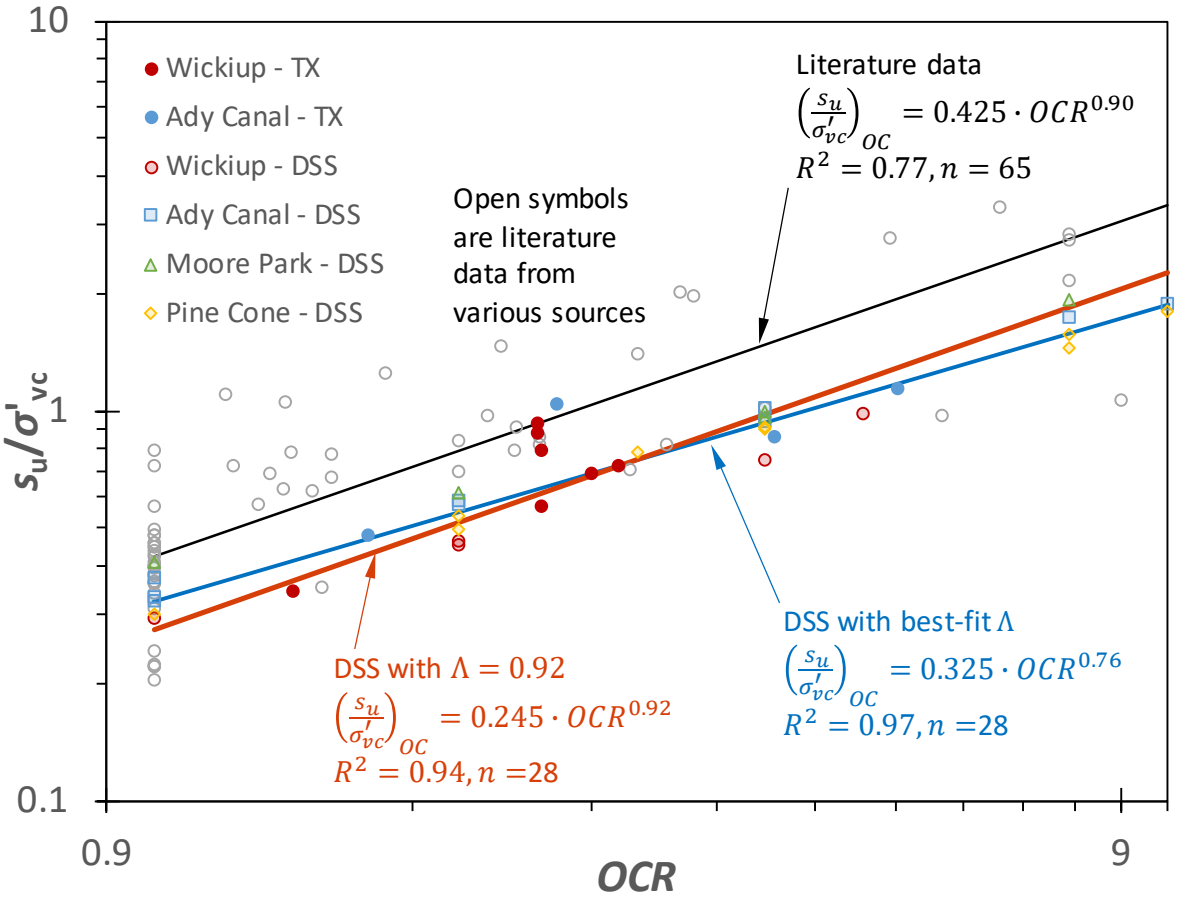

Figure 6.14: Relationship between s_u/σ'_{vc} and OCR from this study and literature data (TX = triaxial tests). The orange line represents the best fit when the plastic volumetric strain potential from Figure 6.12 is used.

6.3.4 Integrated Physical Properties and SPT Resistance

Although $(N_1)_{60}$ values are less accurate in predicting soil properties than CPT results, they are often more available to geotechnical design engineers as a matter of course. In this section, we seek a relationship between $(N_1)_{60}$ and combined physical properties. Generally speaking, LL by itself does not develop a universal trend with the normalized strength, however, $G_s w_n/LL$ can qualitatively relate to $(N_1)_{60}$, seen as Figure 6.15. $(N_1)_{60}$ has a generally decreasing trend with $G_s w_n/LL$. If individually looking how the three parameters (G_s, w_n, and LL) influence soil strength: lower G_s and higher LL indicate higher diatom content which is a positive effect on soil strength, whereas, w_n is a negative effect on soil strength. It is intuitive that soil strength will decrease with $G_s w_n/LL$, which is consistent with the trend shown in Figure 6.15.

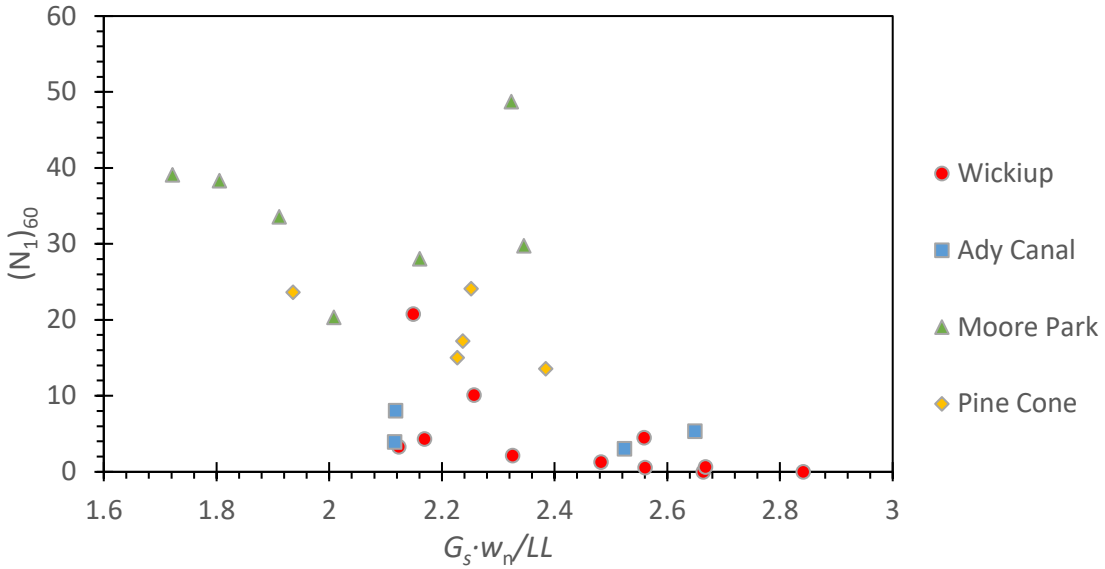

Figure 6.15: $(N_1)_{60}$ vs. $G_s w_n/LL$ on diatomaceous soil

6.4 SYNTHESIS ON *IN-SITU* RESULTS AND COMPARISONS WITH LAB RESULTS

6.4.1 Refined Soil Layers

In Chapter 3, preliminary soil layers purely based on the apparent textures/consistency/color of split spoon samples were identified, which provides a basic idea of subsurface appearance of diatomaceous soil deposits. After running a series of laboratory tests and combining with *in-situ* results, more refined soil layers can be identified. The focus is to separate non-diatomaceous soil layers from diatomaceous soil layers, where the SEM imaging plays an important role with additional knowledge on physical properties such as w_n, consistency limits, and G_s. Once diatomaceous soil layers are identified, the field characterization (mainly SPT and CPT results) is involved to categorize diatomaceous soil based on its SPT/CPT resistance.

Table 6.1 - Table 6.4 summarizes the refined soil layers for all four sites. Unlike the other three sites where sand layers are the only non-diatomaceous soil layers if any, Wickiup Junction has a thick layer of non-diatomaceous clay layer (15 m thick) which is not possible to verify the soil type visually. The *in-situ* test results of the clay layer also do not differ distinctly from regular soft diatomaceous soil, only after running SEM imaging together with physical characterization was the layer identified as a non-diatomaceous clay layer. Based on the $(N_1)_{60}$ and q_t values, the diatomaceous soils are divided into soft, stiff, and mudstone diatomaceous three categories. The soft and stiff diatomaceous layers are only assigned to Wickiup and Ady Canal, whereas the mudstone diatomaceous layer is only assigned to Moore Park and Pine Cone. Soft diatomaceous layers have the lowest SPT/CPT resistance, whereas the mudstone diatomaceous layers have the highest. The stiff diatomaceous layers have intermediate resistance. In Chapter 2, we introduced that diatomaceous soils from the literature were referred to as soft (or lacustrine, alluvial, colluvial) or mudstone (or soft rock) diatomaceous soils. There is no strict definition in terms of soft and mudstone diatomaceous soils. Generally, mudstone diatomaceous soils show higher resistance and higher apparent OCR (up to 25 to 53) (Maekawa et al., 1992; Hong et al., 2006).

Table 6.1: Refined soil layers in Wickiup Junction

Layer identifier	Depth [m]	Specimen range	General description
Upper sand	0 – 14.94	W1N1–W1N5	–
Non-diatomaceous clay	14.94 – 29.79	W1N6–W1N12 W1U1–W1U6	$w_n = 32-56$ $LL = 27-49$ $PL = 18-35$ $G_s = 2.67-2.81$ $(N_1)_{60} = 0-0.83$ $q_t = 1-2MPa$
Upper Soft diatomaceous	29.79 – 47.62	W1N13–W1N18 W1U7–W1U10	$w_n = 55-206$ $LL = 51-172$ $PL = 29-87$ $G_s = 2.23-2.54$ $(N_1)_{60} = 0-1.2$ $q_t = 1.2-2.6MPa$
Lower sand	47.62 – 50.67	W1N19, W1U11	–
Lower soft diatomaceous	50.67 – 63.86	W1N20–W1N24 W1U12–W1U14	$w_n = 116-171$ $LL = 111-161$ $PL = 68-93$ $G_s = 2.19-2.25$ $(N_1)_{60} = 0.5-4.5$ $q_t = 2.4-3.1MPa$
Stiff diatomaceous	63.68 – 67.17	W1N25–W1N26	$w_n = 135-211$ $LL = 148-200$ $PL = 67-69$ $G_s = 2.13-2.2$ $(N_1)_{60} = 10-21$
Gravels, cobbles	67.17 – 77.37	W1N27–W1N30	–

Table 6.2: Refined soil layers in Ady Canal

Layer identifier	Depth [m]	Specimen range	General description
Upper sand	0 – 9.14	AC1N1–AC1N3 AC1U1–AC1U2	–
Soft diatomaceous	9.14 – 12.19	AC1N4–AC1N5a AC1U3	$w_n = 102-173$ $LL \approx 99$ $PL \approx 50$ $(N_1)_{60} = 1-2.9$ $q_t = 0.76-2.1MPa$
Lower sand	12.19 – 15.70	AC1N5b–AC1N6	–
Upper stiff diatomaceous	15.70 – 17.91	AC1N7	$w_n \approx 160$ $q_t = 1.3-17.8MPa$
Silty sand	17.91–19.66	AC1N8, AC1U4	$w_n \approx 37$ $LL \approx 35$ $PL \approx 30$ $G_s = 2.51$ $(N_1)_{60} = 58$ $q_t = 17-43MPa$
Lower stiff diatomaceous	19.66 – 31.7	AC1N9–AC1N13 AC1U5–AC1U8	$w_n = 126-121$ $LL = 119-166$ $PL = 54-96$ $G_s = 2.20-2.31$ $(N_1)_{60} = 3-11$

Table 6.3: Refined soil layers in Pine Cone Drive

Layer identifier	Depth [m]	Specimen range	General description
Mudstone diatomaceous	0 – 32.77	PC1N1 –PC1N11 PC1U1–PC1U10	$w_n = 83-186$ $LL = 108-185$ $PL = 49-109$ $(N_1)_{60} = 12-36$ $q_t = 1.2-14.3MPa$ refusal with $q_t = 48MPa$

Table 6.4: Refined soil layers in Moore Park

Layer identifier	Depth [m]	Specimen range	Description
Coarse sands	0 – 8	MP1N1–MP1N2 MP1U1–MP1U2 top half	–
Mudstone diatomaceous	8 – 30.94	MP1N3–MP1N14 MP1U2 bottom half–MP1U11	$w_n = 95–208$ $LL = 112–214$ $PL = 53–115$ $(N_1)_{60} = 19–49$ $q_t = 5.4–21.8MPa$ refusal with $q_t = 39MPa$

Table 6.5 summarized $(N_1)_{60}$ and q_t values of different diatomaceous soil layers. The layers of different diatomaceous soils are usually separated by sand layers or abrupt change of SPT/CPT resistance.

Table 6.5: $(N_1)_{60}$ and q_t value range of different diatomaceous soil layers

Layer identifier	$(N_1)_{60}$	q_t [MPa]
Soft diatomaceous	0–4.5	0.76–3.1
Stiff diatomaceous	3–21	1.3–17.8
Mudstone diatomaceous	12–49	1.2–21.8, refusal on 39 MPa for Moore Park, 48 MPa for Pine Cone

6.4.2 Soil Profiles with Refined Soil Stratification

Categorizing diatomaceous soil into soft, stiff, and mudstone is somewhat arbitrary in that there is not a strict definition to distinguish the stiffness of diatomaceous soil. In the literature, different words were used to describe diatomaceous soil. For example, "mudstone" and "soft rock" were used to refer to diatomaceous soil that has relatively high shear strength and stiffness (e.g., Iijima and Tada, 1981; Maekawa et al., 1992; Liao et al., 1998; Verdugo, 2008; Lee et al., 2011; Oka et al., 2011; Zhang et al., 2013; Ovalle and Arenaldi-Perisic, 2021), whereas, "soft clay", "ooze", "lacustrine clay", and "alluvial or colluvial clay" were used to describe diatomaceous soil that has relatively low shear strength and stiffness (e.g., Tanaka et al., 2001; Díaz-Rodríguez, 2003; Vera-Grunauer, 2014; Wiemer et al., 2015; Caicedo et al., 2018).

A detailed discussion and comparison of the two categories was conducted in Chapter 2. It is worth noting that despite diatomaceous soil being both soft-clay-like and mudstone-like, the two soil states were rarely mentioned together in the same reference (e.g. Jardine et al., 1998).

In this project, stiff diatomaceous soil is used to describe a transitional state between soft and mudstone diatomaceous soils. Wickiup and Ady Canal diatomaceous soils are only classified as soft or stiff diatomaceous, whereas Pine Cone and Moore Park diatomaceous soils are only classified as mudstone diatomaceous. Figure 6.16 – Figure 6.19 replot CPTu test results as well

as basic index properties profiles (G_s, w_n, LL, PL) with identified soil layers. Only Wickiup has a non-diatomaceous clay layer whereas the non-diatomaceous layers in other sites are all sands or silty sands. There is little distinction between the non-diatomaceous clay layer and diatomaceous layers in Wickiup in terms of CPTu profiles or soil behavioral charts (see 6.4.3). Therefore, one must conduct necessary laboratory tests to identify diatomaceous soils.

Profiles of q_t and $(N_1)_{60}$ are plotted in the same subplot in order to compare the resistance from CPT and SPT results. For Wickiup and Ady Canal (identified as soft/stiff diatomaceous soil), q_t and $(N_1)_{60}$ synchronize in a way that the coefficient between the two parameters is about 1 (q_t in MPa), whereas, for Moore Park (identified as mudstone diatomaceous soil), q_t and $(N_1)_{60}$ separate apart. Except for Wickiup where CPT advancement stopped near the end of lower soft diatomaceous soil, in all other three sites refusal was encountered where CPT stopped advancing. In Wickiup, G_s gradually decreases with depth whereas q_t gradually increases with depth, which means that the resistance increases with diatom content. The mudstone diatomaceous soil in Pine Cone and Moore Park has slightly lower G_s but a lot higher q_t. Ady Canal has the most versatile soil profiles, however, CPT did not advance into the lower stiff diatomaceous layer.

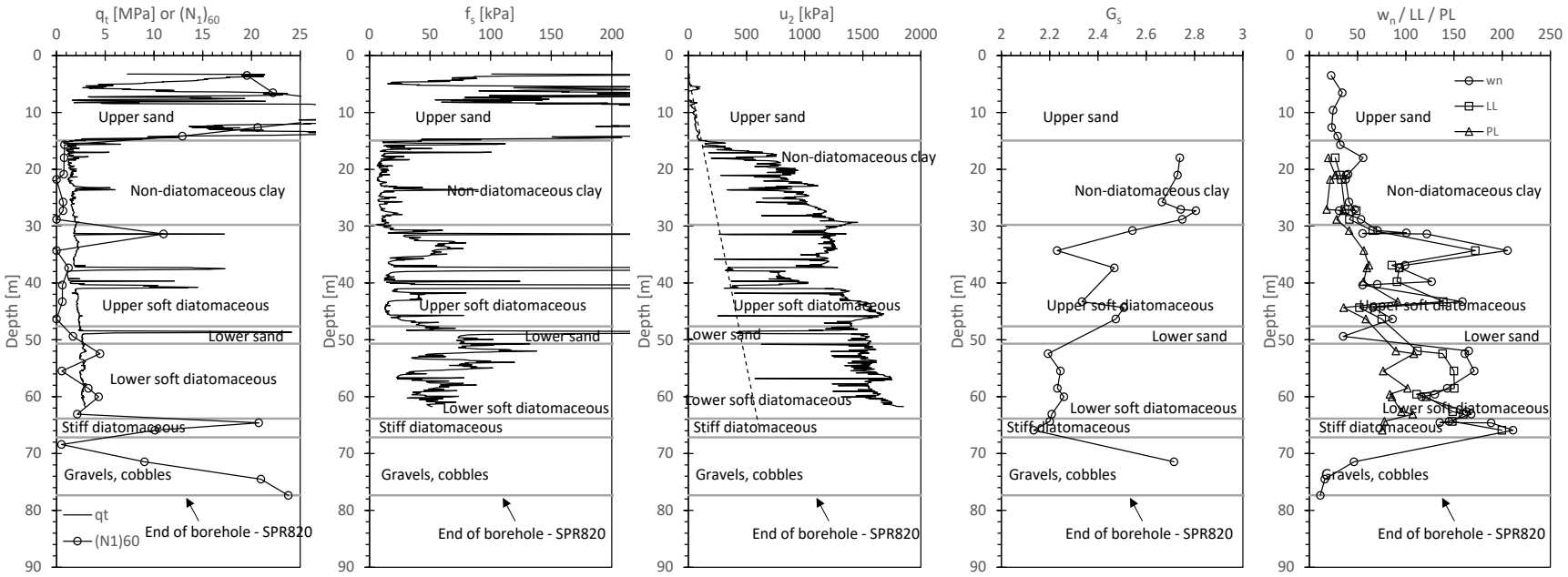

Figure 6.16: $q_t, (N_1)_{60}, f_s, u_2, G_s, w_n/LL/PL$ profiles at Wickiup

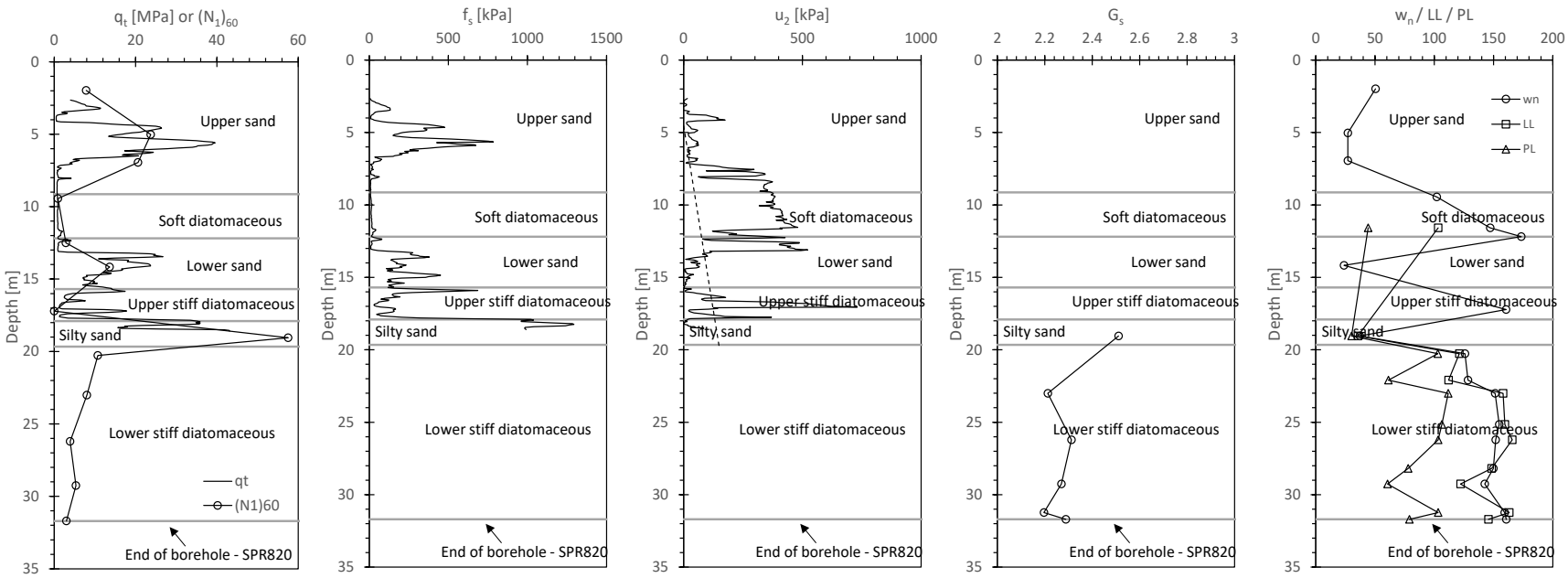

Figure 6.17: $q_t, (N_1)_{60}, f_s, u_2, G_s, w_n/LL/PL$ profiles at Ady Canal

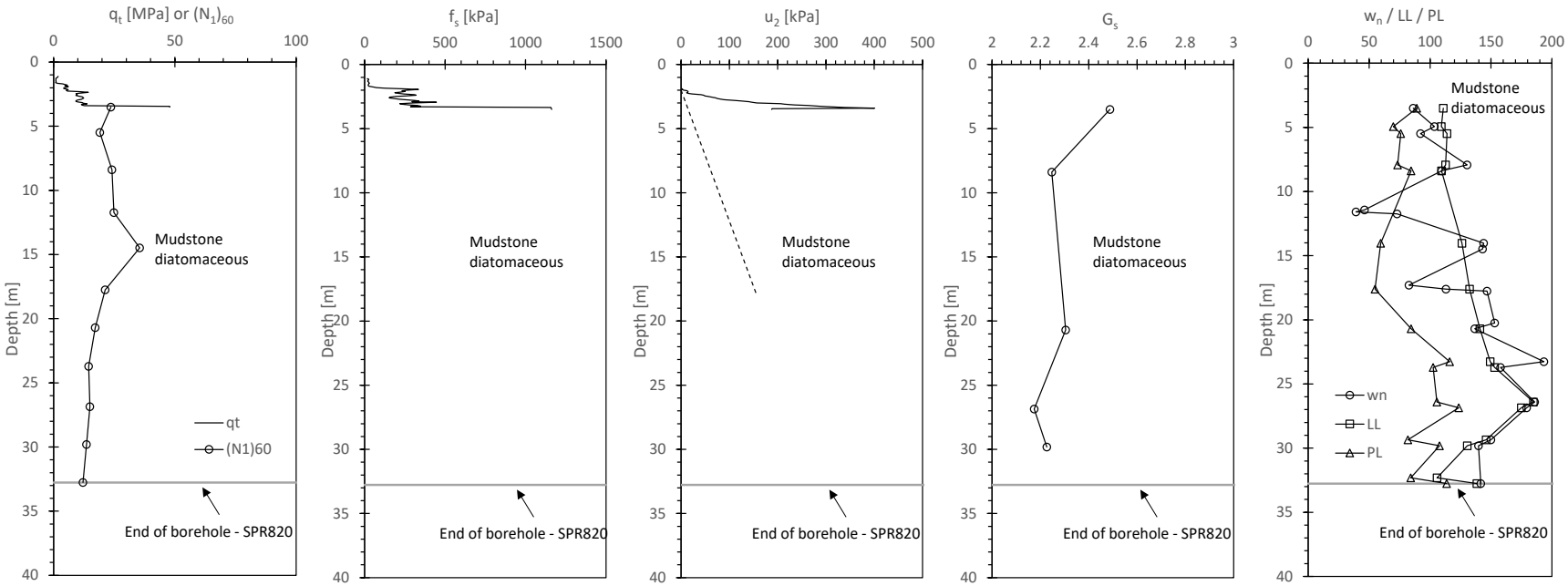

Figure 6.18: $q_t, (N_1)_{60}, f_s, u_2, G_s, w_n/LL/PL$ profiles at Pine Cone Drive

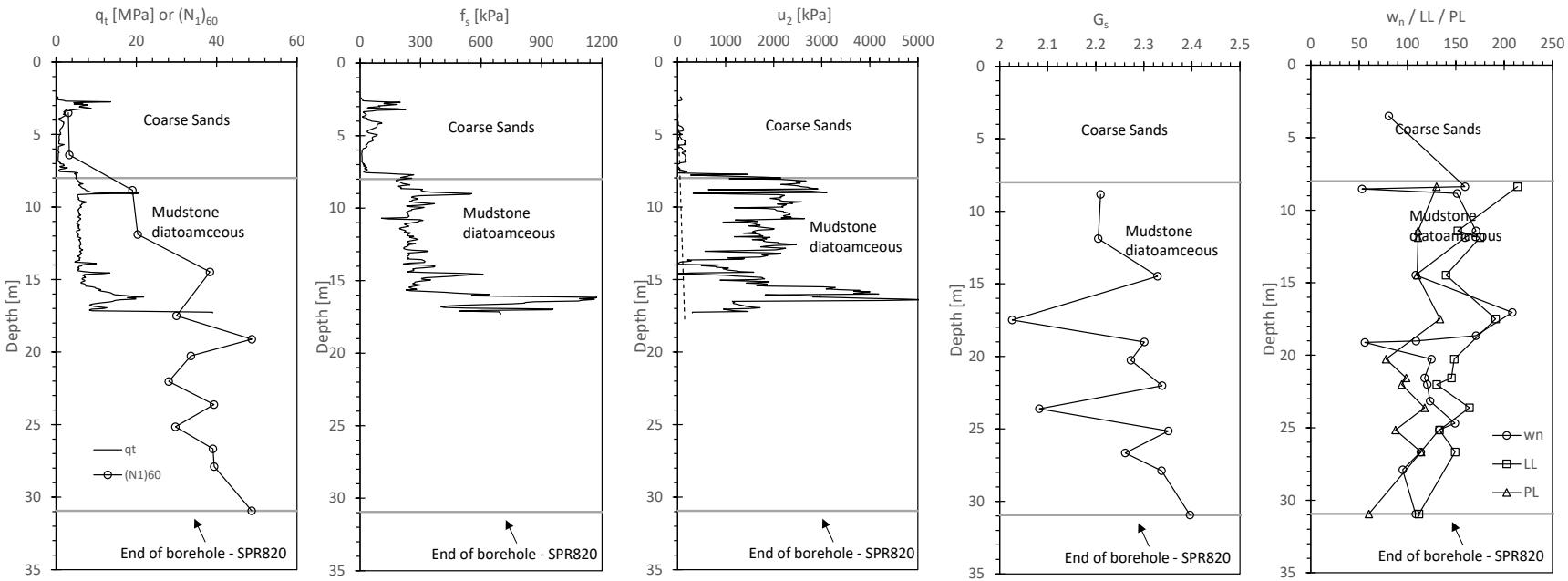

Figure 6.19: $q_t, (N_1)_{60}, f_s, u_2, G_s, w_n/LL/PL$ profiles at Moore Park

Table 6.6: Properties summary of different soil layers

Site	Layer classification	w_n	LL	PL	PI	G_s	$\gamma\ [kN/m^3]$	$(N_1)_{60}$	$q_t[MPa]$
Wickiup	Upper soft diatomaceous	66–205	66–172	36–87	30–122	2.23–2.54	11.8–14.5	0–1.2	2–2.3
	Lower soft diatomaceous	116–171	111–160	68–93	31–82	2.19–2.26	12.3–13.2	0.5–4.5	2.36–2.8
	Stiff diatomaceous	135–211	148–200	67–69	79–133	2.13–2.20	11.1–11.7	10–21	/
Ady Canal	Soft diatomaceous	102–173	103	50	53	–	–	0.9–2.9	0.88–2
	Upper stiff diatomaceous	160	–	–	–	–	–	–	1.8–15
	Lower stiff diatomaceous	126–160	112–166	53–107	34–77	2.2–2.31	12.2–12.6	3–10.7	/
Pine Cone	Mudstone	82–193	109–185	49–109	37–84	2.17–2.49	11.8–14.2	12–35.5	1.8–12(47.8)
Moore Park	Mudstone	95–208	112–214	53–115	45–99	2.03–2.4	12.1–13.5	19–49	6.2–21.8(39)

6.4.3 Soil Classification Chart

Most soil classification systems are based on grain size and plasticity (e.g., Unified Soil Classification System, USCS) which are measured remolded soils, thus, the link to soil *in-situ* behavior can be weak. Efforts have been made to utilize CPTu results to classify soil materials as the test itself has many advantages in investigating soils for being a reliable, cost-effective, rapid, and continuous tool. In Chapter 3, we introduced a most common CPTu-based soil classification method proposed by Robertson (1990, 2009). The application of this approach is adopted in all four sites and the classification charts are plotted in Figure 6.20 - Figure 6.23 (subplot (a) and (b)). Note that Robertson (2016) updated $Q_t - F_N$ to $Q_{tn} - F_N$, where the calculation for Q_t and Q_{tn} are introduced in Chapter 3, but in most cases of fine-grained soils, $Q_t \cong Q_{tn}$. Robertson (2016) introduced contours between contractive and dilative soils (the red lines in subplot (a)) on top of $Q_{tn} - F_N$ chart.

We can see that soils from different layers are located in different zones (i.e., different classification types). In Section 6.4.1, we refined the soil layers mainly based on the soil type (diatomaceous or non-diatomaceous) and the *in-situ* penetration resistance ($(N_1)_{60}$ and q_t), and the diatomaceous soils are classified into soft, stiff, and mudstone types. Looking at the $Q_{tn} - F_N$ chart, the soft diatomaceous soil is mainly located in zone 3 (or zone CC), i.e., clays to silty clay (or clay-like contractive), in contrast, the mudstone diatomaceous soil is located at the boundary between Zones 4, 5, and 6 and Zones 8 and 9, ranging from sandy type to very stiff fine grained type (or dilative zone). That the mudstone diatomaceous soil is classified as sandy type or transitional type from the $Q_{tn} - F_N$ chart indicates that it can be highly overconsolidated fine grained soils (Robertson, 2009), and as a matter of fact, that is the feature of mudstone diatomaceous soil, i.e., showing exceedingly high apparent OCR (e.g., Maekawa et al., 1991; Hong et al., 2006; Wang et al., 2021). Although the CPTu soundings only advanced into the upper stiff diatomaceous layer in Ady Canal, we can see that the stiff diatomaceous soil in Ady Canal acts as intermediate behavior between the soft and mudstone diatomaceous soils. The $Q_t - B_q$ chart is also used. The classification from both charts ($Q_{tn} - F_N$ and $Q_t - B_q$) is mainly in agreement with one another for Wickiup and Ady Canal, but the mudstone diatomaceous soil from Pine Cone and Moore Park shows somewhat differences, for example, mudstone diatomaceous soil from Pine Cone extends to zone 7 (i.e., gravelly sand to sand) in $Q_t - B_q$ chart which is not the case in $Q_{tn} - F_N$ chart. Robertson (1990, 2009) mentioned that soils may fall in different zones at these two charts, generally, $Q_t - B_q$ chart should be used with judgement in interpreting the results.

Robertson (2016) stated that identifying soils with microstructure is important as the effect largely influences the soil *in-situ* behavior. The author has modified a parameter to identify the possible microstructure of soils, shown as Equation (6-12). For most young and uncemented soils, K_G^* is closed to 100 ($K_G^* < 330$), whereas soils with $K_G^* > 330$ tend to have significant microstructure, and the higher K_G^*, the higher cementation. For soils with high cementation or microstructure, the traditional CPT-based empirical correlations may be less reliable. Like all other soil classification approaches, soils located around boundaries between two types should be looked at individually and judgement is needed in classifying the soils. That is, the boundary of uncemented and cemented soils at $K_G^* = 330$ can be somewhat arbitrary since the change of soil behavior is often gradual.

$$K_G^* = \frac{(I_G)}{(Q_{tn})}^{0.75} \tag{6-12}$$

$$I_G = \frac{G_0}{q_n} \tag{6-13}$$

$$G_0 = \rho(V_s)^2 \tag{6-14}$$

$$q_n = q_t - \sigma_v \tag{6-15}$$

where:
K_G^* = modified normalized small-strain rigidity index;
I_G = small-strain strain rigidity index;
G_0 = small-strain stiffness;
ρ = soil mas density;
V_s = shear wave velocity; and
q_n = net cone resistance.

The subplots (c) in Figure 6.20 - Figure 6.23 show the degree of microstructure of diatomaceous soils at different sites. The soft and stiff diatomaceous soils from Wickiup and Ady Canal are well below $K_G^* = 330$ line, indicating an uncemented, young soils whereas mudstone diatomaceous soils have K_G^* around or above 330. This is consistent with the observation that mudstone diatomaceous soil always has OCR that is high and even higher than the geologic justification (Wang et al., 2021). Many researchers have attributed this phenomenon to diagenesis, which is associated with cementation and ageing (Iijima and Tada, 1981; Perisic et al., 2019; Ovalle and Arenaldi-Perisic, 2021).

Schneider et al. (2008) proposed $Q_t - \Delta u_2/\sigma'_{v0}$ chart (subplot(d)) as an improvement to $Q_t - B_q$ chart. The chart shows different paths for the increase of coefficient of consolidation (i.e., c_v) and OCR. From the Schneider et al. (2008) chart, we can still see the distinction between the soft and mudstone diatomaceous soil, where the mudstone diatomaceous extends in line with "increasing OCR".

Table 6.7: Soil behavior type (after Robertson 1990, 2009, 2016)

NO.	Soil behavior type
1	Sensitive fine-grained
2	Organic soils – peat
3	Clays – silty clay to clay
4	Silt mixture – clayey silt to silty clay
5	Sand mixture – silty sand to sandy silt
6	Sands – clean sand to silty sand
7	Gravelly sand to dense sand
8	Very stiff sand to clayey sand
9	Very stiff fine-grained

Table 6.8: Soil behavior type -continued (after Robertson 2016)

Acronym	Soil behavior type
CCS	Clay-like – contractive – sensitive
CC	Clay-like – contractive
CD	Clay-like – dilative
TC	Transitional – contractive
TD	Transitional – dilative
SC	Sand-like – contractive
SD	Sand-like – dilative

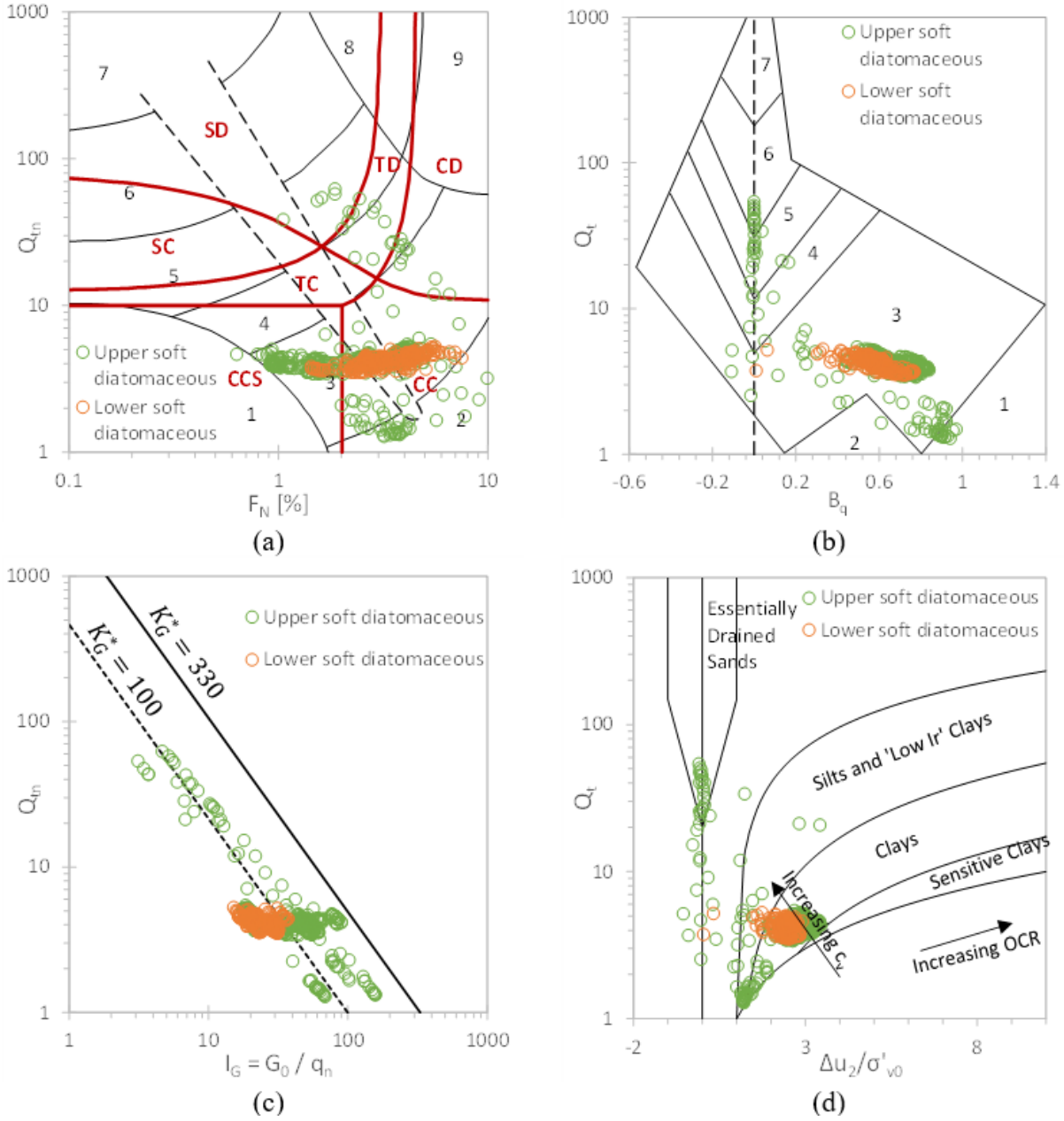

Figure 6.20: Soil behavior type classification chart based on normalized CPT data in Wickiup based on Robertson (2009, 2016) (chart (a), (b), (c)) and Schneider et al. (2008) (chart (d)) (soil behavior types referred to Table 3.3 and Table 6.8)

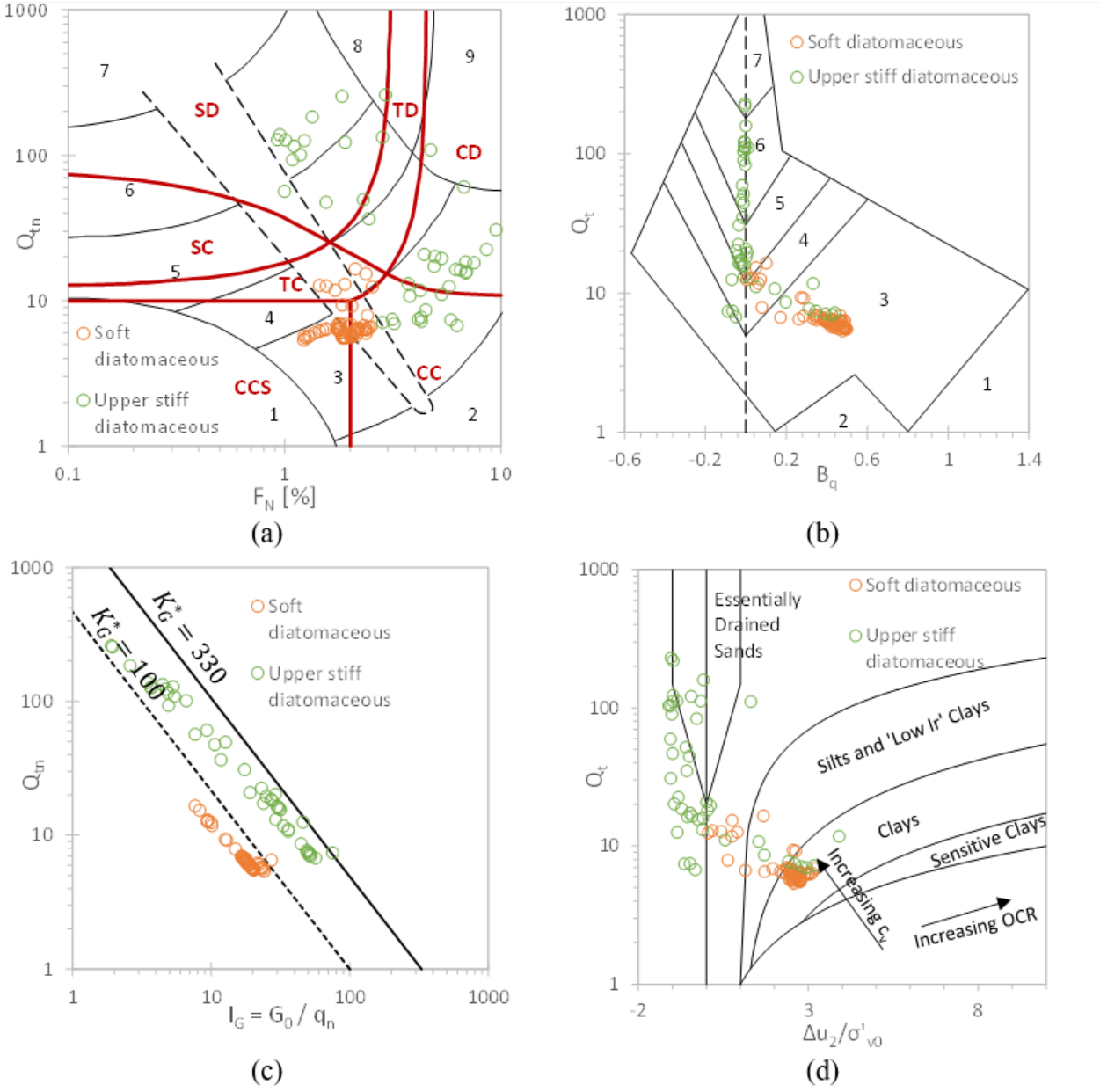

Figure 6.21: Soil behavior type classification chart based on normalized CPT data in Ady Canal based on Robertson (2009, 2016) (chart (a), (b), (c)) and Schneider et al. (2008) (chart (d)) (soil behavior types referred to Table 3.3 and Table 6.8)

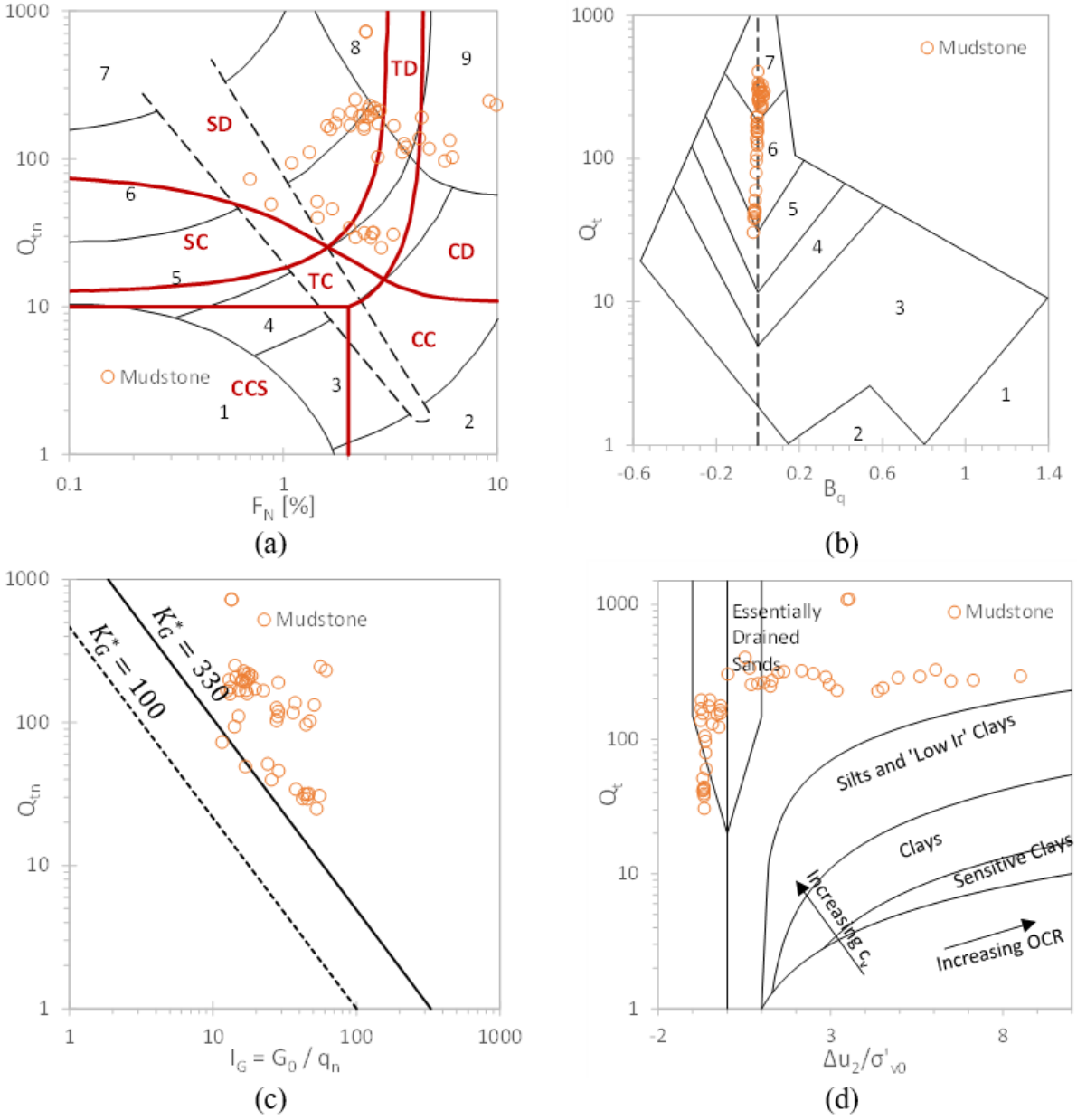

Figure 6.22: Soil behavior type classification chart based on normalized CPT data in Pine Cone based on Robertson (2009, 2016) (chart (a), (b), (c)) and Schneider et al. (2008) (chart (d)) (soil behavior types referred to Table 3.3 and Table 6.8)

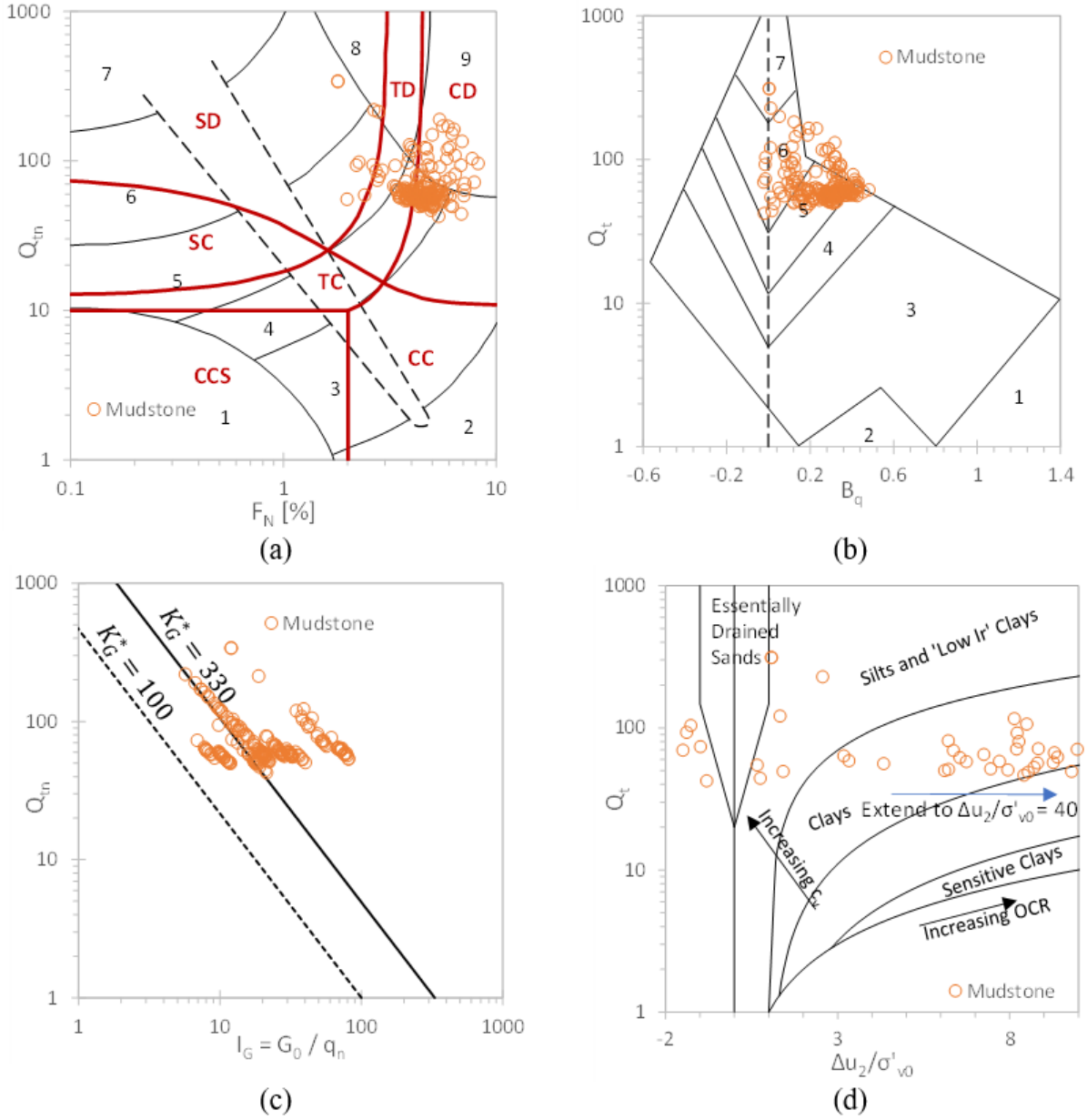

Figure 6.23: Soil behavior type classification chart based on normalized CPT data in Moore Park based on Robertson (2009, 2016) (chart (a), (b), (c)) and Schneider et al. (2008) (chart (d)) (soil behavior types referred to Table 3.3 and Table 6.8)

6.4.4 *In-situ* Correlations Compared with Lab Results

6.4.4.1 Unit weight

As introduced in previous chapters, diatomaceous soil tends to have lower specific gravity and lower unit weight. Therefore, it is important to accurately estimate the unit weight from CPTu results. A couple of empirical correlations are listed in Equation (6-16) – (6-21) proposed by Mayne (2007, 2014). Equation (6-16) is correlated to sleeve

friction (f_s) and specific gravity (G_s), Equation (6-17) and (6-18) are correlated to shear wave velocity (V_s), and Equation (6-19)- (6-21) are correlated to sleeve friction (f_s). Figure 6.24 and Figure 6.25 plot the profiles of unit weight at all four sites. Legend "Measured" refers to the tested unit weight based on the wax method (ASTM D 7263; *American Society for Testing and Materials (ASTM). 2021b.*), legend "Calculated" refers to unit weight calculated from G_s and w_n (assuming $S_r = 100\%$). Both can be referred to as true unit weight, note that they are connected by lines in the figures for better view, though they are discrete data points. Legend "Correlation" refers to the correlated unit weight from Equation (6-16), while legends of other correlations are omitted. Despite no overlaps between unit weight measurement (or calculation based on G_s) and CPTu correlations at Ady Canal and Pine Cone, the measured (or calculated) unit weight agrees well with the correlation from Equation (6-16), while all other correlations (Equation (6-17) – (6-21)) do not provide reasonable estimates for diatomaceous soils. Diatomaceous soils are unique in many ways, the most significant feature of the soil is that many traditional correlations amongst soil properties do not apply. Without knowing G_s, using Equations (6-17) – (6-21) to estimate the unit weight of diatomaceous soil may induce large errors. Therefore, in engineering practice, if a soil is suspected to be diatomaceous, it is important adopt Equation (6-16) to estimate the unit weight to ensure an accurate *in-situ* overburden stress.

$$\gamma_{sat}\left(\text{in}\,\frac{\text{kN}}{\text{m}^3}\right) = 2.6\log\left(f_s\ (\text{in kPa})\right) + 15G_s - 26.5 \tag{6-16}$$

$$\gamma_{total}\left(\text{in}\,\frac{\text{kN}}{\text{m}^3}\right) = 8.32\log\left(V_s\ \left(\text{in}\,\frac{\text{m}}{\text{s}}\right)\right) - 1.61\log\left(z\ (\text{in m})\right) \tag{6-17}$$

$$\gamma_{total}\left(\text{in}\,\frac{\text{kN}}{\text{m}^3}\right) = 7.83\log\left(V_s\ \left(\text{in}\,\frac{\text{m}}{\text{s}}\right)\right) - 0.125 \tag{6-18}$$

$$\gamma_{total}\left(\text{in}\,\frac{\text{kN}}{\text{m}^3}\right) = 26 - \frac{14}{1 + [0.5\log(f_s\ (\text{in kPa}) + 1)]^2} \tag{6-19}$$

$$\gamma_{total}\left(\text{in}\,\frac{\text{kN}}{\text{m}^3}\right) = 12 + 1.5\ln(f_s\ (\text{in kPa}) + 1) \tag{6-20}$$

$$\gamma_{total} = \gamma_{water}\left[1.22 + 0.345\log\left(\frac{100f_s}{p_{atm}} + 0.01\right)\right] \tag{6-21}$$

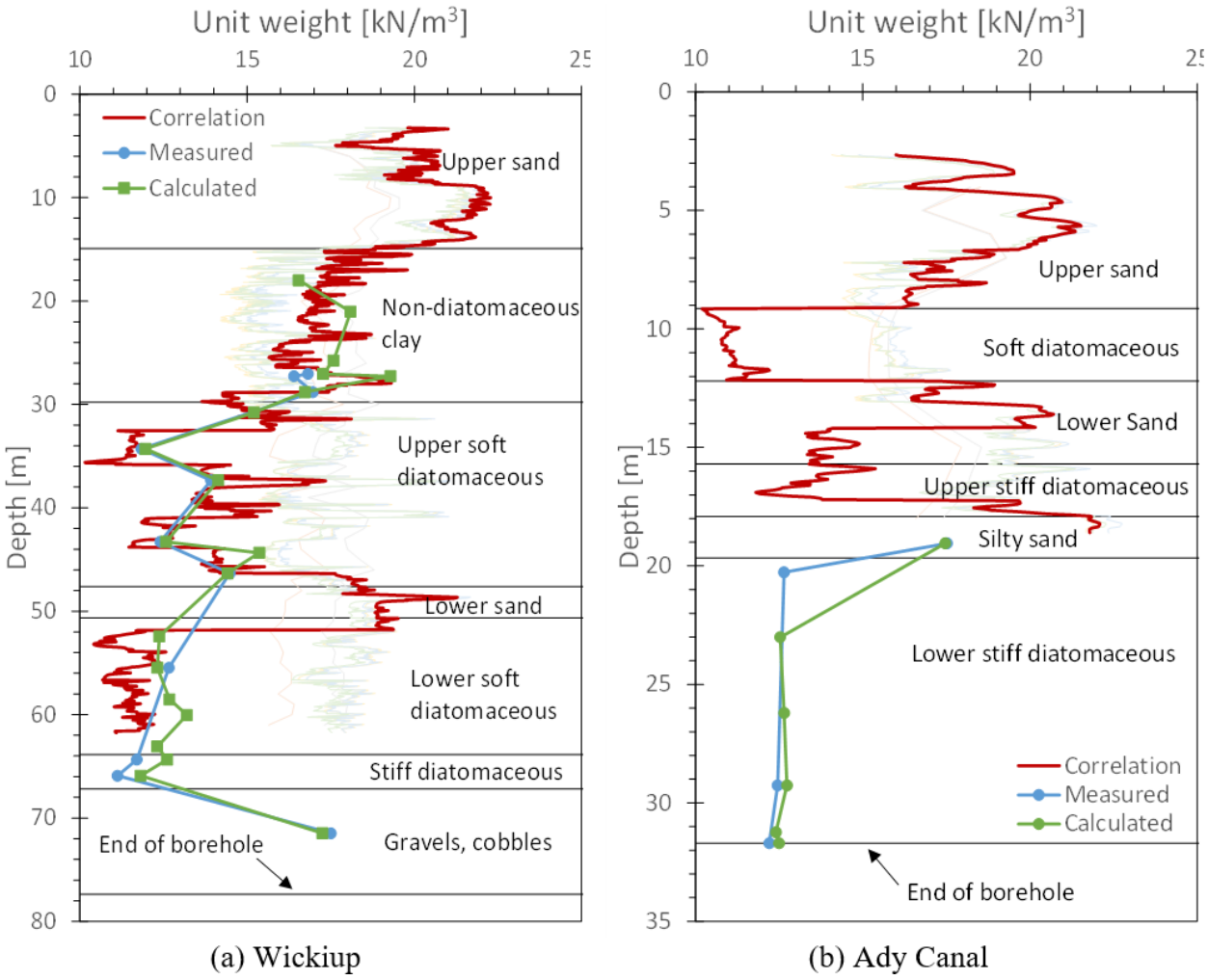

Figure 6.24: Comparisons of unit weight from CPTu correlations and lab results at Wickiup (a) and Ady Canal (b) (note that the measured and calculated are discrete data points)

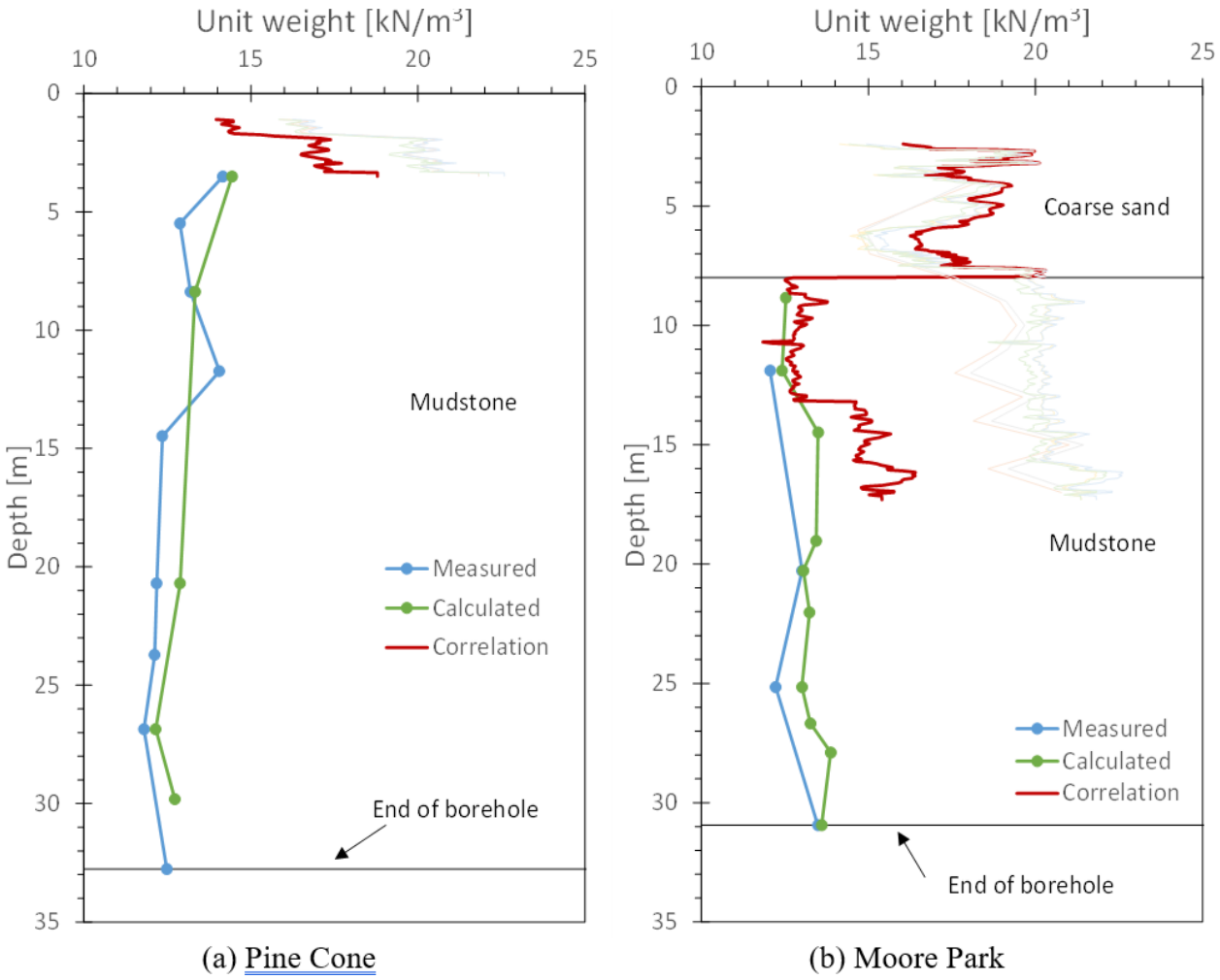

Figure 6.25: Comparisons of unit weight from CPTu correlations and lab results at Pine Cone (a) and Moore Park (b) (note that the measured and calculated are discrete data points)

6.4.4.2 Overconsolidation ratio

Mayne (1991) derived a hybrid analytical solution (Equation (5-4)) of preconsolidation stress (σ_p') from CPTu results by combining spherical cavity expansion theory and critical state soils mechanics (SCE-CSSM). Later, the form is reduced to first-order approximation with some empirical correction (Mayne, 2015; Agaiby and Mayne, 2019), shown as Equation (6-23). The comparisons of CPTu correlated OCR and OCR from laboratory tests are plotted in Figure 6.26. Due to very early refusal (3.5 m) of CPTu sounding in Pine Cone, its OCR profile is omitted. Generally, Equation (6-23) provides a more consistent correlation across all three sites. In Wickiup, both correlations provide reasonable estimates, but Equation (5-4) tends to spike at OCR up to 30. The distinction between the two correlations is more obvious for Ady Canal and Moore Park. For example, OCR predicted by Equation (5-4) ranges between 40 to 200 in the mudstone layer at Moore Park. It appears that Equation (6-23) still predicts a more stable OCR in

Ady Canal and Moore Park, and the limited lab results at least agree reasonably well with Equation (6-23) prediction.

$$\boldsymbol{OCR(1) = 2 \cdot \left[\frac{1}{1.95M + 1}\left(\frac{q_t - u_2}{\sigma'_{v0}}\right)\right]^{\frac{1}{\Lambda}}} \quad \textbf{(6-22)}$$

$$\boldsymbol{OCR(2) = \frac{0.33(q_t - \sigma_{v0})^{m'}\left(\frac{p_{atm}}{100}\right)^{1-m'}}{\sigma'_{v0}}} \quad \textbf{(6-23)}$$

where:

M = strength parameter in critical state soil mechanics, $M = \frac{6\sin\phi'}{3-\sin\phi'}$;
ϕ' = soil friction angle;
q_t = corrected cone tip resistance, calculated as Equation (3-3), kPa;
u_2 = pore water pressure measured at the cone shoulder, kPa;
σ'_{v0} = effective vertical stress in-situ, kPa;
Λ = plastic volumetric strain potential, $\Lambda = 1 - \frac{C_s}{C_c}$;
C_s = swelling index;
C_c = compression index;
σ_{v0} = total vertical stress in-situ, kPa;
m' = exponent parameter, $m' = 1 - \frac{0.28}{1+(I_c/2.65)^{25}}$
I_c = soil behavioral type index, calculated as Equation (3-7) to (3-9); and
p_{atm} = atmosphere pressure, taken as 101.3 kPa.

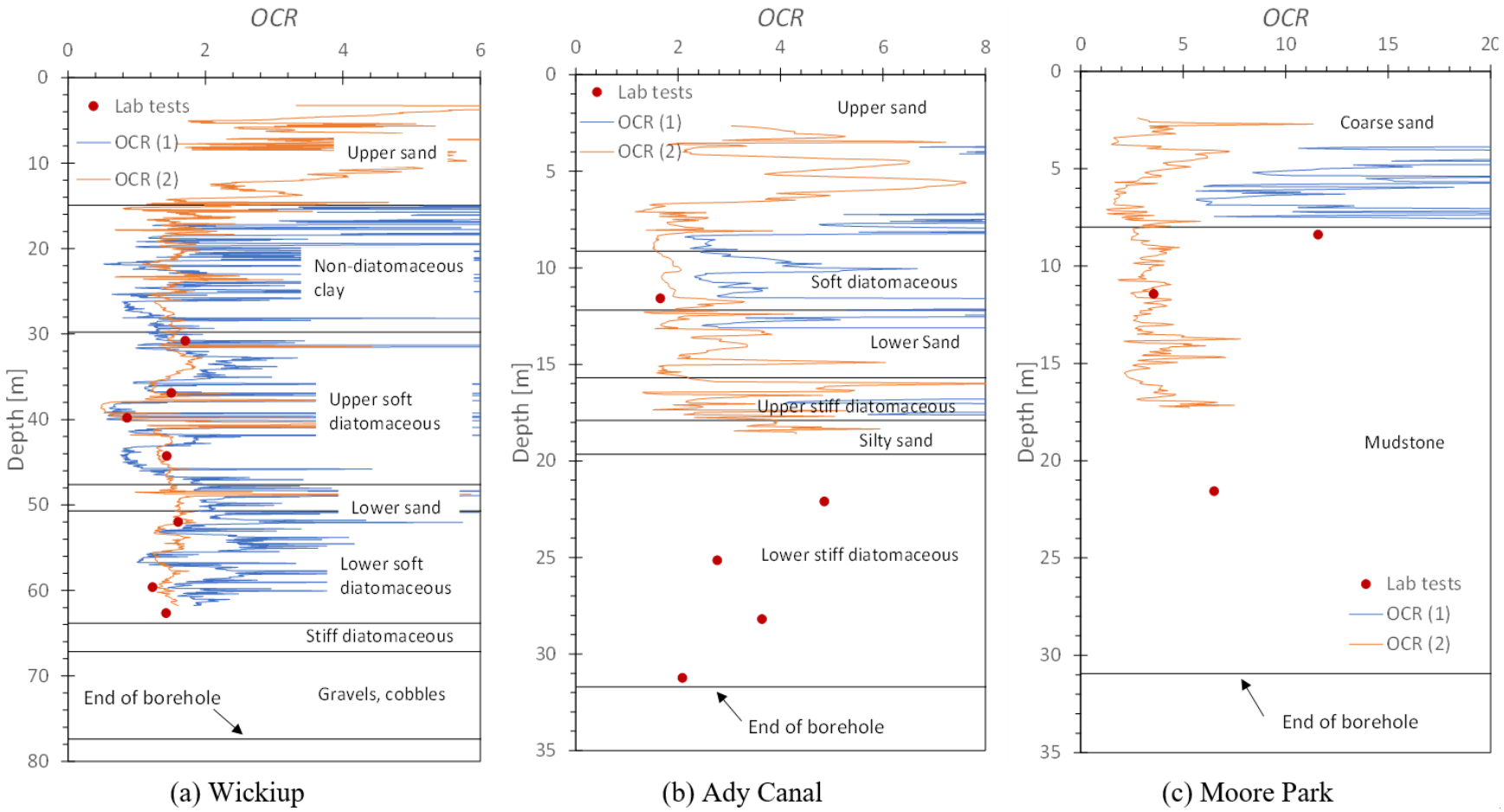

Figure 6.26: Comparisons of OCR from CPTu correlations and lab results

6.4.4.3 Friction angle

Senneset et al. (1989) developed a theoretical relationship between friction angle and CPTu parameters (N_m and B_q) for soft to firm clays. The direct evaluation of friction angle was approximated by Mayne (2007) given as Equation (6-24). This method is restricted for fine-grained soil with OCR less than 2.5 and friction angle between 18° - 45°. Ouyang and Mayne (2019) modified this approach to extend to overconsolidated clays by incorporating OCR in the evaluation (Equation (6-25)). The friction angle of sands will be evaluated by Equation (6-26) proposed by Kulhawy and Mayne (1990). The comparisons of friction angle and CPTu correlations are plotted in Figure 6.27. Note that the modified friction angle evaluation (Equation (6-25)) needs the knowledge of OCR (i.e., OCR correlation presented in 6.4.4.2). The legend "ϕ' (mod 1)" represents Equation (6-25) prediction with OCR (1) evaluation (i.e., Equation (5-4)), while the legend "ϕ' (mod 2)" represents Equation (6-25) prediction with OCR (2) evaluation (i.e., Equation (6-23)). Generally, Equation (6-24) gives higher prediction of ϕ' than the modified approach, though the applicable range for predicted ϕ' is 18° - 45°. Meanwhile, the modified approach using OCR (1) evaluation gives the lowest prediction. In Wickiup, for upper diatomaceous soil, the friction angle was reasonably captured by the unmodified approach (Equation (6-24)), though slightly underpredicted. For lower diatomaceous soil, none of these correlations captures the high friction angle. In Ady Canal, there is only one specimen tested for friction angle that overlaps with CPTu profiles, and the friction angles agree well with the unmodified approach. In Moore Park, three methods largely differ from one another. The unmodified approach (Equation (6-24)) predicts ϕ' to be as high as 60°. It appears that the modified approach with OCR (2) evaluation gives the best estimate of ϕ' of mudstone diatomaceous soil.

$$\mathbf{0.05 < B_q < 1} \qquad \boldsymbol{\phi' = 29.5^\circ B_q^{0.121}\left(0.256 + 0.336 B_q + \log(N_m)\right)}$$

$$\textbf{Restrictions: } \boldsymbol{18^o \le \phi' \le 45^o,\ OCR < 2.5} \qquad \textbf{(6-24)}$$

$$\boldsymbol{\phi'(mod) = 29.5^\circ B_q^{0.121}\left(0.256 + 0.336 B_q + \log(N_{mc})\right)} \qquad \textbf{(6-25)}$$

$$\mathbf{B_q < 0.05} \qquad \boldsymbol{\phi' = 17.6^\circ + 11^\circ \log\left(\frac{q_t}{\sqrt{\sigma'_{v0} q_{atm}}}\right)} \qquad \textbf{(6-26)}$$

where:

B_q = pore pressure ratio, $B_q = \frac{u_2 - u_0}{q_t - \sigma_{v0}}$;

N_m = cone resistance number, $N_m = Q_t = \frac{q_t - \sigma_{v0}}{\sigma'_{v0}}$ when $c' = 0$; and

N_{mc} = modified cone resistance number, $N_{mc} = \frac{N_m}{OCR^\Lambda}$

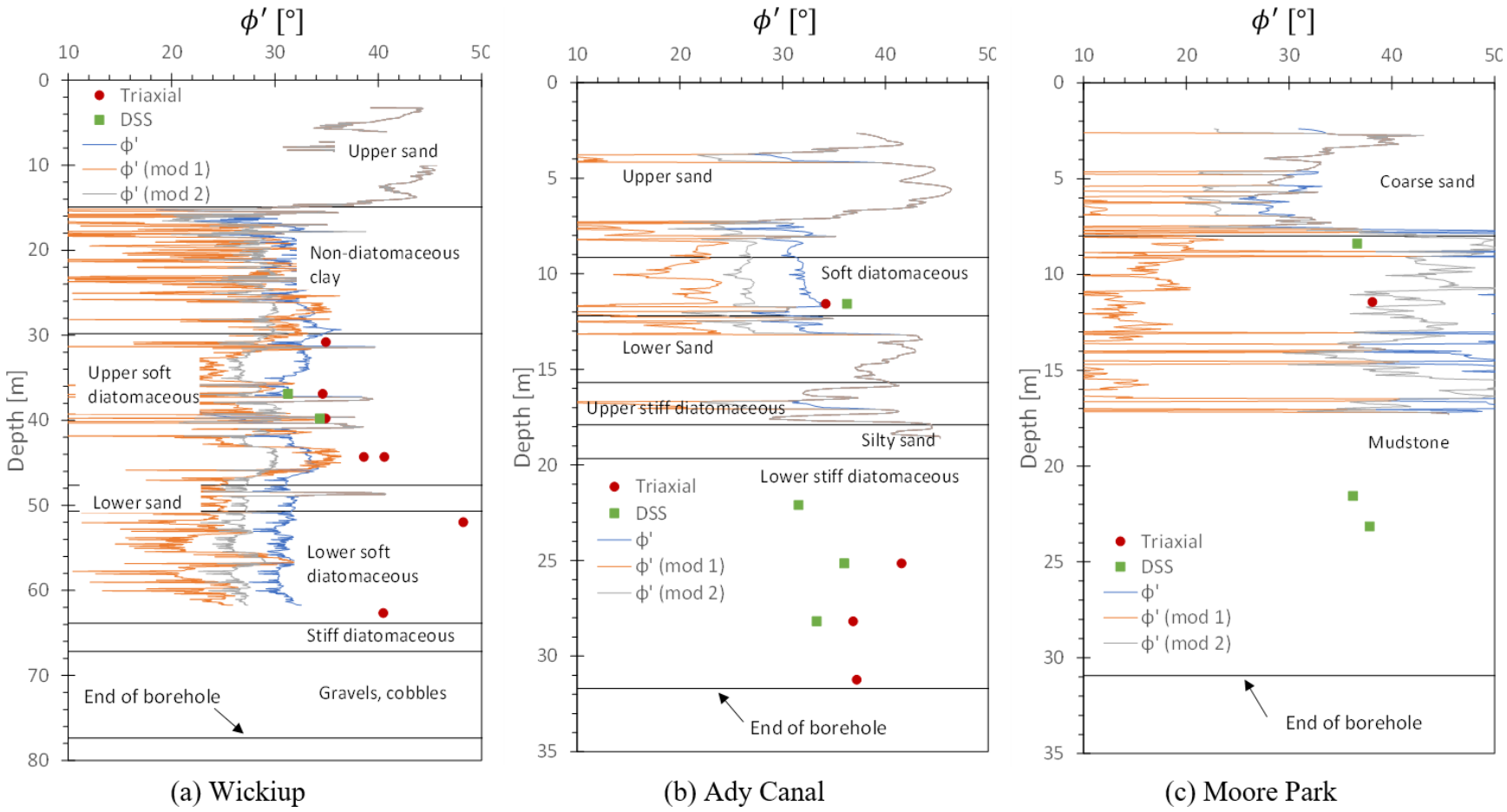

Figure 6.27: Comparisons of ϕ' from CPTu correDlations and lab results

6.4.4.4 Undrained shear strength

The undrained shear strength (s_u) can be developed from critical state soil mechanics (Schofield and Wroth, 1968) and can be evaluated by Equation (6-27). Another common approach to evaluate s_u is using the net cone resistance, shown as Equation (6-28). The comparisons of s_u from both correlations and lab results are shown in Figure 6.28. Note than Equation (6-27) involves the evaluation of OCR and ϕ', sections 6.4.4.2 and 6.4.4.3 show that different approaches induce different results. Generally, OCR (2) (i.e., Equation (6-23)) is adopted since it gives reasonable approximation. Both ϕ' correlations are close to each other. Therefore, in Figure 6.28, the legend "su (1) – 1" refers to the Equation (6-27) evaluation with OCR (2) (i.e., Equation (6-23)) and unmodified ϕ' (i.e., Equation (6-24). The legend "su (1) – 2" use the same evaluation as "su (1) – 1" except with modified ϕ' (i.e., Equation (6-25)). Figure 6.28 shows that all s_u evaluations are close to one another and consistent with lab results at Wickiup and Ady Canal. In Moore Park, Equation (6-28) tends to overpredict s_u and Equation (6-27) is in agreement with the DSS result.

$$\boldsymbol{s_u(1) = \frac{1}{2} M p' \left(\frac{R_0}{2}\right)^{\Lambda}} \tag{6-27}$$

$$\boldsymbol{s_u(2) = \frac{q_t - \sigma_{v0}}{N_{kt}}}$$

$$\boldsymbol{N_{kt} = 25.3 \text{ for } B_q < -0.06}$$

(6-28)

$$\boldsymbol{N_{kt} = 10.5 - 4.6 \ln(0.1 + B_q) \text{ for } B_q \geq -0.06}$$

(6-29)

where:

p' = effective mean stress, $p' = \frac{1+2K_0^{OC}}{3}\sigma'_{v0}$;

K_0^{OC} = coefficient of horizontal stress, $K_0^{OC} = (1 - \sin\phi')OCR^{\sin\phi'}$;

R_0 = preconsolidation stress in terms of p', $R_0 = \left(\frac{1+2(1-\sin\phi')}{1+2K_0^{OC}}\right) \cdot OCR$; and

N_{kt} = bearing factor, calculated by Equation (6-29).

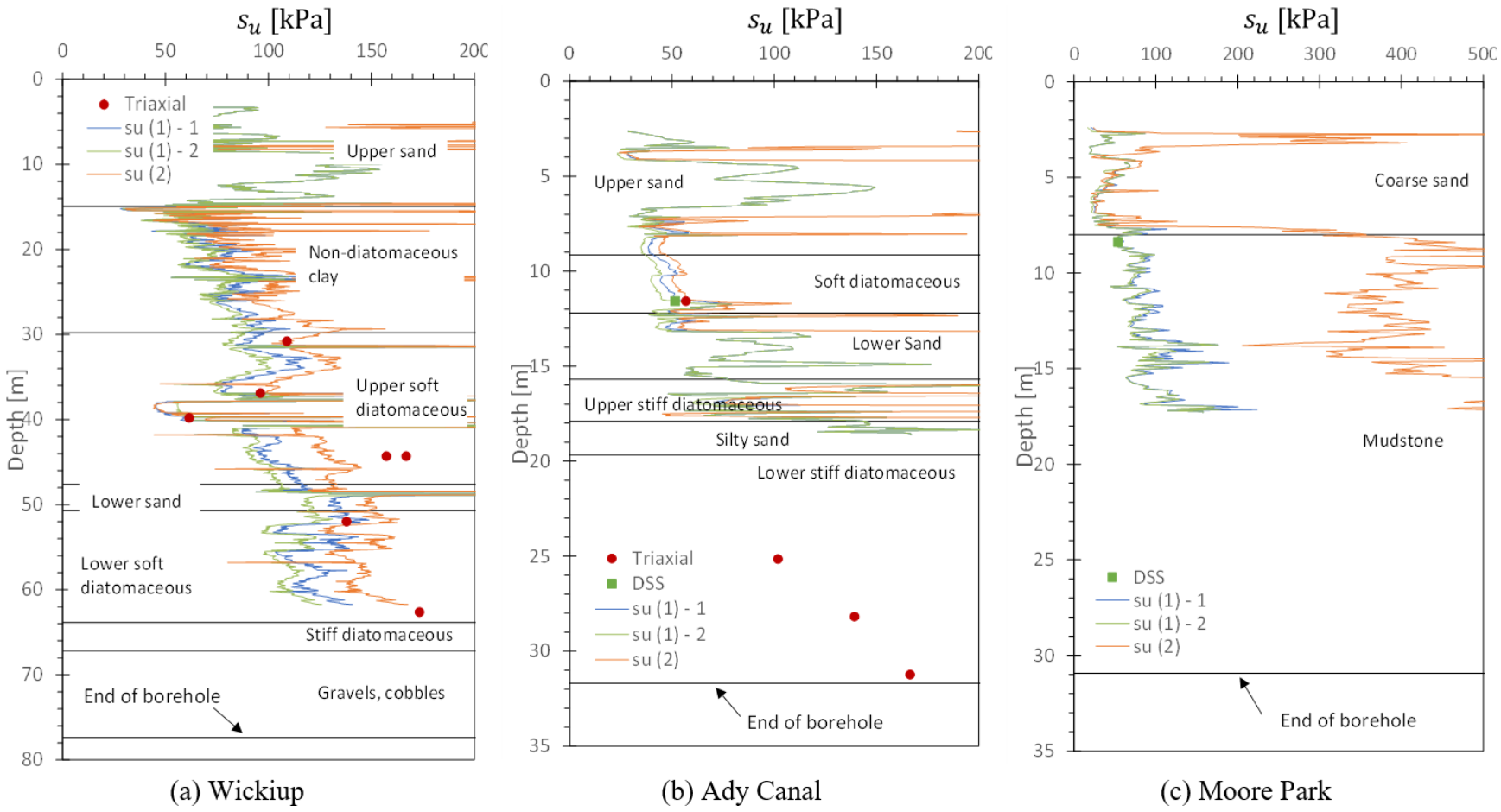

Figure 6.28: Comparisons of s_u from CPTu correlations and lab results

7.0 COMPUTATIONAL MODELING OF DIATOMACEOUS SOIL BEHAVIOR

7.1 INTRODUCTION

Limited attempts to simulate the mechanical behavior of diatomaceous soil with various constitutive models have been reported in the literature. Some have adopted elasto-viscoplastic (EVP) constitutive models (Maekawa et al., 1991; Liao et al., 2003; Oka et al., 2011, with corresponding EVP models: Sekiguchi, 1977; Yin and Graham, 1999; Kimoto and Oka, 2005, respectively) to simulate the time-settlement behavior or shear stress-strain behavior of triaxial tests on Japanese diatomaceous mudstone. Vera-Grunauer (2014) used the SimpleDSS model (Pestana et al., 2000) to predict the stress-strain behavior of a monotonic DSS test of a soft diatomaceous soil from Guayaquil, Ecuador. Perez Leon et al. (2022) adopted the hardening soil (HS) model (Schanz 1998) to simulate both CU triaxial tests and 1D consolidation tests simultaneously on normally consolidated reconstituted specimens of 50% kaolin and 50% diatomaceous soil from Bogota, Colombia. While these researchers concluded that their simulations have good agreement with lab results, they only attempted to simulate one type of soil test, either triaxial shear or oedometric compression. It is less clear that these models can reasonably reconcile the shear and compressive behavior of diatomaceous soils because the soil has very low oedometric stiffness but relatively high elastic modulus. Perez Leon et al. (2022) simulated both triaxial and consolidation tests on diatom-kaolin mixtures using the HS model and concluded that the HS model can capture the shear and compressive behavior of reconstituted diatom mixtures with E_{ur}^{ref} and E_{50}^{ref} (definitions see below) being the main parameters of adjustment. However, in natural (undisturbed) diatomaceous soil the relationship between measured stiffness parameters may not meet the mathematical requirements of the HS model (equations (2-1) and (6-1)) by implementation software (e.g., PLAXIS) due to the exceedingly low E_{oed}^{ref} (i.e., high C_c) and relatively high E_{50}^{ref}.

$$\mathbf{0.1}\ \boldsymbol{E_{50}^{ref}} < \boldsymbol{E_{oed}^{ref}} < \mathbf{3}\ \boldsymbol{E_{50}^{ref}} \tag{7-1}$$

$$\mathbf{2}\ \boldsymbol{E_{50}^{ref}} < \boldsymbol{E_{ur}^{ref}} < \mathbf{20}\ \boldsymbol{E_{50}^{ref}} \tag{7-2}$$

where:
E_{50}^{ref} = secant stiffness in standard drained triaxial test at p^{ref};
E_{oed}^{ref} = tangent stiffness for primary oedometer loading at p^{ref};
E_{ur}^{ref} = unloading/reloading stiffness at p^{ref}; and
p^{ref} = reference pressure, default setting is 100 kPa in PLAXIS software.

The first goal of this chapter is to find a suitable constitutive model for diatomaceous soil and calibrate the model with test results (both shear and consolidation tests) to understand the behaviors of diatomaceous soil. Due to the unique nature of the soil (it has high E_{50}^{ref} and E_{ur}^{ref} but a low E_{oed}^{ref}), common soil models are not capable of capturing both effects (e.g., HS model, Modified Cam-Clay model, Original Cam-Clay model). We adopt the Soft Soil model (Brinkgreve, 1994) to simulate the shear and compressive behavior of nearly normally consolidated diatomaceous soil from Wickiup and Ady Canal. We also consider literature data to compare the similarity of diatomaceous soil from different regions.

7.2 CONSTITUTIVE MODELING OF ELEMENTAL TESTING

The Soft Soil model was formulated through advanced modifications of the Modified Cam-Clay (MCC) model. In this section, we initially delineate the foundational framework of the Modified Cam-Clay model in order to better understand the Soft Soil model and its modifications. Subsequently, we address an inherent limitation observed in the MCC model. Finally, we present the detailed formulation of the Soft Soil model.

7.2.1 Modified Cam-Clay Model

7.2.1.1 Introduction of some key terms

In the MCC model, we concentrate on a saturated soil under axisymmetric loading. The framework is expressed in (q, p') and $(e, \ln p')$ space where p' and q (under axisymmetric loading) are defined by Equation (7-3) and (7-4). Note that some of the key terms adopted in this chapter were introduced in previous chapters, for the easiness to read, they are defined again as necessary.

$$\boldsymbol{p' = \frac{\sigma_1' + 2\sigma_3'}{3}} \tag{7-3}$$

$$\boldsymbol{q = \sigma_1' - \sigma_3'} \tag{7-4}$$

where:
p' = mean effective stress, Equation (7-3) is based upon axisymmetric loading;
q = deviatoric stress or shear stress, Equation (7-4) is based upon axisymmetric loading;
σ_1' = major principal stress; and
σ_3' = minor principal stress.

The isotropic consolidation line is expressed in $(e, \ln p')$ space (see Figure 7.1). The slope of virgin compression is defined as compression index, denoted as λ, and the average slope of unloading/reloading curves is defined as recompression index, denoted as κ. Previously, we introduced oedometric consolidation (i.e., IL and CRS test), the consolidation line is expressed in $(e, \log \sigma_v')$ space. The compression and recompression

indices (C_c and C_r) are defined similarly. The relationships between C_c and λ, and C_r and κ are expressed in Equation (7-5) and (7-6).

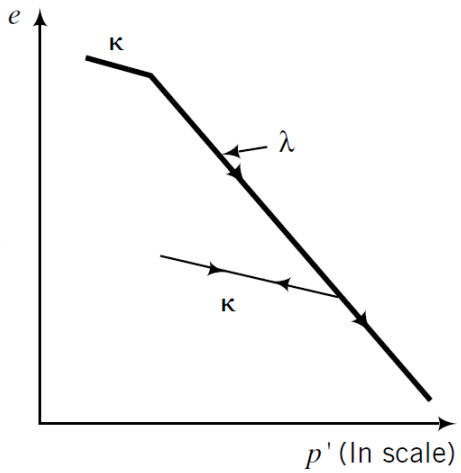

Figure 7.1: Isotropic consolidation line in $(e, \ln p')$ space (after Budhu, 2010)

$$\lambda = \frac{C_c}{\ln 10} = 0.434\, C_c \tag{7-5}$$

$$\kappa = \frac{C_r}{\ln 10} = 0.434\, C_r \tag{7-6}$$

The preconsolidation ratio (R_0) is defined by Equation (7-7).

$$R_0 = \frac{p_c'}{p_0'} \tag{7-7}$$

where:
p_c' = preconsolidation mean effective stress; and
p_0' = current mean effective stress.

7.2.1.2 Failure line

In Critical State Soil Mechanics, the fundamental concept is that the soil fails on the failure line (also referred to as critical state line, CSL), that is, the soil will approach the failure line during shearing. The failure line in (q, p') and $(e, \ln p')$ space is shown in Figure 7.2. In (q, p') space, the failure line is a straight line passing through the origin and has a slope of M, which is directly related to the critical state friction angle. The expression of M for axisymmetric compression is by Equation (7-8). The failure line in $(e, \ln p')$ space is also a straight line that has the same slope as the isotropic consolidation line. The expression of the failure line in $(e, \ln p')$ space is by Equation (7-9).

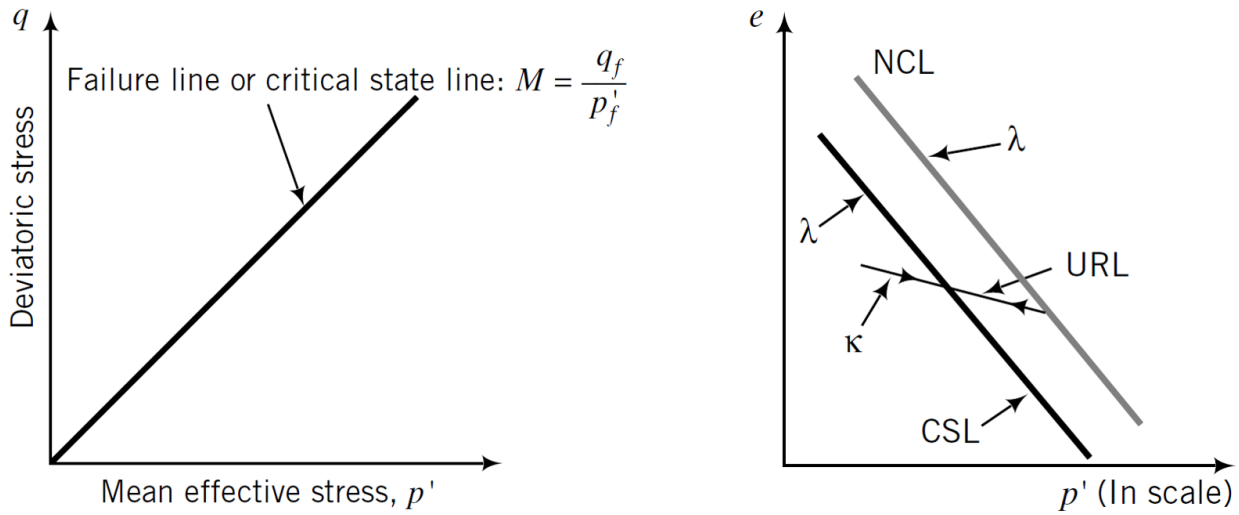

(a) Failure line in (q, p') space (b) Failure line in $(e, \ln p')$ space

Figure 7.2: Failure line in (q, p') and $(e, \ln p')$ space (after Budhu, 2010)

$$M = \frac{6 \sin \phi'_{cs}}{3 - \sin \phi'_{cs}} = \frac{q_f}{p'_f} \tag{7-8}$$

$$e = e_\Gamma - \lambda \ln p' \tag{7-9}$$

where;
M = strength parameter in the MCC model;
q_f = deviatoric stress at failure;
p'_f = mean effective stress at failure;
ϕ'_{cs} = friction angle at critical state;
e_Γ = the void ratio on CSL in $(e, \ln p')$ space when $p' = 1\ kPa$. e_Γ can be derived and written as a function of $e_0, \lambda, \kappa, p'_c$, and p'_0. e_0 is the void ratio corresponding to p'_0.

7.2.1.3 Yield surface

The yield surface is an ellipse in (q, p') space that passes the origin and intersect with the CSL at its co-vertex, shown in Figure 7.3. The function is given by Equation (7-10). The initial size is determined by preconsolidation mean effective stress, p'_c. When the stress states are within the yield surface, the soil will respond elastically. As the soil approaches the yield surface and tends to move outside of the yield surface, the soil starts to behave plastically, and correspondingly, the yield surface expands, the size of which is determined by the current preconsolidation stress, p'_G, see Figure 7.3.

$$F = (p')^2 - p' p'_c + \frac{q^2}{M^2} = 0 \tag{7-10}$$

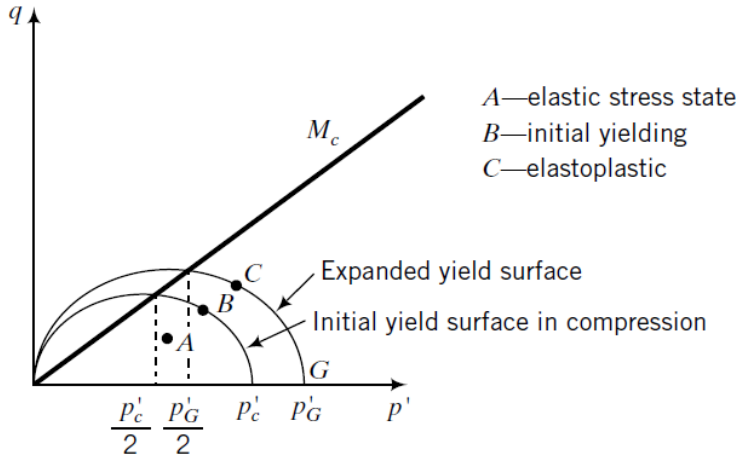

Figure 7.3: Yield surface in (q, p') space (after Budhu, 2010)

7.2.1.4 Elastic properties

The elastic properties are described by the soil stiffness: the shear modulus (G) and the effective bulk modulus (K'). The shear modulus (G) is the ratio between the deviatoric stress (q) and the elastic deviatoric strain (ε_q^e), shown in Equation (7-11). The effective bulk modulus (K') is the ratio between the mean effective stress (p') and the elastic volumetric strain (ε_p^e), shown in Equation (7-12).

$$d\varepsilon_q^e = \frac{dq}{3G} \tag{7-11}$$

$$d\varepsilon_p^e = \frac{dp'}{K'} \tag{7-12}$$

where;
$d\varepsilon_q^e$ = elastic deviatoric strain increment;
dq = deviatoric stress increment;
$d\varepsilon_p^e$ = elastic volumetric strain increment; and
dp' = mean effective stress increment.

From the unloading-reloading curve in $(e, \ln p')$ space and combining Equation (7-12), the effective bulk modulus (K') can be related to κ, shown in Equation (7-13). Based on elasticity theory, G is reliant on K' and Poisson's ratio (ν) by Equation (7-14) and (7-15), where Poisson's ratio (ν) is a parameter input in the MCC model. Therefore, the relationships between ε_q^e and q, ε_p^e and p' are defined.

$$K' = \frac{p'(1 + e_0)}{\kappa} \tag{7-13}$$

$$K' = \frac{E'}{3(1-2\nu)} \tag{7-14}$$

$$G = \frac{E'}{2(1+\nu)} \tag{7-15}$$

where:
E' = effective elastic modulus.

7.2.1.5 Plastic potential and hardening rule

The plastic potential of MCC model has the same function as the yield surface. The plastic strain increment is normal to the plastic potential, which is called the hardening rule. As is shown in Figure 7.4, after the soil reaches the yield surface and continues to deform, the plastic strain (denoted as $d\varepsilon^p$) develops, normal to the yield surface. The projections on p' and q axis are corresponding plastic strains: plastic volumetric strain increment ($d\varepsilon_p^p$) on p' axis, and plastic deviatoric strain increment ($d\varepsilon_q^p$) on q axis. The relationship between $d\varepsilon_p^p$ and $d\varepsilon_q^p$ can be developed based on the function of plastic potential (i.e., yield surface): the tangent or slope of the yield surface at stress state (p', q) is given by Equation (7-16), rearranging to obtain the slope given by Equation (7-17), thus, the normal to the yield surface is expressed as Equation (7-18), which is the ratio between $d\varepsilon_q^p$ and $d\varepsilon_p^p$, shown in Equation (7-19). To get rid of p_c' in Equation (7-19), we apply Equation (7-10), thus we get Equation (7-20).

$$dF = 2p'dp' - p_c'dp' + 2q\frac{dq}{M^2} = 0 \tag{7-16}$$

$$\frac{dq}{dp'} = \frac{\frac{p_c'}{2} - p'}{\frac{q}{M^2}} \tag{7-17}$$

$$-\frac{1}{\frac{dq}{dp'}} = -\frac{dp'}{dq} = -\frac{\frac{q}{M^2}}{\frac{p_c'}{2} - p'} \tag{7-18}$$

$$\frac{d\varepsilon_q^p}{d\varepsilon_p^p} = -\frac{1}{\frac{dq}{dp'}} = -\frac{\frac{q}{M^2}}{\frac{p_c'}{2} - p'} \tag{7-19}$$

$$\frac{d\varepsilon_q^p}{d\varepsilon_p^p} = \frac{\frac{2q}{p'}}{M^2 - \left(\frac{q}{p'}\right)^2} \tag{7-20}$$

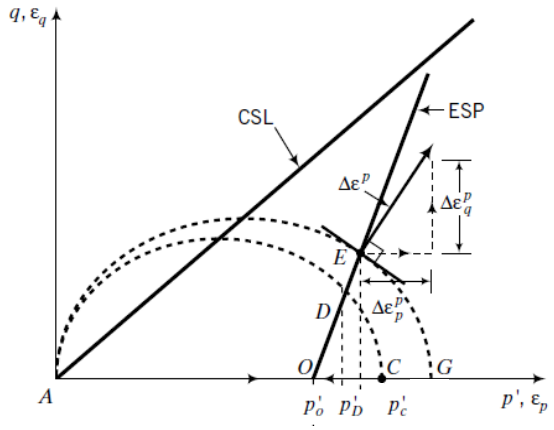

Figure 7.4: Relationship between plastic deviatoric and plastic volumetric strain (after Budhu, 2010)

7.2.1.6 Plastic volumetric strain

With the relationship between plastic volumetric strain increment ($d\varepsilon_p^p$) and plastic deviatoric strain increment ($d\varepsilon_q^p$) derived as Equation (7-19), we only need to know one of the two to compute the plastic strains. Recall the function of normally consolidation line (NCL) given by Equation (7-9), the derivative format can be written as Equation (7-21). The relationship between the total volumetric strain increment ($d\varepsilon_p$) and the void ratio increment (de) is given as Equation (7-22), thus, the total volumetric strain increment ($d\varepsilon_p$) can be written as Equation (7-23). Similarly, the elastic volumetric strain increment ($d\varepsilon_p^e$) can be written as Equation (7-24), inducing the plastic volumetric strain increment ($d\varepsilon_p^p$) written as Equation (7-25). Till now, all strain increment components are expressed as functions of stress increments.

$$de = -\lambda \frac{dp'}{p'} \tag{7-21}$$

$$d\varepsilon_p = -\frac{de}{1 + e_0} \tag{7-22}$$

$$d\varepsilon_p = \frac{\lambda}{1 + e_0} \frac{dp'}{p'} \tag{7-23}$$

$$d\varepsilon_p^e = \frac{\kappa}{1+e_0}\frac{dp'}{p'} \tag{7-24}$$

$$d\varepsilon_p^p = d\varepsilon_p - d\varepsilon_p^e = \frac{\lambda-\kappa}{1+e_0}\frac{dp'}{p'} \tag{7-25}$$

7.2.1.7 Summary

Wood (1990) stated that an elastic-plastic soil constitutive model should contain the following four parts: elastic properties, yield surface, plastic potential, and hardening rule. Sections 7.2.1.1 - 7.2.1.6 introduced these basic components of the MCC model. The model requires five material parameters: $\lambda, \kappa, \nu, e_0$, and M. If a soil's stress history (p_c'), initial mean effective stress (p_0'), and the stress path (drained or undrained) are known, with correct estimates of the material parameters, the soil behaviors can be determined (e.g., failure stresses, stress-strain curves, etc.).

7.2.2 Coupling Effect Between the Strength Parameter and the Coefficient of Lateral Earth Pressure in MCC Model

Based on the MCC model, the coefficient of lateral earth pressure (K_0, the ratio between in-situ horizontal effective stress to in-situ vertical effective stress) is related to the strength parameter (M), however, both parameters are expressed as functions of effective friction angle at critical state (ϕ_{cs}'). The parameter M is given by Equation (7-8), and the parameter K_0 is given by Equation (7-26) and (7-27) (Jaky 1944). Either Equation (7-26) or (7-27), K_0 is coupled with M through ϕ_{cs}', such relationship differs from the relationship (between K_0 and M) derived from MCC model. This is one of the discrepancies of the MCC model, which is elaborated in this section.

$$K_o^{nc} = 1 - \sin\phi_{cs}' \tag{7-26}$$

$$K_o^{oc} = (1 - \sin\phi_{cs}')OCR^{\sin\phi_{cs}'} \tag{7-27}$$

where:
K_o^{nc} = coefficient of lateral earth pressure for normally consolidated soil; and
K_o^{oc} = coefficient of lateral earth pressure for overconsolidated soil.

We first attempt to derive the relationship between K_0 and M from the MCC model. Consider oedometric compression, we denote subscript yy as the vertical direction, subscript xx and zz as the horizontal direction, superscript e as the elastic strain, and superscript p as the plastic strain.

The compression is positive. The basic conditions for oedometric compression are listed by Equation (7-28) – (7-31).

$$d\varepsilon_{zz} = d\varepsilon_{xx} = 0 \tag{7-28}$$

$$d\varepsilon_{zz}^{e} = d\varepsilon_{xx}^{e} \tag{7-29}$$

$$d\varepsilon_{zz}^{p} = d\varepsilon_{xx}^{p} \tag{7-30}$$

$$d\sigma_{xx} = d\sigma_{zz} = K_0\, d\sigma_{yy} \tag{7-31}$$

According to Hooke's law, the elastic strain components on x and y directions are written as Equation (7-32) and (7-33). Combining with Equation (7-31), the stress components ($d\sigma_{xx}$ and $d\sigma_{yy}$) can be eliminated and the relationship between the elastic strain components on x and y directions is shown in Equation (7-34).

$$d\varepsilon_{xx}^{e} = \frac{1}{E'}\left[(1-\nu)\, d\sigma_{xx} - \nu\, d\sigma_{yy}\right] \tag{7-1}$$

$$d\varepsilon_{yy}^{e} = \frac{1}{E'}\left[-2\nu\, d\sigma_{xx} + d\sigma_{yy}\right] \tag{7-2}$$

$$d\varepsilon_{xx}^{e} = \frac{K_0(1-\nu) - \nu}{1 - 2\nu K_0} d\varepsilon_{yy}^{e} \tag{7-3}$$

Now we attempt to derive the expressions of the plastic strain components on x and y directions. The total and elastic volumetric strains can be written as functions of strain components on x and y directions, shown in Equations (7-35) and (7-36). We also recall that the total and elastic volumetric strains are expressed by Equations (7-23) and (7-24), thus, Equation (7-37) is derived. Combining Equations (7-35) – (7-37), we can get Equation (7-38). Combining Equations (7-38) and (7-34), we get Equation (7-39). Therefore, the plastic strain components on x and y directions are derived as Equation (7-40) and (7-41).

$$d\varepsilon_{p} = d\varepsilon_{yy} + 2d\varepsilon_{xx} = d\varepsilon_{yy} \tag{7-4}$$

$$d\varepsilon_{p}^{e} = d\varepsilon_{yy}^{e} + 2d\varepsilon_{xx}^{e} \tag{7-5}$$

$$\frac{d\varepsilon_{p}}{d\varepsilon_{p}^{e}} = \frac{\lambda}{\kappa} \tag{7-6}$$

$$\frac{\boldsymbol{d\varepsilon_{yy}}}{\boldsymbol{d\varepsilon^{e}_{yy} + 2d\varepsilon^{e}_{xx}}} = \frac{\boldsymbol{\lambda}}{\boldsymbol{\kappa}} \tag{7-7}$$

$$\boldsymbol{d\varepsilon_{yy}} = \frac{\boldsymbol{(1-2\nu)(1+2K_0)}}{\boldsymbol{1-2\nu\, K_0}} \cdot \frac{\boldsymbol{\lambda}}{\boldsymbol{\kappa}} \cdot \boldsymbol{d\varepsilon^{e}_{yy}} \tag{7-8}$$

$$\boldsymbol{d\varepsilon^{p}_{yy} = d\varepsilon_{yy} - d\varepsilon^{e}_{yy}} = \left[\frac{\boldsymbol{(1-2\nu)(1+2K_0)}}{\boldsymbol{1-2\nu\, K_0}} \cdot \frac{\boldsymbol{\lambda}}{\boldsymbol{\kappa}} - \boldsymbol{1}\right] \boldsymbol{d\varepsilon^{e}_{yy}} \tag{7-9}$$

$$\boldsymbol{d\varepsilon^{p}_{xx} = -d\varepsilon^{e}_{xx}} = -\frac{\boldsymbol{K_0(1-\nu) - \nu}}{\boldsymbol{1-2\nu\, K_0}} \boldsymbol{d\varepsilon^{e}_{yy}} \tag{7-10}$$

Lastly, we attempt to derive the plastic deviatoric ($d\varepsilon_q^p$) and plastic volumetric ($d\varepsilon_p^p$) strains. The relationship between the deviatoric (or volumetric) strains and strain components on x and y directions is expressed in Equation (7-42) (or (7-44)). Equation (7-42) and (7-44) hold true for situations on elastic, plastic, and total strain components for axisymmetric loading. With expressions of plastic strain components on x and y directions presented in Equations (7-40) and (7-41), Equations (7-42) and (7-44) can be written as Equations (7-43) and (7-45) respectively. Implement Equations (7-43) and (7-45) into the flow rule expressed by Equation (7-20), and recall that the ratio of deviatoric stress to mean effective stress is expressed by Equation (7-46) for oedometric loading, we can get M expressed as a function of K_0, λ/κ, and ν shown in Equation (7-47).

$$\boldsymbol{d\varepsilon^{p}_{q}} = \frac{\boldsymbol{2}}{\boldsymbol{3}}\left(\boldsymbol{d\varepsilon^{p}_{yy} - d\varepsilon^{p}_{xx}}\right) \tag{7-11}$$

$$\boldsymbol{d\varepsilon^{p}_{q}} = \frac{\boldsymbol{2}}{\boldsymbol{3}}\left[\frac{\boldsymbol{(1-2\nu)(1+2K_0)\lambda/\kappa - (1+\nu)(1-K_0)}}{\boldsymbol{1-2\nu\, K_0}}\right] \boldsymbol{d\varepsilon^{e}_{yy}} \tag{7-12}$$

$$\boldsymbol{d\varepsilon^{p}_{p} = d\varepsilon^{p}_{yy} + 2\, d\varepsilon^{p}_{xx}} \tag{7-13}$$

$$\boldsymbol{d\varepsilon^{p}_{p}} = \left[\frac{\boldsymbol{(1-2\nu)(1+2K_0)(\lambda/\kappa - 1)}}{\boldsymbol{1-2\nu\, K_0}}\right] \boldsymbol{d\varepsilon^{e}_{yy}} \tag{7-14}$$

$$\frac{\boldsymbol{q}}{\boldsymbol{p'}} = \frac{\boldsymbol{3(1-K_0)}}{\boldsymbol{1+2K_0}} \tag{7-15}$$

$$M = 3\sqrt{\frac{(1-K_0)^2}{(1+2K_0)^2} + \frac{(1-K_0)(1-2\nu)(\lambda/\kappa - 1)}{(1+2K_0)(1-2\nu)\lambda/\kappa - (1-K_0)(1+\nu)}} \quad \textbf{(7-16)}$$

As described above, K_0 and M can be related to each other through two ways: first is through M as an expression of ϕ'_{cs} given by Equation (7-8) and K_0 as an expression of ϕ'_{cs} given by Equation (7-26) (or (7-27)), the second is through adopting MCC model in oedometric compression given by Equation (7-47). The relationship between K_0 and M derived from the two ways are not consistent with each other. We further illustrate this with an example, suppose a normally consolidated soil has the following properties: $\phi'_{cs} = 20^{\circ}, \lambda/\kappa = 5, \nu = 0.2$. The strength parameter M is 0.77 calculated by Equation (7-8), K_0 is calculated to be 0.8 by Equation (7-47), however, K_0 is supposed to be 0.66 by Equation (7-26). It means that K_0 is overpredicted by MCC model. If we choose a correct K_0 ($K_0 = 0.66$ in this case), the MCC model will overpredict M ($M = 1.15$ in this case by Equation (7-47)) where M is supposed to be 0.77 given by Equation (7-8).

7.2.3 Soft Soil Model

7.2.3.1 Yield surface, failure line, and flow rule

Considering the limitation of MCC model described in 7.2.2, the soft soil model (SSM) was then developed by Brinkgreve (1994) which is in the family of critical state soil mechanics (Schofield and Wroth, 1968). The soft soil model breaks the coupling effect between M and K_0 in MCC model by using the yield surface that represents the correct K_0-path and the failure line that represents the correct shear strength. Figure 7.5 shows the yield surface and failure line in (q, p') space, and corresponding functions are given by Equation (7-48) and (7-49). The yield surface in the Soft Soil model has the same shape as that in MCC model, but the determination of the size is slightly different. In the Soft Soil model, cohesion (c') is introduced and the major axis length of the ellipse-shape yield surface is computed as $p'_c + c' \cot \phi'_{cs}$. The yield surface intercept a line that passes $(-c' \cot \phi'_{cs}, 0)$ with a slope of M_{ss} at its co-vertex. Note that the slope M_{ss} is not considered as a strength parameter in SSM, but it represents the correct K_0-path, the value of which is computed by Equation (7-47). Note that in other references of the Soft Soil model (e.g., (Brinkgreve, 1994) or PLAXIS 2D manual, etc.), symbol M is used, here, to differentiate from the MCC model introduced previously, we denote it as M_{ss}. The failure line in SSM is a straight line that passes $(-c' \cot \phi'_{cs}, 0)$ with a slope of α, the strength parameter. If the soil reaches the yield surface before it reaches the failure line, it follows associated flow rule. That is the plastic potential is the same as the yield surface, and the plastic strain is normal to the yield surface. The concept remains the same as the MCC model described in 7.2.1.5. If the soil reaches the failure line first, it recedes to Mohr-Coulomb failure.

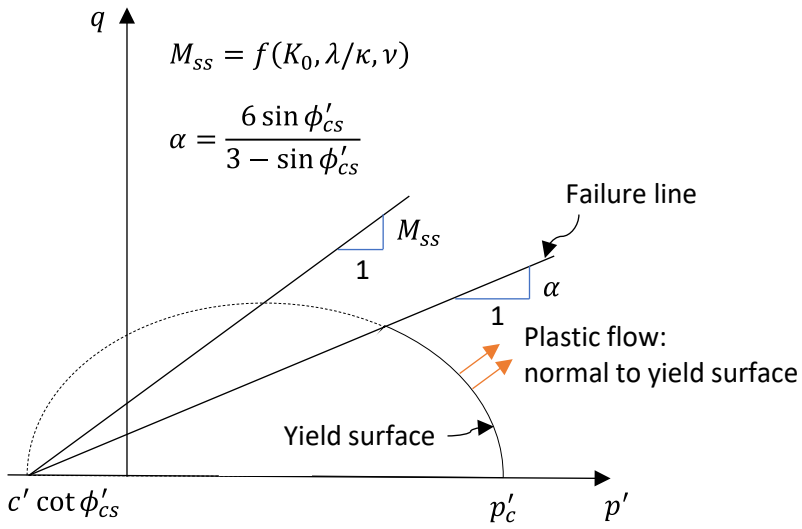

Figure 7.5: Yield surface and failure line of the Soft Soil model (modified after Brinkgreve, 1994)

$$\boldsymbol{f_1 = \frac{q^2}{M_{ss}^2} + p^*(p^* - p_c^*) = 0} \tag{7-17}$$

$$\boldsymbol{f_2 = q - \alpha p^*} \tag{7-18}$$

where:

M_{ss} = value calculated by Equation (7-47), note it is not a strength parameter in SSM;

α = $\frac{6 \sin \phi'_{cs}}{3 - \sin \phi'_{cs}}$ for axisymmetric compression, the strength parameter in SSM;

p^* = $p' + c' \cot \phi'_{cs}$;

p_c^* = $p'_c + c' \cot \phi'_{cs}$; and

c' = the effective cohesion.

7.2.3.2 Plastic volumetric strain

Similar to the MCC model, the flow rule determines the ratio between plastic volumetric strain increment ($d\varepsilon_p^p$) and plastic deviatoric strain increment ($d\varepsilon_q^p$), and we need to know the expression of either one to obtain both $d\varepsilon_p^p$ and $d\varepsilon_q^p$. The Soft Soil model has a logarithmic relation between the change of volumetric strain and the change of mean effective stress, shown in Equations (7-50) and (7-51). Since the Soft Soil model introduced the cohesion component, the volumetric strain is a function of $p' + c' \cot \phi'_{cs}$ instead of p' solely. Similar to the MCC model, the derivative formats are written in Equations (7-52) and (7-53). Thus, the plastic component of volumetric strain increment is given by Equation (7-54).

$$\boldsymbol{\varepsilon_p - \varepsilon_p^0 = \frac{\lambda}{1+e_0} \ln\left(\frac{p' + c' \cot \phi'_{cs}}{p'^{,0} + c' \cot \phi'_{cs}}\right)} \tag{7-19}$$

$$\boldsymbol{\varepsilon_p^e - \varepsilon_p^{e0} = \frac{\kappa}{1+e_0} \ln\left(\frac{p' + c' \cot \phi'_{cs}}{p'^{,0} + c' \cot \phi'_{cs}}\right)} \tag{7-20}$$

$$\boldsymbol{d\varepsilon_p = \frac{\lambda}{1+e_0} \cdot \frac{dp'}{p' + c' \cot \phi'_{cs}}} \tag{7-21}$$

$$\boldsymbol{d\varepsilon_p^e = \frac{\kappa}{1+e_0} \cdot \frac{dp'}{p' + c' \cot \phi'_{cs}}} \tag{7-22}$$

$$\boldsymbol{d\varepsilon_p^p = d\varepsilon_p - d\varepsilon_p^e = \frac{\lambda - \kappa}{1+e_0} \cdot \frac{dp'}{p' + c' \cot \phi'_{cs}}} \tag{7-23}$$

Where, ε_p^0 and $p'^{,0}$ are corresponding to each other, when determining the normally consolidation line, ε_p^0 and $p'^{,0}$ can be set at initial state which should be known. ε_p^{e0} is the elastic component of ε_p^0. Other symbols are previously defined.

7.2.3.3 Elastic properties

The elasticity theory still holds true for the Soft Soil model, the relationship between the elastic stress and strain were given by Equation (7-11) and (7-12), but the expression of the effective bulk modulus (K') is different than the MCC model. Based on Equation (7-12) and (7-53), the effective bulk modulus (K') can be derived as Equation (7-55). It is worth to note that the introduction of cohesion (c') would increase the effective bulk modulus of the soil. The shear modulus is a function of the effective bulk modulus (K') and the Poisson's ratio (ν) by combining Equation (7-14) and (7-15), where the Poisson's ratio (ν) is an input parameter.

$$\boldsymbol{K' = \frac{(p' + c' \cot \phi'_{cs}) \cdot (1 + e_0)}{\kappa}} \tag{7-24}$$

7.2.3.4 Soft Soil model parameters

Recall the MCC model parameters: $\lambda, \kappa, \nu, e_0,$ and M. The Soft Soil model uses similar parameters, and we describe each one herein. First, the compression index is denoted as λ^*, the slope of normally consolidation line in $\varepsilon_p - \ln p'$ space, the relationship to λ is expressed by Equation (7-56). Similarly, the swelling index is denoted as κ^*, the slope of unloading-reloading line in $\varepsilon_p - \ln p'$ space, the relationship to κ is expressed by

Equation (7-57). Theoretically, λ^* and κ^* can be obtained from isotropic compression tests, however, the oedometric compression (IL and CRS) tests are typically conducted in the laboratory, and it is C_c and C_r that are determined from the laboratory oedometric consolidation tests, the relationships between λ^* and C_c, κ^* and C_r are expressed by Equations (7-58) and (7-59). Note that there is no exact relation between κ^* and C_r because the ratio (K_0) of the horizontal and vertical stresses during unloading is not a constant (when unloading, the soil becomes overconsolidated). Equation (7-59) is an approximation. Second, the effective cohesion is introduced in the Soft Soil model, facilitating expansion of the elastic region into the tension zone. Modifying this parameter will change the effective bulk modulus (Equation (7-55)). Third, the effective friction angle at critical state (ϕ'_{cs}) is an equivalent parameter to M in the MCC model. Last, the Poisson's ratio is the same as that from MCC model. Measurement of ν is less straightforward and would require knowledge of either lateral stress in oedometric loading or radial deformation in triaxial loading, neither of which is routinely measured. As such, a value of $\nu = 0.15$ is typically adopted. Model is not particularly sensitive to the value of ν. In addition to these basic parameters, K_0 represents the coefficient of lateral earth pressure, it is computed by Equation (7-26) or (7-27). In PLAXIS 2D, the default value of K_0 is computed by Equation (7-26), alternatively, the user can set the value of their choice. The model parameters are summarized in Table 7.1.

$$\boldsymbol{\lambda^* = \frac{\lambda}{1 + e_0}} \tag{7.25}$$

$$\boldsymbol{\kappa^* = \frac{\kappa}{1 + e_0}} \tag{7.26}$$

$$\boldsymbol{\lambda^* = \frac{0.434\, C_c}{1 + e_0}} \tag{7.27}$$

$$\boldsymbol{\kappa^* \approx \frac{0.434\, C_r}{1 + e_0}} \tag{7.28}$$

Table 7.1: Soft soil model parameters

	Symbol	Parameters	Calculation / typical values
Basic parameters	λ^*	Modified compression index	Equations (7-56) or (7-58)
	κ^*	Modified swelling index	Equations (7-57) or (7-59)
	ν	Poisson's ratio on the unload-reload line	Typically $0.1 \leq \nu \leq 0.2$
	c' [kPa]	Effective cohesion	Material dependent
	ϕ'_{cs} [°]	Effective friction angle	$\frac{6 \sin \phi'_{cs}}{3 - \sin \phi'_{cs}} = \frac{q_f}{p'_f + c' \cot \phi'_{cs}}$
Miscellaneous parameters	K_0	Coefficient of lateral stress in normal consolidation	Default setting: $K_0 = 1 - \sin \phi'_{cs}$ Or set by user
	M_{ss}	K_0-dependent	Equation (7-47)

7.3 MODEL CALIBRATION WITH LAB RESULTS

Parameters for the Soft Soil model were calibrated in PLAXIS 2D (PLAXIS 2D material models manual, Brinkgreve et al., 2023) using the *SoilTest* module which facilitates simulation of laboratory tests with the selection of soil model and parameters on the basis of a single point algorithm. Because some triaxial tests exhibit extensive post-peak strain softening behavior and it is difficult for a relatively simple model to capture this complex behavior, we only attempted to simulate pre-peak stress-strain behavior of the shear tests.

The PLAXIS 2D material models manual (Brinkgreve et al., 2023) briefly describes the formulation of the Soft Soil Model and model parameters. In relationship between the modified swelling index (κ^*) and one-dimensional swelling index (C_s), the manual adopts Equation (7-60) while we presented Equation (7-59). Both equations are approximation because ratio of horizontal and vertical stresses changes during one-dimensional unloading. Equation (7-60) assumes that the average stress state during unloading is an isotropic stress state (i.e., $K_0 = 1$), which is reasonable for lightly overconsolidated soils with friction angle between $20^\circ - 30^\circ$ (Brinkgreve et al., 2023). In addition, the manual stated that κ^* should be based on swelling index (C_s) rather than recompression index (C_r). However, in this study, we measure C_r based on unloading-reloading line (URL), therefore, we use C_r to estimate κ^* by Equation (7-61).

$$\boldsymbol{\kappa^* \approx \frac{2 \times 0.434 C_s}{(1 + e_0)}} \quad \textbf{(7-29)}$$

$$\boldsymbol{\kappa^* \approx \frac{2 \times 0.434 C_r}{(1 + e_0)}} \quad \textbf{(7-30)}$$

In this section, we demonstrate two model calibrations on lightly overconsolidated specimen (W1U9) and heavily overconsolidated specimen (W1U10) to understand the soil behaviors. Moreover, we attempted to calibrate the literature laboratory data to compare with diatomaceous soil from this study.

7.3.1 Model Calibration on Lightly-overconsolidated Specimen: W1U9 as an Example

In this section, we use the triaxial and consolidation tests on W1U9 to calibrate the Soft Soil Model. The basic model parameters (λ^*, κ^*, ϕ'_{cs}) can be determined from the laboratory data, and we assume $\nu = 0.15$ and no cohesion ($c' = 0$). The K_0-parameters (both K_0 and M_{ss}) use the default setting. Hence, the parameters determination is presented in Table 7.2 as well as the calculations. We use the laboratory triaxial and consolidation test configurations (presented in Table 7.3 and Table 7.4) in the *SoilTest* module in PLAXIS 2D and perform single element testing numerically. The preconsolidation stress (σ'_p) for W1U9 from laboratory consolidation test is 243.7 kPa, and the initial mean effective stress (p'_0) in triaxial test is 177.6 kPa. The OCR during triaxial test is around 1.4, therefore, the specimen is considered lightly overconsolidated.

Table 7.2: Back calculated parameters from laboratory results for W1U9

	Parameters	Value	Calculation or source
Basic parameters	λ^*	0.1505	$C_c = 1.54$, $e_0 = 3.449$, and Equations (7-58)
	κ^*	0.029	$C_r = 0.1491$, $e_0 = 3.449$, and Equations (7-61)
	ν	0.15	Reasonable assumption
	c' [kPa]	0	Not introducing cohesion yet
	ϕ'_{cs} [°]	34.9°	$\frac{6\sin\phi'_{cs}}{3-\sin\phi'_{cs}} = \frac{q_f}{p'_f}$, obtained from triaxial test
Miscellaneous parameters	K_0	0.4277	$K_0 = 1 - \sin\phi'_{cs}$
	M_{ss}	1.827	Equation (7-47)

Table 7.3: Triaxial test configuration for W1U9

Type of test	Direction	Consolidation	p'_0 [kPa]	σ'_p [kPa]
Undrained	Compression	Isotropic	177.6	243.7

Table 7.4: Consolidation test configuration for W1U9

Type of test	σ'_p [kPa]	Strain - loading [%]	Strain - unloading [%]
CRS	243.7	37.28	1.004

The results from laboratory and numerical simulation based on parameters back calculated (i.e., Table 7.2) are presented in Figure 7.6. We can see that the Soft Soil model overpredicts shear strength (Figure 7.6 (a)) and underpredicts excess pore water pressure (Figure 7.6 (b)) during triaxial test. Looking at the consolidation curve predicted by Soft Soil model (Figure 7.6 (c) and (d)), the initial swelling line is not consistent with lab result. Therefore, we attempt to modify the parameters to make the model better predict soil laboratory behaviors. It is worth noting that the deviatoric stress and excess pore water pressure curves are internally related, so we only try to obtain better results on the deviatoric stress which may be achieved by lowering ϕ'_{cs}. In terms of initial swelling part of the consolidation curve, on one hand, we could decrease κ^* to increase the initial stiffness, on the other hand, we could assign some cohesion to increase the bulk modulus

(K', see Equation (7-55)). We obtain the proper parameters by manually adjusting these parameters, although somewhat arbitrary, the goal is to change the least amount of parameters to obtain the optimal results. The adjusted parameters as well as the rationale are presented in Table 7.5. The numerical results with adjusted parameters are presented in Figure 7.6. We can see that there is a good agreement in consolidation test, and the model reasonably captures the peak deviatoric stress in the triaxial test. However, such modifications further decrease the excess pore water pressure generated during the undrained triaxial test (Figure 7.6 (b)). Next, we take a look at the effective stress path and yield surface in order to better understand the excess pore water pressure generation.

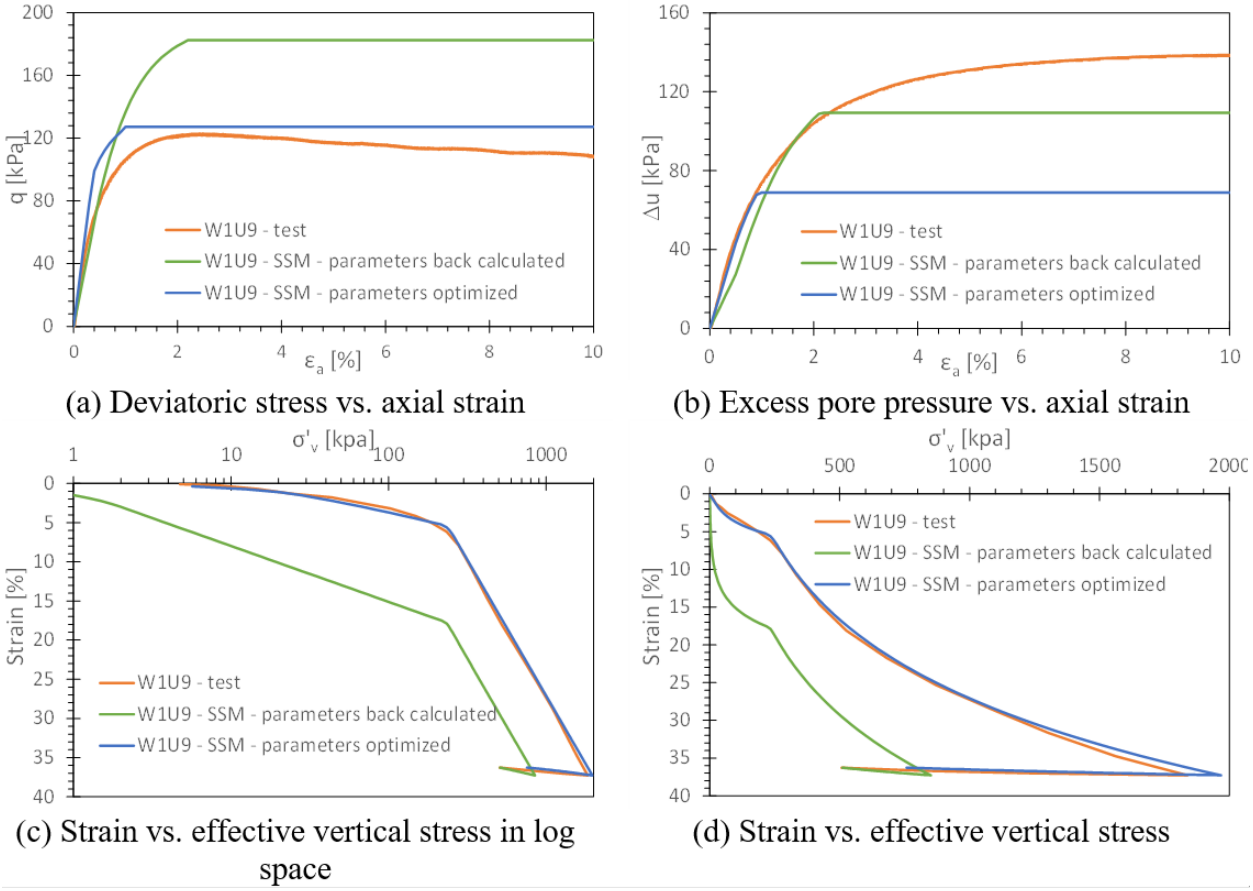

(a) Deviatoric stress vs. axial strain

(b) Excess pore pressure vs. axial strain

(c) Strain vs. effective vertical stress in log space

(d) Strain vs. effective vertical stress

Figure 7.6: Test curves from laboratory and Soft Soil Model (SSM) for W1U9

Table 7.5: Optimized SSM parameters for W1U9

	Parameters	Value	Rationale
Basic parameters	λ^*	0.1505	No need to modify
	κ^*	0.02	Lower slightly to increase K' (Equation (7-55))
	ν	0.15	It's a reasonable assumption and has little impact
	c' [kPa]	5	Assign small amount to increase K' (Equation (7.55))
	ϕ'_{cs} [°]	20°	Lower significantly to obtain the shear strength needed
Miscellaneous parameters	K_0	0.658	Default setting, $K_0 = 1 - \sin\phi'_{cs}$
	M_{ss}	1.178	Default setting, Equation (7.47)

The function of yield surface for Soft Soil model is presented in Equation (7-48). Basically, we need to know p_c^* and M_{ss} to draw the yield surface. M_{ss} is directly related to ϕ'_{cs} which is either back calculated from laboratory triaxial test or parameters optimization. p_c^* is computed from the preconsolidation stress (σ'_p). The computation process is shown in Table 7.6 for both sets of model parameters (laboratory back calculated and parameters optimization).

Table 7.6: Parameters for yield surface calculation for W1U9

	Parameters back calculated from laboratory	Parameters optimized	Equation / source
$\boldsymbol{c'}$ **[kPa]**	0	5	Laboratory or optimized
$\boldsymbol{\phi'_{cs}}$ [°]	34.9°	20°	Laboratory or optimized
$\boldsymbol{K_0}$	0.4277	0.658	$K_0 = 1 - \sin\phi'_{cs}$
$\boldsymbol{M_{ss}}$	1.827	1.178	Equation (7.47)
$\boldsymbol{\sigma'_p}$ **[kPa]**	243.7	243.7	Laboratory
$\boldsymbol{q}$ **[kPa]**	139.5	83.4	$q = (1 - K_0) \cdot \sigma'_p$
$\boldsymbol{p'}$ **[kPa]**	150.7	188.2	$p' = \sigma'_p \cdot (1 + 2K_0)/3$
$\boldsymbol{p^*}$ **[kPa]**	150.7	201.9	$p^* = p' + c' \cot\phi'_{cs}$ (see Equation (7-48))
$\boldsymbol{p_c^*}$ **[kPa]**	189.4	228.5	Equation (7-48)
$\boldsymbol{p'_c}$ **[kPa]**	189.4	214.8	$p'_c = p_c^* - c' \cot\phi'_{cs}$

The effective stress paths and yield surface are presented in Figure 7.7 and Figure 7.8 for the two scenarios we discussed above. Figure 7.7 presents the effective stress path from laboratory test and simulation based on parameters back calculated. Since we assume no cohesion in the model, the failure line passes the origin and the end points (i.e., critical state) of both effective stress paths. Clearly, the model overestimates the peak deviatoric stress. It appears that the specimen started yielding from the beginning of the triaxial test, which may indicate it is normally consolidated under shearing. The different effective stress paths by laboratory test and model

may also indicate that diatomaceous soil does not follow the flow rule that Soft Soil model undertakes, which is further elaborated in later section 7.3.3.

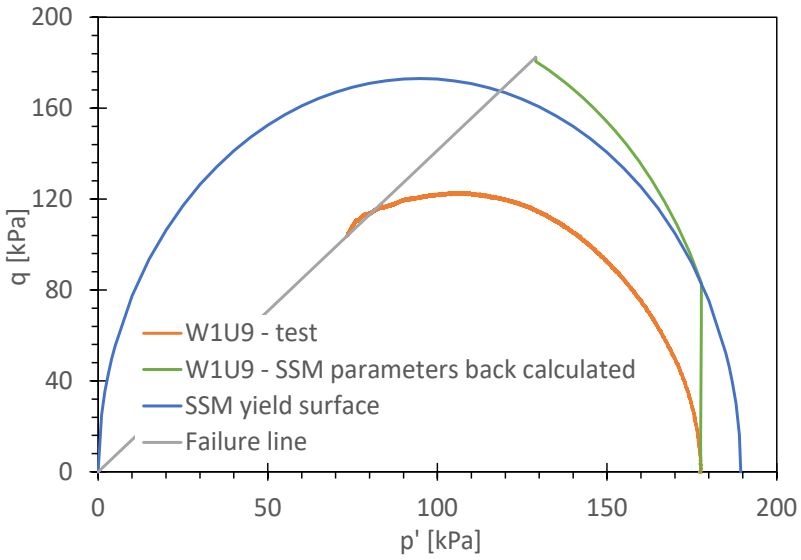

Figure 7.7: Stress path and yield surface for W1U9 (SSM with parameters back calculated from laboratory)

After we adjust the model parameters to match the peak deviatoric stress and the consolidation curve, the model yield surface and effective stress paths are presented in Figure 7.8. Because we introduce cohesion, the failure line does not pass the origin. It can be seen that during triaxial test, although there is slightly post-peak softening behavior, the excess pore water pressure generation is even more pronounced as p' keeps decreasing. Similar phenomena also happen in diatomaceous soil from literature discussed in 7.3.3.

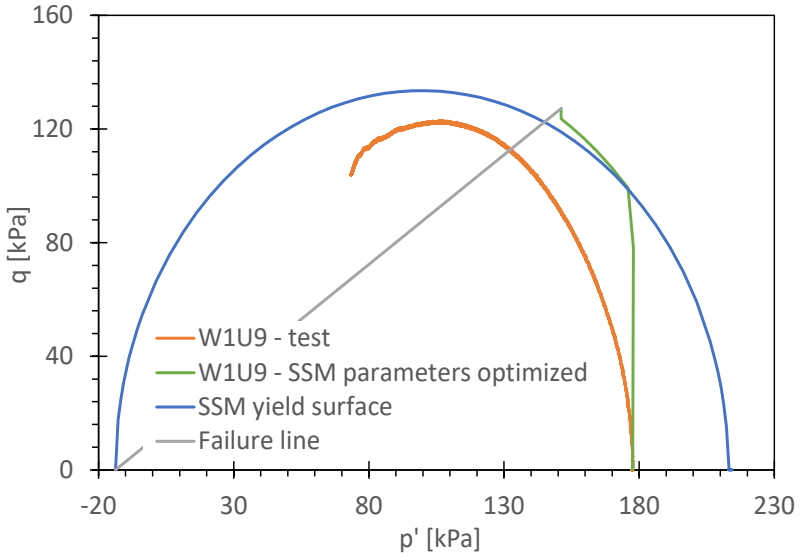

Figure 7.8: Stress path and yield surface for W1U9 (SSM with parameters optimized)

In short summary, the Soft Soil model is capable of capturing the peak deviatoric stress in triaxial tests and consolidation behaviors. However, the predicted effective stress path is somewhat different, if we tend to make the model have good predictions on peak deviatoric stress, the excess pore water pressure is usually underpredicted.

7.3.2 Model Calibration on Heavily-overconsolidated Specimen: W1U10 as an Example

In this section, we use the same procedure of calibration but on a heavily-overconsolidated specimen (W1U10) during triaxial test. The parameters back calculated from laboratory and test configurations are presented in Table 7.7 - Table 7.9. The overconsolidation ratio is about 2.4 (σ_p'/p_0').

Table 7.7: Back calculated parameters from laboratory results for W1U10

	Parameters	Value	Calculation or source
Basic parameters	λ^*	0.1305	$C_c = 0.788$, $e_0 = 1.627$, and Equations (7-58)
	κ^*	0.014	$C_r = 0.0425$, $e_0 = 1.627$, and Equations (7-61)
	ν	0.15	Reasonable assumption
	c' [kPa]	0	Not introducing cohesion yet
	ϕ_{cs}' [°]	39°	$\frac{6\sin\phi_{cs}'}{3-\sin\phi_{cs}'} = \frac{q_f}{p_f'}$, obtained from triaxial test
Miscellaneous parameters	K_0	0.3707	$K_0 = 1 - \sin\phi_{cs}'$
	M_{ss}	2.068	Equation (7-47)

Table 7.8: Triaxial test configuration for W1U10

Type of test	Direction	Consolidation	p_0' [kPa]	σ_p' [kPa]
Undrained	Compression	Isotropic	180	430.2

Table 7.9: Consolidation test configuration for W1U10

Type of test	σ_p' [kPa]	Strain - loading [%]	Strain - unloading [%]
CRS	430.2	15.87	1.032

The results from laboratory and numerical simulation based on parameters back calculated (i.e., Table 7.7) are presented in Figure 7.12. W1U10 exhibited more significant post-peak strain softening behavior during triaxial tests, but the Soft Soil model with laboratory back calculated parameters reasonably captured its peak deviatoric stress. Similarly, the excess pore water pressure is underpredicted by the model. Similar phenomenon in consolidation curve simulation is observed that the initial swelling stiffness is underpredicted. To calibrate the model, we assign small amount of cohesion and adjust λ^* and ϕ_{cs}' slightly. Table 7.10 summarizes the fitted parameters and the rationale. After calibration, we can see that the model better captures the consolidation behavior, and plots for triaxial test do not change significantly (Figure 7.9).

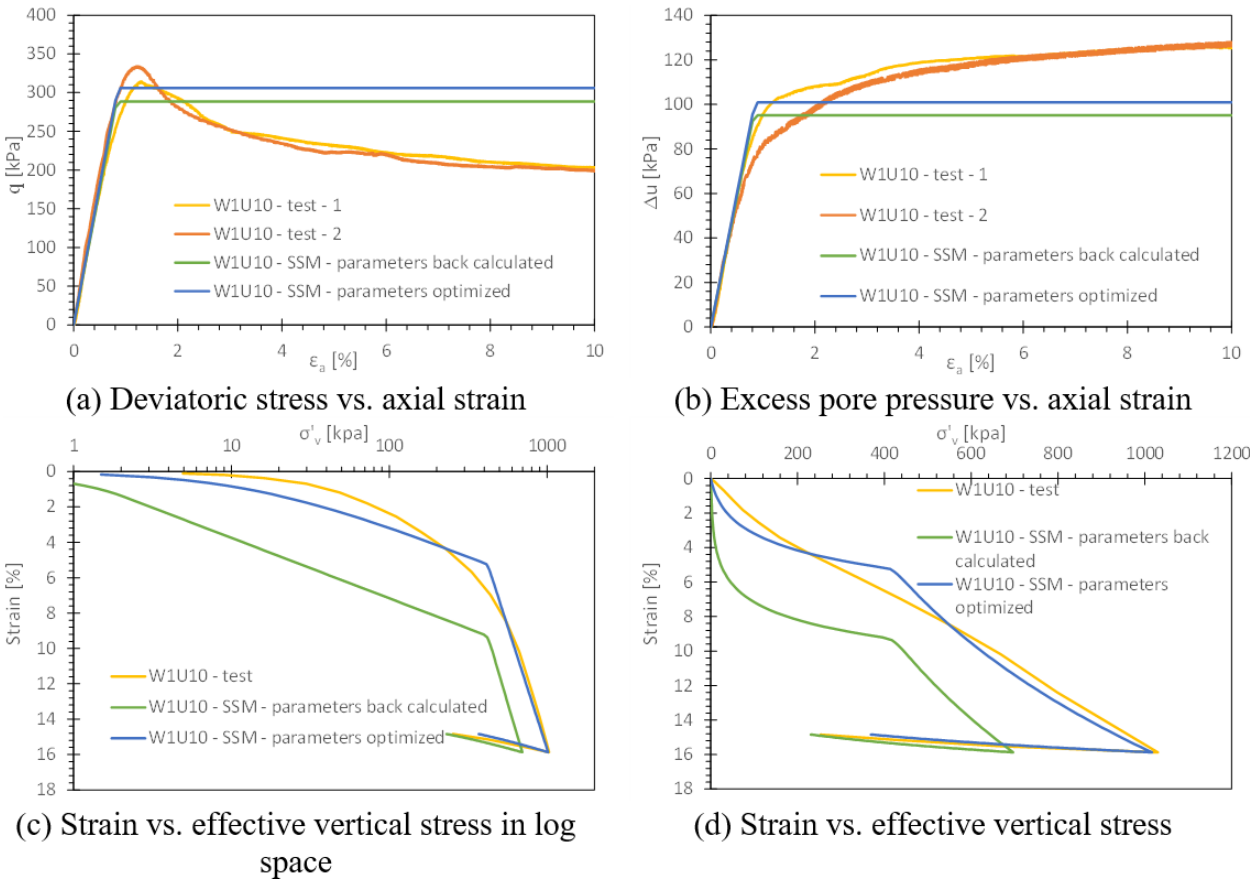

(a) Deviatoric stress vs. axial strain

(b) Excess pore pressure vs. axial strain

(c) Strain vs. effective vertical stress in log space

(d) Strain vs. effective vertical stress

Figure 7.9: Test curves from laboratory and Soft Soil Model (SSM) for W1U10

Table 7.10: Optimized SSM parameters for W1U10

	Parameters	Value	Rationale
Basic parameters	λ^*	0.12	Slightly lower to match virgin compression line
	κ^*	0.014	No need to adjust
	ν	0.15	It's a reasonable assumption and has little impact
	c' [kPa]	5	Assign small amount to increase K' (Equation (7-55))
	ϕ'_{cs} [°]	40°	Slightly increase to match the peak stress (by 1°)
Miscellaneous parameters	K_0	0.3572	Default setting, $K_0 = 1 - \sin\phi'_{cs}$
	M_{ss}	2.116	Default setting, Equation (7-47)

Parameters that determined the yield surface are summarized in Table 7.11. The effective stress paths and yield surface are plotted in Figure 7.10 and Figure 7.11.

Table 7.11: Parameters for yield surface calculation for W1U10

	Parameters back calculated from laboratory	Parameters optimized	Equation / source
c' [kPa]	0	5	Laboratory or optimized
ϕ'_{cs} [°]	39°	40°	Laboratory or optimized
K_0	0.3707	0.3572	$K_0 = 1 - \sin\phi'_{cs}$
M_{ss}	2.068	2.116	Equation (7-47)
σ'_p [kPa]	430.2	430.2	Laboratory
q [kPa]	270.8	276.5	$q = (1 - K_0) \cdot \sigma'_p$
p' [kPa]	249.7	245.9	$p' = \sigma'_p \cdot (1 + 2K_0)/3$
p^* [kPa]	249.7	251.8	$p^* = p' + c' \cot\phi'_{cs}$ (see Equation (7-48)
p^*_c [kPa]	318.4	319.7	Equation (7-48)
p'_c [kPa]	318.4	313.7	$p'_c = p^*_c - c' \cot\phi'_{cs}$

Here, we see that the effective stress paths from Soft Soil model deteriorated to be a vertical line that stops on the failure line. The Soft Soil model recedes to be the Mohr-Coulomb criterion when the OCR is greater than 2 (i.e., heavily overconsolidated). This matches the laboratory behavior of diatomaceous soil. For laboratory tests, after the soil reaches peak deviatoric stress, it decreases exhibiting strain-softening behavior, while the excess pore pressure continues generating.

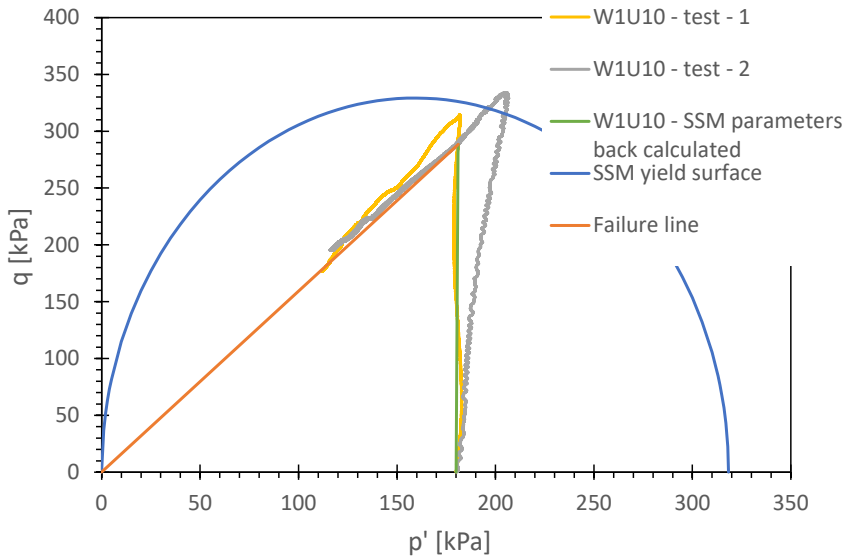

Figure 7.10: Stress path and yield surface for W1U10 (SSM with parameters back calculated from laboratory)

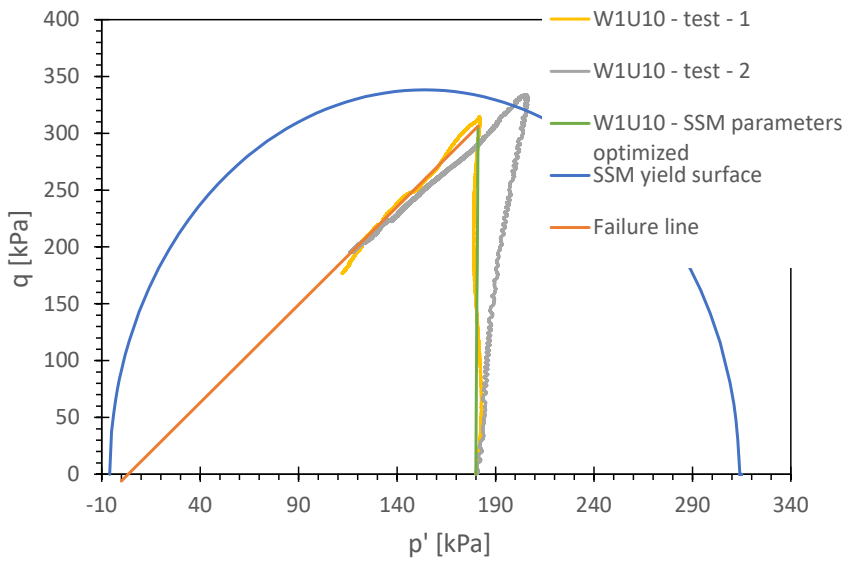

Figure 7.11: Stress path and yield surface for W1U10 (SSM with parameters optimized)

7.3.3 Model Calibration on Literature Data

While the Soft Soil Model is capable of capturing pre-peak stress-strain and oedometric compression behavior, model prediction of excess pore water pressure generation in diatomaceous soils does not match measured behavior. Typically, diatomaceous soils generate exceedingly high excess pore pressures, which implies a higher friction angle at constant deviatoric stress. To further explore this behavior, we use the Soft Soil Model to simulate diatomaceous soil behaviors reported in the literature. Specifically, we consider diatomaceous mudstone from Japan (Liao et al., 1998; Liao et al., 2003) and Chile (Ovalle and Arenaldi-Perisic, 2021) and diatomaceous soft-clay from Mexico City (Díaz-Rodríguez et al., 2009) and Bogota (Caicedo et al., 2018). Our approach is to adjust ϕ' to match the peak stress and κ^* to match the stiffness in triaxial test curves while λ^* is taken from reported compressive parameters. ν_{ur} is set as 0.15, and c' is set as 0 as we do not have the consolidation curves to calibrate. K_0 is used with the default value.

Liao et al. (2003) conducted triaxial tests and numerical analysis on Japanese diatomaceous mudstone from Noto Peninsula. They adopted a 3D EVP model (Yin and Graham, 1999) to simulate the triaxial behavior. While their results showed good agreement between the model and test results, here we attempt to use Soft Soil model to simulate their laboratory behavior. Liao et al. (2003) conducted triaxial tests on normally consolidated soil at $p_0' = 1.5, 2, 2.5, 3, 3.5\ MPa$ and reported a friction angle of $\phi' = 42.6°$ across all tested specimens.

However, in the Soft Soil Model, ϕ' varies with p_0'. The fitted parameters for the Soft Soil Model are shown in Table 7.12. Stress-strain and excess pore pressure-strain curves are shown in Figure 7.12. The Soft Soil Model captures the pre-peak stress-strain behavior in triaxial tests well, but not the peak excess pore pressure.

An interesting feature of normally consolidated diatomaceous soil tested in triaxial compression is that the excess pore pressure continues to be generated after the deviatoric stress reaches a steady state value. This phenomenon is observed in soft Bogota diatomaceous clay, as reported by Caicedo et al. (2018). Stress-strain plots and stress paths are shown in Figure 7.13. The stress-strain curves are well-predicted by the Soft Soil Model, and the character of the effective stress paths is captured, though there is some deviation from measured values. Another example is shown in Figure 7.14, where only effective stress paths were reported by Ovalle and Arenaldi-Perisic (2021). For $p_0' \leq 1800\ kPa$, the model captures the pre-peak stress path quite well, but does not match the excess pore pressure generation after peak deviatoric stress is reached.

Table 7.12: Fitted Soft Soil model parameters using laboratory data from Liao et al. (2003)

p_0' [kPa]	λ^*	κ^*	ν_{ur}	c [kPa]	ϕ' [°]
1.5	0.1664	0.03	0.2	0	42.64
2	0.1664	0.03	0.2	0	32
2.5	0.1664	0.03	0.2	0	28
3	0.1664	0.03	0.2	0	26
3.5	0.1664	0.03	0.2	0	27

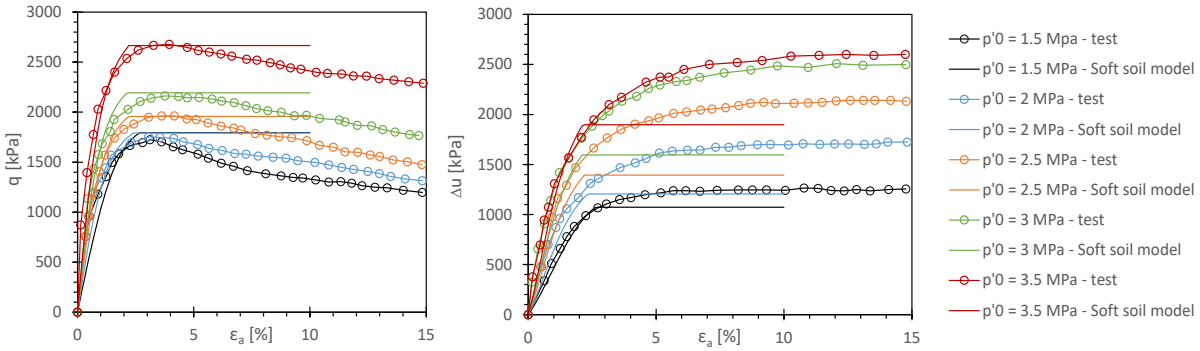

Figure 7.12: Soft soil model simulation, after (Liao et al., 2003)

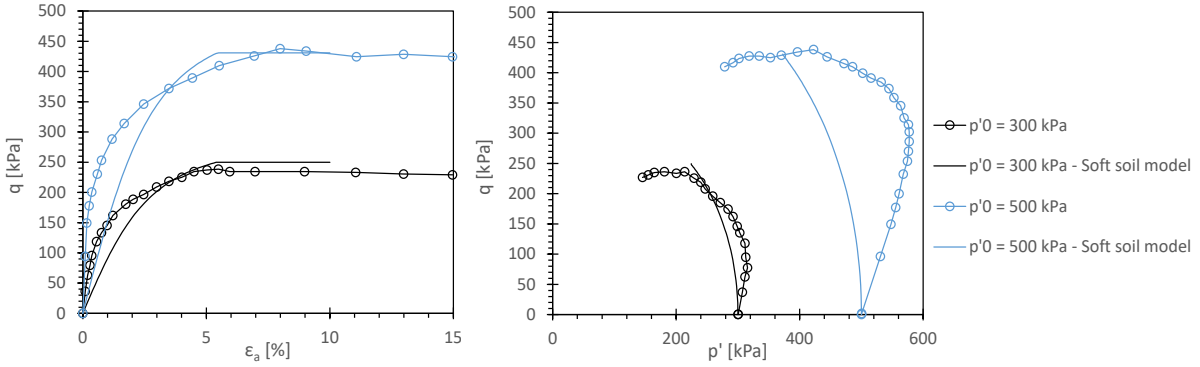

Figure 7.13: Soft soil model simulation, after (Caicedo et al., 2018)

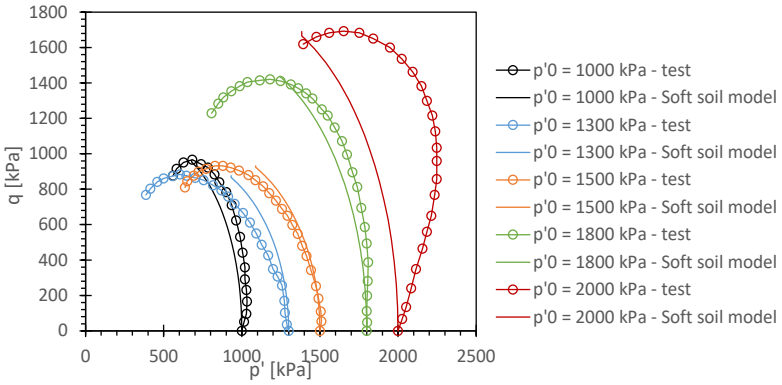

Figure 7.14: Soft soil model simulation, after (Ovalle and Arenaldi-Perisic, 2021)

8.0 PILE DESIGN IN DIATOMACEOUS SOIL

8.1 INTRODUCTION

Current design methodology for deep foundations in diatomaceous soils is often judgment-based rather than founded in analytical, numerical, or empirical design methods. This may result in costly project delays and change orders during construction due to the lack of reliable geotechnical engineering methods and standards of practice for building in these unique subsurface conditions. There have been limited case studies on deep foundation design or projects on diatomaceous soil. Yazdani et al. (2021) discussed the difficulties associated with driving closed-end pipe piles in a mudstone-like diatomaceous deposit at a site in Klamath County, OR, USA. High pile rebound resulting in premature refusal was observed for closed-end pipe piles in this project. Jardine et al. (1998) introduced a new effective stress design procedure for driven displacement piles in clay, termed the Imperial College Pile (ICP) design method, that exhibited promising performance in predicting capacity for load tests in two Japanese diatomaceous soil deposits. The ICP method was subsequently applied to driven piles in Mexico City clay (Saldivar and Jardine, 2005) and again showed reasonable agreement with pile load test results. In this chapter, the ICP design method is introduced, and several calculation examples are demonstrated.

8.2 IMPERIAL COLLEGE PILE METHOD IN CLAY

Pile design using the ICP method for diatomaceous soil should follow the design in clay method as opposed to the design in sand. Although the design method in sand is also introduced in section 8.3 in case of when diatomaceous deposits have sand layers.

8.2.1 Shaft Capacity

8.2.1.1 Overview

The ICP design method for shaft capacity is a modified application of the so-called "beta method" (β-method; Burland, 1973) for determination of pile shaft capacity. The β-method is a straightforward effective stress approach that models shaft capacity as an interface shear failure between a Mohr-Coulomb soil and a continuum counter face. As such, the shear stress required to cause failure may be expressed as Equation (8-1):

$$\tau_f = \sigma'_{rf} \tan(\delta_f) \quad \textbf{(8-1)}$$

where:

τ_f = local shear stress at failure;
σ'_{rf} = local radial effective stress at failure; and
δ_f = pile-soil interface friction angle.

Because pile failure is a large displacement problem, the effective stress cohesion (or, more appropriately, adhesion for a soil-continuum interface) is always neglected (i.e., $c' = 0$).

The normal effective stress on the interface (σ'_{rf}) must be known (or approximated) to determine the failure stresses. However, this is not a readily measurable quantity and is thus often computed using a lateral earth stress coefficient, K. Prior to pile installation, the lateral geostatic stress is typically defined using the coefficient of lateral earth stress at-rest, K_0: $\sigma'_r = K_0\sigma'_{v0}$. Pile installation massively disrupts the geostatic stress state, so K_0 is not appropriate for approximating the radial stresses acting on the pile. Rather, an empirically determined lateral stress coefficient, K_c, which can be computed in two ways (Equation (8-2) and (8-3)), is used in the ICP method:

$$\boldsymbol{K_c = \left[2.2 + 0.016\, OCR - 0.87\, \Delta I_{vy}\right] OCR^{0.42} \left(\frac{h}{R^*}\right)^{-0.2}} \tag{8-2}$$

$$\boldsymbol{K_c = \left[2.0 - 0.625\, \Delta I_{v0}\right] OCR^{0.42} \left(\frac{h}{R^*}\right)^{-0.2}} \tag{8-3}$$

where:
ΔI_{vy} = sensitivity parameter referenced to void ratio at yield vertical effective stress, see Section 8.2.1.2;
ΔI_{v0} = sensitivity parameter referenced to void ratio at *in-situ* vertical effective stress, see Section 8.2.1.2;
h = distance from the point of stress calculation to the pile tip; and
R^* = characteristic radius of the pile and $h/R^* \geq 8$.

Thus, prior to loading, the lateral stress on the pile may be approximated by $\sigma'_{rc} = K_c\sigma'_{v0}$ where σ'_{v0} is the *in-situ* vertical effective stress. Stress measurements during pile load tests (McClelland, 1974) have shown a decrease in radial effective stress from post-installation equalized at-rest conditions (σ'_{rc}) to the failure state (σ'_{rf}). As such, the ICP method recommends a reduction factor when calculating the lateral stress on the pile at failure:

$$\boldsymbol{\sigma'_{rf} = 0.8\sigma'_{rc}} \tag{8-4}$$

$$\boldsymbol{\sigma'_{rc} = K_c\sigma'_{v0}} \tag{8-5}$$

The pile characteristic radius (R^*) depends on pile geometry – closed-end, open-end, or square. It may be calculated as shown below.

Closed-end pipe piles:

$$\boldsymbol{R^* = R} \tag{8-6}$$

Open-end pipe piles:

$$\boldsymbol{R^* = \sqrt{\left(R_o^2 - R_i^2\right)}} \tag{8-7}$$

Solid square-section piles:

$$\boldsymbol{R^* = \frac{b}{\sqrt{\pi}}} \tag{8-8}$$

where:

R_o = outer radius of an open-end pile;
R_i = inner radius of an open-end pile; and
b = side width of a square section pile.

Additional details about model input parameters are provided hereinafter.

8.2.1.2 Sensitivity parameters

The ICP method uses a sensitivity parameter to capture the behavior of soils in response to pile driving, which effectively remolds the soil in the vicinity of the pile (Figure 8.1). The sensitivity S_t of a soil is typically defined as the ratio of its intact shear strength to its fully remolded shear strength (i.e., Equation (8-9)):

$$S_t = \frac{s_{u0}}{s_{ur}} \tag{8-9}$$

where:

S_t = sensitivity;
s_{u0} = peak undrained shear strength; and
s_{ur} = fully remolded shear strength.

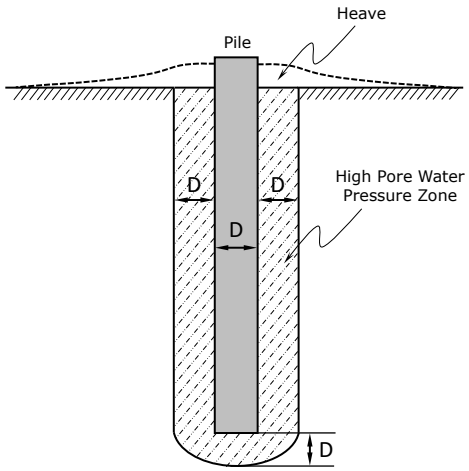

Figure 8.1: Schematic representation of the region of highly disturbed (i.e., remolded) soil in the vicinity of a large displacement pile (after Hannigan et al., 2016)

In practice, s_{u0} is often determined through unconsolidated undrained (UU) triaxial tests on intact specimens, but there is considerable variability in the measured strength values. This may be somewhat mitigated by using s_{u0} values from K_0–consolidated undrained triaxial compression (CK_0UC) tests or *in-situ* test data. The remolded shear strength (s_{ur}) can be measured in UU tests, but in the absence of test data may be calculated using Equations (8-10) and (8-11) (Wroth, 1979).

$$\boldsymbol{s_{ur} = 1.7\ \text{kPa} \cdot \left[10^{2(1-LI)}\right]} \tag{8-10}$$

$$\boldsymbol{LI = \frac{w - PL}{LL - PL}} \tag{8-11}$$

Where LI is the liquidity index of the soil and w is its water content. Equation (8-10) represents a logarithmic decrease in shear strength from 170 kPa at the PL to 1.7 kPa at the LL, which are generally accepted values for remolded soils (e.g., Norman, 1958; Youssef, 1965; Sherwood and Ryley, 1970). Once the sensitivity of the soil is known, the ICP method sensitivity parameter may be calculated:

OC soils:

$$\boldsymbol{\Delta I_{vy} = \log_{10} S_t} \tag{8-12}$$

NC or lightly OC soils:

$$\boldsymbol{\Delta I_{v0} \approx \log_{10} \frac{S_t}{OCR}} \tag{8-13}$$

However, due to the difficulties associated with measuring reliable sensitivities in triaxial tests, Jardine et al. (2005) recommended that oedometrically-based sensitivity parameters

be used in the ICP method. These definitions of ΔI_{vy} and ΔI_{v0} are presented graphically in Figure 8.2. The solid line represents the measured oedometric compression curve for an undisturbed specimen, and the dashed line represents the intrinsic compression line (ICL). The ICL was defined by Burland (1990) as the oedometric compression line of a remolded specimen slurry-reconstituted at a water content equal to 125% of the liquid limit. The definitions for ΔI_{vy} and ΔI_{v0} are expressed mathematically in Equation (8-14) and (8-15).

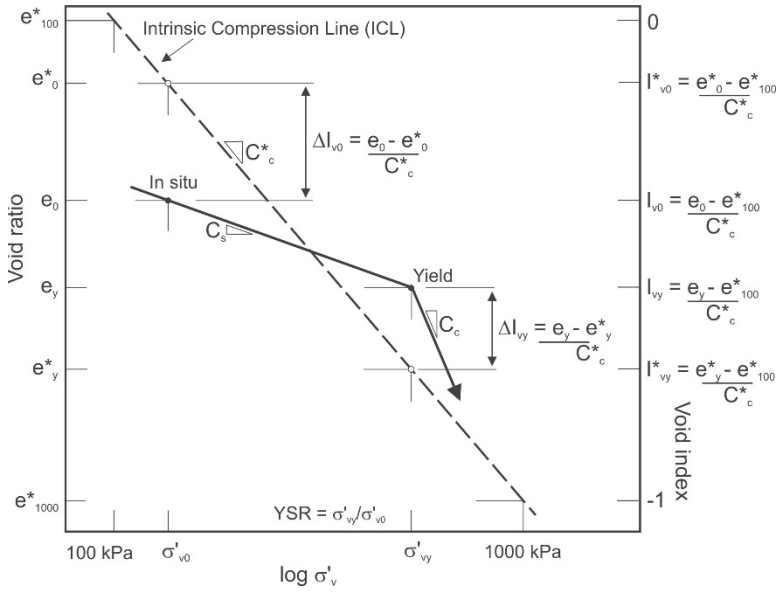

Figure 8.2: Definitions of sensitivity parameters ΔI_{vy} and ΔI_{v0} (after Jardine et al., 2005)

$$\Delta I_{vy} = \frac{e_y - e_y^*}{C_c^*} \tag{8-14}$$

$$\Delta I_{v0} = \frac{e_0 - e_0^*}{C_c^*} \tag{8-15}$$

where:

e_y = corresponding void ratio at yield stress on the compression curve of the undisturbed specimen;

e_y^* = corresponding void ratio at yield stress on the ICL of the reconstituted specimen;

e_0 = initial void ratio at *in-situ* vertical effective stress of the undisturbed specimen;

e_0^* = corresponding void ratio at *in-situ* vertical effective stress on the ICL of the reconstituted specimen; and

C_c^* = the compression index on the ICL.

When results from an oedometer test on a reconstituted specimen is not available, the empirical correlations given in Equation (8-16) and (8-17) may be used to develop the ICL (Burland, 1990):

$$e_{100}^{*} = 0.109 + 0.679e_L - 0.089e_L^2 + 0.016e_L^3 \quad \textbf{(8-16)}$$

$$C_c^{*} = 0.256e_L - 0.04 \quad \textbf{(8-17)}$$

where:
e_{100}^{*} = the void ratio at 100 kPa on ICL; and
e_L = the void ratio at the LL of the reconstituted specimen.

According to Jardine et al. (2005), determination of ΔI_{vy} or ΔI_{v0} by Equation (8-14) or (8-15) is less prone to error than the approximation by Equation (8-12), although it would be helpful to check both methods against each other.

8.2.1.3 Interface friction angle

Ideally, the interface friction angle between the pile material and the host soil is measured using laboratory tests, such as the ring shear interface test (e.g., Yoshimi and Kishida, 1981). Interface strength will be a function of the normal effective stress level, pile surface roughness, shearing history, strain rate, and median particle size of the soil (Uesugi and Kishida, 1986a; b; Uesugi et al., 1988; Frost et al., 2004). However, this is a highly specialized test that is typically not available as a matter of course. Thus, the interface friction angle is often approximated as some fraction of the critical state friction angle (ϕ') of the soil, typically between $2\phi'/3$ and ϕ' (e.g., Potyondy, 1961; Aksoy et al., 2018). Jardine et al. (2005) noted that there is no universal relationship between δ_f and PI, with diatomaceous Mexico City clay having both high PI and high δ_f being a prime example.

8.2.1.4 Calculation procedure

The ICP design method for shaft resistance in clay soils is summarized below.

a) Divide the shaft into sufficiently short sections

The shaft should be divided into sufficiently short sections in accordance with the soil layering and variations. Jardine et al. (2005) recommended at least 15 subdivisions regardless of how uniform the soil profile is.

b) Calculate the local shear stress (τ_f) at each subdivision

The sequential procedures are as follows:

- Calculate pile characteristic radius (R^*) based on pile geometry following Equations (8-6) to (8-8).

- At the relevant depth, determine the distance to the pile tip (h), OCR, and ΔI_{vy} (or ΔI_{v0}). Calculate ΔI_{vy} by Equation (8-12) or (8-14); or calculate ΔI_{v0} by Equation (8-13) or (8-15).

- Calculate the lateral stress coefficient (K_c) by Equation (8-2) or (8-3). Recall $h/R^* \geq 8$.

- Compute local radial effective stress at failure (σ'_{rf}) using Equations (8-4) and (8-5).

- Using the pile-soil interface friction angle (δ_f) calculate the local shear stress at failure (τ_f) using Equation (2-1).

Repeat the calculations for each subdivision to obtain the local shear stress (τ_f) along the pile profile.

c) Integrate the shear stresses (τ_f) along the length of the embedded shaft

The shaft resistance capacity (Q_s) can be calculated using Equation (8-18).

$$\boldsymbol{Q_s = \pi D \int_0^L \tau_f \, dz} \qquad \textbf{(8-18)}$$

where:

Q_s	=	ultimate shaft resistance;
z	=	depth below ground surface, positive downward;
L	=	pile length; and
D	=	diameter of the pile.

8.2.2 Base Resistance

Base resistance usually comprises a relatively small fraction of the total capacity of floating deep foundations (i.e., those that are not driven to a competent bearing stratum). For the ICP method, Jardine et al. (2005) propose that base resistance be computed using CPT tip resistance rather than more conventional s_u–based approaches.

8.2.2.1 Closed-ended piles

The base capacity (Q_b) for closed-ended piles is calculated using Equations (8-19) – (8-22):

Circular cross-section:

$$\boldsymbol{Q_b = \frac{q_b \pi D^2}{4}} \qquad \textbf{(8-19)}$$

Square cross-section:

$$\boldsymbol{Q_b = q_b b^2} \tag{8-20}$$

For undrained loading:

$$\boldsymbol{q_b = 0.8 q_t} \tag{8-21}$$

For drained loading:

$$\boldsymbol{q_b = 1.3 q_t} \tag{8.22}$$

where:
Q_b = ultimate base (toe) resistance; and
q_t = CPT tip resistance averaged over 1.5 pile diameters above and below the pile toe.

8.2.2.2 Open-end piles

Toe resistance for an open-end pile depends on whether the pile is fully plugged. A simplified empirical criterion may be used to determine whether a pile is fully plugged. If Equation (8-23) is satisfied, then the pile may be considered as plugged.

$$\boldsymbol{\frac{D_i}{D_{CPT}} + \frac{0.45 q_t}{p_a} < 36} \tag{8-23}$$

where:
D_i = inner diameter of the pile;
D_{CPT} = diameter of CPT probe, value for standard size is 35.7 mm; and
p_a = atmospheric pressure (101.3 kPa).

For fully plugged open-end piles, Q_b is calculated using Equation (8-19) or (8-20), but with the following modifications to q_b:

For undrained loading:

$$\boldsymbol{q_b = 0.4 q_t} \tag{8-24}$$

For drained loading:

$$\boldsymbol{q_b = 0.65 q_t} \tag{8-25}$$

For unplugged open-end piles, Q_b is calculated by Equation (8-26):

$$\boldsymbol{Q_b = q_{ba} \pi \left(R_o^2 - R_i^2 \right)} \tag{8-26}$$

For undrained loading:

$$q_{ba} = q_t \tag{8-27}$$

For drained loading:

$$q_{ba} = 1.6q_t \tag{8-28}$$

8.2.3 Total Pile Capacity

Once the shaft capacity and base resistance have been calculated, the total single pile capacity (Q_t) is the sum of Q_s and Q_b, as shown in Equation (8-29).

$$Q_t = Q_s + Q_b \tag{8-29}$$

8.3 IMPERIAL COLLEGE PILE METHOD IN SANDS

The focus of this work is on the engineering behavior of diatomaceous soils, but piles are generally installed through layered subsurface profiles. The ICP design method for sands can be used when a site contains sandy strata. Thus, this method is presented briefly below for completeness. We also note that, while diatomaceous soils are fine-grained, they also exhibit some behaviors more often associated with coarse-grained soils, such as high effective stress friction angles and rapid dissipation of excess pore water pressure. As such, some aspects of the ICP sand method that could be applicable to diatomaceous soils.

8.3.1 Shaft Capacity

The framework for predicting shaft capacity in sands is similar to that used for clays. Specifically, the failure envelope for the shaft-soil interface system is assumed to be of the Mohr-Coulomb type, similar to that described by Equation (2-1). However, the manner by which the inputs for that calculation are determined is somewhat different. Specifically, Equations (8-30) through (8-35) are used to compute shaft capacity for a pile embedded in sand:

$$\tau_f = \sigma'_{rf} \tan(\delta_{cv}) \tag{8-30}$$

$$\sigma'_{rf} = \sigma'_{rc} + \Delta\sigma'_{rd} \tag{8-31}$$

$$\sigma'_{rc} = 0.029q_t \left(\frac{\sigma'_{v0}}{p_a}\right)^{0.13} \left(\frac{h}{R^*}\right)^{-0.38} \tag{8-32}$$

$$\Delta\sigma'_{rd} = 2G\,\frac{\Delta r}{R} \tag{8-33}$$

$$G = \frac{q_t}{[0.0203 + 0.00125\eta - 1.216 \cdot 10^{-6}\eta^2]} \quad \textbf{(8-34)}$$

$$\eta = \frac{q_t}{\sqrt{p_a \sigma'_{v0}}} \quad \textbf{(8-35)}$$

where:
δ_{cv} = constant volume (i.e., failure) interface friction angle;
$\Delta\sigma'_{rd}$ = the dilatant increase in local radial effective stress during pile loading; and
Δr = a quantifier of pile surface roughness, ($= 0.02\ mm$ for lightly rusted steel piles, but should be evaluated case by case, may be higher for concrete piles).

Other terms are as previously defined and $h/R^* \geq 8$. The steps for calculation for shaft capacity in sand are generally consistent with the calculation in clay. The steps are summarized as follows:

1. Divide the shaft into sufficiently short sections

The shaft should be divided into sufficiently short sections in accordance with the soil layering and variations. Jardine et al. (2005) recommended at least 15 subdivisions regardless of how uniform the soil profile is.

2. Calculate the local shear stress (τ_f) at each subdivision

The sequential procedures are as follows:

- Calculate pile characteristic radius (R^*) based on pile geometry following Equations (8-6) to (8-8).
- At each depth, find the CPT resistance (q_t) and *in-situ* vertical effective stress (σ'_{v0}) and calculate the local radial effective stress (σ'_{rc}) using Equation (8-32) with $h/R^* \geq 8$.
- Use Equations (8-33) to (8-35) to calculate $\Delta\sigma'_{rd}$.This is the dilatant increase in local radial effective stress observed during pile loading ($\Delta\sigma'_{rd}$) in the ICP field tests (Jardine et al. 2005).
- The local radial effective stress at failure (σ'_{rf}) is then the sum of σ'_{rc} and $\Delta\sigma'_{rd}$, i.e., Equation (8-31).
- Determine the pile-soil interface friction angle (δ_{cv}) from the ring shear test or estimate from d_{50} using Figure 8.3.
- Finally, calculate the local shear stress (τ_f) using Equation (8-30).

Repeat the calculations for each subdivision to obtain the local shear stress (τ_f) along the pile profile.

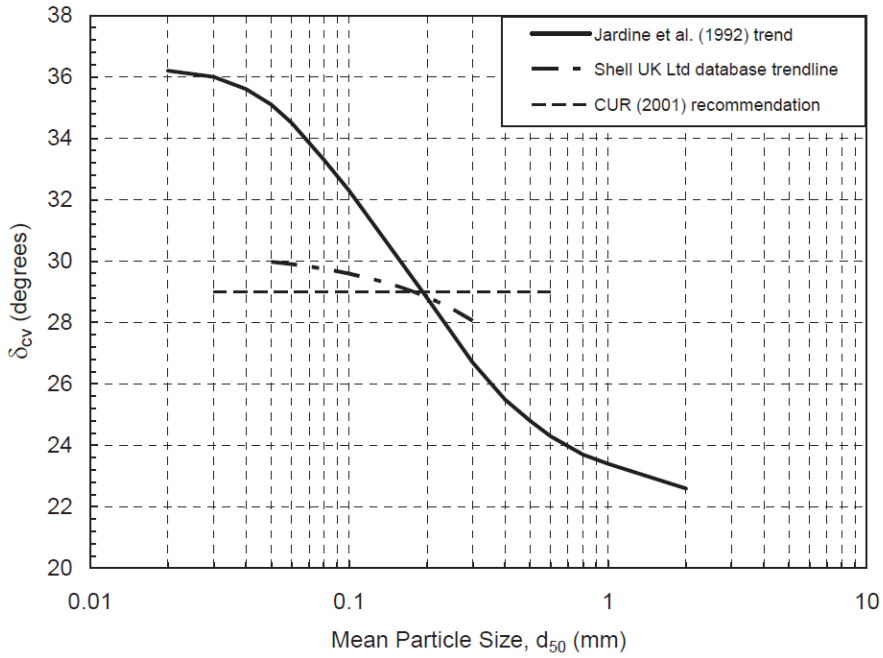

Figure 8.3: Interface friction angle in sand (δ_{cv}) empirically correlated with d_{50} (after Jardine et al., 2005)

3. Integrate the shear stresses (τ_f) along the embedded shaft

The shaft resistance capacity (Q_s) can be calculated using Equation (8-18).

8.3.2 Base Resistance

Similar to the case of clay, the base resistance in sand is computed using CPT tip resistance as well, and is illustrated in Sections 8.3.2.1 and 8.3.2.2.

8.3.2.1 Closed-end piles

The base capacity (Q_b) for closed-ended piles is calculated using Equations (8-36) – (8-38).

$$q_b = q_t \left[1 - 0.5 \log\left(\frac{D}{D_{CPT}}\right)\right] \quad \textbf{(8-36)}$$

Circular cross-section:

$$\boldsymbol{Q_b = \frac{q_b \pi D^2}{4}}$$

(8-37)

Square cross-section:

$$\boldsymbol{Q_b = q_b b^2}$$

(8-38)

where:

q_b = unit base resistance, $\geq 0.3\ q_t$;
D = pile diameter; and
D_{CPT} = diameter of CPT probe, value for standard size is 35.7 mm.

8.3.2.2 Open-end piles

Toe resistance for an open-end pile depends on whether the pile is fully plugged. A pile may be considered to be fully plugged if Equations (8-39) and (8-40) are satisfied.

$$\boldsymbol{D_i < 0.02\ (D_r - 30)}$$

(8-39)

$$\boldsymbol{\frac{D_i}{D_{CPT}} < 0.083\ \frac{q_t}{p_a}}$$

(8-40)

where:

D_i = inner diameter of the pile, in meters;
D_r = relative density of the sand, in %;

For fully plugged open-end piles, Q_b is calculated using Equations (8-41) and (8-42):

$$\boldsymbol{q_b = q_t \left[0.5 - 0.25\ \log_{10}\left(\frac{D}{D_{CPT}}\right)\right]}$$

(8-41)

$$\boldsymbol{Q_b = q_b \pi R_o^2}$$

(8-42)

For unplugged open-end piles, Q_b is calculated by Equations (8-43) and (8-44):

$$q_{ba} = q_t$$

(8-43)

$$Q_b = q_{ba}\pi\left(R_o^2 - R_i^2\right)$$

(8-44)

8.3.3 Total pile capacity

With the shaft capacity and base resistance, the total single pile capacity (Q_t) is simply the sum of Q_s and Q_b, shown in Equation (8-29).

8.4 CASE STUDIES

8.4.1 Example Calculation: Saldivar and Jardine (2005)

Saldivar and Jardine (2005) implemented ICP design method for concrete piles driven in Mexico City clay and compared results with the measured pile capacity. This section demonstrates the reproducibility of the ICP method on one of the driven piles, Pile BC12. The pile dimensions and soil/site properties are summarized in Table 8.1.

Table 8.1: Basic site, pile, and soil properties for Pile BC12 in Saldivar and Jardine (2005)

Category	Parameter	Value
Site	Ground water table	6 m
Pile dimensions	Pile length	22 m
	Pre-boring length	14.5 m
	Side width (b)	0.5 m
	R^* (Equation (8-8))	0.282 m
Soil properties	S_t	11.9
	ΔI_{vy} (Equation (8-12))	1.0755
	δ_f	36°
	OCR	2
	γ	11.3 kN/m^3

The pile (BC 12) has a pre-boring length of 14.5 m, and the total length is 22 m. Therefore, the shaft capacity should be calculated from depth 14.5 to 22 m. We divided the pile shaft into 0.5-m sections and considered the middle depth of each section as the representative depth for this section. There are a total of 15 subdivisions when calculating the shaft capacity. The calculation of shaft capacity between 14.5 – 15 m is summarized in Table 8.2; the same calculation procedures should be followed for each subdivision. The detailed shaft capacities at each

subdivision are summarized in Appendix H. The total shaft capacity of Pile BC 12 is calculated to be 783.2 kN.

Table 8.2: Shaft capacity calculation at 14.5 - 15 m subdivision for Pile BC 12 in Saldivar and Jardine (2005)

Parameter	Value	Equation
Depth range of subdivision	14.5 – 15 m	–
Δz	0.5 m	$15\ m - 14.5\ m = 0.5\ m$
Representative depth	14.75 m	$(15\ m\ +\ 14.5\ m)/2 = 14.75\ m$
h	7.25 m	$22\ m - 14.75\ m = 7.25\ m$
h/R^*	25.7	$7.25\ m/0.282\ m = 25.7$
K_c	0.91	Equation (8-2)
σ_{v0}	166.68 kPa	$11.3\ kN/m^3 \times 14.75\ m = 166.68\ kPa$
u	85.75 kPa	$9.8\ kN/m^3 \times (14.75\ m - 6\ m) = 85.75\ kPa$
σ'_{v0}	80.93 kPa	$166.68\ kPa - 85.75\ kPa = 80.93$ kPa
σ'_{rc}	73.65 kPa	$\sigma'_{rc} = K_c\sigma'_{v0} = 0.91 \times 80.93\ kPa$
σ'_{rf}	58.92 kPa	$\sigma'_{rf} = 0.8\sigma'_{rc} = 0.8 \times 73.65\ kPa$
τ'_f	42.81 kPa	$\tau_f = \sigma'_{rf}\tan(\delta_f) = 58.92\ kPa \times \tan 36^\circ$
$\tau'_f \cdot \Delta z$	21.40 kN/m	$42.81\ kPa \times 0.5\ m = 21.40\ kN/m$
ΔQ_s	42.8 kN	$21.40\ \ kN/m \times 0.5\ m \times 4 = 42.8\ kN$

To calculate the base resistance, the cone tip resistance (q_t) is needed. Saldivar and Jardine (2005) provided the CPT tip resistance profile in the deposit of Mexico City clay. For the demonstration, q_t is taken as 1200 kPa at depth 22 m. Then based on Equations (8-20) and (8-21), the base resistance (Q_b) is 240 kN, as shown in Table 8.3.

Table 8.3: Base resistance calculation for Pile BC 12 in Saldivar and Jardine (2005)

Parameter	Value	Equation
q_t	1200 kPa	–
q_b	960 kPa	$q_b = 0.8q_t = 0.8 \times 1200\ kPa$
Q_b	240 kN	$Q_b = q_b b^2 = 960\ kPa \times (0.5\ m)^2$

Finally, the total pile capacity (Q_t) is the sum of Q_s and Q_b. Table 8.4 summarizes the results from this demonstration and Saldivar and Jardine (2005). Our result is consistent with the results provided by Saldivar and Jardine (2005), demonstrating correct implementation of the ICP method for clays.

Table 8.4: Results comparison for Pile BC 12 in Saldivar and Jardine (2005)

Parameter	Value	Source
Q_t	1023 kN	Demonstration in the current section
Q_t	1013 kN	Total resistance calculated in Saldivar and Jardine (2005)
Q_m	1048 kN	Total resistance measured in Saldivar and Jardine (2005)

8.4.2 Example Calculation: Yazdani et al. (2021)

There have only been limited cases of pile installation in diatomaceous soil reported in the literature. Two references (Jardine et al., 1998; Saldivar and Jardine, 2005) were related to application of the ICP method in Japanese and Mexico City clays, both of which contain a high proportion of diatoms in addition to their clay minerals. Yazdani et al. (2021) reported a case study of a driven pile foundation in diatomaceous soil located in Buck Creek, OR. Unexpected high pile rebound was observed during driving a closed-end pipe pile, and open-end piles were subsequently driven. In this section, we apply the ICP method for clays to compute the capacity of one pile (B2P2) and compare to the pile resistance from CAPWAP and WEAP measurements obtained during driving.

8.4.2.1 Parameter determination

In order to apply ICP method, the sensitivity parameters (ΔI_{vy} or ΔI_{v0}) are needed. As introduced in section 8.2.1.2, ΔI_{vy} (or ΔI_{v0}) can be determined from oedometric compressive behaviors or shear behaviors. However, neither the ICL nor S_t is provided by Wang et al. (2021) or Yazdani et al. (2021). Therefore, it is necessary to estimate the ICL from empirical correlations or to assume S_t. In this section, we will use different approaches to estimate the sensitivity parameters and evaluate different results.

The location of the ICL in $e - \log \sigma_v'$ is specified by e_{100}^* and C_c^*, which are empirically correlated with e_L, as discussed previously. The parameters (G_s, LL) to calculate e_L as well as e_{100}^* and C_c^* are summarized in Table 8.5.

Table 8.5: Basic parameters to determine the ICL

Parameter	Value	Source or equation
G_s	2.28	Wang et al. (2021)
LL	142	Wang et al. (2021)
e_L	3.24	$e_L = G_s \times LL$
e_{100}^*	1.920	Equation (8-16)
C_c^*	0.790	Equation (8-17)

The consolidation curves of undisturbed soil samples reported in Wang et al. (2021) are simplified to two-straight lines in $e - \log \sigma_v'$ space. The consolidation test curve and simplified consolidation curve are plotted in Figure 8.4. The parameters to determine the simplified consolidation curve are summarized in Table 8.6.

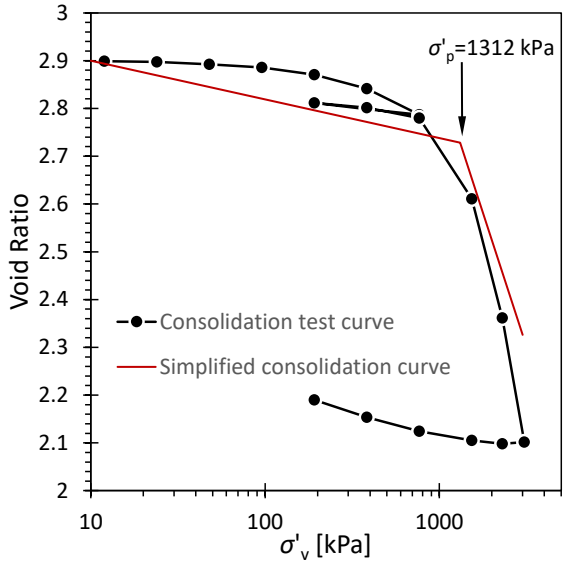

Figure 8.4: Consolidation curve on an undisturbed specimen from Buck Creek

Table 8.6: Basic parameters to determine consolidation curve on undisturbed specimen

e_0	σ'_{v0} [kPa]	σ'_p [kPa]	C_c	C_r	OCR
2.90	38.1	1312	1.12	0.081	34

With parameters summarized in Table 8.5 and Table 8.6, we can plot the ICL and the simplified consolidation curve on undisturbed soil sample in $e - \log \sigma_v'$ space, shown in Figure 8.5. The sensitivity parameters can then be computed by Equations (8-14) and (8-15). Although we lack data on S_t for this case study, Jardine et al. (1998) and Saldivar and Jardine (2005) report S_t to be around 10 for diatomaceous soils. Thus, we assume that it is reasonable to use $S_t = 10$ for this case study and computer ΔI_{vy} by Equation (8-12) as well. Thus, we use three approaches to estimate the sensitivity parameters and summarize them in Table 8.7.

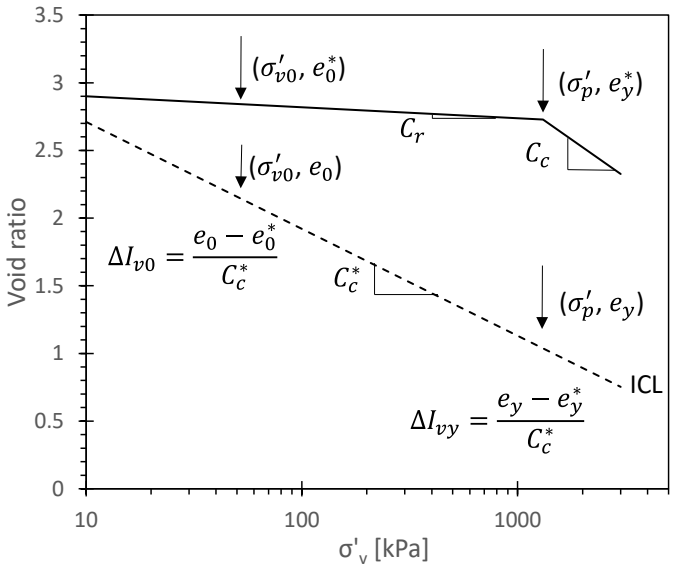

Figure 8.5: The correlated ICL (dashed line) and consolidation curve (solid line) from undisturbed soil sample for the case study Wang et al. (2021)

Table 8.7: Sensitivity parameters from different approaches

Parameters	Value	Source
ΔI_{vy}	2.141	Figure 8.5 and Equation (8-14)
ΔI_{v0}	0.822	Figure 8.5 and Equation (8-15)
ΔI_{vy}	1	Assume $S_t = 10$ and Equation (8-12)

The pile-soil interface friction angle (δ_f) for this case study is assumed to be 35° due to lack of data. This is reasonable for diatomaceous soil as the soil tends to have quite high friction angle, as high as $40^\circ - 55^\circ$, with δ_f typically between $2\phi'/3$ and ϕ' (e.g., Potyondy 1961; Aksoy et al. 2018). Saldivar and Jardine (2005) reported the Mexico City clay with $\delta_f = 36^\circ$. Jardine et al. (1998) reported two Japanese diatomaceous soils with $\delta_f = 25^\circ - 29^\circ$. Both imply that 35° is a reasonable approximation of δ_f for diatomaceous soil.

With the discussions on ΔI_{vy}, ΔI_{v0}, and δ_f above, the other paramters are relatively straightforward. Yazdani et al. (2021) reported the pile dimensions, while the companion paper (Wang et al. 2021) reported the results of site investigation: soil profiles, soil parameters, and CPTu results. A summary of necessary parameters is shown in Table 8.8. Note that the sand parameters are estimated and the default value of $\Delta r = 0.02\ mm$ (related to roughness of pile surface) is used. These estimated parameters (Δr, δ_{cv}, γ_{sand}) are all for the shaft resistance calculation in the sand layer which is a smaller portion of the total shaft resistance.

Table 8.8: Basic site, pile, and soil properties of Pile B2P2 in Wang et al. (2021) and Yazdani et al. (2021)

Category	Parameter		Value
Site	Groundwater table depth		2.7 m
	Sand layer		0 – 4 m
	Diatomaceous soil layer		4 – 17 m
Pile dimensions or property	Pile length		16.2 m
	Outer diameter (D_o)		0.4064 m
	Inner diameter (D_i)		0.3874 m
	R^* (Equation (8-7))		0.0615 m
	Δr		0.02 mm
Diatomaceous soil properties	γ		13 kN/m^3
	OCR		34
	Sensitivity parameters	ΔI_{vy} (Figure 8.5 and Equation (8-14))	2.141
		ΔI_{v0} (Figure 8.5 and Equation (8-15))	0.822
		ΔI_{vy} (Assume $S_t = 10$ and Equation (8-12))	1
	δ_f		35°
Sand properties	δ_{cv}		30°
	γ_{sand}		17 kN/m^3

8.4.2.2 Calculation demonstration

The sand layer exists in the upper 4 m, we divide into 0.05-m intervals to obtain 80 subdivisions. We demonstrate the shaft resistance calculation for the 1 – 1.05 m section, as shown in Table 8.9. The same calculation procedures should be repeated for each subdivision. The detailed shaft capacities at each subdivision are summarized in Appendix H. The total shaft capacity of Pile B2P2 in the sand layer (0-4 m) is calculated to be 71.4 kN.

Table 8.9: Shaft capacity calculation at 1 – 1.05 m subdivision for Pile B2P2 in Yazdani et al. (2021)

Parameter	Value	Source or equation
Depth range of subdivision	1 – 1.05 m	–
Δz	0.05 m	$1.05\ m - 1\ m = 0.05\ m$
Representative depth	1.025 m	$(1.05\ m + 1\ m)/2 = 1.025\ m$
h	15.175 m	$16.2\ m - 1.025\ m = 15.175\ m$
h/R^*	246.75	$15.175\ m/0.0615\ m = 246.75$
q_t	1696 kPa	Wang et al. (2021)
σ'_{v0}	17.43 kPa	$17\ kN/m^3 \times 1.025\ m = 17.43\ kPa$
σ'_{rc}	4.82 kPa	Equation (8-32)
η	40.37	Equation (8-35)
G	24.659 MPa	Equation (8-34)
$\Delta\sigma'_{rd}$	4.85 kPa	Equation (8-33)
σ'_{rf}	9.68 kPa	Equation (8-31)
τ'_f	5.59 kPa	Equation (8-30)
$\tau'_f \cdot \Delta z$	0.28 kN/m	$5.59\ kPa \times 0.05\ m = 0.28\ kN/m$
ΔQ_s	0.36 kN	$0.28\ kN/m \times 0.4064\ m \times \pi = 0.36\ kN$

The shaft resistance in the diatomaceous soil layer is calculated following section 8.2.1. The total pile length is 16.2 m, and the diatomaceous soil layer is 4 – 16.2 m depth. We divide it into 0.05-m intervals. We selected the 4 – 4.05 m section to demonstrate the shaft resistance calculation, and incorporate the three evaluations of the sensitivity parameters discussed in the above section (Table 8.7), that is, three evaluations of shaft resistance are computed. The demonstration for shaft resistance in 4 – 4.05 m section is presented in Table 8.10 and Table 8.11. The same calculation procedures should be repeated for each subdivision. The detailed shaft capacities at each subdivision are summarized in Appendix H.

Table 8.10: Shaft capacity calculation at 4 – 4.05 m subdivision for Pile B2P2 in Yazdani et al. (2021)

Parameter	Value	Equation
Depth range of subdivision	4 – 4.05 m	
Δz	0.05 m	$4.05\ m - 4\ m = 0.05\ m$
Representative depth	4.025 m	$(4.05\ m + 4\ m)/2 = 4.025\ m$
h	12.175 m	$16.2\ m - 4.025\ m = 12.175\ m$
h/R^*	198	$12.175\ m/0.0615\ m = 198$
σ_{v0}	68.33 kPa	$17\ kN/m^3 \times 4\ m + 13\ kN/m^3 \times 0.025\ m = 68.33\ kPa$
u	12.99 kPa	$9.8\ kN/m^3 \times (4.025\ m - 2.7\ m) = 12.99\ kPa$
σ'_{v0}	55.34 kPa	$68.33\ kPa - 12.99\ kPa = 58.34$ kPa

Table 8.11: Shaft capacity calculation at 4 – 4.05 m subdivision for Pile B2P2 in Yazdani et al. (2021) - continued

Parameter	Value			Equation
	$\Delta I_{vy} = 2.141$	$\Delta I_{v0} = 0.822$	$\Delta I_{vy} = 1$	
K_c	1.35	2.27	2.86	Equation (8-2) or (8-3)
σ'_{rc} [kPa]	74.45	125.63	158.38	Equation (8-5)
σ'_{rf} [kPa]	59.56	100.50	126.70	Equation (8-4)
τ'_f [kPa]	41.71	70.37	88.72	Equation (2-1)
$\tau'_f \cdot \Delta z$ [kN/m]	2.09	3.52	4.44	$\tau'_f \times 0.05\ m$
ΔQ_s [kN]	2.66	4.49	5.66	$\tau'_f \cdot \Delta z \times 0.4064\ m \times \pi$

The total shaft capacities of Pile B2P2 in the diatomaceous layer (4-16.2 m) based on different evaluated sensitivity parameters are summarized in Table 8.12. It can be seen that Q_s computed with $\Delta I_{v0} = 0.822$ is about 70% higher than Q_s computed with $\Delta I_{vy} = 2.141$. Indeed, Jardine et al. (2005) mentioned that ΔI_{v0}-approach evaluation is less conservative. The oedometrically-based ΔI_{vy} (i.e., $\Delta I_{vy} = 2.141$) evaluation is equivalent to $S_t = 138.5$, which may be too high for diatomaceous soil. The third evaluation based on $\Delta I_{vy} = 1$ gives Q_s equal to 2355.91 kN.

Table 8.12: Total shaft capacity in diatomaceous layer evaluated from different sensitivity parameters

Sensitivity parameter	$\Delta I_{vy} = 2.141$	$\Delta I_{v0} = 0.822$	$\Delta I_{vy} = 1$
Q_s [kN] (4-16.2 m)	1107.53	1868.78	2355.91

The ICP method to evaluate base resistance requires CPT tip resistance. In this case study, $q_t \cong 7036.5\ kPa$ near the pile tip (Wang et al. 2021). Since the plugging situation

is not mentioned in Yazdani et al. (2021), we use Equation (8-23) to evaluate, and calculation (8-45) shows that there is no plugging based on the criterion. Simply using Equations (8-26) and (8-27), we get the base resistance (Q_b) to be 83.6 kN.

$$\frac{\boldsymbol{D_i}}{\boldsymbol{D_{CPT}}}+\frac{\boldsymbol{0.45q_c}}{\boldsymbol{p_a}}=\frac{\boldsymbol{0.38735\ m}}{\boldsymbol{0.0357\ m}}+\frac{\boldsymbol{0.45\times 7036.5\ kPa}}{\boldsymbol{101.3\ kPa}}=\boldsymbol{42.1>36} \tag{8-45}$$

The capacity of Pile B2P2 evaluted from different sensitivity parameters is summarized in Table 8.13.

Table 8.13: Summary of capacity of Pile B2P2 in Yazdani et al. (2021)

Sensitivity parameter	Q_s [kN] in diatomaceous layer	Q_s [kN] in sand layer	Q_b [kN]	Q_t [kN]
$\Delta I_{vy}=2.141$	1107.53	71.4	83.6	1262.5
$\Delta I_{v0}=0.822$	1868.78			2023.8
$\Delta I_{vy}=1$	2355.91			2510.9

8.4.2.3 Comparison to measured capacity

The capacity of Buck Creek Pile B2P2 was computed based on a CAPWAP analysis (Rausche et al., 1972). Shaft resistance was estimated as 3003 kN and toe resistance was 555 kN, resulting in a total predicted capacity of 3558 kN (Shannon &Wilson, 2018). These values are higher than those predicted using the ICP design method. The ratios of measured to calculated shaft, base and total capacity are presented in Table 8.14. These results imply that the ICP method, as developed, is possibly not a reasonable predictor of pile capacity in Oregon diatomaceous deposits. To better understand the implication of these findings, we perform parametric analyses to determine the effects of varying inputs on computed pile capacity, as presented subsequently.

Table 8.14: Ratios of CAPWAP-measured pile capacity to ICP method predicted capacity for Buck Creek Pile B2P2

Sensitivity parameter	$\left(\frac{Q_{meas}}{Q_{pred}}\right)_{shaft}$	$\left(\frac{Q_{meas}}{Q_{pred}}\right)_{base}$	$\left(\frac{Q_{meas}}{Q_{pred}}\right)_{total}$
$\Delta I_{vy}=2.141$	2.55	6.64	2.82
$\Delta I_{v0}=0.822$	1.55		1.76
$\Delta I_{vy}=1$	1.24		1.42

8.5 PARAMETRIC ANALYSES

Despite some uncertainties of δ_f and ΔI_{vy} (i.e., S_t), we have a good understanding of γ and OCR of diatomaceous soil at the Buck Creek site and reasonable estimates of δ_f and ΔI_{vy}. Apparently,

the calculated shaft resistance of the open-end driven pile is lower than the measured shaft resistance. In order to study the influence of the four paramters, the shaft resistances are calculated on 4 - 16.2 m depth of the pile by varying parameter values, shown in Figure 8.6. From Equations (2-1) through (8.5) we can see that Q_s increases with γ, OCR, and δ_f and decreases with S_t. The accuracy of these parameters actually plays an important role of the final shaft resistance.

While the ICP design method has been applied in both stiff (e.g., Japanese mudstone, Jardine et al., 1998) and soft (e.g., Mexico City clays, Saldivar and Jardine, 2005) diatomaceous soil, it is not necessarily strictly applicable to diatomaceous soils in Oregon. There is not enough information to know for certain why there is discrepancy between the ICP calculated pile capacity and measured pile capacity for the open-end driven pile in Buck Creek. Pile load tests and more accurate site and soil information are needed in order to assess the validity of the ICP design method. Nonetheless, we can parametrically assess the performance of the ICP method at Buck Creek and make some informed modifications to the approach to better reflect local conditions. The sensitivity of the computed shaft capacity to the input parameters γ, S_t, OCR, and δ_f is shown in Figure 8.6. These trends partially inform the proposed modifications to the ICP method presented subsequently.

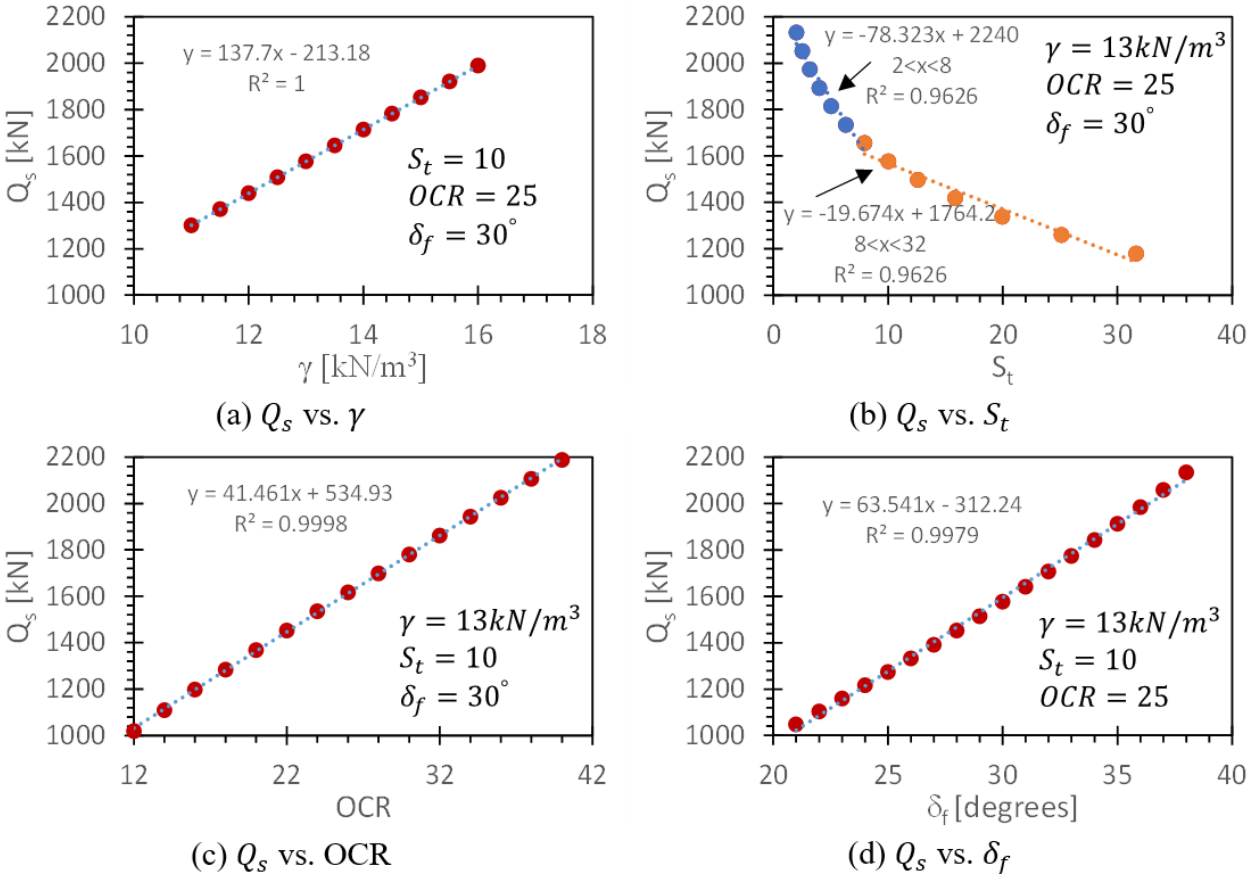

Figure 8.6: Shaft resistance of the open-end pile driven in Buck Creek in the diatomaceous layer from 4.7–16.2 m depth (in each subplot, a linear trendline is fitted with data plotted, in each equation, y is Q_s and x is the corresponding influence factor).

8.6 MODIFIED ICP METHOD FOR DIATOMACEOUS SOILS

As presented previously, the ICP method is implemented differently for clays and for sands. Diatomaceous soils (specifically, those present in Oregon) are silts, exhibiting behaviors in some ways similar to clays but in other ways more similar to sands – and this complexity is in addition to the known peculiar engineering response of diatomaceous soils. As such, we propose that the ICP method for clays be modified slightly to better reflect the expected behaviors of diatomaceous soils in-situ – specifically, high shear strength, stress history dependency, dilation on shear, and rapid dissipation of excess pore water pressure. We outline these suggested modifications below and present their overall effect.

To employ the ICP method, we require a geostatic stress profile based on the unit weight of the soil in-situ. As noted in Chapter 6, friction sleeve measurements are a reasonable predictor of unit weight in diatomaceous soils as long as the correlation includes information about the soil's specific gravity. We use Equation (8-46) to compute unit weight of the soil:

$$\boldsymbol{\gamma_t = \left[2.6 \log\left(\frac{f_s}{1\ kPa}\right) + 15 G_s - 26.5\right] \cdot \frac{kN}{m^3}}$$

(8-46)

where all terms are previously defined. Geostatic effective stress at the depth of each cone measurement is then computed in the usual manner.

The original ICP method specifies that the pile-soil interface friction angle (δ_f) be measured directly in the laboratory. While soil-continuum interface friction tests are not necessarily complicated, they require highly specialized equipment and are not typically run as a matter of course in most geotechnical projects. In the absence of measured δ_f values, the engineer might choose to select a conservative value for this parameter (e.g., $20° - 30°$). However, diatomaceous soils are known to exhibit high effective stress friction angles, often exceeding 40°, which implies that ultra-conservative interface strength parameters may not be appropriate. We suggest that the effective stress friction angle of the soil be inferred from CPT results and then δ_f assumed as some fraction of that value. The effective stress friction angle may be calculated using the NTH method by Equation (8-47) and (8-48) (Ouyang and Mayne 2019, 2020, 2023).

$$\boldsymbol{\phi' = 29.5° \cdot B_q^{0.121}\left[0.256 + 0.336 B_q + \log(N_m)\right]}$$
$$\textbf{if}$$
$$\boldsymbol{0.05 \le B_q \le 1.0}$$

(8-47)

$$\boldsymbol{\phi' = 8.18 \cdot \ln(2.13 N_m)}$$
$$\textbf{if}$$
$$\boldsymbol{B_q < 0.05}$$

(8-48)

where:
B_q = normalized pore pressure parameter [$= (u_2 - u_0)/(q_t - \sigma_{v0})$]; and
N_m = cone resistance number [$= (q_t - \sigma_{v0})/\sigma'_{v0}$].

Ouyang and Mayne (2019, 2020, 2023) suggest incorporating stress history effects by using a modified cone resistance number, $N_{mc} = N_m/OCR^{\Lambda}$, where $\Lambda = 1 - C_r/C_c \approx 0.8$ is the plastic volumetric strain potential and all other terms are previously defined. Using the modified cone resistance number serves to decrease the predicted value of the friction angle. Diatomaceous soils can exhibit extremely high apparent overconsolidation ratios, thus resulting in artificially low calculated values of friction angle. Ironically, this can also result in underprediction of OCR as the two properties are interdependent (i.e., the calculation is iterative), as discussed below. Thus, we suggest that the cone resistance number (N_m) should be used and not the modified cone resistance number (N_{mc}).

We also require an estimation of the OCR for soil layers that are particularly influenced by stress history. At the Buck Creek site, only the diatomaceous layers have a strong dependence on their stress history. The conventional approach for assessing OCR in fine-grained soils is to use the solution based on spherical cavity expansion theory and critical state soil mechanics (SCE-CSSM) developed by (Mayne 1991, 2001) shown as Equation (8-49):

$$\boldsymbol{OCR = 2\left[\frac{q_t - u_2}{\sigma'_{v0}(1.95M + 1)}\right]^{\frac{1}{\Lambda}}} \quad \textbf{(8-49)}$$

where $M = 6\sin\phi'/(3 - \sin\phi')$ is the slope of the frictional failure envelope in Cambridge University-type $q - p'$ space and other terms are previously defined. However, diatomaceous soils are quickly draining in shear (e.g., during penetration or laboratory measurement of M), and we find that this expression tends to significantly underestimates the expected OCR at Buck Creek bridge. Thus, we suggest using an alternative expression developed through a database approach for freely-draining materials (Mayne, 2001, 2005) shown as Equation (8-50):

$$\boldsymbol{OCR = \left[\frac{0.192\left(\frac{q_t}{\sigma_{atm}}\right)^{0.22}}{(1 - \sin\phi')\left(\frac{\sigma'_{v0}}{\sigma_{atm}}\right)^{0.31}}\right]^{\frac{1}{\sin\phi' - 0.27}}} \quad \textbf{(8-50)}$$

The final soil parameter needed for calculation of side resistance in the diatomaceous layer is the sensitivity parameter, ΔI_{vy}. To be consistent with the other parameters calculated from CPT data, we use a value of soil sensitivity computed based on undrained shear strength from CSSM and the measured sleeve friction, shown as Equation (8-51) and (8-52):

$$s_u = \frac{1}{2} M \cdot p_0' \left(\frac{R_0}{2}\right)^{\Lambda}$$

(8-51)

$$\Delta I_{vy} = \log\left(\frac{s_u}{f_s}\right)$$

(8-52)

where $R_0 = p_c'/p_0'$ is the isotropic overconsolidation ratio (the maximum past mean effective stress normalized by the current mean effective stress, sometimes referred to as the preconsolidation ratio) and we take the fully remolded shear strength ($s_{u,r}$) to be equal to the measured sleeve friction (f_s; e.g., Robertson 2009, 2016). We make use of the following theoretical relationship to compute R_0 from the OCR value determined through Equation (8-53):

$$R_0 = \frac{1 + 2(1 - \sin\phi')}{1 + 2(1 - \sin\phi')OCR^{\sin\phi'}} OCR$$

(8-53)

The parameters described above are sufficient to perform the modified ICP design method calculations once the effective stress friction angle is adjusted to represent a soil-pile interface friction angle (δ). In practice, this value is typically assumed to be in the range $2\phi'/3 \leq \delta \leq \phi'$, so we select an intermediate value of $3\phi'/4$. Thus, based on the interpretations introduced above, the profiles of computed friction angle, OCR, and sensitivity parameter (ΔI_{vy}) are presented in Figure 8.7.

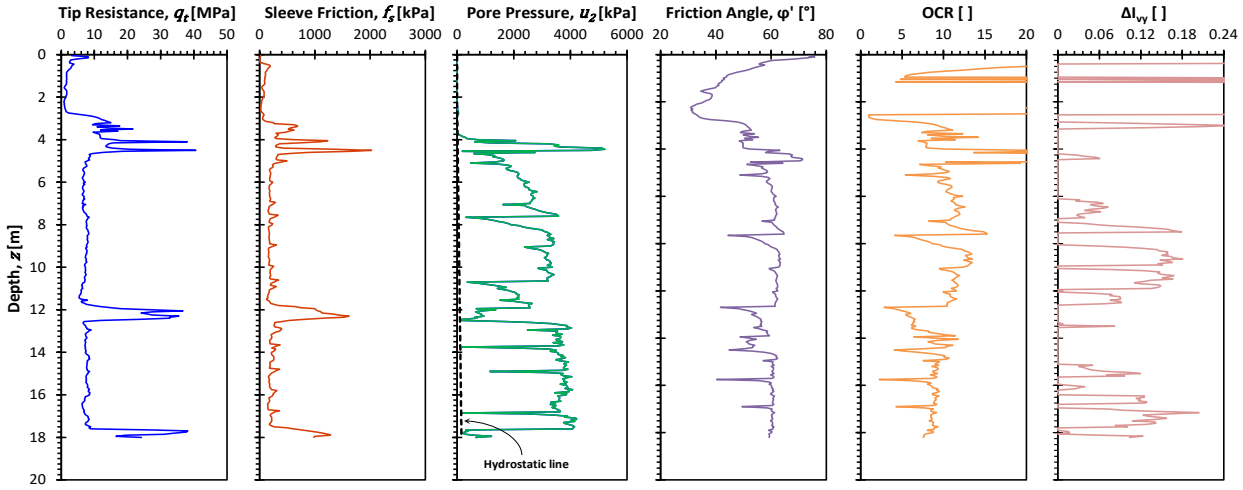

Figure 8.7: CPTu and interpretations of friction angle, OCR, and sensitivity at Buck Creek

Results from the modified ICP design method calculations using the input parameters described above result in the capacity values presented in Table 8.15. We note that the modified ICP method calculations underpredict measured total capacity by 16% and 9% for the unplugged and

plugged cases, respectively. However, the difference can be attributed almost entirely to the predicted values of base resistance, as the shaft capacity is only underpredicted by 5%. The base resistance is typically a small part of the total capacity of an open-ended pipe pile and requires a much greater deformation to be fully mobilized than the skin friction. We note here that CAPWAP is only an approximation of actual static capacity for the pile and that it is very preferable to underpredict total capacity than to overpredict it.

Table 8.15: Modified ICP method predicted capacity and CAPWAP-measured pile capacity for Buck Creek Pile B2P2

	Unplugged		**Plugged**		**CAPWAP**
	Q_{pred} **[kN]**	$\frac{Q_{pred}}{Q_{meas}}$ [%]	Q_{pred} **[kN]**	$\frac{Q_{pred}}{Q_{meas}}$ [%]	Q_{meas} **[kN]**
Q_s **[kN]**	2852.04	94.8	2852.04	94.8	3010
Q_b **[kN]**	139.73	25.4	381.56	69.2	551
Q_t **[kN]**	2991.77	84.0	3233.60	90.8	3561

9.0 SUMMARY, CONCLUSIONS, AND RECOMMENDATIONS FOR FUTURE RESEARCH

9.1 SUMMARY AND CONTRIBUTIONS

Diatomaceous soil has been widely discovered and studied by researchers around the world. However, most of the studies tended to focus on a specific subset of those material behaviors, leaving a void in a holistic understanding of the soil's behavior, and large amount of research targeted on the mixtures of diatomite and other types of soil to underscore the significant influence of diatomite on soil behavior. In this study, a relatively exhaustive investigation, encompassing both *in-situ* and laboratory characterization, was undertaken to elucidate the geotechnical properties of natural diatomaceous soil from Oregon. This study not only illuminated the inherent characteristics of such soils but also delved into the broader implications these findings hold for geotechnical design practices. The contributions of this study are summarized as follows:

1. The consistency of natural diatomaceous deposits varies between a soft, fine-grained and mudstone-like behavior. Laboratory and in-situ test data for mudstone diatomaceous soil has been technically challenging due to impediments in extracting Shelby tube samples and advancing CPTu probes. The soft fine-grained diatomaceous soil, as typified by the Wickiup and Ady Canal cases, is better delineated owing to a more exhaustive test program. Conversely, the mudstone diatomaceous soil, exemplified by Moore Park and Pine Cone cases, has less laboratory and in-situ test data to fully understand the behaviors. Disparities between these two diatomaceous classifications will be elaborated upon in subsequent bullet points.

2. Diatomaceous soil exhibits distinctive physical properties on natural water content (w_n), in-situ unit weight (γ), and specific gravity (G_s) from regular soils. The ranges of these properties of diatomaceous soil from this study are: $w_n \cong 50\% - 200\%, \gamma \cong 11 - 14\ kN/m^3, G_s \cong 2 - 2.5$. Both this study and the literature show that the properties of diatomaceous soil exhibit large variations across different sources. Conversely, parameters like fines content, grain size distribution (GSD), and specific surface area (SSA) did not manifest a discernible distinction between diatomaceous and non-diatomaceous soils. Because of these unique characteristics, special care must be exercised when determining the in-situ unit weight of diatomaceous soils compared to other soils. For example, specific gravity, which is not always measured as a matter of course in geotechnical practice, is necessary for correct determination of unit weight through either laboratory or in-situ means. Neglecting this fact may result in erroneous prediction of the geostatic stress profile for a given deposit.

3. The consistency limits of diatomaceous soil were systematically evaluated. Liquid limit (LL) was ascertained using Casagrande cup, fall cone, and miniature vane tests, while the plastic limit (PL) was determined through thread rolling, dual-cone (Wood and Wroth, 1978), and fall cone methods (Feng 2001). Validation of the fall cone test for LL was affirmed by the miniature vane test, highlighting an average

underestimation of LL of approximately 18% by the Casagrande method. The dual-cone approach for PL showed high variability and is not advocated. Despite consistent results between the latter two PL tests, the thread rolling method is recommended for diatomaceous soil due to two reasons: it is directly related to the cohesion-based plastic limit definition; and Feng (2001) method yields different results depending on the test directions (wet-to-dry or dry-to-wet).

4. The compressibility and stress history of diatomaceous soil has been evaluated through IL and CRS consolidation tests. The compression and recompression indices for the diatomaceous specimens tested are mostly in the range of $0.5 \lesssim C_c \lesssim 2.9$ and $0.04 \lesssim C_r \lesssim 0.22$, respectively. The ratios of C_r to C_c generally fall in the range of $0.04 \lesssim C_r/C_c \lesssim 0.2$. The distinction between soft fine-grained and mudstone diatomaceous soils is markedly evident in their apparent overconsolidation ratios (OCR). While the former displays characteristics of normal consolidation, the latter is predominantly heavily overconsolidated ($OCR \cong 6 - 13$).

5. High shear strength is another feature of diatomaceous soil. The ranges for friction angle and normalized undrained shear strength are: $\phi'_{cs} \cong 34^\circ - 48^\circ$, and $(s_u/\sigma'_v)_{NC} \cong 0.28 - 0.4$ for this study, which is consistent with values reported from various sources across the literature: $\phi'_{cs} \cong 20^\circ - 60^\circ$, and $(s_u/\sigma'_v)_{NC} \cong 0.2 - 0.8$.

6. This work has shown that G_s serves as an indicative metric for diatom content, signifying an inverse relationship between the two properties. Of all physical properties subjected to correlative analysis with G_s, the consistency limits, predominantly LL, manifest the most pronounced correlation with G_s. Decreased G_s corresponds to increased consistency limits. Efforts were made to correlate compressive parameters with LL, evidencing that an elevated LL directly results in increased C_c and C_r. Similarly, shear strengths were explored in relation to LL, OCR, and the amalgamated physical property metric ($G_s w_n/LL$).

7. The CPTu test data were used to interpret diatomaceous soil behaviors and properties. It is noteworthy that the mudstone diatomaceous soil manifests behavior markedly divergent from the soft fine-grained category. Each diatomaceous soil type occupies discrete regions on soil behavior charts (e.g., $Q_{tn} - F_N$ and $Q_t - B_q$). Different interpretations of unit weight, OCR, friction angle, and undrained shear strength from CPTu tests are presented and evaluated. The unit weight is best correlated by Equation (6.16) for all diatomaceous soil considered in this work. However, for the mudstone diatomaceous soil, the correlations concerning the other three properties remain inconclusive, attributable to the limited scope of laboratory tests and CPTu data available. For soft fine-grained diatomaceous soil, OCR is best correlated by Equation (6.23), friction angle is best correlated by Equation (6.24), undrained shear strength is best correlated by Equation (6.27).

8. Owing to the intricate and unique properties of diatomaceous soil, simple constitutive models (e.g., Mohr-Coulomb) exhibit inadequate performance in accurately predicting its behavior. The Soft Soil Model was identified as an appropriate constitutive model, demonstrating its capacity to overall capture macroscopic

behaviors and provide credible predictions at the system scale based on elemental test outcomes. Practitioners can deduce the model parameters through CPT interpretations, coupled with correlations to basic geotechnical properties (e.g., LL), as outlined in Chapter 6. Efforts were also directed towards calibrating the model using previously documented laboratory tests on diatomaceous soil from the literature. A notable observation was the propensity of diatomaceous soil to produce elevated excess pore water pressure during consolidated undrained (CU) triaxial tests, surpassing the model's predictions.

9. The Imperial College Pile (ICP) design methodology was subjected to a rigorous evaluation against the on-site pile dynamic capacity measurements at Buck Creek Bridge. Discrepancies were observed, with the predicted total and shaft pile capacities registering 30% - 60% lower than the measured values, contingent on parameter selection. Subsequently, modifications were proposed to the ICP methodology to integrate CPTu-derived parameters for pile capacity prediction. The revised ICP methodology exhibited an underprediction of the measured total capacity by 16% and 9% for unplugged and plugged scenarios, respectively. Moreover, the modified method shaft capacity demonstrated a mere 5% underprediction. Thus, the optimized ICP methodology offers potential efficacy for pile capacity estimations within Oregon diatomaceous soil deposits.

9.2 RECOMMENDATIONS FOR FUTURE RESEARCH

Diatomaceous soil manifests in two predominant geotechnical states: those analogous to soft fine-grained soil and those akin to mudstone. The geotechnical behavior of soft diatomaceous soil, such as that observed at Wickiup Junction and Ady Canal, is better documented, partially due to the challenges inherent in extracting undisturbed samples from and conducting CPTu in diatomaceous mudstone (e.g., Moore Park and Pine Cone). Advancing the understanding of the engineering behavior of diatomaceous mudstone can be facilitated through additional in-situ testing and more robust procedures for extracting intact samples during drilling.

Simulation of the shear and compression characteristics of diatomaceous soil is reasonably facilitated by the Soft Soil Model. Nonetheless, calibration from laboratory tests conducted in this study and data sourced from existing literature indicates that diatomaceous soils often generate higher excess pore water pressures than those predicted by the model. A more advanced constitutive model that can accurately account for post-peak softening and the generation of excess pore water pressure during CU tests of diatomaceous soil should be considered for further investigation.

Results in the literature indicate that the ICP design method may be appropriate for predicting pile capacity in some diatomaceous soils. However, challenges in pile driving, such as pronounced pile rebound, have also been documented, and this cannot be predicted via the ICP method. A comprehensive instrumented full-scale pile static test program to directly measure capacity in diatomaceous soil is needed. Modifications to the current design methodologies beyond those proposed herein or the formulation of a novel approach are necessary. These

efforts should be integrated with numerical simulations to collect information that is otherwise inaccessible in physical experiments or model tests.

REFERENCES

AASHTO T 89; Standard Method of Test for Determining the Liquid Limit of Soils. (n.d.). American Association of State Highway and Transportation Officials (AASHTO).

Agaiby, S. S., and Mayne, P. W. (2019). "CPT evaluation of yield stress profiles in soils." *Journal of Geotechnical and Geoenvironmental Engineering*, American Society of Civil Engineers, 145(12), 4019104.

Aggour, M. S., and Radding, W. R. (2001). "Standard penetration test (SPT) correction." *Report No. MD02-007B48, Maryland State Highway Administration, Baltimore*, 87.

Aksoy, H. S., Mesut, G. Ö. R., and Esen, İ. (2018). "Determination of friction angles between soil and steel-FRP piles." *Turkish Journal of Science and Technology*, 13(1), 19–23.

American Society for Testing and Materials. 2018a. "Test Method for Field Vane Shear Test in Saturated Fine-Grained Soils." (n.d.). D2573/D2573M-18. West Conshohocken, PA: ASTM International.

American Society for Testing and Materials (ASTM). 2014. (n.d.). "Test Methods for Specific Gravity of Soil Solids by Water Pycnometer." D854-14. West Conshohocken, PA: ASTM International.

American Society for Testing and Materials (ASTM). 2016c. (n.d.). "Test Method for Laboratory Miniature Vane Shear Test for Saturated Fine-Grained Clayey Soil." D4648/D4648M − 16. West Conshohocken, PA: ASTM International.

American Society for Testing and Materials (ASTM). 2016d. (n.d.). "Test Methods for Measurement of Hydraulic Conductivity of Saturated Porous Materials Using a Flexible Wall Permeameter." D5084-16a. West Conshohocken, PA: ASTM International.

American Society for Testing and Materials (ASTM). 2017. (n.d.). "Standard Practice for Using Hollow-Stem Augers for Geotechnical Exploration and Soil Sampling." D6151-97. West Conshohocken, PA: ASTM International.

American Society for Testing and Materials (ASTM). 2017. (n.d.). "Standard Test Method for Consolidated Undrained Direct Simple Shear Testing of Fine Grain Soils" D6528-17. West Conshohocken, PA: ASTM International.

American Society for Testing and Materials (ASTM). 2017c. (n.d.). "Test Methods for Determining the Amount of Material Finer than 75-μm (No. 200) Sieve in Soils by Washing." D1140-17. West Conshohocken, PA: ASTM International.

American Society for Testing and Materials (ASTM). 2017d. (n.d.). "Test Methods for Liquid Limit, Plastic Limit, and Plasticity Index of Soils." D4318-17. West Conshohocken, PA: ASTM International.

American Society for Testing and Materials (ASTM). 2017e. (n.d.). "Test Methods for Particle-Size Distribution (Gradation) of Soils Using Sieve Analysis." D6913/D6913M-17. West Conshohocken, PA: ASTM International.

American Society for Testing and Materials (ASTM). 2018. (n.d.). "Standard Guide for Use of Direct Rotary Drilling with Water-Based Drilling Fluid for Geoenvironmental Exploration and the Installation of Subsurface Water-Quality Monitoring Devices". D5783-18. West Conshohocken, PA: ASTM International.

American Society for Testing and Materials (ASTM). 2018a. (n.d.). "Test Method for Field Vane Shear Test in Saturated Fine-Grained Soils." D2573/D2573M-18. West Conshohocken, PA: ASTM International.

American Society for Testing and Materials (ASTM). 2018b. (n.d.). "Test Method for Standard Penetration Test (SPT) and Split-Barrel Sampling of Soils." D1586/D1586M-18e1. West Conshohocken, PA: ASTM International.

American Society for Testing and Materials (ASTM). 2019. (n.d.). "Test Methods for Laboratory Determination of Water (Moisture) Content of Soil and Rock by Mass." D2216-19. West Conshohocken, PA: ASTM International.

American Society for Testing and Materials (ASTM). 2020. (n.d.). "Test Method for Electronic Friction Cone and Piezocone Penetration Testing of Soils." D5778-20. West Conshohocken, PA: ASTM International.

American Society for Testing and Materials (ASTM). 2020a. (n.d.). "Test Method for Consolidated Drained Triaxial Compression Test for Soils." D7181-20. West Conshohocken, PA: ASTM International.

American Society for Testing and Materials (ASTM). 2020b. (n.d.). "Test Method for Consolidated Undrained Triaxial Compression Test for Cohesive Soils." D4767-11. West Conshohocken, PA: ASTM International.

American Society for Testing and Materials (ASTM). 2020d. (n.d.). "Test Methods for One-Dimensional Consolidation Properties of Soils Using Incremental Loading." D2435-11. West Conshohocken, PA: ASTM International.

American Society for Testing and Materials (ASTM). 2021. (n.d.). "Standard test method for one-dimensional consolidation properties of saturated cohesive soils using controlled-strain loadingr." D4186-20. West Conshohocken, PA: ASTM International.

American Society for Testing and Materials (ASTM). 2021a. (n.d.). "Test Method for Particle-Size Distribution (Gradation) of Fine-Grained Soils Using the Sedimentation (Hydrometer) Analysis." D7928-16. West Conshohocken, PA: ASTM International.

American Society for Testing and Materials (ASTM). 2021b. (n.d.). "Test Methods for Laboratory Determination of Density (Unit Weight) of Soil Specimens." D7263-21. West Conshohocken, PA: ASTM International.

Antonides, L. E. (1998). "Diatomite." *Minerals Yearbook Metals and Minerals 1998*, US Geological Survey, 1, 21–24.

Atterberg, A. (1911). "Die plastizitat der Tone." *Intern mitt. boden.*, 4–37.

Baligh, M. M., and Levadoux, J.-N. (1986). "Consolidation after undrained piezocone penetration. II: Interpretation." *Journal of geotechnical engineering*, American Society of Civil Engineers, 112(7), 727–745.

Bardet, J.-P. (1997). *Experimental soil mechanics*. Prentice Hall.

Barros, P. L. A., and Pinto, P. R. O. (2008). "Oedometer consolidation test analysis by nonlinear regression." *Geotechnical Testing Journal*, ASTM International, 31(1), 76–83.

Becker, D. E., Crooks, J. H. a, Been, K., and Jefferies, M. G. (1987). "Work as a criterion for determining in situ and yield stresses in clays." *Canadian Geotechnical Journal*, 24(4), 549–564.

Benson, B. D., and Rippe, A. H. (2008). "Dike Breach Repair Design in Inundated, Scoured Conditions." *GeoCongress 2008*, K. R. Reddy, M. V. Khire, and A. N. Alshawabkeh, eds., American Society of Civil Engineers, Reston, VA, 239–246.

Bjerrum, L. (1967). "Engineering geology of norwegian normally-consolidated marine clays as related to settlements of buildings." *Geotechnique*, 17(2), 83–118.

Bjerrum, L., and Simons, N. E. (1960). "Comparison of shear strength characteristics of normally consolidated clays." *Proceedings, Research Conference on Shear Strength of Cohesive Soils*, ASCE, Boulder, CO, 711–726.

Bliss, M. (2005). "Jet Grouting for Seismic Remediation of Wickiup Dam, Oregon." *Journal of Dam Safety*, 3(1).

Bolton, M. D. (1986). "The strength and dilatancy of sands." *Géotechnique*, 36(1), 65–78.

Brinkgreve, R. B. J. (1994). "Geomaterial models and numerical analysis of softening(Ph. D. Thesis)."

Brinkgreve, R. B. J., Swolfs, W. M., Engin, E., Waterman, D., Chesaru, A., Bonnier, P. G., and Galavi, V. (2023). "PLAXIS 2D 2023 material models manual." *PLAXIS BV*.

BSI. (2022). "BS EN ISO 17892-12: 2022. Geotechnical investigation and testing. Laboratory testing of soil. Determination of liquid and plastic limits." BSI London.

Budhu, M. (2010). *Soil mechanics and foundations*. John Wiley & Sons, Inc., New York.

Burland, J. (1973). “Shaft friction of piles in clay--a simple fundamental approach.” *Publication of: Ground Engineering/UK/*, 6(3).

Burland, J. B. (1990). “On the compressibility and shear strength of natural clays.” *Géotechnique*, Thomas Telford Ltd, 40(3), 329–378.

Burns, S. E., and Mayne, P. W. (1998a). “Penetrometers for soil permeability and chemical detection, geosystems engineering group.” *School of Civil and Environmental Engineering, Georgia Institute of Technology Atlanta, Georgia*, 30332–30355.

Burns, S. E., and Mayne, P. W. (1998b). “Penetrometers for soil permeability and chemical detection.” *Funding provided by NSF and ARO issued by Georgia Institute of Technology Report No GITGEEGEO-98-1*.

Caicedo, B., Mendoza, C., Lizcano, A., and Lopez-Caballero, F. (2019a). “Some contributions to mechanical behaviors of lacustrine deposit in Bogotá, Colombia.” *Journal of Rock Mechanics and Geotechnical Engineering*, Elsevier, 11(4), 837–849.

Caicedo, B., Mendoza, C., López, F., and Lizcano, A. (2018). “Behavior of diatomaceous soil in lacustrine deposits of Bogotá, Colombia.” *Journal of rock mechanics and geotechnical engineering*, Elsevier, 10(2), 367–379.

Caicedo, B., Zuluaga, D., and Slebi, C. (2019b). “Effects of micro-features of fossil diatom on the macroscopic behaviour of soils.” *Géotechnique Letters*, Thomas Telford Ltd, 9(4), 322–327.

Campanella, R. (1988). “Current status of the piezocone test.” *Proc. 1st Int. Symp. on Penetration Testing*, ISOPT, 93–116.

Casagrande, A. (1936). “The determination of pre-consolidation load and it’s practical significance.” *Proc. Int. Conf. Soil Mech. Found. Eng. Cambridge, Mass., 1936*, 60.

Casagrande, A., and Fadum, R. E. (1940). “Notes on soil testing for engineering purposes.”

Chai, J. C., Iribe, K., and Hino, T. (2006). “Comparison of incremental load and constant rate of strain consolidation test results.” *Proceedings of the 4th Asia Joint Symposium on Geotechnical and Geoenvironmental Engineering, Dalian*, Citeseer, 47–52.

Coduto, D. P. (2003). “Foundation Design on Problematic Soils: Principles and Practices.” Prentice-Hall.

Covarrubias Ornelas, A., Wang, J., Moug, D., Evans, T. M., and Walter, A. (2022). “Relating the Proportion of Diatom Particles to the Physical Properties of Natural Diatomaceous Soil.” *Geo-Congress 2022*, 479–489.

Dadashi, A. (2022). “Laboratory Investigation of the Cyclic Response of Transitional Soils: Bridging Element-Scale and In-Situ Responses.” Oregon State University.

Day, R. W. (1995). “Engineering Properties of Diatomaceous Fill.” *Journal of Geotechnical Engineering*, 121(12), 908–910.

Day, R. W. (1997). “Laboratory testing of air-dried diatomaceous fill.” *Environmental & Engineering Geoscience*, EEGS, 3(3), 449–452.

Diaz-Rodríguez, J. A. (2011). “Diatomaceous soils: monotonic behavior.” *Deformation characteristics of geomaterials*, IOS Press, 865–871.

Díaz-Rodríguez, J. A. (2003). “Characterization and engineering properties of Mexico City lacustrine soils.” *Characterization and engineering properties of natural soils*, Sweets and Zeitlinger, 1, 725–755.

Díaz-Rodríguez, J. A., Cruz, R. L.-S., Dávila-Alcocer, V. M., Vallejo, E., and Girón, P. (1998). “Physical, chemical, and mineralogical properties of Mexico City sediments: a geotechnical perspective.” *Canadian Geotechnical Journal*, NRC Research Press, 35(4), 600–610.

Díaz-Rodríguez, J. A., and González-Rodríguez, R. (2013). “Influence of diatom microfossils on soil compressibility.” *Proceedings of the 18th International Conference on Soil Mechanics and Geotechnical Engineering*, P. Delage, J. Desrues, F. Roger, Puech Alain, and F. Schlosser, eds., Presses des Ponts, Paris, France.

Diaz-Rodriguez, J. A., Leroueil, S., and Aleman, J. D. (1992). “Yielding of Mexico City clay and other natural clays.” *Journal of geotechnical engineering*, American Society of Civil Engineers, 118(7), 981–995.

Díaz-Rodríguez, J. A., and López-Flores, L. (1999). “A study of microstructure using resonant-column tests.” *Earthquake Geotechnical Engineering*, 89–94.

Díaz-Rodríguez, J. A., and Lopez-Molina, J. A. (2009). “Cyclic behavior of diatomaceous soils.” *Proceedings of the 17th International Conference on Soil Mechanics and Geotechnical Engineering: The Academia and Practice of Geotechnical Engineering*, M. Hamza, M. Shahien, and Y. El-Mossallamy, eds., IOS Press, Alexandria, Egypt, 159–162.

Díaz-Rodríguez, J. A., and Martínez-Vásquez, J. J. (2008). “One-dimensional consolidation testing of lacustrine soil from Mexico City.” *Proceedings of the 4th International Symposium on Deformation6 Characteristics of Geomaterials, At Atlanta, Georgia, USA. https://doi. org/10.13140/2.1*.

Díaz-Rodríguez, J. A., Martínez-Vasquez, J. J., and Santamarina, J. C. (2009). “Strain-Rate Effects in Mexico City Soil.” *Journal of Geotechnical and Geoenvironmental Engineering*, 135(2), 300–305.

Díaz-Rodríguez, J. A., and Moreno-Arriaga, A. (2017). “Contributions of diatom microfossils to soil compressibility.” *Proceedings of the 19th International Conference on Soil Mechanics and Geotechnical Engineering*, W. Lee, J.-S. Lee, H.-K. Kim, and D.-S. Kim, eds., Korean Geotechnical Society, Seoul, Korea, 349–352.

Díaz-Rodríguez, J. A., and Santamarina, J. C. (1999). "Thixotropy: the case of Mexico city soils." *XI Panamerican Conf. on Soil Mech. and Geotech. Eng*, Foz do Iguaçu, Brazil, 441–448.

Dyvik, R., Berre, T., Lacasse, S., and Raadim, B. (1987). "Comparison of Truly Undrained and Constant Volume Direct SImple Shear Tests." *Géotechnique*, 37(1), 3–10.

Evans, T. M., and Simpson, D. C. (2015). "Innovative data acquisition for the fall cone test in teaching and research." *Geotechnical Testing Journal*, 38(3), 346–354.

Feng, T.-W. (2001). "A linear log *d* – log *w* model for the determination of consistency limits of soils." *Canadian Geotechnical Journal*, 38(6), 1335–1342.

Finn, W. D. L., and Vaid, Y. P. (1977). "Liquefaction potential from drained constant volume cyclic simple shear tests." *Proceedings of the 6th World Conference on Earthquake Engineering*, New Delhi, India, 10–14.

Franklin, D. (2004). "Gas Guzzlers." *Smithsonian*, Smithsonian Magazine, 34(11), 25.

Fredlund, M. D., Fredlund, D. G., and Wilson, G. W. (2000). "An equation to represent grain-size distribution." *Canadian Geotechncial Journal*, 37, 817–827.

Frost, J. D., Hebeler, G. L., Evans, T. M., and DeJong, J. T. (2004). "Interface behavior of granular soils." *Engineering, construction, and operations in challenging environments: earth and space 2004*, 65–72.

Frýbová, P., Erbenová, A., Glisníková, V., and Drápalová, R. (2017). "Changes in the basic index properties of clays in relation to the content of diatoms." *Advanced Engineering Forum*, Trans Tech Publ, 335–345.

Gillette, D. R. (2008). "Review of In Situ Measurements as Indications of Liquefaction Potential at Numerous Sites." *Sixth International Conference on Case Histories in Geotechnical Engineering*, Arlington, VA, 9.

Gorman, C. T. (1976). "Constant-rate-of-strain and controlled-gradient consolidation testing."

Grim, R. E. (1949). "Mineralogical composition in relation to the properties of certain soils." *Geotechnique*, Thomas Telford Ltd, 1(3), 139–147.

Hagerty, M. M., Hite, D. R., Ullrich, C. R., and Hagerty, D. J. (1993). "One-Dimensional High-Pressure Compression of Granular Media." *Journal of Geotechnical Engineering*, 119(1), 1–18.

Hang, P. T., and Brindley, G. W. (1970). "Methylene blue absorption by clay minerals. Determination of surface areas and cation exchange capacities (clay-organic studies XVIII)." *Clays and clay minerals*, Springer, 18(4), 203–212.

Hannigan, P. J., Rausche, F., Likins, G. E., Robinson, B., Becker, M., and Berg, R. R. (2016). *Design and construction of driven pile foundations–Volume I*. National Highway Institute (US).

Hansbo, S. (1957). *New approach to the determination of the shear strength of clay by the fall-cone test*.

Hoang, N. Q., Kim, S. Y., and Lee, J.-S. (2022). "Compressibility, stiffness and electrical resistivity characteristics of sand–diatom mixtures." *Géotechnique*, Thomas Telford Ltd, 72(12), 1068–1081.

Hong, Z.-S., Yin, J., and Cui, Y.-J. (2010). "Compression behaviour of reconstituted soils at high initial water contents." *Géotechnique*, 60(9), 691–700.

Hong, Z., Tateishi, Y., and Han, J. (2006). "Experimental Study of Macro-and Microbehavior of Natural Diatomite." *Journal of Geotechnical and Geoenvironmental Engineering*, 132(5), 603–610.

Houlsby, G. T. (1982). "Theoretical analysis of the fall cone test." *Geotechnique*, Thomas Telford Ltd, 32(2), 111–118.

Iijima, A., and Tada, R. (1981). "Silica diagenesis of Neogene diatomaceous and volcaniclastic sediments in northern Japan." *Sedimentology*, Wiley Online Library, 28(2), 185–200.

Israelachvili, J. N. (2011). *Intermolecular and Surface Forces*. Elsevier, Waltham, MA.

Jaky, J. (1944). "The coefficient of earth pressure at rest." *Journal of the Society of Hungarian Architects and engineers*.

Jardine, R., Chow, F., Overy, R., and Standing, J. (2005). *ICP design methods for driven piles in sands and clays*. Thomas Telford London.

Jardine, R. J., Chow, F. C., Matsumoto, T., and Lehane, B. M. (1998). "A new design procedure for driven piles and its application to two Japanese clays." *Soils and foundations*, The Japanese Geotechnical Society, 38(1), 207–219.

Kenney, T. C. (1959). "Discussion of 'Geotechnical Properties of Glacial Lake Clays' by Tien H. Wu." *Journal of the Soil Mechanics and Foundations Division*, 85(SM3), 67–79.

Kimoto, S., and Oka, F. (2005). "An elasto-viscoplastic model for clay considering destructuralization and consolidation analysis of unstable behavior." *Soils and Foundations*, Elsevier, 45(2), 29–42.

Kulhawy, F. H., and Mayne, P. W. (1990). *Manual on estimating soil properties for foundation design*. Electric Power Research Inst., Palo Alto, CA (USA); Cornell Univ., Ithaca ….

Ladd, C. C., and Foott, R. (1974). “New design procedure for stability of soft clays.” *Journal of the Geotechnical Engineering Division*, American Society of Civil Engineers, 100(7), 763–786.

Ladd, C. C., Foott, R., Ishihara, K., and Schlosser, F. (1977). “Stress-deformation and strength characteristics.”

Lambe, T. W., and Whitman, R. V. (1969). “Soil mechanics, 553 pp.” John Wiley, New York.

Lee, C., Yun, T. S., Lee, J.-S., Bahk, J. J., and Santamarina, J. C. (2011). “Geotechnical characterization of marine sediments in the Ulleung Basin, East Sea.” *Engineering Geology*, Elsevier, 117(1–2), 151–158.

Lee, J. (2014). “Evaluation of Diatomaceous Earth Content in Natural Soils for Potential Engineering Applications.”

Liao, H.-J., Su, L.-J., Pu, W.-C., and Yin, J.-H. (2003). “Test and numerical analysis of the constitutive relation of a diatomaceous soft rock.” *Marine Georesources and Geotechnology*, Taylor & Francis, 21(3–4), 183–200.

Liao, H., Ning, C., Akaishi, M., and Zhou, L. (1998). “Effects of the time-dependent behavior on strain softening of diatomaceous soft rock.” *Metals and Materials*, Springer, 4, 1093–1096.

Locat, J., and Tanaka, H. (2001). “A new class of soils: Fossiliferous soils?” *Proceedings of the 15th International Conference on Soil Mechanics and Geotechnical Engineering*, Istanbul, Turkey, 2295–2300.

Locat, J., Tanaka, H., Tan, T. S., Dasari, G. R., and Lee, H. (2003). “Natural soils: geotechnical behavior and geological knowledge.” *Characterisation and engineering properties of natural soils*, CRC Press, 1, 3.

Ludwig, E. E. (1997). *Applied Process Design for Chemical and Petrochemical Plants: Volume 2*. gulf professional publishing.

Maekawa, H., Miyakita, K., and Ohta, H. (1992). “Yield locus of a diatomaceous mudstone with artificially made plane of separation.” *Soils and Foundations*, The Japanese Geotechnical Society, 32(2), 21–34.

Maekawa, H., Miyakita, K., and Sekiguchi, H. (1991). “Elasto-Viscoplastic Consolidation of a Diatomaceous Mudstone.” *Soils and Foundations*, 31(2), 93–107.

Matsumoto, T., Michi, Y., and Hirano, T. (1995). “Performance of Axially Loaded Steel Pipe Piles Driven in Soft Rock.” *Journal of Geotechnical Engineering*, 121(4), 305–315.

Mayne, P. W. (1985). “A review of undrained strength in direct simple shear.” *Soils and foundations*, The Japanese Geotechnical Society, 25(3), 64–72.

Mayne, P. W. (1991). “DETERMINATION OF OCR IN CLAYS BY PIEZOCONE TESTS USING CAVITY EXPANSI0N AND CRITICAL STATE C0NCEPTS.” *Soils and foundations*, The Japanese Geotechnical Society, 31(2), 65–76.

Mayne, P. W. (2001). “Stress-strain-strength-flow parameters from enhanced in-situ tests.” *Proc. Int. Conf. on In Situ Measurement of Soil Properties and Case Histories, Bali*, 27–47.

Mayne, P. W. (2005). “Integrated ground behavior: In-situ and lab tests.” *Deformation characteristics of geomaterials*, Taylor & Francis London, 2, 155–177.

Mayne, P. W. (2007). *Cone penetration testing*. Transportation Research Board.

Mayne, P. W. (2014). “Interpretation of geotechnical parameters from seismic piezocone tests.” *Proceedings, 3rd International Symposium on Cone Penetration Testing*, 47–73.

Mayne, P. W. (2015). “In-situ geocharacterization of soils in the year 2016 and beyond.” *Advances in Soil Mechanics*, Geot. Synergy (PCSMGE, Buenos Aires), IOS, 5, 139–161.

McClelland, B. (1974). “Design of deep penetration piles for ocean structures.” *Journal of the Geotechnical Engineering Division*, American Society of Civil Engineers, 100(7), 709–747.

Mendoza, C., Caicedo, B., and Lopez-Caballero, F. (2019). “Geotechnical behavior of Bogotá lacustrine soil through its geological history.” *Proceedings of the 17th European Conference on Soil Mechanics and Geotechnical Engineering, ECSMGE, Reykjavik, Iceland*, 1–6.

Mesri, G., Rokhsar, A., and Bohor, B. F. (1975). “Composition and compressibility of typical samples of Mexico City clay.” *Geotechnique*, Thomas Telford Ltd, 25(3), 527–554.

Nishida, Y. (1985). “Drivability of steel pipe piles into diatomaceous mudstone in the construction of Notojima Bridge.” *Proc. Int. Symp. on Penetrability and Drivability of Piles*, 187–190.

Norman, L. E. J. (1958). “A comparison of values of liquid limit determined with apparatus having bases of different hardness.” *Geotechnique*, Thomas Telford Ltd, 8(2), 79–83.

ODOT. (1996). *Foundation Report - Geary Canal Bridge*. Oregon Department of Transportaion.

Oka, F., Kimoto, S., Higo, Y., Ohta, H., Sanagawa, T., and Kodaka, T. (2011). “An elasto-viscoplastic model for diatomaceous mudstone and numerical simulation of compaction bands.” *International Journal for Numerical and Analytical Methods in Geomechanics*, Wiley Online Library, 35(2), 244–263.

Ouyang, Z., and Mayne, P. W. (2019). “Modified NTH method for assessing effective friction angle of normally consolidated and overconsolidated clays from piezocone tests.” *Journal of Geotechnical and Geoenvironmental Engineering*, American Society of Civil Engineers, 145(10), 4019067.

Ouyang, Z., and Mayne, P. W. (2020). "Effective Stress Friction Angle of Normally Consolidated and Overconsolidated Intact Clays from Piezocone Tests." *Geotechnical Engineering (00465828)*, 51(2).

Ouyang, Z., and Mayne, P. W. (2023). "Evaluating friction angles for clays: piezocone tests compared with Atterberg limits." *Proceedings of the Institution of Civil Engineers-Geotechnical Engineering*, Thomas Telford Ltd, 1–11.

Ovalle, C., and Arenaldi-Perisic, G. (2021). "Mechanical behaviour of undisturbed diatomaceous soil." *Marine Georesources & Geotechnology*, Taylor & Francis, 39(5), 623–630.

Ovalle, C., Arenaldi-Perisic, G., and Barrios, A. (2019). "Compressibility and Dynamic Properties of Diatomaceous Soils from Mejillones, Chile." *Geotechnical Engineering in the XXI Century: Lessons learned and future challenges: Proceedings of the XVI Pan-American Conference on Soil Mechanics and Geotechnical Engineering (XVI PCSMGE), 17-20 November 2019, Cancun, Mexico*, IOS Press, 294.

Pacheco Silva, F. (1970). "A new graphical construction for determination of the preconsolidation stress of a soil sample." *Proceedings of the 4th Brazilian Conference on Soil Mechanics and Foundation Engineering, Rio de Janeiro, Brazil*, 225–232.

Palomino, A. M., Kim, S., Summitt, A., and Fratta, D. (2010). "Influence of ionic concentration and internal porosity on the behavior of diatom-clay mixtures." *GeoFlorida 2010: advances in analysis, modeling & design*, 628–637.

Palomino, A. M., Kim, S., Summitt, A., and Fratta, D. (2011). "Impact of diatoms on fabric and chemical stability of diatom–kaolin mixtures." *Applied Clay Science*, Elsevier, 51(3), 287–294.

Pearse-Danker, E. (2013). "Liquefaction potential of Rotorua soils." *19th New Zealand Geotechnical Society Geotechnical Symposium*, C. Y. Chin, ed., Queenstown, NZ, 7.

Perez Leon, R. F., Rodríguez Rebolledo, J. F., and Caicedo Hormaza, B. (2022). "Stiffness and strength parameters for the hardening soil model of a reconstituted diatomaceous soil." *European Journal of Environmental and Civil Engineering*, Taylor & Francis, 1–21.

Peric, D., Runesson, K., and Sture, S. (1992). "Evaluation of plastic bifurcation for plane strain versus axisymmetry." *Journal of engineering mechanics*, American Society of Civil Engineers, 118(3), 512–524.

Perisic, G. A., Ovalle, C., and Barrios, A. (2019). "Compressibility and creep of a diatomaceous soil." *Engineering Geology*, Elsevier, 258, 105145.

Pestana, J. M., Biscontin, G., Nadim, F., and Andersen, K. (2000). "Modeling cyclic behavior of lightly overconsolidated clays in simple shear." *Soil Dynamics and Earthquake Engineering*, Elsevier, 19(7), 501–519.

Petersen, L. W., Moldrup, P., Jacobsen, O. H., and Rolston, D. E. (1996). "Relations between specific surface area and soil physical and chemical properties." *Soil Science*, LWW, 161(1), 9–21.

Pittenger, A., Taylor, E., and Bryant, W. R. (1989). "43. THE INFLUENCE OF BIOGENIC SILICA ON THE GEOTECHNICAL STRATIGRAPHY OF THE VORING PLATEAU, NORWEGIAN SEA1."

Potyondy, J. G. (1961). "Skin friction between various soils and construction materials." *Geotechnique*, Thomas Telford Ltd, 11(4), 339–353.

Puzrin, A. (2012). *Constitutive modelling in geomechanics: introduction*. Springer Science & Business Media.

Rausche, F., Moses, F., and Goble, G. G. (1972). "Soil resistance predictions from pile dynamics." *Journal of the soil mechanics and foundations division*, American Society of Civil Engineers, 98(9), 917–937.

Robertson, P. K. (1990). "Soil classification using the cone penetration test." *Canadian Geotechnical Journal*, NRC Research Press Ottawa, Canada, 27(1), 151–158.

Robertson, P. K. (2009). "Interpretation of cone penetration tests—a unified approach." *Canadian geotechnical journal*, 46(11), 1337–1355.

Robertson, P. K. (2016). "Cone penetration test (CPT)-based soil behaviour type (SBT) classification system—an update." *Canadian Geotechnical Journal*, NRC Research Press, 53(12), 1910–1927.

Robertson, P. K., and Fear, C. E. (1997). "Cyclic liquefaction and its evaluation based on the SPT and CPT." *Proceeding of the NCEER workshop on evaluation of liquefaction resistance of soils*, 41–87.

Robinson, R. G. (2003). "A study on the beginning of secondary compression of soils." *Journal of testing and evaluation*, ASTM International, 31(5), 388–397.

Saldivar, E. E., and Jardine, R. J. (2005). "Application of an effective stress design method to concrete piles driven in Mexico City clay." *Canadian geotechnical journal*, NRC Research Press, 42(6), 1495–1508.

Santamarina, J. C., Klein, A., and Fam, M. A. (2001a). "Soils and waves: Particulate materials behavior, characterization and process monitoring." *Journal of Soils and Sediments*, Springer Nature BV, 1(2), 130.

Santamarina, J. C., Klein, K. A., and Fam, M. A. (2001b). *Soils and Waves*. J. Wiley & Sons, New York.

Santamarina, J. C., Klein, K. A., Wang, Y. H., and Prencke, E. (2002). "Specific surface: determination and relevance." *Canadian Geotechnical Journal*, 39, 233–241.

Schanz, T. (1998). *Zur Modellierung des mechanischen verhaltens von Reibungsmaterialien*. na.

Schellart, W. P. (2000). "Shear test results for cohesion and friction coefficients for different granular materials: scaling implications for their usage in analogue modelling." *Tectonophysics*, Elsevier, 324(1–2), 1–16.

Schneider, J. A., Randolph, M. F., Mayne, P. W., and Ramsey, N. R. (2008). "Analysis of factors influencing soil classification using normalized piezocone tip resistance and pore pressure parameters." *Journal of geotechnical and geoenvironmental engineering*, American Society of Civil Engineers, 134(11), 1569–1586.

Schofield, A. N., and Wroth, C. P. (1968). *Critical State Soil Mechanics*. London.

Sekiguchi, H. (1977). "Rheological characteristics of clays." *Proc. 9th ICSMFE, 1977*, 1, 289–292.

Senneset, K., Sandven, R., and Janbu, N. (1989). "Evaluation of soil parameters from piezocone tests." *Transportation research record*, (1235).

Shannon &Wilson, I. (2018). *Report of Dynamic Testing, OR 140: Buck Creek Bridge Replacement Project, Klamath County, Oregon. Oregon Department of Transportation.*

Shatnawi, H. H., and Bandini, P. (2018). "Limitations of Classifications for Soils that Contain Diatom Microfossils." *IFCEE 2018*, American Society of Civil Engineers, Orlando, FL, 123–132.

Shatnawi, H. H. Al, and Bandini, P. (2019). "Oedometric Behavior of a Diatom-Kaolin Mixture." *Geo-Congress 2019: Geotechnical Materials, Modeling, and Testing*, American Society of Civil Engineers Reston, VA, 673–681.

Sherwood, P. T., and Ryley, M. D. (1970). "An investigation of a cone-penetrometer method for the determination of the liquid limit." *Géotechnique*, Thomas Telford Ltd, 20(2), 203–208.

Shiwakoti, D. R., Tanaka, H., Tanaka, M., and Locat, J. (2002). "Influences of Diatom Microfossils on Engineering Properties of Soils." *Soils and Foundations*, 42(3), 1–17.

Simpson, D. C., and Evans, T. M. (2016). "Behavioral thresholds in mixtures of sand and kaolinite clay." *Journal of Geotechnical and Geoenvironmental Engineering*, 142(2).

Skempton, A. W., and Northey, R. D. (1952). "The sensitivity of clays." *Geotechnique*, Thomas Telford Ltd, 3(1), 30–53.

Skempton, A. W. (1948). "A possible relationship between true cohesion and the mineralogy of clays." *Proceedings of the second International Conference, Rotterdam*, 45–46.

Skempton, A. W. (1953). "Soil mechanics in relation to geology." *Proceedings of the Yorkshire Geological Society*, The Geological Society of London Bath, 29(1), 33–62.

Skempton, A. W. (1984). *Selected papers on soil mechanics*. Thomas Telford.

Skempton, A. W., and Bishop, A. W. (1950). "The measurement of the shear strength of soils." *Geotechnique*, Thomas Telford Ltd, 2(2), 90–108.

Slebi-Acevedo, C. J., Zuluaga-Astudillo, D. A., Ruge, J. C., and Castro-Fresno, D. (2021). "Influence of the diatomite specie on the peak and residual shear strength of the fine-grained soil." *Applied Sciences*, MDPI, 11(4), 1352.

Smith, R. E., and Wahls, H. E. (1969). "Consolidation under constant rates of strain." *Journal of the Soil Mechanics and Foundations Division*, American Society of Civil Engineers, 95(2), 519–539.

Sonyok, D. R. (2015). "Effect of Diatoms on Index Properties, Compressibility, Suction, and Stiffness of Diatomite-Kaolin Mixtures." Ph.D. thesis, New Mexico State University, Las Cruces, NM.

Sonyok, D. R., and Bandini, P. (2019). "Oedometric Behavior of Diatomite–Kaolin Mixtures." *Journal of Geotechnical and Geoenvironmental Engineering*, American Society of Civil Engineers, 145(9), 6019005.

Tamaki, K., Suyehiro, K., Allan, J., and McWilliams, M. (1989). "71. CONSOLIDATION CHARACTERISTICS AND PERMEABILITIES OF SEDIMENTS FROM THE JAPAN SEA (SITES 798 AND 799)." *Proceedings of the Ocean Drilling Program: Scientific results*, The Program, 1123.

Tanaka, H., and Locat, J. (1999). "A microstructural investigation of Osaka Bay clay: the impact of microfossils on its mechanical behaviour." *Canadian Geotechnical Journal*, 36, 493–508.

Tanaka, M., Tanaka, H., Kamei, T., and Hayashi, S. (2003). "Effects of diatom microfossil contents on engineering properties of soils." *The Thirteenth International Offshore and Polar Engineering Conference*, OnePetro.

Tanaka, M., Tanaka, H., and Shiwakoti, D. R. (2001). "Sample quality evaluation of soft clays using six types of samplers." *The Eleventh International Offshore and Polar Engineering Conference*, OnePetro.

Tanaka, M., Watabe, Y., and Kaihatsu, K. (2013). "Effects of Crushed Diatom Microfossils Content on Physical Properties of Japanese Clays." *Proceedings of the Twenty-third International Offshore and Polar Engineering*, International Society of Offshore and Polar Engineers (ISOPE), Anchorage, AK, 513–517.

Tanaka, M., Watabe, Y., Tomita, R., and Kamei, T. (2012). "Effects of diatom microfossils content on physical properties of clays." *The Twenty-second International Offshore and Polar Engineering Conference*, OnePetro.

Taylor, D. (1948). *Fundamentals of soil mechanics*. Chapman And Hall, Limited.; New York.

Teh, C. I., and Houlsby, G. T. (1991). “An analytical study of the cone penetration test in clay.” *Geotechnique*, 41(1), 17–34.

Terzaghi, K. (1943). “1943, Theoretical Soil Mechanics, John Wiley & Sons, New York.”

Uesugi, M., and Kishida, H. (1986a). “Influential factors of friction between steel and dry sands.” *Soils and foundations*, The Japanese Geotechnical Society, 26(2), 33–46.

Uesugi, M., and Kishida, H. (1986b). “Frictional resistance at yield between dry sand and mild steel.” *Soils and foundations*, Elsevier, 26(4), 139–149.

Uesugi, M., Kishida, H., and Tsubakihara, Y. (1988). “Behavior of sand particles in sand-steel friction.” *Soils and foundations*, The Japanese Geotechnical Society, 28(1), 107–118.

Vardanega, P. J., and Haigh, S. K. (2014). “The undrained strength-liquidity index relationship.” *Canadian Geotechnical Journal*, 51, 1073–1086.

Vardoulakis, I. (1979). “Bifurcation analysis of the triaxial test on sand samples.” *Acta Mechanica*, Springer, 32(1–3), 35–54.

Vardoulakis, I. (1983). “Rigid granular plasticity model and bifurcation in the triaxial test.” *Acta Mechanica*, Springer, 49(1–2), 57–79.

Vardoulakis, I. (1985). “Stability and bifurcation of undrained, plane rectilinear deformations on water-saturated granular soils.” *International journal for numerical and analytical methods in geomechanics*, Wiley Online Library, 9(5), 399–414.

Vera-Grunauer, X. (2014). “Seismic Response of a Soft, High Plasticity, Diatomaceous Naturally Cemented Clay Deposit.” University of California, Berkeley.

Verdugo, R. (2008). “Singularities of Geotechnical Properties of Complex Soils in Seismic Regions.” *Journal of Geotechnical and Geoenvironmental Engineering*, 134(July), 982–991.

VJ Tech. (n.d.). “Direct Simple Shear - An Introduction.” <https://www.vjtech.co.uk/blog/introduction-to-direct-simple-shear-dss-testing> (Jul. 15, 2023).

Wang, J., Chin, T., Moug, D., and Evans, T. M. (2022). “On the liquid limit of diatomaceous soils: Complex behavior of a non-standard material.” *Geo-Congress 2022*, 45–55.

Wang, J., Yazdani, E., and Evans, T. M. (2021). “Case study of a driven pile foundation in diatomaceous soil. I: Site characterization and engineering properties.” *Journal of Rock Mechanics and Geotechnical Engineering*, Elsevier, 13(2), 431–445.

Wiemer, G., Dziadek, R., and Kopf, A. (2017). “The enigmatic consolidation of diatomaceous sediment.” *Marine Geology*, Elsevier, 385, 173–184.

Wiemer, G., and Kopf, A. (2017). “Influence of diatom microfossils on sediment shear strength and slope stability.” *Geochemistry, Geophysics, Geosystems*, Wiley Online Library, 18(1), 333–345.

Wiemer, G., Moernaut, J., Stark, N., Kempf, P., De Batist, M., Pino, M., Urrutia, R., Ladrón De Guevara, B., Strasser, M., and Kopf, A. (2015). “The role of sediment composition and behavior under dynamic loading conditions on slope failure initiation: a study of a subaqueous landslide in earthquake-prone South-Central Chile.” *Int J Earth Sci*, 104, 1439–1457.

Wikipedia. (n.d.). “Preconsolidation pressure.” <https://en.wikipedia.org/wiki/Preconsolidation_pressure> (Jul. 15, 2023).

Wood, D. M. (1985). “Some fall-cone tests.” *Geotechnique*, Thomas Telford Ltd, 35(1), 64–68.

Wood, D. M. (1990). *Soil Behaviour and Critical State Soil Mechanics*. Cambridge University Press, Cambridge.

Wood, D. M., and Wroth, C. P. (1978). “The use of the cone penetrometer to determine the plastic limit of soils.” *Ground Engineering*, 11(3).

Wroth, C. P. (1979). “Correlations of some engineering properties of soils.” *Proceedings of the Second International Conference on the Behaviour of Off-Shore Structures, held at Imperial College, London, England*.

Wroth, C. P. (1984). “The interpretation of in situ soil tests.” *Geotechnique*, Thomas Telford Ltd, 34(4), 449–489.

Wroth, C. P., and Wood, D. M. (1978). “The correlation of index properties with some basic engineering properties of soils.” *Canadian Geotechnical Journal*, NRC Research Press, 15(2), 137–145.

Xu, Y., Zhang, X., Liu, X., and Wang, G. (2022). “Alterations of physical properties and microstructure of marine diatomite owing to variation of diatom content.” *Marine Georesources & Geotechnology*, Taylor & Francis, 1–12.

Yazdani, E., Wang, J., and Evans, T. M. (2021). “Case Study of a Driven Pile Foundation in Diatomaceous Soil II: Pile Installation.” *Journal of Rock Mechanics and Geotechnical Engineering*, in review.

Yin, J.-H., and Graham, J. (1999). “Elastic viscoplastic modelling of the time-dependent stress-strain behaviour of soils.” *Canadian geotechnical journal*, NRC Research Press Ottawa, Canada, 36(4), 736–745.

Yoshimi, Y., and Kishida, T. (1981). “A ring torsion apparatus for evaluating friction between soil and metal surfaces.” *Geotechnical testing journal*, ASTM International, 4(4), 145–152.

Youssef, M. S. (1965). “Relationships between shear strength, consolidation, liquid limit, and plastic limit for remoulded clays.” *Proc. 6th Int. Conf. on SMFE*, Tronto Univ. press, 126–129.

Zhang, L. (2017). “A Discrete Numerical Study of the Micromechanics of Sand Liquefaction.” Oregon State University.

Zhang, Y., Guo, C., Yao, X., Qu, Y., and Zhou, N. (2013). “Engineering geological characterization of clayey diatomaceous earth deposits encountered in highway projects in the Tengchong region, Yunnan, China.” *Engineering Geology*, Elsevier, 167, 95–104.

Zuluaga-Astudillo, D. A., Slebi-Acevedo, C. J., Ruge, J. C., and Olarte, M. C. (2022). “Physical Modeling in Geotechnical Centrifuge of Foundations Supported on Diatomaceous Soils.” *Indian Geotechnical Journal*, Springer, 1–10.

Zuluaga, D. A., Sabogal, D., Buenaventura, C. A., and Slebi, C. J. (2021). “Physical and mechanical behavior of fine soil according to the content of multispecies diatoms.” *Journal of Physics: Conference Series*, IOP Publishing, 12011.

APPENDIX A: SCANNING ELECTRON MICROSCOPE IMAGES

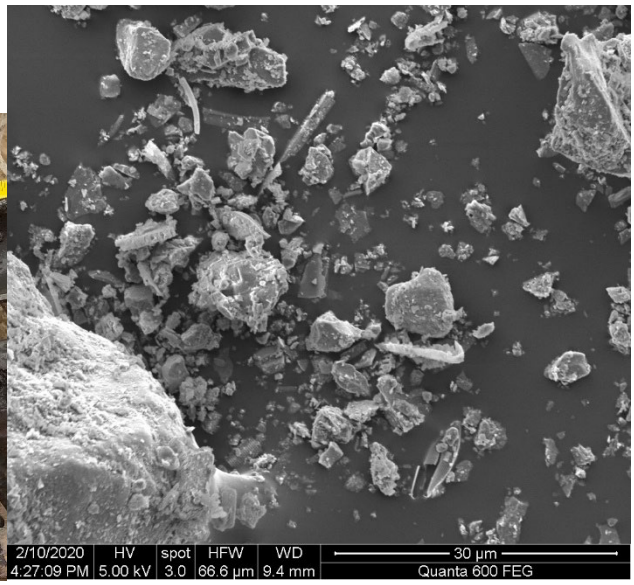

W1N6

$$\boldsymbol{depth = 15.7m}$$

$$\boldsymbol{w_n = 32, (N_1)_{60} = 0.8}$$

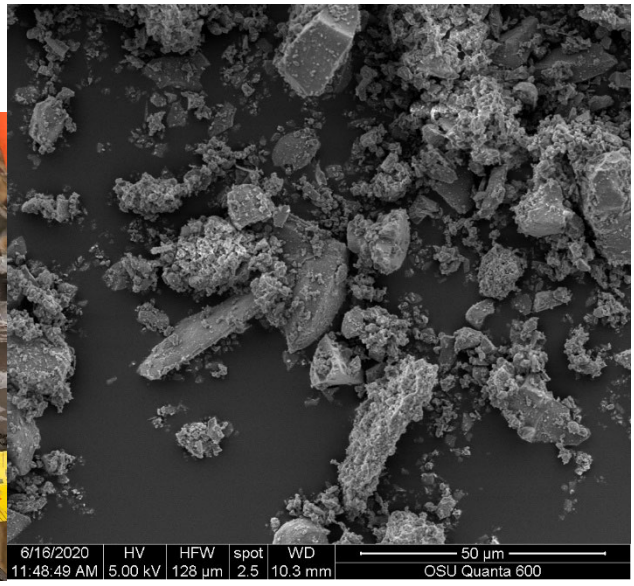

W1N8

$$\boldsymbol{depth = 20.9m}$$

$$\boldsymbol{w_n = 40, (N_1)_{60} = 0.7}$$

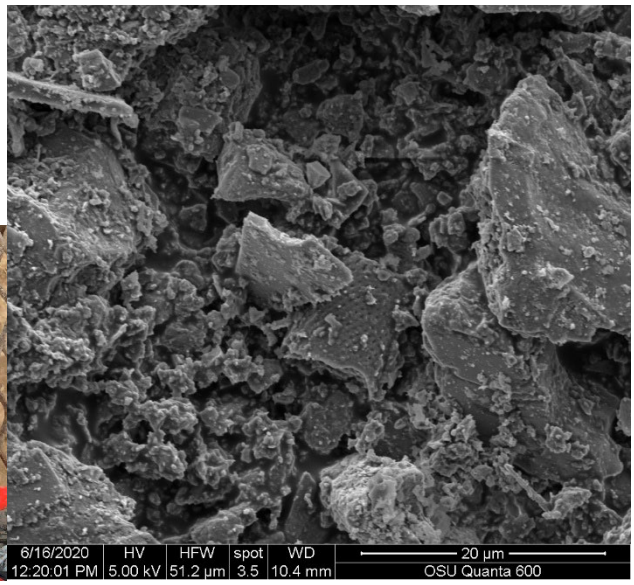

W1N11a

$\boldsymbol{depth = 27m}$

$\boldsymbol{w_n = 47, LL = 37, PL = 18}$

$\boldsymbol{\gamma = 16.81 kN/m^3, G_s = 2.74}$

$\boldsymbol{S_r = 95.5\%, FC = 79.4\%,\ (N_1)_{60} = 0.7}$

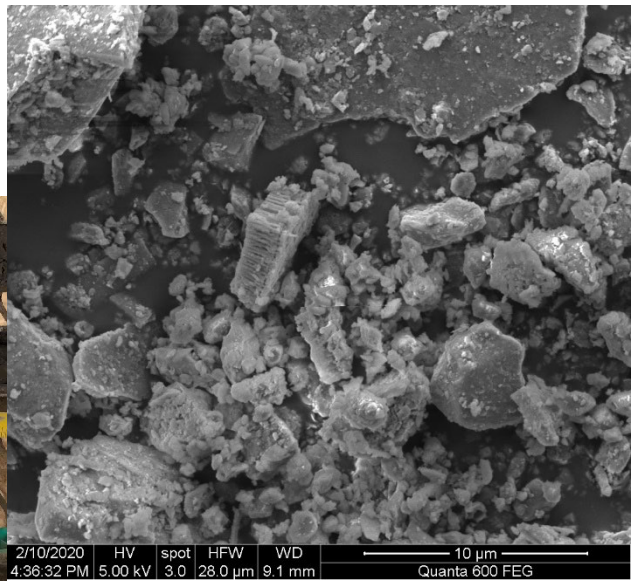

W1N11b

$\boldsymbol{depth = 27.3m}$

$\boldsymbol{w_n = 31, LL = 49, PL = 35}$

$\boldsymbol{\gamma = 16.4 kN/m^3, G_s = 2.8}$

$\boldsymbol{S_r = 72.5\%, FC = 96.6\%,\ (N_1)_{60} = 0.7}$

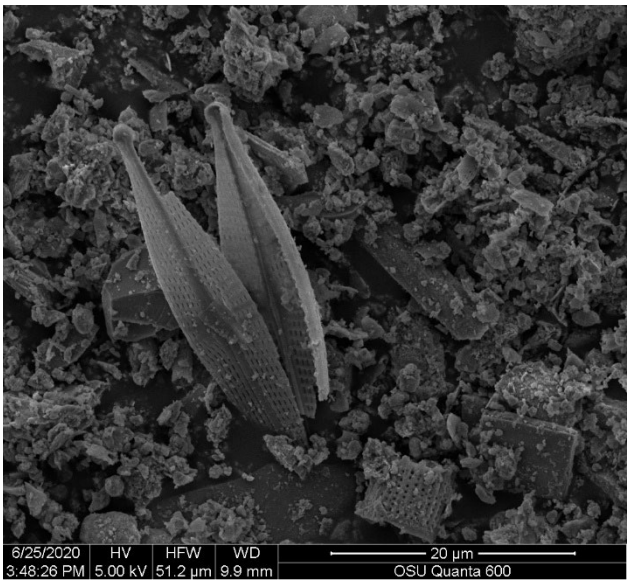

W1U7

$$\boldsymbol{depth = 30.8m}$$
$$\boldsymbol{w_n = 71, LL = 66, PL = 36}$$
$$\boldsymbol{\gamma_{calc} = 15.2kN/m^3, G_s = 2.54}$$
$$\boldsymbol{FC = 98.4\%}$$

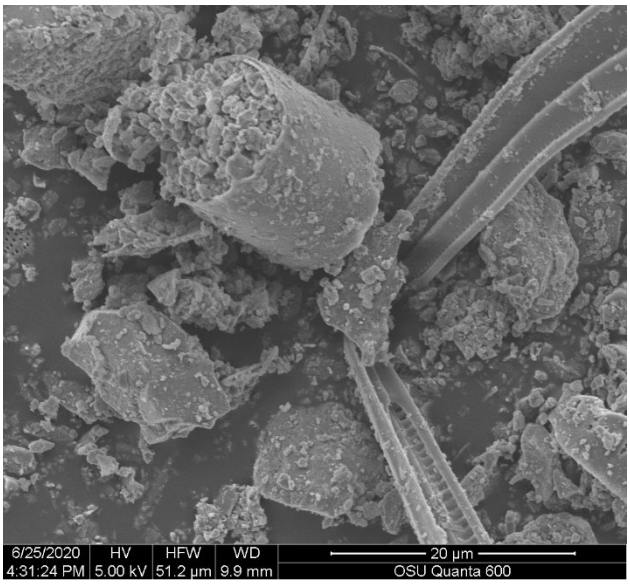

W1U10

$$\boldsymbol{depth = 44.4m}$$
$$\boldsymbol{w_n = 66, LL = 52, PL = 29}$$
$$\boldsymbol{\gamma_{calc} = 15.4kN/m^3, G_s = 2.5}$$
$$\boldsymbol{FC = 99.6\%}$$

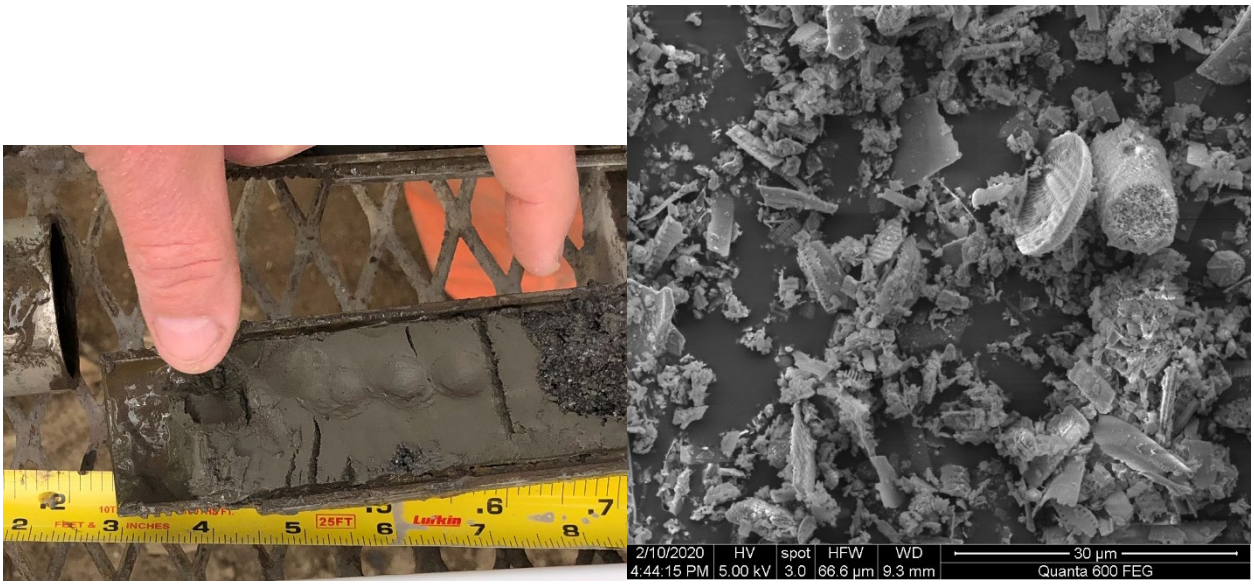

W1N13a
$\boldsymbol{depth = 31.4m}$
$\boldsymbol{w_n = 122}$

W1N13c
$\boldsymbol{depth = 31.2m}$
$\boldsymbol{w_n = 100}$

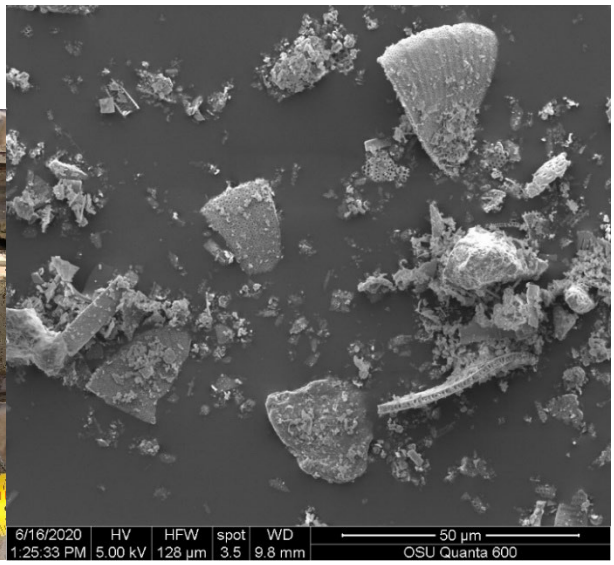

W1N14

$$depth = 34.29m$$
$$w_n = 205.5, LL = 172, PL = 50$$
$$\gamma = 11.84kN/m^3, G_s = 2.23$$
$$S_r = 98.8\%, FC = 93.9\%$$
$$(N_1)_{60} = 0$$

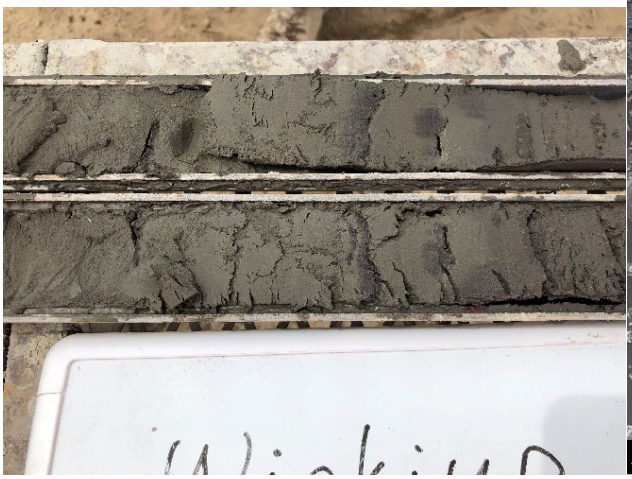

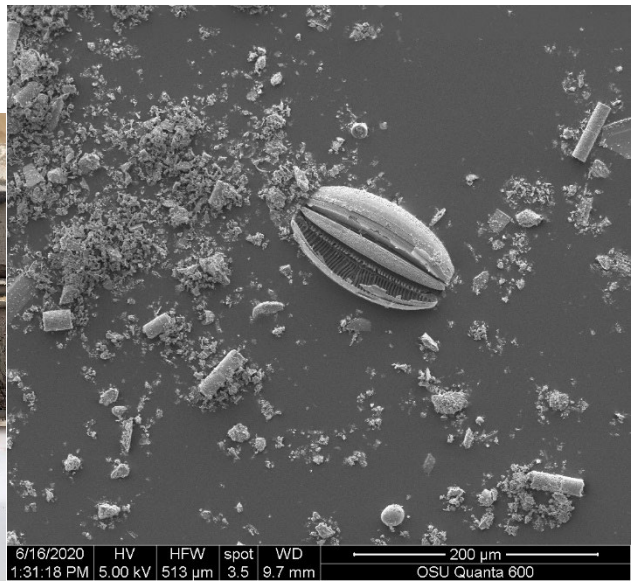

W1N15

$$depth = 37.34m$$
$$w_n = 93.8, LL = 93, PL = 48$$
$$\gamma = 13.92kN/m^3, G_s = 2.47$$
$$S_r = 97.8\%, FC = 95.5\%$$
$$(N_1)_{60} = 1.2$$

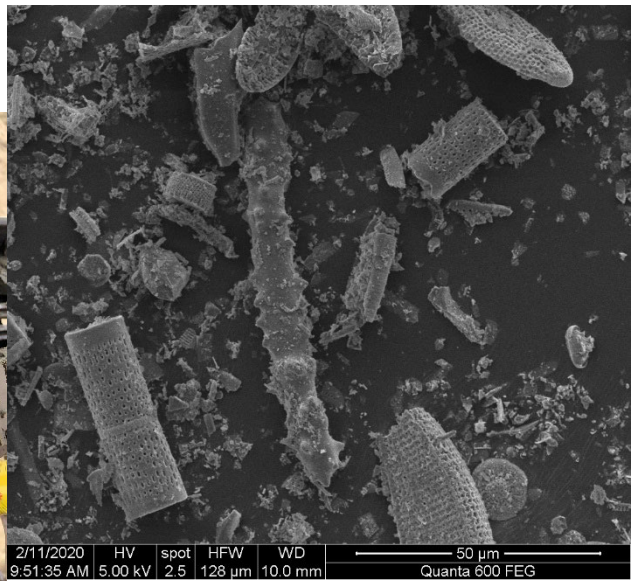

W1N17

$\boldsymbol{depth = 43.28m}$

$\boldsymbol{w_n = 158.8, LL = 139, PL = 87}$

$\boldsymbol{\gamma = 12.4kN/m^3, G_s = 2.33}$

$\boldsymbol{S_r = 98.2\%, FC = 99.5\%}$

$\boldsymbol{(N_1)_{60} = 0.6}$

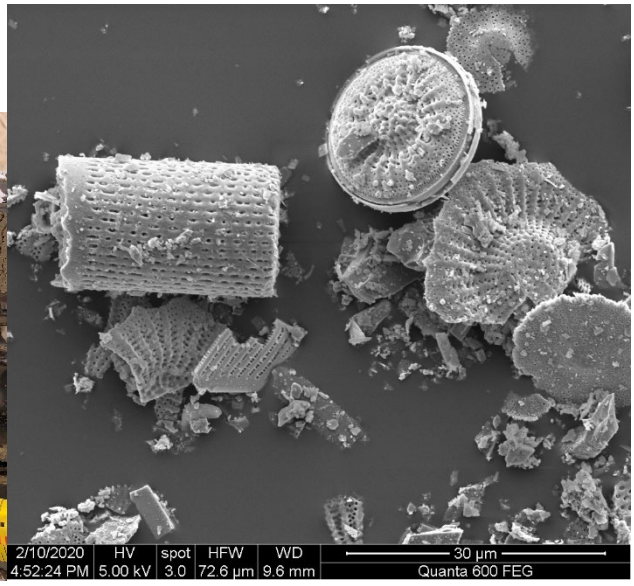

W1N21

$\boldsymbol{depth = 55.47m}$

$\boldsymbol{w_n = 171, LL = 150, PL = 68}$

$\boldsymbol{\gamma = 12.66kN/m^3, G_s = 2.24}$

$\boldsymbol{S_r = 103.5\%, FC = 97.3\%}$

$\boldsymbol{(N_1)_{60} = 0.6}$

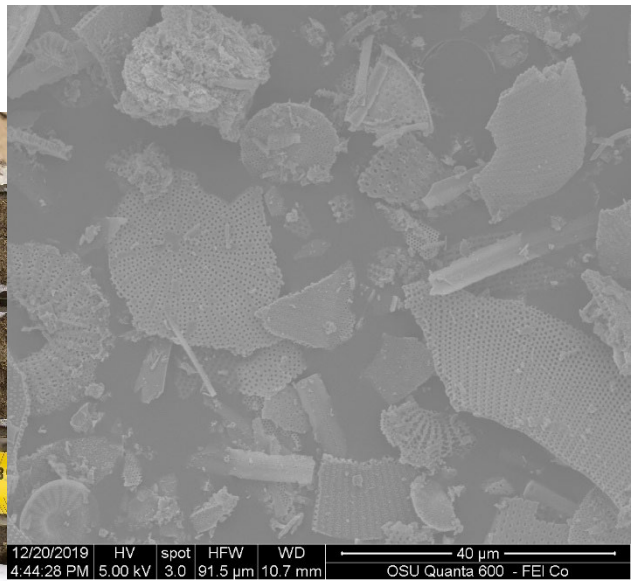

W1N26

$\boldsymbol{depth = 65.9m}$
$\boldsymbol{w_n = 211.3, LL = 200, PL = 67}$
$\boldsymbol{\gamma = 11.12kN/m^3, G_s = 2.13}$
$\boldsymbol{S_r = 92.9\%, FC = 87.2\%}$
$\boldsymbol{(N_1)_{60} = 10}$

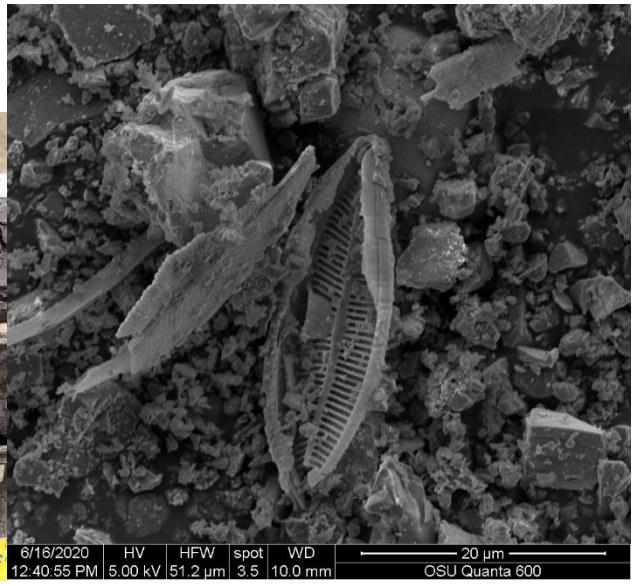

W1N28

$\boldsymbol{depth = 71.5m}$
$\boldsymbol{w_n = 46}$
$\boldsymbol{\gamma = 17.5kN/m^3, G_s = 2.7}$
$\boldsymbol{S_r = 102.7\%, FC = 98.5\%}$
$\boldsymbol{(N_1)_{60} = 9}$

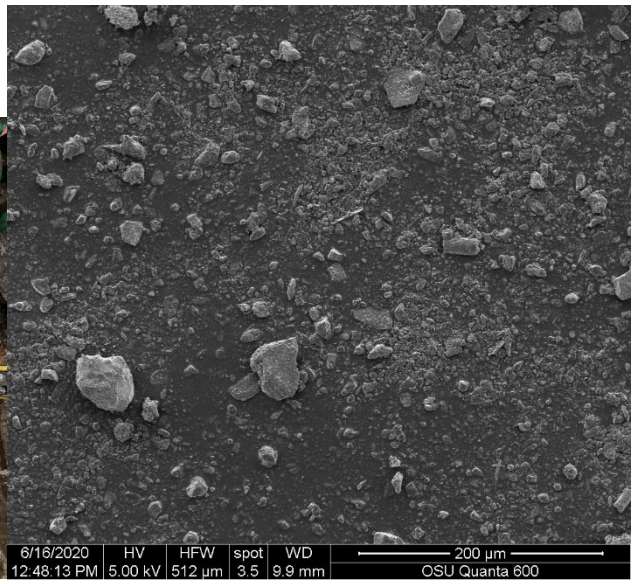

W2N1

$\boldsymbol{depth = 21m}$

$\boldsymbol{w_n = 38,\ SSA_{MB} = 23m^2/g}$

$\boldsymbol{\gamma = 18kN/m^3, G_s = 2.73}$

$\boldsymbol{FC = 97.8\%}$

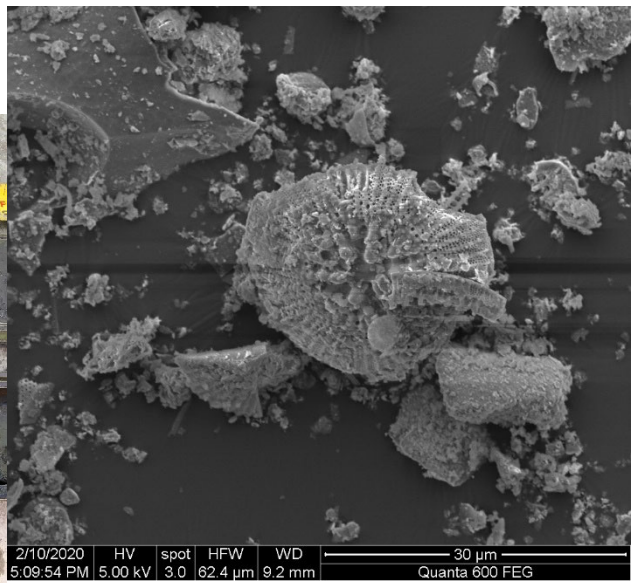

AC1N4

$\boldsymbol{depth = 9.4m}$

$\boldsymbol{w_n = 102}$

$\boldsymbol{(N_1)_{60} = 0.9}$

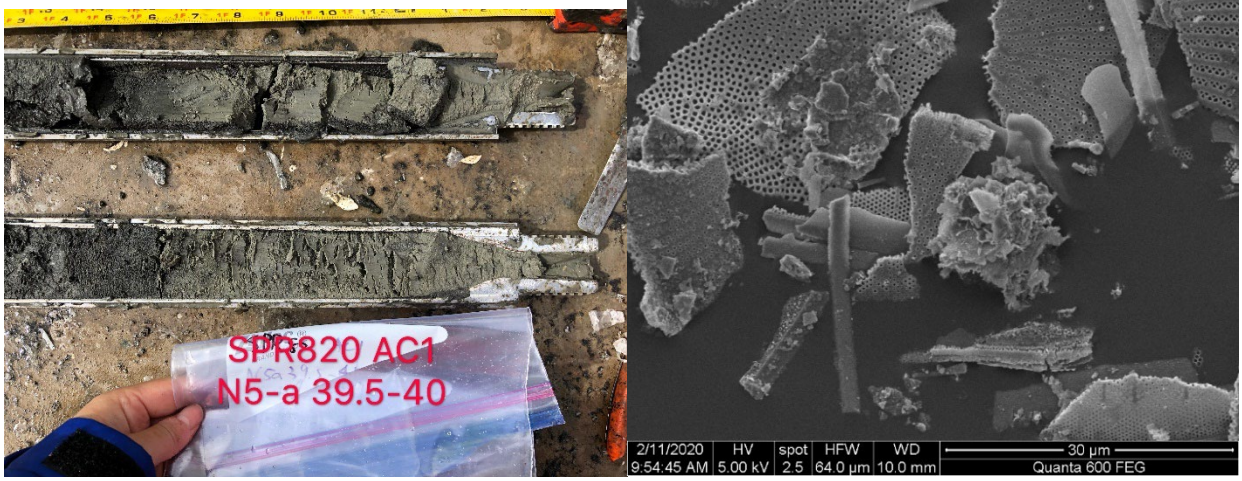

AC1N5a

$\boldsymbol{depth = 12.2m}$

$\boldsymbol{w_n = 173}$

$\boldsymbol{(N_1)_{60} = 2.9}$

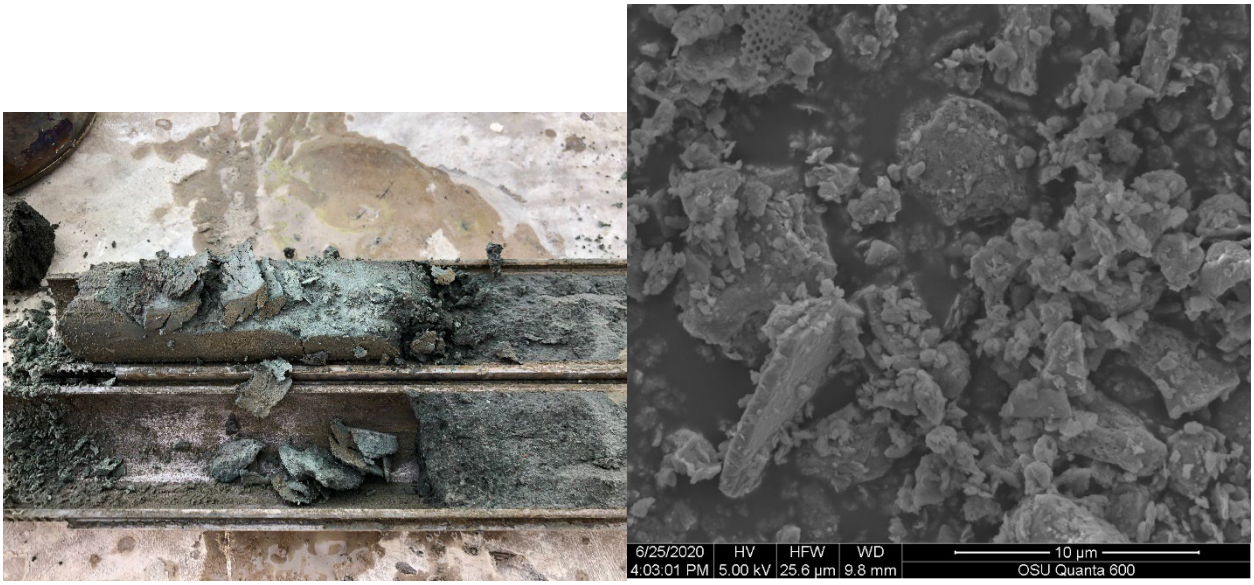

AC1N8

$\boldsymbol{depth = 19m}$

$\boldsymbol{w_n = 37, LL = 35, PL = 30,\ SSA_{MB} = 120.5m^2/g}$

$\boldsymbol{\gamma = 17.5kN/m^3, G_s = 2.5}$

$\boldsymbol{S_r = 100.7\%, FC = 64.7\%}$

$\boldsymbol{(N_1)_{60} = 57.5}$

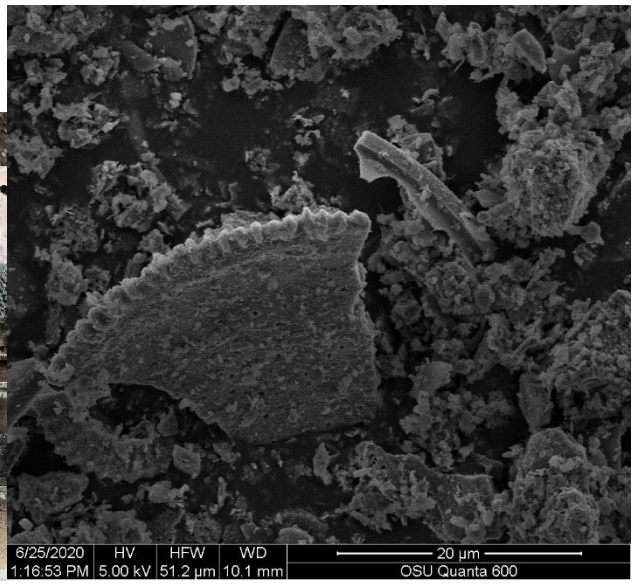

AC1N9

$\boldsymbol{depth = 20.27m}$
$\boldsymbol{w_n = 126, LL = 121, PL = 85,\ SSA_{MB} = 223m^2/g}$
$\boldsymbol{\gamma = 12.6kN/m^3}$
$\boldsymbol{FC = 96.5\%}$
$\boldsymbol{(N_1)_{60} = 10.7}$

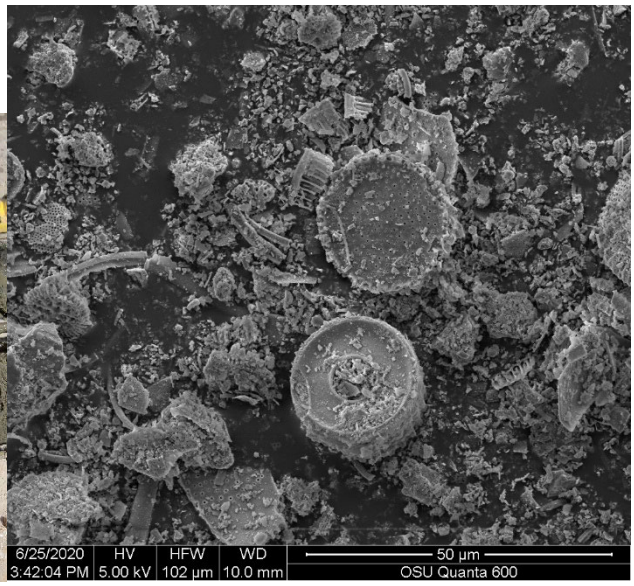

AC1N11

$\boldsymbol{depth = 26.2m}$
$\boldsymbol{w_n = 151.7, LL = 166, PL = 89}$
$\boldsymbol{\gamma_{calc} = 12.65kN/m^3, G_s = 2.31}$
$\boldsymbol{FC = 90\%}$
$\boldsymbol{(N_1)_{60} = 3.9}$

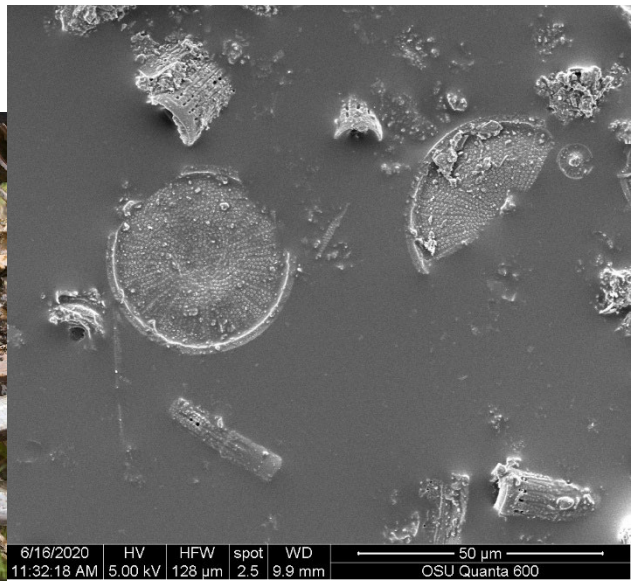

PC1N1

$\boldsymbol{depth = 3.5m}$

$\boldsymbol{w_n = 86, LL = 111, PL = 73}$

$\boldsymbol{\gamma = 14.2kN/m^3, G_s = 2.49}$

$\boldsymbol{S_r = 97.3\%, FC = 91\%}$

$\boldsymbol{(N_1)_{60} = 23.6}$

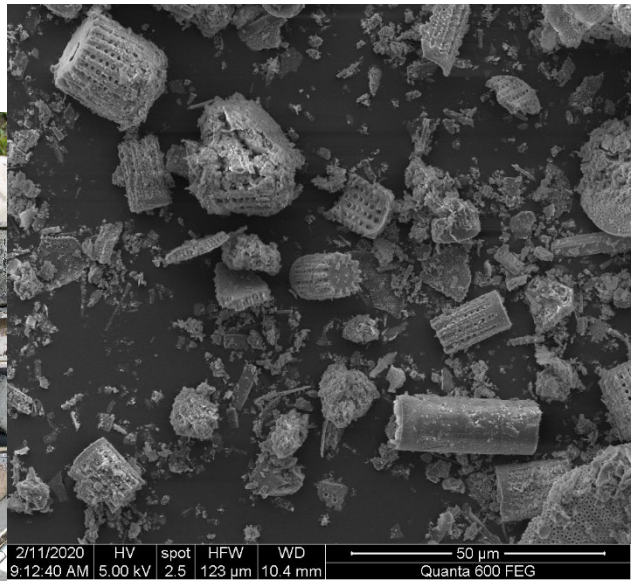

PC1N2

$\boldsymbol{depth = 5.49m}$

$\boldsymbol{w_n = 92, LL = 114, PL = 49}$

$\boldsymbol{\gamma = 12.9kN/m^3}$

$\boldsymbol{FC = 87.6\%}$

$\boldsymbol{(N_1)_{60} = 19}$

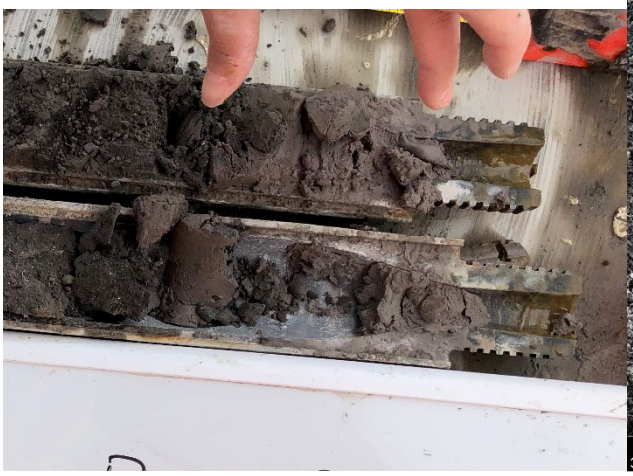

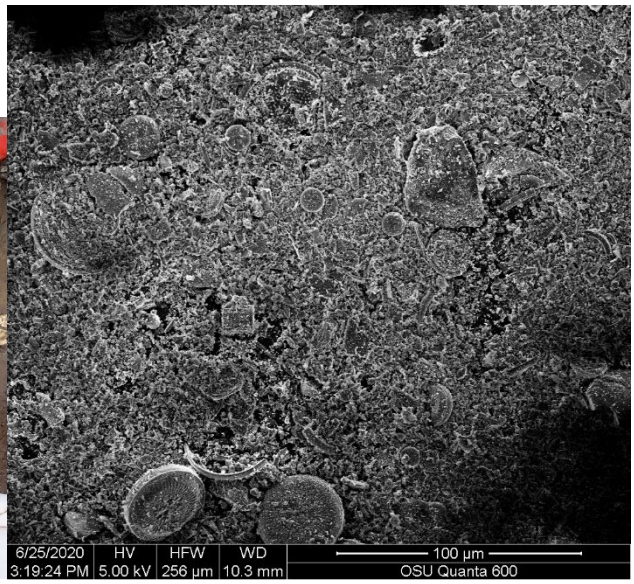

PC1N4a
$\boldsymbol{depth = 11.4m}$
$\boldsymbol{w_n = 46}$
$\boldsymbol{(N_1)_{60} = 25}$

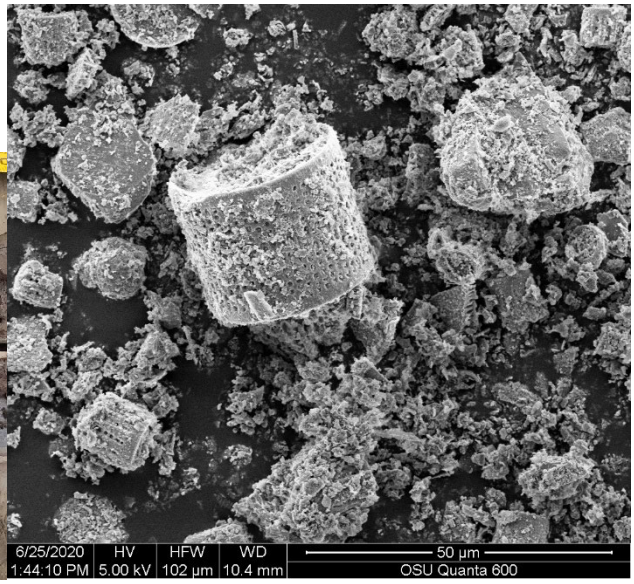

PC1N4b
$\boldsymbol{depth = 11.6m}$
$\boldsymbol{w_n = 39}$
$\boldsymbol{(N_1)_{60} = 25}$

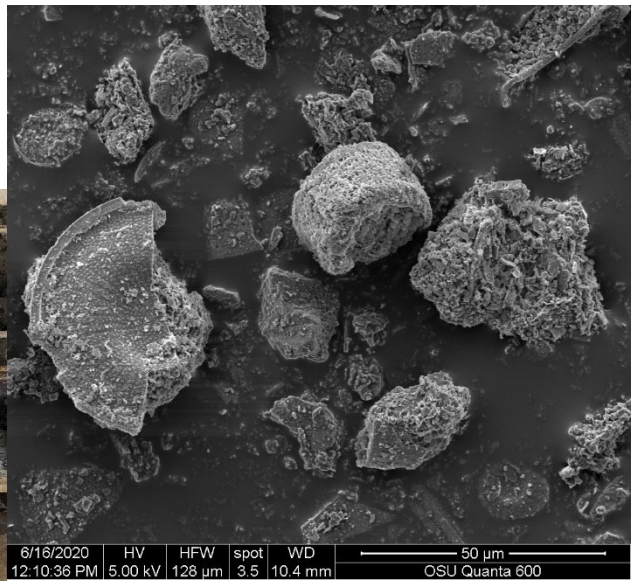

PC1N4c

$\boldsymbol{depth = 11.7m}$

$\boldsymbol{w_n = 73}$

$\boldsymbol{\gamma = 14kN/m^3}$

$\boldsymbol{(N_1)_{60} = 25}$

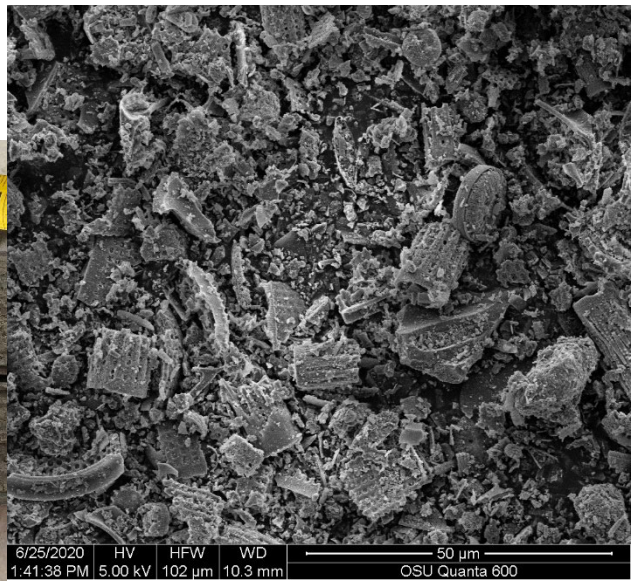

PC1N6b

$\boldsymbol{depth = 17.8m}$

$\boldsymbol{w_n = 147}$

$\boldsymbol{(N_1)_{60} = 21.3}$

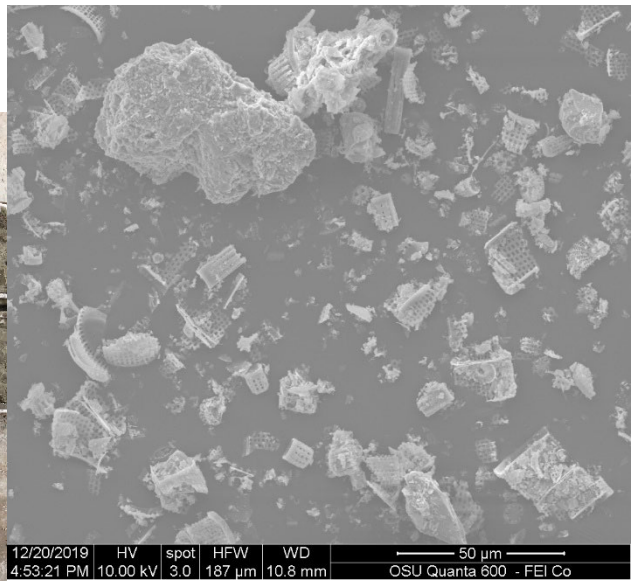

PC1N8

$\boldsymbol{depth = 23.7m}$

$\boldsymbol{w_n = 158, LL = 153, PL = 91}$

$\boldsymbol{\gamma = 12.1kN/m^3}$

$\boldsymbol{(N_1)_{60} = 14.5}$

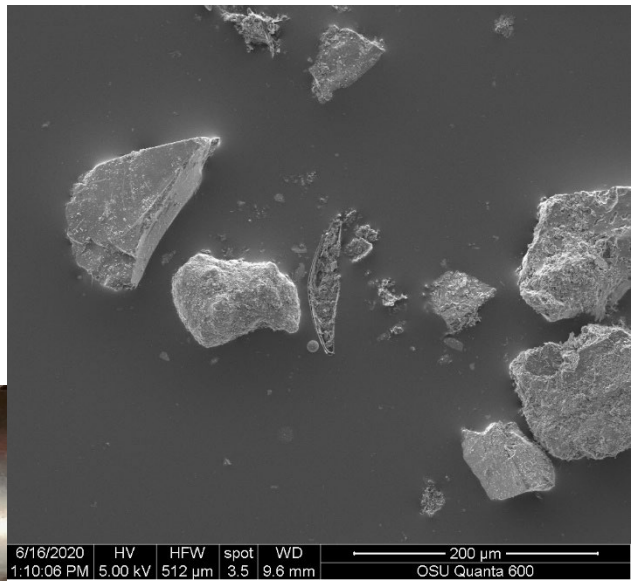

MP1N3a

$\boldsymbol{depth = 8.5m}$

$\boldsymbol{w_n = 53}$

$\boldsymbol{(N_1)_{60} = 19}$

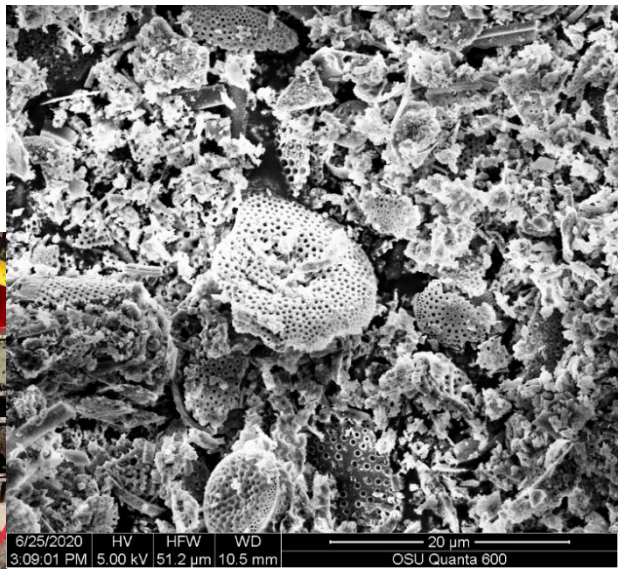

MP1N3b

$\boldsymbol{depth = 8.8m}$

$\boldsymbol{w_n = 151}$

$\boldsymbol{\gamma_{calc} = 12.5kN/m^3, G_s = 2.2}$

$\boldsymbol{FC = 92.6\%}$

$\boldsymbol{(N_1)_{60} = 19}$

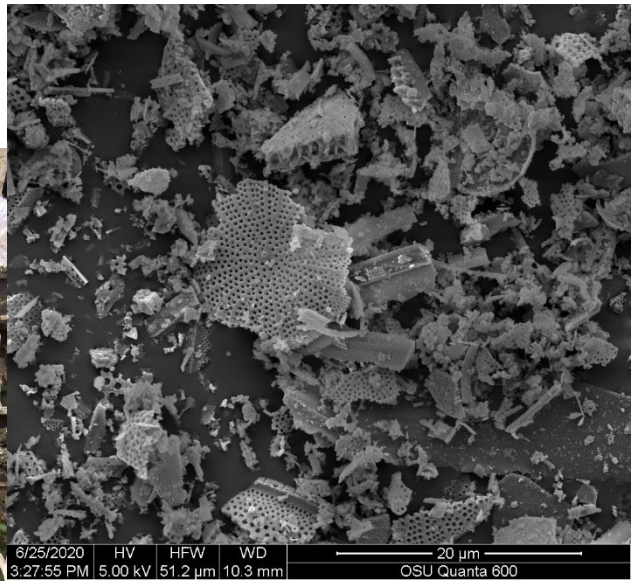

MP1N7a

$\boldsymbol{depth = 19m}$

$\boldsymbol{w_n = 109}$

$\boldsymbol{\gamma_{calc} = 13.4kN/m^3, G_s = 2.3}$

$\boldsymbol{FC = 75.5\%}$

$\boldsymbol{(N_1)_{60} = 48.8}$

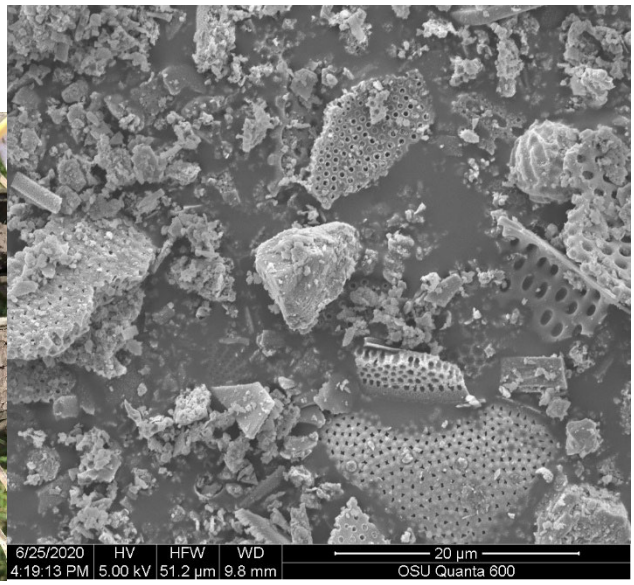

MP1N9

$\boldsymbol{depth = 22m}$

$\boldsymbol{w_n = 120.4, LL = 130, PL = 81}$

$\boldsymbol{\gamma_{calc} = 13.2kN/m^3, G_s = 2.34}$

$\boldsymbol{FC = 98.28\%}$

$\boldsymbol{(N_1)_{60} = 28}$

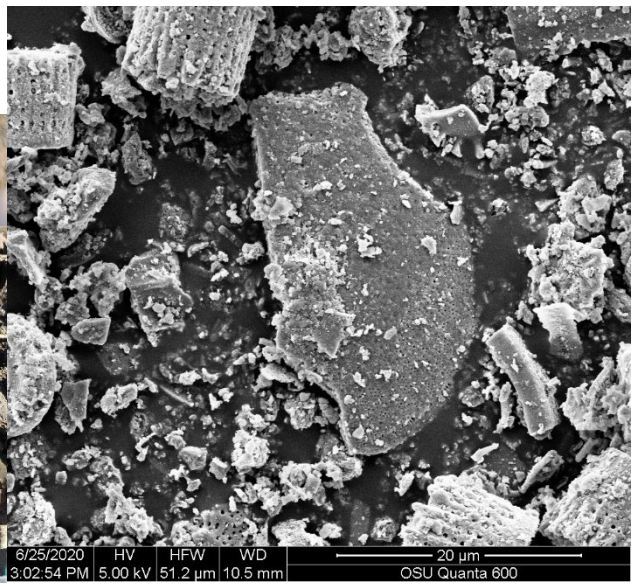

MP1N12

$\boldsymbol{depth = 26.67m}$

$\boldsymbol{w_n = 113.7, LL = 149, PL = 98}$

$\boldsymbol{\gamma_{calc} = 13.26kN/m^3, G_s = 2.26}$

$\boldsymbol{FC = 98.4\%}$

$\boldsymbol{(N_1)_{60} = 39}$

APPENDIX B: DIATOMACEOUS SPLIT SPOON SAMPLES

W1N14, $depth = 34.29m$
$w_n = 205.5, LL = 172, PL = 50$
$\gamma = 11.84kN/m^3, G_s = 2.23$
$S_r = 98.8\%, FC = 93.9\%, (N_1)_{60} = 0$

W1N17, $depth = 43.28m$
$w_n = 158.8, LL = 139, PL = 87$
$\gamma = 12.4kN/m^3, G_s = 2.33$
$S_r = 98.2\%, FC = 99.5\%, (N_1)_{60} = 0.6$

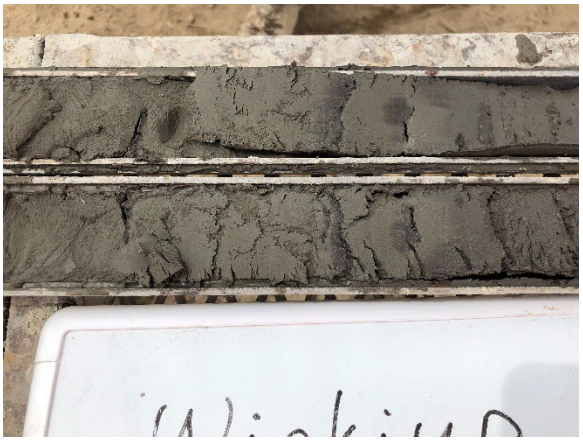

W1N15, $depth = 37.34m$
$w_n = 93.8, LL = 93, PL = 48$
$\gamma = 13.92kN/m^3, G_s = 2.47$
$S_r = 97.8\%, FC = 95.5\%, (N_1)_{60} = 1.2$

W1N18, $depth = 46.33m$
$w_n = 86.2, LL = 75, PL = 53$
$\gamma = 14.48kN/m^3, G_s = 2.47$
$S_r = 100.7\%, FC = 97.2\%, (N_1)_{60} = 0$

W1N20, $depth = 52.42m$
$w_n = 161.3, LL = 138, PL = 93$
$\gamma_{calc} = 12.38kN/m^3, G_s = 2.19$
$FC = 93.9\%, (N_1)_{60} = 4.5$

W1N22, $depth = 58.52m$
$w_n = 143, LL = 150, PL = 88$
$\gamma_{calc} = 12.68kN/m^3, G_s = 2.23$
$FC = 98\%, (N_1)_{60} = 3.3$

W1N21, $depth = 55.47m$
$w_n = 171, LL = 150, PL = 68$
$\gamma = 12.66kN/m^3, G_s = 2.24$
$S_r = 103.5\%, FC = 97.3\%, (N_1)_{60} = 0.6$

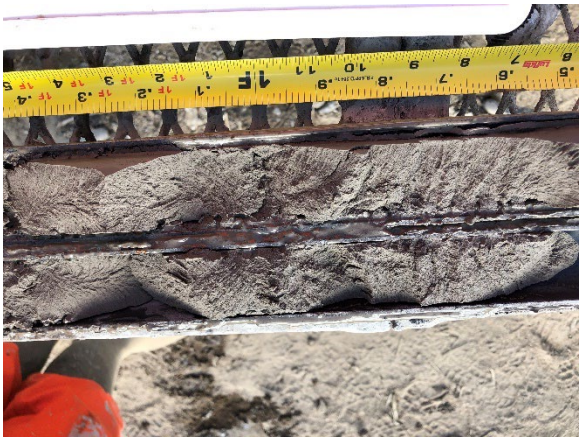

W1N23, $depth = 60.0m$
$w_n = 116.5, LL = 121, PL = 74$
$\gamma_{calc} = 13.2kN/m^3, G_s = 2.26$
$FC = 99\%, (N_1)_{60} = 4.3$

W1N24, $depth = 63.1m$
$w_n = 143, LL = 160, PL = 92$
$\gamma_{calc} = 12.31kN/m^3, G_s = 2.21$
$FC = 95.7\%, (N_1)_{60} = 2.1$

W1N26, $depth = 65.9m$
$w_n = 211.3, LL = 200, PL = 67$
$\gamma = 11.12kN/m^3, G_s = 2.13$
$S_r = 92.9\%, FC = 87.2\%, (N_1)_{60} = 10.1$

W1N25c, $depth = 64.34m$
$w_n = 144.9, LL = 148, PL = 69$
$\gamma = 11.7kN/m^3, G_s = 2.2$
$S_r = 90.8\%, FC = 97.5\%, (N_1)_{60} = 20.8$

AC1N9, $depth = 20.27m$
$w_n = 126, LL = 121, PL = 85, SSA_{MB} = 223m^2/g$
$\gamma = 12.6kN/m^3$
$FC = 96.5\%, (N_1)_{60} = 10.7$

AC1N10, $depth = 23m$
$w_n = 151.3, LL = 158, PL = 96$
$\gamma_{calc} = 12.53kN/m^3, G_s = 2.21$
$FC = 97.78\%, (N_1)_{60} = 8$

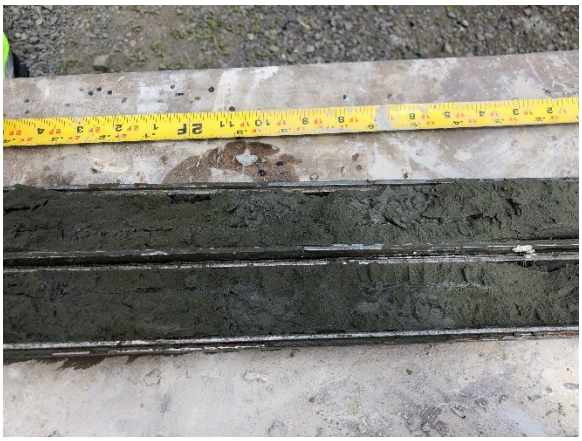

AC1N12, $depth = 29.26m$
$w_n = 143, LL = 122, PL$
$= 54,\ SSA_{MB}$
$= 66.7m^2/g$
$\gamma = 12.45kN/m^3, G_s = 2.27$
$S_r = 97\%, FC = 96.9\%, (N_1)_{60}$
$= 5.3$

AC1N11, $depth = 26.2m$
$w_n = 151.7, LL = 166, PL = 89$
$\gamma_{calc} = 12.65kN/m^3, G_s = 2.31$
$FC = 90\%, (N_1)_{60} = 3.9$

AC1N13, $depth = 31.7m$
$w_n = 161, LL = 146, PL$
$= 70,\ SSA_{MB}$
$= 56.3m^2/g$
$\gamma = 12.2kN/m^3, G_s = 2.29$
$S_r = 97\%, FC = 95.8\%, (N_1)_{60} = 3$

MP1N6, $depth = 17.5m$
$LL = 191, PL = 115$
$G_s = 2.03$
$FC = 99.7\%, (N_1)_{60} = 30$

MP1N9, $depth = 22m$
$w_n = 120.4, LL = 130, PL = 81$
$\gamma_{calc} = 13.2kN/m^3, G_s = 2.34$
$FC = 98.28\%, (N_1)_{60} = 28$

MP1N8, $depth = 20.27m$
$w_n = 125, LL = 148, PL$
$= 69,\ SSA_{MB}$
$= 28m^2/g$
$\gamma = 13kN/m^3, G_s = 2.27$
$S_r = 99.6\%, FC = 94.7\%, (N_1)_{60}$
$= 33.6$

MP1N10, $depth = 23.6m$
$LL = 164, PL = 101$
$G_s = 2.08$
$FC = 99.7\%, (N_1)_{60} = 39.3$

MP1N11, $depth = 25.1m$
$w_n = 133, LL = 133, PL = 75,\ SSA_{MB} = 51.7m^2/g$
$\gamma = 12.2kN/m^3, G_s = 2.35$
$S_r = 92\%, (N_1)_{60} = 29.7$

MP1N14, $depth = 30.94m$
$w_n = 108, LL = 112, PL = 53,\ SSA_{MB} = 93.6m^2/g$
$\gamma = 13.5kN/m^3, G_s = 2.4$
$S_r = 98.8\%, FC = 97.8\%, (N_1)_{60} = 48.7$

MP1N12, $depth = 26.67m$
$w_n = 113.7, LL = 149, PL = 98$
$\gamma_{calc} = 13.26kN/m^3, G_s = 2.26$
$FC = 98.4\%, (N_1)_{60} = 39.1$

PC1N1, $depth = 3.5m$
$w_n = 86, LL = 111, PL = 73$
$\gamma = 14.2kN/m^3, G_s = 2.49$
$S_r = 97.3\%, FC = 91\%, (N_1)_{60} = 23.6$

PC1N2, $depth = 5.49m$
$w_n = 92, LL = 114, PL = 49$
$\gamma = 12.9kN/m^3$
$FC = 87.6\%, (N_1)_{60} = 19.1$

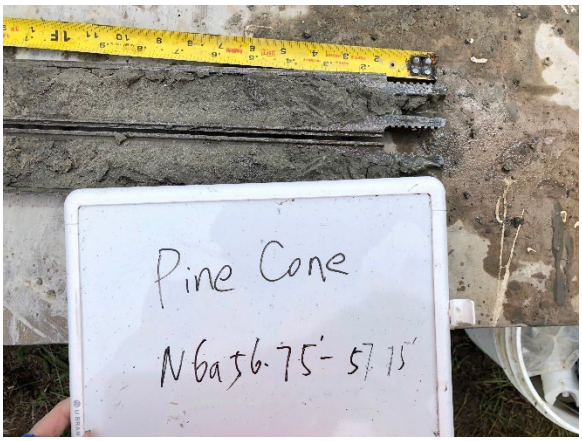

PC1N6a, $depth = 17.6m$
$w_n = 113, LL = 132, PL = 49$
$FC = 81.9\%, (N_1)_{60} = 21.3$

PC1N3, $depth = 8.38m$
$w_n = 109.6, LL = 109, PL = 75$
$\gamma = 13.2kN/m^3, G_s = 2.25$
$S_r = 98.5\%, FC = 97.9\%, (N_1)_{60} = 24.1$

PC1N7, $depth = 20.7m$
$w_n = 137, LL = 141, PL = 75$
$\gamma = 12.2kN/m^3, G_s = 2.3$
$S_r = 93\%, FC = 95.2\%, (N_1)_{60} = 17.2$

PC1N8, $depth = 23.7m$
$w_n = 158, LL = 153, PL = 91$
$\gamma = 12.1kN/m^3, (N_1)_{60} = 14.5$

PC1N10, $depth = 29.8m$
$w_n = 139.7, LL = 130, PL = 93$
$\gamma_{calc} = 12.7kN/m^3, G_s = 2.23$
$FC = 98.3\%, (N_1)_{60} = 13.6$

PC1N9, $depth = 26.9m$
$w_n = 179, LL = 175, PL = 109$
$\gamma = 11.8kN/m^3, G_s = 2.17$
$S_r = 96.4\%, FC = 99.9\%, (N_1)_{60} = 15$

PC1N11, $depth = 32.77m$
$w_n = 141.6, LL = 138, PL = 101$
$\gamma = 12.48kN/m^3$
$FC = 99.8\%, (N_1)_{60} = 12.2$

APPENDIX C: NON-DIATOMACEOUS SPLITSPOON SAMPLES

W1N7, $depth = 20m$
$w_n = 55.8, LL = 27, PL = 20$
$\gamma_{calc} = 16.54kN/m^3, G_s = 2.74,$
$FC = 95.1\%$

W1N11a, $depth = 27.05m$
$w_n = 46.9, LL = 37, PL = 18$
$\gamma = 16.8kN/m^3, G_s = 2.74$
$S_r = 95.5\%, FC = 79.4\%$

W1N9, $depth = 21.8m$
$w_n = 37.7, LL = 33, PL = 22$
$FC = 94\%$

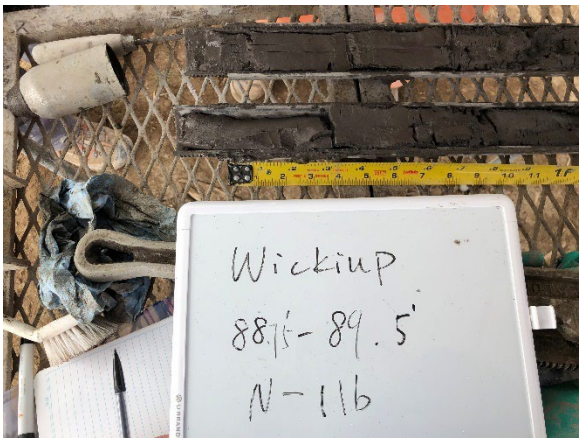

W1N11b, $depth = 27.27m$
$w_n = 30.9, LL = 49, PL = 35, SSA_{MB} = 31.8m^2/g$
$\gamma = 16.4kN/m^3, G_s = 2.8$
$S_r = 72.5\%, FC = 96.6\%$

W1N12, $\boldsymbol{depth = 28.8m}$
$\boldsymbol{w_n = 53.6, LL = 42, PL = 28}$
$\boldsymbol{\gamma = 17kN/m^3, G_s = 2.75}$
$\boldsymbol{S_r = 102.4\%, FC = 91\%}$

AC1N8, $\boldsymbol{depth = 19.05m}$
$\boldsymbol{w_n = 37, LL = 35.5, PL = 30}$
$\boldsymbol{\gamma = 17.5kN/m^3, G_s = 2.51}$
$\boldsymbol{S_r = 100.7\%, FC = 63.7\%}$

APPENDIX D: GRAIN SIZE DISTRIBUTION

Diatomaceous soil specimens

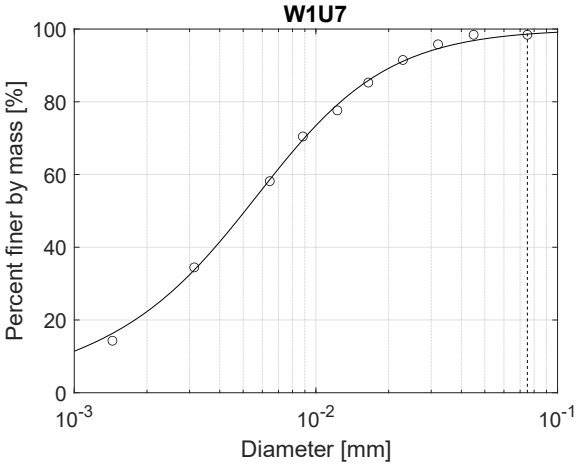

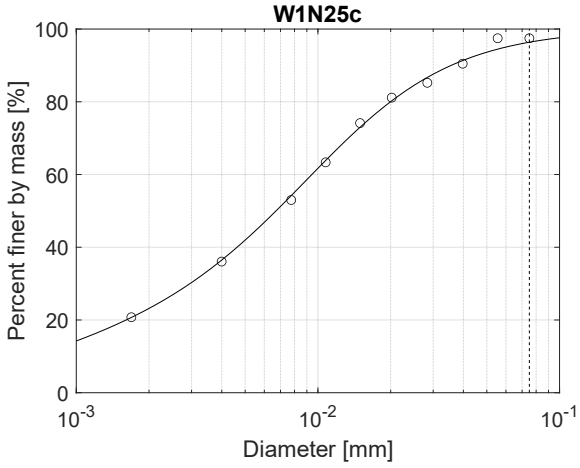

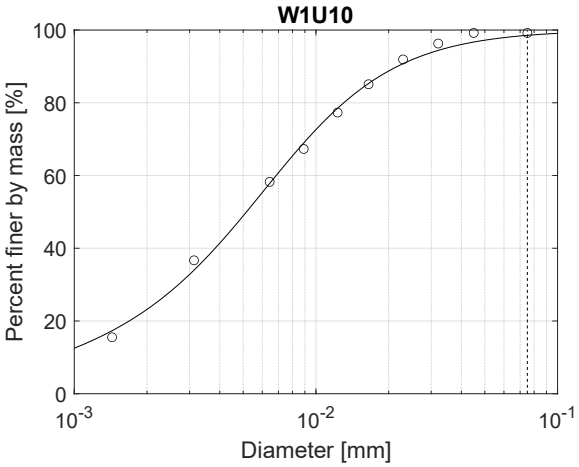

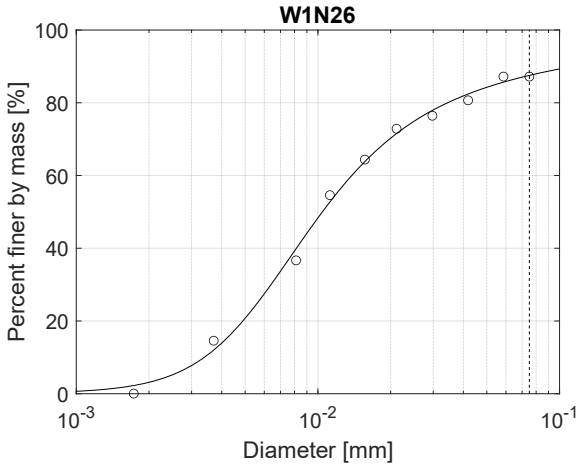

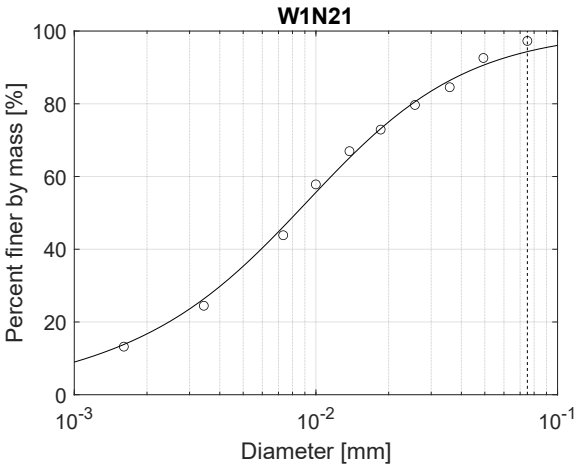

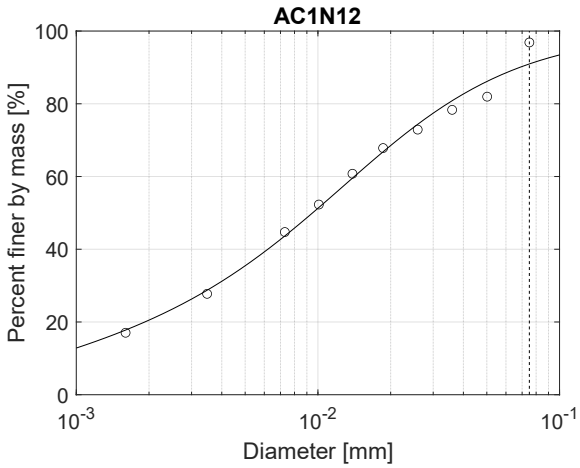

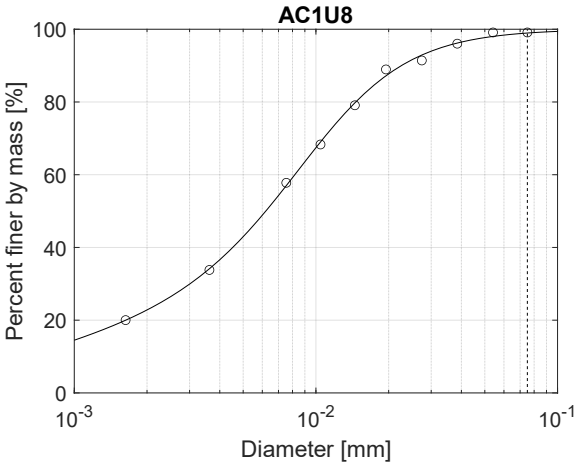
AC1U8
Percent finer by mass [%]
Diameter [mm]

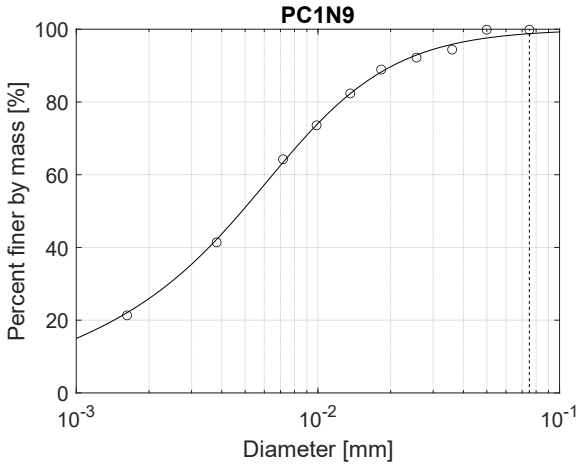
PC1N9
Percent finer by mass [%]
Diameter [mm]

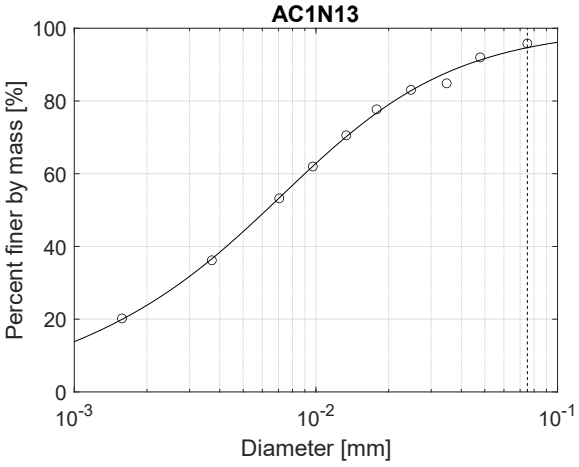
AC1N13
Percent finer by mass [%]
Diameter [mm]

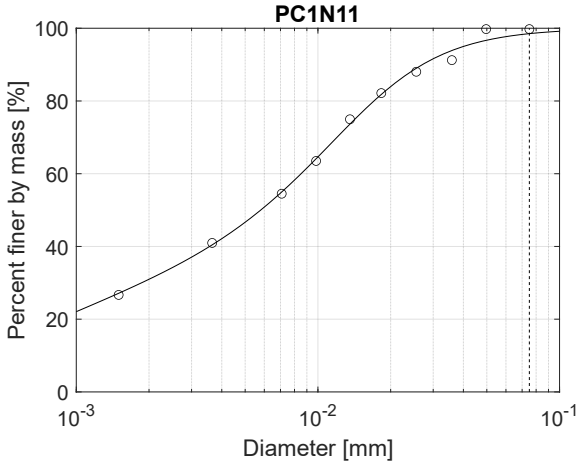
PC1N11
Percent finer by mass [%]
Diameter [mm]

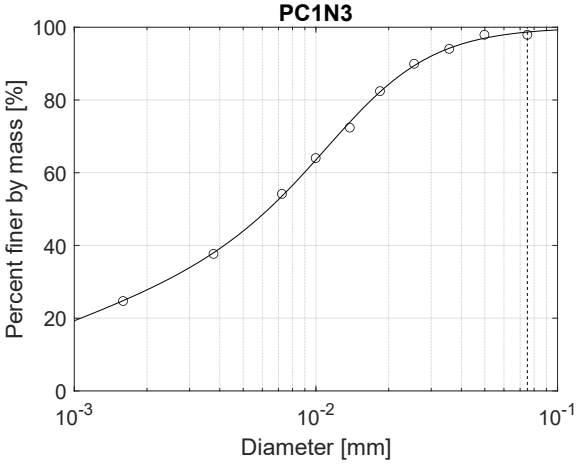
PC1N3
Percent finer by mass [%]
Diameter [mm]

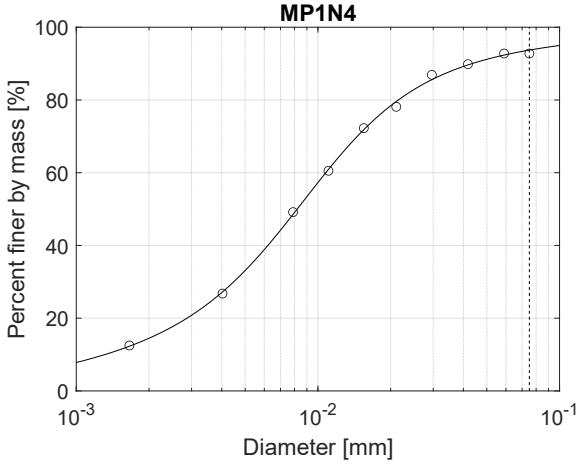
MP1N4
Percent finer by mass [%]
Diameter [mm]

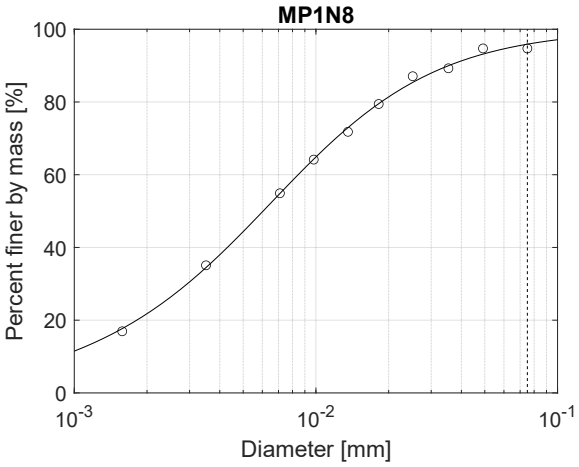

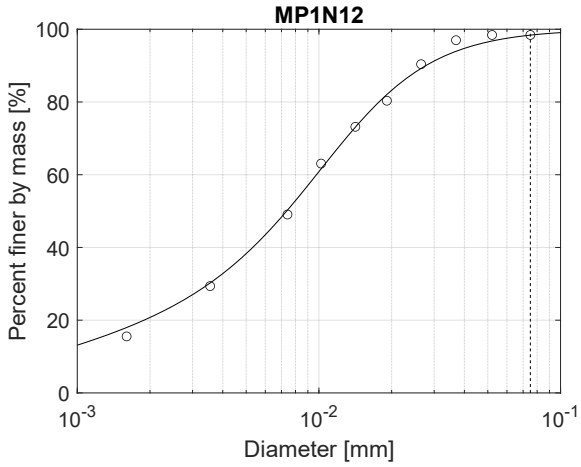

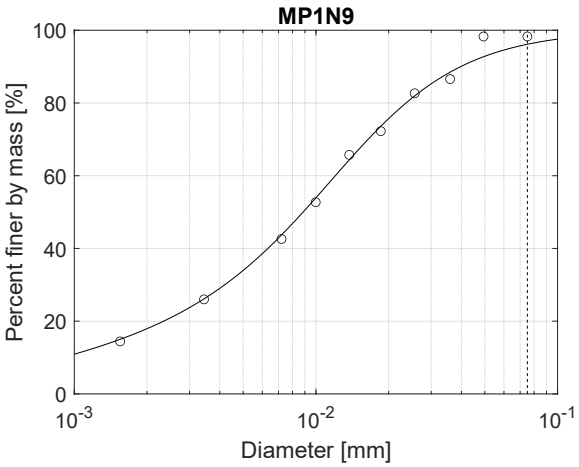

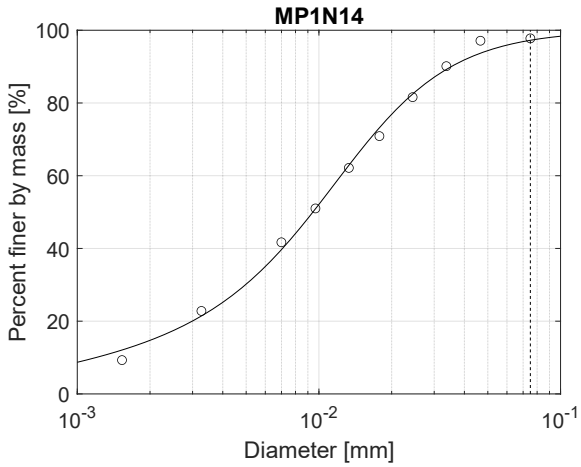

Non-diatomaceous soil specimens

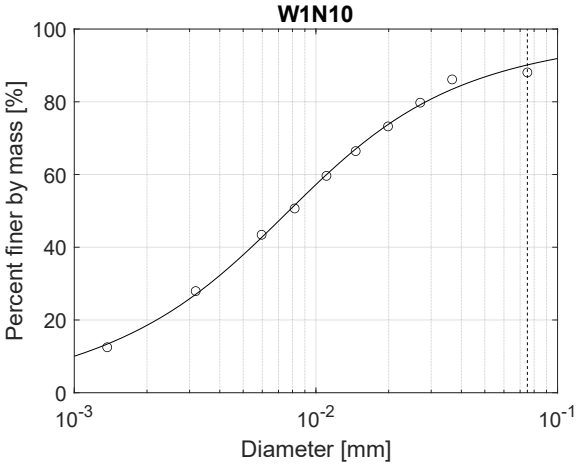

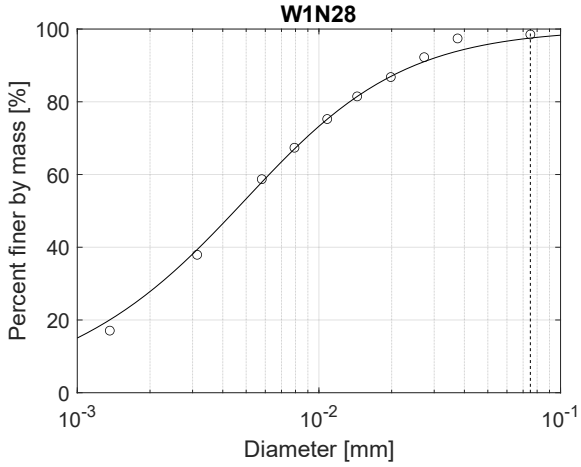

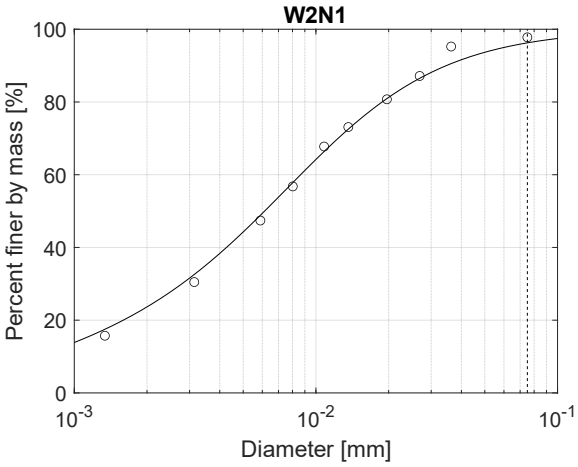
W2N1
Percent finer by mass [%]
Diameter [mm]
100
80
60
40
20
0
10^{-3}
10^{-2}
10^{-1}

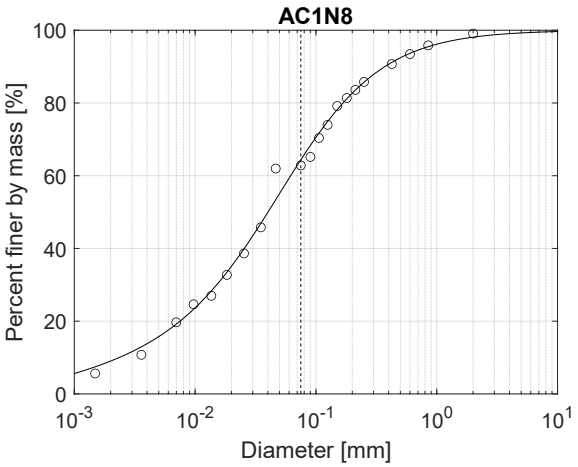
AC1N8
Percent finer by mass [%]
Diameter [mm]
100
80
60
40
20
0
10^{-3}
10^{-2}
10^{-1}
10^{0}
10^{1}

APPENDIX E: CONSOLIDATION TEST SPECIMENS

W1U7

CRS: before trimming

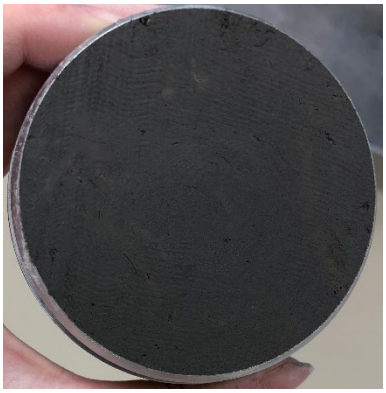

CRS: after trimming

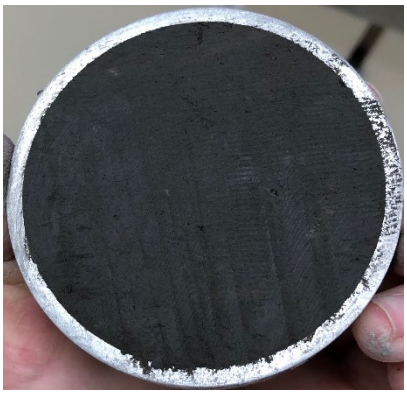

CRS: after trimming

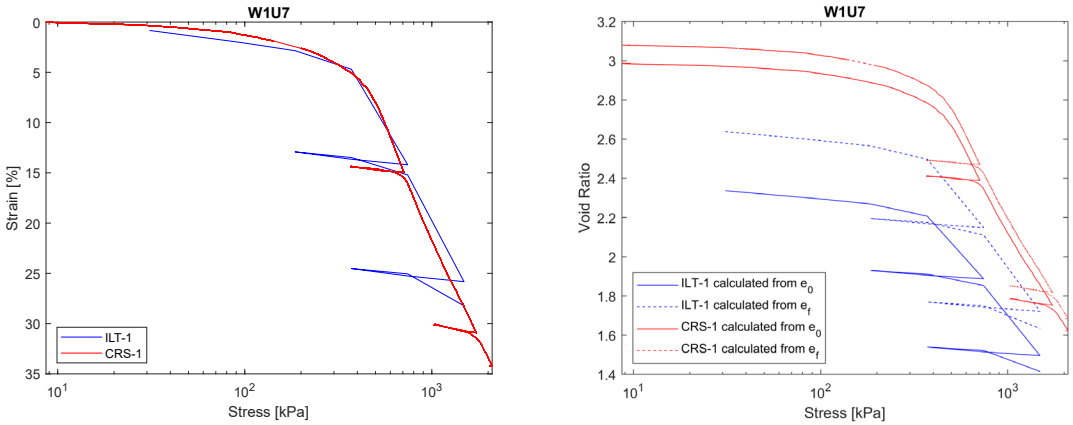

Wickiup Sample W1U7 Consolidation Testing

Wickiup Sample W1U7 Consolidation Testing Results

	C_c	C_r	σ'_p [kPa] Becker method	σ'_p [kPa] Casagrande method	σ'_p [kPa] Silva method
ILT	1.288	0.113	350.9	399.0	367.4
CRS	1.763	0.173	431.4	458.0	420.0

Note: No photos taken for the ILT test, but both tests had good quality specimens. Soil is relatively soft, clayey like.

W1U8

ILT-1: before trimming

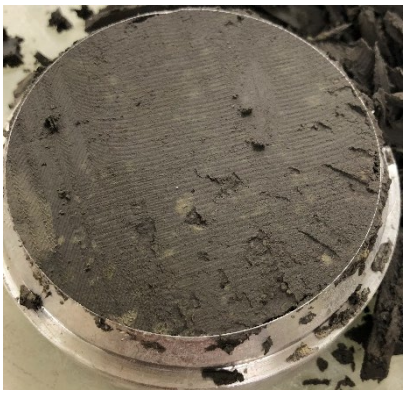

ILT-2: before trimming

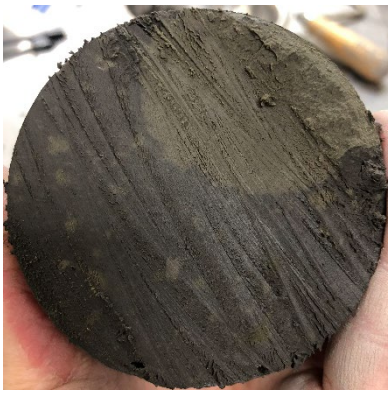

CRS: before trimming

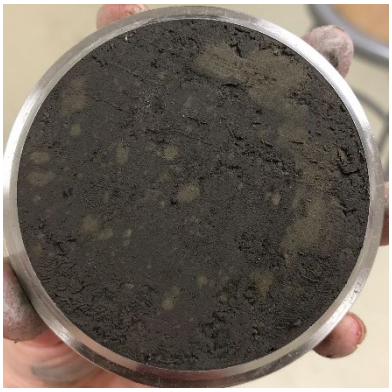

ILT-1: after trimming

ILT-2: after trimming

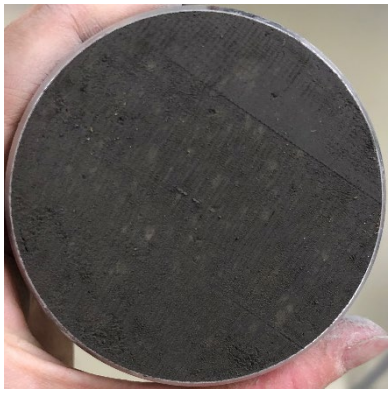

CRS: after trimming

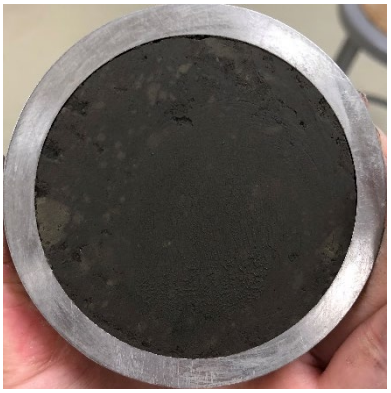

ILT-1: after trimming

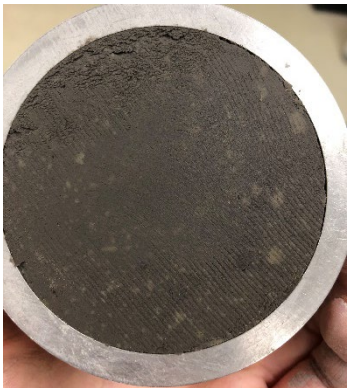

ILT-2: after trimming

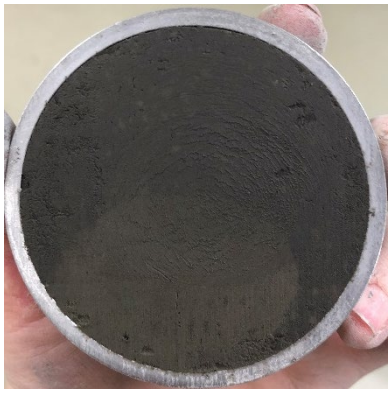

CRS: after trimming

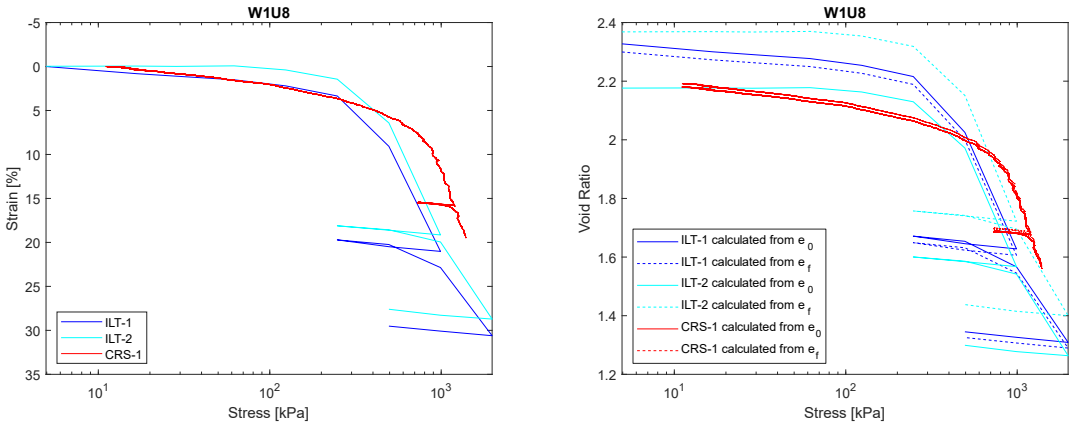

Wickiup Sample W1U8 Consolidation Testing

Wickiup Sample W1U8 Consolidation Testing Results

	C_c	C_r	σ'_p [kPa] Becker method	σ'_p [kPa] Casagrande method	σ'_p [kPa] Silva method
ILT-1	1.180	0.129	375.2	365.9	380.2
ILT-2	1.247	0.084	408.7	398.9	422.5
CRS	1.711	0.051	728.9	810.1	764.8

Note: ILT-2 was 24hr loading procedure. Soil is relatively soft, clayey like.

W1U9

ILT-1: before trimming

ILT-2: before trimming

CRS-1: before trimming

ILT-1: after trimming

ILT-2: after trimming

CRS-1: after trimming

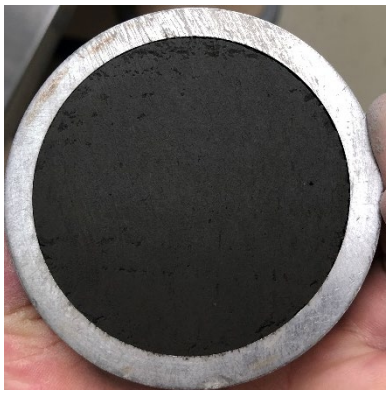

ILT-1: after trimming

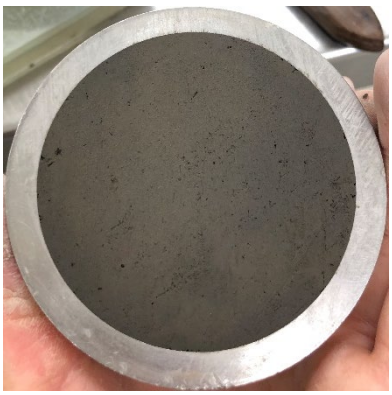

ILT-2: after trimming

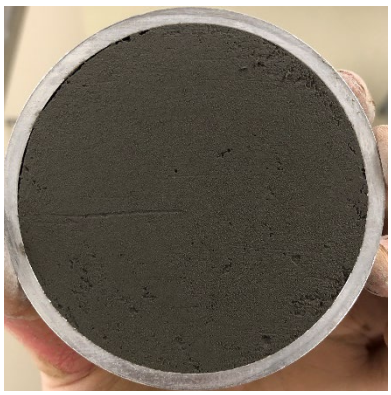

CRS-1: after trimming

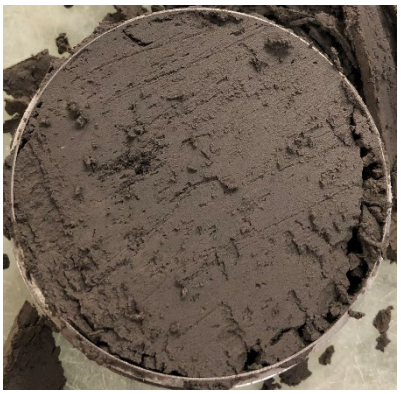

CRS-2: before trimming

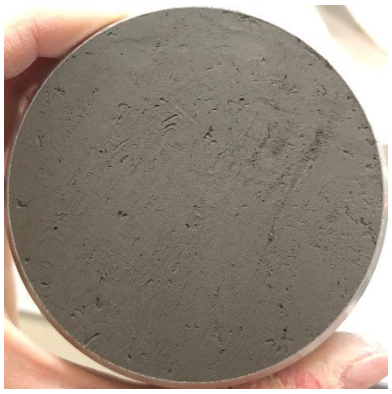

CRS-2: after trimming

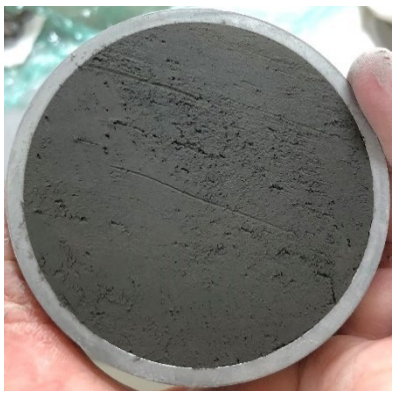

CRS-2: after trimming

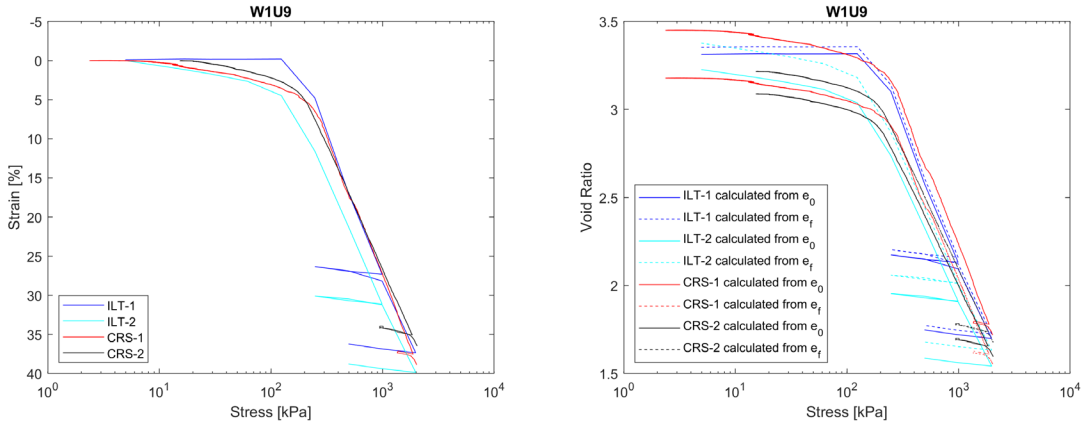

Wickiup Sample W1U9 Consolidation Testing

Wickiup Sample W1U9 Consolidation Testing Results

	C_c	C_r	σ'_p $[kPa]$ Becker method	σ'_p $[kPa]$ Casagrande method	σ'_p $[kPa]$ Silva method
ILT-1	1.573	0.105	196.2	198.3	212.2
ILT-2	1.382	0.079	163.5	150.9	138.1
CRS-1	1.540	0.149	243.8	250.4	235.8
CRS-2	1.336	0.022	185.7	206.0	182.5

Note: ILT-1 was 24 hr loading procedure. Generally, ILT-1 and CRS-1 were better quality specimens than ILT-2 and CRS-2. Soil is relatively soft, clayey like.

W1U10

ILT-1: before trimming

ILT-2: before trimming

CRS: before trimming

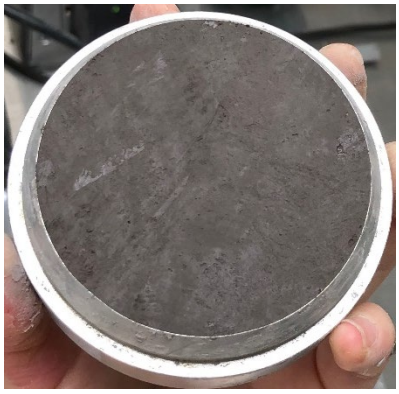

ILT-1: after trimming

ILT-2: after trimming

CRS: after trimming

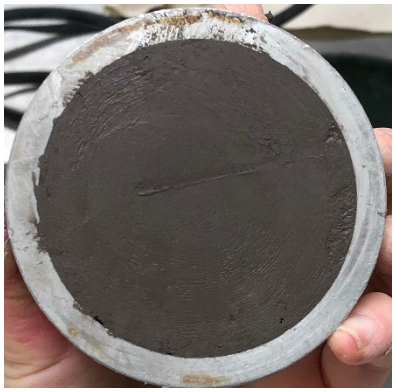

ILT-1: after trimming

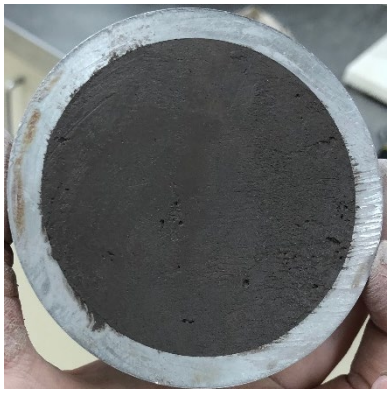

ILT-2: after trimming

CRS: after trimming

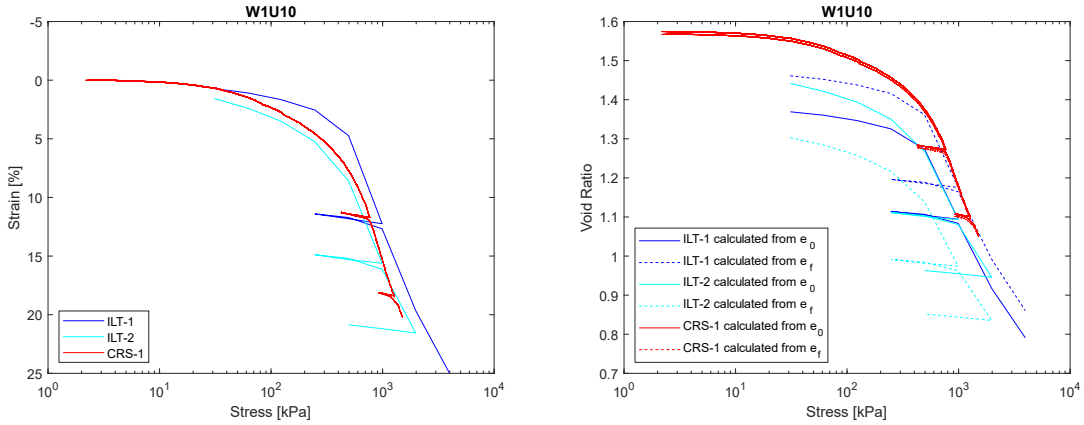

Wickiup Sample W1U10 Consolidation Testing

Wickiup Sample W1U10 Consolidation Testing Results

	C_c	C_r	σ'_p [kPa] Becker method	σ'_p [kPa] Casagrande method	σ'_p [kPa] Silva method
ILT-1	0.614	0.045	442.9	454.5	440.9
ILT-2	0.504	0.040	420.2	390.3	350.8
CRS	0.788	0.042	430.2	435.3	475.8

Note: ILT-2 was 24 hr loading procedure. All good quality specimens. Soil is relatively soft, clayey like.

W1U12

ILT: before trimming

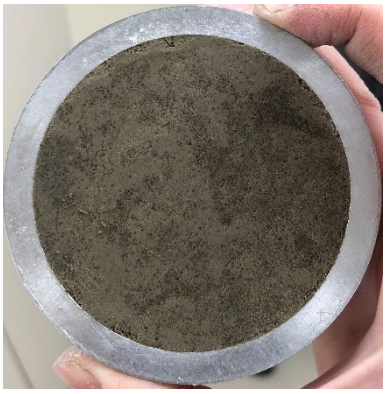

ILT: after trimming

CRS: after trimming

ILT: after trimming

CRS: after trimming

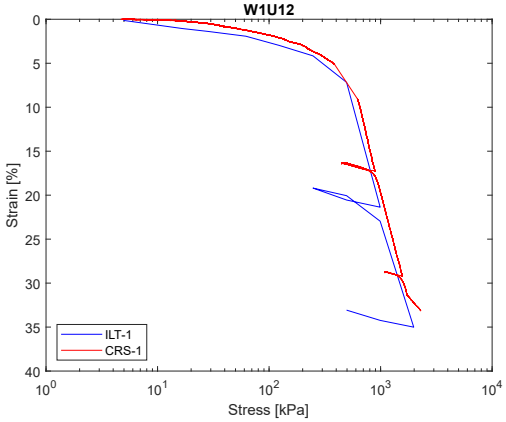

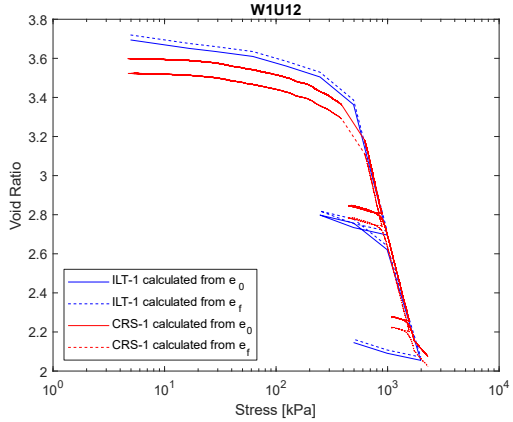

Wickup Sample W1U12 Consolidation Testing

Wickiup Sample W1U12 Consolidation Testing Results

	C_c	C_r	σ'_p [kPa] Becker method	σ'_p [kPa] Casagrande method	σ'_p [kPa] Silva method
ILT	2.185	0.241	454.4	460.7	437.0
CRS	2.207	0.153	540.8	511.9	504.2

Note: The soil is stiffer than previous specimens (W1U7, W1U8, W1U9, W1U10). Both tests were quality specimens.

W1U13

ILT: before trimming

ILT: after trimming

CRS: before trimming

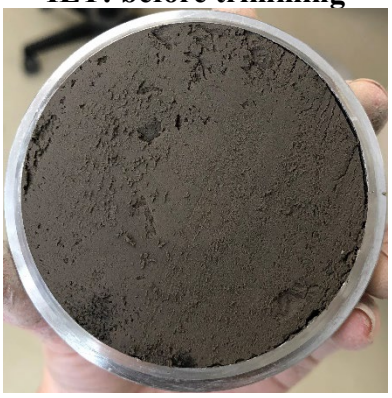

ILT: after trimming

CRS: before trimming

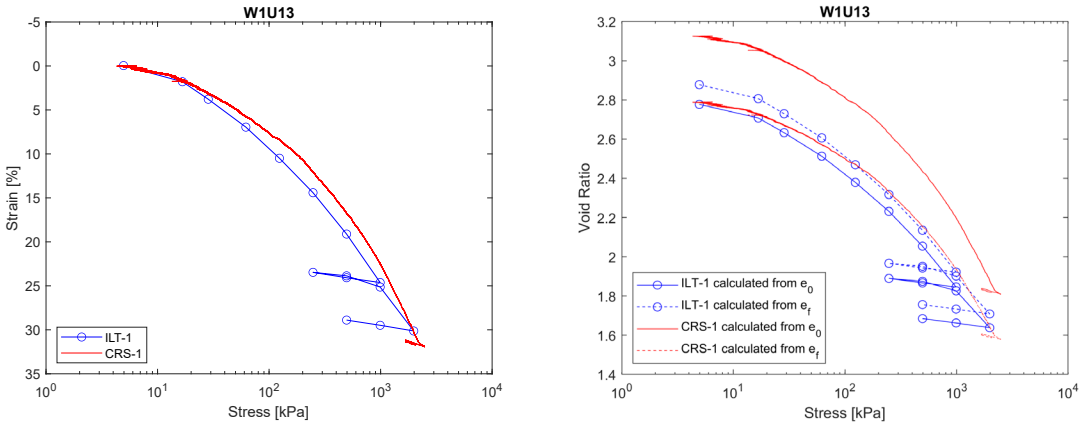

Wickup Sample W1U13 Consolidation Testing

Wickup Sample W1U13 Consolidation Testing Results

	C_c	C_r	σ'_p [kPa] Becker method	σ'_p [kPa] Casagrande method	σ'_p [kPa] Silva method
ILT	0.643	0.095	196.8	164.9	81.5
CRS	1.031	0.160	442.2	394.3	314.4

Note: Soil is soft. It was hard to trim a smooth surface. Results also show disturbance.

W1U14

ILT: before trimming

ILT: after trimming

ILT: after trimming

CRS: before rimming

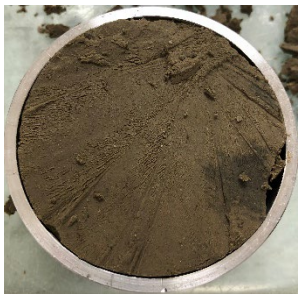

CRS: before trimming

CRS: after trimming

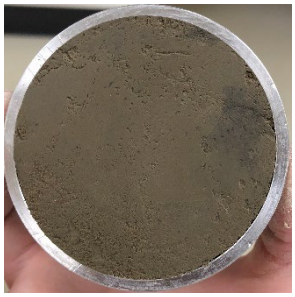

CRS: after trimming

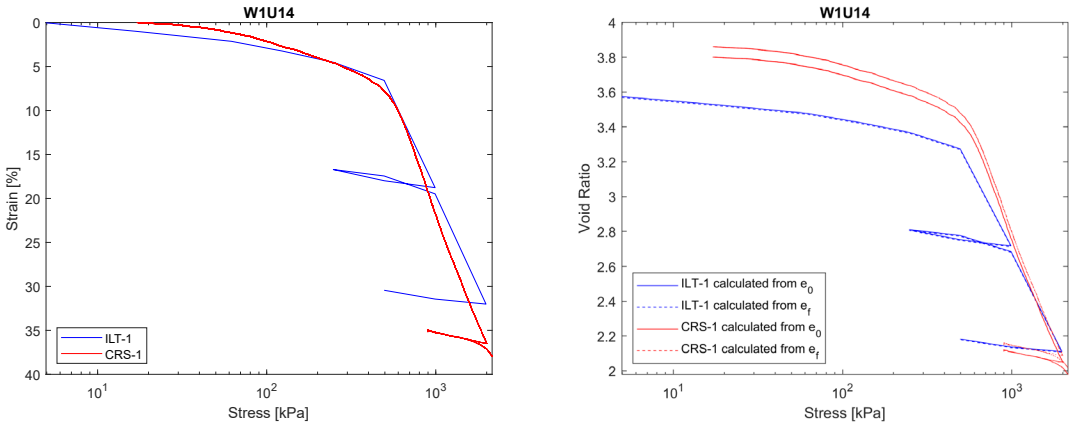

Wickiup Sample W1U14 Consolidation Testing

Wickiup Sample W1U14 Consolidation Testing Results

	C_c	C_r	σ'_p [kPa] Becker method	σ'_p [kPa] Casagrande method	σ'_p [kPa] Silva method
ILT	1.931	0.187	504.4	494.2	453.1
CRS	2.048~2.707	0.205	525.1	544.3	523.7

Note: Soil is stiff.

AC1U3

ILT: before trimming

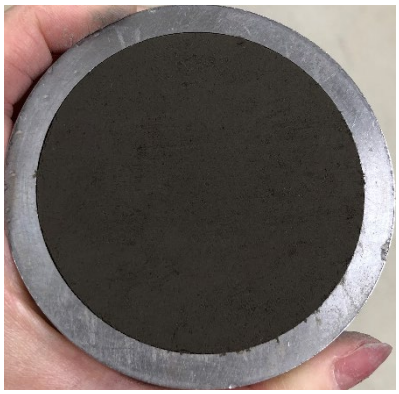

ILT: after trimming

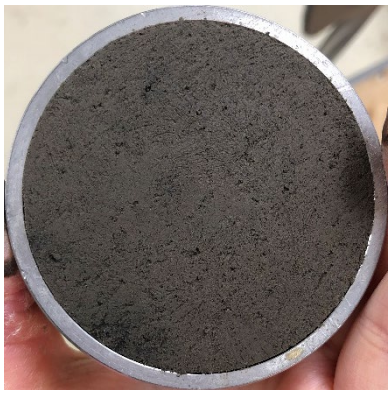

CRS: after trimming

ILT: after trimming

CRS: after trimming

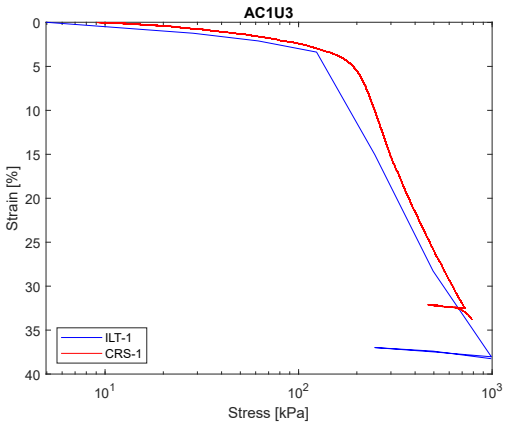

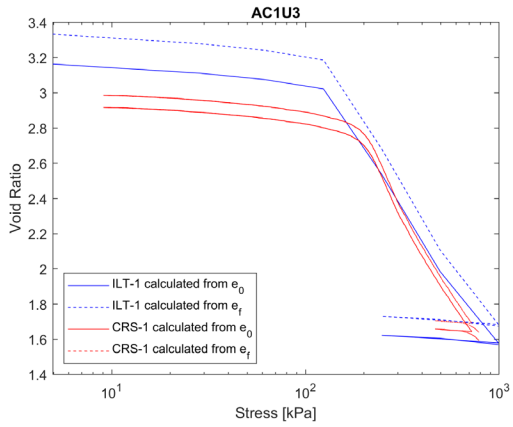

Ady Canal Sample AC1U3 Consolidation Testing

Ady Canal Sample AC1U3 Consolidation Testing Results

	C_c	C_r	σ'_p [kPa] Becker method	σ'_p [kPa] Casagrande method	σ'_p [kPa] Silva method
ILT	1.632	0.086	126.1	123.6	121.0
CRS	1.624~2.316	0.087	193.0	207.7	193.1

Note: Both were good quality specimens. CRS specimen had a few sandy parts.

AC1U5

ILT: before trimming

ILT: after trimming

CRS: after trimming

ILT: after trimming

CRS: before trimming

CRS: after trimming

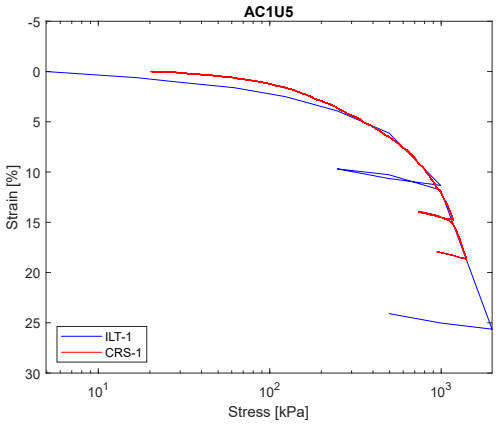

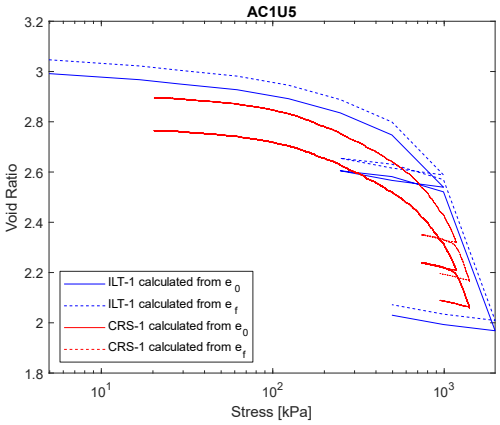

Ady Canal Sample AC1U5 Consolidation Testing

Ady Canal Sample AC1U5 Consolidation Testing Results

	C_c	C_r	σ'_p [kPa] Becker method	σ'_p [kPa] Casagrande method	σ'_p [kPa] Silva method
ILT	1.861	0.129	836.8	764.4	757.2
CRS	1.897	0.170	811.8	770.4	805.7

Note: Soil is stiff.

AC1U6

ILT: before trimming

ILT: before trimming

ILT: after trimming

ILT: after trimming

CRS: before trimming

CRS: after trimming

CRS: after trimming

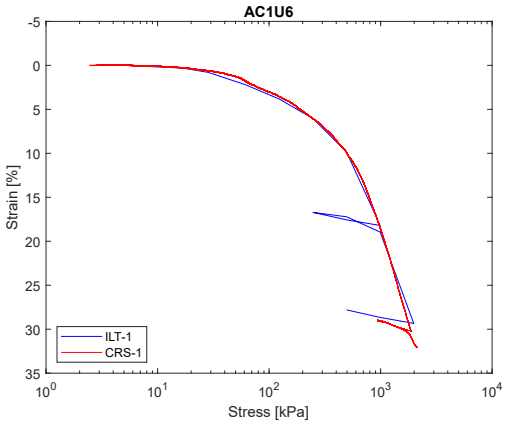

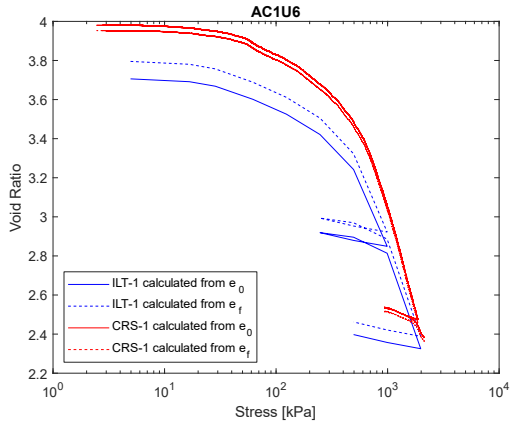

Ady Canal Sample AC1U6 Consolidation Testing

Ady Canal Sample AC1U6 Consolidation Testing Results

	C_c	C_r	σ'_p [kPa] Becker method	σ'_p [kPa] Casagrande method	σ'_p [kPa] Silva method
ILT	1.552	0.154	372.1	418.4	363.1
CRS	2.155	0.222	486.0	474.3	519.4

Note: Soil is stiff, CRS specimen was slightly better than ILT specimen.

AC1U7

ILT: before trimming

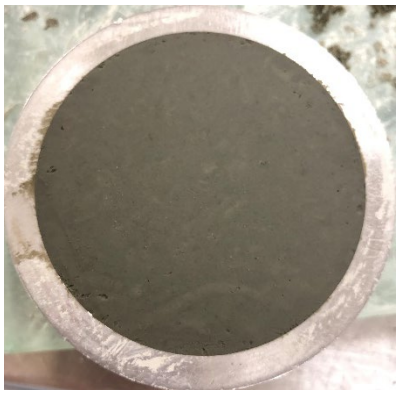

ILT: after trimming

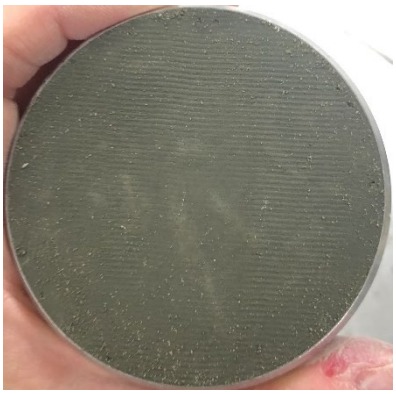

CRS: after trimming

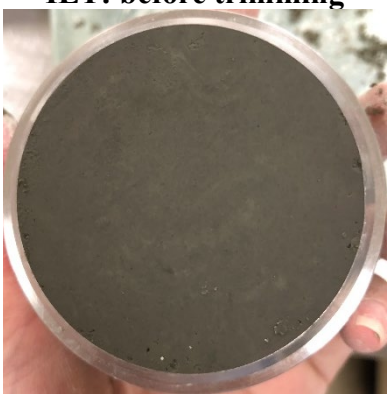

ILT: after trimming

CRS: before trimming

CRS: after trimming

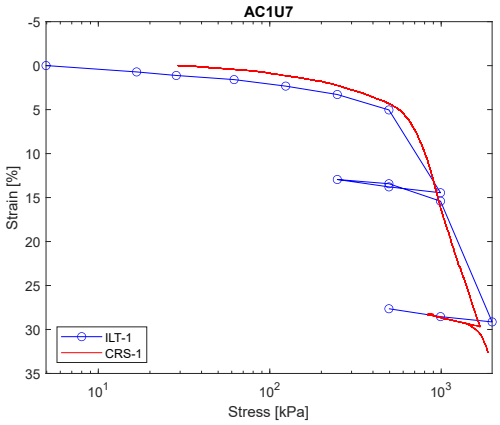

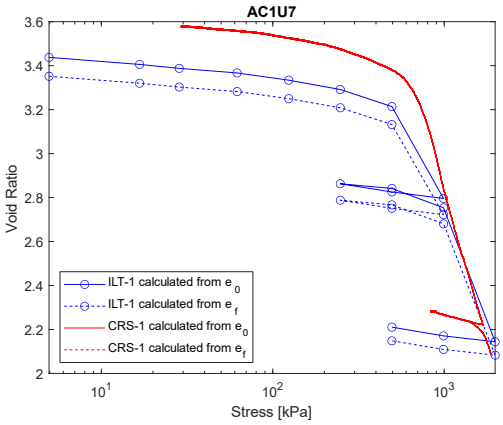

Ady Canal Sample AC1U7 Consolidation Testing

Ady Canal Sample AC1U7 Consolidation Testing Results

	C_c	C_r	σ'_p [kPa] Becker method	σ'_p [kPa] Casagrande method	σ'_p [kPa] Silva method
ILT	1.980	0.150	622.0	590.6	574.6
CRS	2.516~3.252	0.202	669.3	708.3	672.0

Note: Soil is stiff.

AC1U8

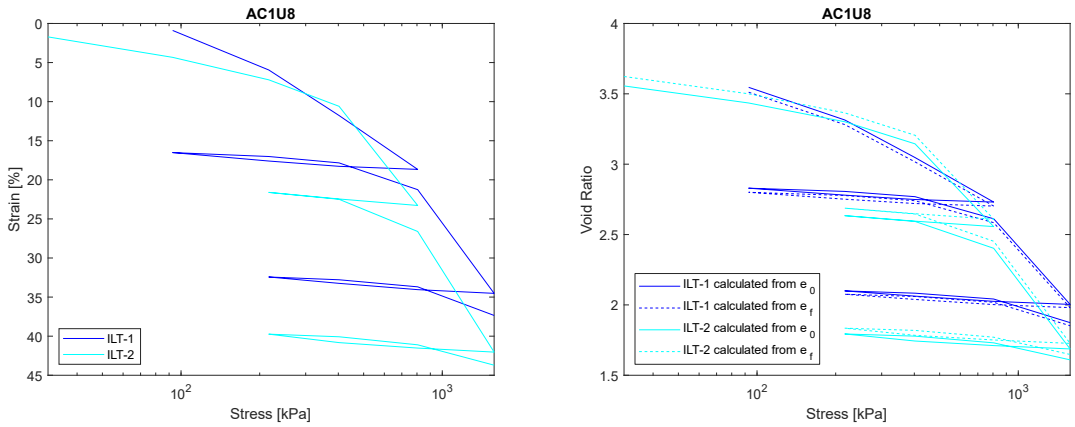

Ady Canal Sample AC1U8 Consolidation Testing

Ady Canal Sample AC1U8 Consolidation Testing Results

	C_c	C_r	σ_p' $[kPa]$ Becker method	σ_p' $[kPa]$ Casagrande method	σ_p' $[kPa]$ Silva method
ILT-1	2.064	0.190	/	/	/
ILT-2	2.490	0.173	400.0	449.2	385.1

Note: No photos taken. These were the very first consolidation tests run.

MP1U2

CRS-1: raw specimen

CRS-2: before trimming

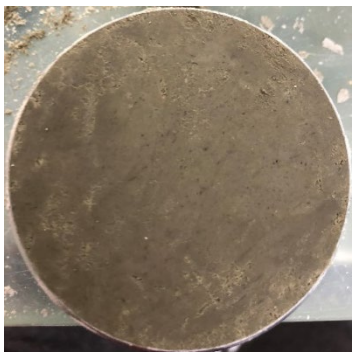

CRS-2: after trimming

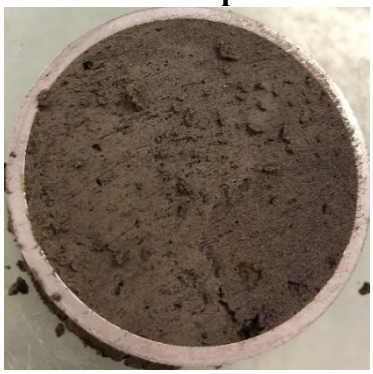

CRS-1: before trimming

CRS-2: before trimming

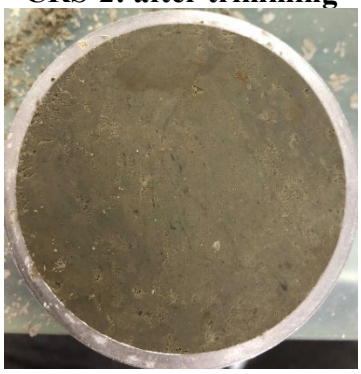

CRS-2: after trimming

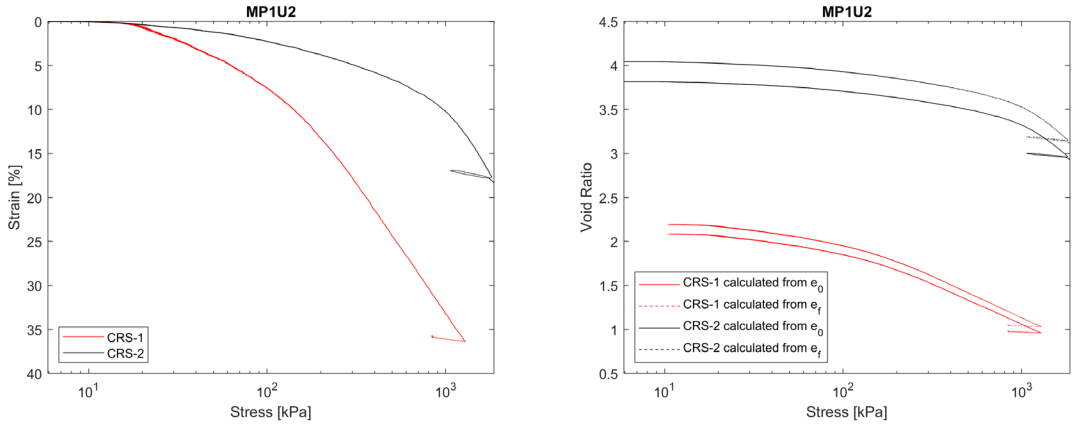

Moore Park Sample MP1U2 Consolidation Testing

Moore Park Sample MP1U2 Consolidation Testing Results

	C_c	C_r	σ_p' $[kPa]$ Becker method	σ_p' $[kPa]$ Casagrande method	σ_p' $[kPa]$ Silva method
CRS-1	0.949	0.092	135.8	181.1	117.2
CRS-2	1.796	0.203	909.6	1119.7	864.6

Note: CRS-1 is more clayey, CRS-2 is more mudstone like. There is layer intersection inside MP1U2, implied by the two different CRS specimens. Other tests conducted from MP1U2 are

mudstone stone like (DSS, consistency limits), therefore, CRS-1 is not used in the whole section 5.3.2 due to the irrelevance of the soil nature, only CRS-2 will be used.

MP1U3

ILT: before trimming

ILT: after trimming

CRS: after trimming

ILT: before trimming

CRS: before trimming

CRS: after trimming

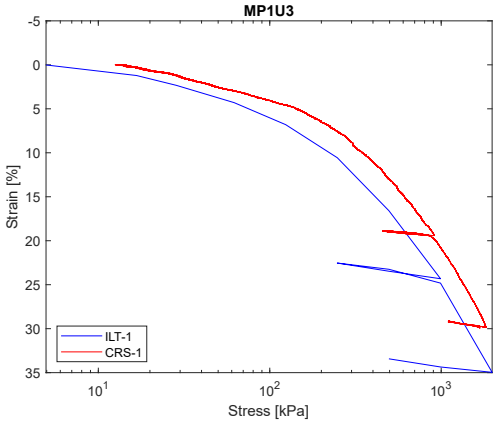

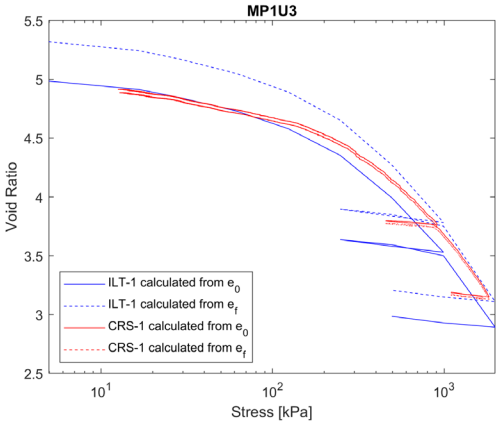

Moore Park Sample MP1U3 Consolidation Testing

Moore Park Sample MP1U3 Consolidation Testing Results

	C_c	C_r	$\sigma_p' \ [kPa]$ Becker method	$\sigma_p' \ [kPa]$ Casagrande method	$\sigma_p' \ [kPa]$ Silva method
ILT	2.130	0.219	237.6	408.2	315.5
CRS	2.083	0.162	304.2	427.6	360.8

Note: The specimen was hard to trim and fill well. The rock-like pieces are easily crushed into fine grained soil when pinched between fingertips. It can be seen that there are hollow parts on the wall surface of ILT specimen, which might induce disturbance.

MP1U8

CRS: before trimming

CRS: before trimming

CRS: after trimming

CRS: before trimming

CRS: after trimming

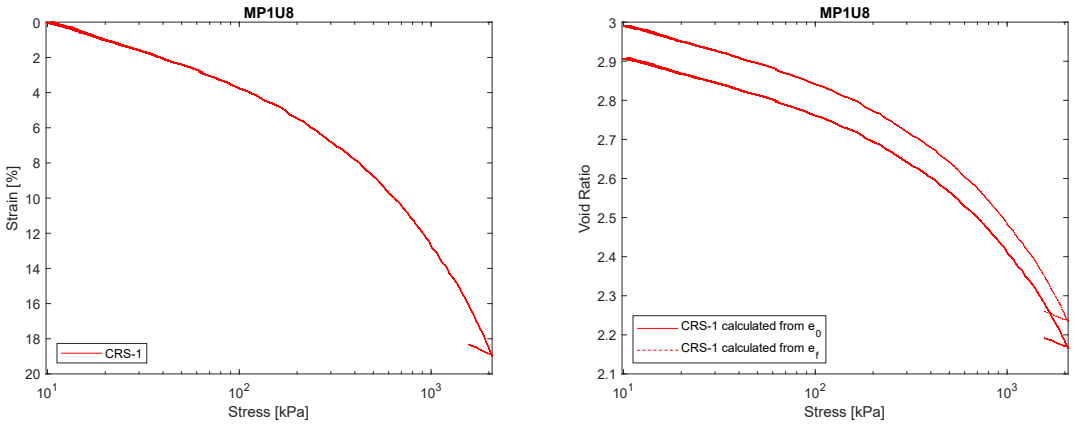

Moore Park Sample MP1U8 Consolidation Testing

Moore Park Sample MP1U8 Consolidation Testing Results

	C_c	C_r	$\sigma_p' \ [kPa]$ Becker method	$\sigma_p' \ [kPa]$ Casagrande method	$\sigma_p' \ [kPa]$ Silva method
CRS	1.105	0.199	792.3	778.7	652.6

Note: The specimen was disturbed.

PC1U1

CRS: before trimming **CRS: before trimming** **CRS: after trimming** **CRS: after trimming**

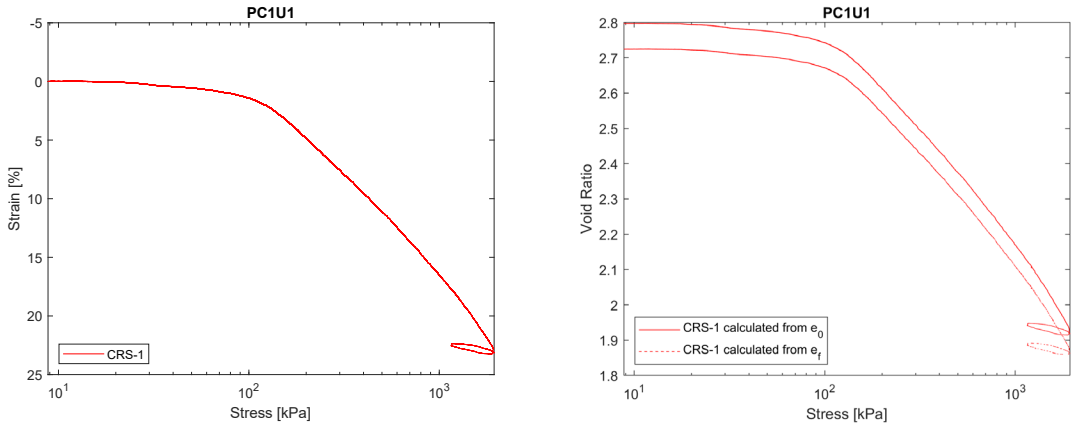

Pine Cone Drive Sample PC1U1 Consolidation Testing

Pine Cone Drive Sample PC1U1 Consolidation Testing Results

	C_c	C_r	$\sigma_p' \ [kPa]$ Becker method	$\sigma_p' \ [kPa]$ Casagrande method	$\sigma_p' \ [kPa]$ Silva method
CRS	0.962	0.102	504.8	297.9	435.9

Note: Similar to MP1U3-CRS specimen but slightly softer, the soil broke into rock-like particles which could be crushed into find grained soil when pinched between fingertips.

PC1U2

CRS-1: before trimming

CRS-1: after trimming

CRS-1: after trimming

CRS-2: before trimming

CRS-2: before trimming

CRS-2: after trimming

CRS-2: after trimming

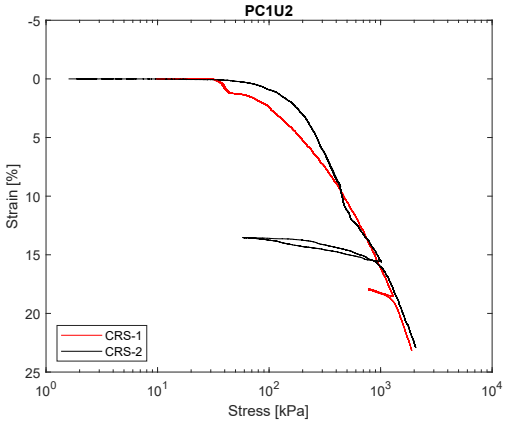

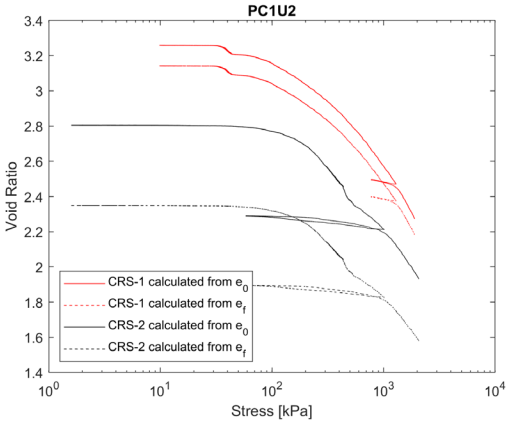

Pine Cone Drive Sample PC1U2 Consolidation Testing

Pince Cone Drive Sample PC1U2 Consolidation Testing Results

	C_c	C_r	σ_p' $[kPa]$ Becker method	σ_p' $[kPa]$ Casagrande method	σ_p' $[kPa]$ Silva method
CRS-1	1.140	0.127	328.4	336.6	309.8
CRS-2	0.808	0.054	377.4	199.7	182.8

Note: Both specimens were very difficult to trim because of the rock-like particles which can be crushed into fined grained soil.

PC1U4


CRS: before trimming


CRS: before trimming


CRS: after trimming

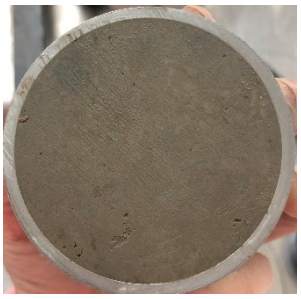
CRS: after trimming

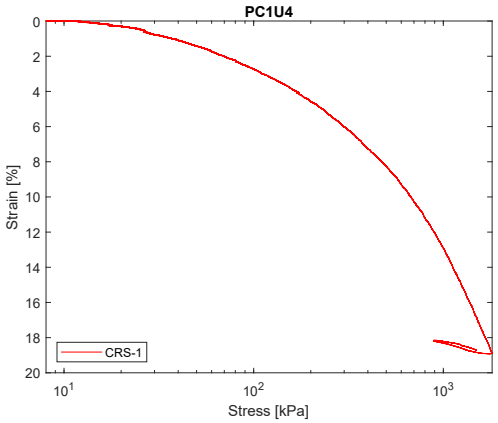

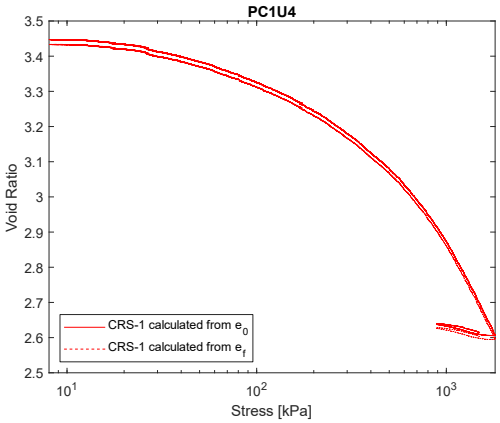

Pine Cone Drive Sample PC1U4 Consolidation Testing

Pine Cone Drive Sample PC1U4 Consolidation Testing Results

	C_c	C_r	$\sigma_p' \ [kPa]$ Becker method	$\sigma_p' \ [kPa]$ Casagrande method	$\sigma_p' \ [kPa]$ Silva method
CRS	1.262	0.121	615.7	569.2	551.2

Note: The rock-like particles are slightly softer than those of PC1U2 CRS-1 and MP1U3 CRS.

PC1U7

ILT: no trimming

ILT: no trimming

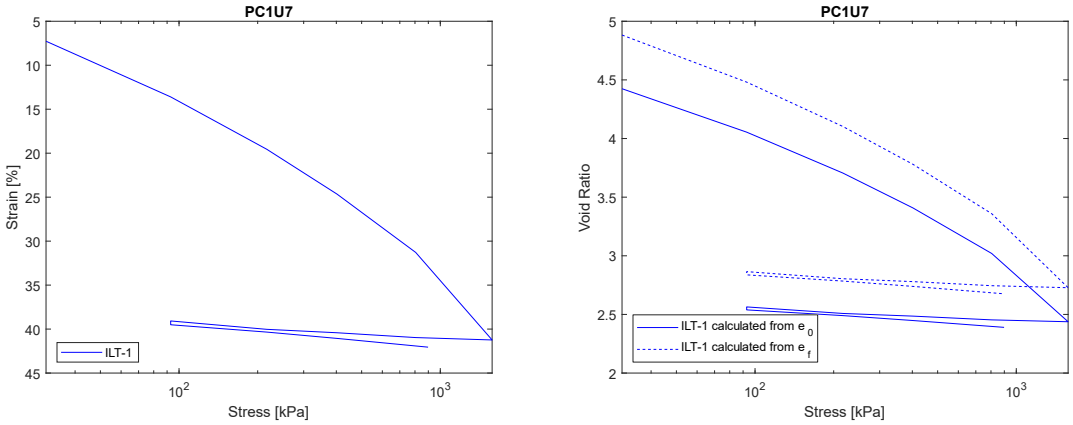

Pine Cone Drive Sample PC1U7 Consolidation Testing

Pine Cone Drive Sample PC1U7 Consolidation Testing Results

	C_c	C_r	$\sigma_p' \ [kPa]$ Becker method	$\sigma_p' \ [kPa]$ Casagrande method	$\sigma_p' \ [kPa]$ Silva method
ILT	0.170	0.121	/	/	/

Note: The soil inside the tube was fragile and broken apart. It was impossible to obtain intact specimen out of PC1U7. Results of PC1U7 are not included in analysis in the whole section 5.3.2 due to the poor quality of specimen.

PC1U8

CRS: before trimming

CRS: before trimming

CRS: before trimming

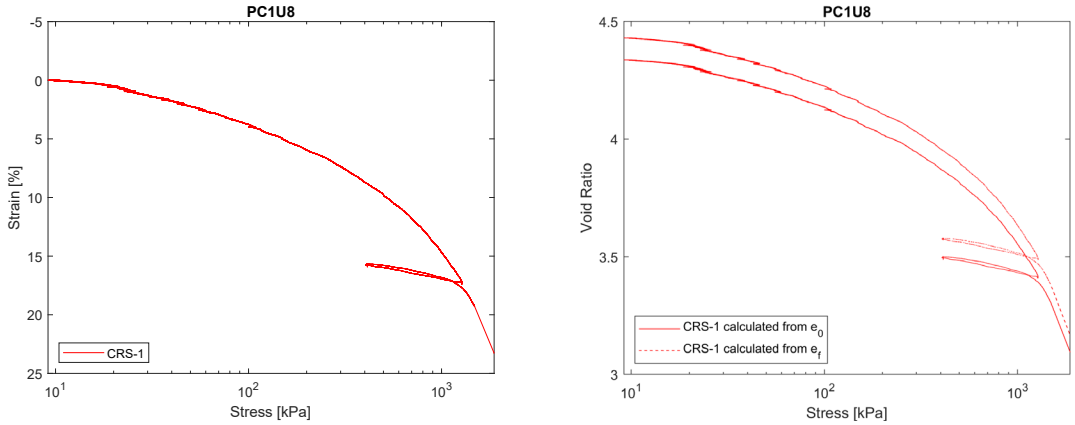

Pine Cone Drive Sample PC1U8 Consolidation Testing

Pine Cone Drive Consolidation Testing Results

	C_c	C_r	σ_p' $[kPa]$ Becker method	σ_p' $[kPa]$ Casagrande method	σ_p' $[kPa]$ Silva method
CRS	1.633	0.180	592.0	793.1	826.7

Note: No photos taken after the specimen was trimmed and filled. But the final surfaces were smooth after filling. There are rock-like particles but much softer than those of PC1U2 CRS-1 and MP1U3 CRS.

PC1U9

CRS: before trimming

CRS: before trimming

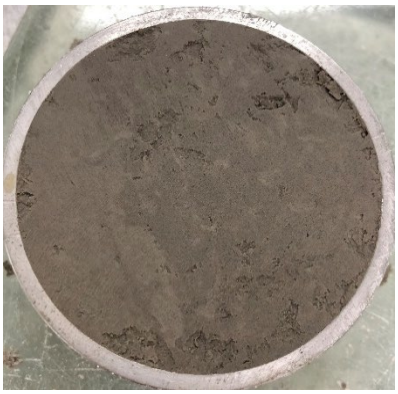

CRS: after trimming

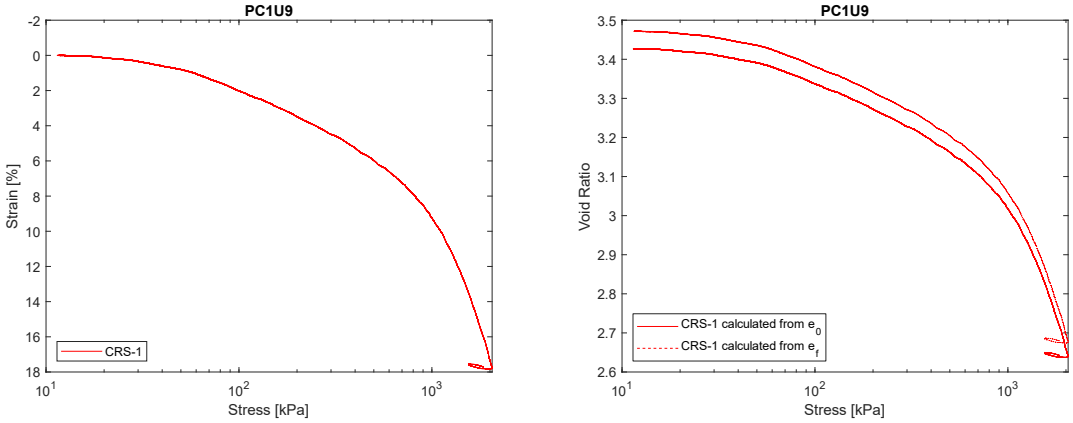

Pine Cone Drive Sample PC1U9 Consolidation Testing

Pine Cone Drive Sample PC1U9 Consolidation Testing Results

	C_c	C_r	σ_p' $[kPa]$ Becker method	σ_p' $[kPa]$ Casagrande method	σ_p' $[kPa]$ Silva method
CRS	1.800	0.092	1014.3	962.8	951.1

Note: The specimen was good quality.

APPENDIX F: TRIAXIAL TEST SPECIMENS

(a)

(b)

W1U7 (before trimming: (a); after trimming: (b))

(a)

(b)

(c)

W1U8 (before trimming: (a) (b); after trimming: (c))

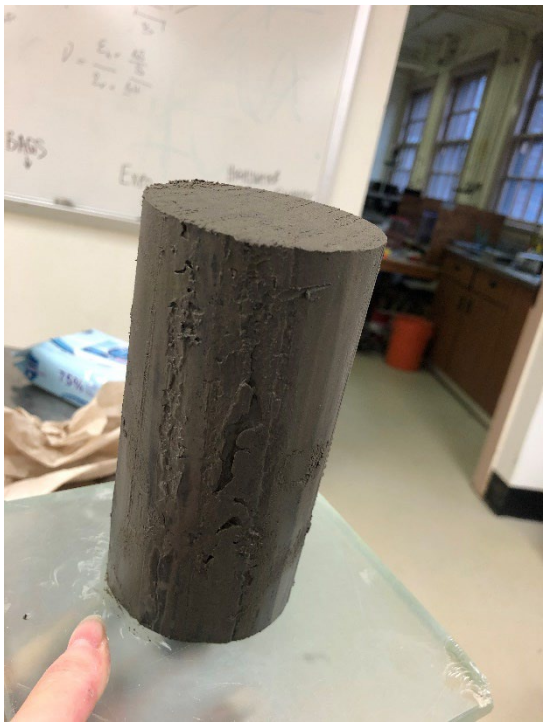

W1U9 (the specimen almost needed no trimming)

(a)

(b)

W1U10-1 (before trimming: (a); after trimming: (b))

(a)

(b)

W1U10-2 (before trimming: (a); after trimming: (b))

(a)

(b)

W1U12 (before trimming: (a); after trimming: (b))

W1U14 (specimen trimmed, but photo not taken)

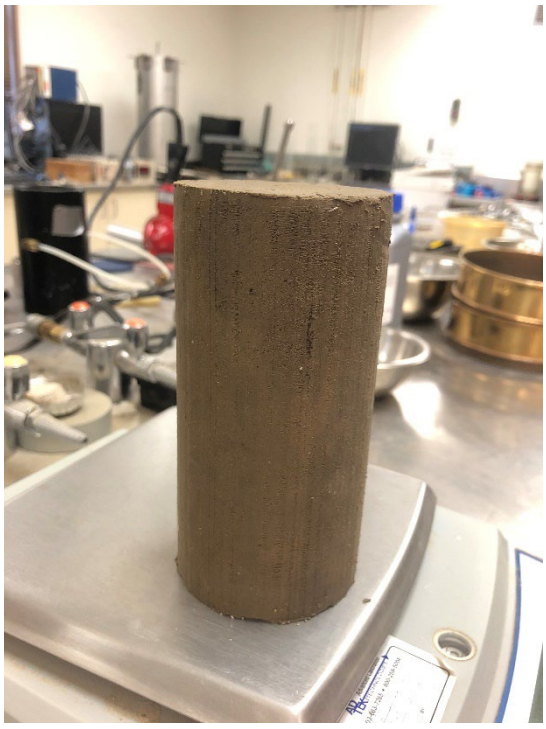

AC1U3 (the specimen almost needed no trimming)

(a)

(b)

AC1U6 (before trimming: (a); after trimming: (b))

(a)

(b)

AC1U7 (before trimming: (a); after trimming: (b))

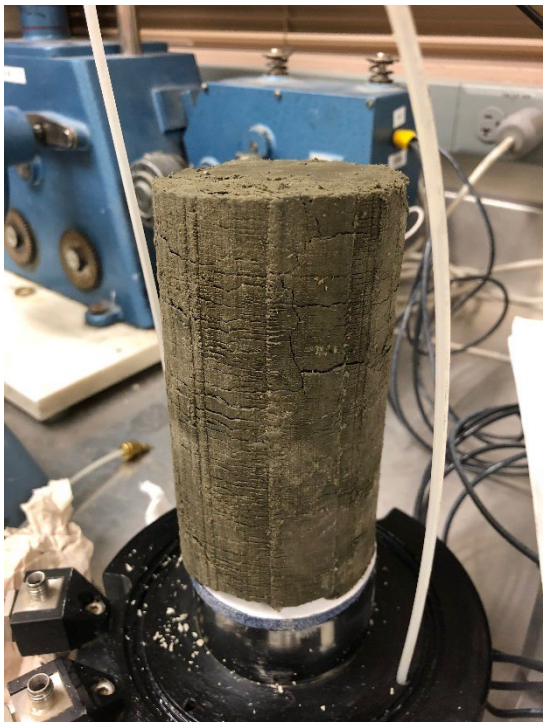

AC1U8 (specimen trimmed, but photo not taken)

(a)

(b)

MP1U3 (before trimming: (a); after trimming: (b))

APPENDIX G: DIRECT SIMPLE SHEAR TEST CURVES

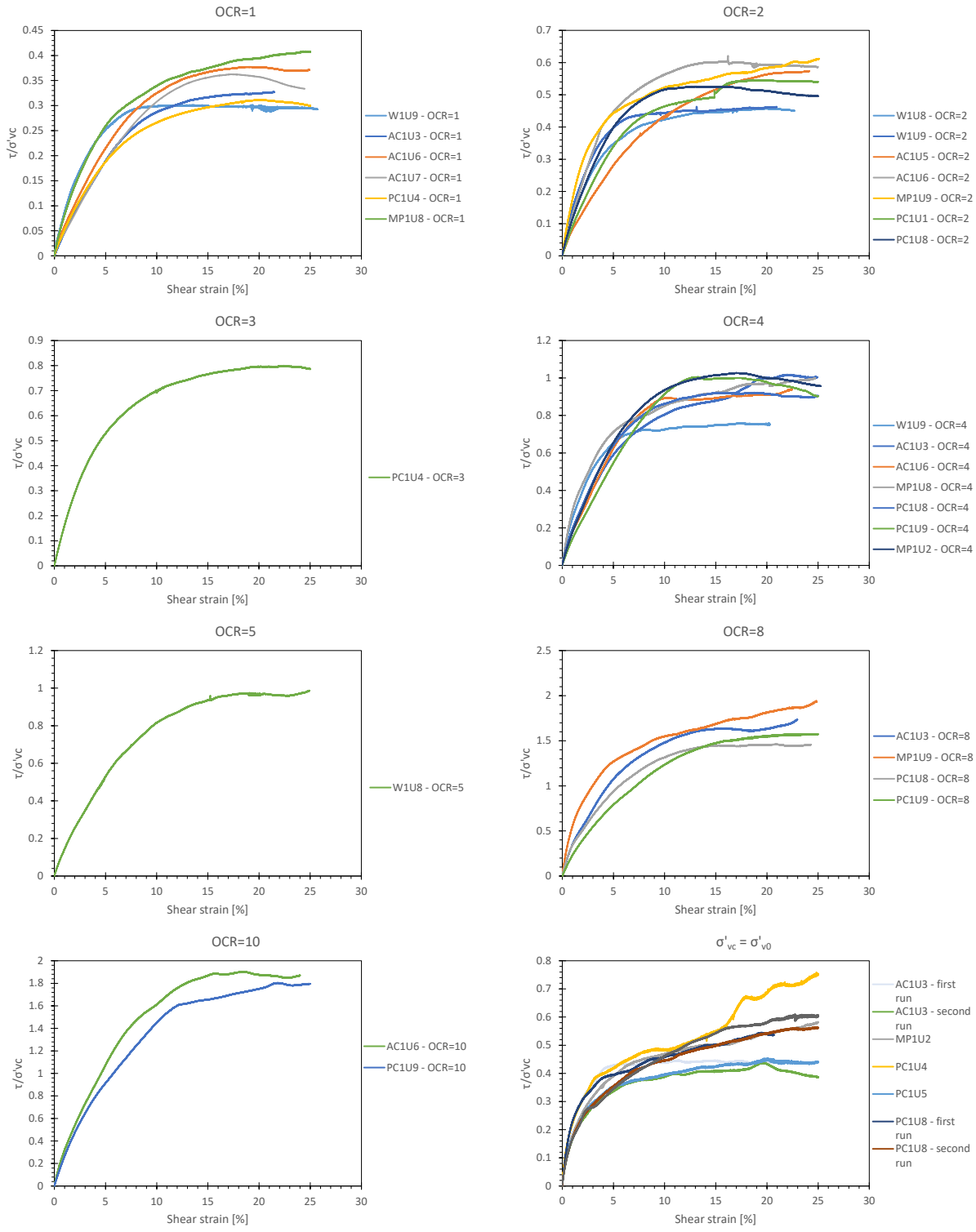

τ/σ'_{vc} vs. shear strain (γ) curves

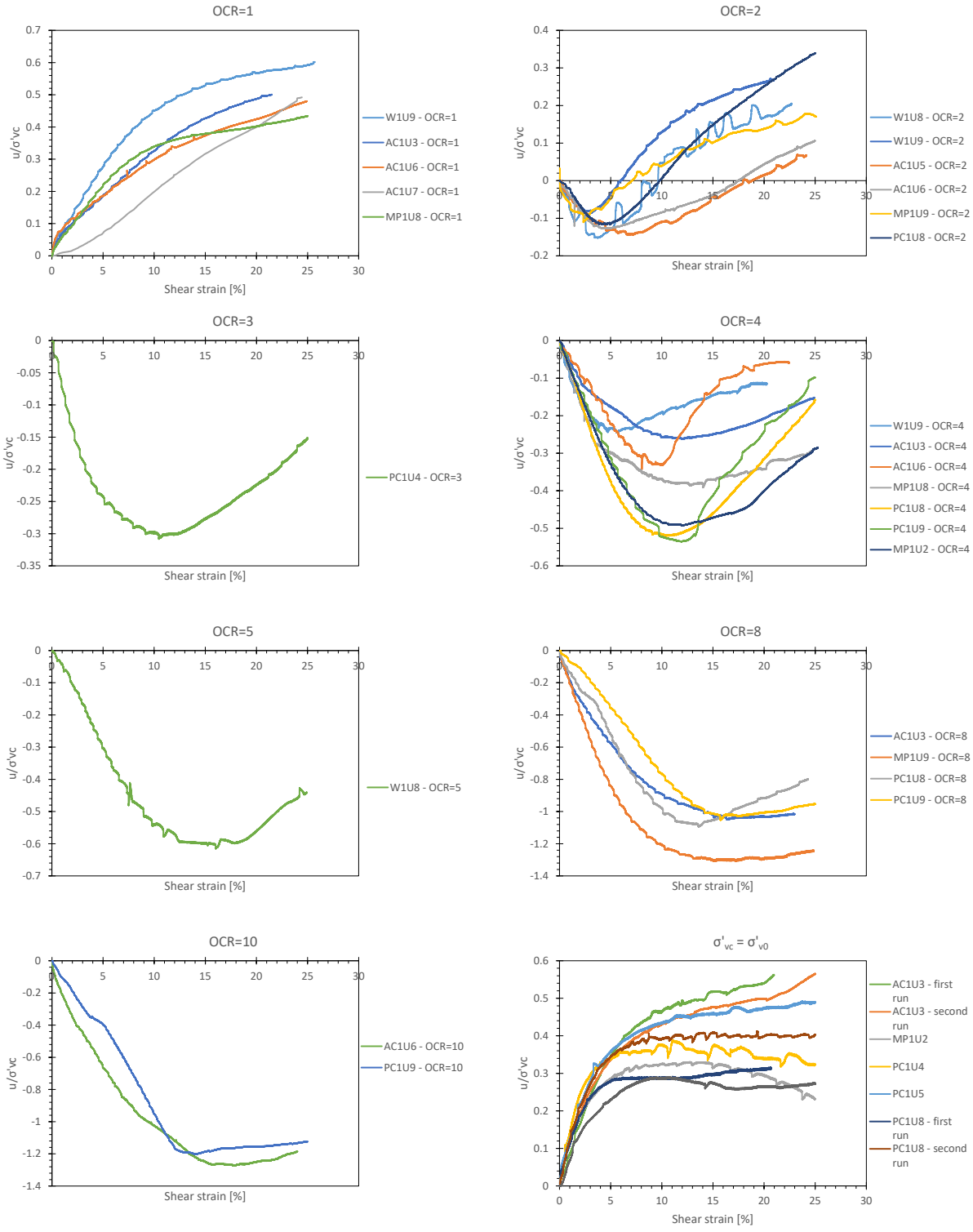

u/σ'_{vc} vs. shear strain (γ) curves

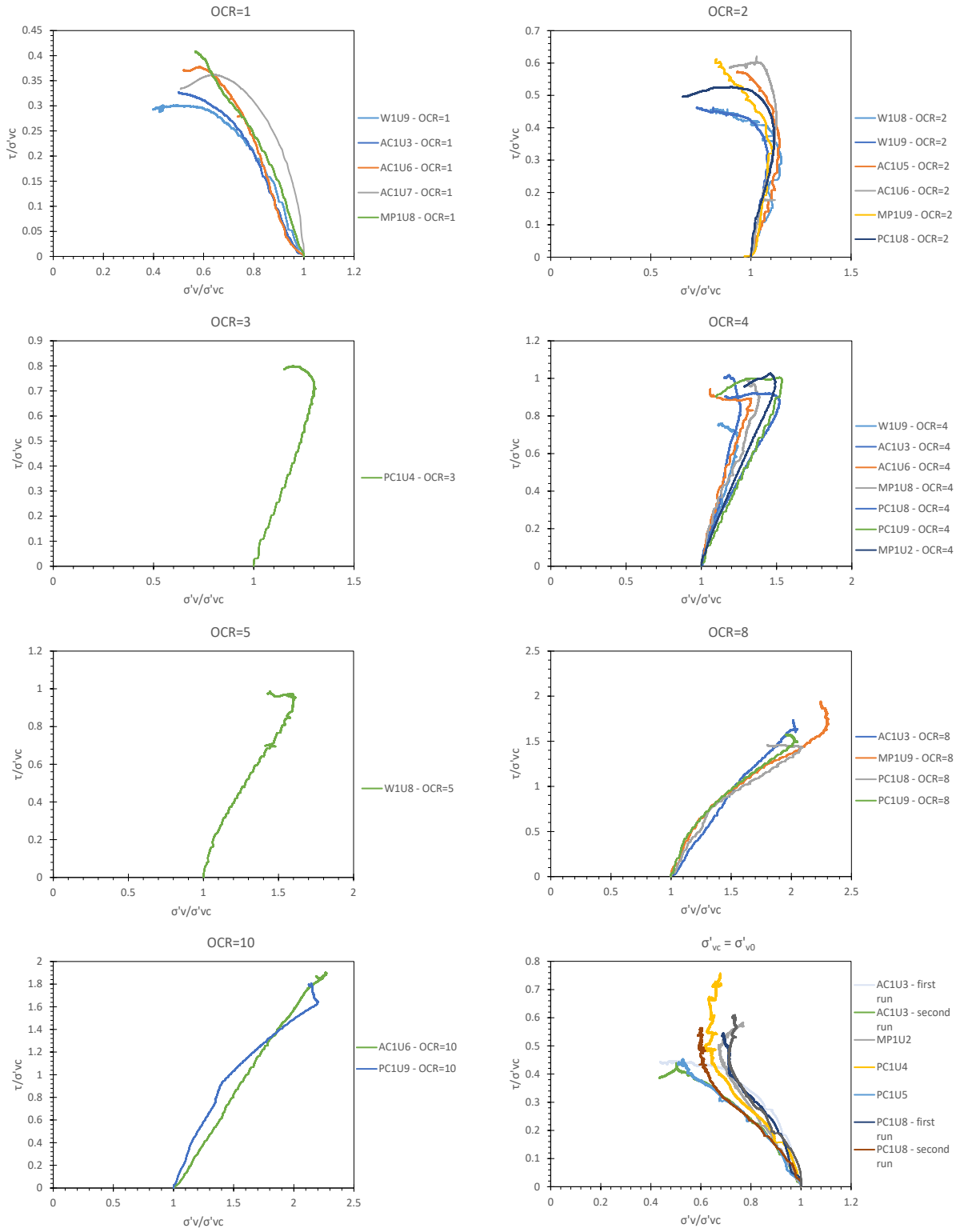

Effective stress paths

APPENDIX H: TABLES OF PILE CAPACITY CALCULATIONS

Table 10.1: Shaft capacity calculation for Pile BC 12 in Saldivar and Jardine (2005)

Depth range	Δz	Avg. depth	h	h/R^*	K_c	σ'_{v0}	σ'_{rc}	σ'_{rf}	τ'_f	$\tau'_f \Delta z$	ΔQ_s
[m]	[m]	[m]	[m]	/	/	[kPa]	[kPa]	[kPa]	[kPa]	kN/m	kN
14.5-15	0.5	14.75	7.25	25.70	0.91	80.93	73.65	58.92	42.81	21.4	42.80
15-15.5	0.5	15.25	6.75	23.93	0.92	81.68	75.06	60.05	43.63	21.82	43.63
15.5-16	0.5	15.75	6.25	22.16	0.93	82.43	76.93	61.54	44.71	22.36	44.71
16-16.5	0.5	16.25	5.75	20.38	0.95	83.18	78.93	63.15	45.88	22.94	45.88
16.5-17	0.5	16.75	5.25	18.61	0.97	83.93	81.11	64.89	47.14	23.57	47.14
17-17.5	0.5	17.25	4.75	16.84	0.99	84.68	83.49	66.79	48.53	24.26	48.53
17.5-18	0.5	17.75	4.25	15.07	1.01	85.43	86.12	68.90	50.06	25.03	50.06
18-18.5	0.5	18.25	3.75	13.29	1.03	86.18	89.08	71.26	51.78	25.89	51.78
18.5-19	0.5	18.75	3.25	11.52	1.06	86.93	92.46	73.97	53.74	26.87	53.74
19-19.5	0.5	19.25	2.75	9.75	1.10	87.68	96.43	77.14	56.05	28.02	56.05
19.5-20	0.5	19.75	2.25	8.00	1.14	88.43	101.18	80.94	58.81	29.40	58.81
20-20.5	0.5	20.25	1.75	8.00	1.14	89.18	102.04	81.63	59.31	29.65	59.31
20.5-21	0.5	20.75	1.25	8.00	1.14	89.93	102.89	82.32	59.81	29.90	59.81
21-21.5	0.5	21.25	0.75	8.00	1.14	90.68	103.75	83.00	60.30	30.15	60.30
21.5-22	0.5	21.75	0.25	8.00	1.14	91.43	104.61	83.69	60.80	30.40	60.80
										$\sum Q_s$ [kN] =	783.2

Table 10.2: Shaft capacity calculation in sand layer for Pile B2P2 in Yazdani et al. (2021)

Section bottom depth	Δz	Avg. depth	h	h/R^*	q_c	σ'_{v0}	σ'_{rc}	η	G	$\Delta\sigma'_{rd}$	σ'_{rf}	τ'_f	$\tau'_f \Delta z$	ΔQ_s
[m]	[m]	[m]	[m]	/	[kPa]	[kPa]	[kPa]	/	[kPa]	[kPa]	[kPa]	[kPa]	kN/m	kN
0.05	0.05	0.025	16.175	263.08	3134	0.43	5.37	477.68	9220	1.81	7.18	4.15	0.21	0.26
0.1	0.05	0.075	16.125	262.27	8133	1.28	16.09	715.63	27844	5.48	21.57	12.45	0.62	0.79
0.15	0.05	0.125	16.075	261.45	8120	2.13	17.18	553.41	23906	4.71	21.89	12.64	0.63	0.81
0.2	0.05	0.175	16.025	260.64	5366	2.98	11.88	309.13	18473	3.64	15.52	8.96	0.45	0.57
0.25	0.05	0.225	15.975	259.83	2936	3.83	6.72	149.16	16339	3.22	9.94	5.74	0.29	0.37
0.3	0.05	0.275	15.925	259.01	2689	4.68	6.33	123.56	17216	3.39	9.72	5.61	0.28	0.36
0.35	0.05	0.325	15.875	258.20	2495	5.53	6.01	105.44	18000	3.54	9.55	5.51	0.28	0.35
0.4	0.05	0.375	15.825	257.39	2585	6.38	6.35	101.71	19166	3.77	10.12	5.84	0.29	0.37
0.45	0.05	0.425	15.775	256.57	3840	7.23	9.60	141.94	22167	4.36	13.96	8.06	0.40	0.51
0.5	0.05	0.475	15.725	255.76	3434	8.08	8.72	120.07	22466	4.42	13.14	7.59	0.38	0.48
0.55	0.05	0.525	15.675	254.95	3170	8.93	8.16	105.42	22876	4.50	12.67	7.31	0.37	0.47
0.6	0.05	0.575	15.625	254.13	3012	9.78	7.86	95.71	23383	4.60	12.46	7.19	0.36	0.46
0.65	0.05	0.625	15.575	253.32	2817	10.63	7.44	85.87	23739	4.67	12.11	6.99	0.35	0.45
0.7	0.05	0.675	15.525	252.51	2432	11.48	6.50	71.34	23549	4.64	11.13	6.43	0.32	0.41
0.75	0.05	0.725	15.475	251.69	2067	12.33	5.58	58.48	23155	4.56	10.13	5.85	0.29	0.37
0.8	0.05	0.775	15.425	250.88	1813	13.18	4.94	49.62	22850	4.50	9.44	5.45	0.27	0.35
0.85	0.05	0.825	15.375	250.07	1629	14.03	4.48	43.22	22608	4.45	8.93	5.16	0.26	0.33
0.9	0.05	0.875	15.325	249.25	1588	14.88	4.41	40.90	22880	4.50	8.91	5.14	0.26	0.33
0.95	0.05	0.925	15.275	248.44	1659	15.73	4.64	41.56	23645	4.65	9.30	5.37	0.27	0.34
1	0.05	0.975	15.225	247.63	1536	16.58	4.33	37.49	23469	4.62	8.95	5.17	0.26	0.33
1.05	0.05	1.025	15.175	246.81	1696	17.43	4.82	40.37	24659	4.85	9.68	5.59	0.28	0.36
1.1	0.05	1.075	15.125	246.00	1586	18.28	4.54	36.86	24503	4.82	9.37	5.41	0.27	0.35
1.15	0.05	1.125	15.075	245.19	1671	19.13	4.82	37.96	25317	4.98	9.81	5.66	0.28	0.36
1.2	0.05	1.175	15.025	244.37	1588	19.98	4.61	35.30	25240	4.97	9.58	5.53	0.28	0.35
1.25	0.05	1.225	14.975	243.56	1538	20.83	4.50	33.48	25298	4.98	9.48	5.47	0.27	0.35
1.3	0.05	1.275	14.925	242.75	1665	21.68	4.90	35.54	26354	5.19	10.09	5.83	0.29	0.37
1.35	0.05	1.325	14.875	241.93	1554	22.53	4.60	32.54	26041	5.13	9.73	5.62	0.28	0.36

Section bottom depth	Δz	Avg. depth	h	h/R^*	q_c	σ'_{v0}	σ'_{rc}	η	G	$\Delta\sigma'_{rd}$	σ'_{rf}	τ'_f	$\tau'_f\Delta z$	ΔQ_s
[m]	[m]	[m]	[m]	/	[kPa]	[kPa]	[kPa]	/	[kPa]	[kPa]	[kPa]	[kPa]	kN/m	kN
1.4	0.05	1.375	14.825	241.12	1551	23.38	4.62	31.88	26332	5.18	9.81	5.66	0.28	0.36
1.45	0.05	1.425	14.775	240.31	1251	24.23	3.75	25.25	24483	4.82	8.57	4.95	0.25	0.32
1.5	0.05	1.475	14.725	239.49	1053	25.08	3.18	20.90	22952	4.52	7.70	4.44	0.22	0.28
1.55	0.05	1.525	14.675	238.68	911	25.93	2.76	17.77	21616	4.26	7.02	4.05	0.20	0.26
1.6	0.05	1.575	14.625	237.87	1100	26.78	3.36	21.13	23833	4.69	8.05	4.65	0.23	0.30
1.65	0.05	1.625	14.575	237.06	1453	27.63	4.45	27.46	27047	5.32	9.78	5.65	0.28	0.36
1.7	0.05	1.675	14.525	236.24	1629	28.48	5.02	30.33	28531	5.62	10.64	6.14	0.31	0.39
1.75	0.05	1.725	14.475	235.43	1675	29.33	5.19	30.73	29096	5.73	10.92	6.30	0.32	0.40
1.8	0.05	1.775	14.425	234.62	1684	30.18	5.24	30.47	29420	5.79	11.04	6.37	0.32	0.41
1.85	0.05	1.825	14.375	233.80	1700	31.03	5.32	30.32	29777	5.86	11.18	6.46	0.32	0.41
1.9	0.05	1.875	14.325	232.99	1624	31.88	5.11	28.58	29511	5.81	10.92	6.30	0.32	0.40
1.95	0.05	1.925	14.275	232.18	1456	32.73	4.60	25.28	28471	5.60	10.20	5.89	0.29	0.38
2	0.05	1.975	14.225	231.36	1353	33.58	4.29	23.20	27814	5.48	9.77	5.64	0.28	0.36
2.05	0.05	2.025	14.175	230.55	1237	34.43	3.95	20.95	26922	5.30	9.24	5.34	0.27	0.34
2.1	0.05	2.075	14.125	229.74	1029	35.28	3.30	17.22	24826	4.89	8.18	4.73	0.24	0.30
2.15	0.05	2.125	14.075	228.92	980	36.13	3.15	16.19	24355	4.79	7.95	4.59	0.23	0.29
2.2	0.05	2.175	14.025	228.11	876	36.98	2.83	14.32	23090	4.55	7.38	4.26	0.21	0.27
2.25	0.05	2.225	13.975	227.30	860	37.83	2.79	13.89	22974	4.52	7.31	4.22	0.21	0.27
2.3	0.05	2.275	13.925	226.48	959	38.68	3.12	15.31	24479	4.82	7.94	4.59	0.23	0.29
2.35	0.05	2.325	13.875	225.67	914	39.53	2.99	14.44	23982	4.72	7.71	4.45	0.22	0.28
2.4	0.05	2.375	13.825	224.86	996	40.38	3.27	15.57	25232	4.97	8.24	4.76	0.24	0.30
2.45	0.05	2.425	13.775	224.04	1000	41.23	3.30	15.47	25408	5.00	8.30	4.79	0.24	0.31
2.5	0.05	2.475	13.725	223.23	1111	42.08	3.68	17.01	26951	5.31	8.99	5.19	0.26	0.33
2.55	0.05	2.525	13.675	222.42	1223	42.93	4.07	18.54	28397	5.59	9.66	5.58	0.28	0.36
2.6	0.05	2.575	13.625	221.60	1309	43.78	4.37	19.66	29481	5.80	10.18	5.87	0.29	0.38
2.65	0.05	2.625	13.575	220.79	1401	44.63	4.70	20.84	30577	6.02	10.72	6.19	0.31	0.39
2.7	0.05	2.675	13.525	219.98	1645	45.48	5.54	24.24	32979	6.49	12.03	6.95	0.35	0.44
2.75	0.05	2.725	13.475	219.16	2204	46.08	7.44	32.26	37133	7.31	14.75	8.52	0.43	0.54

Section bottom depth	Δz	Avg. depth	h	h/R^*	q_c	σ'_{v0}	σ'_{rc}	η	G	$\Delta\sigma'_{rd}$	σ'_{rf}	τ'_f	$\tau'_f \Delta z$	ΔQ_s
[m]	[m]	[m]	[m]	/	[kPa]	[kPa]	[kPa]	/	[kPa]	[kPa]	[kPa]	[kPa]	kN/m	kN
2.8	0.05	2.775	13.425	218.35	4670	46.44	15.81	68.09	46807	9.21	25.02	14.45	0.72	0.92
2.85	0.05	2.825	13.375	217.54	7321	46.80	24.84	106.33	52495	10.33	35.17	20.31	1.02	1.30
2.9	0.05	2.875	13.325	216.72	9236	47.16	31.41	133.63	55766	10.98	42.39	24.47	1.22	1.56
2.95	0.05	2.925	13.275	215.91	10635	47.52	36.26	153.29	58009	11.42	47.68	27.53	1.38	1.76
3	0.05	2.975	13.225	215.10	11590	47.88	39.61	166.42	59544	11.72	51.33	29.63	1.48	1.89
3.05	0.05	3.025	13.175	214.28	12169	48.24	41.69	174.08	60528	11.91	53.60	30.95	1.55	1.98
3.1	0.05	3.075	13.125	213.47	13165	48.60	45.21	187.63	62091	12.22	57.43	33.16	1.66	2.12
3.15	0.05	3.125	13.075	212.66	14001	48.96	48.19	198.81	63425	12.49	60.68	35.03	1.75	2.24
3.2	0.05	3.175	13.025	211.85	14951	49.32	51.59	211.52	64921	12.78	64.37	37.16	1.86	2.37
3.25	0.05	3.225	12.975	211.03	10334	49.68	35.74	145.66	58521	11.52	47.26	27.29	1.36	1.74
3.3	0.05	3.275	12.925	210.22	9439	50.04	32.73	132.58	57329	11.29	44.01	25.41	1.27	1.62
3.35	0.05	3.325	12.875	209.41	17602	50.40	61.17	246.34	69180	13.62	74.79	43.18	2.16	2.76
3.4	0.05	3.375	12.825	208.59	10786	50.76	37.57	150.41	59654	11.74	49.32	28.47	1.42	1.82
3.45	0.05	3.425	12.775	207.78	13772	51.12	48.10	191.38	64060	12.61	60.71	35.05	1.75	2.24
3.5	0.05	3.475	12.725	206.97	21659	51.48	75.82	299.93	75778	14.92	90.74	52.39	2.62	3.34
3.55	0.05	3.525	12.675	206.15	11851	51.84	41.59	163.54	61660	12.14	53.72	31.02	1.55	1.98
3.6	0.05	3.575	12.625	205.34	17121	52.20	60.22	235.45	69260	13.63	73.86	42.64	2.13	2.72
3.65	0.05	3.625	12.575	204.53	9593	52.56	33.82	131.47	58631	11.54	45.37	26.19	1.31	1.67
3.7	0.05	3.675	12.525	203.71	10652	52.92	37.65	145.49	60380	11.89	49.54	28.60	1.43	1.83
3.75	0.05	3.725	12.475	202.90	11621	53.28	41.17	158.19	61946	12.19	53.37	30.81	1.54	1.97
3.8	0.05	3.775	12.425	202.09	11604	53.64	41.21	157.42	62073	12.22	53.43	30.85	1.54	1.97
3.85	0.05	3.825	12.375	201.27	11795	54.00	41.99	159.47	62500	12.30	54.29	31.35	1.57	2.00
3.9	0.05	3.875	12.325	200.46	11721	54.36	41.83	157.95	62545	12.31	54.14	31.26	1.56	2.00
3.95	0.05	3.925	12.275	199.65	12112	54.72	43.32	162.68	63258	12.45	55.78	32.20	1.61	2.06
4	0.05	3.975	12.225	198.83	16059	55.08	57.58	214.99	68972	13.58	71.16	41.08	2.05	2.62
													$\sum Q_s$ [kN] =	71.4

Table 10.3: Shaft capacity calculation in diatomaceous layer for Pile B2P2 in Yazdani et al. (2021) - $\Delta I_{vy} = 2.141$

Section bottom depth	Δz	Avg. depth	h	h/R^*	σ'_{v0}	K_c	σ'_{rc}	σ'_{rf}	τ'_f	$\tau'_f \Delta z$	ΔQ_s
[m]	[m]	[m]	[m]	/	[kPa]	/	[kPa]	[kPa]	[kPa]	kN/m	kN
4.05	0.05	4.025	12.175	198.02	55.34	1.35	74.45	59.56	41.71	2.09	2.66
4.1	0.05	4.075	12.125	197.21	55.50	1.35	74.73	59.78	41.86	2.09	2.67
4.15	0.05	4.125	12.075	196.39	55.66	1.35	75.01	60.01	42.02	2.10	2.68
4.2	0.05	4.175	12.025	195.58	55.82	1.35	75.29	60.23	42.17	2.11	2.69
4.25	0.05	4.225	11.975	194.77	55.98	1.35	75.56	60.45	42.33	2.12	2.70
4.3	0.05	4.275	11.925	193.95	56.14	1.35	75.84	60.68	42.49	2.12	2.71
4.35	0.05	4.325	11.875	193.14	56.30	1.35	76.12	60.90	42.64	2.13	2.72
4.4	0.05	4.375	11.825	192.33	56.46	1.35	76.40	61.12	42.80	2.14	2.73
4.45	0.05	4.425	11.775	191.51	56.62	1.35	76.69	61.35	42.96	2.15	2.74
4.5	0.05	4.475	11.725	190.70	56.78	1.36	76.97	61.57	43.12	2.16	2.75
4.55	0.05	4.525	11.675	189.89	56.94	1.36	77.25	61.80	43.27	2.16	2.76
4.6	0.05	4.575	11.625	189.07	57.10	1.36	77.54	62.03	43.43	2.17	2.77
4.65	0.05	4.625	11.575	188.26	57.26	1.36	77.82	62.26	43.59	2.18	2.78
4.7	0.05	4.675	11.525	187.45	57.42	1.36	78.10	62.48	43.75	2.19	2.79
4.75	0.05	4.725	11.475	186.64	57.58	1.36	78.39	62.71	43.91	2.20	2.80
4.8	0.05	4.775	11.425	185.82	57.74	1.36	78.68	62.94	44.07	2.20	2.81
4.85	0.05	4.825	11.375	185.01	57.90	1.36	78.96	63.17	44.23	2.21	2.82
4.9	0.05	4.875	11.325	184.20	58.06	1.37	79.25	63.40	44.39	2.22	2.83
4.95	0.05	4.925	11.275	183.38	58.22	1.37	79.54	63.63	44.56	2.23	2.84
5	0.05	4.975	11.225	182.57	58.38	1.37	79.83	63.86	44.72	2.24	2.85
5.05	0.05	5.025	11.175	181.76	58.54	1.37	80.12	64.10	44.88	2.24	2.87
5.1	0.05	5.075	11.125	180.94	58.70	1.37	80.41	64.33	45.04	2.25	2.88
5.15	0.05	5.125	11.075	180.13	58.86	1.37	80.70	64.56	45.21	2.26	2.89
5.2	0.05	5.175	11.025	179.32	59.02	1.37	81.00	64.80	45.37	2.27	2.90
5.25	0.05	5.225	10.975	178.50	59.18	1.37	81.29	65.03	45.54	2.28	2.91
5.3	0.05	5.275	10.925	177.69	59.34	1.37	81.58	65.27	45.70	2.29	2.92
5.35	0.05	5.325	10.875	176.88	59.50	1.38	81.88	65.50	45.87	2.29	2.93

Section bottom depth	Δz	Avg. depth	h	h/R^*	σ'_{v0}	K_c	σ'_{rc}	σ'_{rf}	τ'_f	$\tau'_f \Delta z$	ΔQ_s
[m]	[m]	[m]	[m]	/	[kPa]	/	[kPa]	[kPa]	[kPa]	kN/m	kN
5.4	0.05	5.375	10.825	176.06	59.66	1.38	82.17	65.74	46.03	2.30	2.94
5.45	0.05	5.425	10.775	175.25	59.82	1.38	82.47	65.98	46.20	2.31	2.95
5.5	0.05	5.475	10.725	174.44	59.98	1.38	82.77	66.22	46.36	2.32	2.96
5.55	0.05	5.525	10.675	173.62	60.14	1.38	83.07	66.45	46.53	2.33	2.97
5.6	0.05	5.575	10.625	172.81	60.30	1.38	83.37	66.69	46.70	2.33	2.98
5.65	0.05	5.625	10.575	172.00	60.46	1.38	83.67	66.93	46.87	2.34	2.99
5.7	0.05	5.675	10.525	171.18	60.62	1.39	83.97	67.17	47.04	2.35	3.00
5.75	0.05	5.725	10.475	170.37	60.78	1.39	84.27	67.42	47.20	2.36	3.01
5.8	0.05	5.775	10.425	169.56	60.94	1.39	84.57	67.66	47.37	2.37	3.02
5.85	0.05	5.825	10.375	168.74	61.10	1.39	84.88	67.90	47.54	2.38	3.04
5.9	0.05	5.875	10.325	167.93	61.26	1.39	85.18	68.14	47.72	2.39	3.05
5.95	0.05	5.925	10.275	167.12	61.42	1.39	85.49	68.39	47.89	2.39	3.06
6	0.05	5.975	10.225	166.30	61.58	1.39	85.79	68.63	48.06	2.40	3.07
6.05	0.05	6.025	10.175	165.49	61.74	1.39	86.10	68.88	48.23	2.41	3.08
6.1	0.05	6.075	10.125	164.68	61.90	1.40	86.41	69.13	48.40	2.42	3.09
6.15	0.05	6.125	10.075	163.86	62.06	1.40	86.72	69.37	48.58	2.43	3.10
6.2	0.05	6.175	10.025	163.05	62.22	1.40	87.03	69.62	48.75	2.44	3.11
6.25	0.05	6.225	9.975	162.24	62.38	1.40	87.34	69.87	48.92	2.45	3.12
6.3	0.05	6.275	9.925	161.43	62.54	1.40	87.65	70.12	49.10	2.45	3.13
6.35	0.05	6.325	9.875	160.61	62.70	1.40	87.96	70.37	49.27	2.46	3.15
6.4	0.05	6.375	9.825	159.80	62.86	1.40	88.28	70.62	49.45	2.47	3.16
6.45	0.05	6.425	9.775	158.99	63.02	1.41	88.59	70.87	49.63	2.48	3.17
6.5	0.05	6.475	9.725	158.17	63.18	1.41	88.91	71.13	49.80	2.49	3.18
6.55	0.05	6.525	9.675	157.36	63.34	1.41	89.23	71.38	49.98	2.50	3.19
6.6	0.05	6.575	9.625	156.55	63.50	1.41	89.54	71.63	50.16	2.51	3.20
6.65	0.05	6.625	9.575	155.73	63.66	1.41	89.86	71.89	50.34	2.52	3.21
6.7	0.05	6.675	9.525	154.92	63.82	1.41	90.18	72.15	50.52	2.53	3.22
6.75	0.05	6.725	9.475	154.11	63.98	1.41	90.50	72.40	50.70	2.53	3.24

Section bottom depth	Δz	Avg. depth	h	h/R^*	σ'_{v0}	K_c	σ'_{rc}	σ'_{rf}	τ'_f	$\tau'_f \Delta z$	ΔQ_s
[m]	[m]	[m]	[m]	/	[kPa]	/	[kPa]	[kPa]	[kPa]	kN/m	kN
6.8	0.05	6.775	9.425	153.29	64.14	1.42	90.83	72.66	50.88	2.54	3.25
6.85	0.05	6.825	9.375	152.48	64.30	1.42	91.15	72.92	51.06	2.55	3.26
6.9	0.05	6.875	9.325	151.67	64.46	1.42	91.47	73.18	51.24	2.56	3.27
6.95	0.05	6.925	9.275	150.85	64.62	1.42	91.80	73.44	51.42	2.57	3.28
7	0.05	6.975	9.225	150.04	64.78	1.42	92.13	73.70	51.61	2.58	3.29
7.05	0.05	7.025	9.175	149.23	64.94	1.42	92.46	73.96	51.79	2.59	3.31
7.1	0.05	7.075	9.125	148.41	65.10	1.43	92.78	74.23	51.97	2.60	3.32
7.15	0.05	7.125	9.075	147.60	65.26	1.43	93.11	74.49	52.16	2.61	3.33
7.2	0.05	7.175	9.025	146.79	65.42	1.43	93.45	74.76	52.35	2.62	3.34
7.25	0.05	7.225	8.975	145.97	65.58	1.43	93.78	75.02	52.53	2.63	3.35
7.3	0.05	7.275	8.925	145.16	65.74	1.43	94.11	75.29	52.72	2.64	3.37
7.35	0.05	7.325	8.875	144.35	65.90	1.43	94.45	75.56	52.91	2.65	3.38
7.4	0.05	7.375	8.825	143.53	66.06	1.43	94.78	75.83	53.09	2.65	3.39
7.45	0.05	7.425	8.775	142.72	66.22	1.44	95.12	76.10	53.28	2.66	3.40
7.5	0.05	7.475	8.725	141.91	66.38	1.44	95.46	76.37	53.47	2.67	3.41
7.55	0.05	7.525	8.675	141.09	66.54	1.44	95.80	76.64	53.66	2.68	3.43
7.6	0.05	7.575	8.625	140.28	66.70	1.44	96.14	76.91	53.86	2.69	3.44
7.65	0.05	7.625	8.575	139.47	66.86	1.44	96.49	77.19	54.05	2.70	3.45
7.7	0.05	7.675	8.525	138.65	67.02	1.44	96.83	77.46	54.24	2.71	3.46
7.75	0.05	7.725	8.475	137.84	67.18	1.45	97.17	77.74	54.43	2.72	3.47
7.8	0.05	7.775	8.425	137.03	67.34	1.45	97.52	78.02	54.63	2.73	3.49
7.85	0.05	7.825	8.375	136.22	67.50	1.45	97.87	78.30	54.82	2.74	3.50
7.9	0.05	7.875	8.325	135.40	67.66	1.45	98.22	78.58	55.02	2.75	3.51
7.95	0.05	7.925	8.275	134.59	67.82	1.45	98.57	78.86	55.22	2.76	3.52
8	0.05	7.975	8.225	133.78	67.98	1.46	98.92	79.14	55.41	2.77	3.54
8.05	0.05	8.025	8.175	132.96	68.14	1.46	99.28	79.42	55.61	2.78	3.55
8.1	0.05	8.075	8.125	132.15	68.30	1.46	99.63	79.71	55.81	2.79	3.56
8.15	0.05	8.125	8.075	131.34	68.46	1.46	99.99	79.99	56.01	2.80	3.58

Section bottom depth	Δz	Avg. depth	h	h/R^*	σ'_{v0}	K_c	σ'_{rc}	σ'_{rf}	τ'_f	$\tau'_f \Delta z$	ΔQ_s
[m]	[m]	[m]	[m]	/	[kPa]	/	[kPa]	[kPa]	[kPa]	kN/m	kN
8.2	0.05	8.175	8.025	130.52	68.62	1.46	100.35	80.28	56.21	2.81	3.59
8.25	0.05	8.225	7.975	129.71	68.78	1.46	100.71	80.57	56.41	2.82	3.60
8.3	0.05	8.275	7.925	128.90	68.94	1.47	101.07	80.85	56.61	2.83	3.61
8.35	0.05	8.325	7.875	128.08	69.10	1.47	101.43	81.14	56.82	2.84	3.63
8.4	0.05	8.375	7.825	127.27	69.26	1.47	101.80	81.44	57.02	2.85	3.64
8.45	0.05	8.425	7.775	126.46	69.42	1.47	102.16	81.73	57.23	2.86	3.65
8.5	0.05	8.475	7.725	125.64	69.58	1.47	102.53	82.02	57.43	2.87	3.67
8.55	0.05	8.525	7.675	124.83	69.74	1.48	102.90	82.32	57.64	2.88	3.68
8.6	0.05	8.575	7.625	124.02	69.90	1.48	103.27	82.62	57.85	2.89	3.69
8.65	0.05	8.625	7.575	123.20	70.06	1.48	103.64	82.91	58.06	2.90	3.71
8.7	0.05	8.675	7.525	122.39	70.22	1.48	104.02	83.21	58.27	2.91	3.72
8.75	0.05	8.725	7.475	121.58	70.38	1.48	104.39	83.51	58.48	2.92	3.73
8.8	0.05	8.775	7.425	120.76	70.54	1.49	104.77	83.82	58.69	2.93	3.75
8.85	0.05	8.825	7.375	119.95	70.70	1.49	105.15	84.12	58.90	2.95	3.76
8.9	0.05	8.875	7.325	119.14	70.86	1.49	105.53	84.42	59.11	2.96	3.77
8.95	0.05	8.925	7.275	118.32	71.02	1.49	105.91	84.73	59.33	2.97	3.79
9	0.05	8.975	7.225	117.51	71.18	1.49	106.30	85.04	59.55	2.98	3.80
9.05	0.05	9.025	7.175	116.70	71.34	1.50	106.69	85.35	59.76	2.99	3.82
9.1	0.05	9.075	7.125	115.88	71.50	1.50	107.08	85.66	59.98	3.00	3.83
9.15	0.05	9.125	7.075	115.07	71.66	1.50	107.47	85.97	60.20	3.01	3.84
9.2	0.05	9.175	7.025	114.26	71.82	1.50	107.86	86.29	60.42	3.02	3.86
9.25	0.05	9.225	6.975	113.44	71.98	1.50	108.25	86.60	60.64	3.03	3.87
9.3	0.05	9.275	6.925	112.63	72.14	1.51	108.65	86.92	60.86	3.04	3.89
9.35	0.05	9.325	6.875	111.82	72.30	1.51	109.05	87.24	61.09	3.05	3.90
9.4	0.05	9.375	6.825	111.01	72.46	1.51	109.45	87.56	61.31	3.07	3.91
9.45	0.05	9.425	6.775	110.19	72.62	1.51	109.85	87.88	61.54	3.08	3.93
9.5	0.05	9.475	6.725	109.38	72.78	1.51	110.26	88.21	61.76	3.09	3.94
9.55	0.05	9.525	6.675	108.57	72.94	1.52	110.67	88.53	61.99	3.10	3.96

Section bottom depth	Δz	Avg. depth	h	h/R^*	σ'_{v0}	K_c	σ'_{rc}	σ'_{rf}	τ'_f	$\tau'_f \Delta z$	ΔQ_s
[m]	[m]	[m]	[m]	/	[kPa]	/	[kPa]	[kPa]	[kPa]	kN/m	kN
9.6	0.05	9.575	6.625	107.75	73.10	1.52	111.08	88.86	62.22	3.11	3.97
9.65	0.05	9.625	6.575	106.94	73.26	1.52	111.49	89.19	62.45	3.12	3.99
9.7	0.05	9.675	6.525	106.13	73.42	1.52	111.90	89.52	62.68	3.13	4.00
9.75	0.05	9.725	6.475	105.31	73.58	1.53	112.32	89.86	62.92	3.15	4.02
9.8	0.05	9.775	6.425	104.50	73.74	1.53	112.74	90.19	63.15	3.16	4.03
9.85	0.05	9.825	6.375	103.69	73.90	1.53	113.16	90.53	63.39	3.17	4.05
9.9	0.05	9.875	6.325	102.87	74.06	1.53	113.58	90.87	63.63	3.18	4.06
9.95	0.05	9.925	6.275	102.06	74.22	1.54	114.01	91.21	63.86	3.19	4.08
10	0.05	9.975	6.225	101.25	74.38	1.54	114.44	91.55	64.10	3.21	4.09
10.05	0.05	10.025	6.175	100.43	74.54	1.54	114.87	91.90	64.35	3.22	4.11
10.1	0.05	10.075	6.125	99.62	74.70	1.54	115.30	92.24	64.59	3.23	4.12
10.15	0.05	10.125	6.075	98.81	74.86	1.55	115.74	92.59	64.83	3.24	4.14
10.2	0.05	10.175	6.025	97.99	75.02	1.55	116.18	92.94	65.08	3.25	4.15
10.25	0.05	10.225	5.975	97.18	75.18	1.55	116.62	93.30	65.33	3.27	4.17
10.3	0.05	10.275	5.925	96.37	75.34	1.55	117.07	93.65	65.58	3.28	4.19
10.35	0.05	10.325	5.875	95.55	75.50	1.56	117.51	94.01	65.83	3.29	4.20
10.4	0.05	10.375	5.825	94.74	75.66	1.56	117.96	94.37	66.08	3.30	4.22
10.45	0.05	10.425	5.775	93.93	75.82	1.56	118.42	94.73	66.33	3.32	4.23
10.5	0.05	10.475	5.725	93.11	75.98	1.56	118.87	95.10	66.59	3.33	4.25
10.55	0.05	10.525	5.675	92.30	76.14	1.57	119.33	95.47	66.85	3.34	4.27
10.6	0.05	10.575	5.625	91.49	76.30	1.57	119.80	95.84	67.11	3.36	4.28
10.65	0.05	10.625	5.575	90.67	76.46	1.57	120.26	96.21	67.37	3.37	4.30
10.7	0.05	10.675	5.525	89.86	76.62	1.58	120.73	96.58	67.63	3.38	4.32
10.75	0.05	10.725	5.475	89.05	76.78	1.58	121.20	96.96	67.89	3.39	4.33
10.8	0.05	10.775	5.425	88.23	76.94	1.58	121.68	97.34	68.16	3.41	4.35
10.85	0.05	10.825	5.375	87.42	77.10	1.58	122.16	97.73	68.43	3.42	4.37
10.9	0.05	10.875	5.325	86.61	77.26	1.59	122.64	98.11	68.70	3.43	4.39
10.95	0.05	10.925	5.275	85.80	77.42	1.59	123.13	98.50	68.97	3.45	4.40

Section bottom depth	Δz	Avg. depth	h	h/R^*	σ'_{v0}	K_c	σ'_{rc}	σ'_{rf}	τ'_f	$\tau'_f \Delta z$	ΔQ_s
[m]	[m]	[m]	[m]	/	[kPa]	/	[kPa]	[kPa]	[kPa]	kN/m	kN
11	0.05	10.975	5.225	84.98	77.58	1.59	123.62	98.89	69.25	3.46	4.42
11.05	0.05	11.025	5.175	84.17	77.74	1.60	124.11	99.29	69.52	3.48	4.44
11.1	0.05	11.075	5.125	83.36	77.90	1.60	124.61	99.68	69.80	3.49	4.46
11.15	0.05	11.125	5.075	82.54	78.06	1.60	125.11	100.09	70.08	3.50	4.47
11.2	0.05	11.175	5.025	81.73	78.22	1.61	125.61	100.49	70.36	3.52	4.49
11.25	0.05	11.225	4.975	80.92	78.38	1.61	126.12	100.90	70.65	3.53	4.51
11.3	0.05	11.275	4.925	80.10	78.54	1.61	126.63	101.31	70.94	3.55	4.53
11.35	0.05	11.325	4.875	79.29	78.70	1.62	127.15	101.72	71.23	3.56	4.55
11.4	0.05	11.375	4.825	78.48	78.86	1.62	127.67	102.14	71.52	3.58	4.57
11.45	0.05	11.425	4.775	77.66	79.02	1.62	128.20	102.56	71.81	3.59	4.58
11.5	0.05	11.475	4.725	76.85	79.18	1.63	128.73	102.98	72.11	3.61	4.60
11.55	0.05	11.525	4.675	76.04	79.34	1.63	129.26	103.41	72.41	3.62	4.62
11.6	0.05	11.575	4.625	75.22	79.50	1.63	129.80	103.84	72.71	3.64	4.64
11.65	0.05	11.625	4.575	74.41	79.66	1.64	130.35	104.28	73.02	3.65	4.66
11.7	0.05	11.675	4.525	73.60	79.82	1.64	130.90	104.72	73.32	3.67	4.68
11.75	0.05	11.725	4.475	72.78	79.98	1.64	131.45	105.16	73.63	3.68	4.70
11.8	0.05	11.775	4.425	71.97	80.14	1.65	132.01	105.61	73.95	3.70	4.72
11.85	0.05	11.825	4.375	71.16	80.30	1.65	132.57	106.06	74.26	3.71	4.74
11.9	0.05	11.875	4.325	70.34	80.46	1.65	133.14	106.52	74.58	3.73	4.76
11.95	0.05	11.925	4.275	69.53	80.62	1.66	133.72	106.98	74.91	3.75	4.78
12	0.05	11.975	4.225	68.72	80.78	1.66	134.30	107.44	75.23	3.76	4.80
12.05	0.05	12.025	4.175	67.90	80.94	1.67	134.89	107.91	75.56	3.78	4.82
12.1	0.05	12.075	4.125	67.09	81.10	1.67	135.48	108.38	75.89	3.79	4.84
12.15	0.05	12.125	4.075	66.28	81.26	1.67	136.08	108.86	76.23	3.81	4.87
12.2	0.05	12.175	4.025	65.46	81.42	1.68	136.68	109.35	76.57	3.83	4.89
12.25	0.05	12.225	3.975	64.65	81.58	1.68	137.30	109.84	76.91	3.85	4.91
12.3	0.05	12.275	3.925	63.84	81.74	1.69	137.91	110.33	77.25	3.86	4.93
12.35	0.05	12.325	3.875	63.02	81.90	1.69	138.54	110.83	77.60	3.88	4.95

Section bottom depth	Δz	Avg. depth	h	h/R^*	σ'_{v0}	K_c	σ'_{rc}	σ'_{rf}	τ'_f	$\tau'_f \Delta z$	ΔQ_s
[m]	[m]	[m]	[m]	/	[kPa]	/	[kPa]	[kPa]	[kPa]	kN/m	kN
12.4	0.05	12.375	3.825	62.21	82.06	1.70	139.17	111.34	77.96	3.90	4.98
12.45	0.05	12.425	3.775	61.40	82.22	1.70	139.81	111.85	78.32	3.92	5.00
12.5	0.05	12.475	3.725	60.59	82.38	1.70	140.46	112.36	78.68	3.93	5.02
12.55	0.05	12.525	3.675	59.77	82.54	1.71	141.11	112.89	79.04	3.95	5.05
12.6	0.05	12.575	3.625	58.96	82.70	1.71	141.77	113.42	79.41	3.97	5.07
12.65	0.05	12.625	3.575	58.15	82.86	1.72	142.44	113.95	79.79	3.99	5.09
12.7	0.05	12.675	3.525	57.33	83.02	1.72	143.12	114.49	80.17	4.01	5.12
12.75	0.05	12.725	3.475	56.52	83.18	1.73	143.80	115.04	80.55	4.03	5.14
12.8	0.05	12.775	3.425	55.71	83.34	1.73	144.50	115.60	80.94	4.05	5.17
12.85	0.05	12.825	3.375	54.89	83.50	1.74	145.20	116.16	81.34	4.07	5.19
12.9	0.05	12.875	3.325	54.08	83.66	1.74	145.92	116.73	81.74	4.09	5.22
12.95	0.05	12.925	3.275	53.27	83.82	1.75	146.64	117.31	82.14	4.11	5.24
13	0.05	12.975	3.225	52.45	83.98	1.75	147.37	117.90	82.55	4.13	5.27
13.05	0.05	13.025	3.175	51.64	84.14	1.76	148.11	118.49	82.97	4.15	5.30
13.1	0.05	13.075	3.125	50.83	84.30	1.77	148.87	119.09	83.39	4.17	5.32
13.15	0.05	13.125	3.075	50.01	84.46	1.77	149.63	119.71	83.82	4.19	5.35
13.2	0.05	13.175	3.025	49.20	84.62	1.78	150.41	120.33	84.25	4.21	5.38
13.25	0.05	13.225	2.975	48.39	84.78	1.78	151.19	120.96	84.69	4.23	5.41
13.3	0.05	13.275	2.925	47.57	84.94	1.79	151.99	121.60	85.14	4.26	5.44
13.35	0.05	13.325	2.875	46.76	85.10	1.80	152.81	122.25	85.60	4.28	5.46
13.4	0.05	13.375	2.825	45.95	85.26	1.80	153.63	122.91	86.06	4.30	5.49
13.45	0.05	13.425	2.775	45.13	85.42	1.81	154.47	123.58	86.53	4.33	5.52
13.5	0.05	13.475	2.725	44.32	85.58	1.81	155.32	124.26	87.01	4.35	5.55
13.55	0.05	13.525	2.675	43.51	85.74	1.82	156.19	124.95	87.49	4.37	5.59
13.6	0.05	13.575	2.625	42.69	85.90	1.83	157.08	125.66	87.99	4.40	5.62
13.65	0.05	13.625	2.575	41.88	86.06	1.84	157.97	126.38	88.49	4.42	5.65
13.7	0.05	13.675	2.525	41.07	86.22	1.84	158.89	127.11	89.00	4.45	5.68
13.75	0.05	13.725	2.475	40.25	86.38	1.85	159.82	127.86	89.53	4.48	5.72

Section bottom depth	Δz	Avg. depth	h	h/R^*	σ'_{v0}	K_c	σ'_{rc}	σ'_{rf}	τ'_f	$\tau'_f \Delta z$	ΔQ_s
[m]	[m]	[m]	[m]	/	[kPa]	/	[kPa]	[kPa]	[kPa]	kN/m	kN
13.8	0.05	13.775	2.425	39.44	86.54	1.86	160.77	128.62	90.06	4.50	5.75
13.85	0.05	13.825	2.375	38.63	86.70	1.87	161.74	129.39	90.60	4.53	5.78
13.9	0.05	13.875	2.325	37.81	86.86	1.87	162.73	130.19	91.16	4.56	5.82
13.95	0.05	13.925	2.275	37.00	87.02	1.88	163.74	130.99	91.72	4.59	5.86
14	0.05	13.975	2.225	36.19	87.18	1.89	164.78	131.82	92.30	4.62	5.89
14.05	0.05	14.025	2.175	35.38	87.34	1.90	165.83	132.66	92.89	4.64	5.93
14.1	0.05	14.075	2.125	34.56	87.50	1.91	166.91	133.53	93.50	4.67	5.97
14.15	0.05	14.125	2.075	33.75	87.66	1.92	168.01	134.41	94.11	4.71	6.01
14.2	0.05	14.175	2.025	32.94	87.82	1.93	169.14	135.31	94.75	4.74	6.05
14.25	0.05	14.225	1.975	32.12	87.98	1.94	170.30	136.24	95.40	4.77	6.09
14.3	0.05	14.275	1.925	31.31	88.14	1.95	171.49	137.19	96.06	4.80	6.13
14.35	0.05	14.325	1.875	30.50	88.30	1.96	172.70	138.16	96.74	4.84	6.18
14.4	0.05	14.375	1.825	29.68	88.46	1.97	173.95	139.16	97.44	4.87	6.22
14.45	0.05	14.425	1.775	28.87	88.62	1.98	175.24	140.19	98.16	4.91	6.27
14.5	0.05	14.475	1.725	28.06	88.78	1.99	176.56	141.25	98.90	4.95	6.31
14.55	0.05	14.525	1.675	27.24	88.94	2.00	177.92	142.34	99.67	4.98	6.36
14.6	0.05	14.575	1.625	26.43	89.10	2.01	179.33	143.46	100.45	5.02	6.41
14.65	0.05	14.625	1.575	25.62	89.26	2.03	180.78	144.62	101.26	5.06	6.46
14.7	0.05	14.675	1.525	24.80	89.42	2.04	182.27	145.82	102.10	5.11	6.52
14.75	0.05	14.725	1.475	23.99	89.58	2.05	183.82	147.06	102.97	5.15	6.57
14.8	0.05	14.775	1.425	23.18	89.74	2.07	185.42	148.34	103.87	5.19	6.63
14.85	0.05	14.825	1.375	22.36	89.90	2.08	187.09	149.67	104.80	5.24	6.69
14.9	0.05	14.875	1.325	21.55	90.06	2.10	188.81	151.05	105.77	5.29	6.75
14.95	0.05	14.925	1.275	20.74	90.22	2.11	190.61	152.49	106.77	5.34	6.82
15	0.05	14.975	1.225	19.92	90.38	2.13	192.48	153.98	107.82	5.39	6.88
15.05	0.05	15.025	1.175	19.11	90.54	2.15	194.43	155.55	108.92	5.45	6.95
15.1	0.05	15.075	1.125	18.30	90.70	2.17	196.48	157.18	110.06	5.50	7.03
15.15	0.05	15.125	1.075	17.48	90.86	2.19	198.62	158.90	111.26	5.56	7.10

Section bottom depth	Δz	Avg. depth	h	h/R^*	σ'_{v0}	K_c	σ'_{rc}	σ'_{rf}	τ'_f	$\tau'_f \Delta z$	ΔQ_s
[m]	[m]	[m]	[m]	/	[kPa]	/	[kPa]	[kPa]	[kPa]	kN/m	kN
15.2	0.05	15.175	1.025	16.67	91.02	2.21	200.88	160.70	112.53	5.63	7.18
15.25	0.05	15.225	0.975	15.86	91.18	2.23	203.25	162.60	113.86	5.69	7.27
15.3	0.05	15.275	0.925	15.04	91.34	2.25	205.77	164.61	115.26	5.76	7.36
15.35	0.05	15.325	0.875	14.23	91.50	2.28	208.43	166.74	116.76	5.84	7.45
15.4	0.05	15.375	0.825	13.42	91.66	2.30	211.27	169.01	118.34	5.92	7.55
15.45	0.05	15.425	0.775	12.60	91.82	2.33	214.30	171.44	120.04	6.00	7.66
15.5	0.05	15.475	0.725	11.79	91.98	2.37	217.55	174.04	121.87	6.09	7.78
15.55	0.05	15.525	0.675	10.98	92.14	2.40	221.07	176.86	123.84	6.19	7.91
15.6	0.05	15.575	0.625	10.17	92.30	2.44	224.89	179.91	125.97	6.30	8.04
15.65	0.05	15.625	0.575	9.35	92.46	2.48	229.07	183.25	128.32	6.42	8.19
15.7	0.05	15.675	0.525	8.54	92.62	2.52	233.68	186.94	130.90	6.54	8.36
15.75	0.05	15.725	0.475	8.00	92.78	2.56	237.15	189.72	132.84	6.64	8.48
15.8	0.05	15.775	0.425	8.00	92.94	2.56	237.56	190.05	133.07	6.65	8.50
15.85	0.05	15.825	0.375	8.00	93.10	2.56	237.97	190.38	133.30	6.67	8.51
15.9	0.05	15.875	0.325	8.00	93.26	2.56	238.38	190.70	133.53	6.68	8.52
15.95	0.05	15.925	0.275	8.00	93.42	2.56	238.79	191.03	133.76	6.69	8.54
16	0.05	15.975	0.225	8.00	93.58	2.56	239.20	191.36	133.99	6.70	8.55
16.05	0.05	16.025	0.175	8.00	93.74	2.56	239.61	191.68	134.22	6.71	8.57
16.1	0.05	16.075	0.125	8.00	93.90	2.56	240.01	192.01	134.45	6.72	8.58
16.15	0.05	16.125	0.075	8.00	94.06	2.56	240.42	192.34	134.68	6.73	8.60
16.2	0.05	16.175	0.025	8.00	94.22	2.56	240.83	192.67	134.91	6.75	8.61
										$\sum Q_s$ [kN] =	1107.53

Table 10.4: Shaft capacity calculation in diatomaceous layer for Pile B2P2 in Yazdani et al. (2021) - $\Delta I_{v0} = 0.822$

Section bottom depth	Δz	Avg. depth	h	h/R^*	σ'_{v0}	K_c	σ'_{rc}	σ'_{rf}	τ'_f	$\tau'_f \Delta z$	ΔQ_s
[m]	[m]	[m]	[m]	/	[kPa]	/	[kPa]	[kPa]	[kPa]	kN/m	kN
4.05	0.05	4.025	12.175	198.02	55.34	2.27	125.63	100.50	70.37	3.52	4.49
4.1	0.05	4.075	12.125	197.21	55.50	2.27	126.10	100.88	70.63	3.53	4.51
4.15	0.05	4.125	12.075	196.39	55.66	2.27	126.56	101.25	70.90	3.54	4.53
4.2	0.05	4.175	12.025	195.58	55.82	2.28	127.03	101.63	71.16	3.56	4.54
4.25	0.05	4.225	11.975	194.77	55.98	2.28	127.50	102.00	71.42	3.57	4.56
4.3	0.05	4.275	11.925	193.95	56.14	2.28	127.97	102.38	71.69	3.58	4.58
4.35	0.05	4.325	11.875	193.14	56.30	2.28	128.45	102.76	71.95	3.60	4.59
4.4	0.05	4.375	11.825	192.33	56.46	2.28	128.92	103.14	72.22	3.61	4.61
4.45	0.05	4.425	11.775	191.51	56.62	2.29	129.40	103.52	72.48	3.62	4.63
4.5	0.05	4.475	11.725	190.70	56.78	2.29	129.87	103.90	72.75	3.64	4.64
4.55	0.05	4.525	11.675	189.89	56.94	2.29	130.35	104.28	73.02	3.65	4.66
4.6	0.05	4.575	11.625	189.07	57.10	2.29	130.83	104.66	73.29	3.66	4.68
4.65	0.05	4.625	11.575	188.26	57.26	2.29	131.31	105.05	73.55	3.68	4.70
4.7	0.05	4.675	11.525	187.45	57.42	2.30	131.79	105.43	73.82	3.69	4.71
4.75	0.05	4.725	11.475	186.64	57.58	2.30	132.27	105.82	74.09	3.70	4.73
4.8	0.05	4.775	11.425	185.82	57.74	2.30	132.75	106.20	74.36	3.72	4.75
4.85	0.05	4.825	11.375	185.01	57.90	2.30	133.24	106.59	74.64	3.73	4.76
4.9	0.05	4.875	11.325	184.20	58.06	2.30	133.73	106.98	74.91	3.75	4.78
4.95	0.05	4.925	11.275	183.38	58.22	2.31	134.21	107.37	75.18	3.76	4.80
5	0.05	4.975	11.225	182.57	58.38	2.31	134.70	107.76	75.45	3.77	4.82
5.05	0.05	5.025	11.175	181.76	58.54	2.31	135.19	108.15	75.73	3.79	4.83
5.1	0.05	5.075	11.125	180.94	58.70	2.31	135.68	108.55	76.00	3.80	4.85
5.15	0.05	5.125	11.075	180.13	58.86	2.31	136.17	108.94	76.28	3.81	4.87
5.2	0.05	5.175	11.025	179.32	59.02	2.32	136.67	109.33	76.56	3.83	4.89
5.25	0.05	5.225	10.975	178.50	59.18	2.32	137.16	109.73	76.83	3.84	4.90
5.3	0.05	5.275	10.925	177.69	59.34	2.32	137.66	110.13	77.11	3.86	4.92
5.35	0.05	5.325	10.875	176.88	59.50	2.32	138.16	110.53	77.39	3.87	4.94

Section bottom depth	Δz	Avg. depth	h	h/R^*	σ'_{v0}	K_c	σ'_{rc}	σ'_{rf}	τ'_f	$\tau'_f \Delta z$	ΔQ_s
[m]	[m]	[m]	[m]	/	[kPa]	/	[kPa]	[kPa]	[kPa]	kN/m	kN
5.4	0.05	5.375	10.825	176.06	59.66	2.32	138.66	110.93	77.67	3.88	4.96
5.45	0.05	5.425	10.775	175.25	59.82	2.33	139.16	111.33	77.95	3.90	4.98
5.5	0.05	5.475	10.725	174.44	59.98	2.33	139.66	111.73	78.23	3.91	4.99
5.55	0.05	5.525	10.675	173.62	60.14	2.33	140.16	112.13	78.51	3.93	5.01
5.6	0.05	5.575	10.625	172.81	60.30	2.33	140.67	112.53	78.80	3.94	5.03
5.65	0.05	5.625	10.575	172.00	60.46	2.34	141.17	112.94	79.08	3.95	5.05
5.7	0.05	5.675	10.525	171.18	60.62	2.34	141.68	113.35	79.37	3.97	5.07
5.75	0.05	5.725	10.475	170.37	60.78	2.34	142.19	113.75	79.65	3.98	5.08
5.8	0.05	5.775	10.425	169.56	60.94	2.34	142.70	114.16	79.94	4.00	5.10
5.85	0.05	5.825	10.375	168.74	61.10	2.34	143.21	114.57	80.22	4.01	5.12
5.9	0.05	5.875	10.325	167.93	61.26	2.35	143.73	114.98	80.51	4.03	5.14
5.95	0.05	5.925	10.275	167.12	61.42	2.35	144.24	115.40	80.80	4.04	5.16
6	0.05	5.975	10.225	166.30	61.58	2.35	144.76	115.81	81.09	4.05	5.18
6.05	0.05	6.025	10.175	165.49	61.74	2.35	145.28	116.22	81.38	4.07	5.20
6.1	0.05	6.075	10.125	164.68	61.90	2.36	145.80	116.64	81.67	4.08	5.21
6.15	0.05	6.125	10.075	163.86	62.06	2.36	146.32	117.06	81.96	4.10	5.23
6.2	0.05	6.175	10.025	163.05	62.22	2.36	146.84	117.48	82.26	4.11	5.25
6.25	0.05	6.225	9.975	162.24	62.38	2.36	147.37	117.90	82.55	4.13	5.27
6.3	0.05	6.275	9.925	161.43	62.54	2.36	147.90	118.32	82.85	4.14	5.29
6.35	0.05	6.325	9.875	160.61	62.70	2.37	148.42	118.74	83.14	4.16	5.31
6.4	0.05	6.375	9.825	159.80	62.86	2.37	148.95	119.16	83.44	4.17	5.33
6.45	0.05	6.425	9.775	158.99	63.02	2.37	149.49	119.59	83.74	4.19	5.35
6.5	0.05	6.475	9.725	158.17	63.18	2.37	150.02	120.02	84.04	4.20	5.36
6.55	0.05	6.525	9.675	157.36	63.34	2.38	150.55	120.44	84.34	4.22	5.38
6.6	0.05	6.575	9.625	156.55	63.50	2.38	151.09	120.87	84.64	4.23	5.40
6.65	0.05	6.625	9.575	155.73	63.66	2.38	151.63	121.30	84.94	4.25	5.42
6.7	0.05	6.675	9.525	154.92	63.82	2.38	152.17	121.74	85.24	4.26	5.44
6.75	0.05	6.725	9.475	154.11	63.98	2.39	152.71	122.17	85.54	4.28	5.46

Section bottom depth	Δz	Avg. depth	h	h/R^*	σ'_{v0}	K_c	σ'_{rc}	σ'_{rf}	τ'_f	$\tau'_f \Delta z$	ΔQ_s
[m]	[m]	[m]	[m]	/	[kPa]	/	[kPa]	[kPa]	[kPa]	kN/m	kN
6.8	0.05	6.775	9.425	153.29	64.14	2.39	153.26	122.60	85.85	4.29	5.48
6.85	0.05	6.825	9.375	152.48	64.30	2.39	153.80	123.04	86.15	4.31	5.50
6.9	0.05	6.875	9.325	151.67	64.46	2.39	154.35	123.48	86.46	4.32	5.52
6.95	0.05	6.925	9.275	150.85	64.62	2.40	154.90	123.92	86.77	4.34	5.54
7	0.05	6.975	9.225	150.04	64.78	2.40	155.45	124.36	87.08	4.35	5.56
7.05	0.05	7.025	9.175	149.23	64.94	2.40	156.00	124.80	87.39	4.37	5.58
7.1	0.05	7.075	9.125	148.41	65.10	2.40	156.56	125.25	87.70	4.38	5.60
7.15	0.05	7.125	9.075	147.60	65.26	2.41	157.12	125.69	88.01	4.40	5.62
7.2	0.05	7.175	9.025	146.79	65.42	2.41	157.68	126.14	88.32	4.42	5.64
7.25	0.05	7.225	8.975	145.97	65.58	2.41	158.24	126.59	88.64	4.43	5.66
7.3	0.05	7.275	8.925	145.16	65.74	2.42	158.80	127.04	88.95	4.45	5.68
7.35	0.05	7.325	8.875	144.35	65.90	2.42	159.37	127.49	89.27	4.46	5.70
7.4	0.05	7.375	8.825	143.53	66.06	2.42	159.93	127.95	89.59	4.48	5.72
7.45	0.05	7.425	8.775	142.72	66.22	2.42	160.50	128.40	89.91	4.50	5.74
7.5	0.05	7.475	8.725	141.91	66.38	2.43	161.07	128.86	90.23	4.51	5.76
7.55	0.05	7.525	8.675	141.09	66.54	2.43	161.65	129.32	90.55	4.53	5.78
7.6	0.05	7.575	8.625	140.28	66.70	2.43	162.23	129.78	90.87	4.54	5.80
7.65	0.05	7.625	8.575	139.47	66.86	2.43	162.80	130.24	91.20	4.56	5.82
7.7	0.05	7.675	8.525	138.65	67.02	2.44	163.38	130.71	91.52	4.58	5.84
7.75	0.05	7.725	8.475	137.84	67.18	2.44	163.97	131.17	91.85	4.59	5.86
7.8	0.05	7.775	8.425	137.03	67.34	2.44	164.55	131.64	92.18	4.61	5.88
7.85	0.05	7.825	8.375	136.22	67.50	2.45	165.14	132.11	92.51	4.63	5.91
7.9	0.05	7.875	8.325	135.40	67.66	2.45	165.73	132.58	92.84	4.64	5.93
7.95	0.05	7.925	8.275	134.59	67.82	2.45	166.32	133.06	93.17	4.66	5.95
8	0.05	7.975	8.225	133.78	67.98	2.46	166.92	133.53	93.50	4.68	5.97
8.05	0.05	8.025	8.175	132.96	68.14	2.46	167.51	134.01	93.84	4.69	5.99
8.1	0.05	8.075	8.125	132.15	68.30	2.46	168.11	134.49	94.17	4.71	6.01
8.15	0.05	8.125	8.075	131.34	68.46	2.46	168.71	134.97	94.51	4.73	6.03

Section bottom depth	Δz	Avg. depth	h	h/R^*	σ'_{v0}	K_c	σ'_{rc}	σ'_{rf}	τ'_f	$\tau'_f \Delta z$	ΔQ_s
[m]	[m]	[m]	[m]	/	[kPa]	/	[kPa]	[kPa]	[kPa]	kN/m	kN
8.2	0.05	8.175	8.025	130.52	68.62	2.47	169.32	135.46	94.85	4.74	6.05
8.25	0.05	8.225	7.975	129.71	68.78	2.47	169.93	135.94	95.19	4.76	6.08
8.3	0.05	8.275	7.925	128.90	68.94	2.47	170.54	136.43	95.53	4.78	6.10
8.35	0.05	8.325	7.875	128.08	69.10	2.48	171.15	136.92	95.87	4.79	6.12
8.4	0.05	8.375	7.825	127.27	69.26	2.48	171.76	137.41	96.22	4.81	6.14
8.45	0.05	8.425	7.775	126.46	69.42	2.48	172.38	137.90	96.56	4.83	6.16
8.5	0.05	8.475	7.725	125.64	69.58	2.49	173.00	138.40	96.91	4.85	6.19
8.55	0.05	8.525	7.675	124.83	69.74	2.49	173.62	138.90	97.26	4.86	6.21
8.6	0.05	8.575	7.625	124.02	69.90	2.49	174.25	139.40	97.61	4.88	6.23
8.65	0.05	8.625	7.575	123.20	70.06	2.50	174.88	139.90	97.96	4.90	6.25
8.7	0.05	8.675	7.525	122.39	70.22	2.50	175.51	140.41	98.32	4.92	6.28
8.75	0.05	8.725	7.475	121.58	70.38	2.50	176.15	140.92	98.67	4.93	6.30
8.8	0.05	8.775	7.425	120.76	70.54	2.51	176.78	141.43	99.03	4.95	6.32
8.85	0.05	8.825	7.375	119.95	70.70	2.51	177.42	141.94	99.39	4.97	6.34
8.9	0.05	8.875	7.325	119.14	70.86	2.51	178.07	142.45	99.75	4.99	6.37
8.95	0.05	8.925	7.275	118.32	71.02	2.52	178.71	142.97	100.11	5.01	6.39
9	0.05	8.975	7.225	117.51	71.18	2.52	179.36	143.49	100.47	5.02	6.41
9.05	0.05	9.025	7.175	116.70	71.34	2.52	180.02	144.01	100.84	5.04	6.44
9.1	0.05	9.075	7.125	115.88	71.50	2.53	180.67	144.54	101.21	5.06	6.46
9.15	0.05	9.125	7.075	115.07	71.66	2.53	181.33	145.07	101.58	5.08	6.48
9.2	0.05	9.175	7.025	114.26	71.82	2.53	182.00	145.60	101.95	5.10	6.51
9.25	0.05	9.225	6.975	113.44	71.98	2.54	182.66	146.13	102.32	5.12	6.53
9.3	0.05	9.275	6.925	112.63	72.14	2.54	183.33	146.66	102.70	5.13	6.56
9.35	0.05	9.325	6.875	111.82	72.30	2.55	184.00	147.20	103.07	5.15	6.58
9.4	0.05	9.375	6.825	111.01	72.46	2.55	184.68	147.74	103.45	5.17	6.60
9.45	0.05	9.425	6.775	110.19	72.62	2.55	185.36	148.29	103.83	5.19	6.63
9.5	0.05	9.475	6.725	109.38	72.78	2.56	186.04	148.84	104.22	5.21	6.65
9.55	0.05	9.525	6.675	108.57	72.94	2.56	186.73	149.39	104.60	5.23	6.68

Section bottom depth	Δz	Avg. depth	h	h/R^*	σ'_{v0}	K_c	σ'_{rc}	σ'_{rf}	τ'_f	$\tau'_f \Delta z$	ΔQ_s
[m]	[m]	[m]	[m]	/	[kPa]	/	[kPa]	[kPa]	[kPa]	kN/m	kN
9.6	0.05	9.575	6.625	107.75	73.10	2.56	187.42	149.94	104.99	5.25	6.70
9.65	0.05	9.625	6.575	106.94	73.26	2.57	188.12	150.49	105.38	5.27	6.73
9.7	0.05	9.675	6.525	106.13	73.42	2.57	188.82	151.05	105.77	5.29	6.75
9.75	0.05	9.725	6.475	105.31	73.58	2.58	189.52	151.62	106.16	5.31	6.78
9.8	0.05	9.775	6.425	104.50	73.74	2.58	190.23	152.18	106.56	5.33	6.80
9.85	0.05	9.825	6.375	103.69	73.90	2.58	190.94	152.75	106.96	5.35	6.83
9.9	0.05	9.875	6.325	102.87	74.06	2.59	191.65	153.32	107.36	5.37	6.85
9.95	0.05	9.925	6.275	102.06	74.22	2.59	192.37	153.90	107.76	5.39	6.88
10	0.05	9.975	6.225	101.25	74.38	2.60	193.10	154.48	108.17	5.41	6.90
10.05	0.05	10.025	6.175	100.43	74.54	2.60	193.82	155.06	108.57	5.43	6.93
10.1	0.05	10.075	6.125	99.62	74.70	2.60	194.56	155.64	108.98	5.45	6.96
10.15	0.05	10.125	6.075	98.81	74.86	2.61	195.29	156.23	109.40	5.47	6.98
10.2	0.05	10.175	6.025	97.99	75.02	2.61	196.03	156.83	109.81	5.49	7.01
10.25	0.05	10.225	5.975	97.18	75.18	2.62	196.78	157.42	110.23	5.51	7.04
10.3	0.05	10.275	5.925	96.37	75.34	2.62	197.53	158.02	110.65	5.53	7.06
10.35	0.05	10.325	5.875	95.55	75.50	2.63	198.28	158.63	111.07	5.55	7.09
10.4	0.05	10.375	5.825	94.74	75.66	2.63	199.04	159.24	111.50	5.57	7.12
10.45	0.05	10.425	5.775	93.93	75.82	2.64	199.81	159.85	111.93	5.60	7.15
10.5	0.05	10.475	5.725	93.11	75.98	2.64	200.58	160.46	112.36	5.62	7.17
10.55	0.05	10.525	5.675	92.30	76.14	2.64	201.36	161.08	112.79	5.64	7.20
10.6	0.05	10.575	5.625	91.49	76.30	2.65	202.14	161.71	113.23	5.66	7.23
10.65	0.05	10.625	5.575	90.67	76.46	2.65	202.92	162.34	113.67	5.68	7.26
10.7	0.05	10.675	5.525	89.86	76.62	2.66	203.71	162.97	114.11	5.71	7.28
10.75	0.05	10.725	5.475	89.05	76.78	2.66	204.51	163.61	114.56	5.73	7.31
10.8	0.05	10.775	5.425	88.23	76.94	2.67	205.31	164.25	115.01	5.75	7.34
10.85	0.05	10.825	5.375	87.42	77.10	2.67	206.12	164.90	115.46	5.77	7.37
10.9	0.05	10.875	5.325	86.61	77.26	2.68	206.94	165.55	115.92	5.80	7.40
10.95	0.05	10.925	5.275	85.80	77.42	2.68	207.76	166.20	116.38	5.82	7.43

Section bottom depth	Δz	Avg. depth	h	h/R^*	σ'_{v0}	K_c	σ'_{rc}	σ'_{rf}	τ'_f	$\tau'_f \Delta z$	ΔQ_s
[m]	[m]	[m]	[m]	/	[kPa]	/	[kPa]	[kPa]	[kPa]	kN/m	kN
11	0.05	10.975	5.225	84.98	77.58	2.69	208.58	166.87	116.84	5.84	7.46
11.05	0.05	11.025	5.175	84.17	77.74	2.69	209.41	167.53	117.31	5.87	7.49
11.1	0.05	11.075	5.125	83.36	77.90	2.70	210.25	168.20	117.78	5.89	7.52
11.15	0.05	11.125	5.075	82.54	78.06	2.70	211.10	168.88	118.25	5.91	7.55
11.2	0.05	11.175	5.025	81.73	78.22	2.71	211.95	169.56	118.73	5.94	7.58
11.25	0.05	11.225	4.975	80.92	78.38	2.72	212.81	170.25	119.21	5.96	7.61
11.3	0.05	11.275	4.925	80.10	78.54	2.72	213.67	170.94	119.69	5.98	7.64
11.35	0.05	11.325	4.875	79.29	78.70	2.73	214.55	171.64	120.18	6.01	7.67
11.4	0.05	11.375	4.825	78.48	78.86	2.73	215.43	172.34	120.68	6.03	7.70
11.45	0.05	11.425	4.775	77.66	79.02	2.74	216.31	173.05	121.17	6.06	7.74
11.5	0.05	11.475	4.725	76.85	79.18	2.74	217.21	173.77	121.67	6.08	7.77
11.55	0.05	11.525	4.675	76.04	79.34	2.75	218.11	174.49	122.18	6.11	7.80
11.6	0.05	11.575	4.625	75.22	79.50	2.76	219.02	175.22	122.69	6.13	7.83
11.65	0.05	11.625	4.575	74.41	79.66	2.76	219.94	175.95	123.20	6.16	7.86
11.7	0.05	11.675	4.525	73.60	79.82	2.77	220.87	176.69	123.72	6.19	7.90
11.75	0.05	11.725	4.475	72.78	79.98	2.77	221.80	177.44	124.25	6.21	7.93
11.8	0.05	11.775	4.425	71.97	80.14	2.78	222.75	178.20	124.77	6.24	7.97
11.85	0.05	11.825	4.375	71.16	80.30	2.79	223.70	178.96	125.31	6.27	8.00
11.9	0.05	11.875	4.325	70.34	80.46	2.79	224.66	179.73	125.85	6.29	8.03
11.95	0.05	11.925	4.275	69.53	80.62	2.80	225.63	180.51	126.39	6.32	8.07
12	0.05	11.975	4.225	68.72	80.78	2.81	226.61	181.29	126.94	6.35	8.10
12.05	0.05	12.025	4.175	67.90	80.94	2.81	227.60	182.08	127.49	6.37	8.14
12.1	0.05	12.075	4.125	67.09	81.10	2.82	228.60	182.88	128.06	6.40	8.17
12.15	0.05	12.125	4.075	66.28	81.26	2.83	229.61	183.69	128.62	6.43	8.21
12.2	0.05	12.175	4.025	65.46	81.42	2.83	230.63	184.51	129.19	6.46	8.25
12.25	0.05	12.225	3.975	64.65	81.58	2.84	231.66	185.33	129.77	6.49	8.28
12.3	0.05	12.275	3.925	63.84	81.74	2.85	232.71	186.17	130.35	6.52	8.32
12.35	0.05	12.325	3.875	63.02	81.90	2.85	233.76	187.01	130.95	6.55	8.36

Section bottom depth	Δz	Avg. depth	h	h/R^*	σ'_{v0}	K_c	σ'_{rc}	σ'_{rf}	τ'_f	$\tau'_f \Delta z$	ΔQ_s
[m]	[m]	[m]	[m]	/	[kPa]	/	[kPa]	[kPa]	[kPa]	kN/m	kN
12.4	0.05	12.375	3.825	62.21	82.06	2.86	234.83	187.86	131.54	6.58	8.40
12.45	0.05	12.425	3.775	61.40	82.22	2.87	235.91	188.72	132.15	6.61	8.44
12.5	0.05	12.475	3.725	60.59	82.38	2.88	237.00	189.60	132.76	6.64	8.47
12.55	0.05	12.525	3.675	59.77	82.54	2.88	238.10	190.48	133.37	6.67	8.51
12.6	0.05	12.575	3.625	58.96	82.70	2.89	239.21	191.37	134.00	6.70	8.55
12.65	0.05	12.625	3.575	58.15	82.86	2.90	240.34	192.28	134.63	6.73	8.59
12.7	0.05	12.675	3.525	57.33	83.02	2.91	241.49	193.19	135.27	6.76	8.64
12.75	0.05	12.725	3.475	56.52	83.18	2.92	242.65	194.12	135.92	6.80	8.68
12.8	0.05	12.775	3.425	55.71	83.34	2.93	243.82	195.05	136.58	6.83	8.72
12.85	0.05	12.825	3.375	54.89	83.50	2.93	245.01	196.00	137.24	6.86	8.76
12.9	0.05	12.875	3.325	54.08	83.66	2.94	246.21	196.97	137.92	6.90	8.80
12.95	0.05	12.925	3.275	53.27	83.82	2.95	247.43	197.94	138.60	6.93	8.85
13	0.05	12.975	3.225	52.45	83.98	2.96	248.66	198.93	139.29	6.96	8.89
13.05	0.05	13.025	3.175	51.64	84.14	2.97	249.92	199.93	140.00	7.00	8.94
13.1	0.05	13.075	3.125	50.83	84.30	2.98	251.19	200.95	140.71	7.04	8.98
13.15	0.05	13.125	3.075	50.01	84.46	2.99	252.48	201.98	141.43	7.07	9.03
13.2	0.05	13.175	3.025	49.20	84.62	3.00	253.79	203.03	142.16	7.11	9.08
13.25	0.05	13.225	2.975	48.39	84.78	3.01	255.12	204.09	142.91	7.15	9.12
13.3	0.05	13.275	2.925	47.57	84.94	3.02	256.47	205.17	143.66	7.18	9.17
13.35	0.05	13.325	2.875	46.76	85.10	3.03	257.84	206.27	144.43	7.22	9.22
13.4	0.05	13.375	2.825	45.95	85.26	3.04	259.23	207.38	145.21	7.26	9.27
13.45	0.05	13.425	2.775	45.13	85.42	3.05	260.65	208.52	146.00	7.30	9.32
13.5	0.05	13.475	2.725	44.32	85.58	3.06	262.09	209.67	146.81	7.34	9.37
13.55	0.05	13.525	2.675	43.51	85.74	3.07	263.55	210.84	147.63	7.38	9.42
13.6	0.05	13.575	2.625	42.69	85.90	3.09	265.04	212.03	148.47	7.42	9.48
13.65	0.05	13.625	2.575	41.88	86.06	3.10	266.56	213.25	149.32	7.47	9.53
13.7	0.05	13.675	2.525	41.07	86.22	3.11	268.10	214.48	150.18	7.51	9.59
13.75	0.05	13.725	2.475	40.25	86.38	3.12	269.68	215.74	151.06	7.55	9.64

Section bottom depth	Δz	Avg. depth	h	h/R^*	σ'_{v0}	K_c	σ'_{rc}	σ'_{rf}	τ'_f	$\tau'_f \Delta z$	ΔQ_s
[m]	[m]	[m]	[m]	/	[kPa]	/	[kPa]	[kPa]	[kPa]	kN/m	kN
13.8	0.05	13.775	2.425	39.44	86.54	3.13	271.28	217.02	151.96	7.60	9.70
13.85	0.05	13.825	2.375	38.63	86.70	3.15	272.92	218.33	152.88	7.64	9.76
13.9	0.05	13.875	2.325	37.81	86.86	3.16	274.59	219.67	153.81	7.69	9.82
13.95	0.05	13.925	2.275	37.00	87.02	3.18	276.29	221.03	154.77	7.74	9.88
14	0.05	13.975	2.225	36.19	87.18	3.19	278.03	222.43	155.74	7.79	9.94
14.05	0.05	14.025	2.175	35.38	87.34	3.20	279.81	223.85	156.74	7.84	10.01
14.1	0.05	14.075	2.125	34.56	87.50	3.22	281.63	225.30	157.76	7.89	10.07
14.15	0.05	14.125	2.075	33.75	87.66	3.23	283.49	226.79	158.80	7.94	10.14
14.2	0.05	14.175	2.025	32.94	87.82	3.25	285.40	228.32	159.87	7.99	10.21
14.25	0.05	14.225	1.975	32.12	87.98	3.27	287.35	229.88	160.96	8.05	10.28
14.3	0.05	14.275	1.925	31.31	88.14	3.28	289.35	231.48	162.09	8.10	10.35
14.35	0.05	14.325	1.875	30.50	88.30	3.30	291.41	233.13	163.24	8.16	10.42
14.4	0.05	14.375	1.825	29.68	88.46	3.32	293.52	234.82	164.42	8.22	10.50
14.45	0.05	14.425	1.775	28.87	88.62	3.34	295.69	236.55	165.64	8.28	10.57
14.5	0.05	14.475	1.725	28.06	88.78	3.36	297.92	238.34	166.89	8.34	10.65
14.55	0.05	14.525	1.675	27.24	88.94	3.38	300.22	240.18	168.17	8.41	10.74
14.6	0.05	14.575	1.625	26.43	89.10	3.40	302.59	242.07	169.50	8.47	10.82
14.65	0.05	14.625	1.575	25.62	89.26	3.42	305.03	244.03	170.87	8.54	10.91
14.7	0.05	14.675	1.525	24.80	89.42	3.44	307.56	246.05	172.28	8.61	11.00
14.75	0.05	14.725	1.475	23.99	89.58	3.46	310.17	248.13	173.75	8.69	11.09
14.8	0.05	14.775	1.425	23.18	89.74	3.49	312.87	250.30	175.26	8.76	11.19
14.85	0.05	14.825	1.375	22.36	89.90	3.51	315.68	252.54	176.83	8.84	11.29
14.9	0.05	14.875	1.325	21.55	90.06	3.54	318.59	254.87	178.46	8.92	11.39
14.95	0.05	14.925	1.275	20.74	90.22	3.56	321.62	257.30	180.16	9.01	11.50
15	0.05	14.975	1.225	19.92	90.38	3.59	324.78	259.82	181.93	9.10	11.61
15.05	0.05	15.025	1.175	19.11	90.54	3.62	328.08	262.46	183.78	9.19	11.73
15.1	0.05	15.075	1.125	18.30	90.70	3.66	331.53	265.22	185.71	9.29	11.86
15.15	0.05	15.125	1.075	17.48	90.86	3.69	335.15	268.12	187.74	9.39	11.98

Section bottom depth	Δz	Avg. depth	h	h/R^*	σ'_{v0}	K_c	σ'_{rc}	σ'_{rf}	τ'_f	$\tau'_f \Delta z$	ΔQ_s
[m]	[m]	[m]	[m]	/	[kPa]	/	[kPa]	[kPa]	[kPa]	kN/m	kN
15.2	0.05	15.175	1.025	16.67	91.02	3.72	338.95	271.16	189.87	9.49	12.12
15.25	0.05	15.225	0.975	15.86	91.18	3.76	342.96	274.37	192.11	9.61	12.26
15.3	0.05	15.275	0.925	15.04	91.34	3.80	347.20	277.76	194.49	9.72	12.42
15.35	0.05	15.325	0.875	14.23	91.50	3.84	351.69	281.35	197.01	9.85	12.58
15.4	0.05	15.375	0.825	13.42	91.66	3.89	356.48	285.18	199.69	9.98	12.75
15.45	0.05	15.425	0.775	12.60	91.82	3.94	361.59	289.28	202.55	10.13	12.93
15.5	0.05	15.475	0.725	11.79	91.98	3.99	367.09	293.67	205.63	10.28	13.13
15.55	0.05	15.525	0.675	10.98	92.14	4.05	373.02	298.42	208.95	10.45	13.34
15.6	0.05	15.575	0.625	10.17	92.30	4.11	379.46	303.57	212.56	10.63	13.57
15.65	0.05	15.625	0.575	9.35	92.46	4.18	386.51	309.21	216.51	10.83	13.82
15.7	0.05	15.675	0.525	8.54	92.62	4.26	394.29	315.43	220.87	11.04	14.10
15.75	0.05	15.725	0.475	8.00	92.78	4.31	400.16	320.12	224.15	11.21	14.31
15.8	0.05	15.775	0.425	8.00	92.94	4.31	400.85	320.68	224.54	11.23	14.33
15.85	0.05	15.825	0.375	8.00	93.10	4.31	401.54	321.23	224.93	11.25	14.36
15.9	0.05	15.875	0.325	8.00	93.26	4.31	402.23	321.78	225.31	11.27	14.38
15.95	0.05	15.925	0.275	8.00	93.42	4.31	402.92	322.33	225.70	11.28	14.41
16	0.05	15.975	0.225	8.00	93.58	4.31	403.61	322.88	226.09	11.30	14.43
16.05	0.05	16.025	0.175	8.00	93.74	4.31	404.30	323.44	226.47	11.32	14.46
16.1	0.05	16.075	0.125	8.00	93.90	4.31	404.99	323.99	226.86	11.34	14.48
16.15	0.05	16.125	0.075	8.00	94.06	4.31	405.68	324.54	227.25	11.36	14.51
16.2	0.05	16.175	0.025	8.00	94.22	4.31	406.37	325.09	227.63	11.38	14.53
										$\sum Q_s$ [kN] =	1868.78

Table 10.5: Shaft capacity calculation in diatomaceous layer for Pile B2P2 in Yazdani et al. (2021) - $\Delta I_{vy} = 1$

Section bottom depth	Δz	Avg. depth	h	h/R^*	σ'_{v0}	K_c	σ'_{rc}	σ'_{rf}	τ'_f	$\tau'_f \Delta z$	ΔQ_s
[m]	[m]	[m]	[m]	/	[kPa]	/	[kPa]	[kPa]	[kPa]	kN/m	kN
4.05	0.05	4.025	12.175	198.02	55.34	2.86	158.38	126.70	88.72	4.44	5.66
4.1	0.05	4.075	12.125	197.21	55.50	2.86	158.96	127.17	89.05	4.45	5.68
4.15	0.05	4.125	12.075	196.39	55.66	2.87	159.55	127.64	89.38	4.47	5.71
4.2	0.05	4.175	12.025	195.58	55.82	2.87	160.15	128.12	89.71	4.49	5.73
4.25	0.05	4.225	11.975	194.77	55.98	2.87	160.74	128.59	90.04	4.50	5.75
4.3	0.05	4.275	11.925	193.95	56.14	2.87	161.33	129.07	90.37	4.52	5.77
4.35	0.05	4.325	11.875	193.14	56.30	2.88	161.93	129.54	90.71	4.54	5.79
4.4	0.05	4.375	11.825	192.33	56.46	2.88	162.53	130.02	91.04	4.55	5.81
4.45	0.05	4.425	11.775	191.51	56.62	2.88	163.12	130.50	91.38	4.57	5.83
4.5	0.05	4.475	11.725	190.70	56.78	2.88	163.73	130.98	91.71	4.59	5.85
4.55	0.05	4.525	11.675	189.89	56.94	2.89	164.33	131.46	92.05	4.60	5.88
4.6	0.05	4.575	11.625	189.07	57.10	2.89	164.93	131.94	92.39	4.62	5.90
4.65	0.05	4.625	11.575	188.26	57.26	2.89	165.53	132.43	92.73	4.64	5.92
4.7	0.05	4.675	11.525	187.45	57.42	2.89	166.14	132.91	93.07	4.65	5.94
4.75	0.05	4.725	11.475	186.64	57.58	2.90	166.75	133.40	93.41	4.67	5.96
4.8	0.05	4.775	11.425	185.82	57.74	2.90	167.36	133.89	93.75	4.69	5.98
4.85	0.05	4.825	11.375	185.01	57.90	2.90	167.97	134.38	94.09	4.70	6.01
4.9	0.05	4.875	11.325	184.20	58.06	2.90	168.58	134.87	94.43	4.72	6.03
4.95	0.05	4.925	11.275	183.38	58.22	2.91	169.20	135.36	94.78	4.74	6.05
5	0.05	4.975	11.225	182.57	58.38	2.91	169.81	135.85	95.12	4.76	6.07
5.05	0.05	5.025	11.175	181.76	58.54	2.91	170.43	136.34	95.47	4.77	6.09
5.1	0.05	5.075	11.125	180.94	58.70	2.91	171.05	136.84	95.82	4.79	6.12
5.15	0.05	5.125	11.075	180.13	58.86	2.92	171.67	137.34	96.16	4.81	6.14
5.2	0.05	5.175	11.025	179.32	59.02	2.92	172.29	137.83	96.51	4.83	6.16
5.25	0.05	5.225	10.975	178.50	59.18	2.92	172.92	138.33	96.86	4.84	6.18
5.3	0.05	5.275	10.925	177.69	59.34	2.92	173.54	138.83	97.21	4.86	6.21
5.35	0.05	5.325	10.875	176.88	59.50	2.93	174.17	139.34	97.56	4.88	6.23

Section bottom depth	Δz	Avg. depth	h	h/R^*	σ'_{v0}	K_c	σ'_{rc}	σ'_{rf}	τ'_f	$\tau'_f \Delta z$	ΔQ_s
[m]	[m]	[m]	[m]	/	[kPa]	/	[kPa]	[kPa]	[kPa]	kN/m	kN
5.4	0.05	5.375	10.825	176.06	59.66	2.93	174.80	139.84	97.92	4.90	6.25
5.45	0.05	5.425	10.775	175.25	59.82	2.93	175.43	140.34	98.27	4.91	6.27
5.5	0.05	5.475	10.725	174.44	59.98	2.94	176.06	140.85	98.62	4.93	6.30
5.55	0.05	5.525	10.675	173.62	60.14	2.94	176.70	141.36	98.98	4.95	6.32
5.6	0.05	5.575	10.625	172.81	60.30	2.94	177.33	141.87	99.34	4.97	6.34
5.65	0.05	5.625	10.575	172.00	60.46	2.94	177.97	142.38	99.69	4.98	6.36
5.7	0.05	5.675	10.525	171.18	60.62	2.95	178.61	142.89	100.05	5.00	6.39
5.75	0.05	5.725	10.475	170.37	60.78	2.95	179.26	143.40	100.41	5.02	6.41
5.8	0.05	5.775	10.425	169.56	60.94	2.95	179.90	143.92	100.77	5.04	6.43
5.85	0.05	5.825	10.375	168.74	61.10	2.95	180.55	144.44	101.14	5.06	6.46
5.9	0.05	5.875	10.325	167.93	61.26	2.96	181.19	144.95	101.50	5.07	6.48
5.95	0.05	5.925	10.275	167.12	61.42	2.96	181.84	145.47	101.86	5.09	6.50
6	0.05	5.975	10.225	166.30	61.58	2.96	182.49	146.00	102.23	5.11	6.53
6.05	0.05	6.025	10.175	165.49	61.74	2.97	183.15	146.52	102.59	5.13	6.55
6.1	0.05	6.075	10.125	164.68	61.90	2.97	183.80	147.04	102.96	5.15	6.57
6.15	0.05	6.125	10.075	163.86	62.06	2.97	184.46	147.57	103.33	5.17	6.60
6.2	0.05	6.175	10.025	163.05	62.22	2.98	185.12	148.10	103.70	5.18	6.62
6.25	0.05	6.225	9.975	162.24	62.38	2.98	185.78	148.63	104.07	5.20	6.64
6.3	0.05	6.275	9.925	161.43	62.54	2.98	186.45	149.16	104.44	5.22	6.67
6.35	0.05	6.325	9.875	160.61	62.70	2.98	187.11	149.69	104.81	5.24	6.69
6.4	0.05	6.375	9.825	159.80	62.86	2.99	187.78	150.22	105.19	5.26	6.71
6.45	0.05	6.425	9.775	158.99	63.02	2.99	188.45	150.76	105.56	5.28	6.74
6.5	0.05	6.475	9.725	158.17	63.18	2.99	189.12	151.30	105.94	5.30	6.76
6.55	0.05	6.525	9.675	157.36	63.34	3.00	189.80	151.84	106.32	5.32	6.79
6.6	0.05	6.575	9.625	156.55	63.50	3.00	190.47	152.38	106.70	5.33	6.81
6.65	0.05	6.625	9.575	155.73	63.66	3.00	191.15	152.92	107.08	5.35	6.84
6.7	0.05	6.675	9.525	154.92	63.82	3.01	191.83	153.47	107.46	5.37	6.86
6.75	0.05	6.725	9.475	154.11	63.98	3.01	192.52	154.01	107.84	5.39	6.88

Section bottom depth	Δz	Avg. depth	h	h/R^*	σ'_{v0}	K_c	σ'_{rc}	σ'_{rf}	τ'_f	$\tau'_f \Delta z$	ΔQ_s
[m]	[m]	[m]	[m]	/	[kPa]	/	[kPa]	[kPa]	[kPa]	kN/m	kN
6.8	0.05	6.775	9.425	153.29	64.14	3.01	193.20	154.56	108.23	5.41	6.91
6.85	0.05	6.825	9.375	152.48	64.30	3.02	193.89	155.11	108.61	5.43	6.93
6.9	0.05	6.875	9.325	151.67	64.46	3.02	194.58	155.67	109.00	5.45	6.96
6.95	0.05	6.925	9.275	150.85	64.62	3.02	195.28	156.22	109.39	5.47	6.98
7	0.05	6.975	9.225	150.04	64.78	3.03	195.97	156.78	109.78	5.49	7.01
7.05	0.05	7.025	9.175	149.23	64.94	3.03	196.67	157.33	110.17	5.51	7.03
7.1	0.05	7.075	9.125	148.41	65.10	3.03	197.37	157.89	110.56	5.53	7.06
7.15	0.05	7.125	9.075	147.60	65.26	3.04	198.07	158.46	110.95	5.55	7.08
7.2	0.05	7.175	9.025	146.79	65.42	3.04	198.78	159.02	111.35	5.57	7.11
7.25	0.05	7.225	8.975	145.97	65.58	3.04	199.48	159.59	111.74	5.59	7.13
7.3	0.05	7.275	8.925	145.16	65.74	3.05	200.19	160.16	112.14	5.61	7.16
7.35	0.05	7.325	8.875	144.35	65.90	3.05	200.91	160.73	112.54	5.63	7.18
7.4	0.05	7.375	8.825	143.53	66.06	3.05	201.62	161.30	112.94	5.65	7.21
7.45	0.05	7.425	8.775	142.72	66.22	3.06	202.34	161.87	113.34	5.67	7.24
7.5	0.05	7.475	8.725	141.91	66.38	3.06	203.06	162.45	113.75	5.69	7.26
7.55	0.05	7.525	8.675	141.09	66.54	3.06	203.78	163.03	114.15	5.71	7.29
7.6	0.05	7.575	8.625	140.28	66.70	3.07	204.51	163.61	114.56	5.73	7.31
7.65	0.05	7.625	8.575	139.47	66.86	3.07	205.24	164.19	114.97	5.75	7.34
7.7	0.05	7.675	8.525	138.65	67.02	3.07	205.97	164.78	115.38	5.77	7.37
7.75	0.05	7.725	8.475	137.84	67.18	3.08	206.71	165.37	115.79	5.79	7.39
7.8	0.05	7.775	8.425	137.03	67.34	3.08	207.44	165.96	116.20	5.81	7.42
7.85	0.05	7.825	8.375	136.22	67.50	3.08	208.18	166.55	116.62	5.83	7.44
7.9	0.05	7.875	8.325	135.40	67.66	3.09	208.93	167.14	117.03	5.85	7.47
7.95	0.05	7.925	8.275	134.59	67.82	3.09	209.68	167.74	117.45	5.87	7.50
8	0.05	7.975	8.225	133.78	67.98	3.10	210.42	168.34	117.87	5.89	7.52
8.05	0.05	8.025	8.175	132.96	68.14	3.10	211.18	168.94	118.29	5.91	7.55
8.1	0.05	8.075	8.125	132.15	68.30	3.10	211.93	169.55	118.72	5.94	7.58
8.15	0.05	8.125	8.075	131.34	68.46	3.11	212.69	170.15	119.14	5.96	7.61

Section bottom depth	Δz	Avg. depth	h	h/R^*	σ'_{v0}	K_c	σ'_{rc}	σ'_{rf}	τ'_f	$\tau'_f \Delta z$	ΔQ_s
[m]	[m]	[m]	[m]	/	[kPa]	/	[kPa]	[kPa]	[kPa]	kN/m	kN
8.2	0.05	8.175	8.025	130.52	68.62	3.11	213.45	170.76	119.57	5.98	7.63
8.25	0.05	8.225	7.975	129.71	68.78	3.11	214.22	171.38	120.00	6.00	7.66
8.3	0.05	8.275	7.925	128.90	68.94	3.12	214.99	171.99	120.43	6.02	7.69
8.35	0.05	8.325	7.875	128.08	69.10	3.12	215.76	172.61	120.86	6.04	7.72
8.4	0.05	8.375	7.825	127.27	69.26	3.13	216.54	173.23	121.30	6.06	7.74
8.45	0.05	8.425	7.775	126.46	69.42	3.13	217.31	173.85	121.73	6.09	7.77
8.5	0.05	8.475	7.725	125.64	69.58	3.13	218.10	174.48	122.17	6.11	7.80
8.55	0.05	8.525	7.675	124.83	69.74	3.14	218.88	175.11	122.61	6.13	7.83
8.6	0.05	8.575	7.625	124.02	69.90	3.14	219.67	175.74	123.05	6.15	7.86
8.65	0.05	8.625	7.575	123.20	70.06	3.15	220.46	176.37	123.50	6.17	7.88
8.7	0.05	8.675	7.525	122.39	70.22	3.15	221.26	177.01	123.94	6.20	7.91
8.75	0.05	8.725	7.475	121.58	70.38	3.16	222.06	177.65	124.39	6.22	7.94
8.8	0.05	8.775	7.425	120.76	70.54	3.16	222.86	178.29	124.84	6.24	7.97
8.85	0.05	8.825	7.375	119.95	70.70	3.16	223.67	178.94	125.29	6.26	8.00
8.9	0.05	8.875	7.325	119.14	70.86	3.17	224.48	179.59	125.75	6.29	8.03
8.95	0.05	8.925	7.275	118.32	71.02	3.17	225.30	180.24	126.20	6.31	8.06
9	0.05	8.975	7.225	117.51	71.18	3.18	226.12	180.89	126.66	6.33	8.09
9.05	0.05	9.025	7.175	116.70	71.34	3.18	226.94	181.55	127.12	6.36	8.12
9.1	0.05	9.075	7.125	115.88	71.50	3.19	227.77	182.21	127.59	6.38	8.14
9.15	0.05	9.125	7.075	115.07	71.66	3.19	228.60	182.88	128.05	6.40	8.17
9.2	0.05	9.175	7.025	114.26	71.82	3.19	229.43	183.55	128.52	6.43	8.20
9.25	0.05	9.225	6.975	113.44	71.98	3.20	230.27	184.22	128.99	6.45	8.23
9.3	0.05	9.275	6.925	112.63	72.14	3.20	231.12	184.89	129.46	6.47	8.26
9.35	0.05	9.325	6.875	111.82	72.30	3.21	231.97	185.57	129.94	6.50	8.30
9.4	0.05	9.375	6.825	111.01	72.46	3.21	232.82	186.26	130.42	6.52	8.33
9.45	0.05	9.425	6.775	110.19	72.62	3.22	233.68	186.94	130.90	6.54	8.36
9.5	0.05	9.475	6.725	109.38	72.78	3.22	234.54	187.63	131.38	6.57	8.39
9.55	0.05	9.525	6.675	108.57	72.94	3.23	235.41	188.33	131.87	6.59	8.42

Section bottom depth	Δz	Avg. depth	h	h/R^*	σ'_{v0}	K_c	σ'_{rc}	σ'_{rf}	τ'_f	$\tau'_f \Delta z$	ΔQ_s
[m]	[m]	[m]	[m]	/	[kPa]	/	[kPa]	[kPa]	[kPa]	kN/m	kN
9.6	0.05	9.575	6.625	107.75	73.10	3.23	236.28	189.02	132.35	6.62	8.45
9.65	0.05	9.625	6.575	106.94	73.26	3.24	237.15	189.72	132.85	6.64	8.48
9.7	0.05	9.675	6.525	106.13	73.42	3.24	238.04	190.43	133.34	6.67	8.51
9.75	0.05	9.725	6.475	105.31	73.58	3.25	238.92	191.14	133.84	6.69	8.54
9.8	0.05	9.775	6.425	104.50	73.74	3.25	239.81	191.85	134.33	6.72	8.58
9.85	0.05	9.825	6.375	103.69	73.90	3.26	240.71	192.57	134.84	6.74	8.61
9.9	0.05	9.875	6.325	102.87	74.06	3.26	241.61	193.29	135.34	6.77	8.64
9.95	0.05	9.925	6.275	102.06	74.22	3.27	242.52	194.01	135.85	6.79	8.67
10	0.05	9.975	6.225	101.25	74.38	3.27	243.43	194.74	136.36	6.82	8.70
10.05	0.05	10.025	6.175	100.43	74.54	3.28	244.35	195.48	136.87	6.84	8.74
10.1	0.05	10.075	6.125	99.62	74.70	3.28	245.27	196.21	137.39	6.87	8.77
10.15	0.05	10.125	6.075	98.81	74.86	3.29	246.20	196.96	137.91	6.90	8.80
10.2	0.05	10.175	6.025	97.99	75.02	3.29	247.13	197.71	138.43	6.92	8.84
10.25	0.05	10.225	5.975	97.18	75.18	3.30	248.07	198.46	138.96	6.95	8.87
10.3	0.05	10.275	5.925	96.37	75.34	3.31	249.02	199.21	139.49	6.97	8.90
10.35	0.05	10.325	5.875	95.55	75.50	3.31	249.97	199.98	140.02	7.00	8.94
10.4	0.05	10.375	5.825	94.74	75.66	3.32	250.93	200.74	140.56	7.03	8.97
10.45	0.05	10.425	5.775	93.93	75.82	3.32	251.89	201.51	141.10	7.06	9.01
10.5	0.05	10.475	5.725	93.11	75.98	3.33	252.86	202.29	141.65	7.08	9.04
10.55	0.05	10.525	5.675	92.30	76.14	3.33	253.84	203.07	142.19	7.11	9.08
10.6	0.05	10.575	5.625	91.49	76.30	3.34	254.83	203.86	142.74	7.14	9.11
10.65	0.05	10.625	5.575	90.67	76.46	3.35	255.82	204.65	143.30	7.16	9.15
10.7	0.05	10.675	5.525	89.86	76.62	3.35	256.81	205.45	143.86	7.19	9.18
10.75	0.05	10.725	5.475	89.05	76.78	3.36	257.82	206.25	144.42	7.22	9.22
10.8	0.05	10.775	5.425	88.23	76.94	3.36	258.83	207.06	144.99	7.25	9.26
10.85	0.05	10.825	5.375	87.42	77.10	3.37	259.85	207.88	145.56	7.28	9.29
10.9	0.05	10.875	5.325	86.61	77.26	3.38	260.88	208.70	146.13	7.31	9.33
10.95	0.05	10.925	5.275	85.80	77.42	3.38	261.91	209.53	146.71	7.34	9.37

Section bottom depth	Δz	Avg. depth	h	h/R^*	σ'_{v0}	K_c	σ'_{rc}	σ'_{rf}	τ'_f	$\tau'_f \Delta z$	ΔQ_s
[m]	[m]	[m]	[m]	/	[kPa]	/	[kPa]	[kPa]	[kPa]	kN/m	kN
11	0.05	10.975	5.225	84.98	77.58	3.39	262.95	210.36	147.30	7.36	9.40
11.05	0.05	11.025	5.175	84.17	77.74	3.40	264.00	211.20	147.88	7.39	9.44
11.1	0.05	11.075	5.125	83.36	77.90	3.40	265.06	212.05	148.48	7.42	9.48
11.15	0.05	11.125	5.075	82.54	78.06	3.41	266.12	212.90	149.07	7.45	9.52
11.2	0.05	11.175	5.025	81.73	78.22	3.42	267.20	213.76	149.68	7.48	9.55
11.25	0.05	11.225	4.975	80.92	78.38	3.42	268.28	214.62	150.28	7.51	9.59
11.3	0.05	11.275	4.925	80.10	78.54	3.43	269.37	215.50	150.89	7.54	9.63
11.35	0.05	11.325	4.875	79.29	78.70	3.44	270.47	216.38	151.51	7.58	9.67
11.4	0.05	11.375	4.825	78.48	78.86	3.44	271.58	217.27	152.13	7.61	9.71
11.45	0.05	11.425	4.775	77.66	79.02	3.45	272.70	218.16	152.76	7.64	9.75
11.5	0.05	11.475	4.725	76.85	79.18	3.46	273.83	219.06	153.39	7.67	9.79
11.55	0.05	11.525	4.675	76.04	79.34	3.47	274.97	219.97	154.03	7.70	9.83
11.6	0.05	11.575	4.625	75.22	79.50	3.47	276.11	220.89	154.67	7.73	9.87
11.65	0.05	11.625	4.575	74.41	79.66	3.48	277.27	221.82	155.32	7.77	9.92
11.7	0.05	11.675	4.525	73.60	79.82	3.49	278.44	222.75	155.97	7.80	9.96
11.75	0.05	11.725	4.475	72.78	79.98	3.50	279.62	223.69	156.63	7.83	10.00
11.8	0.05	11.775	4.425	71.97	80.14	3.50	280.81	224.65	157.30	7.86	10.04
11.85	0.05	11.825	4.375	71.16	80.30	3.51	282.01	225.61	157.97	7.90	10.08
11.9	0.05	11.875	4.325	70.34	80.46	3.52	283.22	226.58	158.65	7.93	10.13
11.95	0.05	11.925	4.275	69.53	80.62	3.53	284.44	227.56	159.34	7.97	10.17
12	0.05	11.975	4.225	68.72	80.78	3.54	285.68	228.54	160.03	8.00	10.22
12.05	0.05	12.025	4.175	67.90	80.94	3.54	286.93	229.54	160.73	8.04	10.26
12.1	0.05	12.075	4.125	67.09	81.10	3.55	288.19	230.55	161.43	8.07	10.31
12.15	0.05	12.125	4.075	66.28	81.26	3.56	289.46	231.57	162.15	8.11	10.35
12.2	0.05	12.175	4.025	65.46	81.42	3.57	290.75	232.60	162.87	8.14	10.40
12.25	0.05	12.225	3.975	64.65	81.58	3.58	292.05	233.64	163.60	8.18	10.44
12.3	0.05	12.275	3.925	63.84	81.74	3.59	293.37	234.69	164.33	8.22	10.49
12.35	0.05	12.325	3.875	63.02	81.90	3.60	294.69	235.76	165.08	8.25	10.54

Section bottom depth	Δz	Avg. depth	h	h/R^*	σ'_{v0}	K_c	σ'_{rc}	σ'_{rf}	τ'_f	$\tau'_f \Delta z$	ΔQ_s
[m]	[m]	[m]	[m]	/	[kPa]	/	[kPa]	[kPa]	[kPa]	kN/m	kN
12.4	0.05	12.375	3.825	62.21	82.06	3.61	296.04	236.83	165.83	8.29	10.59
12.45	0.05	12.425	3.775	61.40	82.22	3.62	297.40	237.92	166.59	8.33	10.63
12.5	0.05	12.475	3.725	60.59	82.38	3.63	298.77	239.02	167.36	8.37	10.68
12.55	0.05	12.525	3.675	59.77	82.54	3.64	300.16	240.13	168.14	8.41	10.73
12.6	0.05	12.575	3.625	58.96	82.70	3.65	301.57	241.26	168.93	8.45	10.78
12.65	0.05	12.625	3.575	58.15	82.86	3.66	302.99	242.39	169.73	8.49	10.83
12.7	0.05	12.675	3.525	57.33	83.02	3.67	304.43	243.55	170.53	8.53	10.89
12.75	0.05	12.725	3.475	56.52	83.18	3.68	305.89	244.71	171.35	8.57	10.94
12.8	0.05	12.775	3.425	55.71	83.34	3.69	307.37	245.90	172.18	8.61	10.99
12.85	0.05	12.825	3.375	54.89	83.50	3.70	308.87	247.10	173.02	8.65	11.04
12.9	0.05	12.875	3.325	54.08	83.66	3.71	310.39	248.31	173.87	8.69	11.10
12.95	0.05	12.925	3.275	53.27	83.82	3.72	311.92	249.54	174.73	8.74	11.15
13	0.05	12.975	3.225	52.45	83.98	3.73	313.48	250.79	175.60	8.78	11.21
13.05	0.05	13.025	3.175	51.64	84.14	3.74	315.06	252.05	176.49	8.82	11.27
13.1	0.05	13.075	3.125	50.83	84.30	3.76	316.67	253.33	177.39	8.87	11.32
13.15	0.05	13.125	3.075	50.01	84.46	3.77	318.29	254.63	178.30	8.91	11.38
13.2	0.05	13.175	3.025	49.20	84.62	3.78	319.94	255.95	179.22	8.96	11.44
13.25	0.05	13.225	2.975	48.39	84.78	3.79	321.62	257.29	180.16	9.01	11.50
13.3	0.05	13.275	2.925	47.57	84.94	3.81	323.32	258.65	181.11	9.06	11.56
13.35	0.05	13.325	2.875	46.76	85.10	3.82	325.05	260.04	182.08	9.10	11.62
13.4	0.05	13.375	2.825	45.95	85.26	3.83	326.80	261.44	183.06	9.15	11.69
13.45	0.05	13.425	2.775	45.13	85.42	3.85	328.59	262.87	184.06	9.20	11.75
13.5	0.05	13.475	2.725	44.32	85.58	3.86	330.40	264.32	185.08	9.25	11.81
13.55	0.05	13.525	2.675	43.51	85.74	3.88	332.25	265.80	186.11	9.31	11.88
13.6	0.05	13.575	2.625	42.69	85.90	3.89	334.13	267.30	187.17	9.36	11.95
13.65	0.05	13.625	2.575	41.88	86.06	3.90	336.04	268.83	188.24	9.41	12.02
13.7	0.05	13.675	2.525	41.07	86.22	3.92	337.99	270.39	189.33	9.47	12.09
13.75	0.05	13.725	2.475	40.25	86.38	3.94	339.97	271.98	190.44	9.52	12.16

Section bottom depth	Δz	Avg. depth	h	h/R^*	σ'_{v0}	K_c	σ'_{rc}	σ'_{rf}	τ'_f	$\tau'_f \Delta z$	ΔQ_s
[m]	[m]	[m]	[m]	/	[kPa]	/	[kPa]	[kPa]	[kPa]	kN/m	kN
13.8	0.05	13.775	2.425	39.44	86.54	3.95	341.99	273.59	191.57	9.58	12.23
13.85	0.05	13.825	2.375	38.63	86.70	3.97	344.06	275.24	192.73	9.64	12.30
13.9	0.05	13.875	2.325	37.81	86.86	3.99	346.16	276.93	193.91	9.70	12.38
13.95	0.05	13.925	2.275	37.00	87.02	4.00	348.31	278.65	195.11	9.76	12.46
14	0.05	13.975	2.225	36.19	87.18	4.02	350.50	280.40	196.34	9.82	12.53
14.05	0.05	14.025	2.175	35.38	87.34	4.04	352.75	282.20	197.60	9.88	12.61
14.1	0.05	14.075	2.125	34.56	87.50	4.06	355.04	284.03	198.88	9.94	12.70
14.15	0.05	14.125	2.075	33.75	87.66	4.08	357.39	285.91	200.20	10.01	12.78
14.2	0.05	14.175	2.025	32.94	87.82	4.10	359.79	287.83	201.54	10.08	12.87
14.25	0.05	14.225	1.975	32.12	87.98	4.12	362.25	289.80	202.92	10.15	12.95
14.3	0.05	14.275	1.925	31.31	88.14	4.14	364.78	291.82	204.34	10.22	13.04
14.35	0.05	14.325	1.875	30.50	88.30	4.16	367.37	293.90	205.79	10.29	13.14
14.4	0.05	14.375	1.825	29.68	88.46	4.18	370.03	296.02	207.28	10.36	13.23
14.45	0.05	14.425	1.775	28.87	88.62	4.21	372.76	298.21	208.81	10.44	13.33
14.5	0.05	14.475	1.725	28.06	88.78	4.23	375.58	300.46	210.39	10.52	13.43
14.55	0.05	14.525	1.675	27.24	88.94	4.26	378.47	302.78	212.01	10.60	13.53
14.6	0.05	14.575	1.625	26.43	89.10	4.28	381.46	305.17	213.68	10.68	13.64
14.65	0.05	14.625	1.575	25.62	89.26	4.31	384.54	307.63	215.41	10.77	13.75
14.7	0.05	14.675	1.525	24.80	89.42	4.34	387.72	310.18	217.19	10.86	13.86
14.75	0.05	14.725	1.475	23.99	89.58	4.36	391.02	312.81	219.03	10.95	13.98
14.8	0.05	14.775	1.425	23.18	89.74	4.40	394.43	315.54	220.94	11.05	14.10
14.85	0.05	14.825	1.375	22.36	89.90	4.43	397.96	318.37	222.92	11.15	14.23
14.9	0.05	14.875	1.325	21.55	90.06	4.46	401.63	321.31	224.98	11.25	14.36
14.95	0.05	14.925	1.275	20.74	90.22	4.49	405.46	324.36	227.12	11.36	14.50
15	0.05	14.975	1.225	19.92	90.38	4.53	409.44	327.55	229.35	11.47	14.64
15.05	0.05	15.025	1.175	19.11	90.54	4.57	413.60	330.88	231.68	11.58	14.79
15.1	0.05	15.075	1.125	18.30	90.70	4.61	417.95	334.36	234.12	11.71	14.95
15.15	0.05	15.125	1.075	17.48	90.86	4.65	422.51	338.01	236.67	11.83	15.11

Section bottom depth	Δz	Avg. depth	h	h/R^*	σ'_{v0}	K_c	σ'_{rc}	σ'_{rf}	τ'_f	$\tau'_f \Delta z$	ΔQ_s
[m]	[m]	[m]	[m]	/	[kPa]	/	[kPa]	[kPa]	[kPa]	kN/m	kN
15.2	0.05	15.175	1.025	16.67	91.02	4.69	427.30	341.84	239.36	11.97	15.28
15.25	0.05	15.225	0.975	15.86	91.18	4.74	432.36	345.88	242.19	12.11	15.46
15.3	0.05	15.275	0.925	15.04	91.34	4.79	437.70	350.16	245.18	12.26	15.65
15.35	0.05	15.325	0.875	14.23	91.50	4.85	443.37	354.69	248.36	12.42	15.85
15.4	0.05	15.375	0.825	13.42	91.66	4.90	449.40	359.52	251.74	12.59	16.07
15.45	0.05	15.425	0.775	12.60	91.82	4.96	455.85	364.68	255.35	12.77	16.30
15.5	0.05	15.475	0.725	11.79	91.98	5.03	462.77	370.22	259.23	12.96	16.55
15.55	0.05	15.525	0.675	10.98	92.14	5.10	470.25	376.20	263.42	13.17	16.82
15.6	0.05	15.575	0.625	10.17	92.30	5.18	478.37	382.70	267.97	13.40	17.11
15.65	0.05	15.625	0.575	9.35	92.46	5.27	487.26	389.81	272.95	13.65	17.42
15.7	0.05	15.675	0.525	8.54	92.62	5.37	497.07	397.65	278.44	13.92	17.77
15.75	0.05	15.725	0.475	8.00	92.78	5.44	504.46	403.57	282.58	14.13	18.04
15.8	0.05	15.775	0.425	8.00	92.94	5.44	505.33	404.26	283.07	14.15	18.07
15.85	0.05	15.825	0.375	8.00	93.10	5.44	506.20	404.96	283.56	14.18	18.10
15.9	0.05	15.875	0.325	8.00	93.26	5.44	507.07	405.66	284.04	14.20	18.13
15.95	0.05	15.925	0.275	8.00	93.42	5.44	507.94	406.35	284.53	14.23	18.16
16	0.05	15.975	0.225	8.00	93.58	5.44	508.81	407.05	285.02	14.25	18.19
16.05	0.05	16.025	0.175	8.00	93.74	5.44	509.68	407.74	285.51	14.28	18.23
16.1	0.05	16.075	0.125	8.00	93.90	5.44	510.55	408.44	285.99	14.30	18.26
16.15	0.05	16.125	0.075	8.00	94.06	5.44	511.42	409.14	286.48	14.32	18.29
16.2	0.05	16.175	0.025	8.00	94.22	5.44	512.29	409.83	286.97	14.35	18.32
										$\sum Q_s$ [kN] =	2355.91